STARS

Electronic Theses and Dissertations, 2004-2019

2018

Design, Synthesis, Stability, and Photocatalytic Studies of Sustainable Metal-Organic Frameworks

Matthew Logan
University of Central Florida

Part of the Chemistry Commons

Find similar works at: https://stars.library.ucf.edu/etd

University of Central Florida Libraries http://library.ucf.edu

University of Central Florida

STARS
Showcase of Text, Archives, Research & Scholarship

DESIGN, SYNTHESIS, STABILITY, AND PHOTOCATALYTIC STUDIES OF SUSTAINABLE METAL-ORGANIC FRAMEWORKS

by:

MATTHEW WADE LOGAN
B.S. in Chemistry Wheeling Jesuit University, 2013

A dissertation submitted in partial fulfillment of the requirements
for the degree of Doctor of Philosophy
in the Department of Chemistry
in the College of Sciences
at the University of Central Florida
Orlando, Florida

Summer Term
2018

Major Professor: Fernando J. Uribe-Romo

ABSTRACT

The presented dissertation focuses on the design, synthesis, and characterization of metal-organic frameworks (MOFs) composed of earth-abundant elements the exhibit photoredox activity and studied their application as heterogeneous photocatalysts in organic synthesis and in solar-to-chemical energy conversion. In particular, the structure-property relationships of titanium-based MOFs relating the structure of the organic building unit and the photophysical and photochemical activity of the solid material is studied. The first novel family of seven MOFs isoreticular to MIL-125-NH$_2$, includes functionalized with *N*-alkyl groups with increasing chain length (methyl to heptyl) and with varying connectivity (primary or secondary). The functionalized materials displayed reduced optical bandgaps correlated with the increased inductive donor ability of the alkyl substituents, enhanced excited-state lifetimes, mechanistic information towards visible light CO_2 reduction, and improved water stability. The second family of titanium MOFs was prepared with a new secondary building unit and organic links of varying lengths, for which Their crystal structure was solved utilizing powder X-ray diffraction crystallography. This work provides guidelines for the next generation of photocatalyst for the conversion of solar-to-chemical energy and other organic transformations.

to my mother and my family

to my friends

ACKNOWLEDGMENTS

TABLE OF CONTENTS

LIST OF FIGURES

LIST OF TABLES

CHAPTER 1: THE USE OF EARTH ABUNDANT METAL-ORGANIC FRAMEWORKS FOR HETEROGENEOUS PHOTOREDOX CATALYSIS

1.1 <u>Photoredox Catalysis</u>

The necessity for more efficient and sustainable chemical processes has been of great concern of synthetic chemistry in recent years, which has, in turn, stimulated ingenuity and innovation. This ingenuity is prominent in the century-old field of photocatalysis,[1] which has evoked interest due to the development of visible light organic photoredox catalysis since the late 1970s.[2-5] Remarkable advances have been made in chemical bond formation under mild conditions promoted solely by visible light, approaching genuinely sustainable bond-forming processes.[6-8] Photoredox catalysis, the field, encompasses an increasing number of photochemical activation methodologies in which solar irradiation is absorbed by a catalyst. This catalyst, upon excitation, becomes much more redox active, enabling access to both reductive and oxidative pathways and in turn, allows controlled bond forming/breaking through mild electron transfer. In contrast, uncatalyzed reactions require stoichiometric amounts of chemical redox reagents that are rarely reusable. The ability to achieve a rich variety of unique or exotic synthetic methodologies that are not yet realized using only sunlight has added more promise, as highly engineered photocatalytic systems can be designed. [9-11]

The direct conversion of solar energy into chemical energy has its origins in photosynthesis. This process has evolved over millions of years to efficiently utilize solar irradiation to drive a thermodynamically uphill process whereby CO_2 is transformed into glucose. Interestingly, this is also an example of a photocatalytic reaction that turns an otherwise endergonic chemical reaction in the ground state into thermodynamically allowed process via a photo-

generated activated state. This allows the storage of energy in electron-rich molecules, such as glucose. Photosynthesis is vital to sustain life on earth, and it's also the origin of all fossil fuels. This natural system obtains an efficiency of ~3%,[12] which although seemingly low, offers a benchmark for artificial systems using visible light and strategies for materials design. Consequently, there has been a concerted effort towards reproducing this natural system to harvest solar energy and convert it to more useful forms through electron transfer process.[13-15]

Although solar-to-chemical transformations are essential, relatively little is known on how to harness solar energy effectively. The amount of photonic energy (E) in kJ that could potentially be extracted from a specific wavelength (λ) of light can be expressed by the following equation:

$$E = h\nu = \frac{hc}{\lambda} \tag{1-1}$$

where h is Planck's constant (6.626×10^{-34} J s), ν is the frequency of light in s^{-1}, and c is the speed of light (2.998×10^{8} m s^{-1}). This can conveniently be converted to energy in terms of a mole of photons by the following equation:

$$E = N_A h\nu = \frac{N_A hc}{\lambda} \tag{1-2}$$

where E is in units of J mol^{-1}, N_A is Avogadro's number (6.022×10^{23} photons mol^{-1}), and λ is the wavelength of light in nm. For example, the energy of ultraviolet light at a wavelength around 315 nm (381 kJ mol^{-1}) is on the same order as the magnitude of the bond dissociation energy for a C-C single bond. This is the minimal amount of energy that **MIGHT** cause this bond to break, rearrange, or form radicals, assuming the molecule can absorb such light. An example of this process is the light-induced *cis-trans* isomerization of retinal that is responsible for vision.[16]

Unfortunately, it is uncommon for organic compounds to directly absorb solar energy and thus, photocatalyst that can promote such transformations are needed.

The conversion pathway from solar-to-chemical energy and other photochemical transformations with solid semiconductor photocatalysts in heterogeneous phase, occurs in three fundamental steps shown in Figure 1-1. **(1)** First, the absorption of a photon activates the catalyst through the creation of an electron-hole excited state (exciton), by promoting an electron from the valence band to the conduction band, as denoted by the vertical arrow. It should be noted that just because a photon is absorbed does not mean that a photochemical event **will** even take pace. The likelihood of photoexcitation to occur, assuming the excitation circumstances are suitable, depends on the number of photons, intensity of light, or absorption cross-section (extinction coefficient). **(2)** Following excitation, the electron-hole pair must migrate to the surface/interface where each charge carrier can then participate in separate redox half-reactions, **(3)** the electron then will cause reduction and the hole will cause oxidation of surface-bound substrates. In a laboratory setting, one of these pathways is typically quenched though the use of a sacrificial reagent to explore each fundamental step independently, facilitating the determination of the reaction mechanism.[17-19]

Historically, transition metal oxides have been the primary focus of photocatalytically active materials finding use in inorganic transformations such as water splitting,[20-23] CO_2 reduction,[24-26] and photovoltaic materials.[27-30] These heterogeneous systems are simple and represented early attempts at creating artificial systems to drive chemical reactions through solar energy under ambient conditions. Due to their intrinsic stability, ease of recyclability, appropriate redox potentials, low toxicity, and high natural abundance, this class of materials has been the most extensively investigated photoredox systems for a wide variety of practical applications.
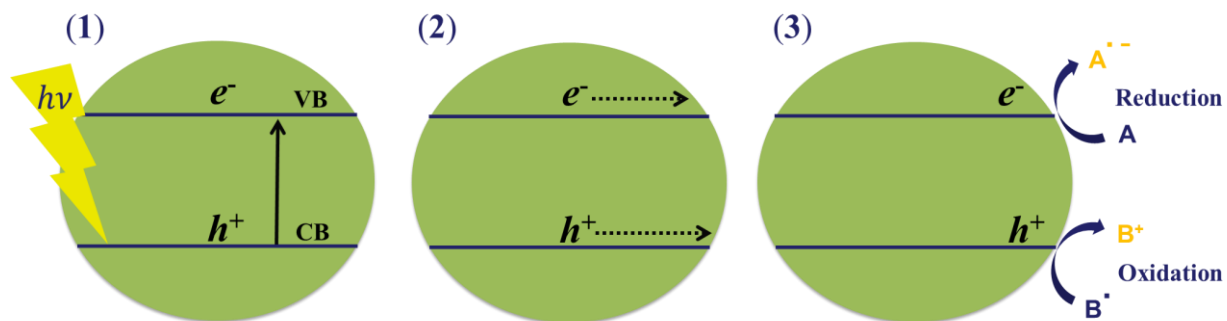
Figure 1-1: Simplified depiction of semiconductor band structure for the photoexcitation (**1**), charge diffusion (**2**), and redox half-reactions (**3**). Energy necessary for excitation is represented by black arrow in (**1**). Black arrow in (**2**) represents charge diffusion to the surface. CB = conduction band and VB = valence band, responsible for reduction and oxidation, respectively. Lightning bolt represents photonic energy.

However, their use has only seen practical implementation in selected applications unrelated to organic transformations or energy production. Their first shortcoming is that they typically have a rather large bandgap,[31] in the range of 3-4 eV (310-410 nm), which limits the absorption of solar irradiation to the UV region, which compromises only less than 5% of the solar spectrum.[32] Moreover, these materials present a high rate of charge carrier recombination, resulting in the material returning to the ground state rendering slow redox activity. Another limitation is their low surface area that results in very low rates due to the smaller number of active sites. Previous research has attempted to overcome this challenge by synthesizing these materials as nanoparticles because the high surface to volume ration, but they have a tendency to aggregate as a result of strong inter-particle forces, effectively reducing accessible reactivities.[33] Despite these drawbacks, great efforts are still being devoted to discovering more active heterogeneous semiconducting photocatalysts for solar-to-chemical conversions and other organic transformations. The majority of this work is concentrated on red-shifting the absorption profile into the visible range to achieve broadband charge separation, transportation, and interfacial redox reactions and to further understand the mechanisms of these processes.

More recently, molecular photoredox systems in homogeneous solution, specifically noble metal-based coordination complexes such as $Ir(ppy)_3$ and $Ru(bpy)_3^{2+}$ (ppy = 2-phenylpyridine; bpy = 2,2'-bipyridine), have emerged as a versatile photocatalyst to mediate organic transformations that could not have otherwise proceeded with ground-state systems.[34-36] In this case, upon the absorption of a visible photon an electron is excited from the HOMO to the LUMO via a singlet metal-to-ligand charge transfer (^{1}MLCT) (*Figure 1-2* (a)). This is subsequently followed by intersystem crossing (ISC) as a result of strong spin-orbit coupling yielding a long-lived (> 1 μs) triplet excited state that is electrochemically active towards single electron transfer

(SET).[37] This extended excited state lifetime allows the participation in both oxidative and reductive process in the same reaction vessel, through which a variety of important organic transformations have been observed. For example, *Figure 1-2* (b) demonstrates examples of photocatalyzed reactions using Ru(bpy)$_3^{2+}$ such as the oxidation of arylboronic acids, reductive elimination, and redox-mediated cycloadditions.[38] Activated C-X moieties can be dehalogenated via reductive pathway producing a carbon-centered radical that can participate in further transformations.[39] These catalysts have also been incorporated in the total synthesis of natural products contributing to increasing the yields while significantly reducing the number of synthetic steps.[37] An example was demonstrated by Yu *et al*. presented Ir(ppy)$_3$ photocatalyzed reduction of acyl oximes into pyridines, quinones, and phenanthridines.[40] The authors constructed bioactive nornitidine and noravicine in five steps (each) in 55% and 53% yields, respectively (Figure 1-2 (c)). Without involving the photoredox step, these products were obtained in 11 steps with overall yields ~20%. Furthermore, the tunability of the electronic structure through the use of ligand modulation enables the control over the redox potentials and an optical gap of these materials. This structure-property relationship allows for the rational design of catalysts with specific properties and applications while being efficient, obtaining quantum yields near unity, and also highly active as a result of their homogeneous nature.[41] Unfortunately, most photoredox catalysts are based on rare and expensive noble metals not very suitable for large-scale use.[42] They also present hazards due to their potential toxicity,[43] often requiring extensive purification.[44] The production of a novel catalytic system that could is necessary for practical applications and more sensible management of natural resources, vital for a sustainable future. This presents countless opportunities for research developing a better understanding of the photophysical and photochemical properties of advanced photocatalytic materials.
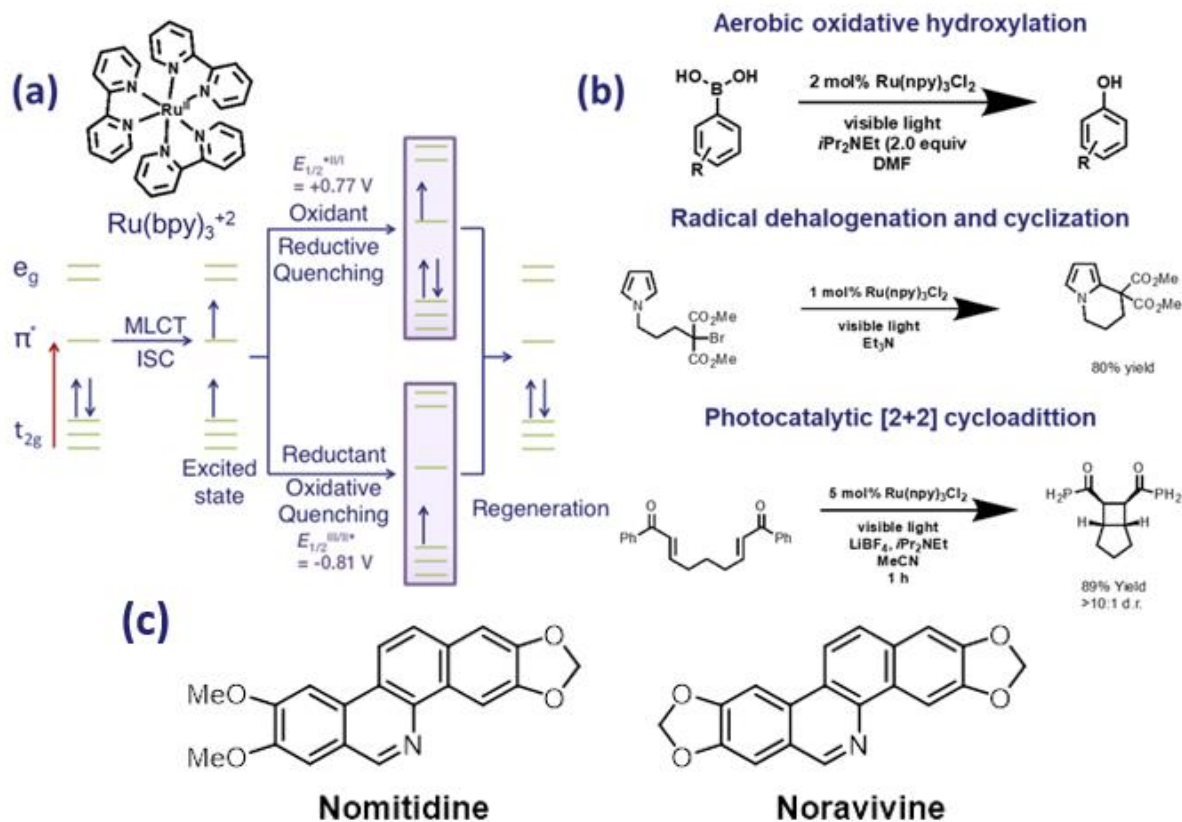
Figure 1-2: (a) Photoinduced SET process mediated by [Ru(bpy)₃]²⁺. Red arrow represents photonic energy required for excitation (b) Examples of [Ru(bpy)3]2+ catalyzed reactions. Nornitidine and noravicine that is synthesized more efficiently with photoredox catalysts. Ref. [38-40, 45]

1.2 <u>Metal-Organic Frameworks</u>

Metal-organic frameworks (MOFs) provide a platform to combine benefits of both heterogeneous and homogeneous systems into a single catalytic structure, due to their high available surface area, crystallinity, large degree of synthetic control, and heterogeneity.[46-47] MOFs are constructed from coordination between well-defined metal oxide clusters, also referred to as nodes, and organic molecules often referred to as linkers or struts. These inorganic nodes can also be represented by simplified geometric shapes called *secondary building units* (SBUs) that dictates the overall topology.[48-49] Molecular linkers connect the oxide clusters together through space to produce highly porous 3D architectures, similar to inorganic zeolites (Figure 1-3), but in this case, MOFs have predictable crystal structures predetermined by the geometry of the SBU and strut of choice (reticular synthesis).[50-52] They are different from other inorganic materials in that they are composed of well-defined, self-assembling molecular building blocks that form an organized hierarchical structure. As of late 2017, MOF synthesis has comprised of > 100 different metal clusters with > 1000 different ditopic, tritopic, or quadratopic linkers to obtain over 70,000 MOFs and a virtually limitless amount of potential structures.[53] This extent of synthetic versatility is unprecedented in inorganic materials, especially for those that express meso- and microporosity. Many applications have been previously demonstrated in gas storage,[54] separation,[55-57] catalysis,[58] photovoltaics,[59-61] sensors,[62-65] and drug delivery,[66-68] with promising potential in innovative applications, due to the ability to tune the chemical, optical, electronic, and magnetic properties by selecting the proper node and linker. This provides the possibility to generate a blueprint for new innovative materials with extraordinary performance.
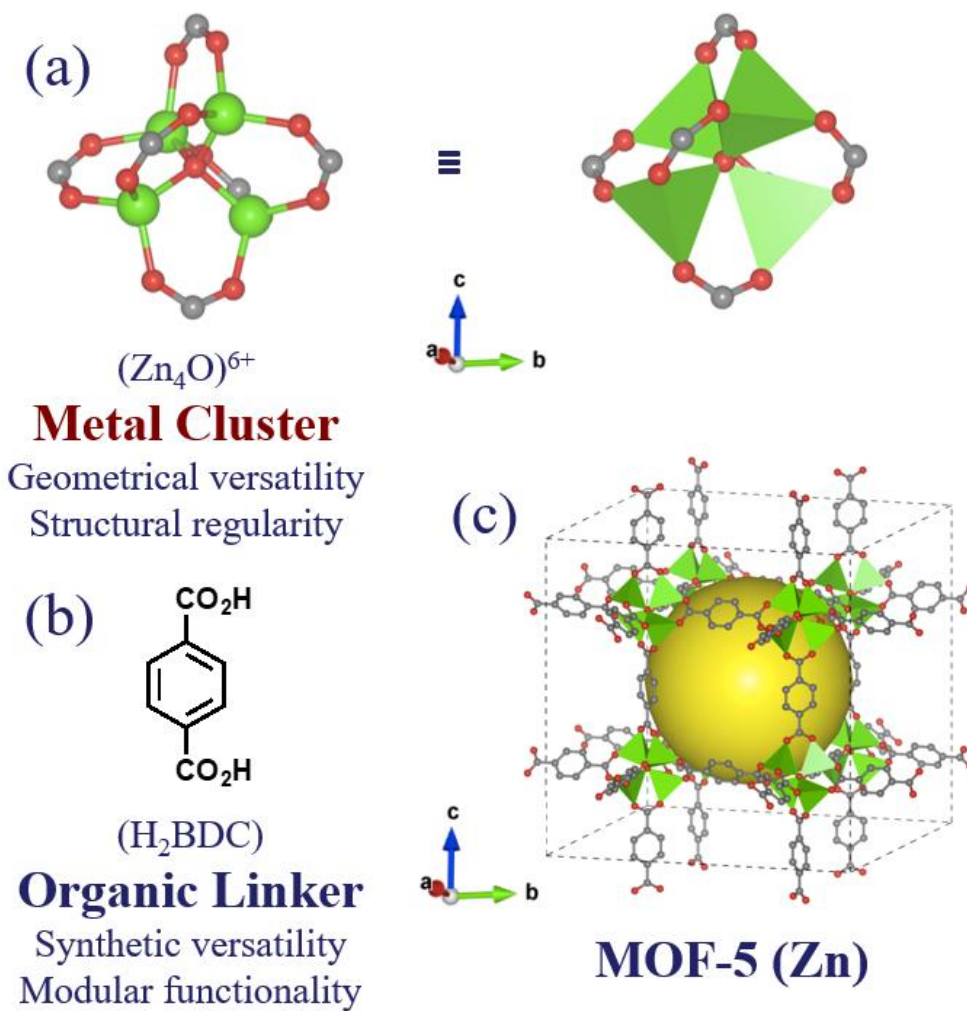
Figure 1-3: *(a) Atomic representation (left) and polyhedral representation (right) of MOF-5 inorganic clusters $(Zn_4O)^{6+}$ connected to carboxylate carbon and oxygen. (b) Organic linker, terephthalic acid (c) MOF-5 crystal structure. Spheres: gray = carbon, red = oxygen, green = Zn. Polyhedra: green = Zn(II). Yellow spheres used to highlight the pore cavity. Created with Vesta 3 and ChemDraw*

Unsurprisingly, this intrinsic degree of high structural organization, porosity, synthetic control and hybrid nature of MOFs has led researchers to investigate their electronic and optical properties for potential use in applied applications.[69-70] MOF-5 is the prototypical MOF, constructed of Zn_4O inorganic semiconducting clusters interconnected by 1,4-benzeodicarboxylate (BDC) (Figure 1-3).[71] Geometrically speaking, MOF-5 is an infinite array of $Zn_4O(CO_2)_6$ octahedra, where the carbon atoms in the carboxylate form octahedra that are connected together through 1,4-phenylene of BDC. The $Zn_4O(CO_2)_6$ cluster forms during MOF crystallization, and this is a secondary building unit with six points of extension. The points of extension are linked together by the carboxylates of the BDC, forming a material composed of inorganic nodes (metal oxide clusters) and organic struts (linkers).

Lin *et al*. rationalized that MOFs should be viewed as molecular catalysts that are self-assembled in a crystalline lattice with discrete nature rather than as an inorganic semiconductor.[72] This rational have been demonstrated through theoretical band structure calculations by Welsh *et al*. for MOF-5, showing that there is no band dispersion. This was later demonstrated experimentally through the photocatalytic behavior of an isoreticular MOF series. Their poor charge carrier properties were contributed to charge localization and should be referred to as **small bandgap insulators**.[73] This localized excited state must be in spatial proximity to the photonic absorption origin and the reaction active sites simultaneously. It was shown experimentally that the charge transport mechanism occurs as thermally activated hopping as opposed to true band transport, where the inorganic nodes are isolated from the organic ligands.[74] The creation of a charge-separated state upon photoexcitation; however, has been demonstrated in MOFs, with such excited state being able to participate in redox reactions.[75-77] The ability of MOFs to bridge the divide between homogeneous and heterogeneous semiconducting catalysts while offering the

advantages of both has made them promising materials in this field. Unfortunately, the fundamental properties of MOFs as solid-state semiconducting materials are yet to be fully understood and developing a generalized understanding is required in order to produce new functional materials.

1.3 <u>MOF Design Principals</u>

The objective of this dissertation is to investigate and understand the photochemical and photocatalytic properties of robust, earth-abundant MOFs as heterogeneous photoredox catalysts for solar-to-chemical energy conversion and organic synthesis. This study was performed through understanding structure-property relationships between the molecular composition of the organic building block in the MOF, and the photocatalytic properties of the solid-state material. Furthermore, in order to enable the possibility of wide spread application, the following requirements are also required: **(1)** The MOFs must be composed of earth-abundant elements, **(2)** must be nontoxic, **(3)** chemically and thermally robust, **(4)** and the MOFs must have accessible, visible light-activated redox potentials.

The **first** requirement is that the MOF must be made of readily available and inexpensive components. Such elements are those that are earth-abundant, easily recoverable from earth's crust, found in convenient forms, and recyclable. Table 1-1 displays the natural abundance in earth's crust of selected metals highlighting their significant differences in abundance.[78] Titanium and zirconium are very abundant metals that meet this requirement and are found to be more than five orders of magnitude more abundant than noble metals such as Ir, Ru, and Re. Using abundant metals facilitates the ability to meet the increasing demands for commodity chemicals, reducing

the energy and cost requirement for production. This includes utilization of elements that are available on earth and energy sources available, using them both sustainability.

Table 1-1: Natural abundance of select elements in Earth's crust. Ref. [78]

Element	Abundance (ppb)
Ti	6,600,000
Zr	130,000
Zn	79,000
Cu	68,000
Ru	1.0
Ir	0.4
Re	2.6

The **second** condition is that the materials used should be nontoxic with no potential for environmental contamination. This means that MOFs made of heavy metals such as Cr, Pb, Cd, Co, *etc*. and organic functionalities that are a potential hazard should not be used. To date there is no relevant environmental or biological role for titanium or zirconium, and are usually not absorbed by digestion in animals due to them typically being found at neutral pH as insoluble metal oxides and have low bioactivity.[79-80] This low bioavailability has been of interest due to the ever-increasing use in consumer goods such as Ti incorporation into pigments, sunscreens, pharmaceuticals, orthopedic implants, and more recently nanomaterials that have displayed

bioactivity.[81-83] Specifically, micro- and nano-particles have become of great concern, since it has been linked to medical complications such as granuloma, pleura effusion, pulmonary fibrosis, and tumor induction upon inhilation.[79, 84]

The **third** requirement is for practical applications; the MOF catalyst must be stable in harsh operating environments. For example, in order to reduce CO_2 from flue gas, the material must be stable above 100 °C with high mass flow under humid environments.[85] These conditions are typically deleterious to the crystallinity of most MOFs.[86-88] This is a result of the meta-stability of the metal-O-(carboxylate) bond, the bond that is formed during MOF assembly under dynamic equilibrium, and typically the weakest link in a MOF. This type of bonding is necessary to form highly ordered materials. As the formation of this bond is driven by metal-coordination via Lewis acid-base interactions, it is prone to be sensitive to water, either aqueous or humid conditions, resulting in the reverse hydrolysis reaction.[89-90] MOFs are also susceptible to thermal decomposition due to the phase transition[91] of the metastable MOF or from the intrinsic decomposition of the organic moiety.[92] This is more of an insignificant factor, since photocatalysis can occur at lower temperatures with no need of added thermal energy to facilitate the reactions other than mass transport of substrates, and lower temperatures can be utilized while having high reaction rates. Furthermore, due to the photoredox transformations progressing through successive SET radical species, the reaction environments can be harsh to the organic components of the materials (organic linkers), and also potentially generate reactive oxygen species (ROS), especially when exposed to UV light. All the mentioned considerations point towards the need for creating MOFs with increased chemical and thermal stability. It has been discussed that carboxylate-based MOFs formed with high oxidation state, early transition metal oxide cluster, offer this desired stability due to strong hard-hard acid-base interactions between the metal ion (acid) and

13

carboxylate (base).[93-94] Thus, this interaction must be stronger than any acid-base interaction that may occur with water which is a hard base. For example, MOFs based on Zr^{4+}, Ti^{4+}, and Y^{3+} metal ions and carboxylate linkers displayed unprecedented stability in water and acidic conditions. The next task involved study is their stability-performance relationship.

The **fourth** and last requirement is to ensure that the photoexcited state has the appropriate redox potentials to initiate the photoredox half-reactions. The alignment of the conduction band and valence band must be more reductive and oxidative than the target reaction, respectively. For example, for a material to photocatalytically split water, the conduction band position must be greater (more negative) than the potential required to reduce $2H^+$ to H_2 (0.0 eV vs. NHE) and the valence band position must be less (more positive) than the potential required to oxidize H_2O to O_2 (1.23 eV vs. NHE). Therefore, under ideal circumstances, the bandgap minimum is 1.23 eV (equivalent to a photon with $\lambda = 1080$ nm). Realistically, the band gap must be larger than this value depending on any overpotential necessary to drive the chemical reaction. These values are challenging to predict for polycrystalline MOFs and difficult to measure directly.[95-98]

Using MOFs in photocatalytic systems has encompassed a variety of roles, from acting as a host or solid substitute to being directly responsible for the entire photoredox process. When acting as the host for other active heterogeneous photocatalyst, the MOFs have little to no participation in the chemical reactions. The catalytically active centers are incorporated into the pores of the MOF through grafting or impregnation that mediate the chemical reactions. MOFs organize these nanomaterials to eliminate the potential of aggregation[99] and self-quenching,[100] even showing enhanced charge separation efficiency.[101]
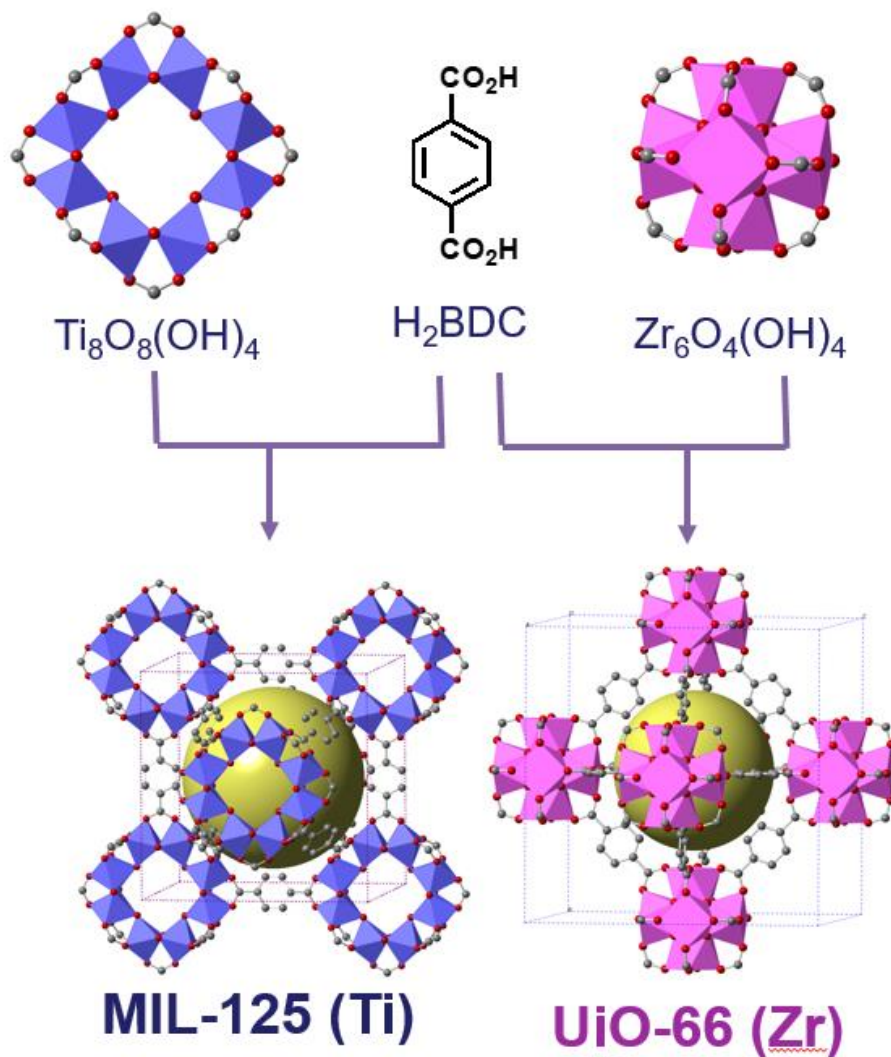
Figure 1-4: Crystal structures of MIL-125 (right) and UiO-66 (left) Spheres: gray = carbon, red = oxygen, white =hydrogen. Polyhedra: green = Zr(IV) and blue = Ti(IV). Yellow spheres used to highlight the pore cavity. Created with Vesta 3 and ChemDraw

When MOFs function as a cocatalyst with other guest components that are not covalently anchored (such as molecular sensitizers[102] or quantum dots)[103] the MOF itself can help promote the photoredox reactions by precisely controlling the nature of the encapsulation. This type of material is best described as an evenly distributed supramolecular system that is segregated by the MOF structure.

In another approach, the entire photoredox process can be solely mediated by the MOF, from the creation of the charge-separated-state to participation in the subsequent redox process.[75-76, 104-107] This ensures there will be no extrinsic factors, like pore clogging[108] or leaching,[109] that lead to the slow loss of active material within the MOF and potential contamination. Also, a decrease in mass transport throughout the entirety of the MOF pores is then expected. In this regard, a stand-alone system that is composed of the inorganic metal-oxide cluster based on earth-abundant elements and organic linker with predesigned electronic and steric structure, with no expensive additives, is desirable. The research presented here is focused on the photoredox activity being an intrinsic property of the material, retaining all the traits of a MOF.

MOFs based on titanium and zirconium, particularly MIL-125(Ti)[110] (MIL = Materials Institute Lavoisier) and UiO-66(Zr) [111] (UiO = University of Oslo (Figure 1-4) are examples of materials that exhibit photoredox behavior and also fulfill the desired requirements. Both MOFs are constructed with BDC linkers (same as in MOF-5). MIL-125 contains $Ti_8O_8(OH)_4(CO_2)_{12}$ ring-shaped clusters, where eight TiO_6 octahedra alternate sharing corners and edges with O^{2-} and OH^- in the inner section of the ring, and carboxylates bridging two titanium ions in the outer section of the ring. The result is a tetragonal structure with a topology closely related to a defect body-centered tetragonal packing (*I4/mmm* symmetry). UiO-66 contains $Zr_6O_4(OH)_4(CO_2)_{12}$ cluster

where the Zr^{4+} occupy the corners of octahedron, O^{2-} and OH- with μ^3-connectivity occupy the faces of the octahedron, alternating positions, and the carboxylates occupy the edges of the octahedron with twelve points of connection, forming a **fcu** topology with cubic symmetry (*Im-3m*). Both materials produce charge-separated states that result in photoredox activity.[76-77, 104, 112-116]

The modular nature of MOFs is unlike inorganic semiconductors, allowing for fine control of their chemical, electronic, and physical properties through synthetic means, decoupling composition from reactivity. Typically, the organic linkers act as light antennae to harvest solar energy and undergo a ligand-to-metal charge transfer (LMCT) that creates a redox active electron-hole pair. Viewing the MOF as an array of self-assembled molecular structures, it can be easily rationalized that the synthetic control over MOF structures allows for control over its properties and performance. The ability to effectively control the energy required to excite the system strongly depends on the nature of the ligand, which functions as electromagnetic antennae. This was first theorized for MOF-5,[117] and later demonstrated with functionalized organic linkers,[118] such as 2-amino terephthalic acid (BDC-NH_2) to increase the level of the HOMO while maintaining the same LUMO (HOMO-LUMO nomenclature when considering molecular, valence-conduction bands when considering solid materials), decreasing the HOMO-LUMO gap (or bandgap) to the visible region. This results from the electron density donation from the lone pair on the nitrogen atom to the antibonding orbital (π^*) of the aromatic ring.[119] This is significant since light harvesting is the first step in the development of new MOFs for photocatalytic applications. This approach gives synthetic control over intrinsic photochemical and photophysical properties of the MOF. Fu *et al.* studied this substitution effect in MIL-125 and MIL-125-NH_2 and its role in the reduction of CO_2 under visible light.[120] Figure 1-5 (1) shows that by introducing

amino groups in the organic link, results in absorption with red shift the near edge absorption band from 350 nm to 500 nm for the MIL-125 and MIL-125-NH$_2$, respectively, evidenced by the color change in the materials (Figure 1-5 (1)). The powder X-ray diffraction pattern shows that the introduction of the amine group does not influence the structure and matches that of the predicted powder pattern (Figure 1-5 (2)). The photoreduction of CO$_2$ to HCO$_2^-$ (formate), which has been shown to be a valuable chemical for fuel cell integration, and even proposed for H$_2$ storage, was performed in acetonitrile (MeCN) using triethanolamine (TEOA) as an electron donor. MIL-125-NH$_2$ showed activity towards the photoreduction of CO$_2$ when irradiation with $\lambda > 450$ nm light, whereas MIL-125 shows no activity under the same conditions. Upon visible light irradiation of MIL-125-NH$_2$ in MeCN with TEOA under a N$_2$ atmosphere, the reaction suspension color changed from yellow to green (Figure 1-5 (4)). The yellow color returned upon the introduction of O$_2$ and CO$_2$. This photochromic behavior is attributed to intervalence electron transfer from electrons hopping between the Ti^{3+} and Ti^{4+} species in the Ti-oxide cluster. This was confirmed using electron spin resonance (ESR) and transient absorption spectroscopy confirming the formation of Ti^{3+} (d^1) upon LMCT.[120]

There are a few reports extending beyond the -NH$_2$ functionality and its influence on the optical band gap of the MOFs. In one study, MIL-125 made with BDC was substituted with varying amounts of BDC-NH$_2$, ranging from one to twelve BDC-NH$_2$ linkers per unit cell, all samples exhibited roughly the same optical bandgap of 2.6 eV with an apparent molar extinction coefficient increasing with the higher density of BDC-NH$_2$.[121]
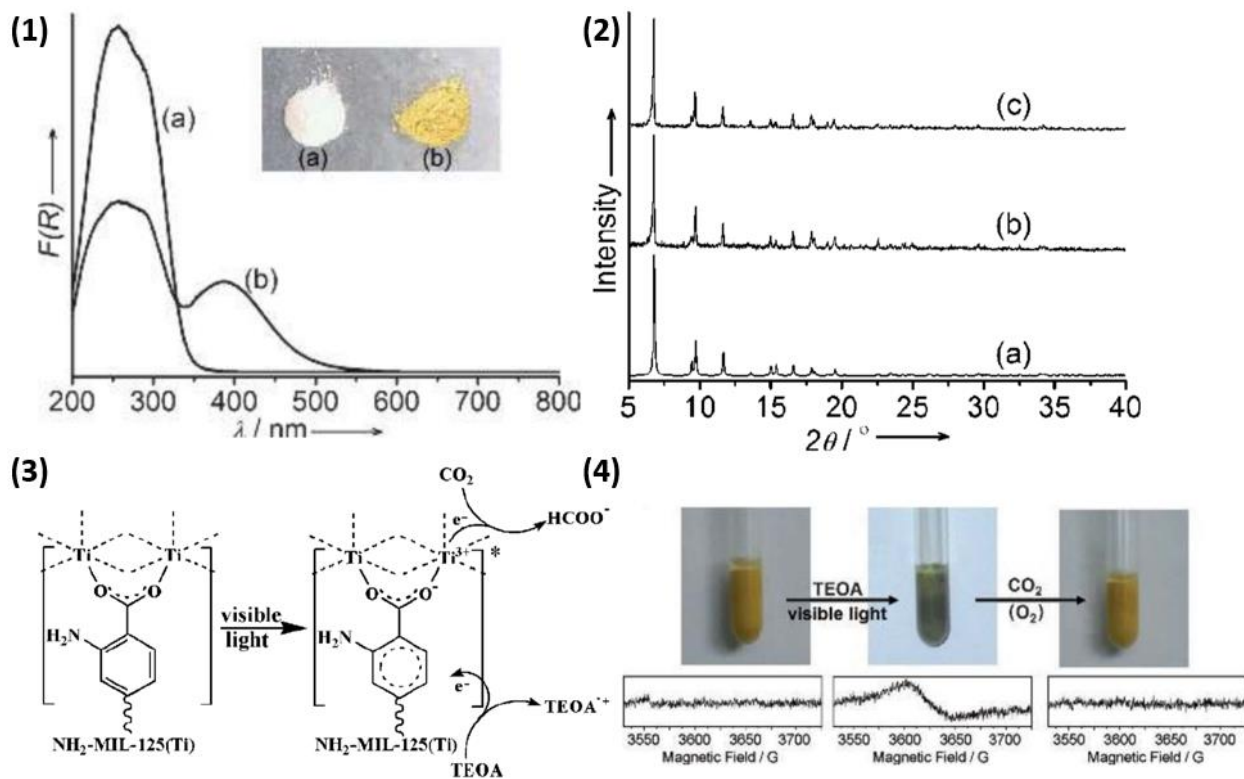
Figure 1-5: (1) Diffuse reflectance absorption spectra of MIL-125(a) and MIL-125-NH$_2$ (b). Insert is an image of samples. (2) PXRD patterns of simulated MIL-125 (a), experimental MIL-125 (b), and experimental MIL-125-NH$_2$ (c). (3) Proposed photoreduction mechanism of CO$_2$ for MIL-125-NH$_2$. (4) ESR spectra (bottom) and photos (top) of fresh MIL-125-NH$_2$ (a), TEOA and visible light under N$_2$ conditions (b), and post CO$_2$ purge (c). Ref. [120]. *Copyright 2012, Wiley-VCH*

19

The addition of a second -NH$_2$ onto the BDC-NH$_2$ ligand of the MIL-125 analog, making BDC-(NH$_2$)$_2$, further destabilized the HOMO and lowered the optical bandgap to 1.3 eV, compared to 2.4 and 3.6 eV for MIL-125-NH$_2$ and MIL-125, respectively. This study provided evidence of ligand substitution for control of optical properties in MOFs, but many questions regarding the specific role of mixed linkers and heterogeneity remain unanswered. In a computational study of the electronic structure of MIL-125, using different substituents such as -CH$_3$, -OH, -NH$_2$, or -Cl revealed that the electronic nature of the substituent is correlated to the bandgap, where greater electron-donating ability of the substituent results in smaller bandgaps, showing that BDC-(NH$_2$)$_2$ has the lowest apparent bandgap in the series.[121] This work demonstrated the significant role that the linker plays on the optical properties and provides initial direction towards the design of highly photoredox active MOF materials. Further studies, also showed that the BDC-NH$_2$ linker prolongs the excited state lifetime by stabilizing the localized hole in the aromatic ring of BDC, increasing probability of redox reactions to take place.[122] Recently, more photoactive linkers have been made and incorporated into MOFs, many inspired by natural photosynthesis, such as the use of porphyrin-like pigments in PCN-222 for the photoelectrochemical oxidation of benzyl alcohol.[123]
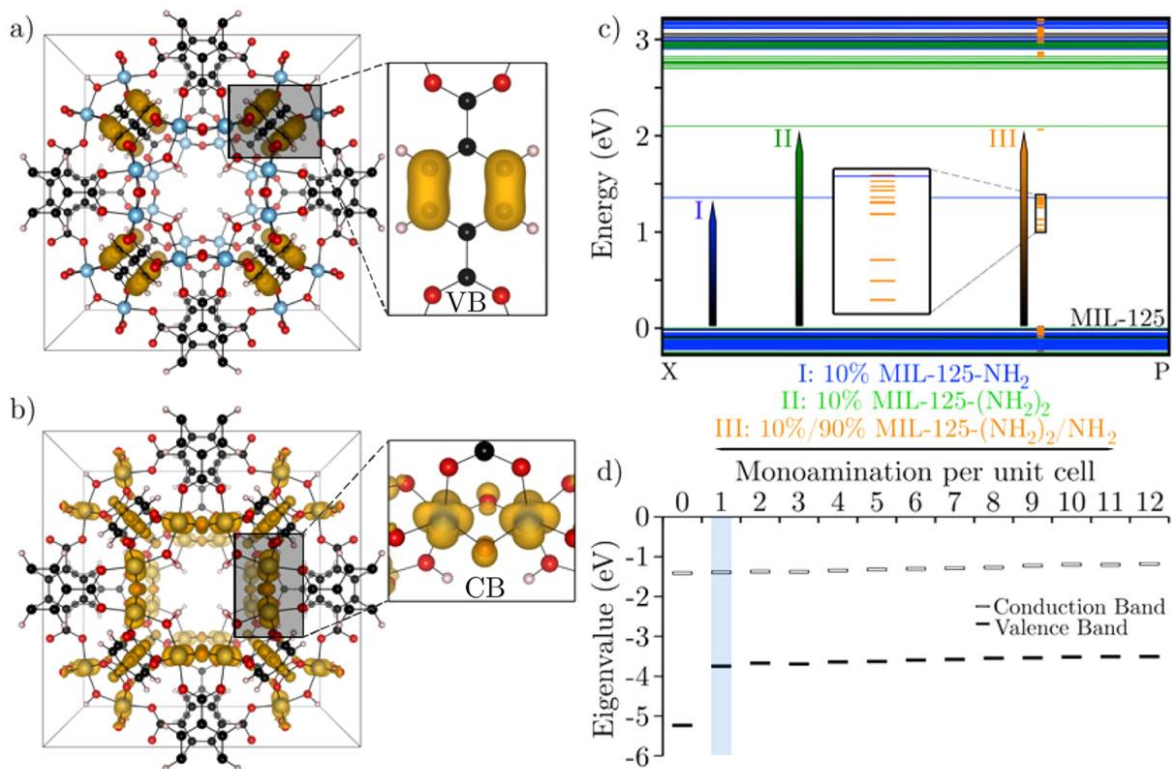
Figure 1-6: (a,b) Frontier orbital electron density for the valence band (a) and conduction band (b) of MIL-125. (c) PBEsol band structure for synthetic MIL-125 (black), 10% MIL-125-NH$_2$ (blue), 90% MIL-125-NH$_2$/10% MIL-125-(NH$_2$)$_2$ (orange), and theoretical 10% MIL-125-(NH$_2$)$_2$ (green). (d) HSE06-calculated VB and CB energies of MIL-125-NH$_2$ with increasing density of BDC-NH$_2$ linkers. Ref [121]. *Copyright 2013, American Chemical Society.*
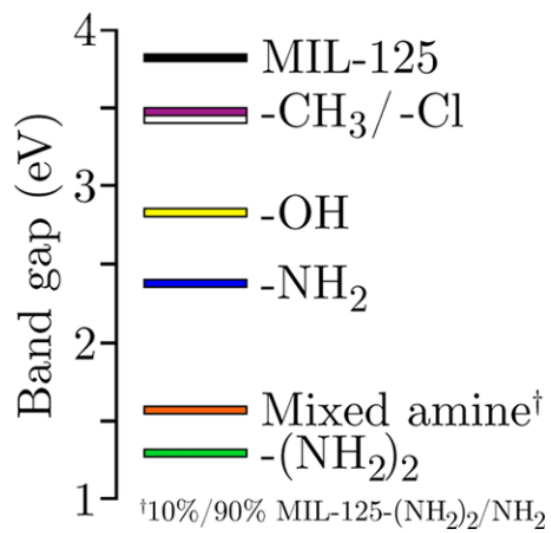
Figure 1-7: DFT-calculated band gaps for MIL-125 and substituted analogs (using HSE06 functional). Ref [121]. Copyright 2013, American Chemical Society.

Similar behavior was observed in the electronic structure of other d^o high valent MOFs with amino-functionalized BDC. The nature of the electronic properties of MIL-125-NH$_2$, UiO-66-NH$_2$(Zr), and UiO-66-NH$_2$(Hf) (isoreticular to UiO, but with Hf instead of Zr) were studied computationally and experimentally for their potential use as a photoredox catalyst. Although they possessed comparable structural features, their electronic properties are significantly different, as shown in Figure 1-8 (a). As already stated, MIL-125 derivatives undergo a LMCT from the HOMO in the organic linker to the LUMO of the metal cluster.[124] This LMCT is long-lived making it suitable for photoredox applications. In contrast, UiO-66-NH$_2$(Zr) and UiO-66-NH$_2$(Hf) exhibit low d-orbital binding energies and cannot overlap with the antibonding orbital of the linker (π^*) of the ligand. This phenomenon has the effect to localize the frontier bands around the organic linker, resulting in fast recombination of the excited state, diminishing the photoredox activity. Electron paramagnetic resonance (EPR) of these MOFs, shown in Figure 1-8 (b), was carried out under similar conditions to that of the photocatalytic redox reactions. When exposed to UV irradiation, there is a LMCT for MIL-125-NH$_2$ that is in agreement with the intense paramagnetic signal ascribed to the Ti^{3+} (d^1) formed with photoexcitation. UiO-66-NH$_2$(Zr) and UiO-66-NH$_2$(Hf) do not display such EPR feature, which agrees with previous observations, trying to use Zr-MOF system to inject electrons into a cocatalyst for H$_2$ evolution from an aqueous solution.[125] These studies altogether suggest that tunable photoredox catalysis in MOFs can be achieved only in MIL-125-like structure, where there is an electronic synergy between the linker and the metal for a long-lived excited state accessible with visible light, and dependent on the electronic features of the linker. **Since it's been shown that there is no electronic communications between linkers and metals in UiO-66, efforts in this dissertation focused on titanium-based MOFs.**
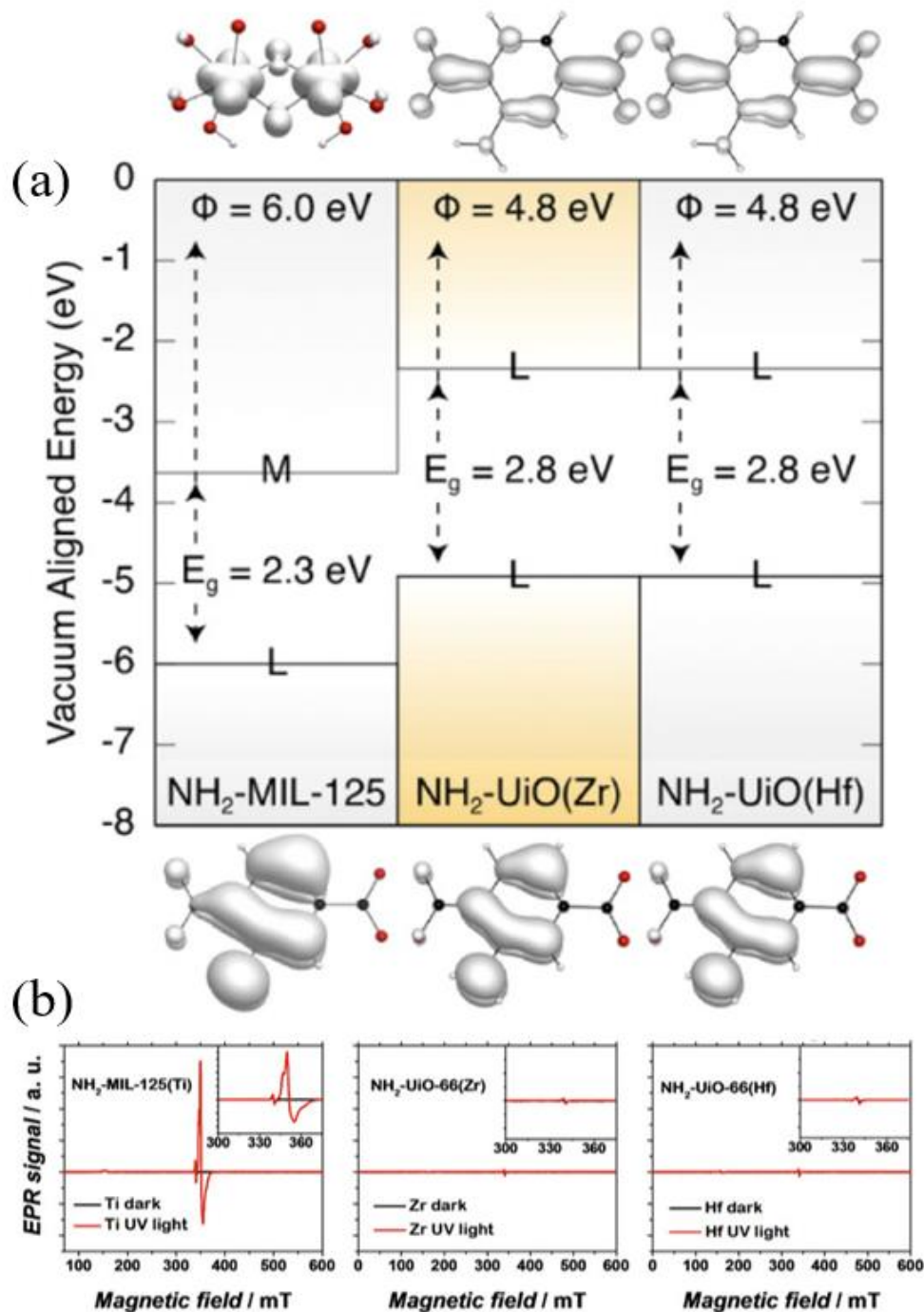
Figure 1-8:(a) Electronic band structure of MIL-125-NH$_2$ (left), UiO-66-NH$_2$(Zr) (center), and UiO-66-NH$_2$ (Hf) (left) relative to vacuum level. Orbitals shown on top and bottom represent the LUMO and HOMO, respectively. M and L indicate metal and ligand, respectively. (b) EPR spectra of MIL-125-NH$_2$ (left), UiO-66-NH$_2$(Zr) (center), and UiO-66-NH$_2$ (Hf) (left) under dark (black) and UV irritation (red). Ref. [124]

The use of post-synthetic modification (PSM) has been demonstrated as an effective method to further functionalize MOFs like gas separation,[126] drug delivery,[67] sensing,[127] and others.[128] This method consists in preforming a targeted chemical transformation or modification of molecular features of the cluster of the linker **after** the MOF is assembled, crystallized and isolated. PSM offers a method to chemically modify the molecular structure of MOFs in a heterogeneous manner that may not be possible before the synthesis of the MOF. There are several advantages of this method which include a rich variety of accessible functional groups, robust synthetic tolerance, facile isolation of newly functionalized MOF, and ambient to mild reaction conditions. Gascon *et al.* demonstrated that the PSM of MIL-125-NH$_2$ by diazotization of the amino groups followed by reaction with dimethylaniline to yield a methyl red derivative moiety (denoted as MIL-125-MR) allowed the extension of the absorption spectrum to nearly 700 nm for the MIL-125-MR due to the increased conjugation of the aromatic linker (Figure 1-9).[129] This bathochromic shift also showed enhanced catalytic activity towards the reduction of benzyl alcohol to form benzaldehyde at higher rates for the MIL-125-MR compared to MIL-125-NH$_2$ and MIL-125 because of the large molecular size of diethyl aniline, it is very likely that this transformation only occurs near the surface of the MOF particles and also likely that the photoredox reaction occurs only at this interface.

The number of reported Ti-based MOFs in the literature is small, compared to MOFs with other metal composites. Titanium MOFs have proved to be synthetically elusive due to the high reactivity of Ti precursors in solution that makes bond association/dissociation challenging and inhibits the dynamic processes necessary for high crystallinity. Synthetic control over crystallization is essential for the successful synthesis of titanium MOFs.
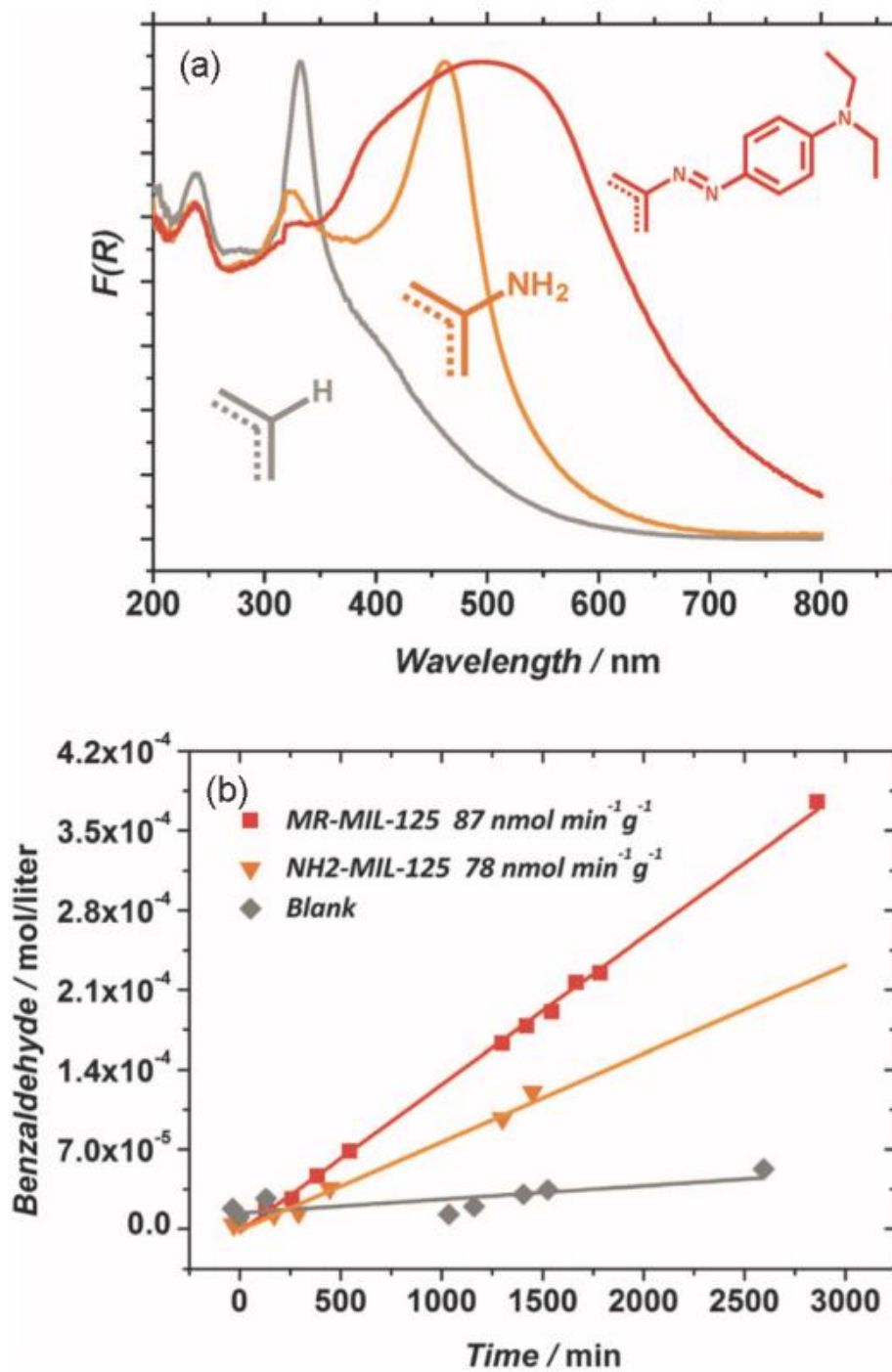
Figure 1-9: (a) Diffuse reflectance absorption spectra of MIL-125 (gray), MIL-125-NH₂ (orange), and Mil-125-MR (red). (b) Photocatalyzed reduction of benzoyl alcohol to benzaldehyde using no catalyst (gray), MIL-125-NH₂ (orange), and Mil-125-MR (red). Ref. [129]. *Copyright 2013, Royal Society of Chemistry*

To circumvent this problem, precondensed titanium-oxo carboxylate (TOC) cluster precursors can be utilized for greater synthetic flexibility, resulting in higher product yields with less TiO_2 phase formation.[130-131] This stepwise approach has proved valuable in the preparation of titanium MOFs, by eliminating the possibility of hydrolysis and slowing down the dynamic crystallization environment. An important point to mention is that there has been significant work beyond the scope of this introduction. Metal deposition was demonstrated by Li *et al*. using Ti-deposited around the Zr-oxy cluster of UiO-66-NH_2(Zr/Ti) to explore the effects of this bimetallic interaction on its photophysical and photochemical properties.[132] Compared to the parent MOF, the bimetallic material had enhanced CO_2 reduction and H_2 evolution ability. DFT and EPR reveal that Ti acts to mediate the electron transfer process into the Zr-oxide cluster. Other, more sophisticated, bimetallic examples were first demonstrated by Lin *et al.* with the inclusion of organometallic complexes of Ru and Ir into UiO-type MOFs, but in this case, all the photoredox activity centers around the Ru/Ir complex, disregarding any role that the metal-oxide can provide.[133]

This description serves as an introduction on how robust MOFs have been designed towards photoredox catalysis and as a guideline for further development for the conversion of solar energy to fuel production and organic synthesis. This is a rich field that offers synthetic versatility from the tunable structure that makes MOFs a promising material for photocatalysis and an ideal platform to study mechanistic processes. MOFs as photocatalysts are still in their infancy with the reported examples of redox reactions being relatively simplistic, while focusing efforts on strategies to enhance light absorption and charge separation to promote MOF photocatalysis. This offers a significant chance for contribution to this field from a platform that facilitates a fundamental understanding of the photophysical and photochemical properties of MOFs. The organic linkers act as light antennae that connect and stabilize the discrete semiconductor metal

oxide centers and play a significant role in determining the properties related to the photocatalytic activity of the MOFs. In an effort to have broadband light absorption, most work towards producing more efficient MOF systems has been focused on producing highly π-conjugated linkers. The difficulty lies in predicting and controlling the energy levels, lifetimes, and other properties related to the transient charge-separated state in MOFs. In addition, the majority of MOFs offer minimal stability under photocatalytic environments. As such, limitations remain that need to be overcome prior to sustainable development and utilization for wide-scale production of photocatalytic MOFs materials.

1.4 <u>Dissertation Outline</u>

This dissertation describes the design, synthesis, and characterization of MOFs composed of earth-abundant elements that exhibit photoredox activity, specifically studying their application as heterogeneous photocatalysts to drive organic transformations and solar-to-chemical energy conversion. I examined the structure-property relationships of titanium-based MOFs by exploring the effect of the structure of the organic component on the photophysical and photochemical activity of its solid-state composition.

Chapter 2 focuses on the mild oxidation of *N*-hydroxy-carbamate compounds from a surveyed library of known MOFs that are chemically stable and constructed of earth-abundant elements including Ti, Zr, Fe, Cu, V, and Al. Upon oxidation, *N*-hydroxy-carbamate produces a reactive acyl-nitroso intermediate that can react with intramolecular pendant alkene moieties through a nitroso-ene reaction to afford *N*-hydroxy-oxazolidones, which are nitrogen-containing building-blocks found in biologically active compounds in pharmaceuticals and natural products. This reaction has been previously reported to occur with mild oxidants such as $CuCl/O_2$ and

Fe(II)/H_2O_2 in the ground state and with Ru(bpy)$_3^{2+}$ as a molecular photoredox catalyst. The library of prepared MOFs was tested towards this oxidation photocatalytically using a UV-Vis Xe lamp and blue LEDs in aerobic conditions. The heterogeneous nature allowed easy isolation of the catalyst from the reaction mixture and in regeneration of the catalyst upon drying; product isolation was achieved by simple filtration and evaporation of the solvent, while the homogeneous methods reported require extensive purification methods (*e.g.,* column chromatography). Upon oxidation of increasingly more complex *N*-hydroxy-carbamates, it was found that the MOFs induce diastereoselectivities similar to those obtained in solution. Mechanistic information was obtained through chemical kinetics studies, photochemical quantum yield measurements, and the determination of the photogenerated reactive species. Temperature dependence in the kinetic studies enabled the identification of the photoredox process as the rate-limiting step of the reaction, a result that is often seen when using non-porous heterogeneous catalysts like TiO_2. This result is also consistent with previous studies on the dependence of the external surface area/external interface of MOF crystallites on the control of the reaction kinetics. *This initial study helped to point out two primary methods of increasing MOFs photocatalytic redox activity: (1) decreasing the bandgap and (2) gaining access to the internal pore structure of the MOF.*

Chapter 3 describes the systematic functionalization of the 2-amino-terephthalate ring with *N*-alkyl groups of increasing chain length (from methyl to heptyl) and varying connectivity (primary and secondary α-carbon). This functionalization increases the electron density of the aromatic ring via inductive effects, which progressively adds electronic density to the aromatic ring in BDC, resulting in decreased bandgap and increasing the photoredox activity. The progressive additions of *N*-alkyl groups also increased the excited state lifetimes and attained high photocatalytic activities towards CO_2 reduction under blue LED illumination, with operating times

up to 120 h. In particular, MIL-125-NHCyp (Cyp = cyclopentyl) exhibited a smaller bandgap, a longer-lived excited-state, and a larger apparent quantum yield compared to the parent MIL-125-NH_2, making it a promising candidate for the next generation of photocatalysts for solar fuel production.

Chapter 4 demonstrates that *N*-alkyl functionalization not only serves to increase the broadband absorption and extend the photogenerated excited state lifetime compared to MIL-125-NH_2, but the successive *N*-alkyklations also provided a means to improve stability towards water, water vapor, and at varied pH and temperatures. It was shown that MIL-125-NHCyp not only exhibited high photocatalytic reduction towards CO_2 in Chapter 3 but also displayed structure and porosity stability in humid and aqueous environments for more than 30 days as well as increased hydrophobicity compared to the parent framework (MIL-125-NH_2). This functionalization also decreased water vapor uptake while allowing the retention BET surface area after multiple adsorption-desorption cycles. This improved stability, in conjunction with its high photocatalytic activity, makes this MOF a very promising candidate for large-scale applications in CO_2 photoreduction.

Chapter 5 describes the strategy followed to access larger pore sizes, using longer linkers and the characterization thereof. This includes a family of three new layered Ti-based MOFs, **UCFMOF** family. This family most likely possesses a nonintepenatrated structure with one-dimensional inorganic clusters. All members of the series exhibit robust porous structures where the unit cell, pore aperture, and the void volume is dependent upon the organic linker length. This is evident by their high permanent porosity and high thermal stability.

Finally, Chapter 6 describes recommendations for future materials based on the titanium MOFs described herein, from the point of view of linker design. Presented is two sequential schemes that impart more sophisticated functionalities that have chemical recognition. The first incorporates electron donation groups and steric constraints through heterocycles to understand the effect on light harvesting and excited state lifetime. The second incorporates chiral molecules to impart preferred spatial configuration on substrates potentially.

1.5 <u>References</u>

1. Ciamician, G., The photochemistry of the future. *Science* **1912,** *36* (926), 385-394.

2. Pac, C.; Ihama, M.; Yasuda, M.; Miyauchi, Y.; Sakurai, H., Tris (2, 2'-bipyridine) ruthenium (2+)-mediated photoreduction of olefins with 1-benzyl-1, 4-dihydronicotinamide: a mechanistic probe for electron-transfer reactions of NAD (P) H-model compounds. *Journal of the American Chemical Society* **1981,** *103* (21), 6495-6497.

3. Ishitani, O.; Pac, C.; Sakurai, H., Redox-photosensitized reactions. 10. Formation of a novel type of adduct between an NADH model and carbonyl compounds by photosensitization using Ru (bpy) 32+. *The Journal of Organic Chemistry* **1983,** *48* (17), 2941-2942.

4. Pac, C.; Miyauchi, Y.; Ishitani, O.; Ihama, M.; Yasuda, M.; Sakurai, H., Redox-photosensitized reactions. 11. Ru (bpy) 32+-photosensitized reactions of 1-benzyl-1, 4-dihydronicotinamide with aryl-substituted enones, derivatives of methyl cinnamate, and substituted cinnamonitriles: electron-transfer mechanism and structure-reactivity relationships. *The Journal of Organic Chemistry* **1984,** *49* (1), 26-34.

5.   Mandler, D.; Willner, I., Solar light induced formation of chiral 2-butanol in an enzyme-catalyzed chemical system. *Journal of the American Chemical Society* **1984,** *106* (18), 5352-5353.

6.   Koike, T.; Akita, M., Visible-light-induced photoredox catalysis: an easy access to green radical chemistry. *Synlett* **2013,** *24* (19), 2492-2505.

7.   Tucker, J. W.; Stephenson, C. R., Shining light on photoredox catalysis: theory and synthetic applications. *The Journal of Organic Chemistry* **2012,** *77* (4), 1617-1622.

8.   Michelin, C.; Hoffmann, N., Photocatalysis applied to organic synthesis–a green chemistry approach. *Current Opinion in Green and Sustainable Chemistry* **2018**.

9.   Fagnoni, M.; Dondi, D.; Ravelli, D.; Albini, A., Photocatalysis for the formation of the C−C bond. *Chemical Reviews* **2007,** *107* (6), 2725-2756.

10.   Yoon, T. P.; Ischay, M. A.; Du, J., Visible light photocatalysis as a greener approach to photochemical synthesis. *Nature Chemistry* **2010,** *2* (7), 527.

11.   Ravelli, D.; Dondi, D.; Fagnoni, M.; Albini, A., Photocatalysis. A multi-faceted concept for green chemistry. *Chemical Society Reviews* **2009,** *38* (7), 1999-2011.

12.   Zhang, T., More efficient together. *Science* **2015,** *350* (6262), 738-739.

13.   Demmig-Adams, B.; Adams Iii, W. W., Harvesting sunlight safely. *Nature* **2000,** *403*, 371.

14.   Balzani, V.; Campagna, S.; Denti, G.; Juris, A.; Serroni, S.; Venturi, M., Harvesting sunlight by artificial supramolecular antennae. *Solar Energy Materials and Solar Cells* **1995,** *38* (1), 159-173.

15.   Ludin, N. A.; Al-Alwani Mahmoud, A. M.; Bakar Mohamad, A.; Kadhum, A. A. H.; Sopian, K.; Abdul Karim, N. S., Review on the development of natural dye photosensitizer

for dye-sensitized solar cells. *Renewable and Sustainable Energy Reviews* **2014,** *31*, 386-396.

16. Hubbard, R.; Wald, G., Cis-trans isomers of vitamin A and retinene in the rhodopsin system. *The Journal of General Physiology* **1952,** *36* (2), 269-315.

17. Pellegrin, Y.; Odobel, F., Sacrificial electron donor reagents for solar fuel production. *Comptes Rendus Chimie* **2017,** *20* (3), 283-295.

18. Schneider, J.; Bahnemann, D. W., Undesired role of sacrificial reagents in photocatalysis. ACS Publications: 2013.

19. Saha, S.; Stoddart, J. F., Photo-driven molecular devices. *Chemical Society Reviews* **2007,** *36* (1), 77-92.

20. Ni, M.; Leung, M. K.; Leung, D. Y.; Sumathy, K., A review and recent developments in photocatalytic water-splitting using TiO2 for hydrogen production. *Renewable and Sustainable Energy Reviews* **2007,** *11* (3), 401-425.

21. Zou, Z.; Ye, J.; Sayama, K.; Arakawa, H., Direct splitting of water under visible light irradiation with an oxide semiconductor photocatalyst. *Nature* **2001,** *414*, 625.

22. Maeda, K.; Domen, K., Photocatalytic Water Splitting: Recent Progress and Future Challenges. *The Journal of Physical Chemistry Letters* **2010,** *1* (18), 2655-2661.

23. Hisatomi, T.; Kubota, J.; Domen, K., Recent advances in semiconductors for photocatalytic and photoelectrochemical water splitting. *Chemical Society Reviews* **2014,** *43* (22), 7520-7535.

24. Liu, L.; Zhao, H.; Andino, J. M.; Li, Y., Photocatalytic CO2 reduction with H2O on TiO2 nanocrystals: Comparison of anatase, rutile, and brookite polymorphs and exploration of surface chemistry. *ACS Catalysis* **2012,** *2* (8), 1817-1828.

25. Sergio, N.; Amarajothi, D.; Mercedes, Á.; Hermenegildo, G., Photocatalytic CO2 Reduction using Non‑Titanium Metal Oxides and Sulfides. *ChemSusChem* **2013,** *6* (4), 562-577.

26. Anpo, M.; Yamashita, H.; Ichihashi, Y.; Fujii, Y.; Honda, M., Photocatalytic Reduction of CO2 with H2O on Titanium Oxides Anchored within Micropores of Zeolites: Effects of the Structure of the Active Sites and the Addition of Pt. *The Journal of Physical Chemistry B* **1997,** *101* (14), 2632-2636.

27. Park, N.-G.; Van de Lagemaat, J.; Frank; AJ, Comparison of dye-sensitized rutile-and anatase-based TiO2 solar cells. *The Journal of Physical Chemistry B* **2000,** *104* (38), 8989-8994.

28. Rajan, J.; Velmurugan, T.; Seeram, R., Metal Oxides for Dye‑Sensitized Solar Cells. *Journal of the American Ceramic Society* **2009,** *92* (2), 289-301.

29. C., A. A.; R., J. L.; N., B. V.; Z., S.; A., C. S.; H.‑H., H., Efficient Titanium Oxide/Conjugated Polymer Photovoltaics for Solar Energy Conversion. *Advanced Materials* **2000,** *12* (22), 1689-1692.

30. Shrotriya, V.; Li, G.; Yao, Y.; Chu, C.-W.; Yang, Y., Transition metal oxides as the buffer layer for polymer photovoltaic cells. *Applied Physics Letters* **2006,** *88* (7), 073508.

31. Ivano, E. C.; Juan María, G.-L.; Falco, H.; Kristian, S. T.; Karsten, W. J., Stability and bandgaps of layered perovskites for one- and two-photon water splitting. *New Journal of Physics* **2013,** *15* (10), 105026.

32. Frederick, J.; Snell, H.; Haywood, E., Solar ultraviolet radiation at the earth's surface. *Photochemistry and Photobiology* **1989,** *50* (4), 443-450.

33. Jiang, J.; Oberdörster, G.; Biswas, P., Characterization of size, surface charge, and agglomeration state of nanoparticle dispersions for toxicological studies. *Journal of Nanoparticle Research* **2009,** *11* (1), 77-89.

34. Prier, C. K.; Rankic, D. A.; MacMillan, D. W., Visible light photoredox catalysis with transition metal complexes: applications in organic synthesis. *Chemical Reviews* **2013,** *113* (7), 5322-5363.

35. Jun, X.; Wen‑Jing, X., Visible‑Light Photoredox Catalysis. *Angewandte Chemie International Edition* **2012,** *51* (28), 6828-6838.

36. Kirsten, Z., Photoredox Catalysis with Visible Light. *Angewandte Chemie International Edition* **2009,** *48* (52), 9785-9789.

37. Damrauer, N. H.; Cerullo, G.; Yeh, A.; Boussie, T. R.; Shank, C. V.; McCusker, J. K., Femtosecond dynamics of excited-state evolution in [Ru (bpy) 3] 2+. *Science* **1997,** *275* (5296), 54-57.

38. Zou, Y. Q.; Chen, J. R.; Liu, X. P.; Lu, L. Q.; Davis, R. L.; Jørgensen, K. A.; Xiao, W. J., Highly efficient aerobic oxidative hydroxylation of arylboronic acids: photoredox catalysis using visible light. *Angewandte Chemie* **2012,** *124* (3), 808-812.

39. Tucker, J. W.; Narayanam, J. M.; Krabbe, S. W.; Stephenson, C. R., Electron transfer photoredox catalysis: intramolecular radical addition to indoles and pyrroles. *Organic Letters* **2009,** *12* (2), 368-371.

40. Jiang, H.; An, X.; Tong, K.; Zheng, T.; Zhang, Y.; Yu, S., Visible‑Light‑Promoted Iminyl‑Radical Formation from Acyl Oximes: A Unified Approach to Pyridines,

Quinolines, and Phenanthridines. *Angewandte Chemie International Edition* **2015,** *54* (13), 4055-4059.

41. Adamson, A. W.; Demas, J. N., New photosensitizer. Tris (2, 2'-bipyridine) ruthenium (II) chloride. *Journal of the American Chemical Society* **1971,** *93* (7), 1800-1801.

42. Larsen, C. B.; Wenger, O. S., Photoredox Catalysis with Metal Complexes Made from Earth‑Abundant Elements. *Chemistry‑A European Journal* **2018,** *24* (9), 2039-2058.

43. Limburg, B.; Bouwman, E.; Bonnet, S., Rate and Stability of Photocatalytic Water Oxidation using [Ru (bpy) 3] 2+ as Photosensitizer. *ACS Catalysis* **2016,** *6* (8), 5273-5284.

44. Zhang, X.; Li, Y.; Hao, X.; Jin, K.; Zhang, R.; Duan, C., Recyclable alkylated Ru (bpy) 32+ complex as a visible-light photoredox catalyst for perfluoroalkylation. *Tetrahedron* **2018,** *74* (15), 1742-1748.

45. Ischay, M. A.; Anzovino, M. E.; Du, J.; Yoon, T. P., Efficient visible light photocatalysis of [2+ 2] enone cycloadditions. *Journal of the American Chemical Society* **2008,** *130* (39), 12886-12887.

46. Zhou, H.-C.; Long, J. R.; Yaghi, O. M., Introduction to metal–organic frameworks. ACS Publications: 2012.

47. Kitagawa, S., Metal–organic frameworks (MOFs). *Chemical Society Reviews* **2014,** *43* (16), 5415-5418.

48. Yaghi, O. M.; O'keeffe, M.; Ockwig, N. W.; Chae, H. K.; Eddaoudi, M.; Kim, J., Reticular synthesis and the design of new materials. *Nature* **2003,** *423* (6941), 705.

49. Yaghi, O. M.; O'Keeffe, M.; Ockwig, N. W.; Chae, H. K.; Eddaoudi, M.; Kim, J., Reticular synthesis and the design of new materials. *Nature* **2003,** *423*, 705.

50.   Furukawa, H.; Cordova, K. E.; O'Keeffe, M.; Yaghi, O. M., The Chemistry and Applications of Metal-Organic Frameworks. *Science* **2013,** *341* (6149).

51.   O'Keeffe, M.; Peskov, M. A.; Ramsden, S. J.; Yaghi, O. M., The Reticular Chemistry Structure Resource (RCSR) Database of, and Symbols for, Crystal Nets. *Accounts of Chemical Research* **2008,** *41* (12), 1782-1789.

52.   Côté, A. P.; El-Kaderi, H. M.; Furukawa, H.; Hunt, J. R.; Yaghi, O. M., Reticular Synthesis of Microporous and Mesoporous 2D Covalent Organic Frameworks. *Journal of the American Chemical Society* **2007,** *129* (43), 12914-12915.

53.   Moghadam, P. Z.; Li, A.; Wiggin, S. B.; Tao, A.; Maloney, A. G.; Wood, P. A.; Ward, S. C.; Fairen-Jimenez, D., Development of a Cambridge Structural Database subset: a collection of metal–organic frameworks for past, present, and future. *Chemistry of Materials* **2017,** *29* (7), 2618-2625.

54.   Ma, S.; Zhou, H.-C., Gas storage in porous metal–organic frameworks for clean energy applications. *Chemical Communications* **2010,** *46* (1), 44-53.

55.   Rodenas, T.; Luz, I.; Prieto, G.; Seoane, B.; Miro, H.; Corma, A.; Kapteijn, F.; i Xamena, F. X. L.; Gascon, J., Metal–organic framework nanosheets in polymer composite materials for gas separation. *Nature Materials* **2015,** *14* (1), 48.

56.   Li, J.-R.; Kuppler, R. J.; Zhou, H.-C., Selective gas adsorption and separation in metal–organic frameworks. *Chemical Society Reviews* **2009,** *38* (5), 1477-1504.

57.   Caro, J., Are MOF membranes better in gas separation than those made of zeolites? *Current Opinion in Chemical Engineering* **2011,** *1* (1), 77-83.

58.   Lee, J.; Farha, O. K.; Roberts, J.; Scheidt, K. A.; Nguyen, S. T.; Hupp, J. T., Metal–organic framework materials as catalysts. *Chemical Society Reviews* **2009,** *38* (5), 1450-1459.

59. Lee, D. Y.; Shinde, D. V.; Yoon, S. J.; Cho, K. N.; Lee, W.; Shrestha, N. K.; Han, S.-H., Cu-based metal–organic frameworks for photovoltaic application. *The Journal of Physical Chemistry C* **2013,** *118* (30), 16328-16334.

60. Kaur, R.; Kim, K.-H.; Paul, A.; Deep, A., Recent advances in the photovoltaic applications of coordination polymers and metal organic frameworks. *Journal of Materials Chemistry A* **2016,** *4* (11), 3991-4002.

61. Li, Y.; Chen, C.; Sun, X.; Dou, J.; Wei, M., Metal‑Organic Frameworks at Interfaces in Dye‑Sensitized Solar Cells. *ChemSusChem* **2014,** *7* (9), 2469-2472.

62. Wang, D.; Tan, Q.; Liu, J.; Liu, Z., A stable europium metal–organic framework as a dual-functional luminescent sensor for quantitatively detecting temperature and humidity. *Dalton Transactions* **2016,** *45* (46), 18450-18454.

63. Xu, H.; Liu, F.; Cui, Y.; Chen, B.; Qian, G., A luminescent nanoscale metal–organic framework for sensing of nitroaromatic explosives. *Chemical Communications* **2011,** *47* (11), 3153-3155.

64. Yu, Y.; Ma, J.-P.; Dong, Y.-B., Luminescent humidity sensors based on porous Ln 3+-MOFs. *CrystEngComm* **2012,** *14* (21), 7157-7160.

65. Gole, B.; Bar, A. K.; Mukherjee, P. S., Fluorescent metal–organic framework for selective sensing of nitroaromatic explosives. *Chemical Communications* **2011,** *47* (44), 12137-12139.

66. Horcajada, P.; Serre, C.; Vallet‑Regí, M.; Sebban, M.; Taulelle, F.; Férey, G., Metal‑organic frameworks as efficient materials for drug delivery. *Angewandte Chemie* **2006,** *118* (36), 6120-6124.

67.   Taylor-Pashow, K. M.; Della Rocca, J.; Xie, Z.; Tran, S.; Lin, W., Postsynthetic modifications of iron-carboxylate nanoscale metal− organic frameworks for imaging and drug delivery. *Journal of the American Chemical Society* **2009,** *131* (40), 14261-14263.

68.   Huxford, R. C.; Della Rocca, J.; Lin, W., Metal–organic frameworks as potential drug carriers. *Current Opinion in Chemical Biology* **2010,** *14* (2), 262-268.

69.   Czaja, A. U.; Trukhan, N.; Müller, U., Industrial applications of metal–organic frameworks. *Chemical Society Reviews* **2009,** *38* (5), 1284-1293.

70.   Mueller, U.; Schubert, M.; Teich, F.; Puetter, H.; Schierle-Arndt, K.; Pastre, J., Metal–organic frameworks—prospective industrial applications. *Journal of Materials Chemistry* **2006,** *16* (7), 626-636.

71.   Li, H.; Eddaoudi, M.; O'Keeffe, M.; Yaghi, O. M., Design and synthesis of an exceptionally stable and highly porous metal-organic framework. *Nature* **1999,** *402* (6759), 276.

72.   Wang, C.; Liu, D.; Lin, W., Metal–organic frameworks as a tunable platform for designing functional molecular materials. *Journal of the American Chemical Society* **2013,** *135* (36), 13222-13234.

73.   Khajavi, H.; Gascon, J.; Schins, J. M.; Siebbeles, L. D.; Kapteijn, F., Unraveling the optoelectronic and photochemical behavior of Zn4O-based metal organic frameworks. *The Journal of Physical Chemistry C* **2011,** *115* (25), 12487-12493.

74.   Coropceanu, V.; Cornil, J.; da Silva Filho, D. A.; Olivier, Y.; Silbey, R.; Brédas, J.-L., Charge transport in organic semiconductors. *Chemical Reviews* **2007,** *107* (4), 926-952.

75.   Zhang, T.; Lin, W., Metal–organic frameworks for artificial photosynthesis and photocatalysis. *Chemical Society Reviews* **2014,** *43* (16), 5982-5993.

76.   Wang, C.-C.; Zhang, Y.-Q.; Li, J.; Wang, P., Photocatalytic CO2 reduction in metal–organic frameworks: a mini review. *Journal of Molecular Structure* **2015,** *1083*, 127-136.

77.   Wang, J.-L.; Wang, C.; Lin, W., Metal–organic frameworks for light harvesting and photocatalysis. *ACS Catalysis* **2012,** *2* (12), 2630-2640.

78.   Winter, M., Abundance in Earth's crust. *The university of Sheffield and web elements Ltd, UK. Accessed* **2016,** *8*.

79.   Dankovic, D.; Kuempel, E.; Wheeler, M., An Approach to Risk Assessment for TiO2. *Inhalation Toxicology* **2007,** *19* (sup1), 205-212.

80.   Buettner, K. M.; Valentine, A. M., Bioinorganic chemistry of titanium. *Chemical Reviews* **2011,** *112* (3), 1863-1881.

81.   Kabata-Pendias, A.; Mukherjee, A. B., *Trace Elements From Soil to Human*. Springer Science & Business Media: 2007.

82.   Att, W.; Hori, N.; Iwasa, F.; Yamada, M.; Ueno, T.; Ogawa, T., The effect of UV-photofunctionalization on the time-related bioactivity of titanium and chromium–cobalt alloys. *Biomaterials* **2009,** *30* (26), 4268-4276.

83.   Vanzillotta, P. S.; Sader, M. S.; Bastos, I. N.; de Almeida Soares, G., Improvement of in vitro titanium bioactivity by three different surface treatments. *Dental Materials* **2006,** *22* (3), 275-282.

84.   Song, Y.; Li, X.; Du, X., Exposure to nanoparticles is related to pleural effusion, pulmonary fibrosis and granuloma. *European Respiratory Journal* **2009,** *34* (3), 559-567.

85.   Aaron, D.; Tsouris, C., Separation of CO2 from flue gas: a review. *Separation Science and Technology* **2005,** *40* (1-3), 321-348.

86. Jasuja, H.; Huang, Y.-g.; Walton, K. S., Adjusting the stability of metal–organic frameworks under humid conditions by ligand functionalization. *Langmuir* **2012,** *28* (49), 16874-16880.

87. Han, S.; Huang, Y.; Watanabe, T.; Nair, S.; Walton, K. S.; Sholl, D. S.; Meredith, J. C., MOF stability and gas adsorption as a function of exposure to water, humid air, SO2, and NO2. *Microporous and Mesoporous Materials* **2013,** *173*, 86-91.

88. Wu, T.; Shen, L.; Luebbers, M.; Hu, C.; Chen, Q.; Ni, Z.; Masel, R. I., Enhancing the stability of metal–organic frameworks in humid air by incorporating water repellent functional groups. *Chemical Communications* **2010,** *46* (33), 6120-6122.

89. Low, J. J.; Benin, A. I.; Jakubczak, P.; Abrahamian, J. F.; Faheem, S. A.; Willis, R. R., Virtual high throughput screening confirmed experimentally: porous coordination polymer hydration. *Journal of the American Chemical Society* **2009,** *131* (43), 15834-15842.

90. Mondloch, J. E.; Katz, M. J.; Planas, N.; Semrouni, D.; Gagliardi, L.; Hupp, J. T.; Farha, O. K., Are Zr 6-based MOFs water stable? Linker hydrolysis vs. capillary-force-driven channel collapse. *Chemical Communications* **2014,** *50* (64), 8944-8946.

91. Bennett, T. D.; Cheetham, A. K., Amorphous metal–organic frameworks. *Accounts of Chemical Research* **2014,** *47* (5), 1555-1562.

92. Kleist, W.; Maciejewski, M.; Baiker, A., MOF-5 based mixed-linker metal–organic frameworks: Synthesis, thermal stability and catalytic application. *Thermochimica Acta* **2010,** *499* (1-2), 71-78.

93. Chen, J.; Li, Y., The Road to MOF‐Related Functional Materials and Beyond: Desire, Design, Decoration, and Development. *The Chemical Record* **2016,** *16* (3), 1456-1476.

94.   Lian, X.; Feng, D.; Chen, Y.-P.; Liu, T.-F.; Wang, X.; Zhou, H.-C., The preparation of an ultrastable mesoporous Cr (III)-MOF via reductive labilization. *Chemical Science* **2015,** *6* (12), 7044-7048.

95.   Butler, K. T.; Hendon, C. H.; Walsh, A., Electronic chemical potentials of porous metal–organic frameworks. *Journal of the American Chemical Society* **2014,** *136* (7), 2703-2706.

96.   Prodan, E.; Kohn, W., Nearsightedness of electronic matter. *Proceedings of the National Academy of Sciences of the United States of America* **2005,** *102* (33), 11635-11638.

97.   Loera-Serna, S.; Oliver-Tolentino, M. A.; de Lourdes López-Núñez, M.; Santana-Cruz, A.; Guzmán-Vargas, A.; Cabrera-Sierra, R.; Beltrán, H. I.; Flores, J., Electrochemical behavior of [Cu3 (BTC) 2] metal–organic framework: the effect of the method of synthesis. *Journal of Alloys and Compounds* **2012,** *540*, 113-120.

98.   Talin, A. A.; Centrone, A.; Ford, A. C.; Foster, M. E.; Stavila, V.; Haney, P.; Kinney, R. A.; Szalai, V.; El Gabaly, F.; Yoon, H. P., Tunable electrical conductivity in metal-organic framework thin-film devices. *Science* **2013**, 1246738.

99.   Gao, S.; Zhao, N.; Shu, M.; Che, S., Palladium nanoparticles supported on MOF-5: A highly active catalyst for a ligand-and copper-free Sonogashira coupling reaction. *Applied Catalysis A: General* **2010,** *388* (1-2), 196-201.

100.   Wen, M.; Mori, K.; Kamegawa, T.; Yamashita, H., Amine-functionalized MIL-101 (Cr) with imbedded platinum nanoparticles as a durable photocatalyst for hydrogen production from water. *Chemical Communications* **2014,** *50* (79), 11645-11648.

101.   Wang, C.; DeKrafft, K. E.; Lin, W., Pt nanoparticles@ photoactive metal–organic frameworks: efficient hydrogen evolution via synergistic photoexcitation and electron injection. *Journal of the American Chemical Society* **2012,** *134* (17), 7211-7214.

102. He, J.; Wang, J.; Chen, Y.; Zhang, J.; Duan, D.; Wang, Y.; Yan, Z., A dye-sensitized Pt@ UiO-66 (Zr) metal–organic framework for visible-light photocatalytic hydrogen production. *Chemical Communications* **2014,** *50* (53), 7063-7066.

103. Jin, S.; Son, H.-J.; Farha, O. K.; Wiederrecht, G. P.; Hupp, J. T., Energy transfer from quantum dots to metal–organic frameworks for enhanced light harvesting. *Journal of the American Chemical Society* **2013,** *135* (3), 955-958.

104. Dhakshinamoorthy, A.; Asiri, A. M.; García, H., Metal–organic framework (MOF) compounds: photocatalysts for redox reactions and solar fuel production. *Angewandte Chemie International Edition* **2016,** *55* (18), 5414-5445.

105. Laurier, K. G.; Vermoortele, F.; Ameloot, R.; De Vos, D. E.; Hofkens, J.; Roeffaers, M. B., Iron (III)-based metal–organic frameworks as visible light photocatalysts. *Journal of the American Chemical Society* **2013,** *135* (39), 14488-14491.

106. Wang, C.-C.; Du, X.-D.; Li, J.; Guo, X.-X.; Wang, P.; Zhang, J., Photocatalytic Cr (VI) reduction in metal-organic frameworks: A mini-review. *Applied Catalysis B: Environmental* **2016,** *193*, 198-216.

107. Du, J.-J.; Yuan, Y.-P.; Sun, J.-X.; Peng, F.-M.; Jiang, X.; Qiu, L.-G.; Xie, A.-J.; Shen, Y.-H.; Zhu, J.-F., New photocatalysts based on MIL-53 metal–organic frameworks for the decolorization of methylene blue dye. *Journal of Hazardous Materials* **2011,** *190* (1-3), 945-951.

108. Roy, S.; Pascanu, V.; Pullen, S.; Miera, G. G.; Martín-Matute, B.; Ott, S., Catalyst accessibility to chemical reductants in metal–organic frameworks. *Chemical Communications* **2017,** *53* (22), 3257-3260.

109. Xamena, F. X. L.; Abad, A.; Corma, A.; Garcia, H., MOFs as catalysts: Activity, reusability and shape-selectivity of a Pd-containing MOF. *Journal of Catalysis* **2007,** *250* (2), 294-298.

110. Dan-Hardi, M.; Serre, C.; Frot, T.; Rozes, L.; Maurin, G.; Sanchez, C.; Férey, G., A new photoactive crystalline highly porous titanium (IV) dicarboxylate. *Journal of the American Chemical Society* **2009,** *131* (31), 10857-10859.

111. Cavka, J. H.; Jakobsen, S.; Olsbye, U.; Guillou, N.; Lamberti, C.; Bordiga, S.; Lillerud, K. P., A new zirconium inorganic building brick forming metal organic frameworks with exceptional stability. *Journal of the American Chemical Society* **2008,** *130* (42), 13850-13851.

112. Sun, D.; Li, Z., Robust Ti‑and Zr‑Based Metal‑Organic Frameworks for Photocatalysis. *Chinese Journal of Chemistry* **2017**.

113. Gomes Silva, C.; Luz, I.; Llabrés i Xamena, F. X.; Corma, A.; García, H., Water stable Zr–benzenedicarboxylate metal–organic frameworks as photocatalysts for hydrogen generation. *Chemistry-A European Journal* **2010,** *16* (36), 11133-11138.

114. Wang, S.; Wang, X., Multifunctional metal–organic frameworks for photocatalysis. *Small* **2015,** *11* (26), 3097-3112.

115. Maurin, G.; Serre, C.; Cooper, A.; Férey, G., The new age of MOFs and of their porous-related solids. *Chemical Society Reviews* **2017,** *46* (11), 3104-3107.

116. Amador, R. N.; Carboni, M.; Meyer, D., Photosensitive titanium and zirconium metal organic frameworks: current research and future possibilities. *Materials Letters* **2016,** *166*, 327-338.

117.   Civalleri, B.; Napoli, F.; Noël, Y.; Roetti, C.; Dovesi, R., Ab-initio prediction of materials properties with CRYSTAL: MOF-5 as a case study. *CrystEngComm* **2006,** *8* (5), 364-371.

118.   Gascon, J.; Hernández‐Alonso, M. D.; Almeida, A. R.; van Klink, G. P.; Kapteijn, F.; Mul, G., Isoreticular MOFs as efficient photocatalysts with tunable band gap: an operando FTIR study of the photoinduced oxidation of propylene. *ChemSusChem* **2008,** *1* (12), 981-983.

119.   Wojciechowski, P. M.; Zierkiewicz, W.; Michalska, D.; Hobza, P., Electronic structures, vibrational spectra, and revised assignment of aniline and its radical cation: Theoretical study. *The Journal of Chemical Physics* **2003,** *118* (24), 10900-10911.

120.   Fu, Y.; Sun, D.; Chen, Y.; Huang, R.; Ding, Z.; Fu, X.; Li, Z., An Amine‐Functionalized Titanium Metal‐Organic Framework Photocatalyst with Visible‐Light‐Induced Activity for CO2 Reduction. *Angewandte Chemie* **2012,** *124* (14), 3420-3423.

121.   Hendon, C. H.; Tiana, D.; Fontecave, M.; Sanchez, C. m.; D'arras, L.; Sassoye, C.; Rozes, L.; Mellot-Draznieks, C.; Walsh, A., Engineering the optical response of the titanium-MIL-125 metal–organic framework through ligand functionalization. *Journal of the American Chemical Society* **2013,** *135* (30), 10942-10945.

122.   de Miguel, M.; Ragon, F.; Devic, T.; Serre, C.; Horcajada, P.; García, H., Evidence of Photoinduced Charge Separation in the Metal‐Organic Framework MIL‐125 (Ti)‐NH2. *ChemPhysChem* **2012,** *13* (16), 3651-3654.

123.   Yuan, S.; Liu, T.-F.; Feng, D.; Tian, J.; Wang, K.; Qin, J.; Zhang, Q.; Chen, Y.-P.; Bosch, M.; Zou, L., A single crystalline porphyrinic titanium metal–organic framework. *Chemical Science* **2015,** *6* (7), 3926-3930.

124. Nasalevich, M. A.; Hendon, C. H.; Santaclara, J. G.; Svane, K.; Van Der Linden, B.; Veber, S. L.; Fedin, M. V.; Houtepen, A. J.; Van Der Veen, M. A.; Kapteijn, F., Electronic origins of photocatalytic activity in d 0 metal organic frameworks. *Scientific Reports* **2016,** *6*, 23676.

125. Horiuchi, Y.; Toyao, T.; Saito, M.; Mochizuki, K.; Iwata, M.; Higashimura, H.; Anpo, M.; Matsuoka, M., Visible-light-promoted photocatalytic hydrogen production by using an amino-functionalized Ti (IV) metal–organic framework. *The Journal of Physical Chemistry C* **2012,** *116* (39), 20848-20853.

126. Gu, Z. Y.; Yan, X. P., Metal‑Organic Framework MIL‑101 for High‑Resolution Gas‑Chromatographic Separation of Xylene Isomers and Ethylbenzene. *Angewandte Chemie International Edition* **2010,** *49* (8), 1477-1480.

127. Cao, J.; Gao, Y.; Wang, Y.; Du, C.; Liu, Z., A microporous metal–organic open framework containing uncoordinated carbonyl groups as postsynthetic modification sites for cation exchange and Tb 3+ sensing. *Chemical Communications* **2013,** *49* (61), 6897-6899.

128. Nguyen, J. G.; Cohen, S. M., Moisture-resistant and superhydrophobic metal− organic frameworks obtained via postsynthetic modification. *Journal of the American Chemical Society* **2010,** *132* (13), 4560-4561.

129. Nasalevich, M. A.; Goesten, M. G.; Savenije, T. J.; Kapteijn, F.; Gascon, J., Enhancing optical absorption of metal–organic frameworks for improved visible light photocatalysis. *Chemical Communications* **2013,** *49* (90), 10575-10577.

130. Nguyen, H. L.; Gándara, F.; Furukawa, H.; Doan, T. L.; Cordova, K. E.; Yaghi, O. M., A titanium–organic framework as an exemplar of combining the chemistry of metal–and

covalent–organic frameworks. *Journal of the American Chemical Society* **2016,** *138* (13), 4330-4333.

131.   Nguyen, H. L.; Vu, T. T.; Le, D.; Doan, T. L.; Nguyen, V. Q.; Phan, N. T., A titanium–organic framework: engineering of the band-gap energy for photocatalytic property enhancement. *ACS Catalysis* **2016,** *7* (1), 338-342.

132.   Sun, D.; Liu, W.; Qiu, M.; Zhang, Y.; Li, Z., Introduction of a mediator for enhancing photocatalytic performance via post-synthetic metal exchange in metal–organic frameworks (MOFs). *Chemical Communications* **2015,** *51* (11), 2056-2059.

133.   Wang, C.; Xie, Z.; deKrafft, K. E.; Lin, W., Doping metal–organic frameworks for water oxidation, carbon dioxide reduction, and organic photocatalysis. *Journal of the American Chemical Society* **2011,** *133* (34), 13445-13454.

CHAPTER 2: HETEROGENEOUS PHOTOREDOX SYNTHESIS OF *N*-HYDROXY-OXOAZOLIDINONES CATALYZED BY METAL-ORGANIC FRAMEWORKS

2.1 <u>Introduction</u>

Metal-organic frameworks (MOFs)[1] composed of earth-abundant elements are attractive candidates for organic photoredox catalysis. By taking advantage of MOF self-assembly, complex hierarchical materials chemically decorated with organic moieties can be easily tailored for specific functions.[2-3] MOFs have shown unprecedented success in many applications such as gas storage,[4] separation,[5] sequestration,[6] payload release,[7] light harvesting,[8] ground-state catalysis,[9] and artificial photosynthesis.[10] A much less explored application, photocatalysis, is particularly attractive since MOFs can act as highly efficient and tunable heterogeneous catalysts that enable many unique photoredox reactions. In such reactions,[11] organic functional groups are transformed by a photoredox catalyst that shuttles a light-induced electron transfer. A vast amount of research has been devoted to using catalysts such as Ru and Ir bipyridyl molecular complexes for homogeneous reactions—pioneered by MacMillan,[12] Stephenson,[13] and Yoon.[14] However, because of their reliance on low abundant, high cost transition metals (especially Ir), their application to large-scale industrial processes might be limited. Moreover; homogeneous catalysis, albeit very fast and efficient, requires tedious processes to separate the heavy metals from reaction mixtures and very rarely can the catalyst be recovered. For these reasons, more efficient, selective and recyclable solid-state catalysts that are composed of earth-abundant elements such as Cu, Ti, Al, or Zr are desirable.

Recently, photoredox activity in MOFs has been observed in relatively simple MOFs containing earth-abundant metal ions: Ti^{+4}, Zr^{+4}, Al^{+3}, Cr^{+3}, and Fe^{+3}. Examples of these include

MIL-125,[15] **UiO-66**,[16] and **MIL-53**[17-19] (Figure 2-2; MIL = Materials Institute Lavoisier, UiO = University of Oslo). This activity has shown promise in the photooxidation of functional groups, such as activated alcohols,[20] and thiols,[21] and in the reduction of carbon dioxide.[22] More complex MOFs, isoreticular to **UiO-66** that contain organic linkers with anchored Ru and Ir complexes were reported by Lin *et al.*[23-24] These MOFs display unprecedented photoredox activity towards the generation of hydrogen, reduction of carbon dioxide, formation of iminium ions and oxidation of thiols. While the observation of photoredox activity with Ru and Ir containing MOFs represents a tremendous advancement in the field of MOF photoredox catalysis, the elimination of precious metals from the active catalysts in more complex reactions has not been achieved. We envision that the next generation of photocatalytic MOFs will incorporate inexpensive organic and inorganic constituents, with tunable steric/electronic features to carry out specific chemical transformations.

In this work, we describe how MOFs can be used as photoredox catalysts, to prepare *N*-hydroxy-oxazolidinones from *N*-hydroxy-carbamates (Figure 2-1). When *N*-hydroxy-carbamate **1** is mildly oxidized, a highly reactive transient acyl-nitroso intermediate (**1a**) is formed, which undergoes an intramolecular nitroso-ene reaction with the pendant alkene to form *N*- hydroxy-oxazolidinone **2**. Oxazolidinones such as **2** are key building blocks in organic chemistry for the synthesis of nitrogen containing natural products and pharmaceuticals. These kinds of oxidation/cyclation reactions have been shown to be highly efficient with the use of mild oxidants in the ground state, such as $CuCl/O_2$ [25] or $FeCl_3/H_2O_2$.[26] We envision that MOFs can provide a photocatalytic alternative for substrates that might be sensitive or incompatible with ground state catalysts.
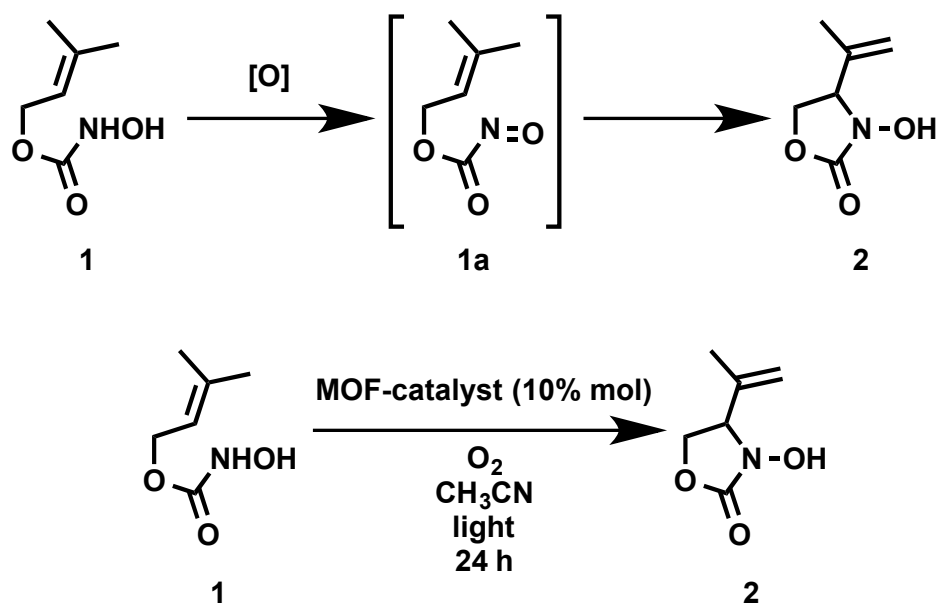
Figure 2-1: Oxidation (top) and MOF-induced photooxidation (bottom) of *N*-hydroxy-carbamates.

2.2 Experimental Section

2.2.1 Materials and methods

All starting materials and solvents, unless otherwise specified, were obtained from commercial sources (Aldrich, Fisher, Strem) and used without further purification. All reactions were performed at ambient laboratory conditions, and no precautions were taken to exclude oxygen or atmospheric moisture unless otherwise specified. Anhydrous acetonitrile (MeCN), and anhydrous *N*,*N*-dimethylformamide (DMF), were purified using a custom-built alumina-column based solvent purification system (Inovative Technology). Anhydrous methanol and anhydrous dioxane were obtained from Aldrich (Sureseal). Mesitylene was dried over activated 4Å molecular sieves. Deuterated solvents (CDCl₃, D₂O, CD₃CN, DCl 30% in D₂O, NaOD 40% in D₂O) were obtained from Cambridge Isotope Lab.

2.2.2 Characterization

High-resolution ^{1}H, and ^{13}C nuclear magnetic resonance (NMR) spectra were recorded using Bruker AVANCE-III 400 MHz spectrometer. The ^{1}H chemical shifts are given relative to tetramethylsilane as zero ppm, calibrated using the residual solvent signal. Data processing was performed using MestReNova (v. 9.0.1). Mass spectra were recorded on an Agilent 6230 TOF LC-MS instrument with an Agilent Zorbax SB-C18 analytical column. Fourier-transform infrared spectra were recorded using a Perkin Elmer Spectrum ONE Universal FT-IR ATR. A total of 32 transients were collected for each sample with a resolution of 0.05 cm^{-1} between 4000-650 cm^{-1}

Powder X-ray diffraction measurements were performed using a Rigaku Miniflex 600 diffractometer, with θ-2θ Bragg-Brentano geometry, and a 600 W (40 kV, 15 mA) Cu X-ray tube source using Kα (λ = 1.5418 Å) radiation, samples were measures from 4 to 40 2θ-degrees with a

step size of 0.02° and a scan rate of 1.5 s per step. Samples were prepared by dropping the powder sample in a glass sample holder and pressing the powder with a razor blade spatula. Measurements were also performed using a PANanalytical Empyrean diffractometer with θ-2θ Bragg-Brentano geometry, and a 1.8 kW (40 kV, 45 mA) Cu X-ray tube source using Kα (λ = 1.5418 Å) radiation, samples were measured from 3 to 40 2θ-degrees with a step size of 0.01671° with spinning sample stage utilizing X'Celerator multi-element detector. Samples were prepared by dropping the powder sample in a zero-background graphite plate and pressing the powder with a razor blade spatula. Simulated of PXRD patterns were calculated using the Reflex module in Materials Studio (v8.0, Biovia) from the CIF file of the respective MOF retrieved from their respective reference.

Scanning Electron Microscopy was performed in a JEOL JSM 6480 microscope at an accelerating voltage of 20 kV operating under low-vacuum mode. Samples were prepared by dispersing powder samples onto sticky carbon surface attached to a flat stainless steel sample holder; excess particulates were removed by tapping the sample holder upside down.

2.2.3   Photocatalytic measurements

Photochemical reactions were carried out in a home-built reactor using a 300 W ozone-free Xe lamp (Newport) equipped with λ > 305 and λ > 385 nm filters to remove lower wavelengths. Reactions at 470 nm were performed utilizing a 60 W blue LED lighting (waterproof LED Flexible Light Strip 12V with 300 SMD 3258 LED, 5 Meter, Amazon). The temperature of the reactor was kept below 30 °C with the aid of an attached fan. Elevated temperatures were achieved by including a temperature programmable stirring plate.

2.2.4 Synthesis

General procedure for the synthesis of 1, 3, 5, 7, 9. 1,1'-Carbonyldiimidazole (6.38 g, 39.4 mmol, 2.0 equiv) was added to a solution of alcohol (1.69 g, 19.7 mmol, 1.0 equiv) in MeCN (50 mL) and stirred, under argon, at room temperature until Thin Layer Chromatography (TLC) indicated complete consumption of the alcohol (typically after 2 h). Imidazole (5.36 g, 78.8 mmol 4.0 equiv) and hydroxylamine hydrochloride (5.48 g, 78.8 mmol, and 4.0 equiv) were added and stirring continued until TLC showed complete consumption of the intermediate. After removal of the reaction solvent, the residue was partitioned between ethyl acetate and 1 M HCl followed by extraction of the aqueous phase with ethyl acetate. The organic phase was washed with brine, dried (Na_2SO_4), filtered, and concentrated under vacuum to afford the crude product, which was purified by flash column chromatography using 40% ethyl acetate-hexane.
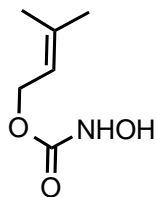
Compound 1: yield: 72%; liquid. ^{1}H NMR (CDCl$_3$, 400 MHz): δ = 7.45 (brs, 2H), 5.36-5.32 (m, 1H), 4.64 (d, J = 7.3 Hz, 2H), 1.75 (s, 3H), 1.71 (s, 3H). ^{13}C NMR (CDCl$_3$, 100 MHz): δ = 159.87, 140.24, 118.30, 63.22, 25.93, 18.20. HRMS (ESI-TOF) m/z calculated for $C_6H_{13}NO_3$ [M+H]$^+$: 146.0812, found 146.0811.
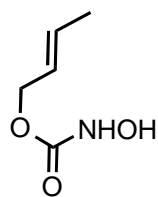
Compound 3: yield: 86%; liquid. ^{1}H NMR (CDCl$_3$, 400 MHz): δ = 7.66 (brs, 1H), 7.62 (brs, 1H), 5.84-5.76 (m, 1H), 5.61-5.53 (m, 1H), 4.55 (dd, J = 6.6, 0.7 Hz, 2H), 1.71 (d, J = 6.5 Hz, 3H). ^{13}C NMR (CDCl$_3$, 100 MHz): δ = 159.62, 132.32, 124.87, 67.02, 17.89. HRMS (ESI-TOF) m/z calculated for C$_5$H$_9$NO$_3$ [M+H]$^+$: 132.0655, found 132.0654.
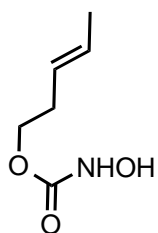
Compound 5: yield: 89%; liquid. ^{1}H NMR (CDCl$_3$, 400 MHz): δ = 7.72 (brs, 1H), 7.59 (brs, 1H), 5.56-5.47 (m, 1H), 5.39-5.32 (m, 1H), 4.13-4.10 (t, J = 7.1 Hz, 2H), 2.30 (q, J = 6.6 Hz, 2H), 1.64 (d, J = 6.3 Hz, 3H). ^{13}C NMR (CDCl$_3$, 100 MHz): δ = 159.79, 128.38, 126.04, 65.98, 32.22, 18.10. HRMS (ESI-TOF) m/z calculated for C$_6$H$_{11}$NO$_3$ [M+H]$^+$: 146.0812, found 146.0813.
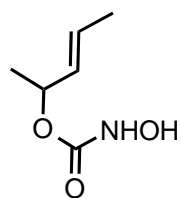
Compound 7: yield: 77%; liquid. ^{1}H NMR (CDCl$_3$, 400 MHz): δ = 7.50 (brs, 2H), 5.78-5.70 (m, 1H), 5.45 (ddd, J = 15.3, 6.9, 1.6 Hz, 1H), 5.28-5.22 (m, 1H), 1.67 (dd, J = 6.5, 0.9 Hz, 3H), 1.30 (d, J = 6.4 Hz, 3H). ^{13}C NMR (CDCl$_3$, 100 MHz): δ = 159.30, 130.45, 129.04, 73.69, 20.52, 17.79. HRMS (ESI-TOF) m/z calculated for C$_6$H$_{11}$NO$_3$ [M+H]$^+$: 146.0812, found 146.0811.

Bu

NHOH

O

O
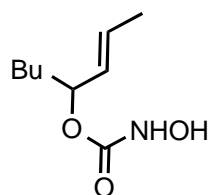
Compound 9: yield: 68%; liquid. ^{1}H NMR (400 MHz, CDCl$_3$) δ = 7.42 (brs, 1H), 5.74 (m, 1H), 5.38 (ddq, J = 15.3, 7.6, 1.6 Hz, 1H), 5.11 (q, J = 6.9 Hz, 1H), 1.68 (ddd, J = 6.5, 1.7, 0.5 Hz, 3H), 1.65-1.60 (m, 1H), 1.56-1.49 (m, 1H), 1.33-1.22 (m, 5H), 0.87 (t, J = 7.0 Hz, 3H). ^{13}C NMR (CDCl$_3$, 100 MHz): δ = 159.44, 130.01, 129.43, 77.60, 34.40, 27.35, 22.57, 17.85, 14.07. HRMS (ESI-TOF) m/z calculated for C$_9$H$_{18}$NO$_3$ [M+H]$^+$: 188.1281, found 188.1293.

General procedure for solvothermal reactions in flame-sealed glass tube vessel. A one m long borosilicate glass tube measuring 10 × 8 mm (o.d × i.d), was divided into six equal portions with a marker. Using a glass cutter, the long tube was cut into three shorter tubes by only cutting every other mark. The cut ends of the tube were etched using an oxygen-propane torch. The final glass tubes were made by melting the intermediate glass tubes at the mark with the torch. After the reactants and solvents were loaded into to the glass tubes, a hose adaptor was used to connect the glass tube to a high vacuum (10 mTorr) using a Schlenk line constructed by fitting the open end of the tube inside a short length of standard rubber hose that was further affixed to a ground glass tap which could be closed to insolate this assembly from dynamic vacuum. The mixture was flash frozen at 77 K (liquid N$_2$), evacuated to an internal pressure of 150 mTorr (± 10 mTorr), and sealed under static vacuum. Upon sealing, the length of the tube was reduced to 18-20 cm; the reactant mixture was allowed to thaw and was placed in an isothermal oven inside a sand bath. After the

55

reaction was complete, the tube was allowed to cool to room temperature and the tube was opened using a glasscutter, and the solids were isolated by filtration.

HKUST-1. Trimesic acid (0.250 g, 1.190 mmol) was dissolved in 50 mL of a 1:1:1 mixture of DMF/Etanol/H_2O in a 250 mL round bottom flask equipped with a magnetic stirrer (Solution A). $CuCl_2(H_2O)_2$ (0.500 g, 2.974 mmol) was dissolved in 50 mL of a 1:1:1 mixture of DMF/EtOH/H_2O (Solution B). Solution B was added drop wise to Solution A at room temperature with stirring. The mixture was stirred for 24 h forming a blue crystalline solid that was isolated by filtration. The solid was rinsed three times with DMF and $CHCl_3$. The blue powder was immersed in $CHCl_3$ and stored 3 days in a desiccator, replacing the solvent six times during this period. The excess solvent was removed by decantation and the solvent-wet powder was dried under dynamic vacuum (10 mTorr) for 24 h at room temperature. The resulting in a bright blue powder was stored under N_2 in a desiccator. Yield: 0.150 g [30% based on $Cu_2(H_2O)_2(C_9H_3O_6)_4$]. FTIR (ATR, cm^{-1}) 664.5, 728.0, 760.0, 994.5, 1082.0, 1106.0, 1256.21, 1372.5, 1432.0, 1448.5, 1611.0, 1635.5.

MIL-53(Al). $AlCl_3$ (0.030 g, 0.225 mmol) was mixed with terephthalic acid (0.037 g, 0.225 mmol) in a borosilicate glass tube. The powders were dissolved in 2.0 mL deionized H_2O and the suspension was mixed in an ultrasonic bath for one minute. The glass tube was flame sealed following the general procedure described above, and heated to 220 °C for 120 hours. After the tube was cooled to room temperature, the solids were separated by filtration, and rinsed three times with DMF and $CHCl_3$. The obtained white powder was immersed in $CHCl_3$ and stored 3 d in a desiccator, replacing the exchange solvent six times during this time. The solvent was removed by decantation and the solvent wet powder was dried under dynamic vacuum (10 mTorr) 24 h at room temperature. The pale yellow solid was stored under N_2 in a desiccator. Yield: 0.029 mg [57

% based on Al(OH)(C$_8$H$_4$O$_4$)$_2$]. FTIR (ATR, cm^{-1}) 730.5, 750.5, 780.0, 822.0, 839.0, 854.5, 880.0, 887.5, 983.5, 1011.5, 1025.5, 1106.0, 1117.5, 1143.5, 1173.5, 1256.5, 1286.0, 1325.5, 1416.0, 1441.0, 1510.0, 1610.5, 1705.5, 3691.0.

MIL-53-NH$_2$(Al). AlCl$_3$ (0.295 g, 2.212 mmol) was mixed with 2-amino-terephthalic acid (0.225 g, 1.242 mmol) in a borosilicate glass tube. The powders were dissolved in 2.0 mL deionized H$_2$O and the suspension was mixed in an ultrasonic bath for one minute. The glass tube was flame sealed following the general procedure described above, and heated to 220 ^{o}C for 120 h. After the tube was cooled to room temperature, the solids were separated by filtration, and rinsed three times with DMF and CHCl$_3$. The obtained white powder was immersed in CHCl$_3$ and stored 3 d in a desiccator, replacing the exchange solvent six times during this time. The solvent was removed by decantation and the solvent wet powder was dried under dynamic vacuum (10 mTorr) 24 h at room temperature. The pale yellow solid was stored under N$_2$ in a desiccator. Yield: 0.027 g [30% based on Al(OH)NH$_2$(C$_8$H$_4$O$_4$)$_2$]. FTIR (ATR, cm^{-1}) 704.0, 755.5, 772.0, 809.0, 818.5, 843.5, 856.5, 890.0, 909.0, 963.5, 1000.5, 1012.0, 1117.5, 1133.5, 1171.5, 1244.5, 1264.0, 1314.0, 1342.5, 1402.0, 1440.5, 1491.5, 1584.5, 1606.0, 1691.5, 3191.0, 3507.5, 3682.0.

UiO-66. ZrCl$_4$ (81.0 mg, 0.348 mmol) was mixed with terephthalic acid (0.058 g, 0.348 mmol) in a 20.0 mL vial. The powders were dissolved in 15.0 mL of anhydrous DMF. The suspension was mixed using an ultrasonic bath for one minute. Water (25.0 µL, 1.392 mmol) was added to the solution. 2.5 mL aliquots were transferred to six borosilicate glass tubes and flame sealed following the general procedure described above. The tube was heated at 120 °C for 24 h yielding a pale yellow solid in a colorless solution. After the tube cooled to room temperature, the solids were separated by filtration and rinsed with three times with DMF and CHCl$_3$. The white

powder was immersed in $CHCl_3$ and stored 3 d in a desiccator, replacing the solvent six times during this period. The solvent was removed by decantation and the solvent wet powder was dried under dynamic vacuum (10 mTorr) 24 h at room temperature. The pale yellow solid was stored under N_2 in a desiccator. Yield: 0.091 g [94 % based on $Zr_6O_4(OH)_4(C_8H_4O_4)_6$]. FTIR (ATR, cm^{-1}) 675.0, 766.0, 836.0, 880.5, 976.5, 1052.5, 1173.0, 1262.5, 1346.5, 1391.0, 1428.5, 1509.0, 1591.0, 1660.5, 3361.0.

UiO-66-NH₂. $ZrCl_4$ (0.080 g, 0.344 mmol) was mixed with 2-amino-terephthalic acid (0.062 g, 0.344 mmol) in a 20.0 mL vial. The powders were dissolved in 20.0 mL of anhydrous DMF. The suspension was mixed in an ultrasonic bath for one minute. Water (25.0 μL, 1.392 mmol) was added to the solution. 2.5 mL aliquots of solution were transferred to eight borosilicate glass tubes and flame sealed following the general procedure described above. The tube was heated at 120 °C for 24 h yielding a yellow solid in a yellow solution. After the tube was cooled to room temperature and the solids were separated by filtration, and rinsed three times with DMF and $CHCl_3$. The yellow powder was immersed in $CHCl_3$ and stored 3 d in a desiccator, replacing the solvent six times during this period. The solvent was removed by decantation and the solvent wet powder was dried under dynamic vacuum (10 mTorr) for 24 h at room temperature. The yellow solid was stored under N_2 in a desiccator. Yield: 0.085 g [84 % based on $Zr_6O_4(OH)_4(C_8H_5NO_4)_6$]. FTIR (ATR, cm^{-1}) 668.0, 707.5, 735.5, 744.0, 789.5, 825.5, 889.0, 1020.5, 1101.0, 1109.5, 1163.0, 1264.0, 1329.5, 1395.5, 1426.0, 1507.5, 1591.0, 1666.0, 3372.0.

MIL-125. Terephthalic acid (0.500 g, 3.012 mmol) was placed in a Teflon Parr reactor acid digestion sleeve and dissolved in anhydrous DMF (9.00 mL). Anhydrous MeOH (0.63 mL) was added to the reactor, followed by $Ti(O^iPr)_4$ (0.213 mL, 0.704 mmol). A stir bar was added and

the mixture was allowed to stir for 30 min at room temperature. The Teflon sleeve was then placed in the stainless-steel reactor vessel and sealed. The sealed reaction tube heated in a 150 ℃ isothermal oven for 20 hours. Upon removal from the oven, the tube was cooled to room temperature and the solids were separated by filtration and rinsed with DMF (~200 mL) and then rinsed three times with MeOH (~200 mL). The obtained white powder was immersed in chloroform and stored 3 days in a desiccator, replacing the exchange solvent eight times during this time. The solvent was removed by decantation and the solvent wet powder was dried under dynamic vacuum (10 mTorr) 24 h at room temperature. The white solid was stored under nitrogen in a desiccator. Yield: 0.125 g [94 % yield based on $Ti_8O_{12}(C_8H_4O_4)_6$]. FTIR (ATR, cm^{-1}) 737.5, 751.5, 777.0, 948.0, 1018.5, 1160.5, 1386.5,1507.5, 1539.0, 1586.0, 1710.5, 3391.0

MIL-125-NH$_2$ (borosilicate glass vessel method). The synthesis was modified from Fu *et al.* [25] 2-amino-terephthalic acid (0.540 g, 2.98 mmol) was placed in a 20 mL disposable scintillation vial with anhydrous DMF (6.5 mL) and mixed thoroughly by immersing the vial in an ultra sonic bath for 1 min. The mixture was separated in equal proportions into two borosilicate glass tubes (see ESI for general method of solvothermal synthesis in flame sealed glass tubes). $Ti(O^iPr)_4$ (0.110 mL, 0.375 mmol), followed by anhydrous MeOH (0.36 mL) were added to the tubes. Immediately after, the tubes were then flash frozen in liquid N_2 and flame sealed. The sealed reaction tubes were heated in an isothermal oven at 150 ℃ for 24 h. Upon removal from the oven, the tubes were cooled to room temperature, the solids were separated by filtration and rinsed with DMF (3x) and CHCl$_3$ (3x). The yellow powder was immersed in CHCl$_3$ and stored 3 d in a desiccator, replacing the solvent during this time (8x). The solvent was removed by decantation and the solvent-wet powder was dried under dynamic vacuum (10 mTorr) for 48 h at room temperature. The degassed yellow solid was stored under N_2 in a desiccator. Yield: 0.102 g [66%

59

yield based on $Ti_8O_{12}(C_8H_5NO_4)_6$]. FTIR (ATR, cm^{-1}) 773.0, 1168.0, 1262.5, 1344.5, 1390.0, 1431.0, 1441.5, 1500.5, 1539.5, 1578.0, 1629.0, 3389.5.

MIL-125-NH$_2$ (PTFE vessel method). The synthesis was modified from Fu *et al.* [25] 2-amino-terephthalic acid (0.560 g, 3.10 mmol) was placed in a in a 20 mL disposable scintillation vial with anhydrous DMF (6 mL) and anhydrous MeOH (1.0 mL) and mixed thoroughly with aid of ultra sonic bath for 1 min. The mixture was transferred to a PTFE-lined steel autoclave (Parr). Ti(O^{i}Pr)$_4$ (0.220 mL, 0.750 mmol) was added, the autoclave was tightly capped and heated to 150 ºC in an isothermal oven for 24 h. Upon removal from the oven, the autoclave was cooled to room temperature and the solids were separated by filtration, and rinsed with DMF (3x) and CHCl$_3$ (3x). The yellow powder was immersed in CHCl$_3$ and stored 3 d in a desiccator, replacing the solvent during this time (8x). The solvent was removed by decantation and the solvent wet powder was dried under dynamic vacuum (10 mTorr) for 24 h at room temperature. The degassed yellow solid was stored under N$_2$ in a desiccator. Yield: 0.088 g [57% yield based on $Ti_8O_{12}(C_8H_5NO_4)_6$]. FTIR (ATR, cm^{-1}) 773.0, 1168.0, 1262.5, 1344.5, 1390.0, 1431.0, 1441.5, 1500.5, 1539.5, 1578.0, 1629.0, 3389.5.

Representative protocol for the photocatalyzed oxidation of 1. Compound **1** (20 mg, 0.138 mmol), **MIL-125-NH$_2$** (3 mg, 0.014 mmol) were loaded in a 4 mL glass vial with a magnetic stirrer, suspended in 1.0 mL of anhydrous MeCN (previously bubbled with O$_2$(*g*) for 20 minutes), and capped with a PTFE septum-cap. The vial was then placed in the photoreactor with a O$_2$(*g*)-filled balloon for positive O$_2$(*g*) pressure, and irradiated at 300 W with stirring for 24 h. The temperature was kept constant below 30 ºC with the aid of a cooling fan. After irradiation, the mixture was filtered through a 0.2 µm nylon syringe membrane (EMD Millipore), rinsed with

CHCl3, and the obtained filtrate was concentrated in a rotary evaporator obtaining a pale oil. ^{1}H

NMR analysis resulted in a mixture of product **2** and starting material **1**. Yield: 19 mg (70% yield

based on recovered starting material, conversion 38% based on ^{1}H NMR.)

1   **2**
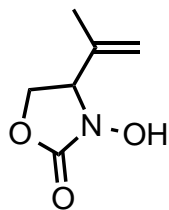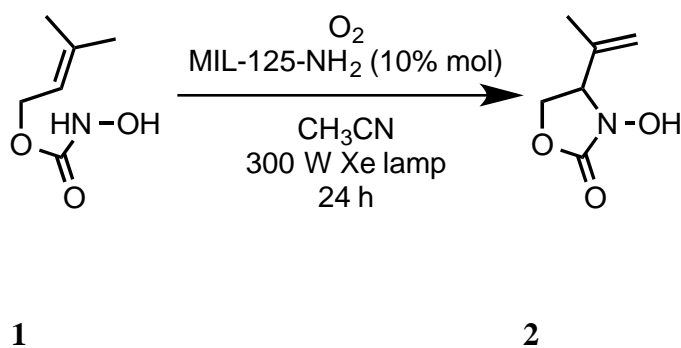
Compound 2: 14 mg (70% yield based on recovered starting material) ^{1}H NMR

(400 MHz, CDCl3) δ = 5.16 - 5.07 (m, 2H), 4.47-4.35 (m, 2H), 4.04 (d, J = 12.1 Hz, 1H), 1.82 -

1.76 (m, 3H). ^{13}C NMR (100 MHz, CDCl3) δ = 160.79 , 139.13 , 117.17 , 65.73 , 65.01 , 17.07 .

HRMS (ESI) m/z calculated for $C_6H_{11}NO_3$ [M+H]$^+$: 144.0661, found 144.0632.
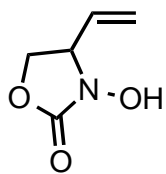
Compound 4: 15 mg (98% yield based on recovered starting material) ^{1}H NMR (CDCl$_3$, 400 MHz): δ = 5.81 (ddd, J = 17.1, 10.2, 7.8 Hz, 1H), 5.55 - 5.38 (m, 2H), 4.43 (dd, J = 8.5, 8.0 Hz, 1H), 4.35 (dtt, J = 9.4, 7.9, 0.7 Hz, 1H), 3.99 (dd, J = 9.1, 8.6 Hz, 1H). ^{13}C NMR (CDCl$_3$, 100 MHz): δ =160.53 , 132.43 , 122.46 , 66.42 , 62.96 . HRMS (ESI-TOF) m/z calculated for C$_5$H$_8$NO$_3$ [M+H]$^+$: 130.0504, found 130.0482.
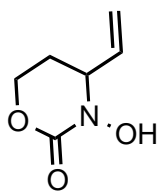
Compound 6: 27 mg (80% yield based on recovered starting material) ^{1}H NMR (CDCl$_3$, 400 MHz): δ = 5.82 (ddd, J = 17.1, 10.3, 6.0 Hz, 1H), 5.46 - 5.28 (m, 2H), 4.33 (q, J = 5.9 Hz, 1H), 4.28 - 4.14 (m, 2H), 2.31 (dddd, J = 13.6, 8.5, 6.5, 4.8 Hz, 1H), 2.02 - 1.90 (m, 1H). ^{13}C NMR (CDCl$_3$, 100 MHz): δ = 154.93 , 135.10 , 118.48 , 63.77 , 60.58 , 28.54 . HRMS (ESI) m/z calculated for C$_6$H$_{10}$NO$_3$ [M+H]$^+$: 144.0661, found 144.0631.
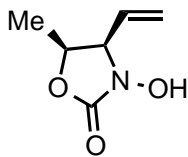
Compound 8a: 6.9 mg (95% yield based on recovered starting material) ^{1}H NMR (400 MHz, CDCl$_3$) δ 5.79 (ddd, J = 16.6, 10.7, 8.6 Hz, 1H), 5.54 – 5.37 (m, 2H), 4.77 – 4.61 (m, 1H), 4.32 (t, J = 8.0 Hz, 1H), 1.33 (d, J = 6.6 Hz, 3H). ^{13}C NMR (100 MHz, CDCl$_3$) δ 160.07,

130.22, 123.08, 73.45, 66.04, 16.16. HRMS (ESI) *m/z* calculated for $C_6H_{11}NO_3$ [M+H]$^+$: 144.0661, found 144.0628.
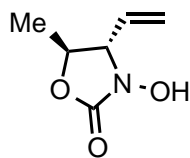
Compound 8b: 3.4 mg (95% yield based on recovered starting material) ^{1}H NMR (400 MHz, CDCl$_3$) δ 5.77 (ddd, *J* = 17.1, 10.2, 8.0 Hz, 1H), 5.54 – 5.40 (m, 2H), 4.22 (dq, *J* = 9.4, 6.2 Hz, 1H), 3.87 – 3.80 (m, 1H), 1.45 (d, *J* = 6.2 Hz, 3H). ^{13}C NMR (100 MHz, CDCl$_3$) δ 132.49, 122.86, 74.88, 70.71, 29.86, 17.82, 1.17, (there is an expected but unobserved resonance at *ca.* 160 ppm). HRMS (ESI) *m/z* calculated for $C_6H_{11}NO_3$ [M+H]$^+$: 144.0661, found 146.0627.
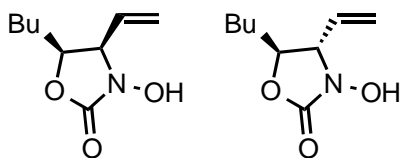
Compounds 10a,b: 12% conversion observed as a mix of diasteromers.

2.2.5 Kinetic measurements

The kinetics of the photochemical reactions were performed in triplicate. Compound **1** (20 mg, 0.138 mmol), dry mesitylene (14 µL, 12 mg, 0.102 mmol), and **MIL-125-NH₂** (3 mg, 0.014 mmol) were loaded in a 4 mL glass vial with a magnetic stirrer. The mixture was dissolved in 1.0 mL of CD$_3$CN, and capped with a PTFE septum-cap. The suspension was bubbled with O$_2$(*g*)

while stirred in the dark for 20 min. The vial was then placed in the photoreactor with an $O_2(g)$-filled balloon for positive $O_2(g)$ pressure, and irradiated at 300 W with stirring. The temperature was kept below 30 ºC with the aid of a cooling fan. At each time interval, a 20 µL aliquot of reaction suspension was sampled, and diluted with 500 µL of $CDCl_3$ and filtered through a 0.2 µm PTFE filter membrane (EMD Millipore) into an NMR tube. Samples were obtained at times 0, 1, 2, 4, 6, 8, 10, 12, 24 and 36 h. After NMR data collection, the intensity of the mesitylene peak was normalized to 100, thus the intensities of the α-ether methylene proton signal in compound **1** (δ = 4.55 ppm) and terminal alkene proton signals in compound **2** (δ = 4.38 ppm) correspond to their concentration in mmol L^{-1}.

2.2.6 Photochemical Quantum Yields

The photochemical quantum yields (Φ_{rxn}) were determined using the decomposition of *p*-cresol by TiO_2 (Degussa P25) in deuterium oxide as standard ($\Phi_{p\text{-}cresol}$ = 0.22 ± 0.04). According to the IUPAC protocol by Serpone *et al.*[27] the photo-chemical quantum yield of a hetereogeneous reaction is defined as:

$$\Phi_\lambda = \frac{R^{in}}{R_{o,\lambda}}$$

$$(2\text{-}1)$$

Where Φ_λ is the photochemical quantum yield at a given wavelength λ, R^{in} is the initial rate of the photochemical reaction, and $R_{o,\lambda}$ is the incident photon flow reaching the reactor at a given wavelength λ. In this context, the quantum yield of a photochemical reaction can be calculated as:

$$F_{rxn} = \frac{R^{in}(reaction)}{R^{in}(stardard)} F_{std}$$

<div align="right">(2-2)</div>

Where R^{in}(*reaction*) is the initial rate of the reaction expressed as substrate consumption and R^{in}(*standard*) is the initial rate of the decomposition of *p*-cresol and Φ_{std} is the photochemical quantum yield of the standard reaction.

p-cresol/TiO$_2$ standard reaction. The initial rate of the decomposition of p-cresol by TiO$_2$ was performed in triplicate. In a 4.0 mL vial equipped with a PTFE stirring bar, p-cresol (38.8 μL, 40 mg, 0.37 mmol) were suspended in 2.0 mL of D$_2$O (for a 185 mM concentration), then 20 μL of 0.10 M DCl in D$_2$O were added (to a pD = 3), followed by the addition of Aeroxide P25 TiO$_2$ (Evonik Degussa, 4.0 mg, 0.05 mmol). The vial was left uncapped and the suspension was stirred in the dark for 5 minutes to allow p-cresol/TiO$_2$ adsorption and O$_2$(g) water/air equilibrium. In parallel, a 92.5 mmol L^{-1} solution of dioxane in D$_2$O was prepared as a standard to calculate the concentration of p-cresol. Anhydrous dioxane (17.1 μL, 16.3 mg 0.185 mmol) was dissolved in 2.0 mL of D$_2$O. At each time point of the photocatalytic degradation of p-cresol, 40 μL of the reaction suspension were transferred to a test tube, followed by adding 20 μL of the dioxane standard, the mixture was diluted with 500 μL of D$_2$O and filtered through a 0.2 μm PTFE filter membrane (EMD Millipore) into an NMR tube. We added dioxane solution as post-reaction standard due to photodegradation of dioxane by TiO$_2$. After NMR data collection, the intensity of the dioxane peak was normalized to 185, thus the intensity of the aromatic peaks would correspond to the concentration of p-cresol. Similarly, the intensity of the methyl peak was multiplied by a 2/3 factor. The intensity of all peaks was averaged for each time point, resulting in the p-cresol concentration. The slope of the of [p-cresol] vs. time corresponds to the R^{in}(*standard*).

2.3 <u>Results and Discussion</u>

We prepared a library of known MOFs (Figure 2-2) with non-noble elements and simple organic linkages, which are chemically and photochemically stable and will not dissolve, decompose, or collapse under the reaction conditions. The prepared MOFs are: **HKUST-1** (HKUST = Hong Kong University of Science and Technology), **MIL-53**, **UiO-66** and **MIL-125**. **HKUST-1** is constructed with 1,3,5-benzene-tricarboxylate organic linker and copper (II) as the metal center.[28] This MOF was selected because its wide use as ground state catalyst,[29-30] and literature precedents of copper (II) mediated oxidation of *N*-hydroxy-carbamates.[25] **MIL-53**, **UiO-66** and **MIL-125** are constructed with terephthalate as linker and Al^{+3}, Zr^{+4} and Ti^{+4} as the metal centers, respectively. Additionally, we prepared **MIL-53-NH₂**, **UiO-66-NH₂**, and **MIL-125-NH₂**, which are isoreticular to the previous three, but with 2-amino-terephthalate as the organic linker. The absorption spectrum of MOFs that are functionalized with 2-amino- terephthalate have been shown to exhibit a red shift with respect to the non-functionalized counterparts.[31] Such spectroscopic shift has been attributed to smaller bandgaps.[32] Moreover, these materials have demonstrated to have higher photocatalytic activities, *e.g.* in the oxidation of benzyl alcohols.[31]
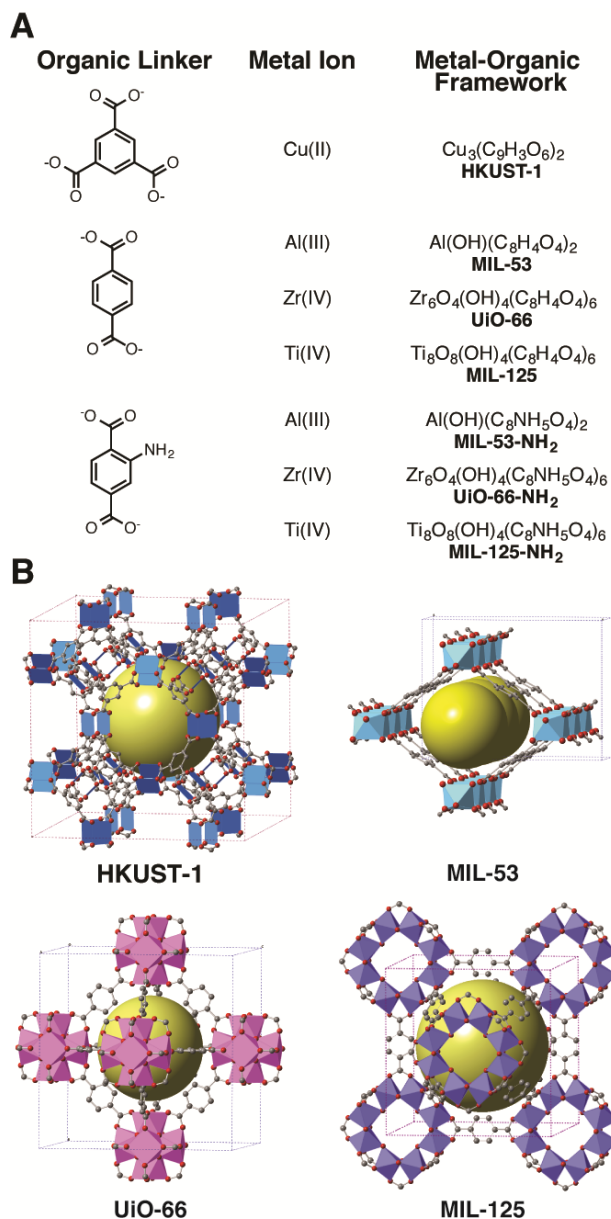
Figure 2-2; Organic linkers, metal ions, and compositions (A), and crystal structures (B) of the MOFs utilized in this study. Spheres: gray = carbon, red = oxygen. Polyhedra: blue = Cu(II), light blue = Al(III), pink = Zr(IV), purple = Ti(IV). Hydrogen and nitrogen are not shown for clarity. Yellow sphere is included to illustrate the size of the pore cavity.

Table 2-1: Photooxidation of **1** with MOFs photocatalysts.[a] Conditions[a]: 0.15 M of **1** in CH_3CN with O_2 (sat.), 300 W Xe-lamp ($\lambda > 305$ or 385 nm) or 60 W blue LED ($\lambda = 470$ nm), 24 h, 25 ℃. Conversion determined by ^{1}H NMR. [b]Entry 10 after re-subjection with fresh MOF and the same conditions. [c]After 96 h.

Entry	MOF	Illumination	Gas	Conversion (%)
1	none	$\lambda > 305$ nm	O_2	0
2	**HKUST-1**	dark	O_2	0
3	**HKUST-1**	$\lambda > 305$ nm	O_2	6
4	**MIL-53**	$\lambda > 305$ nm	O_2	13
5	**UiO-66**	$\lambda > 305$ nm	O_2	3
6	**MIL-125**	$\lambda > 305$ nm	O_2	3
7	**MIL-53-NH₂**	$\lambda > 305$ nm	O_2	16
8	**UiO-66-NH₂**	$\lambda > 305$ nm	O_2	26
9	**MIL-125-NH₂**	$\lambda > 305$ nm	O_2	38
10	**MIL-125-NH₂**	$\lambda > 305$ nm	O_2	50[b]
11	**MIL-125-NH₂**	dark	O_2	0
12	**MIL-125-NH₂**	$\lambda > 305$ nm	Ar	14
13	**MIL-125-NH₂**	$\lambda > 385$ nm	O_2	54[c]
14	**UiO-66-NH₂**	$\lambda > 385$ nm	O_2	43[c]
14	**MIL-125-NH₂**	Blue LED	O_2	24[c]
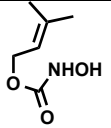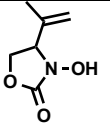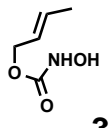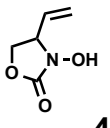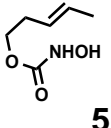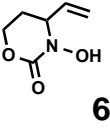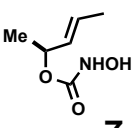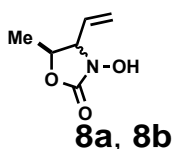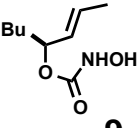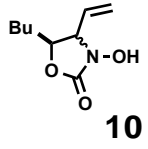
We surveyed the photocatalytic activity of the prepared MOFs towards the oxidation of **1** using a Xe lamp (Newport) with UV-visible ($\lambda > 305$ nm), visible light ($\lambda > 385$ nm), and with blue LED light ($\lambda = 470$ nm). Our experimental protocol allows for easy removal of the catalyst by filtration, followed by solvent evaporation. No further purification is required. In contrast; traditional methods in homogeneous catalysis require expensive column chromatography and have poor catalyst recovery. As shown in Table 1, irradiation of **1** with $\lambda > 305$ nm in CH_3CN with O_2 for 24 h (control), resulted in zero conversion to **2** (Table 1, entry 1), thus the reaction does not occur in the absence of photoredox catalysts. Adding catalytic amounts of **HKUST-1** (10 mol% based on the metal) under similar conditions, resulted in zero conversion to oxazolidinone **2** when the reaction was performed in the dark (entry 2) and only a trace amount of **2** was formed with $\lambda > 305$ nm (entry 3); therefore, the copper (II) embedded in the MOF is unable to interact with the *N*-hydroxy-carbamate; a major difference from Cu mediated oxidations.[32] When using MOFs with non-functionalized terephthalate, **MIL-53**, **UiO-66** and **MIL-125**, only small amounts of **2** were observed (entries 4-6). However, by using the 2-amino-terephthalate isoreticular MOFs, a significant jump in conversion to 16%, 28% and 38%, was observed for **MIL-53-NH₂**, **UiO-66-NH₂** and **MIL-125-NH₂** (entries 7-9). These higher conversions with respect to the non-functionalized MOFs are consistent with the broader red-shifted trend in the photoabsorption.[25] Upon replenishing a new batch of **MIL-125-NH₂** to the crude reaction mixture, improved conversion up to 50% was observed (entry 10), suggesting a limited catalyst lifetime. Performing the reaction with **MIL-125-NH₂** in the dark (control) resulted in no conversion (entry 11). Replacing oxygen from the reaction with argon (entry 12), a significant decrease in conversion was also observed, evidencing the need of an electron sink to regenerate the catalyst. This observation is consistent with other studies that have shown that CO_2 can also be used as an

69

electron acceptor.[33] The use of UV-visible light ($\lambda > 305$ nm) for periods of time longer than 24 h resulted in the appearance of other byproducts, most probably from the photoinduced decomposition alkenes in **1** and **2**, from the presence of highly reactive oxidizing species (see below). The damaging effect of the UV light was alleviated by utilizing visible ($\lambda > 385$ nm), and blue light (LED, $\lambda = 470$ nm). In this case, similar conversions for both **UiO-66-NH₂** and **MIL-125-NH₂** were obtained but only after 96 h: 54 and 43%, with visible light for **MIL-125-NH₂** and **UiO-66-NH₂**, respectively, and 24% with blue LED light for **MIL-125-NH₂**, light with energy slightly above the bandgap of **MIL-125-NH₂** ($E_g = 475$ nm).[31] Only starting material and product were obtained, and little or no decomposition byproducts were observed when utilizing visible light, indicating a clean, and byproduct free reaction.

The scope of the reaction was explored with the conditions that provided higher conversions in shorter times (Table 1 entry 9), and the results are summarized in Table 2. A variety of substrates were tested, including **1** and substrates with varying tether sizes and side chains. The photooxidation of **1** (entry 1) produces **2** in 38% conversion and 70% isolated yield, which was calculated based on recovered starting material. Compound **3** (entry 2), which contains a less reactive alkene, can be transformed to the corresponding oxazolidinone **4** in similar conversion and yield. Increasing the ring size or steric hindrance around the carbamate (entries 3-5), results in significant lower conversion (25% for 6-member ring, 20% and 12% for secondary carbamates).

Table 2-2: Substrate scope for the photooxidation of N-hydroxy-carbamates using MIL-125-NH$_2$.
[a]Conditions: 0.15 M of N-hydroxy-carbamate in CH$_3$CN with O2 (sat.), 10% mol MIL-125-NH$_2$, 300 W Xe-lamp ($\lambda > 305$ nm), 24 h, 25 ºC. [b] Yields are based on recovered starting material, conversion was determined by ^{1}H NMR. [c] Unpurified diasteromer mixture.

Entry	N-hydroxy-carbamate	Product	Yield (Conversion)[b]
1	**1**	**2**	70% (38%)
2	**3**	**4**	98% (34%)
3	**5**	**6**	80% (25%)
4	**7**	**8a**, **8b**	72% (20%) 2:1 dr
5	**9**	**10**	-[c] (12%) 2:1 dr

For substrates **7** and **9**, the nitroso-ene reaction produced a pair of diasteromers and a 2:1 dr was observed for both reactions, which corresponds to the substrate-induced diasteromer ratio observed in solution.[25-26] Given that increasing the molecular size of substrates results in lower conversions, and that the MOF does not induce any particular diasteroselectivity beyond the observed in solution, we suspect that the photocatalytic reaction is not occurring inside the cavities of the MOF, and probably only occurring at or near the surface of solid catalyst particles.

We prepared samples of **MIL-125-NH₂** under different synthetic conditions to probe the effect of the macroscopic particle size and texture,[34] and to provide more evidence to our hypothesis of the catalytic reaction occurring at the MOF particle surface. We observed major differences in the photocatalytic efficiency when **MIL-125-NH₂** was prepared in borosilicate glass tubes or in poly-tetrafluoroethylene (PTFE) vessels. MOF samples that were synthesized in glass tubes yielded the reported conversions of 38 ± 4%; however, **MIL-125-NH₂** prepared in PTFE vessels observed much lower conversions for the photooxidation of **1** (8.3 ± 0.8%). Scanning electron microcopy imaging of both samples (Figures A8-A11) revealed qualitative differences in the sample particle sizes and morphologies. MOF synthesized in glass tubes yielded much smaller and less agglomerated particles than samples prepared in PTFE vessels. PXRD patterns of the MOF prepared under the different reaction vessels revealed no significant difference (Figure 2-3), thus it is very likely that the catalysis occurs at the MOF particle-solvent interphase.

To understand the observed trends in conversion and diasteroselectivity, we performed reaction kinetics study and heterogeneous quantum yield determination. We obtained the concentration of **1** and **2** at different time points using the MOFs with the highest conversions: **MIL-125-NH₂** and **UiO-66-NH₂** (in triplicate), with $\lambda > 305$ nm in CD₃CN. Figure 2-4A displays

the observed ^1H NMR spectra over a 36 h kinetic study using **MIL-125-NH₂**. The indicated

hydrogen signals in **1** and **2** were used to calculate concentrations using mesitylene as internal

standard.[35] These traces indicate the progressive disappearance of **1** with the respective appearance

of **2**. The concentration vs. time plots for both MOFs (Figure 2-4B) exhibit a zero-order rate law

up to 8 h with rate constants of -32.9 ± 4.4 μmol L^{-1} min^{-1} and -40.0 ± 4.2 μmol L^{-1} min^{-1},

respectively for the consumption of **1**. Very similar rate constants (32.9 ± 2.9 μmol L^{-1} min^{-1} and

23.2 ± 1.7 μmol L^{-1} min^{-1}) are obtained for the appearance of **2** from **MIL-125-NH₂** and **UiO-66-**

NH₂, respectively. The similar rate constants for the consumption of **1** and appearance of **2** imply

a clean MOF catalyzed oxidation and nitroso-ene cascade. Typical heterogeneous reactions exhibit

pseudo zero-order rate laws in concentrated conditions,[36] confirming that it is likely the

photooxidation of the *N*-hydroxy-carbamate and the nitroso-ene additions occurs at the surface of

the MOF particles; rather than inside the pores of the MOF. The turnover numbers and frequencies

of the MOF catalysts could be obtained as a function of the number of moles of **2** produced per

mole of catalyst used with respect to the metal ion in the MOF, resulting in turnover numbers

around 1000 after 8 h, and turnover frequencies of 2.35 ± 0.20 min^{-1} and 1.66 ± 0.12 min^{-1},

indicating that the reaction is catalytic.
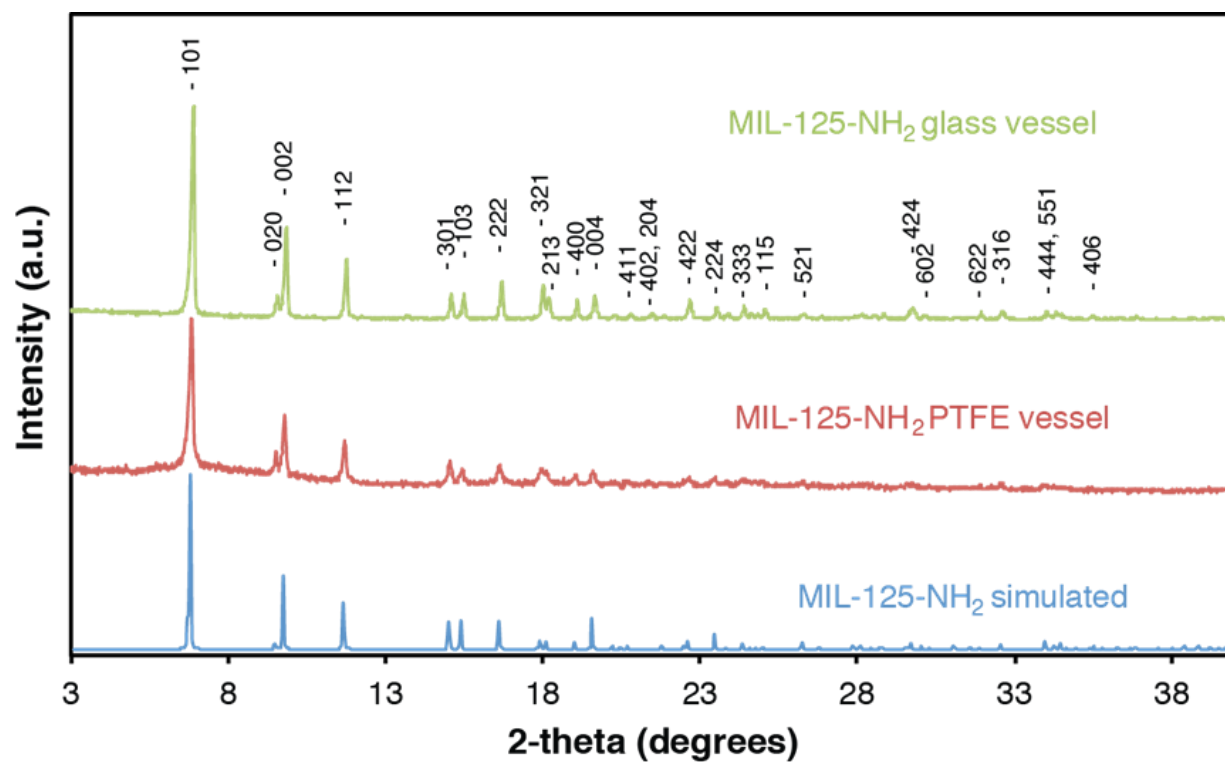
Figure 2-3: PXRD of MIL-125-NH$_2$ as synthesized from both glass and PTFE vessel methods. Peaks are indexed and compared to simulated pattern from single crystal data.
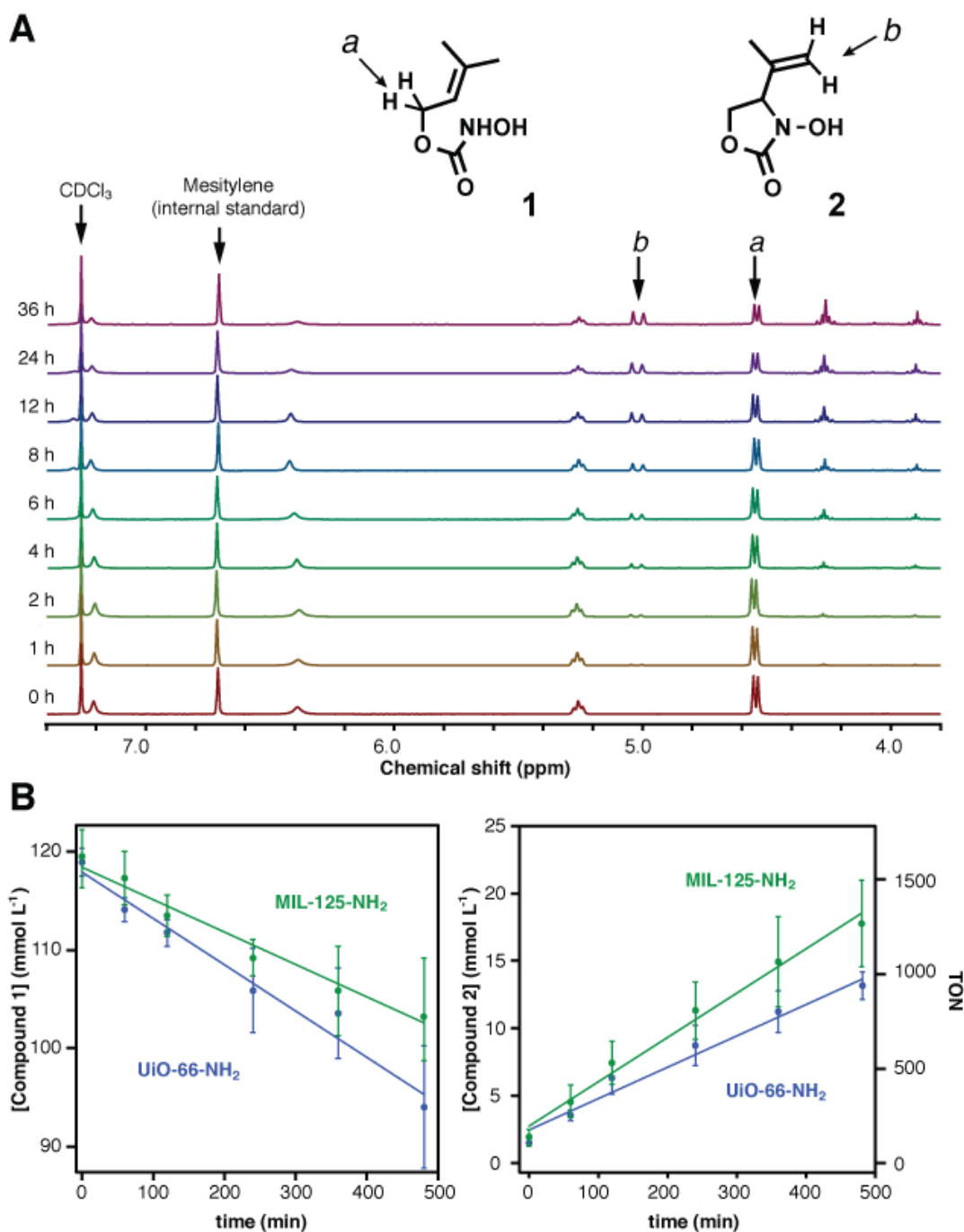
Figure 2-4: A ^{1}H NMR traces of the photooxidation of 1 vs. time using MIL-125-NH$_2$ ($\lambda > 305$ nm). The hydrogen signals used for quantification are indicated for 1 and 2 (other signals not indicated for clarity). B. Kinetic plots for the consumption of 1 (left) and the appearance of 2 (right) using MIL-125-NH$_2$ (green) and UiO-66-NH$_2$ (blue) up to 8 h. The turnover numbers of the catalysts are shown with respect to the appearance of 2 (far right). Data points are the average of three measurements and error bars correspond to one standard deviation. Mesitylene was used as internal standard.

75

The efficiency of the photocatalysis was determined measuring the photochemical quantum yield by heterogeneous actinometry. The heterogeneous photochemical quantum yield of our reaction (Φ_{rxn}) was obtained by following the IUPAC protocol developed by Serpone $et\ al.$,[27] which assumes a pseudo homogeneous treatment of the quantum yield, defined as the rate of chemical events per rate of photons absorbed by the catalyst. Using a standard heterogeneous chemical reaction with known quantum yield Φ_{std}, the photochemical quantum yield can be evaluated by:

$$\mathsf{F}_{rxn} = \frac{R^{in}(rxn)}{R^{in}(std)} \mathsf{F}_{std}$$

(2-2)

where $R^{in}(rxn)$ and $R^{in}(std)$ correspond to the initial rate of starting material consumption of the reaction of interest, and that of a standard reaction, respectively. This method of quantum yield determination is recommended in order to account for the scattering effects of the solid catalysts and the effects of reactor geometry. By using the photochemical decomposition of p-cresol in water by TiO_2 (P25) (Figure 2-5) as standard ($\Phi_{std} = 0.22 \pm 0.04$, $\lambda = 325$ nm), we determined its initial rate of decomposition (Table 2-3, entry 1) and thus the quantum yields of the photooxidation of **1** by **MIL-125-NH₂** and **UiO-66-NH₂** (entries 2, 3). These observed yields suggest that MOFs with proper molecular designs can produce better photoredox catalysts. If the chemical reaction occurs within the MOF cavity, but not at the surface of the crystallite, the reaction kinetics and quantum yield will have a strong correlation with temperature, since higher temperature will facilitate the mass transport inside the MOF pore by allowing faster diffusion of starting materials and products. Reaction kinetics studies performed at 50 and 60 °C yielded increased zero-order rate constants. However, Arrhenius analysis of the rate constants vs. temperature (See appendix A), resulted in

an observed bulk activation energy of $E_a = 8.23$ kJ mol^{-1}. This value is in agreement with the activation energy of photocatalytic reactions (typically <10 kJ mol^{-1}), which is related to the diffusion of the solvent. This temperature dependence is consistent with the photoredox process as the limiting step,[37] which is also encountered in non-porous heterogeneous catalysts, such as TiO$_2$.

We further explored the nature of the photogenerated reactive species that appear during irradiation and are responsible for the oxidation of the *N*-hydroxy-carbamate. For this purpose we added to reaction mixtures an excess amount (10 eq. and $\lambda > 305$ nm) of chemical scavengers that are known to quench specific reactive species.[38] If a targeted reactive species is generated, it will be immediately quenched by the additive and it will be unable to promote the oxidation of **1** to **1a**, thus the conversion to **2** will be significantly reduced. It has been shown by others,[15,39] that the photoirradiation of **MIL-125-NH₂** produces a charge-separated excited state where the positive "hole" is localized in the aromatic organic ligand and is highly oxidant, and the "electron" is localized in a Ti ion of the metal-oxide cluster and is responsible for the reduction of molecular O$_2$ to superoxide. This "hole" can be quenched by the oxalate anion, and the Ti^{III} "electron" can be quenched with persulfate. Adding ammonium oxalate, and potassium persulfate indeed reduces the conversion from $36.7 \pm 3.9\%$ to $17.7 \pm 3.1\%$ and $13.3 \pm 0.6\%$ respectively (Figure 2-6), confirming the presence of these species. Superoxide anion can be quenched by benzoquinone and derivatives; however, benzoquinones can react with nitroso compounds,[40] so we were unable to observe superoxide quenching by chemical means. Nonetheless, the superoxide anion has been observed in photoirradiated **UiO-66**[41] and **MIL-125**,[15] so we believe that superoxide is also generated and contributes to the oxidation of **1**.
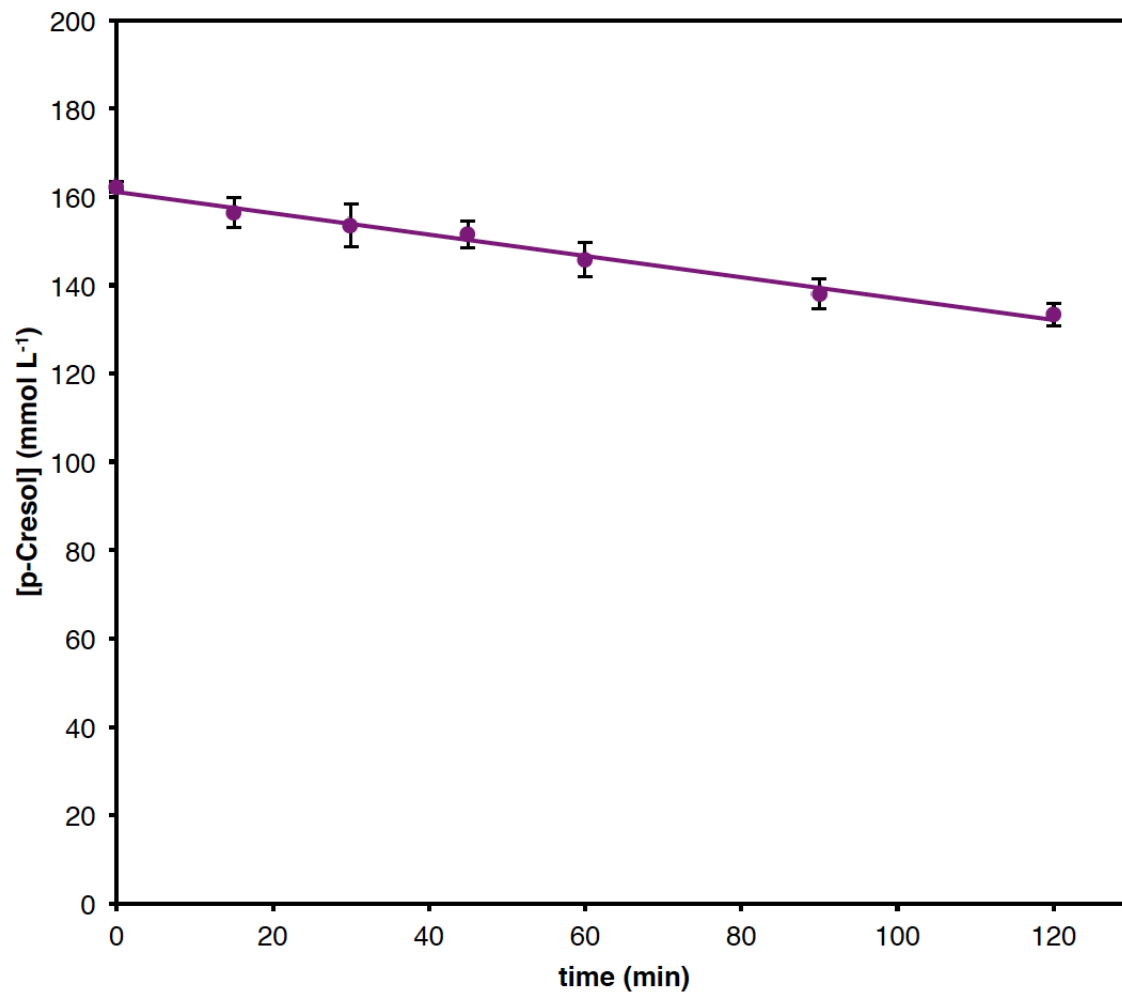
Figure 2-5: Kinetic plot of the standard photodecomposition of p-cresol by TiO_2. Each point corresponds to the average of 3 runs; error bars correspond to one standard deviation.

Table 2-3: Photochemical quantum yields. [a]Standard reaction: Decomposition of p-cresol in DCl/D_2O (pD = 3.0) with TiO_2 (P25) with O_2 and 300 W Xe-lamp (λ > 305 nm) at 25 ºC. More details in the ESI.[24]

Entry	Catalyst	R^{in} (µmol L^{-1} min^{-1})	Φ_{rxn}
1[a]	TiO_2 (P25)	-239 ± 19	0.22 ±0.04
2	**MIL-125-NH$_2$**	-32.9 ± 4.4	0.030± 0.007
3	**UiO-66-NH$_2$**	-40.0 ± 4.2	0.037 ± 0.008
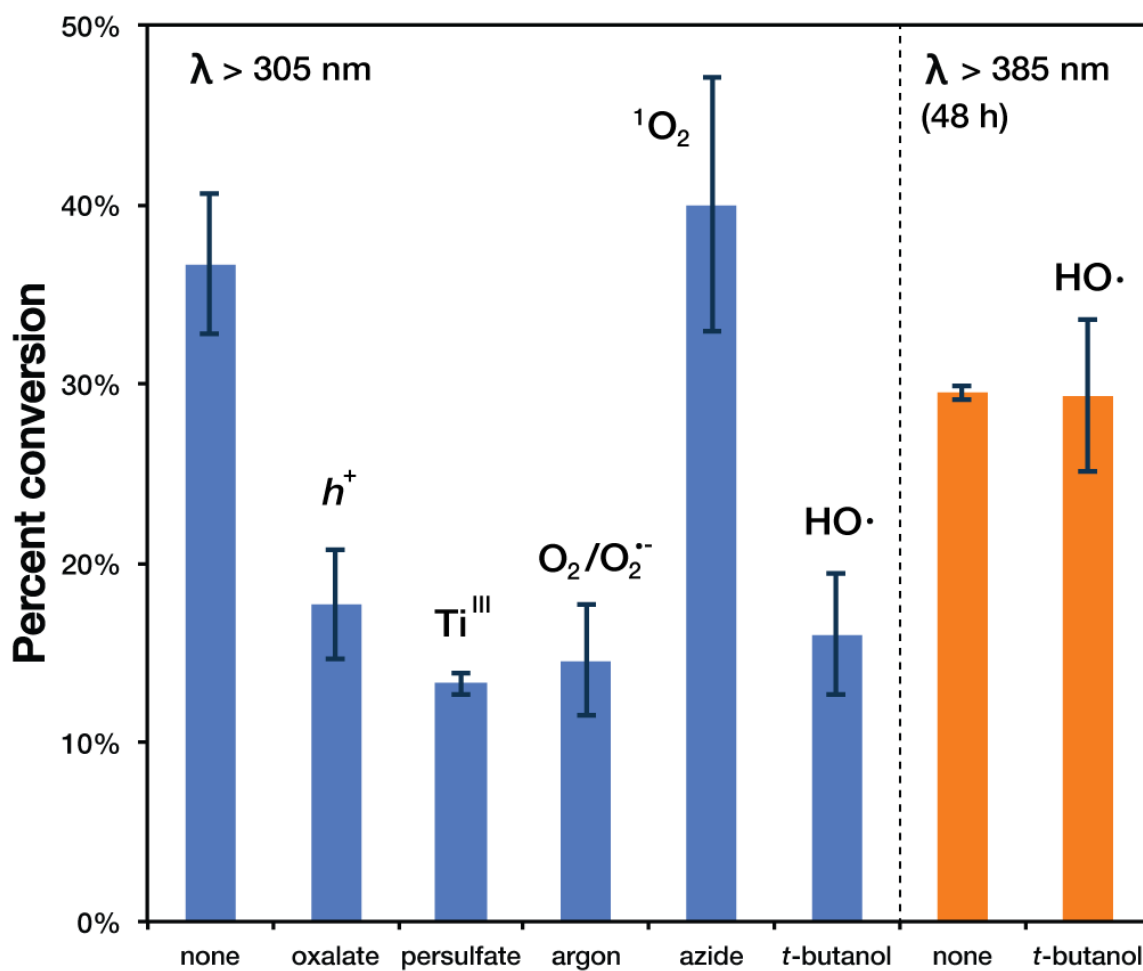
Figure 2-6: Chemical quenching of photogenerated reactive species in **MIL-125-NH$_2$**. Same conditions as in Table 2 Entry 1 (blue traces) plus 10 equivalents of the respective quencher (oxalate = (NH$_4$)$_2$C$_2$O$_4$, persulfate = K$_2$S$_2$O$_8$, azide = NaN$_3$). Reactions at $\lambda > 385$ nm (orange traces) were run for 48 h. All measurements were performed in triplicate, and conversion determined by ^{1}H NMR.

Performing the reaction under argon also reduces the conversion to **2**, suggesting that reduced oxygen also participates in the oxidation. Other possible reactive species that can appear are the highly reactive singlet oxygen and hydroxyl radical, which can be quenched by N_3^- and *tert*-butanol, respectively. Adding excess of sodium azide results in no change in conversion (40.0 ± 7.1%) with respect to the unquenched reaction; therefore, no singlet oxygen is photogenerated. When adding *tert*-butanol as quencher of the hydroxyl radical, we observed significant quenching of the reaction to 16.0 ± 3.4%, so this species also is generated during photoirradiation, and it is perhaps the species responsible for 48 h (29.5 ± 0.4%). This wavelength dependent hydroxyl radical formation is also consistent with the observed photostability of the reaction mixture when the catalysis is performed at $\lambda > 385$ nm; furthermore, it is also possible that the hydroxyl radical generated UV- for the degradation of **1** and **2** after a long irradiation time. To assess this observation, we performed hydroxyl radical quenching with visible light only ($\lambda > 385$ nm) and we did not observe changes in conversion (29.3 ± 4.2%) with respect to the unquenched reaction after irradiating visible light is responsible for the degradation of the 2-amino-terephthalate in **MIL-125-NH₂** photocatalyst.

The structural integrity of the MOFs was determined by powder X-ray diffraction patterns after their removal from the reaction mixtures, and display no change in the diffraction patterns in the case of **MIL-125-NH₂**, **UiO-66-NH₂**, and **HKUST-1** (Figures A5-A7). Furthermore, ^{1}H NMR spectra of crude filtered mixture do not exhibit peaks from the organic linkers. We also observed that reutilizing **MIL-125-NH₂** resulted in decreased conversions, from 30% to 18% to 7% in successive recycling of the same photocatalyst sample. PXRD analysis resulted in no structural change. Moreover, samples of the exhausted catalyst with UV-visible light digested in NaOD 0.1 M in D_2O (Figure 2-7), exhibited ^{1}H NMR signals that correspond to those of the pure ligand and

the pristine MOF. Recycling **MIL-125-NH₂** ten times resulted in the loss of the molecular structure of the 2-amino-terephtalate as well as the diffraction pattern of the MOF. Performing photocatalysis reactions under aerobic conditions it is possible for the $-NH_2$ group to oxidize to $-NO_2$; however, the ^{1}H NMR of 2-nitro-terephthalate in NaOD 0.1 M in D_2O (Figure 2-7), does not relate to the digested exhausted MOF. We suspect that the observed hydroxyl radical participates in the oxidation of the organic linker.

2.4 <u>Conclusion</u>

In summary, we have studied the photoredox activity of chemically stable earth-abundant MOFs towards the oxidation of nitroso intermediates for the subsequent ene reaction for the synthesis of oxazolidinones. We determined that simple MOFs such as **MIL-125-NH₂** and **UiO-66-NH₂**, are able to catalyze the photooxidation in decent conversion, quantum yield and good isolated yields. The oxidation is likely to occur at the surface of the MOF and be very sensitive to steric factors and it is sensitive to the catalysts method of synthesis, probably due to particle size and morphology. The recovery of the photocatalysts is relatively simple; however, the recycled MOF only showed marginal activity. This loss of activity may be related to the chemical stability of the MOF under oxidation conditions and UV light. Study of the photogenerated reactive species revealed the presence of holes, superoxide ion, and hydroxyl radical as oxidant species, with generation of hydroxyl radical that is wavelength dependent. Future optimizations in catalyst stability, particle size non-dependence, and quantum yields are currently under investigation.
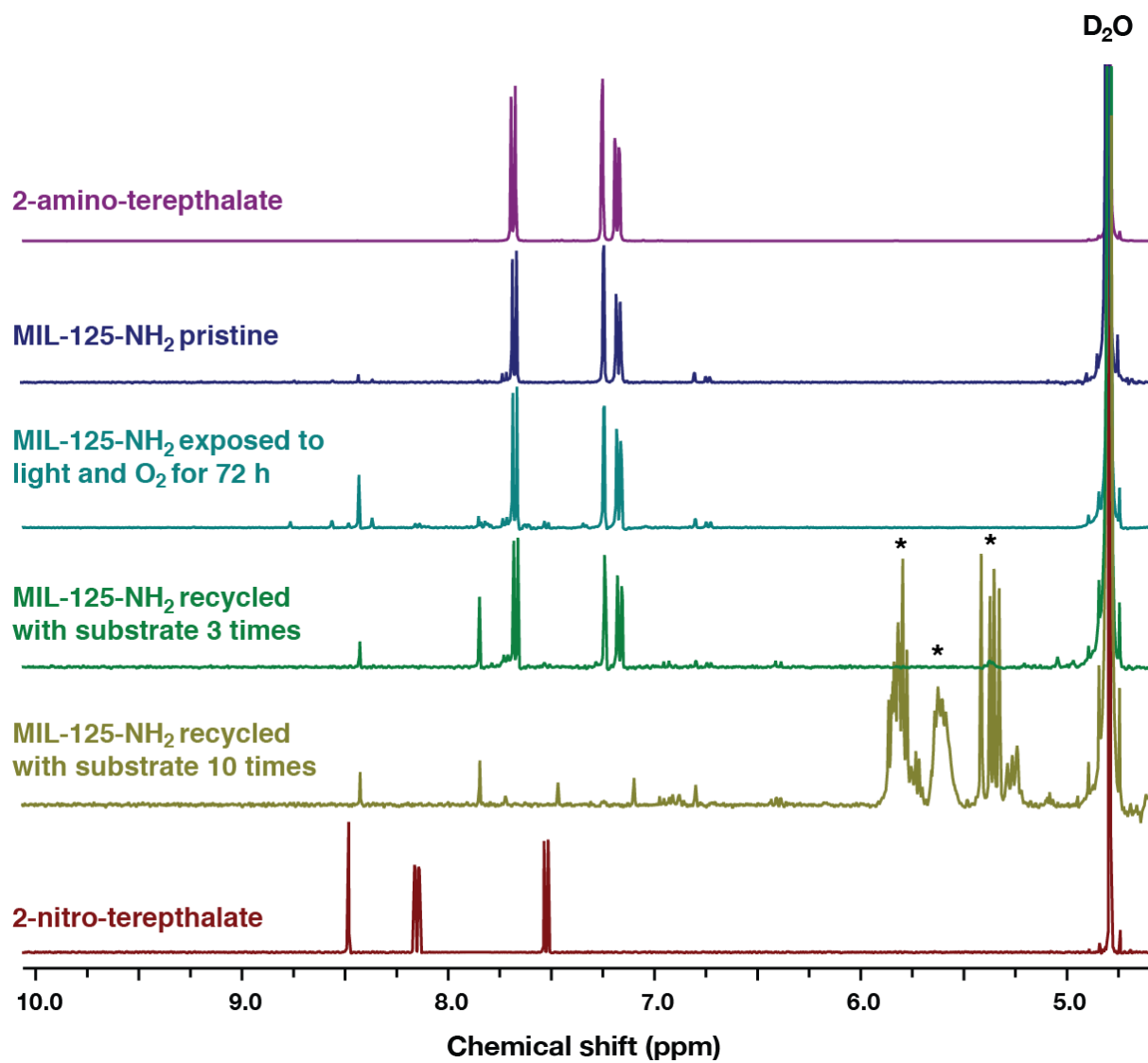
Figure 2-7: ^{1}H NMR spectra of 2-amino-terephtalate, samples of MIL-125-NH$_2$ at different catalyst stages ($\lambda > 305$ nm), and 2-nitro-terephthalate in NaOD 0.1 M/D$_2$O (400 MHz, 25 ºC). Stars indicate signals that are related to **1** and **2**.

2.5 <u>References</u>

1. Furukawa, H.; Cordova, K. E.; O'Keeffe, M.; Yaghi, O. M., The chemistry and applications of metal-organic frameworks. *Science* **2013,** *341* (6149), 1230444.

2. Zhou, H.-C.; Long, J. R.; Yaghi, O. M., Introduction to metal–organic frameworks. ACS Publications: 2012.

3. Kong, X.; Deng, H.; Yan, F.; Kim, J.; Swisher, J. A.; Smit, B.; Yaghi, O. M.; Reimer, J. A., Mapping of functional groups in metal-organic frameworks. *Science* **2013,** *341* (6148), 882-885.

4. Suh, M. P.; Park, H. J.; Prasad, T. K.; Lim, D.-W., Hydrogen storage in metal–organic frameworks. *Chemical Reviews* **2011,** *112* (2), 782-835.

5. Li, J.-R.; Sculley, J.; Zhou, H.-C., Metal–organic frameworks for separations. *Chemical Reviews* **2011,** *112* (2), 869-932.

6. Sumida, K.; Rogow, D. L.; Mason, J. A.; McDonald, T. M.; Bloch, E. D.; Herm, Z. R.; Bae, T.-H.; Long, J. R., Carbon dioxide capture in metal–organic frameworks. *Chemical Reviews* **2011,** *112* (2), 724-781.

7. Horcajada, P.; Gref, R.; Baati, T.; Allan, P. K.; Maurin, G.; Couvreur, P.; Ferey, G.; Morris, R. E.; Serre, C., Metal–organic frameworks in biomedicine. *Chemical Reviews* **2011,** *112* (2), 1232-1268.

8. Lee, C. Y.; Farha, O. K.; Hong, B. J.; Sarjeant, A. A.; Nguyen, S. T.; Hupp, J. T., Light-harvesting metal–organic frameworks (MOFs): efficient strut-to-strut energy transfer in bodipy and porphyrin-based MOFs. *Journal of the American Chemical Society* **2011,** *133* (40), 15858-15861.

9.   Liu, J.; Chen, L.; Cui, H.; Zhang, J.; Zhang, L.; Su, C.-Y., Applications of metal–organic frameworks in heterogeneous supramolecular catalysis. *Chemical Society Reviews* **2014,** *43* (16), 6011-6061.

10.   Zhang, T.; Lin, W., Metal–organic frameworks for artificial photosynthesis and photocatalysis. *Chemical Society Reviews* **2014,** *43* (16), 5982-5993.

11.   Prier, C. K.; Rankic, D. A.; MacMillan, D. W., Visible light photoredox catalysis with transition metal complexes: applications in organic synthesis. *Chemical Reviews* **2013,** *113* (7), 5322-5363.

12.   Nicewicz, D. A.; MacMillan, D. W., Merging photoredox catalysis with organocatalysis: the direct asymmetric alkylation of aldehydes. *Science* **2008,** *322* (5898), 77-80.

13.   Narayanam, J. M.; Stephenson, C. R., Visible light photoredox catalysis: applications in organic synthesis. *Chemical Society Reviews* **2011,** *40* (1), 102-113.

14.   Yoon, T. P.; Ischay, M. A.; Du, J., Visible light photocatalysis as a greener approach to photochemical synthesis. *Nature Chemistry* **2010,** *2* (7), 527.

15.   Dan-Hardi, M.; Serre, C.; Frot, T.; Rozes, L.; Maurin, G.; Sanchez, C.; Férey, G., A new photoactive crystalline highly porous titanium (IV) dicarboxylate. *Journal of the American Chemical Society* **2009,** *131* (31), 10857-10859.

16.   Cavka, J. H.; Jakobsen, S.; Olsbye, U.; Guillou, N.; Lamberti, C.; Bordiga, S.; Lillerud, K. P., A new zirconium inorganic building brick forming metal organic frameworks with exceptional stability. *Journal of the American Chemical Society* **2008,** *130* (42), 13850-13851.

17. Loiseau, T.; Serre, C.; Huguenard, C.; Fink, G.; Taulelle, F.; Henry, M.; Bataille, T.; Ferey, G., A rationale for the large breathing of the porous aluminum terephthalate (mil-53) upon hydration. *Chemistry-A European Journal* **2004,** *10* (6), 1373-1382.

18. Serre, C.; Millange, F.; Thouvenot, C.; Nogues, M.; Marsolier, G.; Louër, D.; Férey, G., Very Large Breathing Effect in the First Nanoporous Chromium (III)-Based Solids: MIL-53 or CrIII (OH)⊙{O2C− C6H4− CO2}⊙{HO2C− C6H4− CO2H} x⊙ H2O y. *Journal of the American Chemical Society* **2002,** *124* (45), 13519-13526.

19. Du, J.-J.; Yuan, Y.-P.; Sun, J.-X.; Peng, F.-M.; Jiang, X.; Qiu, L.-G.; Xie, A.-J.; Shen, Y.-H.; Zhu, J.-F., New photocatalysts based on MIL-53 metal–organic frameworks for the decolorization of methylene blue dye. *Journal of Hazardous Materials* **2011,** *190* (1-3), 945-951.

20. Nasalevich, M. A.; Goesten, M. G.; Savenije, T. J.; Kapteijn, F.; Gascon, J., Enhancing optical absorption of metal–organic frameworks for improved visible light photocatalysis. *Chemical Communications* **2013,** *49* (90), 10575-10577.

21. Johnson, J. A.; Zhang, X.; Reeson, T. C.; Chen, Y.-S.; Zhang, J., Facile control of the charge density and photocatalytic activity of an anionic indium porphyrin framework via in situ metalation. *Journal of the American Chemical Society* **2014,** *136* (45), 15881-15884.

22. Lee, Y.; Kim, S.; Kang, J. K.; Cohen, S. M., Photocatalytic CO 2 reduction by a mixed metal (Zr/Ti), mixed ligand metal–organic framework under visible light irradiation. *Chemical Communications* **2015,** *51* (26), 5735-5738.

23. Wang, C.; Xie, Z.; deKrafft, K. E.; Lin, W., Doping metal–organic frameworks for water oxidation, carbon dioxide reduction, and organic photocatalysis. *Journal of the American Chemical Society* **2011,** *133* (34), 13445-13454.

24.   Wang, C.; Zhang, T.; Lin, W., Rational synthesis of noncentrosymmetric metal–organic frameworks for second-order nonlinear optics. *Chemical Reviews* **2011,** *112* (2), 1084-1104.

25.   Frazier, C. P.; Engelking, J. R.; Read de Alaniz, J., Copper-catalyzed aerobic oxidation of hydroxamic acids leads to a mild and versatile acylnitroso ene reaction. *Journal of the American Chemical Society* **2011,** *133* (27), 10430-10433.

26.   Atkinson, D.; Kabeshov, M. A.; Edgar, M.; Malkov, A. V., Intramolecular carbonyl nitroso ene reaction catalyzed by iron (III) chloride/hydrogen peroxide as an efficient tool for direct allylic amination. *Advanced Synthesis & Catalysis* **2011,** *353* (18), 3347-3351.

27.   Serpone, N.; Salinaro, A., Terminology, relative photonic efficiencies and quantum yields in heterogeneous photocatalysis. Part I: Suggested protocol. *Pure and Applied Chemistry* **1999,** *71* (2), 303-320.

28.   Chui, S. S.-Y.; Lo, S. M.-F.; Charmant, J. P.; Orpen, A. G.; Williams, I. D., A chemically functionalizable nanoporous material [Cu3 (TMA) 2 (H2O) 3] n. *Science* **1999,** *283* (5405), 1148-1150.

29.   Lee, J.; Farha, O. K.; Roberts, J.; Scheidt, K. A.; Nguyen, S. T.; Hupp, J. T., Metal–organic framework materials as catalysts. *Chemical Society Reviews* **2009,** *38* (5), 1450-1459.

30.   Granato, T.; Testa, F.; Olivo, R., Catalytic activity of HKUST-1 coated on ceramic foam. *Microporous and Mesoporous Materials* **2012,** *153*, 236-246.

31.   Hendon, C. H.; Tiana, D.; Fontecave, M.; Sanchez, C. m.; D'arras, L.; Sassoye, C.; Rozes, L.; Mellot-Draznieks, C.; Walsh, A., Engineering the optical response of the titanium-MIL-125 metal–organic framework through ligand functionalization. *Journal of the American Chemical Society* **2013,** *135* (30), 10942-10945.

32.   Chaiyaveij, D.; Cleary, L.; Batsanov, A. S.; Marder, T. B.; Shea, K. J.; Whiting, A., Copper (II)-Catalyzed Room Temperature Aerobic Oxidation of Hydroxamic Acids and Hydrazides to Acyl-Nitroso and Azo Intermediates, and Their Diels–Alder Trapping. *Organic Letters* **2011,** *13* (13), 3442-3445.

33.   Fu, Y.; Sun, D.; Chen, Y.; Huang, R.; Ding, Z.; Fu, X.; Li, Z., An Amine-Functionalized Titanium Metal–Organic Framework Photocatalyst with Visible-Light-Induced Activity for CO2 Reduction. *Angewandte Chemie* **2012,** *124* (14), 3420-3423.

34.   Hu, S.; Liu, M.; Li, K.; Zuo, Y.; Zhang, A.; Song, C.; Zhang, G.; Guo, X., Solvothermal synthesis of NH 2-MIL-125 (Ti) from circular plate to octahedron. *CrystEngComm* **2014,** *16* (41), 9645-9650.

35.   A, S. A.

36.   Dos Santos Afonso, M.; Stumm, W., Reductive dissolution of iron (III)(hydr) oxides by hydrogen sulfide. *Langmuir* **1992,** *8* (6), 1671-1675.

37.   Gaya, U. I., *Heterogeneous photocatalysis using inorganic semiconductor solids*. Springer Science & Business Media: 2013.

38.   Suib, S. L., *New and Future Developments in Catalysis: Solar Photocatalysis*. Newnes: 2013.

39.   de Miguel, M.; Ragon, F.; Devic, T.; Serre, C.; Horcajada, P.; García, H., Evidence of Photoinduced Charge Separation in the Metal–Organic Framework MIL-125 (Ti)-NH2. *ChemPhysChem* **2012,** *13* (16), 3651-3654.

40.   Forrester, A.; Thomson, R., Reaction of quinones with nitrosoarenes. *Zeitschrift für Naturforschung B* **1985,** *40* (11), 1515-1518.

41. Shen, L.; Liang, S.; Wu, W.; Liang, R.; Wu, L., Multifunctional NH 2-mediated zirconium metal–organic framework as an efficient visible-light-driven photocatalyst for selective oxidation of alcohols and reduction of aqueous Cr (vi). *Dalton Transactions* **2013,** *42* (37), 13649-13657.

CHAPTER 3: SYSTEMATIC VARIATION OF THE OPTICAL BANDGAP IN TITANIUM BASED ISORETICULAR METAL-ORGANIC FRAMEWORKS FOR PHOTOCATALYTIC REDUCTION OF CO₂ UNDER BLUE LIGHT

3.1 Introduction

The accumulation of carbon dioxide in the atmosphere as a result of human activity is one of the largest contributing factors in the gradual warming of the Earth.[1] Our planet has a natural system of negative feedback processes to balance these accumulations, primarily by carbon fixation through photosynthesis. However, the amount of carbon dioxide already in the atmosphere is far too large for natural photosynthesis to reduce its accumulation in the short term. Therefore, it is urgent that technologies be developed that are capable of fixating large quantities of CO_2 into organic matter, which are both energetically efficient and capable of creating a usable feedstock of reduced carbon (so-called solar fuel).[2-6] These new technologies require the use of a naturally abundant and sustainable source of energy. Early transition metal oxides, in particular titanium oxides, are capable of reducing CO_2 when excited by UV light.[7] Using sunlight to reduce CO_2 directly would be ideal; however, the majority of the suns rays are in the visible-IR range,[8] which is too low energy to induce photoreduction with these materials, limiting their applicability on environmentally relevant scales. Thus, materials that are able to reduce CO_2 with the use of visible light are an imminent and currently unfulfilled need.

Metal-organic frameworks (MOFs)[9] are a class of porous materials composed of metal-oxide clusters connected through organic links forming highly crystalline open structures that offer a promising alternative to metal-oxide semiconductor photocatalysis. Research in the design and

synthesis of new MOFs (reticular chemistry[10]) has allowed for the creation of functional materials with unprecedented high porosity (surface areas up to 10 000 m^2 g^{-1})[11] and exceptional chemical and thermal stability, with applications in gas storage,[12] gas separation,[13-14] heterogeneous catalysis,[15-16] payload release,[17] and sensing,[18] among others. MOFs are materials with extraordinary chemical and functional versatility, because both the organic and inorganic components can be systematically varied towards targeted applications in a systematic manner.[19-20]

Titanium based MOFs in particular, combine the photocatalytic activity of titanium oxide clusters with the light absorption properties of organic linkers, producing materials that can be photocatalytically active under UV-visible light.[21-28] These catalytic reactions are facilitated through either oxidative,[21, 29-30] or reductive[31-33] photoinduced electron transfer within the Ti-MOF under irradiation. MIL-125-NH$_2$ (MIL = Materials Institut Lavoisier) is a titanium-based MOF constructed from 2-aminoterephthalate and a Ti_8O_{12} ring-shaped cluster (Figure 3-1) that has shown activity towards photocatalytic reduction of carbon dioxide.[34] The biggest challenge in increasing and optimizing this activity for operating in the visible range relies on tuning the bandgap (or HOMO-LUMO gap) of this material (E_g = 2.56 eV). De Miguel *et al.* established that photo irradiation of MIL-125-NH$_2$ with UV-visible light produces a long-lived charge-separated state whose lifetime is directly related to photocatalytic activity.[35] Moreover, it has been demonstrated through high-level DFT calculations that this charge-separated excited state is accessible due to the difference in electronic distribution of the frontier bands/orbitals.[36-39] Hendon *et al.* propose that in this particular MOF, the top of the valence band—or HOMO—is localized in the aromatic ring of the 2-aminoterephthatalate, and the bottom of the conduction band—or LUMO—is localized in the *d*-states of the titanium ions favoring charge separation upon

91

photoexcitation.[36] They also propose that a strategy to decrease the bandgap of this MOF (and thus redshifting the absorption more into the visible range) is by destabilizing the valence band by increasing the electron density in the π-cloud of the terephthalate. It has been previously demonstrated that incorporating 2,5-diaminoterephthalate and 2-aminoterephthalate into the MIL-125 framework effectively decreases the optical bandgap. Other efforts include post synthetic modification of MIL-125-NH$_2$ via diazotization of the amine followed by addition of an electron-rich aniline forming diazo-based groups on the surface of the MOF particles, which exhibit enhanced photooxidation of benzyl alcohols.[29]

Here, we report the synthesis of a family of titanium MOFs isoreticular to MIL-125-NH$_2$, where the amine functionality is decorated with alkyl chains of varying length and connectivity, *i.e.*, methyl, ethyl, isopropyl, *n*-butyl, cyclopentyl, cyclohexyl, and *n*-heptyl (Figure 3-1). Our rationale for this functionalization strategy relies on the hypothesis that sequential addition of carbon atoms in the *N*-alkyl amino group will result in increased electron density in the terephthalate ring as a consequence of subtle inductive effects. These are well-known electronic effects that result from the polarization of a chemical species through σ-bonds due to differences in electronegativity between a heteroatom (in this case nitrogen) and the carbon atoms in the alkyl chains. Moreover, these effects should be more evident in secondary and tertiary alkyls.[40] Thus, increasing the number of σ-bonds in the chain should result in larger electron density around the nitrogen atom in 2-aminoterephthalate, causing an increased density in the aromatic ring, and therefore destabilizing the top of the valence band. By successively destabilizing the valence band in small steps, the bandgap of the MOFs should decrease, and higher photocatalytic activity can be achieved under visible light irradiation.
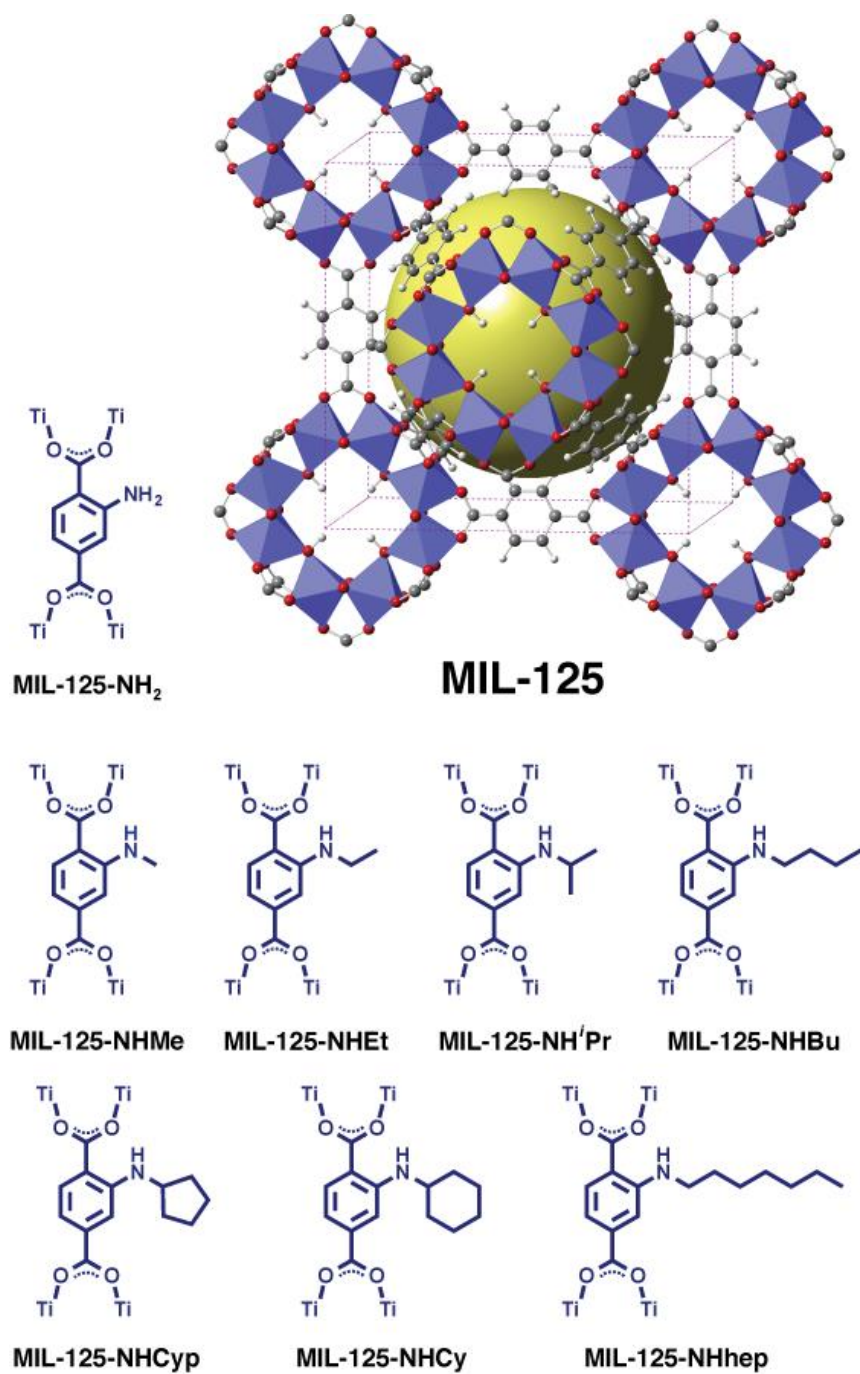
Figure 3-1: Top: Crystal structure of the parent MOF MIL-125 utilized in this study. Bottom: Molecular structure of the organic link in MIL-125-NH$_2$ and the N-substituted isoreticular MOFs prepared in this work. Gray spheres = carbon, white = hydrogen, red = oxygen, blue polyhedral = titanium, the yellow sphere represents the size of the pore in the MOF.

We studied the effect of the *N*-alkyl substitution on the CO_2 adsorption, as well as the photophysical and photocatalytic properties of the materials, particularly the absorption onset, and excited state lifetimes. These parameters were also studied to understand the photocatalytic activity towards reduction of CO_2 utilizing visible light only, in the form of blue LEDs.

3.2 <u>Experimental Section</u>

All starting materials and solvents, unless otherwise specified, were obtained from commercial sources (Aldrich, Fisher, VWR) and used without further purification. All reactions were performed at ambient laboratory conditions, and no precautions were taken to exclude oxygen or atmospheric moisture unless otherwise specified. Anhydrous *N,N*-dimethylformamide (DMF) and tetrahydrofuran (THF) were purified using a custom-built alumina-column based solvent purification system (Inovative Technology). Anhydrous methanol was obtained from Aldrich (Sureseal). Mesitylene and hexamethylphosphoramide (HMPA) were dried over activated 4Å molecular sieves. Deuterated solvents (CDCl$_3$, DMSO, D$_2$O, CD$_3$CN, NaOD 40% in D$_2$O) were obtained from Cambridge Isotope Lab.

3.2.1   Instrumentation

High-resolution ^1H and ^{13}C nuclear magnetic resonance (NMR) spectra were collected using Bruker AVANCE-III 400 MHz spectrometer. The chemical shifts are reported relative to solvent residual signal. NMR data analysis was preformed using MestReNova (*v*. 10.0.2). Liquid chromatography-mass spectra (LC-MS) were recorded using Agilent 6230 TOF with an Agilent Zorbax SB-C18 analytical column. Fourier-transform infrared spectra were performed using a Perkin Elmer Spectrum ONE Universal FT-IR ATR. 32 scans were collected for each sample at a resolution of 120000 cm^{-1} from 4000-650 cm^{-1}. Scanning electron microscopy (SEM) was

conducted using a JEOL JSM 6480 microscope on low-vacuum with an accelerating voltage of 20 kV. Sample preparation involved the dispersion of samples upon carbon tape attached to stainless steel sample holder.

Powder X-ray diffraction (PXRD) data was collected using a Rigaku MiniFlex 600 θ-2θ diffractometer in Bragg-Brentano geometry with a 300 mm goniometer diameter, Ni-filtered CuKα radiation (λ = 1.5418 Å) at 600 W power (40 kV, 15 mA), equipped with a NaI(Tl) SC-70 scintillation detector, 5.0° incident and receiving Soller slits, a 0.625° divergent slit, a 1.25° scattering slit, a 0.3 mm receiving slit and a Ni-CuKβ filter. Samples were analyzed from 3 to 40 2θ-degrees with 0.02° per step and a scan rate of 0.25 2θ-degrees min^{-1}. Samples were prepared by dropping the powder sample in a glass sample holder and pressing the powder with a razor blade spatula forming a smooth surface. Crystal models were created using Materials Studio modeling suite[41] starting from the published crystal of MIL-125 (CCDC code RUPRUQ)[21] by adding the corresponding *N*-alkyl chains. Rietveld refinements were performed with the modeled crystals and the experimental patterns using *GSAS-II* (see SI for more details).[42]

Gas adsorption isotherm analysis was performed using a Micromeritics ASAP 2020 surface area and porosimetry analyzer. Measurements were performed at 77 K (liquid N_2 bath) for $N_2(g)$, and at 273, 283 and 298 K (water circulator bath) for $CO_2(g)$ on thermally activated samples. Brunauer-Emmet-Teller (BET) surface areas were obtained by performing a Rouquerol analysis over the linear isotherm to determine the upper limits of the BET model from the N_2 isotherms. Least squares linear fitting over the BET plot provided the parameter for the volume of the monolayer, BET surface area and *C*-constant were obtained following the recommendation by Snurr *et al*. for determination of the surface area in MOFs.[43] Differential enthalpies of CO_2

adsorption were obtained by fitting the isotherms at the three measured temperatures into a virial equation using the Micromeritics data processing software.

Solid-state absorption spectra were collected at room temperature using an Edinburgh FLS980 spectrometer with the integrating sphere accessory. Light output from a housed 450 W Xe lamp was passed through a single grating (1800 λ mm^{-1}, 250 nm blaze) Czerny-Turner monochromator and then into the integrating sphere containing powder MIL-125-NHR sample or scattering reference (BaSO$_4$). The output from the integrating sphere was passed through a single grating (1800 $\square$/mm, 500 nm blaze) Czerny-Turner and finally detected by a peltier-cooled Hamamatsu R928 photomultiplier tube. Synchronous spectral scans were performed with both excitation and emission monochromators, with zero wavelength offset, stepping through the pre-set spectral range. Absorbance was then calculated using Edinburgh's F900 software package. Tauc plots were obtained assuming $\alpha(\text{h}\nu) = (\text{A}\text{h}\nu)^2$.

Transient Absorption (TA) Measurements: Samples for TA were prepared by suspending MIL-125-NHR in ~3.0 mL of MeCN in a 1 cm × 1 cm quartz cuvette (A ≈ 0.2 O.D.). Measurements were performed on a spectrometer composed of a Continuum Surelite EX Nd:YAG laser combined with a Continuum Horizon OPO (λ_{ex} = 405 nm, 5-7 ns, operated at 1 Hz, beam diameter ~0.5 cm, 5 mJ/pulse) integrated into a commercially available Edinburgh LP980 laser flash photolysis spectrometer. White light probe pulses generated by a pulsed 150 W Xe lamp were passed through the sample, focused into the monochromator, and then, for full spectrum data, were detected by intensified Andor iStar CCD camera. Single wavelength kinetic absorption at 500 nm were detected by a photomultiplier tube with a 435 nm long pass filter placed before the detector to reject unwanted scattered light. Detector outputs were processed using a Tektronix

TDS3012C Digital Phosphor Oscilloscope interfaced to a PC. Single wavelength kinetic data were the result of averaging 50 laser shots. Detector outputs were processed using Edinburgh's L900 (version 8.2.3, build 0) software package. Time-resolved absorption data were fit with the exponential function in equation 1 where τ is the lifetime.

$$I = I_o e^{-t/\tau} \tag{3-1}$$

3.2.2 Synthesis

*Synthesis of N-alkyl-2-amino-terephthalate dimethyl ester (**1a-d, 1g**).* 2-amino-terepthlate dimethyl ester (2.00 g, 9.56 mmol) was suspended in anhydrous DMF (20 mL) and stirred until fully dissolved (HMPA was used instead of DMF for **1g**). K_2CO_3 (5.30 g, 38.2 mmol) was added, followed by dropwise addition of alkyl iodide (14.3 mmol), and the mixture was stirred for 18 h at 100 ºC. The reaction mixture was then cooled to room temperature and quenched with 2 M HCl (*aq*) to a pH = 3. The mixture was extracted with EtOAc (3 × 50 mL), the combined organic extracts were washed with brine (3 × 50 mL), dried over anhydrous $MgSO_4$, filtered through celite and the solvent was removed using a rotary evaporator. The obtained crude was purified using flash chromatography (SiO_2, 15% *v/v* EtOAc:hexanes, dry loading).

*Synthesis of N-cycloalkyl-2-amino-terephthalate dimethyl ester (**1e, 1f**).* Under N_2 (*g*) in a 25 mL two-neck round bottom flask with a magnetic stir bar, 2-aminoterepthlate dimethyl ester (1.00 g, 4.78 mmol) was suspended in anhydrous DMF (3.2 mL) and stirred until fully dissolved. TMSCl (1.30 g, 11.95 mmol) and the corresponding cyclic ketone (5.25 mmol) were added to the solution and the mixture was cooled to 0 ºC in an ice bath. $NaBH_4$ (0.18 g, 4.78 mmol) was added cautiously over 5 min. The mixture was then allowed to warm up to room temperature and monitored by TLC until disappearance of starting material. The mixture was quenched with

97

saturated NaHCO₃ (*aq.*) followed by extraction with EtOAc (3 × 10 mL). The combined organic

fractions were then washed with brine (3 × 10 mL) and dried over MgSO₄, filtered through celite

and the solvent was removed using a rotary evaporator. The obtained crude was purified using

flash chromatography (SiO₂, 5-10% *v/v* EtOAc:hexanes, dry loading).
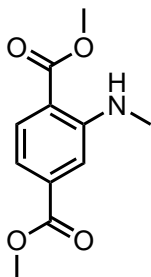
Compound 1a: Yellow solid, yield 0.89 g (45%). ^{1}H NMR (400 MHz, CDCl₃) δ = 7.84 (dd, J =

8.3, 1.7 Hz, 1H), 7.61 (br, NH), 7.24 (s, br, 1H), 7.11 (d, J = 8.3 Hz, 1H), 3.85 (s, 3H), 3.79 (s,

3H), 2.88 (d, J = 5.2 Hz, 3H). ^{13}C NMR (100 MHz, CDCl₃) δ = 168.34, 166.77, 151.48, 134.99,

131.52, 114.59, 112.87, 111.83, 52.15, 51.58, 29.49. HRMS (ESI-TOF) *m/z* calculated for

C₆H₁₃NO₃ [M+H]⁺: 224.0917, found 224.0921.
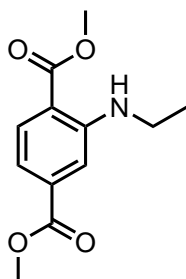
Compound 1b: Yellow solid, yield 0.80 g (40%). ^{1}H NMR (400 MHz, CDCl$_3$) δ = 7.89 (d, J = 8.3

Hz, 1H), 7.59 (br, NH), 7.29 (d, J = 1.7 Hz, 1H), 7.13 (dd, J = 8.3, 1.6 Hz, 1H), 3.87 (s, 3H), 3.83

(s, 3H), 3.24 (qd, J = 7.2, 4.9 Hz, 2H), 1.30 (t, J = 7.2 Hz, 3H). ^{13}C NMR (100 MHz, CDCl$_3$) δ =

168.51, 166.97, 150.74, 135.09, 131.68, 114.54, 112.75, 112.41, 52.26, 51.68, 37.51, 14.47.

HRMS (ESI-TOF) m/z calculated for C$_6$H$_{13}$NO$_3$ [M+H]$^+$: 238.1074, found 238.1055.
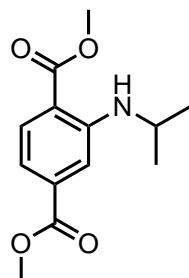
Compound 1c: Yellow solid, yield 0.67 g (34%). ^{1}H NMR (400 MHz, CDCl$_3$) δ = 7.91 (d, J = 8.3

Hz, 1H), 7.68 (br, NH), 7.35 (s, 1H), 7.13 (d, J = 8.4 Hz, 1H), 3.89 (s, 3H), 3.84 (s, 3H), 3.79 (m,

1H), 1.27 (d, J = 6.3 Hz, 6H). ^{13}C NMR (100 MHz, CDCl$_3$) δ = 168.68, 167.04, 150.11, 135.15,

131.98, 114.32, 112.98, 112.74, 52.35, 51.74, 43.50, 22.86. HRMS (ESI-TOF) m/z calculated for

C$_6$H$_{13}$NO$_3$ [M+H]$^+$: 252.1230, found 252.1226.
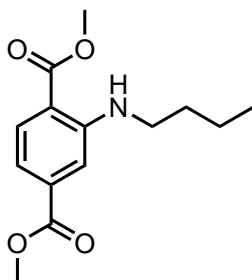
Compound 1d: Yellow solid, yield 0.75 g (38%). ^{1}H NMR (400 MHz, CDCl$_3$) δ = 7.87 (d, J = 8.4

Hz, 1H), 7.67 (br, NH), 7.29 (s, 1H), 7.12 (d, J = 8.2 Hz, 1H), 3.87(s, 3H), 3.83 (s, 3H), 3.23-3.17

(m, 2H), 1.69-1.61 (m, 2H), 1.50-1.40 (m, 3H), 0.97-0.92 (t, J = 7.4, 3H). ^{13}C NMR (100 MHz,

CDCl$_3$) δ = 168.55, 166.92, 150.91, 135.08, 131.70, 114.47, 112.69, 112.44, 52.24, 51.66, 42.62, 31.22, 20.36, 13.87. HRMS (ESI-TOF) *m/z* calculated for C$_6$H$_{13}$NO$_3$ [M+H]$^+$: 266.1387, found 266.1364.
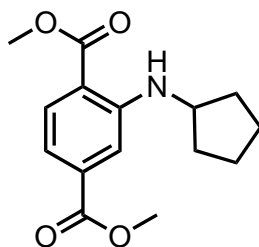
Compound 1e: Yellow liquid, yield 1.20 g (89%). ^{1}H NMR (400 MHz, CDCl$_3$) δ = 7.92 (d, *J* = 8.3 Hz, 1H), 7.79 (br, NH), 7.38 (d, *J* = 1.6 Hz, 1H), 7.15 (dd, *J* = 8.3, 1.6 Hz, 1H), 3.95 (dd, *J* = 9.2, 3.8 Hz, 1H), 3.91 (s, 3H), 3.86 (s, 3H), 2.14 - 2.00 (m, 2H), 1.81 - 1.71 (m, 2H), 1.72 - 1.62 (m, 2H), 1.57 (tdd, *J* = 12.2, 6.2, 3.2 Hz, 2H). ^{13}C NMR (100 MHz, CDCl$_3$) δ = 168.73, 167.11, 150.55, 135.09, 131.87, 114.42, 113.41, 112.82, 53.82, 52.42, 51.81, 33.57, 24.16.
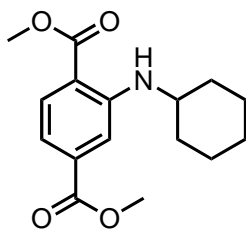
Compound 1f: Yellow liquid, yield 1.24 g (92%). ^{1}H NMR (400 MHz, Chloroform-*d*) δ = 7.93 (d, *J* = 8.3 Hz, 1H), 7.81 (br, NH), 7.12 (dd, *J* = 8.3, 1.6 Hz, 1H), 3.91 (s, 3H), 3.86 (s, 3H), 3.50 (dtd, *J* = 12.6, 8.4, 7.9, 3.6 Hz, 1H), 2.02 (td, *J* = 7.8, 7.3, 3.8 Hz, 2H), 1.77 (dq, *J* = 13.0, 4.2 Hz, 2H),

1.62 (ddt, J = 14.1, 9.6, 4.5 Hz, 1H), 1.51 - 1.22 (m, 5H). ^{13}C NMR (101 MHz, CDCl[3]) δ = 168.79,

167.19, 150.14, 135.18, 132.08, 114.21, 113.06, 112.70, 52.45, 51.82, 50.50, 32.93, 25.96, 24.69.
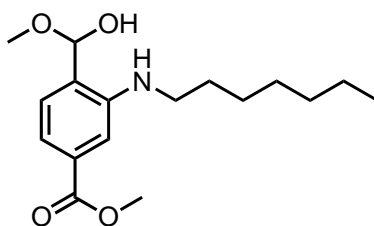
Compound 1g: Yellow liquid, yield 0.53 g (42%). ^{1}H NMR (400 MHz, Chloroform-*d*) δ = 7.93

(d, J = 8.3 Hz, 1H), 7.70 (br, NH), 7.34 (d, J = 1.6 Hz, 1H), 7.17 (dd, J = 8.3, 1.6 Hz, 1H), 4.12 (t,

J = 6.7 Hz, 2H), 3.92 (s, 3H), 3.87 (s, 3H), 1.56 (d, J = 6.4 Hz, 2H), 1.38 - 1.22 (m, 8H), 0.89 (t, J

= 3.1 Hz, 3H). ^{13}C NMR (100 MHz, CDCl[3]) δ = 168.75, 167.15, 151.07, 135.24, 131.88, 114.61,

112.86, 112.64, 52.45, 51.86, 43.11, 31.91, 29.20, 28.84, 27.29, 22.78, 14.20.

Synthesis of N-alkyl-2-amino-terephthalic acid (2a-f). The alkylated diester **1a-f** (0.50 g)

was dissolved in THF (25 mL), followed by addition of 1 M NaOH (*aq*, 12.8 mL). The solution

was heated to 70 ℃ and stirred for 8 h. The mixture was concentrated in a rotary evaporator at 45

℃ to remove the excess THF. The mixture was cooled to room temperature followed by addition

of 1 M HCl (*aq*) until a pH = 3. The observed precipitate was isolated by filtration, rinsed with

water, and dried in air at room temperature for 6 h.
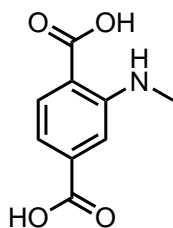
Compound 2a: Yellow solid, yield 0.46 g (92%). ^{1}H NMR (400 MHz, DMSO-d_6) δ = 7.86 (d, J = 8.2 Hz, 1H), 7.21 (d, J = 1.6 Hz, 1H), 7.09 (dd, J = 8.2, 1.6 Hz, 1H), 2.88 (s, 3H). ^{13}C NMR (100 MHz, DMSO-d_6) δ = 169.37, 167.18, 151.27, 135.78, 131.85, 114.27, 113.09, 111.37 , 29.20. HRMS (ESI-TOF) m/z calculated for $C_6H_{13}NO_3$ [M+H]$^+$: 196.0604, found 196.0610.
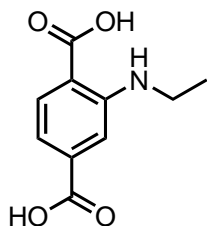
Compound 2b: Yellow solid, yield 0.45 g (90%). ^{1}H NMR (400 MHz, DMSO-d_6) δ = 7.87 (d, J = 8.2 Hz, 1H), 7.23 (d, J = 1.6 Hz, 1H), 7.08 (dd, J = 8.2, 1.6 Hz, 1H), 3.23 (q, J = 7.2 Hz, 2H), 1.23 (t, J = 7.1 Hz, 3H). ^{13}C NMR (100 MHz, DMSO-d_6) δ = 169.46, 167.15, 150.35, 135.78, 131.96,

114.30, 112.91, 111.71, 36.70, 14.26. HRMS (ESI-TOF) *m/z* calculated for $C_6H_{13}NO_3$ [M+H]$^+$: 210.0761, found 210.0746.

Compound 2c: Yellow solid, yield 0.47 g (94%). ^{1}H NMR (400 MHz, DMSO-d_6) δ = 7.87 (d, *J* = 8.2 Hz, 1H), 7.25 (d, *J* = 1.6 Hz, 1H), 7.05 (dd, *J* = 8.2, 1.6 Hz, 1H), 3.74 (hept, *J* = 6.4 Hz, 1H), 1.21 (d, *J* = 6.3 Hz, 6H). ^{13}C NMR (100 MHz, DMSO-d_6) δ = 169.57, 167.19, 149.58, 135.75, 132.11, 114.08, 113.04, 112.14, 42.74, , 22.46. HRMS (ESI-TOF) *m/z* calculated for $C_6H_{13}NO_3$ [M+H]$^+$: 224.0917, found 224.0924.

Compound 2d: Yellow solid, yield 0.48 g (96%). ^{1}H NMR (400 MHz, DMSO-d_6) δ = 7.85 (d, *J* = 8.2 Hz, 1H), 7.24 (d, *J* = 1.5 Hz, 1H), 7.07 (dd, *J* = 8.2, 1.6 Hz, 1H), 3.20 (t, *J* = 7.0 Hz, 2H), 1.60 (m, 2H), 1.40 (m, 2H), 0.93 (t, *J* = 7.1 Hz, 3H). ^{13}C NMR (100 MHz, DMSO-d_6) δ = 169.52,

167.15, 150.51, 135.77, 131.96, 114.25, 112.90, 111.74, 41.72, 30.58, 19.71, 13.68. HRMS (ESI-TOF) m/z calculated for $C_6H_{13}NO_3$ [M+H]$^+$: 238.1074, found 238.1058.

Compound 2e: Yellow solid, yield 0.47 g (93%). ^{1}H NMR (400 MHz, DMSO-d_6) δ = 7.86 (d, J = 8.2 Hz, 1H), 7.27 (d, J = 1.5 Hz, 1H), 7.07 (dd, J = 8.2, 1.5 Hz, 1H), 3.88 (p, J = 6.1 Hz, 1H), 2.02 (dq, J = 12.1, 6.0, 5.1 Hz, 2H), 1.65 (dqd, J = 22.4, 7.8, 3.7 Hz, 4H), 1.45 (dq, J = 11.6, 5.5 Hz, 2H). ^{13}C NMR (100 MHz, DMSO) δ = 169.60, 167.21, 150.05, 135.72, 132.05, 114.28, 112.99, 112.58, 53.08, 32.92, 23.57. HRMS (ESI-TOF) m/z calculated for $C_{13}H_{16}NO_4$ [M+H]$^+$: 250.1079, found 250.1041.
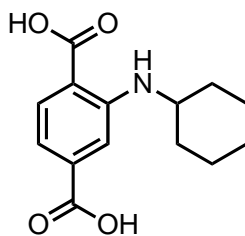
Compound 2f: Yellow solid, yield 0.46 g (92%). ^{1}H NMR (400 MHz, DMSO-d_6) δ = 7.98 (br, NH), 7.86 (d, J = 8.2 Hz, 1H), 7.25 (s, 1H), 7.04 (dd, J = 8.3, 1.4 Hz, 1H), 3.45 (d, J = 8.9 Hz, 2H), 1.93 (dt, J = 12.6, 3.9 Hz, 2H), 1.68 (dt, J = 13.3, 4.3 Hz, 2H), 1.58 (dt, J = 10.0, 4.3 Hz, 1H), 1.49 - 1.34 (m, 2H), 1.34 - 1.19 (m, 3H). ^{13}C NMR (100 MHz, DMSO) δ = 169.67, 167.23, 149.54,

135.74, 132.15, 114.02, 112.11, 49.54, 32.23, 25.33, 23.97. HRMS (ESI-TOF) *m/z* calculated for $C_{14}H_{18}NO_4$ [M+H]$^+$: 264.1235, found 264.1189.
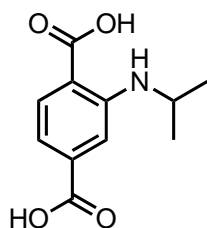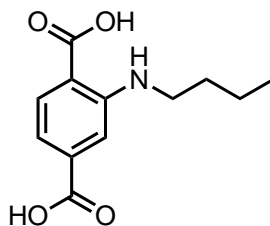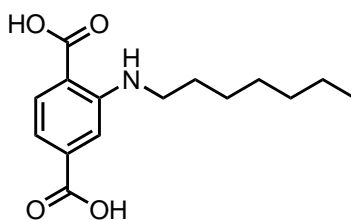

Compound 2g: Yellow solid, yield 0.48 g (96%). ^{1}H NMR (400 MHz, DMSO-d_6) δ = 7.86 (d, *J* = 8.2 Hz, 1H), 7.23 (d, *J* = 1.6 Hz, 1H), 7.07 (dd, *J* = 8.2, 1.5 Hz, 1H), 3.19 (t, *J* = 7.0 Hz, 2H), 1.61 (p, *J* = 7.0 Hz, 2H), 1.44 - 1.20 (m, 8H), 0.92 - 0.80 (m, 3H). ^{13}C NMR (100 MHz, DMSO) δ = 169.54, 167.16, 150.52, 135.77, 131.97, 114.25, 112.89, 111.75, 42.02, 31.20, 28.41, 28.36, 26.45, 22.01, 13.94. HRMS (ESI-TOF) *m/z* calculated for $C_{15}H_{22}NO_4$ [M+H]$^+$: 280.1548, found 280.1500

Synthesis of MIL-125-NHR. Compounds **2a-f** (0.41 mmol) were placed in 20 mL scintillation vials with anhydrous DMF (4.90 mL) and anhydrous MeOH (0.35 mL). The mixture was mixed thoroughly by immersing the vial in an ultra-sonic bath for 1 min then transferred into a borosilicate glass tube (see SI for more details) and bubbled with N_2 (*g*) for 5 min. Ti(O^{i}Pr)$_4$ (0.031 mL, 0.106 mmol) was added to the tube via syringe, immediately flash frozen in liquid N_2, and flame sealed as described in the Appendix B. The sealed tube was heated to 150 ºC for 48 h. After cooling to room temperature, the formed powder was isolated by filtration and rinsed with DMF (3×) and CHCl$_3$ (3×). The powder was immersed in CHCl$_3$ and stored for 3 d in a desiccator, replacing the solvent during this time (8×). The solvent was removed by decantation and the

solvent-wet powder was dried under dynamic vacuum (10 mtorr) for 48 h at room temperature. The degassed yellow solid was stored under N_2 in a desiccator.

MIL-125-NHMe. Yellow solid. Yield: 0.015 g [66% yield based on $Ti_8O_{12}(C_9H_7NO_4)_6$]. FTIR (ATR, cm^{-1}) 3388.88, 2923.01, 1717.1, 1538.36, 1505.04, 1484.73, 1456.67, 1408.86, 1384.32, 1311.53, 1278.29, 1163.53, 1080.44, 1062.15, 1036.26, 950.04, 882.39, 768.58, 632.14, 583.12, 553.84, 507.68, 460.66

MIL-125-NHEt. Yellow solid. Yield: 0.015 g [63% yield based on $Ti_8O_{12}(C_{10}H_9NO_4)_6$]. FTIR (ATR, cm^{-1}) 3364.35, 2969.06, 2927.83, 2871.17, 1622.55, 1574.24, 1538.33, 1504.43, 1480.27, 1454.32, 1385.56, 1304.75, 1279.43, 1269.21, 1157.09, 1081.55, 1058.47, 983.03, 950.64, 886.9, 768.8, 665.76, 630.17, 585.19, 512.73

MIL-125-NH^{i}Pr. Yellow solid. Yield: 0.014 g [56% yield based on $Ti_8O_{12}(C_{11}H_{11}NO_4)_6$]. FTIR (ATR, cm^{-1}) 3354.94, 2965.73, 2927.26, 1622.02, 1573.66, 1538.12, 1503.89, 1454.54, 1445.82, 1410.07, 1384.84, 1279.16, 1246.65, 1117.76, 1006.2, 951.41, 888.56, 850.56, 768.24, 665.95, 636.51, 613.79, 600.93, 538.98, 482.13

MIL-125-NHBu. Yellow solid. Yield: 0.015 g [57% yield based on $Ti_8O_{12}(C_{12}H_{13}NO_4)_6$]. FTIR (ATR, cm^{-1}) 3362.48, 2955.93, 2927.6, 2870.25, 1622.53, 1573.94, 1537.91, 1503.55, 1451.88, 1386.73, 1314.03, 1304.04, 1280.91, 1259.32, 1115.87, 970.85, 951.52, 906.68, 885.87, 837.9, 769.03, 731, 633.97, 616.57, 583.52, 534.70, 503.04

MIL-125-NHCyp. Yellow solid. Yield: 0.010 g [39% yield based on $Ti_8O_{12}(C_{13}H_{13}NO_4)_6$]. FTIR (ATR, cm^{-1}) 3365.09, 2956.52, 2870.11, 1622.59, 1572.58, 1533.02, 1499.83, 1453.63, 1409.16,

1385.58, 1323.65, 1276.65, 1184.97, 1115.98, 1060.09, 980.45, 951.9, 886.01, 768.43, 620.1, 597.1, 523.84, 470.79

MIL-125-NHCy. Yellow solid. Yield: 0.011 g [42% yield based on $Ti_8O_{12}(C_{14}H_{15}NO_4)_6$]. FTIR (ATR, cm^{-1}) 3352.11, 2927.79, 2853.15, 1620.61, 1571.39, 1532.66, 1501.01, 1453.71, 1383.93, 1322.94, 1281.56, 1248.78, 1187.03, 1150.25, 1073.88, 994.46, 959.79, 887.69, 767.44, 664.76, 631.11, 602.49, 526.78, 479.16

MIL-125-NHhept. Yellow solid. Yield: 0.015 g [52% yield based on $Ti_8O_{12}(C_{15}H_{19}NO_4)_6$]. FTIR (ATR, cm^{-1}) 3373.41, 2953.73, 2926, 2854.98, 1622.82, 1573.83, 1537.73, 1532.36, 1504.52, 1454.97, 1403.36, 1385.54, 1311.73, 1278.64, 1123.5, 1063.3, 982.81, 954.74, 884.31, 768.1, 665.83, 617.89, 582.38, 548.52, 505.48

Activation procedure for gas adsorption. The dried MOF powder was placed in a sample tube for gas adsorption, evacuated to ~ 5 mtorr at room temperature and then heated up to 120 ºC under dynamic vacuum for 18 h

3.2.3 Blue LED photochemical reactor setup and calibration.

Photocatalytic reactions were carried out in a home-built reactor using a 60 W blue LED strip (5 m long, MEILI, product # CNMX-Hardlines-464321) with λ = 466 nm (*fwhm* = 20 nm), the strip was coiled and glued inside a 20 cm diameter tin can and mounted on top of a magnetic stirrer. The temperature inside the photo reactor was kept at 25 ºC with the aid of an attached fan and a thermometer. The photon flux of the photoreactor was determined using iron oxalate actinometry at 466 nm following the protocol by Parker *et al*.[44] obtaining a volumetric photon flux of $R_{o,\lambda} = 1.92 \times 10^{-3}$ mol (photons) L^{-1} h^{-1}. The apparent quantum yield, Φ_{app} (also named photonic

efficiency) was determined according to the IUPAC recommended protocol by Serpone *et al.*[45] using the formula:

$$\Phi_{app} = \frac{R^{in}}{R_{o,\lambda}} \qquad (3\text{-}2)$$

where R^{in} corresponds to the initial rate of the reaction (see below), and $R_{o,\lambda}$ is the volumetric photon flux.

3.2.4 Photochemical reduction of carbon dioxide to formate

Measurements were performed under ambient conditions in the photoreactor described above. MIL-125-NHR (3 – 5 mg) was loaded in a 3 mL borosilicate vial with a magnetic stirrer. 1.5 mL of a CO_2-bubbled stock solution containing triethanolamine (TEOA, 0.30 mol L^{-1}) and mesitylene (1.5 mmol L^{-1}) in MeCN-d_3 was added to the vial and tightly capped with a PTFE/rubber septum. A flow of CO_2 (*g*) was bubbled into the vial with the aid of a needle with an input positive pressure of 1 psi for 30 min previous to photoirradiation. During irradiation, 40 µL aliquots were sampled every 12 h with the aid of a syringe, the aliquot was filtered through a 0.2 µm PTFE syringe membrane into an NMR tube. The filtrate was diluted with $CDCl_3$ (~0.6 mL) and a total of 256 transients were measured for each time point. Kinetic plots were obtained in both concentration and turnover number in the ordinate axis. The concentration was obtained by addition of the intensity of the photoreduced-CO_2 signals (formate + HEF + BHEF) and normalizing with respect to the internal standard, and the turnover number was determined as the total number of moles of photoreduced-CO_2 (mol CO_2 + mol HEF + mol BHEF) per mol of photocatalyst (with respect to the organic linker). The initial rate of the reaction was obtained by

fitting a third order polynomial function using linear least squares, then evaluating their first derivative at $t = 0$.

3.2.5   Crystal modeling and Rietveld refinements.

Rietveld refinements were performed in GSAS-II with the experimental diffractograms, and the respective crystal model generated in Materials Studio. Refinements were performed using a Thomson-Cox-Hasting modified pseudo-Voigt function with 6 terms, and Finger-Cox-Jephcoat peak asymmetry with 1 parameter. The background was initially hand fit to a 6th order Shifted Chebyschev polynomial. The profile was initially calculated using the LeBail routine (Peakfit) with manually picked peaks, refining first the Gaussian and then the Lorentzian components, followed by asymmetry and background, observing convergent refinements. Following LeBail fit, Rietveld routine with extraction of the structure factors (F_{obs}) was then used refining the scale factor, unit cell parameters, zero shift and LP function, followed by the background function, the crystallite size and strain broadening, transparency and extinction. Oxygen atoms were included inside the pores to partially correct for the influence of water guest molecules (likely present from the interaction with ambient surroundings over the course of the data collection), and their occupancy factors and positions were refined with convergent results. The atom positions of the alkyl chains were not refined and assumed highly disordered. A preferred orientation correction was added to the refinements using a 2nd order spherical harmonic function. Isotropic atomic displacement parameters (U_{iso}) of all non-hydrogen atoms were refined with constraints (constraining all the chemically equivalent atoms). Final refinements included all parameters, which were refined iteratively until convergent refinements were obtained. F_{obs} were extracted,

bond distances and angles were calculated and a crystallographic information file (CIF) was generated.

Note: MIL-125-NH^{i}Pr, MIL-125-NHBu, and MIL-125-NHCyp exhibit three unindexed peaks at 32.3, 34.0, and 38.8 2-theta degrees. Those peaks do not correspond to starting materials or titanium dioxide polymorphs.

3.2.6 Chemical Actinometry

Calibration of the LED photoreacotor was performed by chemical actionometry though standard photoreduction of $K_3[Fe(C_2O_4)_3]$ to $Fe((C_2O_4)_2^{2-}$ as described by Parker *et al.*[44] After the preparation of a calibration curve of ferrous iron (Figure B-70), the photoreduction of $K_3[Fe(C_2O_4)_3]$ is irradiated over 360 seconds. The absorbance at 510 nm as converted to concentration of ferrous iron using the calibration curve. The radiation dose of a photoreactor using blue LED can be obtained by using the recommended quantum efficiency of 0.925 in the following equation:

$$\Phi_\lambda = \frac{R^{in}}{R_{o,\lambda}}$$

(3-3)

Where Φ_λ is the photochemical quantum yield, R^{in} is the initial rate of the photochemical reaction, and $R_{o,\lambda}$ is the incident volumetric photon flux.

The obtained photon flux in the photoreactor is $R_{o,\lambda} = 1.92 \times 10^{-3}$ mol (photons) L^{-1} h^{-1}.

3.3 Results and Discussion

The isoreticular family of MOFs was prepared via S_N2 reaction of 2-amino terephthalate dimethyl ester (Figure 3-2) with the corresponding alkyl iodide in basic conditions forming intermediates **1a-d** and **1g** in moderate yields. Intermediates **1e-f** were synthesized via reductive amination with cyclopentanone or cyclohexanone in the presence of $NaBH_4$/TMSCl in cold DMF in high yields. Hydrolysis of the dimethyl esters in NaOH/THF afforded linkers **2a-g**, and solvothermal MOF crystallization with $Ti(O^iPr)_4$ in DMF/MeOH in flame sealed borosilicate tubes produced the desired MOFs in high yields (See Appendix B). The molecular integrity of the linkers within the MOFs was determined using ^{1}H NMR by dissolving the synthesized MOFs in NaOD 0.1 M in D_2O (Figure 3-3). These measurements allowed identifying any loss of alkyl chains at the *N*-substitution, as it has been observed by others[46] that solvothermal conditions using tetravalent early transition metal ions (such as Zr^{+4}) in DMF can induce dealkylations at the *N*-substitution. No loss of *N*-alkyl chains was observed in any of the prepared MOFs, indicating a robust and clean crystallization. Attempts to prepare a double methylated aminoterephthalate MIL-125-NMe$_2$ using linker **3** were unsuccessful (Figure 3-5) due to the decomposition of the linker into the monomethylated species **2a**, with 80% conversion while forming non-porous amorphous solids. We deduced that the steric constrain imposed by the double substitution impedes the crystallization of the MOF, while Ti^{+4} induces *N*-dealkylation, similar to Zr-based MOFs, and thus only single *N*-alkylated MOFs were successfully synthesized.

The MOFs were obtained as microcrystalline powders that were analyzed by scanning electron microscopy (SEM) and powder X-ray diffraction (PXRD) crystallography. SEM images (Figures B9-B16) displayed samples with uniform particle shape and texture, suggesting homogeneous materials. All the materials display sharp diffraction peaks (Figure 3-4) starting at

6.8º 2θ, evidencing high degree of crystallinity with large unit cells, as expected in a MOF. All patterns were indexed by comparison to the simulated pattern of MIL-125-NH$_2$,[34] suggesting the formation of frameworks that are isoreticular to MIL-125. Crystal simulation using Materials Studio Modeling Suite[41] produced the library of suitable models for crystal structure solution with the Rietveld method. Refinements of the experimental patterns *vs.* the theoretical crystals allowed the solution of the crystal structures in the high-symmetry tetragonal *I4/mmm* space group with low residuals (see SI), where the –NR groups were assumed to be disordered around the four possible positions in the terephthalate ring and inside the pore.

The porosity of the MOFs was determined using N$_2$ gas adsorption at 77 K. All isotherms display IUPAC Type II isotherm behavior that corresponds to microporous materials with fully reversible adsorption behavior (Figure S18-S47). Application of the Brunauer-Emmet-Teller (BET) model in the low-pressure region of the isotherm resulted in BET surface areas between 200 and 1000 m^2 g^{-1}. A progressive decrease is observed in the order of MIL-125-NH$_2$ (S_{BET} = 1,200 m^2 g^{-1}) > MIL-125-NHMe (S_{BET} = 1,000 m^2 g^{-1}) > MIL-125-NHEt (S_{BET} = 750 m^2 g^{-1}) > MIL-125-NHBu (S_{BET} = 690 m^2 g^{-1}) > MIL-125-NHCyp (S_{BET} = 580 m^2 g^{-1}) > MIL-125-NH^{i}Pr (S_{BET} = 490 m^2 g^{-1}) > MIL-125-NHCy (S_{BET} = 420 m^2 g^{-1}) > MIL-125-NHhep (S_{BET} = 230 m^2 g^{-1}). The total cumulative pore volume, obtained from non-local density functional theory (NLDFT) fitting of the N$_2$ isotherms, resulted in decreasing pore volumes consistent with increased substitution (Figure 3-6) decreasing from 0.73 cm^3 (STP) g^{-1} in MIL-125-NH$_2$ to 0.09 cm^3 (STP) g^{-1} in MIL-125-NHhep.
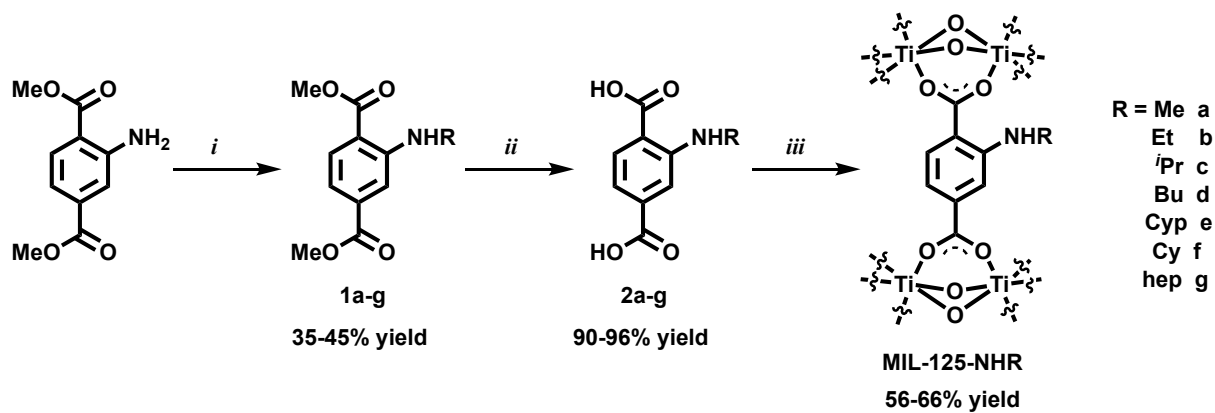
Figure 3-2: Synthesis of isoreticular MIL-125-NHR MOFs. Conditions: [a] (R = Me, Et, ^{i}Pr, Bu, hep) RI, K$_2$CO$_3$, DMF/HPMA, 100 °C, 18 h. [b] (R = Cyp, Cy) cycloketone, TMSCl, NaBH$_4$, DMF, N$_2$ (g), 0 °C, 15 min. ii. NaOH, THF, 70 °C, 8 h. iii. Ti(O^{i}Pr)$_4$, DMF, MeOH, 150 °C, 48 h.
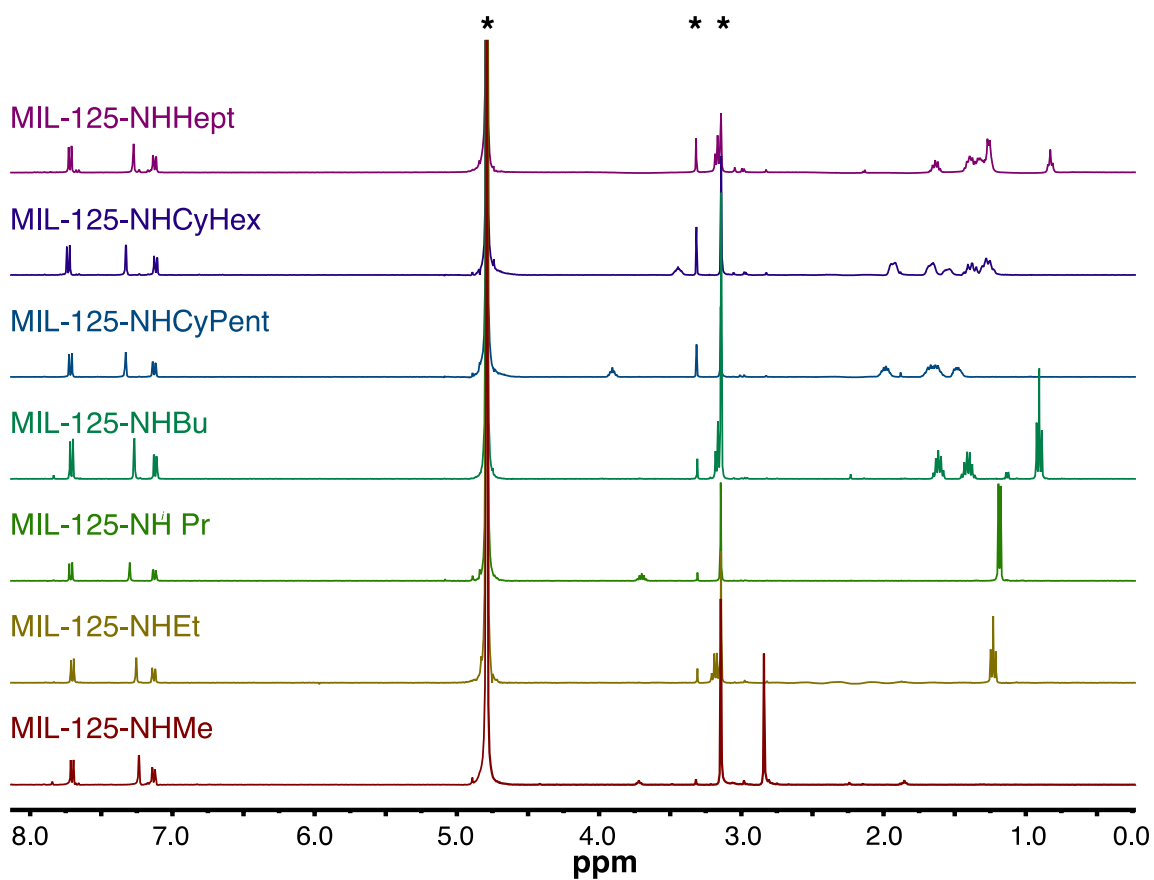
Figure 3-3: ^{1}H NMR spectra (400 MHz, 0.1 M NaOD/D2O, 25 ºC) of NaOD/D_2O digested MOFs (0.1M NaOD in D_2O). * = Residual solvent signals.
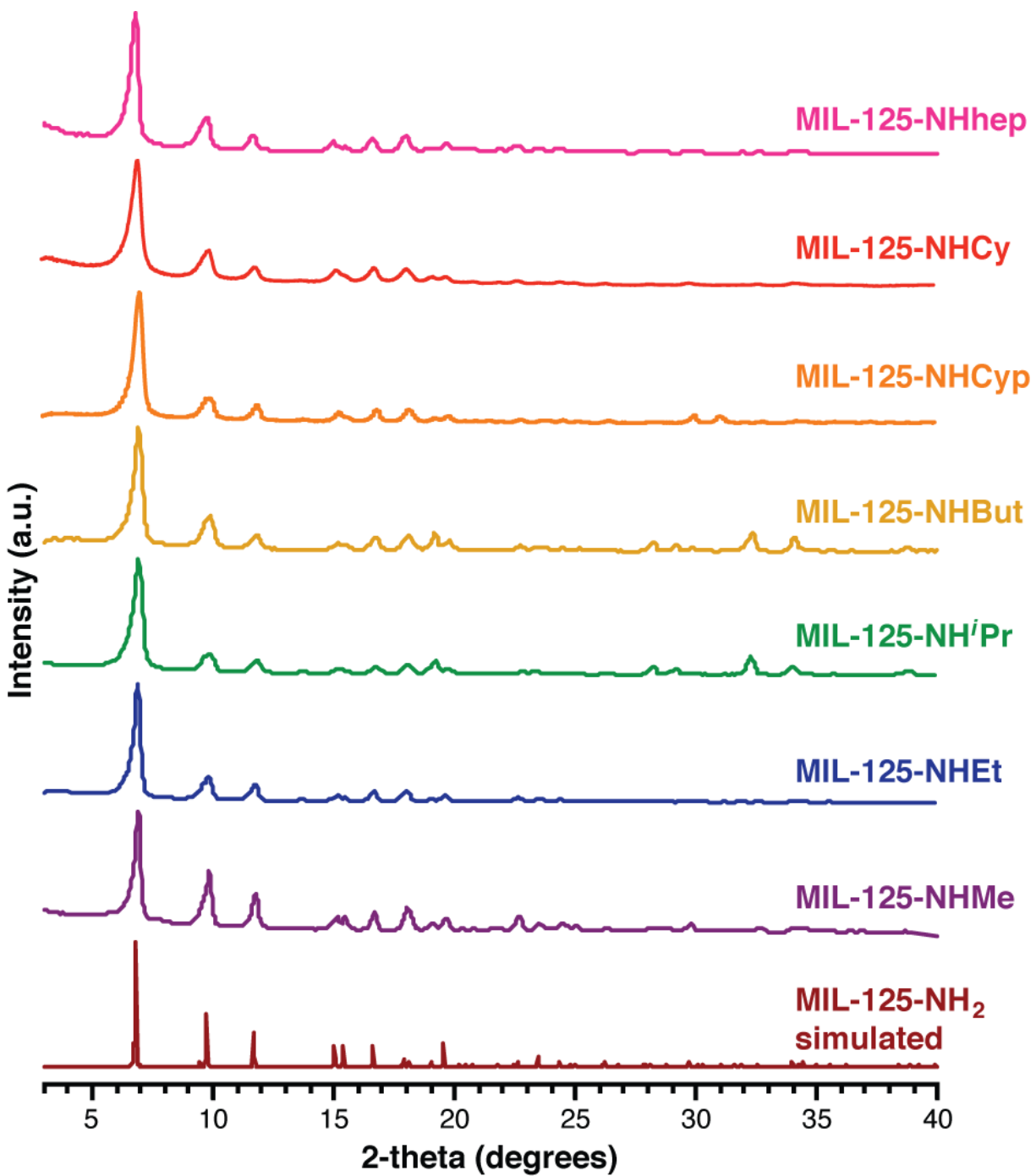
Figure 3-4: Powder X-ray diffraction patterns of the isoreticular family of MIL-125-NHR compared to the simulated pattern of the parent MIL-125-NH_2 (Rietveld refinement parameters in SI).
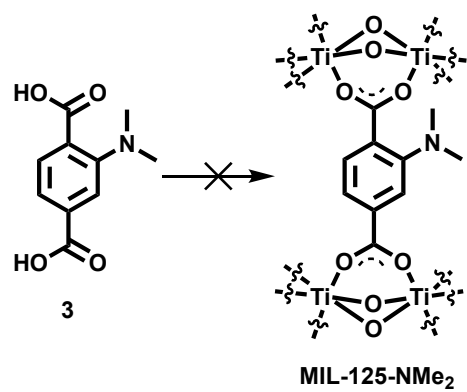
Figure 3-5: Attempted synthesis of MIL-125-NMe₂. Note: Attempts to prepare this MOF under the same conditions as in mono *N*-substituted MOFs resulted in *N*-demethylation of the linker with formation of amorphous non-porous samples.

The CO_2 adsorption isotherms at 273 (Figure 3-7a), 283 and 298 K (Figures B47-S54) exhibit a similar trend in uptake where increased *N*-alkyl substitution results in lower uptakes from 221 cm^3 g^{-1} in MIL-125-NH_2, to 19.1 cm^3 g^{-1} in MIL-125-NHhep. These trends are consistent with: 1) increased amount of weight of the MOF by addition of extra atoms in the *N*-alkyl chain, and 2) the decreased accessibility to the pores as a result of clogging of the pore and pore apertures as the alkyl chains occupy free space of the pores. We also observed that although the functionalized MOFs display lower CO_2 uptakes than the parent MIL-125-NH_2 at room temperature (especially MIL-125-NHCyp, MIL-125-NHCy, and MIL-125-NHhep), their adsorption capacity has little effect in their CO_2 photoreduction rates (see below), which only suggests that mass transport within the pores is not the rate determining step in the photoreduction. Determination of the differential enthalpy of adsorption $\Delta \dot{h}_{ads}$ (Figure 3-7b) allows understanding the thermodynamic interactions between CO_2 and the MOFs. We observed no particular trend given by the systematic *N*-alkyl substitution across the uptake ranges, with all MOFs observing similar $\Delta \dot{h}_{ads}$ than MIL-125-NH_2, ranging from -20 kJ mol^{-1} (MIL-125-NHEt) to -27 kJ mol^{-1} (MIL-125-NHMe) when loading 1 CO_2 molecule per unit cell. This lack on trend in adsorption enthalpy evidences the convoluted effect of: 1) the inherent porosity of the parent MIL-125 framework, 2) the electron rich nature of the amino nitrogen lone pair acting as a Lewis basic site, and 3) the steric hindrance imposed by the bulky alkyl substituents. While the enthalpy of adsorption is a combination of all these effects, the undiluted electronic effects are better understood by determination of the bandgap of the MOFs.

The UV-visible absorption spectra for crystalline powder of the MIL-125-NHR series were acquired using an integrating sphere and the results can be seen in Figure 3-8a. The parent MIL-

125-NH$_2$ exhibits a low energy absorption peak at 375 nm. As expected, a gradual redshift in the absorption is observed for the alkylated derivatives; presumably the shift can be attributed to the alkyl donor group destabilizing the top of the valence band (HOMO) of the amino terephthalate linker. Application of the Tauc model to the photoabsorption plots (Figures S55-S62) allowed for the determination of the optical bandgap (or HOMO-LUMO gap). A decrease in the bandgap of the materials is observed (Figure 3-8b) from MIL-125-NH$_2$ (E_g = 2.56 eV) to MIL-125-NHCy (E_g = 2.29 eV) in a stepwise mode with increased alkyl chain substitution, as expected from the inductive effects of the corresponding alkyl chain. Of the series, the *n*-heptyl substituted MOF displayed a larger bandgap than the cyclopentyl and cyclohexyl, and close in value to *n*-butyl substituted MOF. This behavior is due to the linear nature of the heptyl chain. Inductive effects decrease exponentially as the C–C σ-bonds are further away from the heteroatom, expecting very little induction beyond the fourth σ-bond, as observed in MIL-125-NHBu and MIL-125-NHhep. In contrast, cyclic substituents retain the σ-bonds in close proximity to the amine group, resulting in stronger electronic induction and therefore lower bandgaps. We expect that tertiary carbon substitutions (*e.g.*, *tert*-butyl), or *N*,*N*-dialkyls (*e.g.* MIL-125-NMe$_2$) would result in even lower bandgaps.

The photocatalytic rates and efficiencies of MIL-125-NHR MOFs are known to be dependent on the lifetime of the photo generated charge-separated state.[35] To gain insights into the excited state dynamics, nanosecond transient absorption spectroscopy was performed on suspensions of selected MIL-125-NHR in MeCN and the results can be seen in Figure 3-8c and Figures B63-B67. Upon excitation at 405 nm the parent material, MIL-125-NH$_2$, exhibits bleach from 390 nm to 530 nm and positive ΔA features at λ < 390 nm and λ > 530 nm (Figure B-63).
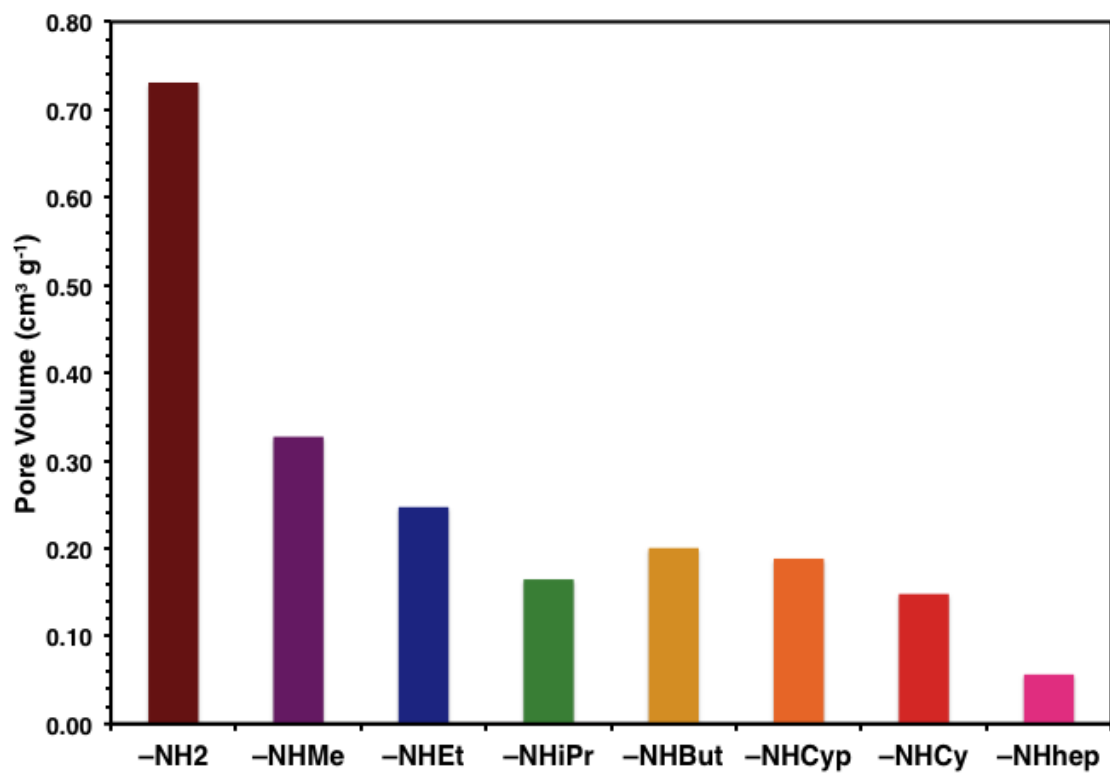
Figure 3-6: Pore volume of as prepared MOFs calculated from NLDFT using data measured from N_2 gas isotherm at 77 K.
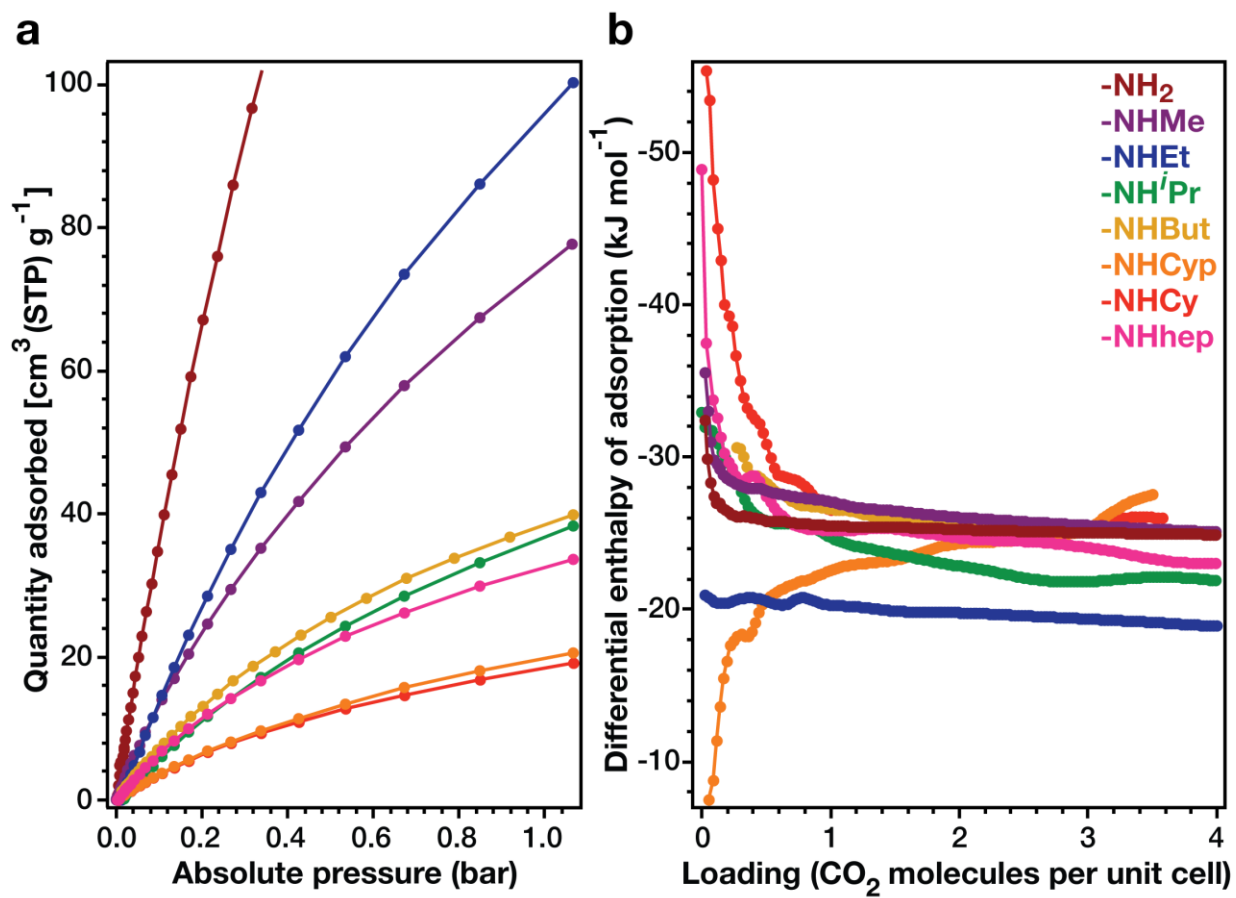
Figure 3-7: (a) CO_2 gas adsorption isotherms (273 K) and (b) Differential (or isosteric) enthalpy of adsorption vs. loading plots of MIL-125-NHR with R = H (brown), Me (purple), Et (blue), ^{i}Pr (green), Bu (yellow), Cyp (orange), Cy (red), hep (pink). CO_2 adsorption points at high pressure in MIL-125-NH$_2$ are not shown for clarity.

These transient spectroscopic features are indicative of the charge-separated state with a hole on the amino terephthalate linker and the electron on the titanium-oxo cluster.[35] Similarly, absorption features are observed for the alkylated derivatives with example spectra for MIL-125-NHMe shown in Figure 3-8c and all other spectra in supporting information. As was observed with the ground state absorption, the alkylated complexes ΔA features are red shifted by ~30 nm compared to MIL-125-NH$_2$. The lifetime of the charge-separated state for the measured set of MIL-125-NHR materials was monitored at 500 nm ($\lambda_{ex} = 405$ nm) and the results can be seen in Figure 3-8d. The lack of signal rise time indicates that the charge-separated state is generated within the instrument response time (< 10 ns). The charge-separated lifetime increases in the order of MIL-125-NH$_2$ ($\tau = 12.8$ ns) < MIL-125-NHMe ($\tau = 38.2$ ns) < MIL-125-NHBu ($\tau = 52.1$ ns) < MIL-125-NHEt ($\tau = 60.63$ ns) < MIL-125-NHCyp ($\tau = 68.9$ ns) < MIL-125-NHCyp ($\tau = 68.8$ ns) < MIL-125-NHhep ($\tau = 69.2$ ns) < MIL-125-NH^{i}Pr ($\tau = 75.11$ ns) < MIL-125-NHCy ($\tau = 91.35$ ns) generally corresponding to a trend of longer lifetimes with greater donor ability of the alkyl substituent. Presumably, the enhanced stabilization of the oxidized terephthalate by the secondary alkyl chain is responsible for the long lifetime observed for MIL-125-NH^{i}Pr, MIL-125-NHCyp and MIL-125-NHCy.

We explored the photocatalytic activity of the isoreticular MOFs towards CO$_2$ photoreduction using blue irradiation (Figure 3-9. A LED light source was utilized because of its accessibility, low cost, high irradiance, low power needs and narrow emission profile, compared to Xe-based lamps.[47] Moreover, using a narrow band aids in circumventing photocatalysis by any residual titanium oxide formed during the MOF synthesis, as these phases require light in the UV region ($\lambda < 350$ nm).[7] Irradiating MIL-125-NHR suspensions in MeCN-d_3 under a flow of CO$_2$ and in the presence of triethanolamine, TEOA (a reducing agent) and mesitylene (an internal

standard) with blue light ($\lambda = 466$ nm) resulted in the formation of formate as the product of CO_2 reduction, which displays a ^{1}H NMR signal at 8.45 ppm (Figure 3-10). Two other signals were also observed at 8.08 and 8.04 ppm, which correspond to *N*-(2-hydroxyethyl)formamide (HEF) and *N*,*N*-bis(2-hydroxyethyl)formamide (BHEF), respectively (Figure 3-11). These two species appear as result of formate reacting with the hydrolyzed products of oxidized TEOA (Figure 3-9), as the photoreduction operates in non-anhydrous conditions.[48-53] Integration of the NMR signals and normalization with respect to the mesitylene internal standard provided kinetic plots (Figures B71-B78) for the three CO_2-photoreduced species. Figure 3-12a displays the kinetic plot of the total CO_2-reduced products over 120 h utilizing MIL-125-NHMe and MIL-125-NHhep. Similar to the trend in photoabsoption and bandgap, the increased number of carbon atoms in the *N*-alkyl chain results in increased photocatalytic activity, with turnover numbers at 120 h between 0.284 for MIL-125-NHMe and 1.151 for MIL-125-NHhep. For comparison purposes, we measured the concentration of formate with our photoreactor ([formate] = 0.165 mmol L^{-1} at t = 12 h) and compared to the observations of Li *et al.* ([formate] = 0.136 mmol L^{-1} at t = 10 h),[34] resulting in very similar values, providing a validation to our approach. Fitting polynomial functions to the concentration-based kinetic plot, followed by evaluation at $t = 0$ h of their first derivative, allowed us to obtain the initial rate of the photoreduction. The initial rates for all the MOFs were utilized to obtain an apparent quantum yield (Φ_{app}, also referred as photonic efficiency[45]) using eq. (2). In this work we use the term *apparent* quantum yield for two reasons: first, the ratio of light absorption/scattering by the MOF is not accounted for (*i.e.* we assume complete light absorption), and second, because the kinetic plots account for two side reactions (amide formation) that occur after the photocatalytic step. As shown in Figure 3-12b, secondary *N*-alkyls, isopropyl, cyclopentyl, and cyclohexyl Figure 3-12b blue histograms) display a larger Φ_{app} (1.5 – 1.8%) than

the primary *N*-alkyls (0.30 – 0.40%, Figure 3-12b orange histograms); especially MIL-125-NHCyp, which displayed the largest apparent quantum yield $\Phi_{app} = 1.80\%$. The increased catalytic activity is consistent with the increased excited-state lifetime and decreased bandgap for the secondary alkyl substituent species.

It is noteworthy to emphasize that we observed no trend or correlation observed between the photocatalytic rates/efficiency and the gas adsorption properties of the MOFs. We believe that electronic effects from *N*-alkyl substitution determine the photocatalytic efficiency with little effect from mass transport. This assessment is consistent with the reaction mechanism proposed by Fu *et al.*,[34] who propose that upon photoexcitation, an electron is promoted from the π-cloud in terephthalate to a Ti *d*-state and is further transferred to CO_2, reducing it to formate. The MOF catalyst is then regenerated by oxidizing TEOA (the latter also serving as proton source). Our observed correlation between excited-state lifetime and apparent quantum yield suggest that the rate-limiting step of the reduction is the electron transfer from Ti^{+3} to CO_2 competing with charge recombination of the MOF. The chemical stability of the MIL-125-NHR MOFs was assessed by PXRD and ^{1}H NMR after 120 h of photoreaction. No changes in the PXRD patterns were observed, suggesting stability of the crystalline framework (Figure 3-13). Moreover, only marginal linker decomposition was observed in the ^{1}H NMR spectra of the base-digested MOFs. The reusability of the MOF photocatalysts was assessed by re-exposing MIL-125-NHCyp for a second photocatalytic run for another 120 h, observing less than 5% variation in concentration of reduced CO_2 species, indicating photochemical stability after reuse (Figure 3-14). Future work includes studying the effect of other reductants (*e.g.* alcohols, hydrogen) and more complex substitutions, such as including tertiary *N*-alkyls and π-donors that will increase the lifetime of the excited state also induce smaller bandgap
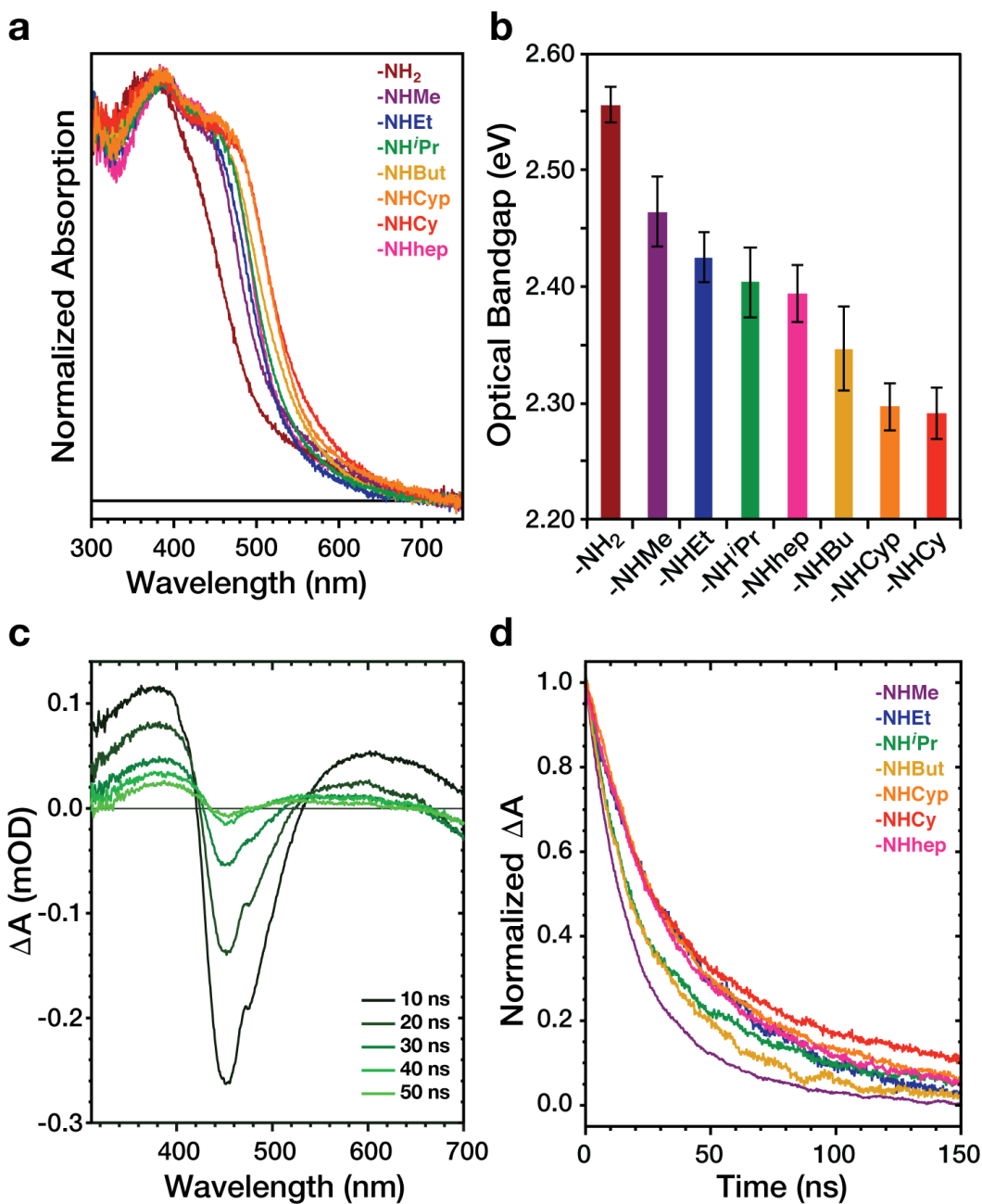
Figure 3-8: (a) Solid-state absorption spectra of MIL-125-NHR MOFs, (b) measured bandgap for MIL-125-NHR MOFs using the Tauc model (error bands correspond to one standard deviation from the linear fitting), (c) transient absorption spectra for MIL-125-NHMe, and d) time-resolved absorption traces at 500 nm for MIL-125-NHR suspended in MeCN (λ_{ex} = 405 nm).
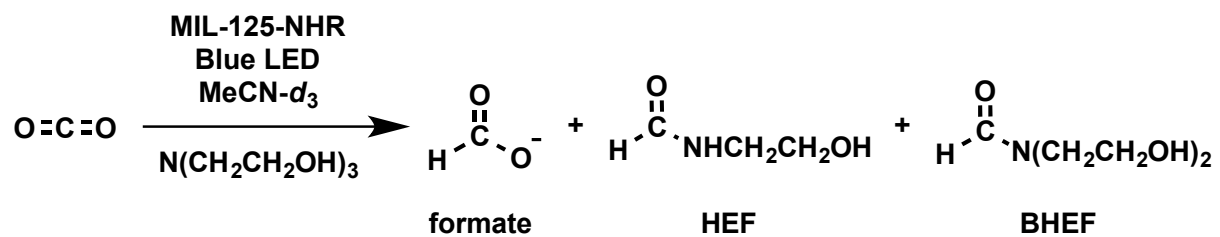
124

Figure 3-9: Photocatalytic reduction of carbon dioxide. Note: HEF and BHEF appear as formate reacts with hydrolyzed products of oxidized triethanolamine.
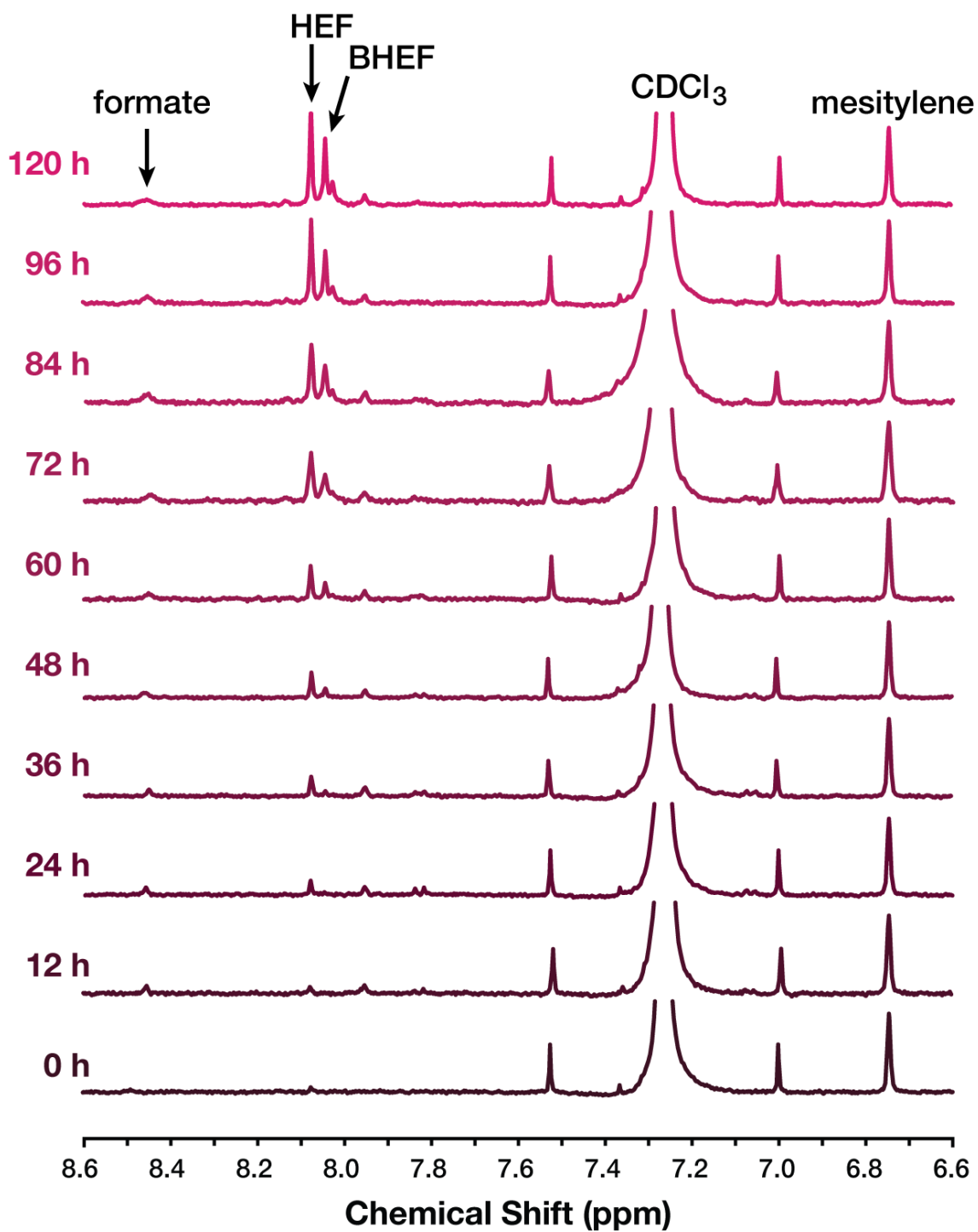
Figure 3-10: 1H NMR traces (400 MHz, CDCl3, 25 ºC) at varying times of the photoreduction of CO2 under blue LED illumination using MIL-125-NHCyp. Signals for formate, HEF, BHEF, residual solvent, and internal standard are indicated.
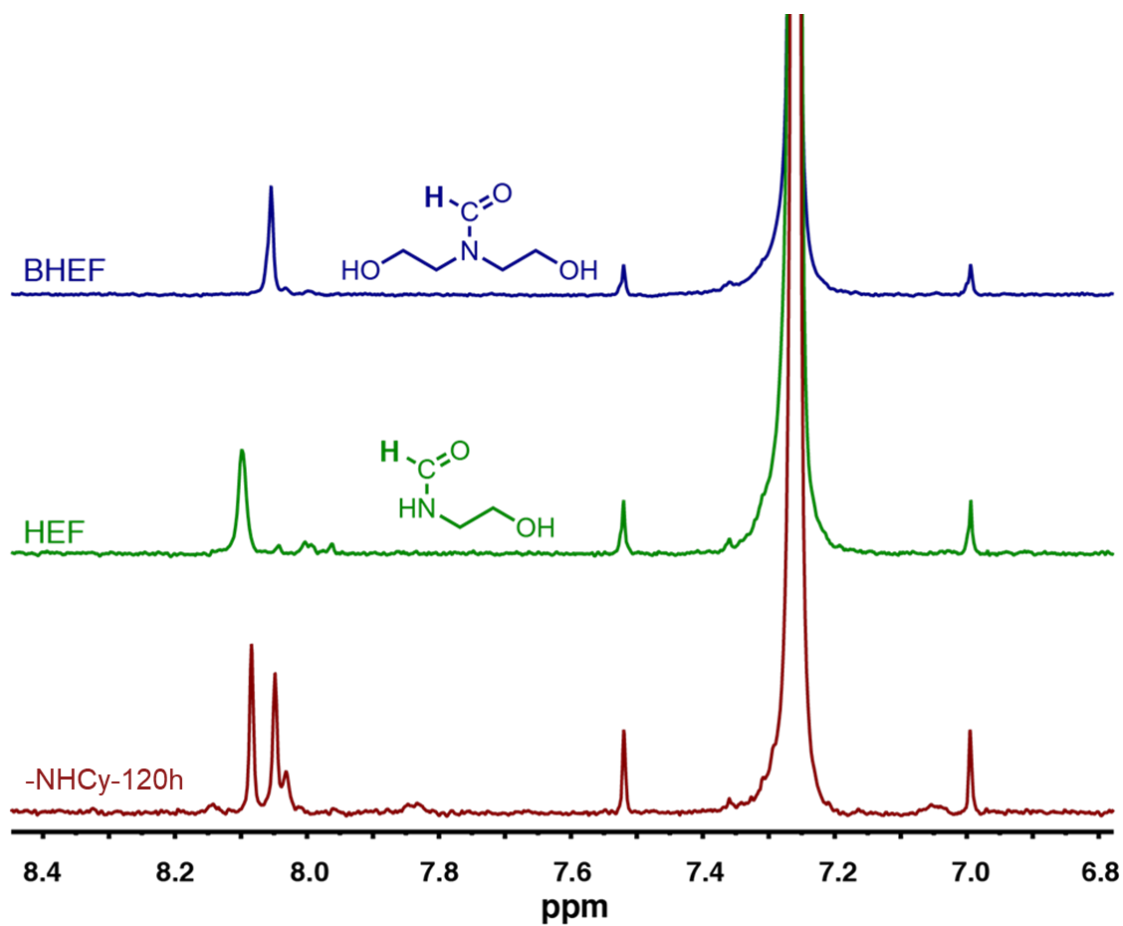
Figure 3-11: ^{1}H NMR (CDCl3, 400 MHz, 25 ℃) of HEF and BHEF compared to CO_2-photoreduced products using MIL-125-NHCy. Signal at 7.26 ppm is residual solvent and it corresponding satellite peaks.
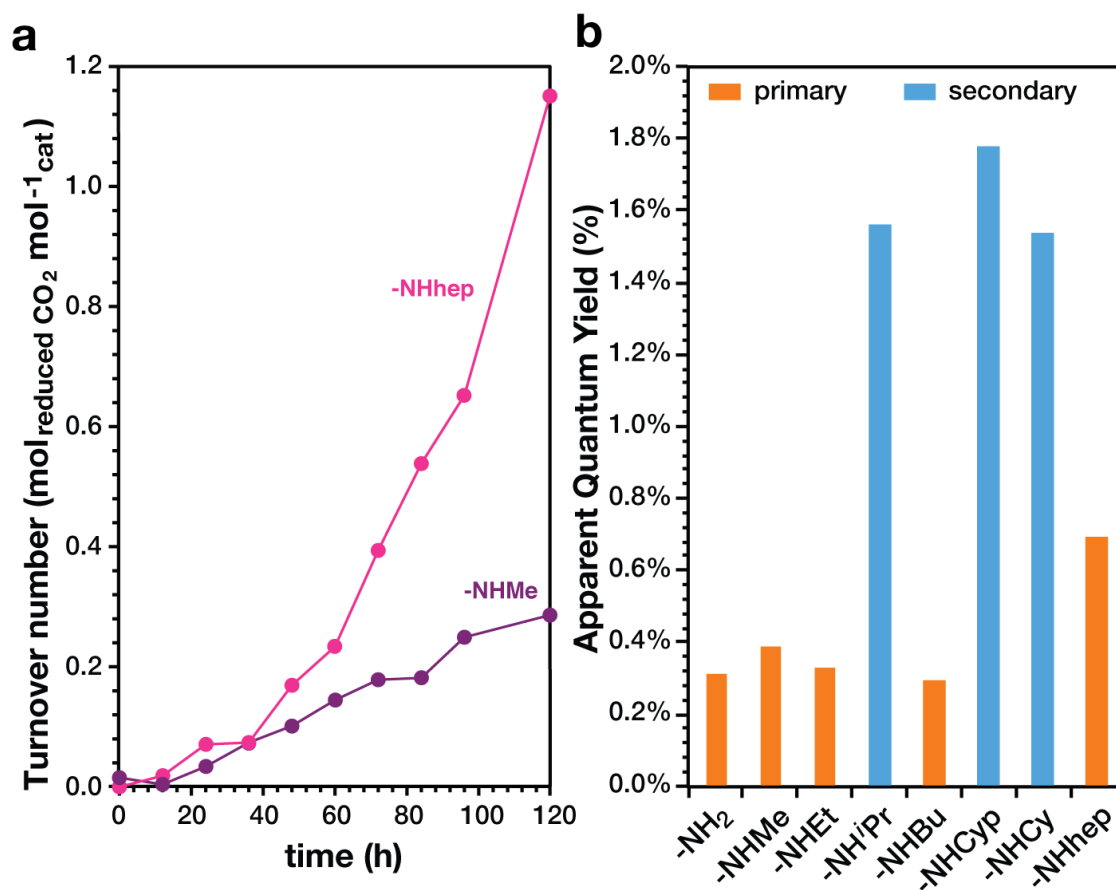
Figure 3-12: (a) Kinetic plot of CO_2-photoreduced products (formate, HEF and BHEF) over time utilizing MIL-125-NHMe (purple) and MIL-125-NHhep (pink). Turnover number determined as total moles of reduced CO_2 per mole of catalyst (based on linker). (b) CO_2 photoreduction apparent quantum yield of the isoreticular MIL-125-NHR MOFs, the histogram color indicates the nature of the alkyl chain.
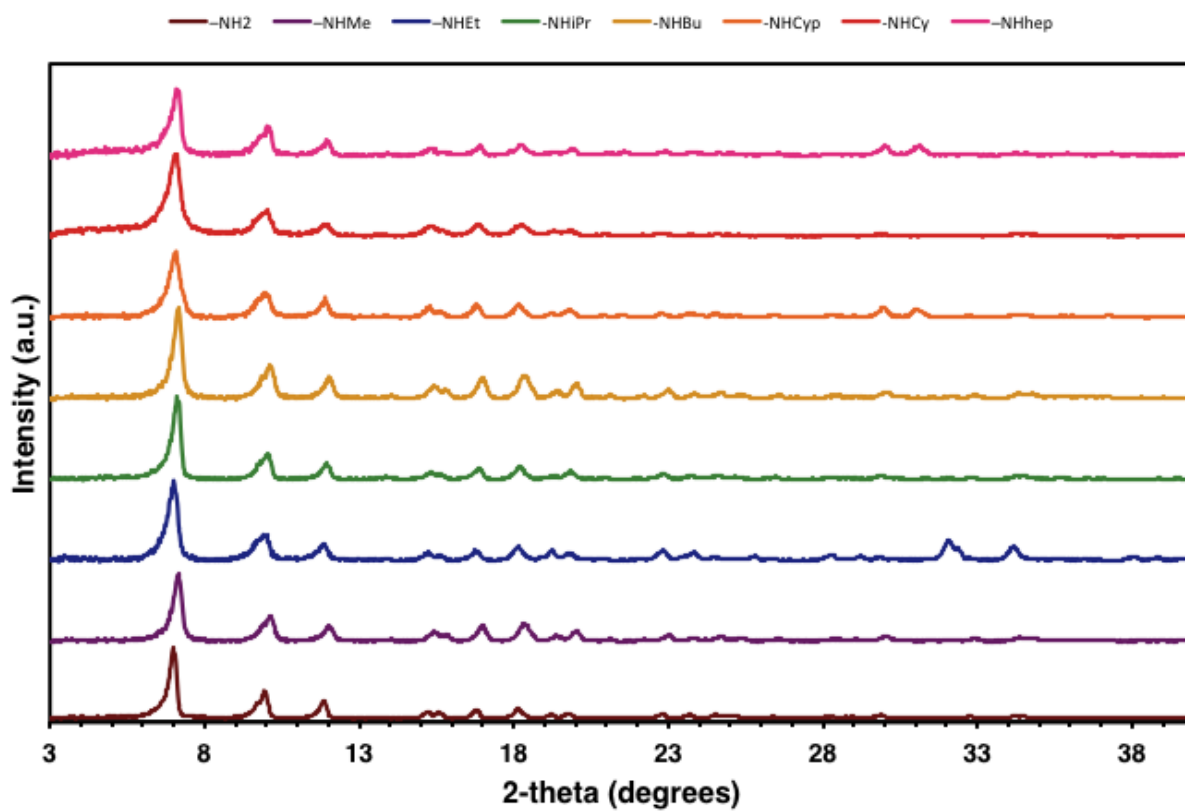
Figure 3-13: Powder X-ray diffraction patterns of the isoreticular family of MIL-125-NHR post photocatalysis showing no significant degradation in crystallinity.
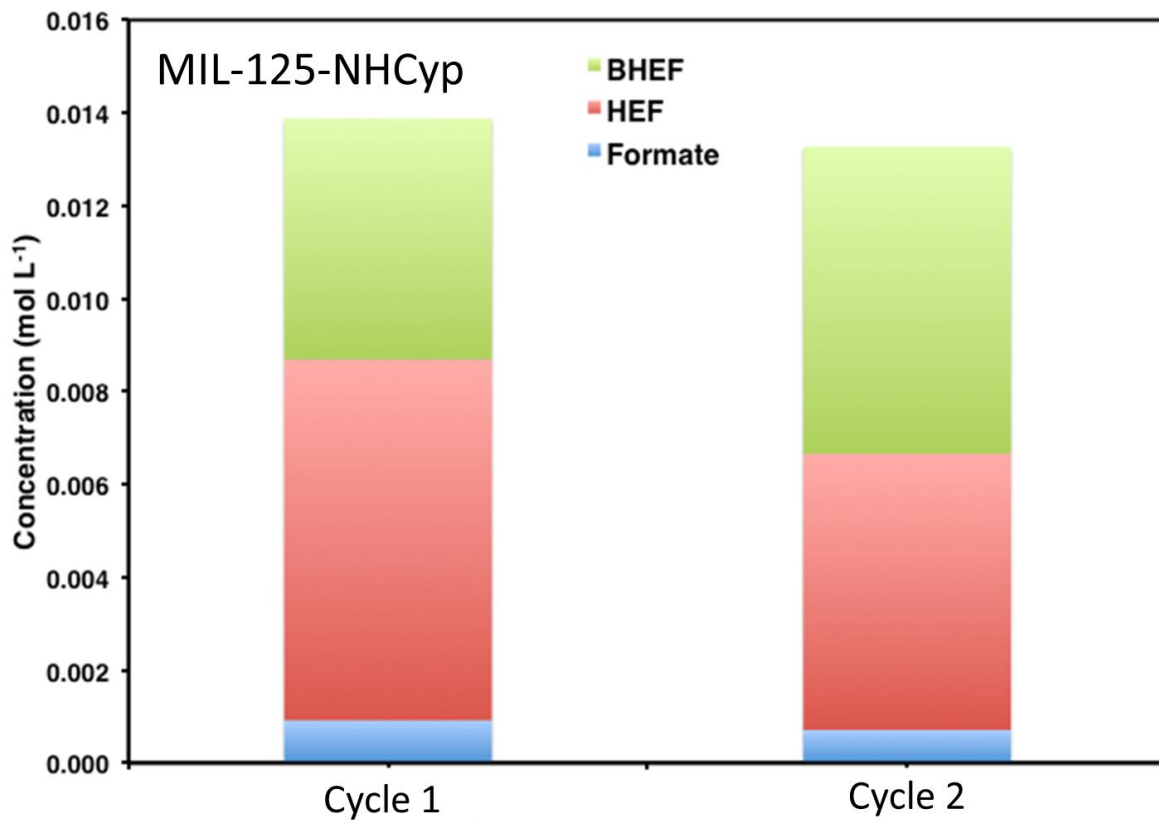
Figure 3-14: Plot showing the concentration in mol L^{-1} of CO_2 reduced species from re-utilized MIL-125-NHCyp after an additional 120 h exposure under blue LED compared to the pristine MOF photocatalyst.

3.4 <u>Conclusion</u>

We prepared an isoreticular series of titanium-based MOF photocatalysts by increasing the *N*-alkyl substitution in MIL-125-NHR, where R varies from methyl, to ethyl, isopropyl, *n*-butyl, cyclopentyl, cyclohexyl, and *n*-heptyl. The isoreticular nature of their crystal structure was studied by powder X-ray crystallography and gas adsorption. Their photophysical and photocatalytic properties were studied displaying a gradual decrease in the optical bandgap from 2.56 eV in MIL-125-NH$_2$ to 2.29 eV in MIL-125-NHCy, consistent with increased electron density around the organic linker via inductive effects of the *N*-alkyl chain. We explored the photocatalytic efficiency of the MOFs towards reduction of carbon dioxide under blue LED light, displaying increased reaction rates and quantum yields consistent with the increased alkyl substitution. We observed that the CO_2 photoreduction quantum yield is higher for MOFs with increased excited-state lifetime, particularly with secondary *N*-alkyls substituents, and concluded that from the current proposed mechanism, the electron transfer from Ti^{+3} to CO_2 is the rate-limiting step in the photoreduction. This study allowed us to understand how small variations in the organic linker of the MOF can result in tuning of the photophysical and photocatalytic properties of the materials, solely by selection of specific substituents in the organic links.

3.5 <u>References</u>

1. Quadrelli, R.; Peterson, S., The energy–climate challenge: Recent trends in CO2 emissions from fuel combustion. *Energy Policy* **2007,** *35* (11), 5938-5952.

2. Tu, W.; Zhou, Y.; Zou, Z., Photocatalytic Conversion of CO2 into Renewable Hydrocarbon Fuels: State-of-the-Art Accomplishment, Challenges, and Prospects. *Advanced Materials* **2014,** *26* (27), 4607-4626.

3. Wang, C.; Thompson, R. L.; Baltrus, J.; Matranga, C., Visible light photoreduction of CO2 using CdSe/Pt/TiO2 heterostructured catalysts. *The Journal of Physical Chemistry Letters* **2009,** *1* (1), 48-53.

4. Woolerton, T. W.; Sheard, S.; Reisner, E.; Pierce, E.; Ragsdale, S. W.; Armstrong, F. A., Efficient and clean photoreduction of CO2 to CO by enzyme-modified TiO2 nanoparticles using visible light. *Journal of the American Chemical Society* **2010,** *132* (7), 2132-2133.

5. Li, P.; Zhou, Y.; Zhao, Z.; Xu, Q.; Wang, X.; Xiao, M.; Zou, Z., Hexahedron prism-anchored octahedronal CeO2: crystal facet-based homojunction promoting efficient solar fuel synthesis. *Journal of the American Chemical Society* **2015,** *137* (30), 9547-9550.

6. Asahi, R.; Morikawa, T.; Ohwaki, T.; Aoki, K.; Taga, Y., Visible-light photocatalysis in nitrogen-doped titanium oxides. *science* **2001,** *293* (5528), 269-271.

7. Habisreutinger, S. N.; Schmidt-Mende, L.; Stolarczyk, J. K., Photocatalytic reduction of CO2 on TiO2 and other semiconductors. *Angewandte Chemie International Edition* **2013,** *52* (29), 7372-7408.

8. Schultz, D. M.; Yoon, T. P., Solar synthesis: prospects in visible light photocatalysis. *Science* **2014,** *343* (6174), 1239176.

9. Furukawa, H.; Cordova, K. E.; O'Keeffe, M.; Yaghi, O. M., The chemistry and applications of metal-organic frameworks. *Science* **2013,** *341* (6149), 1230444.

10. Yaghi, O. M.; O'keeffe, M.; Ockwig, N. W.; Chae, H. K.; Eddaoudi, M.; Kim, J., Reticular synthesis and the design of new materials. *Nature* **2003,** *423* (6941), 705.

11. Furukawa, H.; Ko, N.; Go, Y. B.; Aratani, N.; Choi, S. B.; Choi, E.; Yazaydin, A. Ö.; Snurr, R. Q.; O'Keeffe, M.; Kim, J., Ultrahigh porosity in metal-organic frameworks. *Science* **2010,** *329* (5990), 424-428.

12.   Murray, L. J.; Dincă, M.; Long, J. R., Hydrogen storage in metal–organic frameworks. *Chemical Society Reviews* **2009,** *38* (5), 1294-1314.

13.   Sumida, K.; Rogow, D. L.; Mason, J. A.; McDonald, T. M.; Bloch, E. D.; Herm, Z. R.; Bae, T.-H.; Long, J. R., Carbon dioxide capture in metal–organic frameworks. *Chemical Reviews* **2011,** *112* (2), 724-781.

14.   Li, J.-R.; Kuppler, R. J.; Zhou, H.-C., Selective gas adsorption and separation in metal–organic frameworks. *Chemical Society Reviews* **2009,** *38* (5), 1477-1504.

15.   Zeng, L.; Guo, X.; He, C.; Duan, C., Metal–organic frameworks: Versatile materials for heterogeneous photocatalysis. *ACS Catalysis* **2016,** *6* (11), 7935-7947.

16.   He, H.; Perman, J. A.; Zhu, G.; Ma, S., Metal-Organic Frameworks for CO2 Chemical Transformations. *Small* **2016,** *12* (46), 6309-6324.

17.   Sun, C.-Y.; Qin, C.; Wang, X.-L.; Su, Z.-M., Metal-organic frameworks as potential drug delivery systems. *Expert Opinion on Drug Delivery* **2013,** *10* (1), 89-101.

18.   Kreno, L. E.; Leong, K.; Farha, O. K.; Allendorf, M.; Van Duyne, R. P.; Hupp, J. T., Metal–organic framework materials as chemical sensors. *Chemical Reviews* **2011,** *112* (2), 1105-1125.

19.   Yaghi, O. M., Reticular Chemistry・Construction, Properties, and Precision Reactions of Frameworks. ACS Publications: 2016.

20.   Wang, C.; Liu, D.; Lin, W., Metal–organic frameworks as a tunable platform for designing functional molecular materials. *Journal of the American Chemical Society* **2013,** *135* (36), 13222-13234.

21.   Dan-Hardi, M.; Serre, C.; Frot, T.; Rozes, L.; Maurin, G.; Sanchez, C.; Férey, G., A new photoactive crystalline highly porous titanium (IV) dicarboxylate. *Journal of the American Chemical Society* **2009,** *131* (31), 10857-10859.

22.   Yuan, S.; Liu, T.-F.; Feng, D.; Tian, J.; Wang, K.; Qin, J.; Zhang, Q.; Chen, Y.-P.; Bosch, M.; Zou, L., A single crystalline porphyrinic titanium metal–organic framework. *Chemical Science* **2015,** *6* (7), 3926-3930.

23.   Bueken, B.; Vermoortele, F.; Vanpoucke, D. E.; Reinsch, H.; Tsou, C. C.; Valvekens, P.; De Baerdemaeker, T.; Ameloot, R.; Kirschhock, C. E.; Van Speybroeck, V., A Flexible Photoactive Titanium Metal–Organic Framework Based on a [TiIV3 (µ3-O)(O) 2 (COO) 6] Cluster. *Angewandte Chemie* **2015,** *127* (47), 14118-14123.

24.   Zou, L.; Feng, D.; Liu, T.-F.; Chen, Y.-P.; Yuan, S.; Wang, K.; Wang, X.; Fordham, S.; Zhou, H.-C., A versatile synthetic route for the preparation of titanium metal–organic frameworks. *Chemical Science* **2016,** *7* (2), 1063-1069.

25.   Assi, H.; Pardo Pérez, L. C.; Mouchaham, G.; Ragon, F.; Nasalevich, M.; Guillou, N.; Martineau, C.; Chevreau, H.; Kapteijn, F.; Gascon, J., Investigating the case of titanium (IV) carboxyphenolate photoactive coordination polymers. *Inorganic chemistry* **2016,** *55* (15), 7192-7199.

26.   Nguyen, H. L.; Gándara, F.; Furukawa, H.; Doan, T. L.; Cordova, K. E.; Yaghi, O. M., A titanium–organic framework as an exemplar of combining the chemistry of metal–and covalent–organic frameworks. *Journal of the American Chemical Society* **2016,** *138* (13), 4330-4333.

27.   Serre, C.; Groves, J. A.; Lightfoot, P.; Slawin, A. M.; Wright, P. A.; Stock, N.; Bein, T.; Haouas, M.; Taulelle, F.; Férey, G., Synthesis, structure and properties of related

microporous N, N '-piperazinebismethylenephosphonates of aluminum and titanium. *Chemistry of Materials* **2006,** *18* (6), 1451-1457.

28. Gao, J.; Miao, J.; Li, P.-Z.; Teng, W. Y.; Yang, L.; Zhao, Y.; Liu, B.; Zhang, Q., A p-type Ti (iv)-based metal–organic framework with visible-light photo-response. *Chemical Communications* **2014,** *50* (29), 3786-3788.

29. Logan, M. W.; Lau, Y. A.; Zheng, Y.; Hall, E. A.; Hettinger, M. A.; Marks, R. P.; Hosler, M. L.; Rossi, F. M.; Yuan, Y.; Uribe-Romo, F. J., Heterogeneous photoredox synthesis of N-hydroxy-oxazolidinones catalysed by metal–organic frameworks. *Catalysis Science & Technology* **2016,** *6* (14), 5647-5655.

30. Nasalevich, M. A.; Goesten, M. G.; Savenije, T. J.; Kapteijn, F.; Gascon, J., Enhancing optical absorption of metal–organic frameworks for improved visible light photocatalysis. *Chemical Communications* **2013,** *49* (90), 10575-10577.

31. Toyao, T.; Saito, M.; Horiuchi, Y.; Mochizuki, K.; Iwata, M.; Higashimura, H.; Matsuoka, M., Efficient hydrogen production and photocatalytic reduction of nitrobenzene over a visible-light-responsive metal–organic framework photocatalyst. *Catalysis Science & Technology* **2013,** *3* (8), 2092-2097.

32. Shen, L.; Luo, M.; Huang, L.; Feng, P.; Wu, L., A Clean and General Strategy To Decorate a Titanium Metal–Organic Framework with Noble-Metal Nanoparticles for Versatile Photocatalytic Applications. *Inorganic chemistry* **2015,** *54* (4), 1191-1193.

33. Wang, H.; Yuan, X.; Wu, Y.; Zeng, G.; Chen, X.; Leng, L.; Wu, Z.; Jiang, L.; Li, H., Facile synthesis of amino-functionalized titanium metal-organic frameworks and their superior visible-light photocatalytic activity for Cr (VI) reduction. *Journal of Hazardous Materials* **2015,** *286*, 187-194.

135

34.   Fu, Y.; Sun, D.; Chen, Y.; Huang, R.; Ding, Z.; Fu, X.; Li, Z., An Amine-Functionalized Titanium Metal–Organic Framework Photocatalyst with Visible-Light-Induced Activity for CO2 Reduction. *Angewandte Chemie* **2012,** *124* (14), 3420-3423.

35.   de Miguel, M.; Ragon, F.; Devic, T.; Serre, C.; Horcajada, P.; García, H., Evidence of Photoinduced Charge Separation in the Metal–Organic Framework MIL-125 (Ti)-NH2. *ChemPhysChem* **2012,** *13* (16), 3651-3654.

36.   Hendon, C. H.; Tiana, D.; Fontecave, M.; Sanchez, C. m.; D'arras, L.; Sassoye, C.; Rozes, L.; Mellot-Draznieks, C.; Walsh, A., Engineering the optical response of the titanium-MIL-125 metal–organic framework through ligand functionalization. *Journal of the American Chemical Society* **2013,** *135* (30), 10942-10945.

37.   Lin, C.-K.; Zhao, D.; Gao, W.-Y.; Yang, Z.; Ye, J.; Xu, T.; Ge, Q.; Ma, S.; Liu, D.-J., Tunability of band gaps in metal–organic frameworks. *Inorganic Chemistry* **2012,** *51* (16), 9039-9044.

38.   Sippel, P.; Denysenko, D.; Loidl, A.; Lunkenheimer, P.; Sastre, G.; Volkmer, D., Dielectric Relaxation Processes, Electronic Structure, and Band Gap Engineering of MFU-4-type Metal-Organic Frameworks: Towards a Rational Design of Semiconducting Microporous Materials. *Advanced Functional Materials* **2014,** *24* (25), 3885-3896.

39.   Pham, H. Q.; Mai, T.; Pham-Tran, N.-N.; Kawazoe, Y.; Mizuseki, H.; Nguyen-Manh, D., Engineering of band gap in metal–organic frameworks by functionalizing organic linker: a systematic density functional theory investigation. *The Journal of Physical Chemistry C* **2014,** *118* (9), 4567-4577.

40.   Anslyn, E. V.; Dougherty, D. A., *Modern Physical Organic Chemistry*. University science books: 2006.

41.   Materials Studio, version 8.0; BIOVIA Software Inc.: San Diego CA, 2014.

42.   Toby, B. H.; Von Dreele, R. B., GSAS-II: the genesis of a modern open-source all purpose crystallography software package. *Journal of Applied Crystallography* **2013,** *46* (2), 544-549.

43.   Walton, K. S.; Snurr, R. Q., Applicability of the BET method for determining surface areas of microporous metal− organic frameworks. *Journal of the American Chemical Society* **2007,** *129* (27), 8552-8556.

44.   Hatchard, C.; Parker, C. A., A new sensitive chemical actinometer-II. Potassium ferrioxalate as a standard chemical actinometer. *Proc. R. Soc. Lond. A* **1956,** *235* (1203), 518-536.

45.   Serpone, N.; Salinaro, A., Terminology, relative photonic efficiencies and quantum yields in heterogeneous photocatalysis. Part I: Suggested protocol. *Pure and Applied Chemistry* **1999,** *71* (2), 303-320.

46.   Hahm, H.; Ha, H.; Kim, S.; Jung, B.; Park, M. H.; Kim, Y.; Heo, J.; Kim, M., Synthesis of secondary and tertiary amine-containing MOFs: C–N bond cleavage during MOF synthesis. *CrystEngComm* **2015,** *17* (30), 5644-5650.

47.   Pimputkar, S.; Speck, J. S.; DenBaars, S. P.; Nakamura, S., Prospects for LED lighting. *Nature Photonics* **2009,** *3* (4), 180.

48.   Tlili, A.; Blondiaux, E.; Frogneux, X.; Cantat, T., Reductive functionalization of CO 2 with amines: an entry to formamide, formamidine and methylamine derivatives. *Green Chemistry* **2015,** *17* (1), 157-168.

49.   Ishida, H.; Tanaka, H.; Tanaka, K.; Tanaka, T., Electrochemical Reaction of CO2 with Me2NH to Afford N, N-Dimethylformamide, Catalyzed by [Ru (bpy) 2 (CO) 2] 2+(bpy= 2, 2′-bipyridine). *Chemistry Letters* **1987,** *16* (4), 597-600.

50.   Kobayashi, K.; Kikuchi, T.; Kitagawa, S.; Tanaka, K., Selective Generation of Formamides through Photocatalytic CO2 Reduction Catalyzed by Ruthenium Carbonyl Compounds. *Angewandte Chemie International Edition* **2014,** *53* (44), 11813-11817.

51.   Zhang, L.; Han, Z.; Zhao, X.; Wang, Z.; Ding, K., Highly Efficient Ruthenium-Catalyzed N-Formylation of Amines with H2 and CO2. *Angewandte Chemie* **2015,** *127* (21), 6284-6287.

52.   Pandey, G.; Ghorai, M.; Hajra, S., Design of a photosystem to harvest visible-light into electrons: photosensitised one electron redox reactions in organic synthesis. *Pure and Applied Chemistry* **1996,** *68* (3), 653-658.

53.   Patil, U. B.; Singh, A. S.; Nagarkar, J. M., Nanoceria-catalyzed highly efficient procedure for N-formylation of amines at room temperature under solvent-free conditions. *Chemistry Letters* **2013,** *42* (5), 524-526.

CHAPTER 4: STRUCTURAL STABILITY OF *N*-ALKYL FUNCTIONALIZED TITANIUM METAL-ORGANIC FRAMEWORKS IN AQUEOUS AND HUMID ENVIROMENTS

4.1 Introduction

One of the most common concerns for the widespread realization of metal-organic frameworks (MOFs)[1-3] in real life applications is their perceived instability towards water. Unlike zeolites, which retain crystallinity, porosity, and performance under humid environments, MOFs can be very easily disrupted when exposed to aqueous conditions.[4] Due to the combination of high porosity and the presence oxygen rich metal-oxide clusters, MOFs tend to be hygroscopic, and often water can induce collapse of the structure,[5-8] or interfere with the adsorption of specific guests.[9-11] Improved structural stability in water has been observed in MOFs built with early transition metal ions, in particular with zirconium,[12] titanium,[13] and yttrium.[14] The archetypical zirconium-based **UiO-66** MOFs can remain untouched for long periods of time when boiled in water and acids, without major loss of structural and porosity properties.[15-17] This superior stability towards water is believed to be an effect of the kinetic stability of the $Zr_6O_4(OH)_4(CO_2)_{12}$ cluster,[18,19] and as consequence, this framework type has become very popular for water stable isoreticular MOFs.[20]

Titanium based MOF **MIL-125**, features a stable $Ti_8O_4(OH)_4(CO_2)_{12}$ cluster that also displays water stability; however, a limited number of isoreticular materials have been prepared. These MOFs have gained increased attention due to their exceptional performance as photoredox catalysts.[21-25] In our previous work, we demonstrated that *N*-alkyl functionalization of **MIL-125-NH₂** results in improved photophysical and photocatalytic properties, especially for CO_2 photoreduction.[22] Of the series, **MIL-125-NHCyp** (Cyp = cyclopentyl), which bears a

cyclopentylamine group at the terephthalate linker, exhibits high photocatalytic efficiency at moderate rates under continuous blue LED irradiation without decomposition. The photocatalytic performance of this MOF inspired us to further study its stability in water rich environments to understand how the functionalization of the linker plays a role in their structural stability and water exclusion for improved photocatalysis.

4.2 <u>Experimental Section</u>

All starting materials and solvents, unless otherwise specified, were obtained from commercial sources (Aldrich, Fisher, VWR) and used without further purification. All reactions were performed at ambient laboratory conditions, and no precautions were taken to exclude oxygen or atmospheric moisture unless otherwise specified. Anhydrous *N,N*-dimethylformamide (DMF) and tetrahydrofuran (THF) were purified using a custom-built alumina-column based solvent purification system (Inovative Technology). Anhydrous methanol was obtained from Aldrich (Sureseal). Deuterated solvents (CDCl$_3$, DMSO) were obtained from Cambridge Isotope Lab.

4.2.1   Instrumental

Powder X-ray diffraction (PXRD) data was collected using a Rigaku MiniFlex 600 θ-2θ diffractometer in Bragg-Brentano geometry with a 300 mm goniometer diameter, Ni-filtered CuK$_\alpha$ radiation (λ = 1.5418 Å) at 600 W power (40 kV, 15 mA), equipped with a NaI(Tl) SC-70 scintillation detector, 5.0º incident and receiving Soller slits, a 0.625º divergent slit, a 1.25º scattering slit, a 0.3 mm receiving slit and a Ni-CuK$_\beta$ filter. Samples were analyzed from 3 to 40 2θ-degrees with 0.02º per step and a scan rate of 1.0 degrees min^{-1}. Samples were prepared by dropping the powder sample in a glass sample holder and pressing the powder with a razor blade

spatula forming a smooth surface. Crystal models were created using Materials Studio modeling suite[i] starting from the published crystal of MIL-125 (CCDC code RUPRUQ) by adding the corresponding *N*-alkyl chains.

Gas adsorption isotherm analysis was performed using a Micromeritics ASAP 2020 surface area and porosimetry analyzer. Measurements were performed at 77 K (liquid N_2 bath) for $N_2(g)$, and at 308 K (water circulator bath) for $H_2O(g)$ on thermally activated samples. Brunauer-Emmet-Teller (BET) surface areas were obtained by performing a Rouquerol analysis over the linear isotherm to determine the upper limits of the BET model from the N_2 isotherms. Least squares linear fitting over the BET plot provided the parameter for the volume of the monolayer, BET surface area and *C*-constant were obtained following the recommendation by Snurr *et al*. for determination of the surface area in MOFs.[26]

4.2.2   Synthesis

Synthesis of metal-organic frameworks was performed as described by Logan *et al* also in chapter 3.[13]

The bulk crystallographic stability was measured by immersing power samples (~20 mg) in solvent (~3 mL) for and taking measurements at: 1, 3, 5, 7, 10, 15, 20, 30 day for each sample, or until the sample was completely decomposed. Measurements were carried out until initial powder pattern of MOF is no longer present for all three MOF samples or 30 day was measured. For comparison of MOFs in environments, the onset of decomposition began when the anatase phase of TiO_2 appears (25 and 38 2-theta degrees).

4.2.3   Water Vapor Sorption

Multiple water vapor adsorption isotherms were performed in succession, each cycle being followed by 1 h of dynamic evacuation at 2×10^{-6} torr prior to following cycle. Each adsorption/desorption cycle was from 0.0025-0.45 bar with 30 points in each cycle (20 adsorption, 10 desorption).

4.2.4   Density functional theory

We use density functional theory (DFT) to perform geometry optimization, total energy, and vibrational frequency calculations. Our DFT calculations employ plane-wave basis set and the projector-augmented wave (PAW)[27,28] method as implemented in Vienna ab-initio simulation package (VASP).[29,30] We set cut-off energy for plane-wave expansion at 500 eV. We use Generalized Gradient Approximation (GGA) in the form of Perdew-Burke-Ernzerhof (PBE) functional[31] to describe exchange-correlation interactions between the electrons. We use the implicit solvation model VASPsol[32] to include aquatic solvent effect. All molecules are fully relaxed until all force components reach 10^{-3} eV/Å. Vibrational frequencies are calculated using the finite-different method. In all calculations, the molecules are placed at the center of a box of $L \times L \times L$ Å^3 cubic box ($L = 25$). We apply monopole, dipole, and quadrupole corrections[33,34] to cancel the effect of artificial interactions between periodical images and to correct energy for charged systems. In addition, for charged system, we performed a series of total energy calculations with varying L from 20 to 50 Å with a step of 5 Å the results of which are used to fit to $E = a/L^n + b$ to extrapolate the total energy E for $L \rightarrow \infty$.

We estimate pKa of the dicarboxylic acid linkers by assuming the standard deprotonation reaction, AH $\leftrightharpoons$ A$^-$ + H$^+$, in aqueous solution, and thus p$K_a = \Delta G_{aq}/(RT ln10)$, where ΔG_{aq} is the change of Gibbs free energy and defined as $\Delta G_{aq} = G_{aq}(A^-) + G_{aq}(H^+) - G_{aq}(AH)$. The Gibbs free energy $G_{aq}(AH)$ of AH and $G_{aq}(A^-)$ of A$^-$ are evaluated using standard statistical mechanical treatments in the ideal gas approximation.[35] including zero-point energy correction and entropy including translational, rotational, and vibrational contributions. For the Gibbs free energy of aqueous proton $G_{aq}(H^+)$, we used experimental values as described in Ref. 36. Oftentimes, calculated pKa indicate a linear correlation with experimental values, however the intercept is not 0 and the slop is far from 1.[36-39] While searching for accurate method to calculate pKa is still an active research topic, the problem can be fixed by a simple linear interpolation (ap$K_a + b$, where a and b are two constants that are needed to be determined). In this work, the constants are determined so that pKa_1 and pKa_2 of terephthalic acid (3.54 and 4.43, respectively)[40] are exactly reproduced. The calculated pKa of several carboxylic acids in aqueous solution using the above interpolation, as shown in Table 4-2, are in excellent agreement with experimental ones.[37] This gives us confidence to use it to calculate pKa_1 and pKa_2 of dicarboxylic acid linkers. The results are summarized in Table S1. Note that if we assume the deprotonation reaction as AH + H$_2$O $\leftrightharpoons$ A$^-$ + H$_3$O$^+$ and all Gibbs free energies are calculated, identical results can be obtained with the same interpolation approach.

4.3 <u>Results and Discussion</u>

We studied the bulk crystallographic stability and water vapor adsorption properties of **MIL-125-NHCyp** compared to **MIL-125-NH₂**, and **MIL-125-NHMe**. First, we compared the structural stability of the three MOFs by immersing bulk powder samples in water for varied periods of time

and measured their X-ray power diffraction pattern (PXRD), until the anatase phase of TiO_2 started to appear (Figure 4-1 and Table 1). At 25 ºC and pH 7, we observed that both **MIL-125-NH₂** and **MIL-125-NHCyp** retain their crystallinity up to 20 d. Although neutral water at room temperature did not produce major differences in the stability between these two MOFs, **MIL-125-NHCyp** exhibited an increased stability after raising the temperature and varying the pH. Increasing the temperature to 50 and 70 ºC**, MIL-125-NH₂** decomposes after 5 and 3 d, respectively, whereas **MIL-125-NHCyp** displays decomposition after 10 and 7 d, at the respective temperature. In more acidic environments, decreasing the pH to 4, **MIL-125-NHCyp** retains crystallinity even after being immersed for 20 d, and **MIL-125-NH₂** only up to 15 d. At pH 1, both MOFs remain crystalline, but only up to 7 d. In alkaline media at pH 9, **MIL-125-NHCyp** retains crystallinity up to 15 d and **MIL-125-NH₂** decomposes after 10 d. At pH higher than 9, we observed almost immediate dissolution of all MOFs. In the case of **MIL-125-NHMe**, we observed that this MOF decomposed at much shorter times under all the described conditions (Table 1, see SI), evidencing that the nature of the substitution plays a vital role.
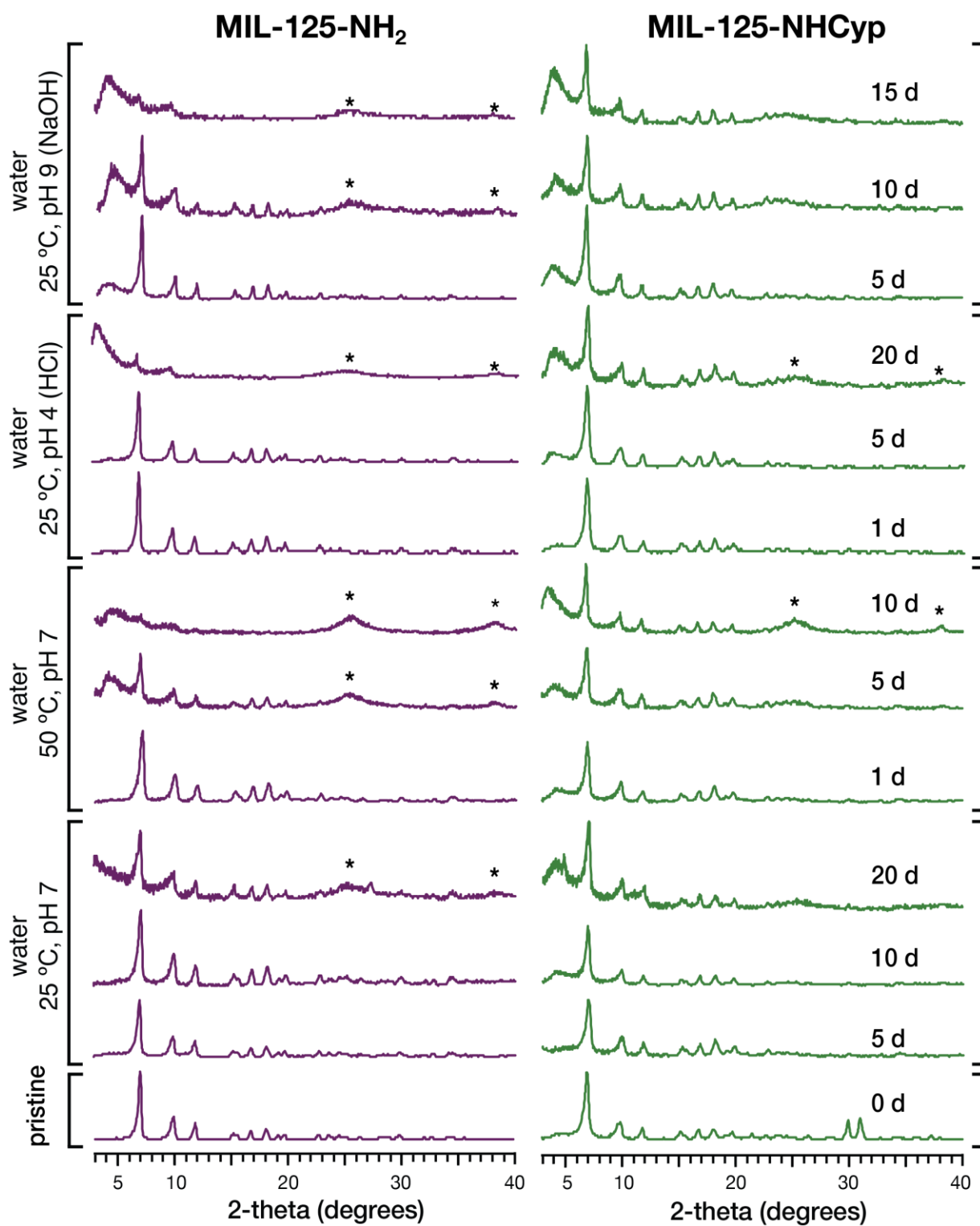
Figure 4-1: Powder X-ray diffraction of MIL-125-NH$_2$ and MIL-125-NHCyp (Cyp = cyclopentyl) after immersion in water at different time, temperatures, and pH. Stars indicate TiO$_2$ anatase phase.

Table 4-1: Water stability data of MIL-125-NHR MOFs. [a]Conditions: 20 mg of MOF in 3.0 mL of solvent at specified pH and temperature. [b]Time at which TiO_2 is observed. [c] 5% v/v H2O in MeCN. [d] At 0.15 M concentration.

Solvent	Temp. (ºC)	pH	Time (d)[b]		
			–NH$_2$	–NHMe	–NHCyp
H$_2$O	25	7	20	10	20
H$_2$O	50	7	5	3	10
H$_2$O	70	7	3	3	7
H$_2$O	25	1	7	3	7
H$_2$O	25	4	15	10	20
H$_2$O	25	9	10	7	15
H$_2$O/MeCN[c]	25	TEOA[d]	>30	>30	>30
MeCN	25	TEOA[d]	>30	>30	>30
MeCN	25	AcOH[d]	>30	>30	>30

Other studies towards water stability in MOFs have been addressed from the point of view of the effect that the pKa of the dicarboxylic acid linker, as well as the hydrophobicity of the side chain functionalization. Long *et al.* proposed that by utilizing less acidic organic linkers, *i.e.* increasing their pKa, should result in stronger metal–linker bonds.[41] In our case, since the only difference between the three linkers is the alkyl functionalization of the aniline in 2-amino-terephtalate (–H, –Me and –Cyp), we rationalize that the small inductive effects of the substituents result in small increases in the pKa value. We previously observed that these small inductive

146

effects indeed affect the electronic properties of the MOF, exhibiting decreased bandgaps, consistent with the expected trend.[22] We performed a DFT calculation on each of the three acids and found that these pKa values are very similar, for **MIL-125-NHMe** and **MIL-125-NHCyp** (see Table 4-2). So the inductive effects are too small to influence Ti–O (carboxylate) bond strength, affecting the stability only marginally.

Table 4-2: Calculated (calc) and experimental value (exp) of pKa of carboxylic acids used in this work. [a] Experimental values are taken from Ref. 37. [b] The values are for pKa_1 and pKa_2, respectively.

Molecule	pKa (calc)	pKa (exp[a])
HCOOH	3.60	3.75
CH_3COOH	4.78	4.76
C_6H_5COOH	4.23	4.20
p-$NH_2C_6H_4COOH$	5.03	4.87
Terephthalic acid	3.54, 4.43 [b]	3.54, 4.43[b]
2-amino-terephtalate (–H)	3.87, 4.77 [b]	NA
2-amino-terephtalate (–Me)	3.89, 4.62 [b]	NA
2-amino-terephtalate (–Cyp)	3.88, 4.79 [b]	NA

A second factor affecting the stability is the hydrophobicity of the linker. Cohen[42] and others[43-46] have studied this effect on the water stability of other MOFs (**MOF-5, MIL-53, UiO-66** types), observing that by adding longer alkyl chains, MOFs that are typically hygroscopic can become superhydrophobic. In our case, the *N*-cyclopentyl group would impart the required hydrophobicity (Figure 4-2) to exclude water from potentially attacking the metal-oxide cluster (see below). A third factor is the Lewis basicity of the aniline nitrogen, as inductive effects cause increased Lewis basicity of the heteroatom. This basicity should affect the hydrogen bonding ability of the linker. We believe that by substituting the amino group with a methyl, the Lewis basicity increases, causing a better interaction with water (see water adsorption below), making it more attractive towards water. This effect should be accentuated even more in **MIL-125-NHCyp**; however, the steric blocking ability of the cyclopentyl group inhibits hydrogen bonds and renders hydrophobicity.

In our previous study,[22] typical photocatalytic conditions with these MOFs were performed in polar organic solvents, such as acetonitrile (MeCN), under non-anhydrous conditions, and in the presence of sacrificial agents, such as basic triethanolamine (TEOA). Here we tested their stability under these conditions by exposing all three MOFs to wet acetonitrile, and in the presence of either TEOA or acetic acid (AcOH), and no decomposition was observed during the measured times (Table 1). The MOFs also remain stable in wet MeCN/TEOA under constant blue LED irradiation for up to 20 d. All the studied MOFs remain crystalline and with optimal photocatalytic operation, even under highly humid environments. This unusual stability prompted us to study how water interacts with the different MOFs, for which we performed water vapor adsorption studies.

MIL-125

MIL-125-NH₂   **MIL-125-NHMe**   **MIL-125-NHCyp**
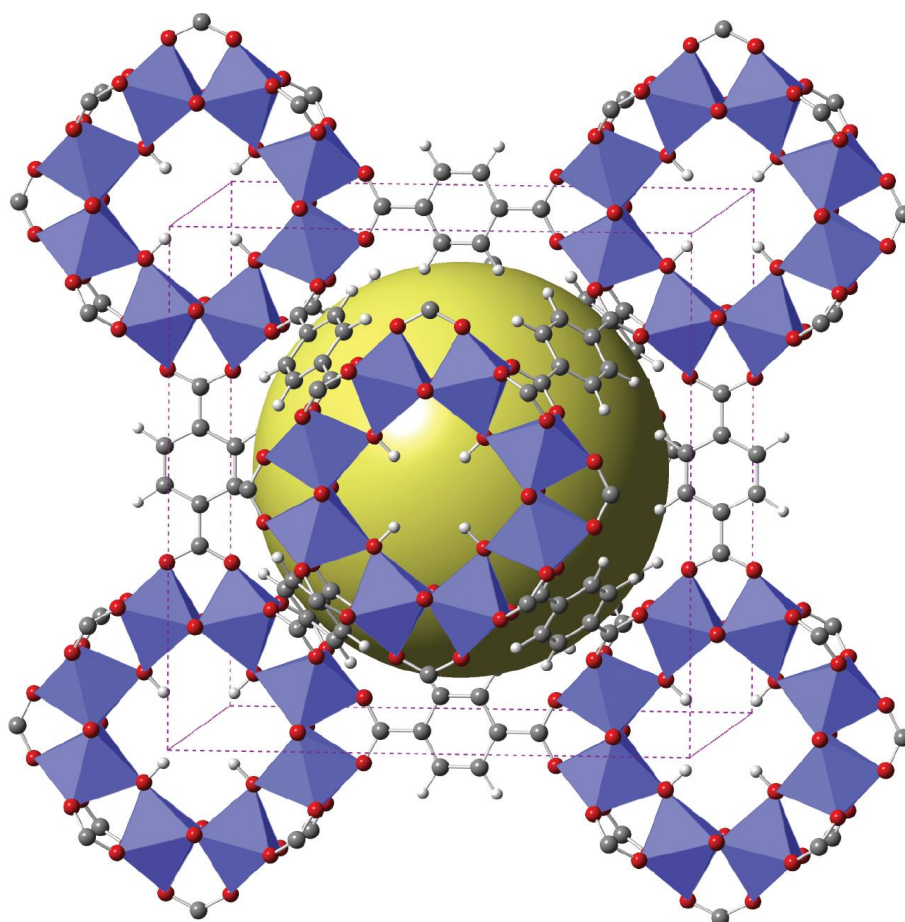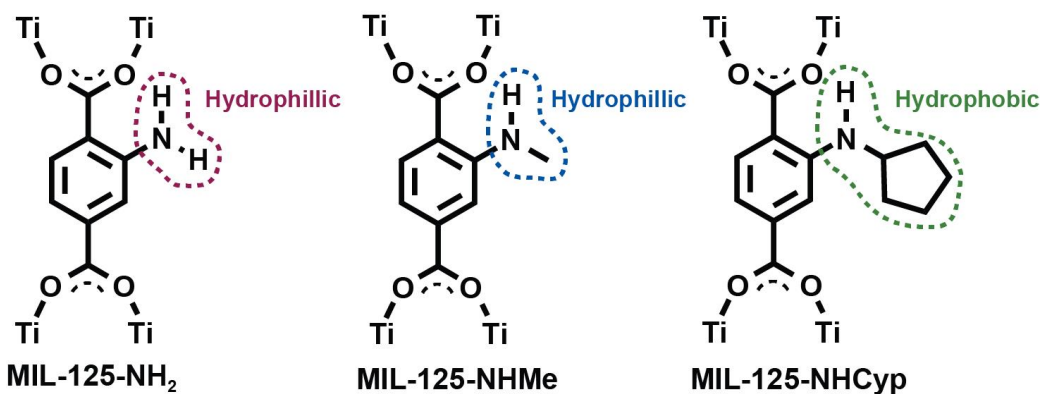
Figure 4-2: Top: crystal structure of the MIL-125 MOFs (gray spheres = carbon, white spheres = hydrogen, red spheres = oxygen, blue polyhedra = titanium, yellow sphere represents the pore, side chains not shown for clarity). Bottom: molecular structure of the –NHR substited linkers indicating hydrophillicity/hydrophobicity of the side chains.

149

We measured the water vapor isotherms at 35 °C (Figure 4-3). As previously observed, **MIL-125-NH₂** displays an IUPAC isotherm Type V, with a characteristic *S*-shape. [47,47] It has been discussed that the shape of the isotherm is due to either pressure-induced pore gating, or clustering of water at the surface of the MOF particles at low pressure, followed by "cooperative adsorption" starting at 20% relative humidity (RH), adsorbing between 30-40% of its weight in water (at 30-80% RH, Table 2). Following a similar trend, **MIL-125-NHMe** also displays the *S*-shaped isotherm, but with slightly decreased water uptake, consistent with its high affinity to water and decreased pore volume,[22] adsorbing water between 20-30 wt% above 30% RH. **MIL-125-NHCyp** on the other hand, exhibits a much smaller water uptake, between 6-12 wt% at the same RH range as the other MOFs, with a very small inflection point at around 20% RH. The isotherm shape and uptake indicate that this MOF is hydrophobic, excluding water more efficiently than the hydrophilic MOFs. This difference in water adsorption is consistent with the increased hydrophobicity of the cyclopentyl group as discussed above. These differences in water adsorption were studied in **UiO-66** MOFs, where functionalization with –NH₂ and –Me groups results in materials with very similar pore volume, but with more than 20% difference in water uptakes, attributing this difference to be a substitution effect,[45] *i.e.* hydrophobicity. Retention of the porous environment after water vapor adsorption was determined by comparison of the change in Brunauer-Emmett-Teller (BET) surface area from their $N_2(g)$ adsorption isotherm before and after water vapor adsorption (Table 4-3). All three MOFs results in retention of their BET surface area decreasing less than 4% of the initial surface area. Moreover, performing five cycles of water vapor adsorption-desorption over **MIL-125-NHCyp** (Figure 4-4), resulted in a decrease of less than 2% in BET surface area, further demonstrating its stability.
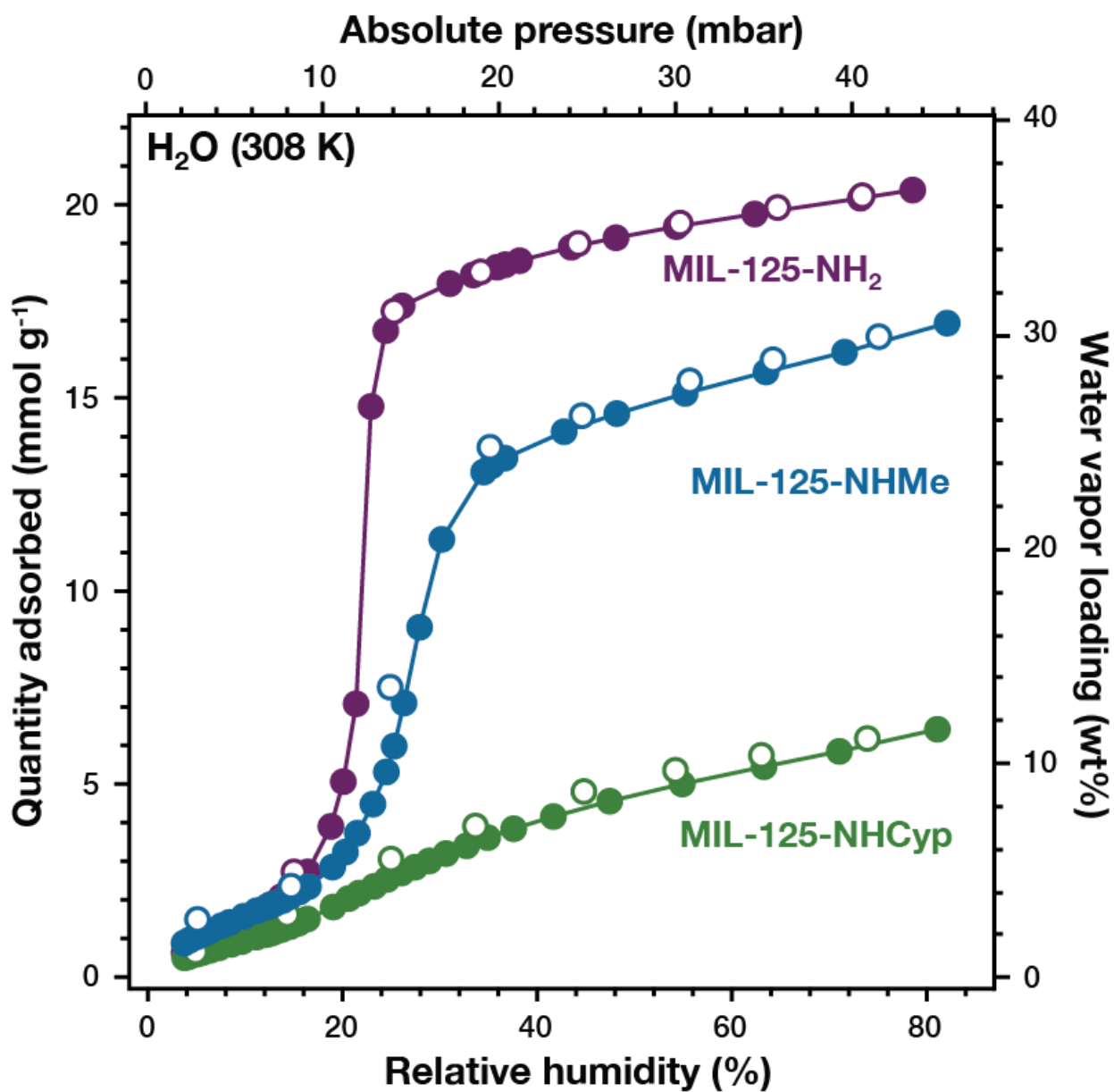
Figure 4-3: Water vapor adsorption isotherms at 308 K (35 ºC) of **MIL-125-NH₂** (purple), **MIL-125-NHMe** (blue), **MIL-125-NHCyp** (green). Closed symbols represent adsorption, open symbols desorption.
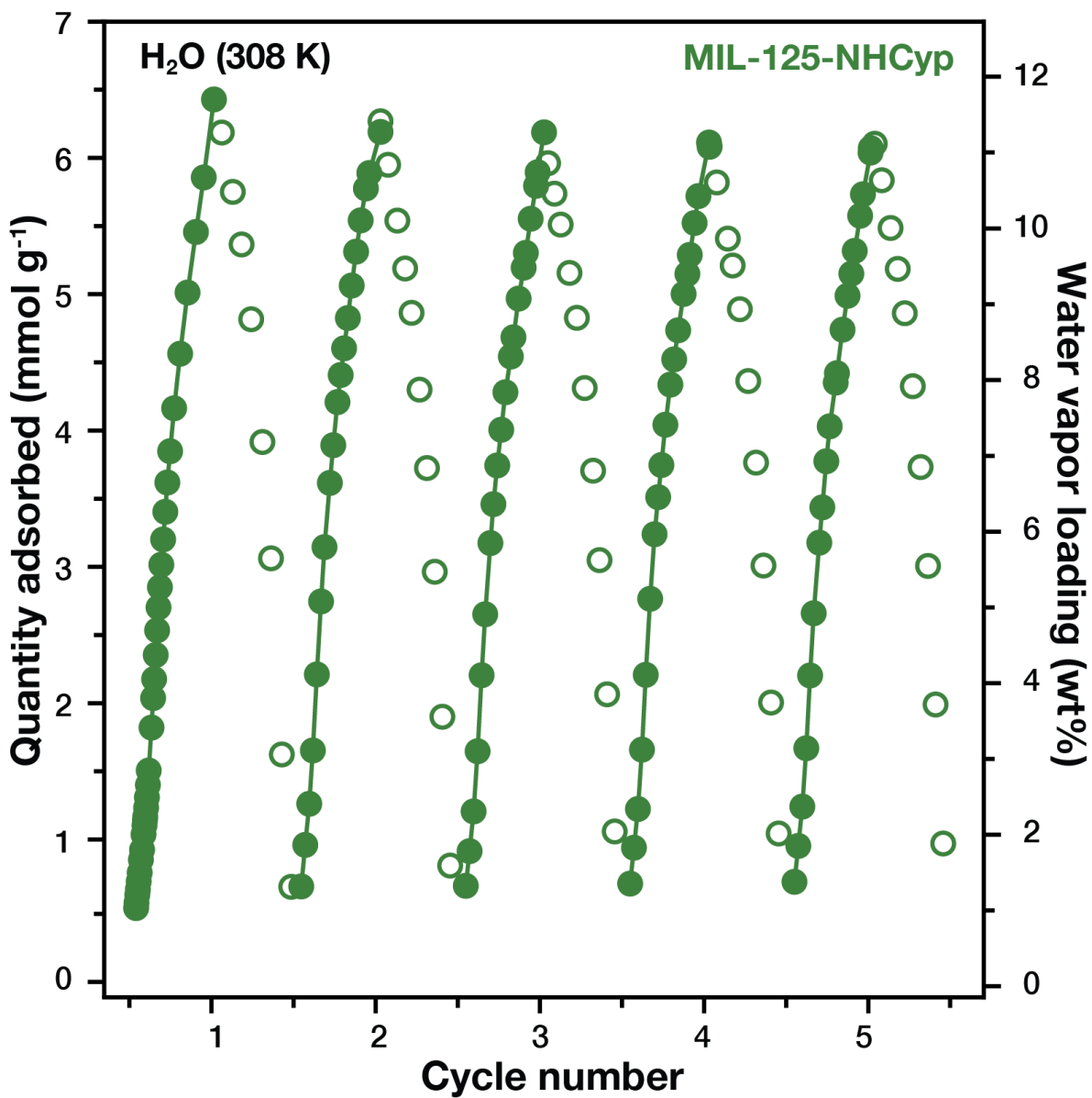
Figure 4-4: Dynamic water vapor (308 K) adsorption/desorption for **MIL-125-NHCyp**. Plot depicts five total cycles beginning from the left with each cycle ranged from 0.0025-0.45 bar with 30 points in each cycle (20 adsorption, 10 desorption). Closed symbols represent adsorption, open symbols, desorption.

Table 4-3: Water adsorption loadings at 30 and 80% relative humidity as well as change in BET surface area before and after water exposure. [a]Brunauer–Emmett–Teller (BET) surface area, calculated from N2(g) isotherm at 77 K (see SI). [b]Loading measured from water adsorption isotherms at 35 °C. [c]After 5 water vapor adsorption cycles (Figure 4-4).

MOF	Loading (wt%)		S_{BET} (m^2 g^{-1})[a]	
	30% RH	80% RH	Before	After
–NH$_2$	32	37	1473	1411
–NHMe	20	30	1047	1010
–NHCyp	6	12	510	503[c]

4.4 Conclusion

We have demonstrated that *N*-alkyl functionalization of photocatalytically active titanium metal-organic frameworks results in enhanced water stability. In particular, **MIL-125-NHCyp** is hydrophobic and exhibits superior structural stability towards humid environments, retaining crystallinity for more than a month under photocatalytic conditions, as well as retaining its porosity after multiple water adsorption-desorption cycles. This study demonstrates the importance of the electronic and steric effects that the organic linker can provide for application of MOFs in real life settings.

4.5 References

1.   Furukawa, H.; Cordova, K. E.; O'Keeffe, M.; Yaghi, O. M. The chemistry and applications of metal-organic frameworks. *Science* 2013, *341*, 1230444.

2.   Zhou, H.-C.; Kitagawa, S. Metal–organic frameworks (MOFs). *Chemistry Society Reviews* **2014**, *43*, 5415-5418.

3.   Zhang, T.; Lin, W. Metal-organic frameworks for artificial photosynthesis and photocatalysis. *Chemistry Society Reviews* **2014**, *43*, 5982-5993.

4.   Low, J. J.; Benin, A. I.; Jakubczak, P.; Abrahamian, J. F.; Faheem, S. A.; Willis, R. R. Virtual high throughput screening confirmed experimentally: porous coordination polymer hydration. *Journal of American Chemical Society* **2009**, *131*, 15834–15842.

5.   Greathouse, J. A.; Allendorf, M. D. The interaction of water with MOF-5 simulated by molecular dynamics. *Journal of American Chemical Society* **2006**, *128*, 10678–10679.

6.   Küsgens, P.; Rose, M.; Senkovska, I.; Fröde, H.; Henschel, A.; Siegle, S.; Kaskel, S. Characterization of metal-organic frameworks by water adsorption. *Microporous and Mesoporous Materials* **2009**, *120*, 325-330.

7.   Liang, Z.; Marshall, M.; Chaffee, A. L. CO_2 adsorption-based separation by metal organic framework (Cu-BTC) versus zeolite (13X). *Energy Fuels* **2009**, *23*, 2785–2789.

8.   Mustafa, D.; Breynaert, E.; Bajpe, S. R.; Martens, J. A.; Kirschhock, C. E. A. Stability improvement of $Cu_3(BTC)_2$ metal–organic frameworks under steaming conditions by encapsulation of a Keggin polyoxometalate. *Chemical Communications.* **2011**, *47*, 8037-8039.

9.   Schröck, K.; Schröder, F.; Heyden, M.; Fischer, R. A.; Havenith, M. Characterization of interfacial water in MOF-5 ($Zn_4(O)(BDC)_3$)—a combined spectroscopic and theoretical study. *Physical Chemistry Chemical Physics* **2008**, *10*, 4732-4739.

10. Borjigin, T.; Sun, F.; Zhang, J.; Cai, K.; Ren, H.; Zhu, G. A microporous metal–organic framework with high stability for GC separation of alcohols from water. *Chemical Communications* **2012**, *48*, 7613-7615.

11. Chen, B.; Ji, Y.; Xue, M.; Fronczek, F. R.; Hurtado, E. J.; Mondal, J. U.; Liang, C.; Dai, S. Metal−organic framework with rationally tuned micropores for selective adsorption of water over methanol. *Inorganic Chemistry* **2008**, *47*, 5543–5545.

12. Cavka, J. H.; Jakobsen, S.; Olsbye, U.; Guillou, N.; Lamberti, C.; Bordiga, S.; Lillerud, K. P. A new zirconium inorganic building brick forming metal organic frameworks with exceptional stability. *Journal of the American Chemical Society* **2008**, *130*, 13850–13851.

13. Dan-Hardi, M.; Serre, C.; Frot Théo; Rozes, L.; Maurin, G.; Sanchez, C.; Férey, G. A new photoactive crystalline highly porous titanium(IV) dicarboxylate. *Journal of the American Chemical Society* **2009**, *131*, 10857–10859.

14. Abdulhalim, R. G.; Bhatt, P. M.; Belmabkhout, Y.; Shkurenko, A.; Adil, K.; Barbour, L. J.; Eddaoudi, M. A Fine-Tuned Metal–Organic Framework for Autonomous Indoor Moisture Control. *Journal of the American Chemical Society* **2017**, *139*, 10715–10722.

15. Guillerm, V.; Ragon, F.; Dan-Hardi, M.; Devic, T.; Vishnuvarthan, M.; Campo, B.; Vimont, A.; Clet, G.; Yang, Q.; Maurin, G.; Férey, G.; Vittadini, A.; Gross, S.; Serre, C. A series of isoreticular, highly stable, porous zirconium oxide based metal–organic frameworks. *Analytical Chemistry* **2012**, *124*, 9401–9405.

16. Kandiah, M.; Nilsen, M. H.; Usseglio, S.; Jakobsen, S.; Olsbye, U.; Tilset, M.; Larabi, C.; Quadrelli, E. A.; Bonino, F.; Lillerud, K. P. Synthesis and stability of tagged UiO-66 Zr-MOFs. *Chemistry of Materials* **2010**, *22*, 6632–6640.

155

17. Decoste, J. B.; Peterson, G. W.; Jasuja, H.; Glover, T. G.; Huang, Y.-G.; Walton, K. S. Stability and degradation mechanisms of metal–organic frameworks containing the $Zr_6O_4(OH)_4$ secondary building unit. *Journal of Materials Chemistry A* **2013**, *1*, 5642-5650.

18. DeCoste, J. B.; Peterson, G. W.; Schindler, B. J.; Killops, K. L.; Browe, M. A.; Mahle, J. J. The effect of water adsorption on the structure of the carboxylate containing metal–organic frameworks Cu-BTC, Mg-MOF-74, and UiO-66. *Journal of Materials Chemistry A* **2013**, *1*, 11922-11932.

19. Mondloch, J. E.; Katz, M. J.; Planas, N.; Semrouni, D.; Gagliardi, L.; Hupp, J. T.; Farha, O. K. Are Zr_6-based MOFs water stable? Linker hydrolysis vs. capillary-force-driven channel collapse. *Chemical Communications* **2014**, *50*, 8944-8946.

20. Jiang, H.-L.; Feng, D.; Wang, K.; Gu, Z.-Y.; Wei, Z.; Chen, Y.-P.; Zhou, H.-C. An exceptionally stable, porphyrinic Zr metal–organic framework exhibiting pH-dependent fluorescence. *Journal of the American Chemical Society* **2013**, *135*, 13934–13938.

21. Fu, Y.; Sun, D.; Chen, Y.; Huang, R.; Ding, Z.; Fu X.; Li, Z. An amine-Functionalized Titanium Metal–Organic Framework Photocatalyst with Visible-Light-Induced Activity for CO_2 Reduction. *Angewandte Chemie* **2012**, *124*, 3420-3423.

22. Logan, M. W.; Ayad, S.; Adamson, J. D.; Dilbeck, T.; Hanson, K.; Uribe-Romo, F. J. Systematic variation of the optical bandgap in titanium based isoreticular metal–organic frameworks for photocatalytic reduction of CO_2 under blue light. *Journal of Materials Chemistry A* **2017**, *5*, 11854–11863.

23.   Nasalevich, M. A.; Goesten, M. G.; Savenije, T. J.; Kapteijn, F.; Gascon, J. Enhancing optical absorption of metal–organic frameworks for improved visible light photocatalysis. *Chemical Communications* **2015**, *51*, 961–962.

24.   Johnson, J. A.; Zhang, X.; Reeson, T. C.; Chen, Y.-S.; Zhang, J. Facile control of the charge density and photocatalytic activity of an anionic indium porphyrin framework via in situ metalation. *Journal of the American Chemical Society* **2014**, *136*, 15881–15884.

25.   Logan, M. W.; Lau, Y. A.; Zheng, Y.; Hall, E. A.; Hettinger, M. A.; Marks, R. P.; Hosler, M. L.; Rossi, F. M.; Yuan, Y.; Uribe-Romo, F. J. Heterogeneous photoredox synthesis of *N*-hydroxy-oxazolidinones catalysed by metal–organic frameworks. *Catalysis Science & Technology* **2016**, *6*, 5647–5655.

26.   Walton, K. S.; Snurr, R. Q. Applicability of the BET Method for Determining Surface Areas of Microporous Metal−Organic Frameworks. *Journal of the American Chemical Society* **2007**, *129*, 8552-8556.

27.   Blöchl, P. E. Projector Augmented-Wave Method. *Phys. Rev. B* **1994**, *50*, 17953–17979.

28.   Kresse, G.; Joubert, D. From Ultrasoft Pseudopotentials to the Projector Augmented-Wave Method. *Physics Reveview B* **1999**, *59*, 1758–1775.

29.   Kresse, G.; Furthmüller, J. Efficient Iterative Schemes for Ab Initio Total-Energy Calculations Using a Plane-Wave Basis Set. *Physics Reveview B* **1996**, *54*, 11169.

30.   Kresse, G.; Hafner, J. Ab Initio Molecular Dynamics for Liquid Metals. *Physics Reveview B* **1993**, *47*, 558–561.

31.   Perdew, J. P.; Burke, K.; Ernzerhof, M. Generalized Gradient Approximation Made Simple. *Physics Reveview Lett*ers **1996**, *77*, 3865–3868.

- 32. Mathew, K.; Sundararaman, R.; Letchworth-Weaver, K.; Arias, T. A.; Hennig, R. G. Implicit Solvation Model for Density-Functional Study of Nanocrystal Surfaces and Reaction Pathways. *Journal of Chemical Physics* **2014**, *140*, 084106.

33. Makov, G.; Payne, M. C. Periodic Boundary-Conditions in Ab-Initio Calculations. *Physics Review B* **1995**, *51*, 4014-4022.

34. Neugebauer, J.; Scheffler, M. Adsorbate-Substrate and Adsorbate-Adsorbate Interactions of Na and K Adlayers on Al(111). *Physics Review B* **1992**, 46, 16067-16080.

35.. Cramer, C. J., Essentials of Computational Chemistry. Second ed.; Wiley: 2004.

36. Thapa, B.; Schlegel, H. B. Density Functional Theory Calculation of Pk(a)'S of Thiols in Aqueous Solution Using Explicit Water Molecules and the Polarizable Continuum Model. *Journal of Physical Chemistry A* **2016**, *120*, 5726-5735.

37. Namazian, M.; Halvani, S. Calculations of Pk(a) Values of Carboxylic Acids in Aqueous Solution Using Density Functional Theory. *Journal of Chemical Thermodynamics* **2006**, *38*, 1495-1502.

38. Ho, J. M.; Coote, M. L. First-Principles Prediction of Acidities in the Gas and Solution Phase. *Wires Computational Molecular Science* **2011**, *1*, 649-660.

39. Muckerman, J. T.; Skone, J. H.; Ning, M.; Wasada-Tsutsui, Y. Toward the Accurate Calculation of Pka Values in Water and Acetonitrile. *Bba-Bioenergetics* **2013**, *1827*, 882-891.

40. Haynes, W. M., Crc Handbook of Chemistry and Physics. 97th ed.; CRC Press/Taylor & Franci: Boca Raton, 2017.

41. Choi, H. J.; Dincă, M.; Dailly, A.; Long, J. R. Hydrogen storage in water-stable metal–organic frameworks incorporating 1, 3- and 1, 4-benzenedipyrazolate. *Energy and Environmental Science* **2010**, *3*, 117–123.

42. Nguyen, J. G.; Cohen, S. M. Moisture-resistant and superhydrophobic metal−organic frameworks obtained via postsynthetic modification. *Journal of the American Chemical Society* **2010**, *132*, 4560–4561.

43. Jasuja, H.; Walton, K. S. Experimental study of CO_2, CH_4, and water vapor adsorption on a dimethyl-functionalized UiO-66 framework. *Journal of Physical Chemistry A* **2013**, *117*, 7062–7068.

44. Cmarik, G. E.; Kim, M.; Cohen, S. M.; Walton, K. S. Tuning the adsorption properties of UiO-66 via ligand functionalization. *Langmuir* **2012**, *28*, 15606–15613.

45. Jasuja, H.; Zang, J.; Sholl, D. S.; Walton, K. S. Rational Tuning of Water Vapor and CO_2 Adsorption in Highly Stable Zr-Based MOFs. *Journal of Physical Chemistry A* **2012**, *116*, 23526-23532.

46. Schoenecker, P. M.; Carson, C. G.; Jasuja, H.; Flemming, C. J. J.; Walton, K. S. Effect of Water Adsorption on Retention of Structure and Surface Area of Metal–Organic Frameworks. *Industrial & Engineering Chemistry Research* **2012**, *51*, 6513-6519

47. Sohail, M.; Yun, Y.-N.; Lee, E.; Kim, S. K.; Cho, K.; Kim, J.-N.; Kim, T. W.; Moon, J.-H.; Kim, H. Synthesis of Highly Crystalline NH_2-MIL-125 (Ti) with S-Shaped Water Isotherms for Adsorption Heat Transformation. *Crystal. Growth Design* **2017**, *17*, 1208–1213.

48.   Jeremias, F.; Lozan, V.; Henninger, S. K.; Janiak, C. Programming MOFs for water sorption: amino-functionalized MIL-125 and UiO-66 for heat transformation and heat storage applications. *Dalton Transactions* **2013**, *42*, 15967-15973

CHAPTER 5: SYNTHESIS AND PRELIMINARY CHARACTERIZATION ON THE ISORETIULAR EXPANSION OF TITANIUM METAL-ORGANIC FRAMEWORKS

5.1 <u>Introduction</u>

As discussed in the precious chapters, there are two proposed methods to increase the photoredox activity of MOF systems.[1] The first was explored by tuning the optical band gap through *N*-alkyl functionalization of 2-amino terephthalic acid.[2] The second one is by increasing the length of the organic linker, to allow larger molecules diffuse into MOF structure. Increasing the length of the linker from a single phenyl ring (terephthalate) to biphenyl, terphenyl, and a quarter phenyl, will result in a systematic increase of crystallographic cell parameters, under the condition of forming the same titanium oxide cluster and retaining their underlying topology. This is known as the "isoreticular principle," one of the principles of reticular chemistry.[3-8] Increasing the cell parameters of a MOF will also result in increasing pore sizes and pore apertures, thus enabling the ability to photocatalyze reactions using more complex and larger substrates.[9-11] Unfortunately, efforts in the synthesis of such MOFs with very large linkers typically results in interpenatration[12-13] or collapse when pore guest are removed from flexibility of longer linkers.[14] Interpenetration is a phenomena in which a framework or multiple frameworks can assemble inside of another framework creating a mechanically interlocked system, similar to the way Hopf links form chains or chain mail. This entanglement of frameworks occurs under three conditions: the MOF contains very long pores, the links in the MOF are large and rod-like, and the topology of the MOF enables interpenetration. The first two conditions are often also desired in a MOF; therefore, interpenetration can be only controlled by careful choice of a MOF topology that doesn't allow for this interpenetration.[15] Interpenetration results in MOFs with decreased porosity, and it

has negative impact for many applications where mass transport and pore accessibility are vital. In this regard, only a few examples of robust structures with isoreticular expansion of non-interpenetrated MOFs have been reported.[16-19] Another challenge for isoreticular expansion of MOFs is the insolubility of the monomers, and increasing the amount of phenylene rings typically enhances π-π stacking of the linker, rendering insoluble and incapable to assemble into MOFs.[20] To avoid insolubility concerns, substitution of the phenylene rings with methyl side groups and other alkyl chains avoids the formation of strong π-π stacking allowing them to dissolve into the MOF-forming cocktail.[21-22]

A strategy to avoid interpenetration is to utilize topologies that contain 1D secondary building units (SUBs), as first demonstrated by Yaghi *et al.*[15] It was shown that limiting one direction in MOF-69A (Zn) allows the organic linkers to come close to one another, such that close mutual CH $\cdots$ π interaction to adjacent organic linkers create an impenetrable wall that stops interpenetration. However, little is known about titanium containing SBUs and titanium MOFs with larger links. Creating titanium based photoredox active MOFs with larger organic links, will result in materials with enhanced porosity, featuring larger cavities, thus allowing the diffusion of large organic substrates for their photoredox transformations. Moreover, these long links can be further modified to tune both the electronic properties and the pore environment of the MOF. For example, electron donating groups can be placed in strategic positions of the link to enhance light absorption, and chiral or molecular recognition functionalities can be added to provide the pore with unique shape-, stereo-, and regioselectivities to drive a chemical reaction through pathways inaccessible in solution.
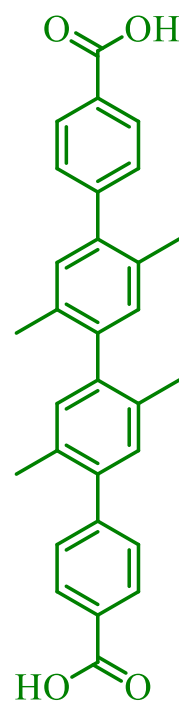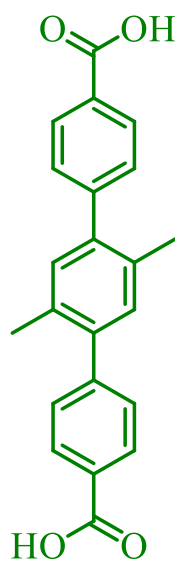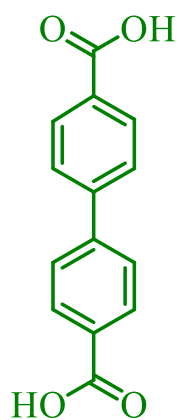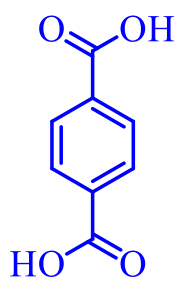
Tetragonal   **Hexagonal**

Figure 5-1: Expansion of organic linkers prepared in this work (green).

In this chapter the primary work is for the isoreticular expansion of titanium MOFs that potentially contain 1D SBU is discussed. To this end, we prepared organic linkers with two, three, and four phenylene rings, shown in Figure 5-1, that were assembled into titanium MOFs producing three new materials that are isoreticular. The work described here includes synthesis, solid-state spectroscopy, spectroscopic studies, preliminary crystallographic work using high-resolution synchrotron diffraction, porosity and thermal properties of this new family of MOFs hereafter called UCFMOFs.

5.2 Experimental Section

All starting materials and solvents, unless otherwise specified, were obtained from commercial sources (Aldrich, Fisher, VWR) and used without further purification. All reactions were performed at ambient laboratory conditions, and no precautions were taken to exclude oxygen or atmospheric moisture unless otherwise specified. Anhydrous *N,N*-dimethylformamide (DMF), acetonitrile, and tetrahydrofuran (THF) were purified using a custom-built alumina-column based solvent purification system (Inovative Technology). Anhydrous methanol was obtained from Aldrich (Sureseal). Deuterated solvents (CDCl$_3$, DMSO) were obtained from Cambridge Isotope Lab.

5.2.1   Instrumentation

High-resolution solution ^{1}H and ^{13}C nuclear magnetic resonance (NMR) spectra was collected using a Bruker AVANCE-III 400 MHz spectrometer. The chemical shifts were reported relative to the solvent residual signal. NMR data was processed using MestReNova package (v. 10.0.2).

Fourier-transform infrared (FT-IR) spectra were recorded using a Perkin Elmer Spectrum ONE universal FT-IR ATR. 32 scans were collected for each sample from 4000-400 cm^{-1}.

Powder X-ray diffraction (PXRD) data for refinement was collected on the 11-BM beam line by synchrotron radiation (λ = 0.41721 Å) of the Advanced Photon Source from Argonne National Laboratory, Chicago IL, USA. Measurements were preformed at ambient pressure and temperature from 0.6 to 50 2θ-degrees with 0.001° per step. *In house laboratory X-ray diffraction* was collected with a Rigaku MiniFlex 600 θ-2θ diffractometer in Bragg-Brentano geometry with a 300 mm goniometer diameter, Ni-filtered CuKα radiation (λ = 1.5418 Å) at 600 W power (40 kV, 15 mA), equipped with a high-resolution D/tex 250 detector, 5.0° incident and receiving Soller slits, a 0.625° divergent slit, a 1.25° scattering slit, a 0.3 mm receiving slit, a Ni-CuKβ filter, and an antiscattering blade. Samples were analyzed from 3 to 40 2θ-degrees with 0.02° per step and a scan rate of 0.25 2θ-degrees min-1. Samples were prepared by dropping the powder sample in a glass sample holder and pressing the powder with a razor blade spatula forming a smooth surface.

Crystal structure indexing was performed using GSAS-II.[23] The background was first hand fit with a 10th order shifted Chebyshev polynomial. The positions of the peaks were manually picked and refined using a LeBail method (GSAS-II peak fit routine), also refining Gaussian and Lorentzian components of the profile function. Next the asymmetry and background were refined. Finally, the Treor90 protocol was preformed, indexing a minimum of 20 peaks with a zero-shift refinement.

Crystal models were created using *Materials Studio* modeling suite.[24] The composition of the SBU and connectivity, Ti$_6$O$_6$(OR)$_6$(CO$_2$R)$_6$ based linker was obtain from previously published literature.[25-26] The organic linkers were piecewise constructed and their geometry was optimized

using the universal force field (UFF) in the *Forcite* module at "fine" optimization quality. The charges were also optimized utilizing the formal charges of each atom as starting point.

Crystal structure refinements were performed using Pawley refinement within GSAS-II. No peaks > 20° 2θ could be resolved and was not considered fir further analysis. A 20th order polynomial functional was used to fit the background with Pearson VII function and Berar-Baldinozzi function for peak asymmetry.

Calculated surface areas were performed using the *Atoms Volumes and Surfaces* tool of *Materials Studio*[24] software. It was used to calculate Connolly specific areas of the refined unit cells. The accessible solvent surface areas were used to calculate the specific surface areas of each MOF in the UCFMOF series.

Gas/vapor adsorption isotherm analysis was performed using a Micromeritics ASAP 2020 surface area and porosimetry analyzer. Measurements were performed at 77 K (liquid N_2 bath) for $N_2(g)$, and at 308 K (water circulator bath) for $H_2O(g)$ on thermally activated samples. Brunauer-Emmet-Teller (BET) surface areas were obtained by first performing a Rouquerol analysis over the linear isotherm to determine the upper limits of the BET model from the N_2 isotherms. Following the recommend by Snurr *et al*. for determination of the surface area in MOFs, a least squares linear fitting over the BET plot provided the parameter for the volume of the monolayer, BET surface area and *C*-constant.[27]

Thermogravimetric analysis was performed using a Shimaszu TGA-50 thermogravimetric analyzed with samples ran in platinum pan in a continuous N_2 gas flow on activated samples. Samples were heated at a constant rate of 10 ºC min^{-1} from 25 ºC to 800 ºC for all experiments. The first minor decrease in weight % is attributed to evaporation of air contaminants collected by

MOF during transfer from activation high vacuum to platinum pan. In each TGA the major weight % loss step is attributed to framework decomposition.

Solid-state ^{13}C nuclear magnetic resonance was measured on an Agilent DD2 500 MHz narrow-bore spectrometer with a frequency 125.6816571 MHz with an Agilent 1.6 mm T3 probe. A spectral width of 37.9 kHz was employed, and 370 complex points were collected with MAS spinning at 19 kHz. All spectra employed 1H decoupling at a frequency of 499.77755 MHz using SPINAL decoupling with a 3.0 μs decoupling pulse. Samples were packed in a 1.6 mm zirconia rotor.

Microwave reactions were performed using a CEM Discover LabMate Microwave reactor, using a IntelliVent Attenuator Assembly as the pressure device for the experiments. The vessels used for the crystallizations were the 10-mL thick walled pyrex reaction vessels with additional sample cooling. The sample vessels were placed in the open vessel attenuator with the spacer and capped with the IntelliVent attenuator for each of the runs. The microwave was set to 300 w, 120 °C, pressure set to 50 psi with varying times according to each sample.

5.2.2 Synthesis

S2
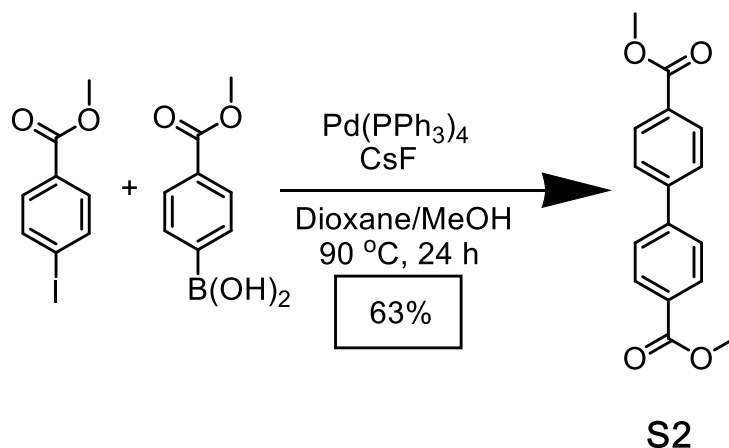
Compound S2: The reaction was carried out under a nitrogen athosphere by using a Schlenk line. A mixture of 4-(methoxycarbonyl)iodobenzene (1.00 g, 3.82 mmol), 4-(methoxycarbonyl)phenylboronic acid (0.75 g, 4.20 mmol), and cesium fluoride (1.74 g, 11.45 mmol) were evacuated and backfilled with N_2 three times. $Pd(PPh_3)_4$ (0.22 g, 0.191 mmol) was then added under positive N_2 flow and then evacuated and backfilled with N_2 gas three more times. While under positive N_2 flow, a solution of dry dioxane / MeOH (1:1 by volume, 38 mL) dispensed. The mixture was heated at 90 °C for 12 h followed by TLC. The reaction was quenched with H_2O and extracted with CH_2Cl_2 (3 x 50 mL), washed with brine (3 x 50 mL), and dried over Na_2SO_4. The crude mixture was then filtered through celite and concentrated under reduced pressure. The product was then purified by recrystallization in EtOH affording **S2** (0.65 g, 2.40 mmol) at 63% yield. ^{1}H NMR (400 MHz, CDCl$_3$) δ (ppm) 8.21 - 8.07 (m, 4H), 7.72 - 7.60 (m, 4H), 3.95 (s, 6H). ^{13}C NMR (100 MHz, CDCl$_3$) δ (ppm) 166.94, 144.50, 130.35, 129.85, 127.40, 52.37.
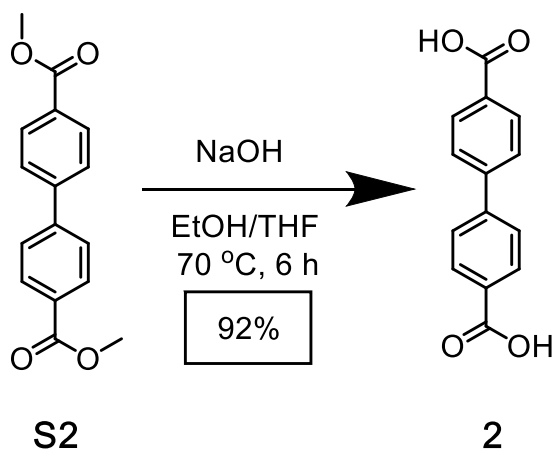
Compound 2: 1 M NaOH (aq*.,* 11.5 mL) was added to a solution of **S1** (0.50 g, 1.85 mmol) in THF (35 mL) in a 100 mL round bottom flask. The solution was stirred at 50 °C for 12 h followed by TLC. THF was removed under reduce pressure, after the solution was allowed to cool to room

temperature. 6M HCl was added dropwise until precipitation of a white solid. The solid was then isolated by vacuum filtration and rinsed with water to afford **1** (0.41 g, 1.70 mmol) as a white solid. (92% yield). ^{1}H NMR (400 MHz, DMSO-d_6) δ (ppm) 8.19 - 8.01 (m, 4H), 8.01 - 7.78 (m, 4H). ^{13}C NMR (100 MHz, DMSO) δ (ppm) 166.98, 143.08, 130.34, 130.00, 127.14.
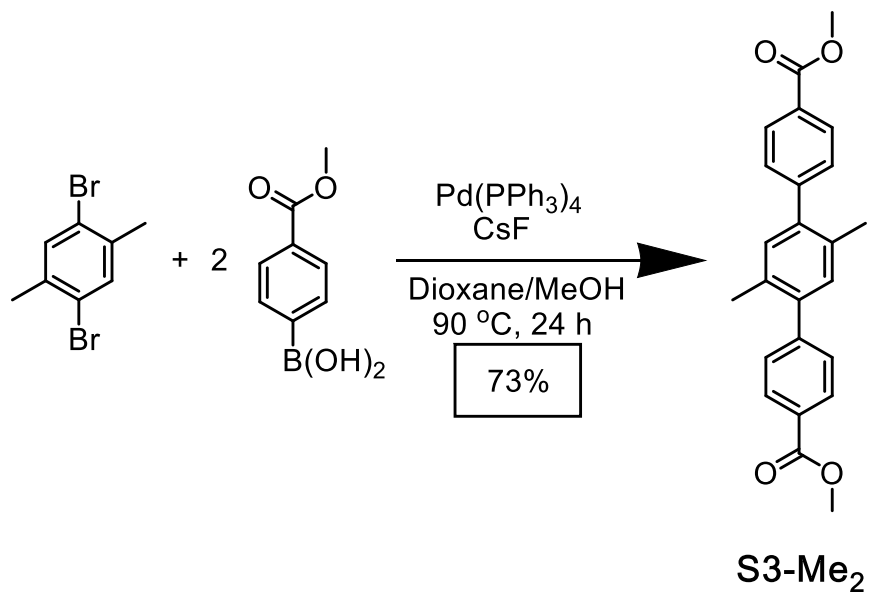
S3-Me$_2$

Compound S3-Me$_2$: The reaction was carried out under a nitrogen athosmosphere by using Schlenk line. A mixture of 1,4-dibromo-2,5-dimethylbenzene (1.00 g, 4.24 mmol), 4-formylbenzeneboronic acid (1.54 g, 8.90 mmol), and CsF (2.57 g, 16.96 mmol) were evacuated and backfilled with N$_2$ three times. Pd(dppf)Cl$_2$ (0.17 g, 0.21 mmol) was then added under positive N$_2$ flow and then evacuated and backfilled with N$_2$ gas three more times. While under positive N$_2$, a solution of anhydrous dioxane/ethanol (3:1 by volume, 42 mL) was added. The mixture was heated at 90 °C for 12 h under N$_2$ and followed by TLC. The reaction was quenched with H$_2$O and extracted with CH$_2$Cl$_2$ (3 x 50 mL), washed with brine (3 x 50 mL), and dried over Na$_2$SO$_4$. The crude mixture was then filtered through celite and concentrated under reduced pressure. The product was then purified by recrystallization in EtOH affording **S3-Me$_2$** (1.16 g, 3.09 mmol) as a

white solid at 73% yield. ^{1}H NMR (400 MHz, CDCl$_3$) δ (ppm) 8.17 (d, J = 8.2 Hz, 4H), 7.51 - 7.37 (m, 4H), 7.16 (s, 2H), 4.42 (q, J = 7.1 Hz, 4H), 2.27 (s, 6H), 1.43 (t, J = 7.1 Hz, 6H). ^{13}C NMR (100 MHz, CDCl$_3$) δ (ppm) 166.69, 146.34, 140.57, 132.82, 131.86, 129.58, 129.35, 129.20, 61.14, 19.99, 14.54.

S3-Me$_2$ **3-Me$_2$**
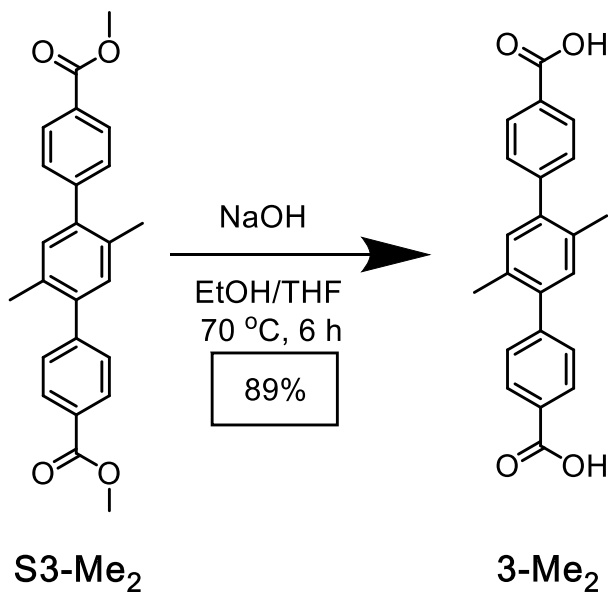
Compound 3-Me$_2$: 1 M NaOH (aq., 11.5 mL) was added to a solution of **S3-Me$_2$** (0.69 g, 1.85 mmol) in THF (35 mL). The solution was stirred at 70 °C for 12 h. THF was removed under reduce pressure once the solution was allowed to cool to room temperature. 6M HCl was added dropwise until precipitation of a solid. The solid was then isolated by vacuum filtration and rinsed with water to afford **3-Me$_2$** (0.56 g, 1.70 mmol) as a white solid at 89% yield. ^{1}H NMR (400 MHz, DMSO-d_6) δ (ppm) 8.02 (d, J = 8.1 Hz, 4H), 7.51 (d, J = 8.2 Hz, 4H), 7.20 (s, 2H). ^{13}C NMR (100 MHz, DMSO-d$_6$) δ (ppm) 167.17, 145.33, 139.79, 132.31, 131.56, 129.44, 129.34, 129.25, 129.21, 40.15, 39.94, 39.73, 39.52, 39.31, 39.10, 38.89, 19.54.
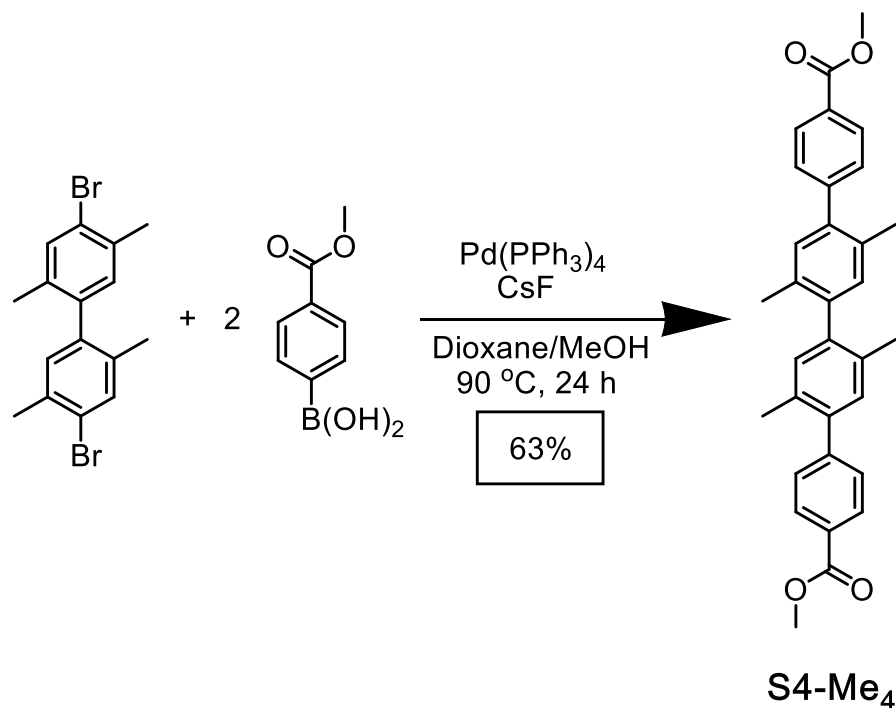
S4-Me₄

Compound S4-Me₄: The reaction was carried out under a nitrogen atmosphere by using

Schlenk line. A mixture of 4,4'-dibromo-2,-2',-5,-5'-tetramethyl-1,1'-biphenyl (1.00 g, 2.71 mmol),

4-formylbenzeneboronic acid (1.03 g, 5.71 mmol), and CsF (1.65 g, 10.84 mmol) were evacuated

and backfilled with N_2 three times. Pd(dppf)Cl$_2$ (0.11 g, 0.14 mmol) was then added under positive

N_2 flow and then evacuated and backfilled with N_2 gas three more times. While under positive N_2,

a solution of anhydrous dioxane/ethanol (3:1 by volume, 27mL) was added. The mixture was

heated at 90 °C for 12 h under N_2. The reaction was quenched with H_2O and extracted with CH_2Cl_2

(3 x 50 mL), washed with brine (3 x 50 mL), and dried over Na_2SO_4. The crude mixture was then

filtered through celite and concentrated under reduced pressure. The product was then purified by

recrystallization in EtOH affording **S4-Me₄** (0.82 g, 1.71 mmol) as a white solid at 63% yield. [1]H

NMR (400 MHz, CDCl₃) δ (ppm) 8.15 - 8.08 (d, 4H), 7.51 - 7.45 (m, 4H), 7.15 (s, 2H), 7.07 (s,

2H), 3.96 (s, 6H), 2.27 (s, 6H), 2.13 (s, 6H). ^{13}C NMR (100 MHz, CDCl$_3$) δ (ppm) 167.25, 146.86, 140.96, 139.80, 133.51, 132.29, 131.66, 131.15, 129.56, 129.49, 128.66, 52.27, 20.05, 19.53.

S4-Me$_4$ 4-Me$_4$
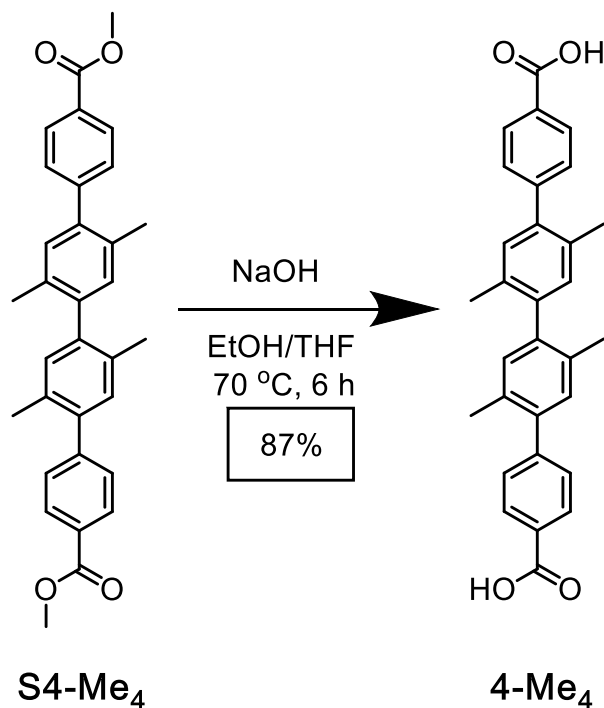
Compound 4-Me₄: 1 M NaOH (aq*.,* 11.5 mL) was added to a solution of **S4-Me₄** (0.89 g, 1.85 mmol) in THF (35 mL). The solution was stirred at 70 °C for 12 h. THF was removed under reduce pressure once the solution was allowed to cool to room temperature. 6M HCl was added dropwise until precipitation of solid. The solid was then isolated by vacuum filtration and rinsed with water to afford **3-Me₂** (0.73 g, 1.61 mmol) as a white solid at 87% yield. ^{1}H NMR (400 MHz, DMSO-d6) δ (ppm) 8.02 (d, J = 6.6 Hz, 4H), 7.54 (d, J = 8.0 Hz, 4H), 7.20 (s, 2H), 7.07 (s, 2H), 2.24 (s, 6H), 2.07 (s, 6H). ^{13}C NMR (100 MHz, DMSO-d6, 25oC) δ (ppm) 167.18, 145.57, 140.25, 139.19, 132.84, 131.84, 131.29, 130.84, 129.28, 129.23, 129.23, 19.62, 19.06.

Synthesis and Characterization of Titanium-oxo Carboxylate Clusters

Synthesis of $[Ti_6O_6(O^iPr)_6(abz)_6]$ (azb = 4-aminobenzoate; O^iPr = isopropoxide) cluster was performed according to previously published procedures by Chun *et al.*[26]

Synthesis of $[Ti_8O_8(O_2C_2(CH_3)_3)_{16}]$ cluster was performed according to previously published procedures by Walsh *et al.*[28]

UCFMOF-2. Linker **2** (0.034 g, 0.141 mmol) and a titanium source (0.071 mmol) were mixed with anhydrous DEF (3.5 mL) in a 10 mL microwave vessel with magnetic stir bar. The mixture was then allowed to stir while being degassed with N_2 gas for 10 min. The degassed sample was then heated by microwave irradiation (300 W) under autogenous pressure for 1 h regulated at 120 °C with external cooling. After the reaction was complete, the tube was allowed to cool to room temperature, opened, and the solids were isolated by filtration. Isolated solid was then rinsed with DMF (~100 mL) and EtOH (3 x ~50 mL). The obtained powder was immersed in EtOH and stored 3 days in a desiccator, replacing the solvent eight times during this time. The solvent was removed by decantation and the solvent wet powder was dried under dynamic vacuum (10 mTorr) 24 h at room temperature. The solid was stored under N_2 in a desiccator.
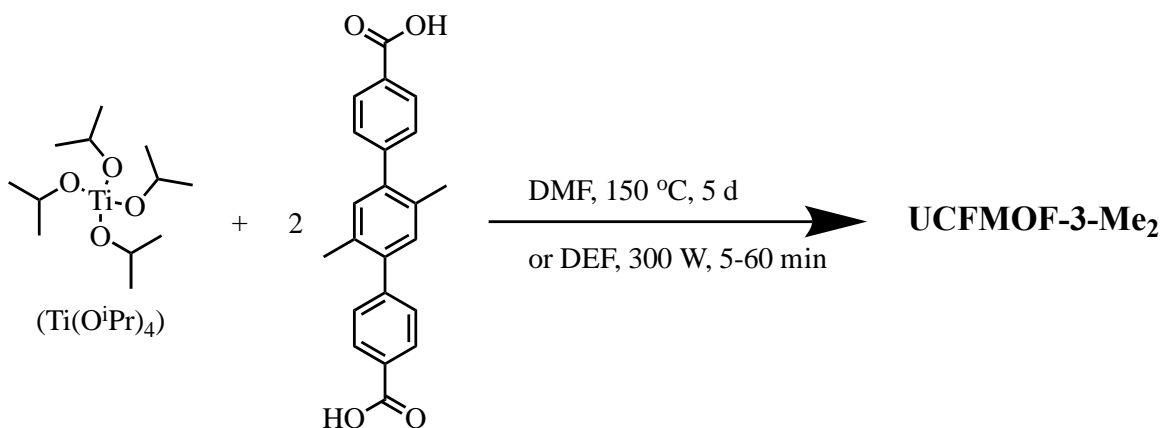
UCFMOF-3-Me₂. Linker **3-Me₂** (0.049 g, 0.141 mmol) was mixed with anhydrous DMF (3.5 mL) in a glass vessel and mixed using an ultrasonic bath. A titanium source (0.071 mmol) was then subsequently added to the mixture followed by sonication for 10 min. The mixture was flash frozen at 77 K (liquid N2), evacuated to an internal pressure of 150 mTorr (± 10 mTorr), and sealed under static vacuum. The sealed reaction tube was placed in a sand bath and heated in a 150 °C isothermal oven for 5 d. After the reaction was complete, the tube was allowed to cool to room temperature, opened, and the solids were isolated by filtration. Isolated solid was then rinsed with DMF (~100 mL) and EtOH (3 x ~50 mL). The obtained powder was immersed in EtOH and stored three days in a desiccator, replacing the exchange solvent eight times during this time. The solvent was removed by decantation and the solvent-wet powder was dried under dynamic vacuum (10 mTorr) 24 h at room temperature. The white solid was stored under nitrogen in a desiccator.

UCFMOF-4-Me₄. Organic linker **4-Me₄** (0.063 g, 0.141 mmol) was mixed with anhydrous DMF (3.5 mL) in a glass vessel by brief sonication. A titanium source (0.071 mmol) was then subsequently added to the mixture followed by sonication for 10 min. The mixture was flash frozen at 77 K (liquid N₂), evacuated to an internal pressure of 150 mTorr (± 10 mTorr), and sealed under static vacuum. The sealed reaction tube was placed in a sand bath and heated in a 150 °C isothermal

oven for 5 d. After the reaction was complete, the tube was allowed to cool to room temperature, opened, and the solids were isolated by filtration. Isolated solid was then rinsed with DMF (~100 mL) and EtOH (3 x ~50 mL). The obtained powder was immersed in EtOH and stored three days in a desiccator, replacing the exchange solvent eight times during this time. The solvent was removed by decantation and the solvent wet powder was dried under dynamic vacuum (10 mTorr) 24 h at room temperature. The white solid was stored under N_2 in a desiccator.

5.3 <u>Results and Discussion</u>

The organic linkers were synthesized by a palladium catalyzed Suzuki reaction followed by hydrolysis in alkaline environment. The corresponding MOF was synthesized in a ligand-to-metal ratio of 2:1. The expansion from the classical single phenylene ring, to two, three, and four dicarboxylate organic linker, yielded three new isoreticular materials termed **UCFMOF-2, UCFMOF-3-Me₂**, and **UCFMOF-4-Me₄**. The synthesis of **UCFMOF-3-Me₂** and **UCFMOF-4-Me₄** were performed solvothermally. Due to the insolubility of linker **2**, the synthesis of **UCFMOF-2** was only obtained though microwave synthesis.

Structural composition of all MOFs was elucidated using powder X-ray diffraction (PXRD) with a synchrotron radiation. The prepared MOFs crystallize as polycrystalline powders and no single crystals could be identified. The experimental diffractograms all depict low-angle diffraction with no evidence of starting material. The experimental powder patterns were indexed in a hexagonal lattice with unit cell parameters displayed in Table 5-1. The appearance of TiO_2 phase impurities in **UCFMOF-2** could not be further removed. Given the hexagonal unit cell and connectivity of the linkers, a SBU with a connectivity of 6 is most probable, also the most observed type of titanium oxo-carboxylate cluster reported.[29-35] Potential structure models were generated

for a three dimensional (3D) supramolecular framework with a hexinuclear SBU that has six carboxylate ligands that extend outward in the (*xy*) place creating an equatorial crown, leading to layered materials.[36-37] The orientation of stacking was modeled with three extreme possibilities using *Forcite* module of *Materials Studio* with geometric and energy minimization (Figure 5-2). **Model A** consists of a layered primitive hexagonal *P6$_3$* (No. 173) system with discrete 0D SBU in an AB-stacking conformation capped with isopropoxy functional groups on the top and bottom. **Model B** is a fully eclipsed structure of **Model A** that consists of layered trigonal *P-3* (No. 147) system in an AA-stacking conformation. **Model C** consists of edge-sharing trigonal pyramidal Ti$_6$O$_9$ clusters that form 1D infinite nanowires [(Ti$_6$O$_9$)$_n$] that eliminates the possibility of interpenetration.

Table 5-1: Indexed cell parameters compared to potential models.

	a (Å)	*a* (Å) Model Parameter			*c* (Å)	*c* (Å) Model Parameters		
Model	Indexed	**A**	**B**	**C**	Indexed	**A**	**B**	**C**
UCFMOF-2	18.41312	18.65234	18.63141	18.54439	11.38132	19.13240	15.26134	11.30219
UCFMOF-3-Me$_2$	22.93292	22.69954	22.75815	22.76060	11.46497	20.62475	15.88039	11.42670
UCFMOF-4-Me$_4$	27.19147	27.07610	26.87281	27.27100	11.46143	19.43110	16.58134	11.52180

The calculated unit cell was then compared with experimentally indexed values (Table 5-1), revealing that **Model C** agrees most closely (Figure 5-3). [13]C Cross-polarization/magic angle-spinning (CP/MAS) on thermally activated samples observed no resonances for titanium alkoxo groups (isopropoxy) that would be expected if **Model A** or **Model B** was formed (Figure 5-4). A Pawley refinement was performed on the experimental powder patter to obtain refined unit cell

176

parameters (Figure 5-5), leading to low residuals (Table D-1) allowing extraction of integrated intensities for electron map reconstruction. Local structure information regarding the titanium-oxo-carboxylate clusters is necessary to definitively determine atomic position and to preform Rietveld refinements for complete crystal structure solution.

To further characterize the porosity properties of **UCFMOF** series, N_2 adsorption (at 77 K) and thermal gravimetric analysis (TGA) was performed on thermally activated samples following EtOH solvent exchange. TGA revealed that the series is thermally stable up to 430 ºC (Figures D-1 to Figure D-3) with no appreciable mass loos below this temperature, suggesting the absence of volatile guests. This was further confirmed with ^{13}C CP/MAS NMR and Fourier transform infrared spectroscopy (FT-IT) by the absence of resonances for residual solvent such as DMF (sample synthesis) and EtOH (sample activation) (Figures D-16 to Figure D-21). N_2 gas adsorption isotherms revealed that all MOFs display a IUPAC type II isotherm that is typical of microporous materials, where gas uptake is governed by accessible pore volume rather than total internal surface area (Figures D-7 to Figure D-15). The application of the Brunauer-Emmett-Teller (BET) model resulted in BET surface areas that increase with increasing linker length, and calculated to be 354 m^2 g^{-1}, 1067 m^2 g^{-1}, and 1679 m^2 g^{-1} for **UCFMOF-2, UCFMOF-3-Me₂**, and **UCFMOF-4-Me₄**, respectively (Figure 5-6). The obtained surface areas are in agreement with those calculated using the refined crystal structure in the *Atoms Volumes and Surfaces* tool of *Materials Studio* with exception of the microwave synthesized **UCFMOF-2** (

Table 5-2, Table D-2).
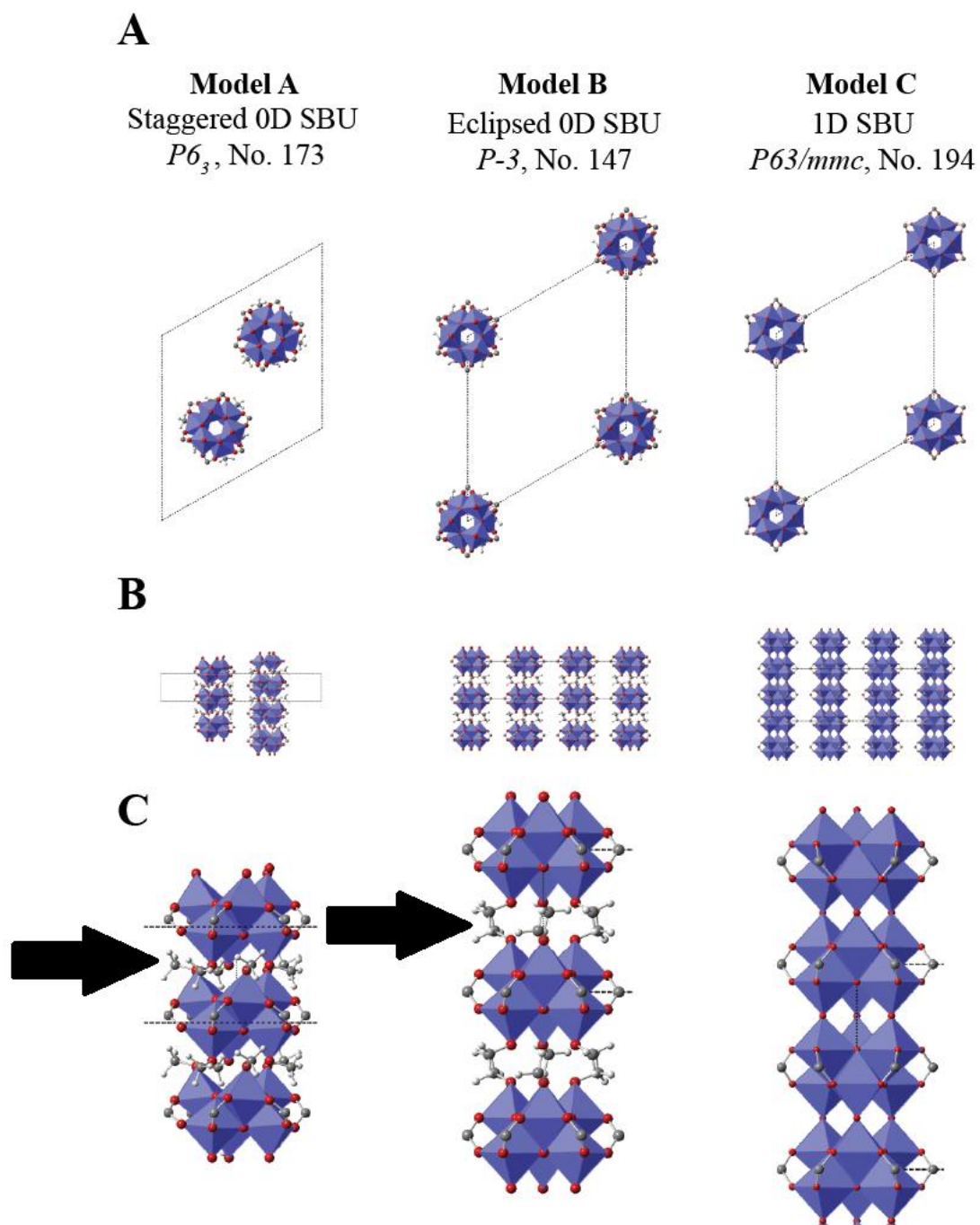
Figure 5-2: Crystal models of titanium clusters. (A) Viewed the clusters along (001) view, (B) (110) view, (C) and magnified to show isopropoxy functional groups presented on top and bottom of each discrete cluster of Model A and Model B, highlighted being pointed out by black arrows. Atom colors: Red = O, White = H, Grey = Carbon. Atom polyhedral: Blue = Ti. Organic moiety omitted for clarity.

3-Me₂

(Ti₆O₉)ₙ
infinate 1D rod
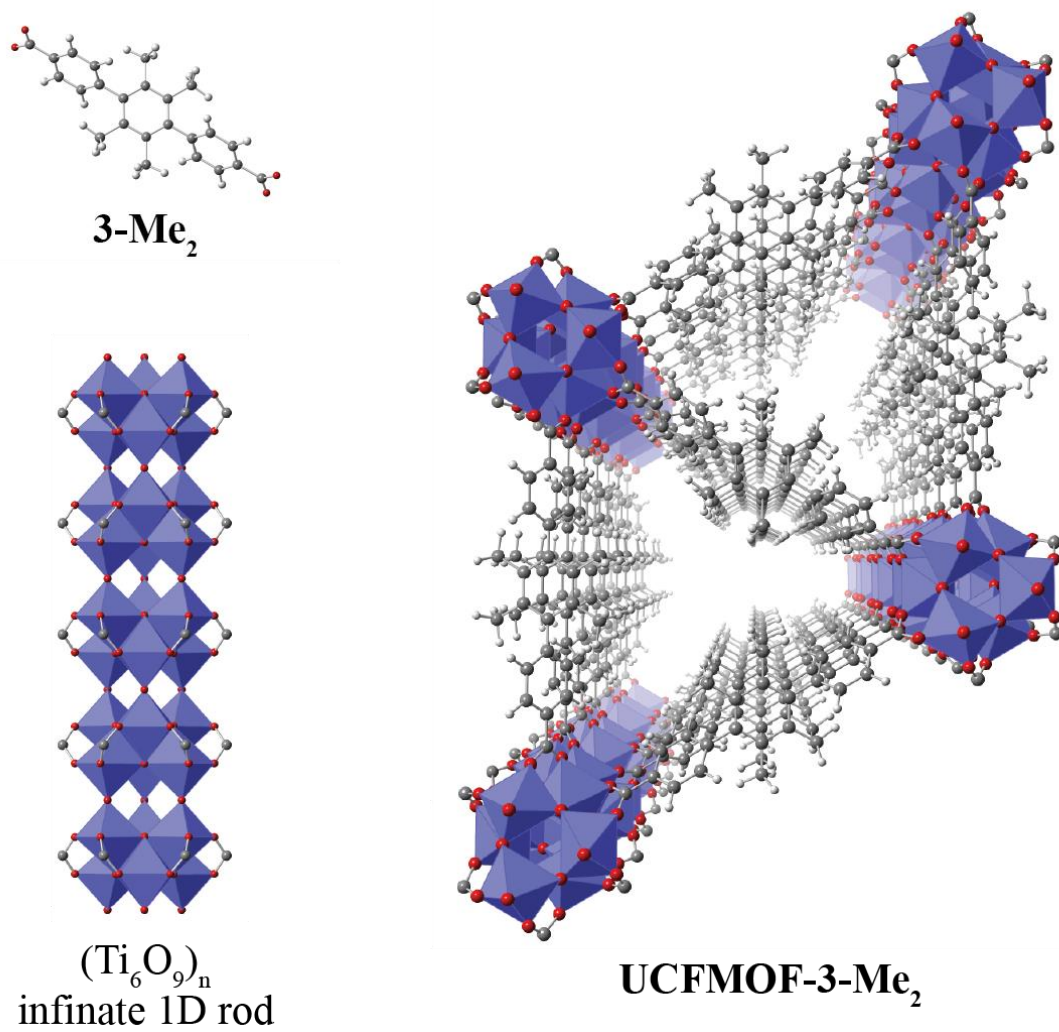
UCFMOF-3-Me₂

Figure 5-3: Proposed crystal model of **UCFMOF-3-Me₂**. Organic linker **3** is solvothermally reacted with metal-oxide SBU to make 3D **UCFMOF-3-Me₂** with 1D channels.
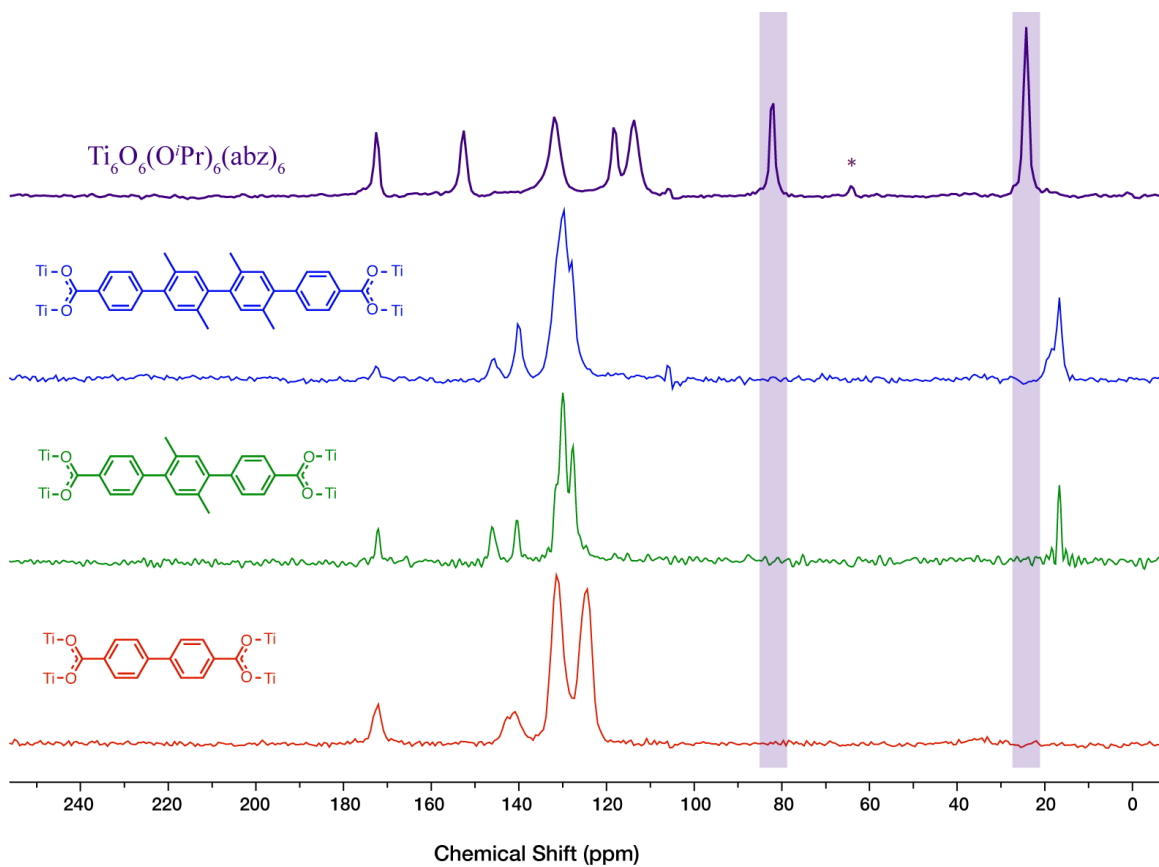
Figure 5-4: ^{13}C CP/MAS spectra analyzing the absence of titanium alkoxide in UCFMOF family. Highlighted in purple is signal of interest. *Denotes excess isopropoxide.
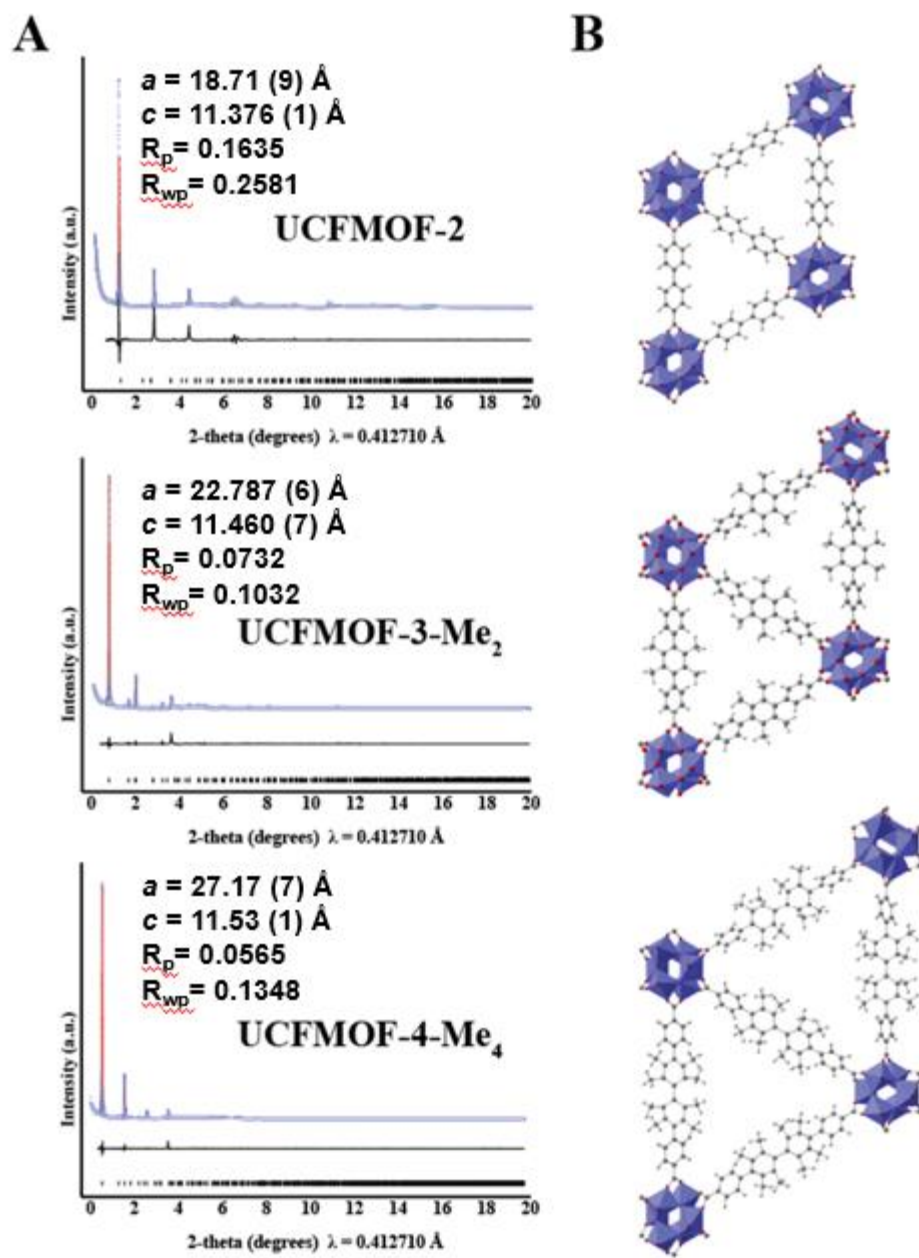
Figure 5-5: (A) PXRD Pawley fitting of thermally activated systems displaying the experimental powder pattern (blue), refined Pawley fitting (red), background (green), difference plot (black line), and the Bragg position (black hashmarks). (B) Refined crystal structures of UCFMOF series.
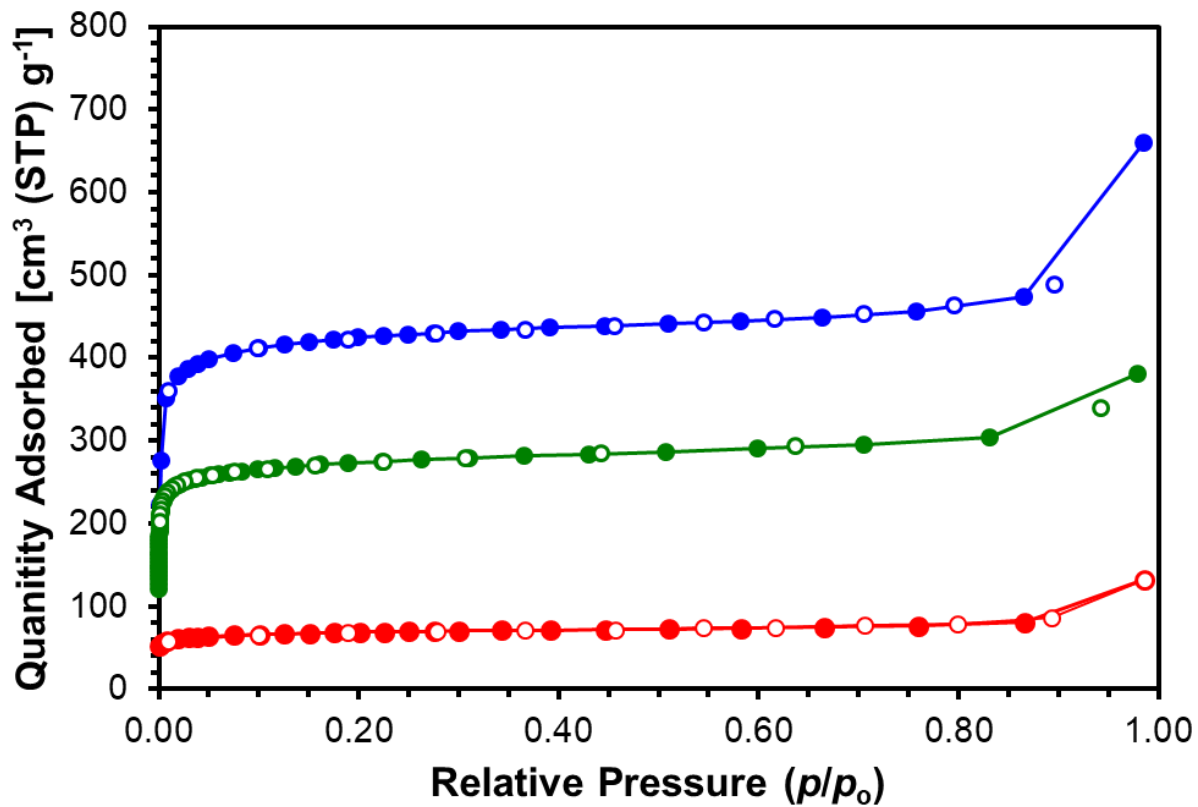
Figure 5-6: N2 isotherm (77 K) of **UCFMOF-2** (blue), **UCFMOF-3-Me₂** (green), and **UCFMOF-4-Me₄** (red)

Table 5-2: BET surface area and pore volume for UCFMOF series. [a]Pore volume measure at 0.05 $p\ p_o^{-1}$.

UCFMOF-	2	3-Me$_2$	4-Me$_4$
BET Surface Area (m^2 g^{-1})	354	1067	1679
Pore volume (cm^3 g^{-1}) [a]	0.064	0.196	0.615

All these MOFs can be synthesized in a wide variety of conditions with little appearance of impurities. The robustness of synthetic conditions and access to rapid production was explored with using microwave assisted synthesis, different titanium sources, concentrations, and different temperatures (depicted conditions shown in Figure 5-7). Ti(O^{i}Pr)$_4$, Ti(OBu)$_4$, TiCl$_4$, and [Ti$_6$O$_6$(O^{i}Pr)$_6$(abz)$_6$] (azb = 4-aminobenzoate; O^{i}Pr = isopropoxide) cluster under identical conditions and with small additions of alcohols as a cosolvent, the same crystalline product was obtained with minor impurities. Interestingly, even when utilizing an 8-fold preassembled titanium-oxo carboxylate cluster [Ti$_8$O$_8$(O$_2$CR)$_{16}$], reconstruction of the cluster core occurs to produce hexagonal materials. In our models, titanium clusters with 8-fold ring shape are incompatible with hexagonal unit cells, so we suspect that reconstruction of the clusters leads to the formation of the 6-fold ring cluster. Temperature has little influence on crystallinity, while conditions appear to be more dependent upon the solubility of the linker.
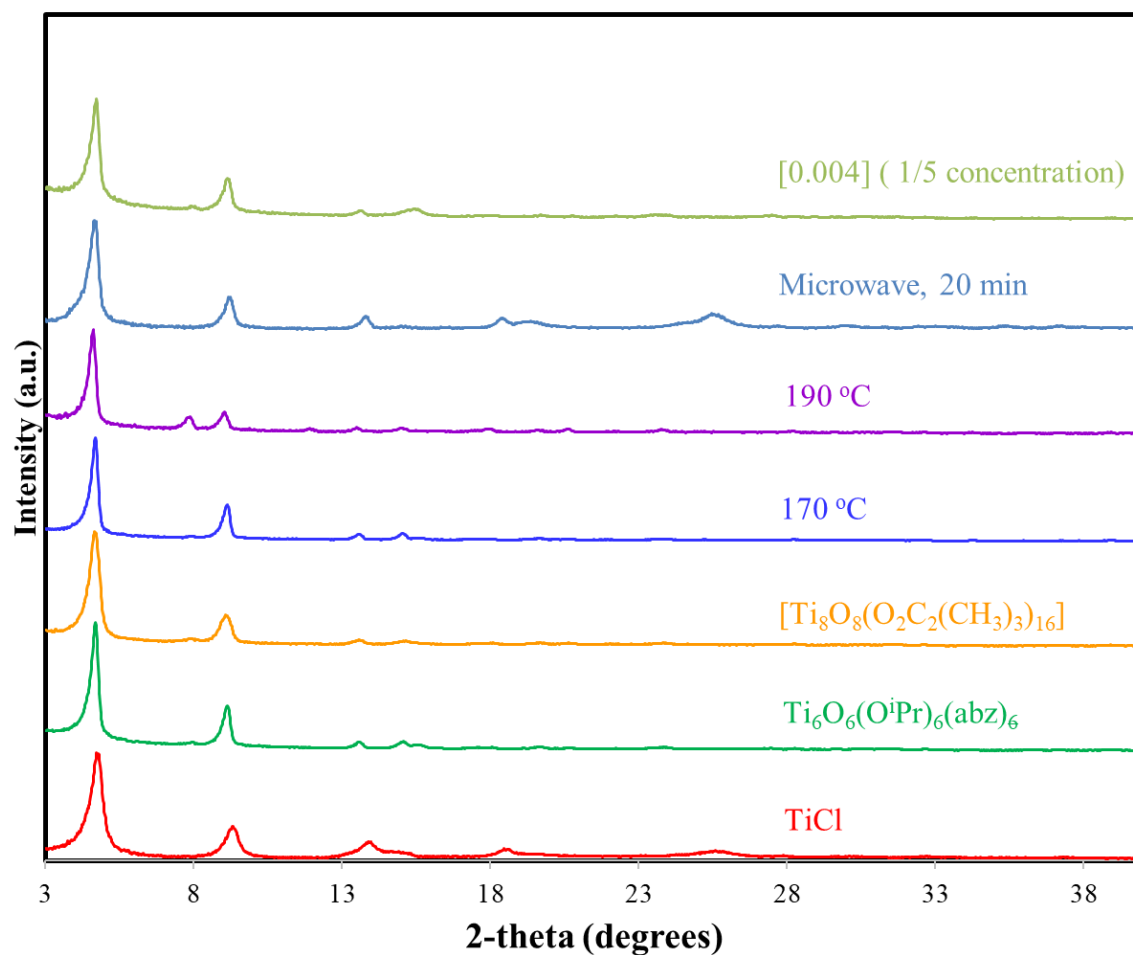
Figure 5-7: PXRD (λ = 1.5418 Å) of selected **UCFMOF-3-Me$_2$** synthesized by changing various conditions.

Complete elucidation of the crystal structure is only possible after preforming Rietveld refinements. In order to have a complete crystal model for refinement, more information on the atomic position of the titanium cluster and linkers is required, since the Rietveld method is very sensitive to this atomic information. Local structure information of titanium will provide a better picture of location of atoms around the cluster. This type of information can be obtained through methods such as X-ray absorption fine structure (XAFS), X-ray absorption near edge spectroscopy (XANES), or total X-ray scattering for pair-distribution function (PDF). These measurements will be performed in future studies.

5.4 <u>Conclusion</u>

In summary, we report three new layered titanium MOF, UCFMOF family, which was synthesized from linear dicarboxylic acid linkers and various titanium metal sources. UCFMOF family most likely possesses a one-dimensional inorganic cluster with a high stability compared to its discrete analogues. All members of UCFMOF series are noninterpenetrated and exhibit robust porous structures where the unit cell, pore aperture, and the void volume is dependent upon the organic linker length. This is evident by their high permanent porosity and high thermal stability (up to 430 ^{o}C). Elucidation of the crystal structure of these MOFs is the last piece of information needed for their complete structural characterization.

5.5 <u>References</u>

1. Logan, M. W.; Lau, Y. A.; Zheng, Y.; Hall, E. A.; Hettinger, M. A.; Marks, R. P.; Hosler, M. L.; Rossi, F. M.; Yuan, Y.; Uribe-Romo, F. J., Heterogeneous photoredox synthesis of N-hydroxy-oxazolidinones catalysed by metal–organic frameworks. *Catalysis Science & Technology* **2016,** *6* (14), 5647-5655.

2. Logan, M. W.; Ayad, S.; Adamson, J. D.; Dilbeck, T.; Hanson, K.; Uribe-Romo, F. J., Systematic variation of the optical bandgap in titanium based isoreticular metal–organic frameworks for photocatalytic reduction of CO_2 under blue light. *Journal of Materials Chemistry A* **2017,** *5* (23), 11854-11863.

3. Ockwig, N. W.; Delgado-Friedrichs, O.; O'Keeffe, M.; Yaghi, O. M., Reticular chemistry: occurrence and taxonomy of nets and grammar for the design of frameworks. *Accounts of chemical research* **2005,** *38* (3), 176-182.

4. O'Keeffe, M.; Peskov, M. A.; Ramsden, S. J.; Yaghi, O. M., The reticular chemistry structure resource (RCSR) database of, and symbols for, crystal nets. *Accounts of chemical research* **2008,** *41* (12), 1782-1789.

5. Tranchemontagne, D. J.; Ni, Z.; O'Keeffe, M.; Yaghi, O. M., Reticular chemistry of metal–organic polyhedra. *Angewandte Chemie International Edition* **2008,** *47* (28), 5136-5147.

6. O'Keeffe, M., Design of MOFs and intellectual content in reticular chemistry: a personal view. *Chemical Society Reviews* **2009,** *38* (5), 1215-1217.

7. Yaghi, O. M.; Li, Q., Reticular chemistry and metal-organic frameworks for clean energy. *MRS bulletin* **2009,** *34* (9), 682-690.

8. Yaghi, O. M., Reticular Chemistry・Construction, Properties, and Precision Reactions of Frameworks. ACS Publications: 2016.

9. Bagshaw, S. A.; Prouzet, E.; Pinnavaia, T. J., Templating of mesoporous molecular sieves by nonionic polyethylene oxide surfactants. *Science* **1995,** *269* (5228), 1242-1244.

10. Zhao, D.; Feng, J.; Huo, Q.; Melosh, N.; Fredrickson, G. H.; Chmelka, B. F.; Stucky, G. D., Triblock copolymer syntheses of mesoporous silica with periodic 50 to 300 angstrom pores. *science* **1998,** *279* (5350), 548-552.

11. Banerjee, R.; Furukawa, H.; Britt, D.; Knobler, C.; O'Keeffe, M.; Yaghi, O. M., Control of pore size and functionality in isoreticular zeolitic imidazolate frameworks and their carbon dioxide selective capture properties. *Journal of the American Chemical Society* **2009,** *131* (11), 3875-3877.

12. Jiang, H.-L.; Makal, T. A.; Zhou, H.-C., Interpenetration control in metal–organic frameworks for functional applications. *Coordination Chemistry Reviews* **2013,** *257* (15), 2232-2249.

13. Eddaoudi, M.; Kim, J.; Rosi, N.; Vodak, D.; Wachter, J.; O'Keeffe, M.; Yaghi, O. M., Systematic Design of Pore Size and Functionality in Isoreticular MOFs and Their Application in Methane Storage. *Science* **2002,** *295* (5554), 469-472.

14. Park, C.; Oh, K.; Lee, S. C.; Kim, C., Controlled release of guest molecules from mesoporous silica particles based on a pH-responsive polypseudorotaxane motif. *Angewandte Chemie International Edition* **2007,** *46* (9), 1455-1457.

15. Rosi, N. L.; Kim, J.; Eddaoudi, M.; Chen, B.; O'Keeffe, M.; Yaghi, O. M., Rod packings and metal− organic frameworks constructed from rod-shaped secondary building units. *Journal of the American Chemical Society* **2005,** *127* (5), 1504-1518.

16. Furukawa, H.; Go, Y. B.; Ko, N.; Park, Y. K.; Uribe-Romo, F. J.; Kim, J.; O'Keeffe, M.; Yaghi, O. M., Isoreticular expansion of metal–organic frameworks with triangular and square building units and the lowest calculated density for porous crystals. *Inorganic Chemistry* **2011,** *50* (18), 9147-9152.

17. Ma, L.; Falkowski, J. M.; Abney, C.; Lin, W., A series of isoreticular chiral metal–organic frameworks as a tunable platform for asymmetric catalysis. *Nature Chemistry* **2010,** *2* (10), 838.

18. Guillerm, V.; Ragon, F.; Dan-Hardi, M.; Devic, T.; Vishnuvarthan, M.; Campo, B.; Vimont, A.; Clet, G.; Yang, Q.; Maurin, G., A series of isoreticular, highly stable, porous zirconium oxide based metal–organic frameworks. *Angewandte Chemie International Edition* **2012,** *51* (37), 9267-9271.

19. Dybtsev, D. N.; Yutkin, M. P.; Peresypkina, E. V.; Virovets, A. V.; Serre, C.; Férey, G.; Fedin, V. P., Isoreticular Homochiral Porous Metal− Organic Structures with Tunable Pore Sizes. *Inorganic Chemistry* **2007,** *46* (17), 6843-6845.

20. Grigor'eva, L. G.; Sergeev, V. A.; Shitikov, V. K.; Korshak, V. V., Some properties of oligophenylenes produced by the reaction of polycyclotrimerization. *Bulletin of the Academy of Sciences of the USSR, Division of chemical science* **1973,** *22* (7), 1446-1450.

21. Pasco, S.; Baker, G., Rotational barriers and conjugation in polyphenylene oligomers. *Synthetic Metals* **1997,** *84* (1-3), 275-276.

22. Deng, H.; Grunder, S.; Cordova, K. E.; Valente, C.; Furukawa, H.; Hmadeh, M.; Gándara, F.; Whalley, A. C.; Liu, Z.; Asahina, S., Large-pore apertures in a series of metal-organic frameworks. *science* **2012,** *336* (6084), 1018-1023.

23. Toby, B. H.; Von Dreele, R. B., GSAS-II: the genesis of a modern open-source all purpose crystallography software package. *Journal of Applied Crystallography* **2013,** *46* (2), 544-549.

24. Materials Studio, version 8.0; BIOVIA Software Inc.: San Diego CA, 2014.

25. Wang, S.; Kitao, T.; Guillou, N.; Wahiduzzaman, M.; Martineau-Corcos, C.; Nouar, F.; Tissot, A.; Binet, L.; Ramsahye, N.; Devautour-Vinot, S., A phase transformable ultrastable titanium-carboxylate framework for photoconduction. *Nature Communications* **2018,** *9*.

26. Hong, K.; Chun, H., Nonporous Titanium–Oxo Molecular Clusters That Reversibly and Selectively Adsorb Carbon Dioxide. *Inorganic Chemistry* **2013,** *52* (17), 9705-9707.

27. Walton, K. S.; Snurr, R. Q., Applicability of the BET method for determining surface areas of microporous metal− organic frameworks. *Journal of the American Chemical Society* **2007,** *129* (27), 8552-8556.

28. Hendon, C. H.; Tiana, D.; Fontecave, M.; Sanchez, C. m.; D'arras, L.; Sassoye, C.; Rozes, L.; Mellot-Draznieks, C.; Walsh, A., Engineering the optical response of the titanium-MIL-125 metal–organic framework through ligand functionalization. *Journal of the American Chemical Society* **2013,** *135* (30), 10942-10945.

29. Rozes, L.; Sanchez, C., Titanium oxo-clusters: precursors for a Lego-like construction of nanostructured hybrid materials. *Chemical Society Reviews* **2011,** *40* (2), 1006-1030.

30. Hubert-Pfalzgraf, L.; Goncalves, M. H. B., Synthesis and characterization of new titanium hexanuclear oxo carboxylato alkoxides. Molecular structure of [Ti 6 (Á 3-O) 6 (Á-O 2 CC 6 H 4 OPh) 6 (OEt) 6]. *Journal of the Chemical Society, Dalton Transactions* **1998,** (14), 2285-2288.

31. Rozes, L.; Steunou, N.; Fornasieri, G.; Sanchez, C., Titanium-oxo clusters, versatile nanobuilding blocks for the design of advanced hybrid materials. *Monatshefte für Chemie/Chemical Monthly* **2006,** *137* (5), 501-528.

32. Hou, J.-L.; Luo, W.; Guo, Y.; Zhang, P.; Yang, S.; Zhu, Q.-Y.; Dai, J., Titanium oxo cluster with six peripheral ferrocene units and its photocurrent response properties for saccharides. *Inorganic Chemistry* **2017,** *56* (11), 6451-6458.

33.   Piszczek, P.; Richert, M.; Wojtczak, A., Crystal structure and spectral characterization of hexanuclear oxo titanium (IV) clusters:[Ti 6 O 6 (OSi (CH 3) 3) 6 (OOCR) 6](R= Bu t, CH 2 Bu t, C (CH 3) 2 Et). *Polyhedron* **2008,** *27* (2), 602-608.

34.   Fang, W.-H.; Wang, J.-F.; Zhang, L.; Zhang, J., Titanium–Oxo Cluster Based Precise Assembly for Multidimensional Materials. *Chemistry of Materials* **2017,** *29* (7), 2681-2684.

35.   Rozes, L.; Cochet, S.; Frot, T.; Fornasieri, G.; Sassoye, C.; Popall, M.; Sanchez, C., Titanium Oxo-Clusters: Vesatile Nano-Objects for the Design of Hybrid Compounds. *MRS Online Proceedings Library Archive* **2007,** *1007*.

36.   Piszczek, P.; Richert, M.; Radtke, A.; Muzioł, T.; Wojtczak, A., Synthesis of titanium dioxide nanocrystalline layers using hexaprismatic shaped μ-oxo Ti (IV) alkoxo carboxylates as precursors. *Polyhedron* **2009,** *28* (17), 3872-3880.

37.   Nguyen, H. L.; Gándara, F.; Furukawa, H.; Doan, T. L.; Cordova, K. E.; Yaghi, O. M., A titanium–organic framework as an exemplar of combining the chemistry of metal–and covalent–organic frameworks. *Journal of the American Chemical Society* **2016,** *138* (13), 4330-4333.

CHAPTER 6: CONCLUSION AND OUTLOOK

This body of work represents a contribution to photoredox active metal-organic frameworks. MOFs offer structural advantages as a tunable photocatalyst for photoredox transformation. The primary design of this research followed a comprehensive approach that combines experimental and theoretical research along with mechanistic information to understand how to optimize photoredox activity and stability in humid environments. This helps to provide guidelines intended for further development of advanced earth-abundant catalytic MOF-systems for targeted applications. Presented here are eleven new Ti-MOFs which nearly doubles the number of existing Ti-MOFs, all are crystalline powders that were characterized by means of powder X-ray diffractions crystallography, gas and vapor adsorption, and solid-state spectroscopy. Their electronic and photocatalytic properties of seven of them were tuned by careful selection of the substituents in the organic building blocks, and expansion if the pore size in four of them was research by increasing the molecular size of the linker. The future tasks of this project is to be able to combine tuning of both electronic and porosity properties for the preparation of an optimal photocatalyst that operates with broadband visible light and it is accessible to large substrates for their site- and shape-selective transformation via photoredox process.

Future research includes elucidation of the crystal structure of the UCFMOF family by determining the local structure around the Ti-cluster. This can be achieved with the use of pair-distribution function (PDF) and potentially with the help of synchrotron-based X-ray absorption measurements. Further prospects include the design of novel UCFMOF-based systems that impart more sophisticated functionalities that include chemical recognition. There are **two** schemes that

are sequential for the future development of the UCFMOF series. The **first** scheme is the incorporation of electron donation groups and steric constraints through heterocycles to see the effect on light harvesting and excited state lifetime. **Second**, incorporation of chiral or shape-selective molecules to impart preferred spatial configuration on substrates. The use of such functional groups can produce diastereomer or enantiopure MOFs with large well-defined asymmetric catalytic sites to facilitate substrate diffusion and pore design that has further selectivity towards shape, size, chemical environment enabling true substrate shape-selectivity. The combination of these two research goals could virtually drive new and highly specific chemical transformation.

Enhancing the optical properties of the organic linker is the next step in the development of the UCFMOF series. The building blocks used in chapter 5 involve linkers that do not promote ligand-to-metal charge transfer in the visible region. This can be addressed with the incorporation of functional groups with electron donating groups in the aromatic rings. Synthetically, UCFMOF family can be chemically altered so the aromatic rings are substituted with electron donating (compounds **2**-**4** and **9**-**10,** Figure 6-1) and electron withdrawing groups (compounds **5-8**, Figure 6-1). The effect heterocycles and their partially restricted rotation can be probed to observe if there is a role in their bandgap, the excited state lifetime, and potential charge recombination effect (compounds **4** and **10**). These can even be utilized as in Chapter 3 and Chapter 4 to study this effect as it pertained to photophysical and photochemical properties. Furthermore, such substitution can probe the effect of distance the elector must travel from the aromatic ring of the valence band (typically reside on ring substituted with electron donating group) to the conduction band (inorganic cluster) and its role on photochemical activity.

UCFMOF-4 family can be modified to allow the core to be altered with chiral groups (Figure 6-2). This imparts a special pore shape and selectivity where it is possible that the MOF steric constraints dictating the chemical pathway after excitation occurs. Covalent attached groups such as 1,1'-bi-2-napthol (BINOL, **11**) will be explored to see the effect that such steric functionalities have on driving potential stereo- and regio-selective reactions that are inaccessible in solutions, for example the photoxidation of compounds **9** and **11** in Chapter 2 of this dissertation produces two diastereomers, and a chiral MOF could aid in the preferential formation of a diastereomer. It is also possible to chemically alter the linkers to study other the effect of other functionalities such as various polarities (**12**), active Brønsted acid photoredox catalyst (**13**), and metal alkoxides (**14**) or even molecular recognition sites. Finally, there is also the possibility to synthesize mixed linker based MOF can generate even more complex photocatalyst with multiple reaction sites for synergistic transformations.
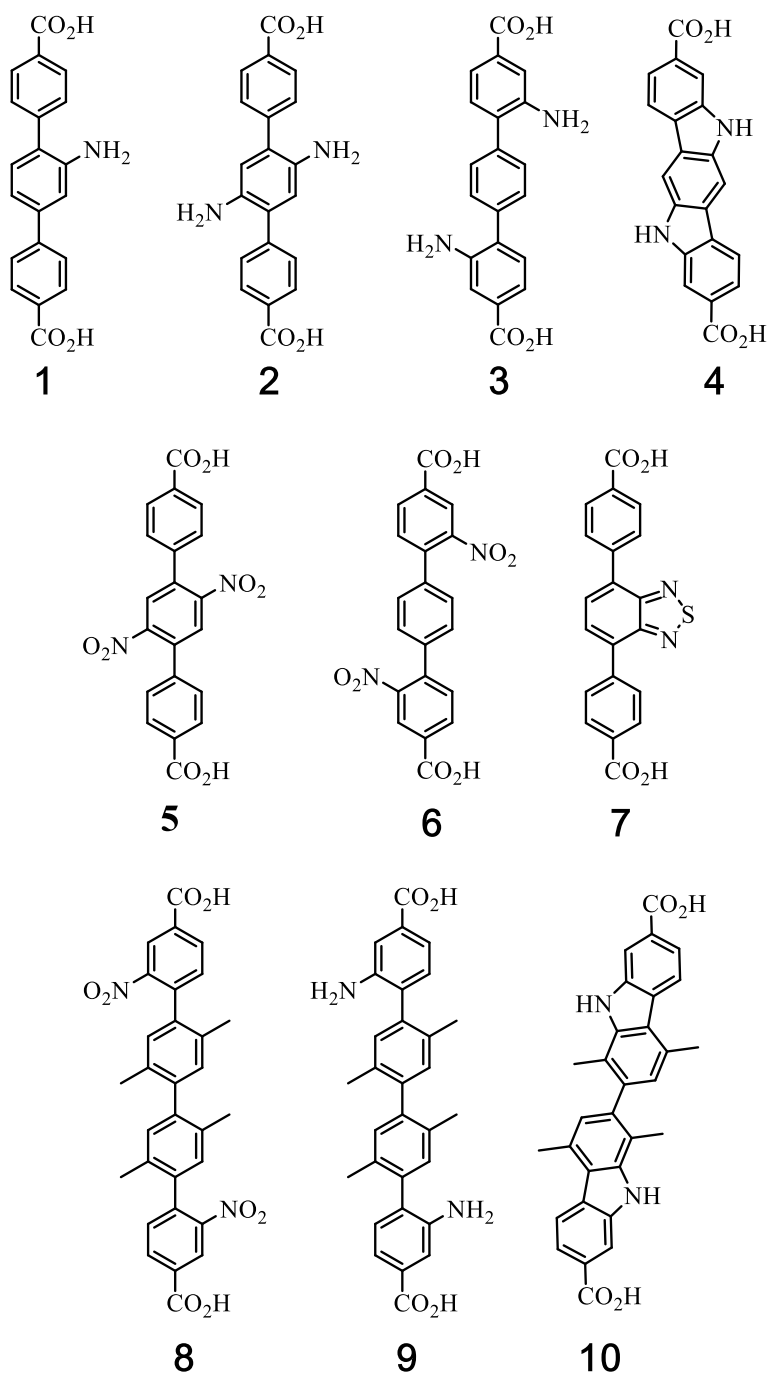
Figure 6-1: Proposed linkers with enhanced electronic structure.
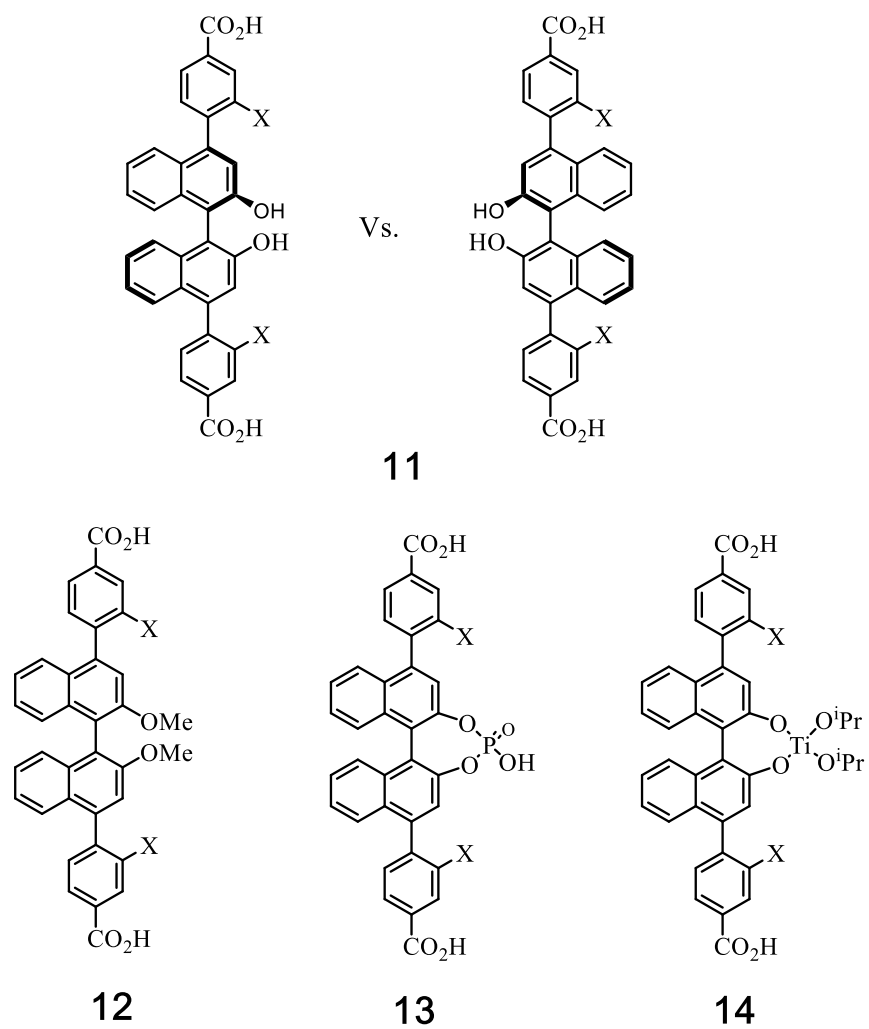
Figure 6-2: Proposed linkers with enhanced steric control. "X" represents functionality with optimal optical properties.

APPENDIX A: **SUPPLEMENTARY MATERIAL FOR CHAPTER 2**

A.1 Powder X-ray Diffractograms
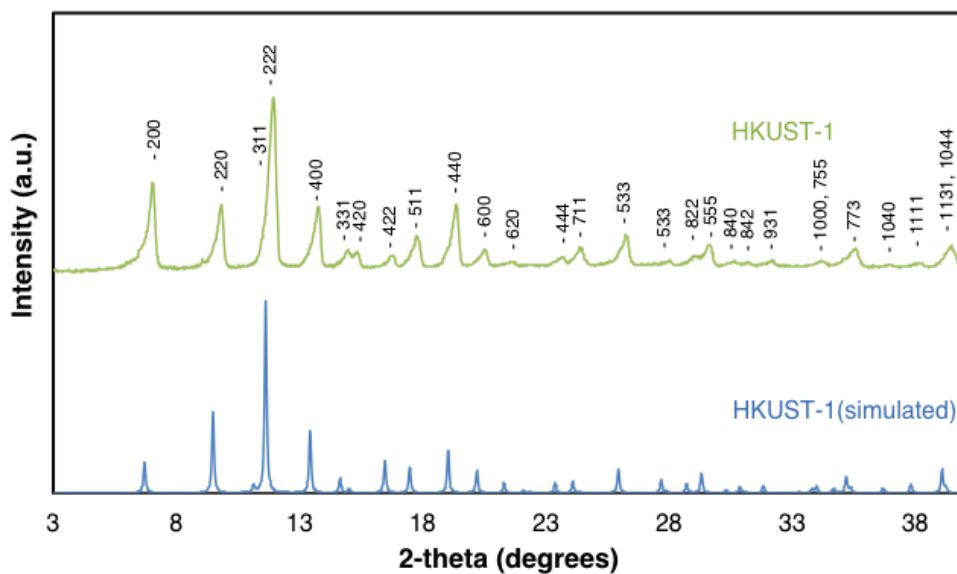
Figure A-1: PXRD of UiO-66 and UiO-66-NH2 as synthesized, peaks are indexed and compared to simulated pattern from single crystal data.
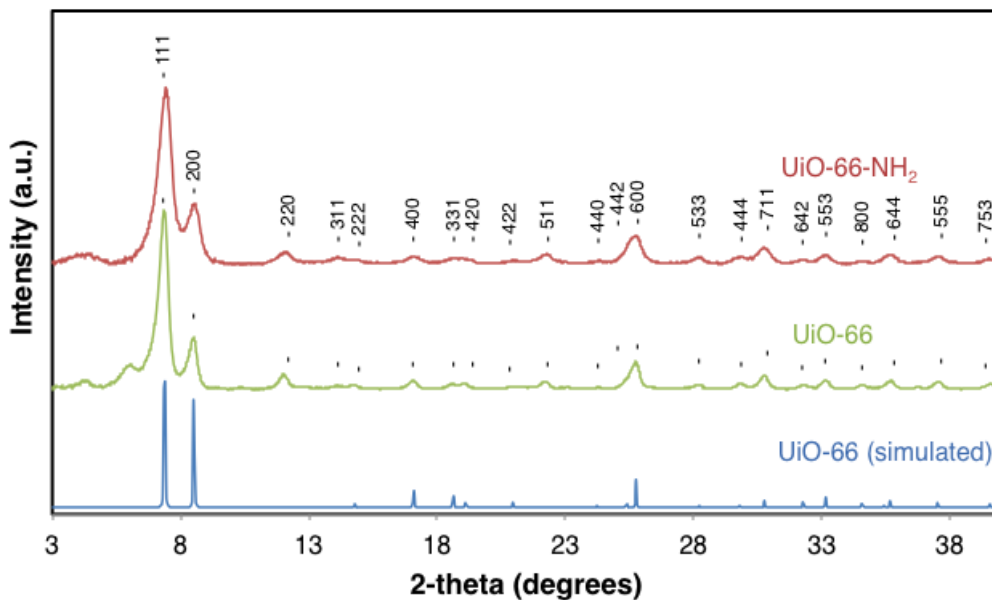
Figure A-2: PXRD of UiO-66 and UiO-66-NH2 as synthesized, peaks are indexed and compared to simulated pattern from single crystal data.
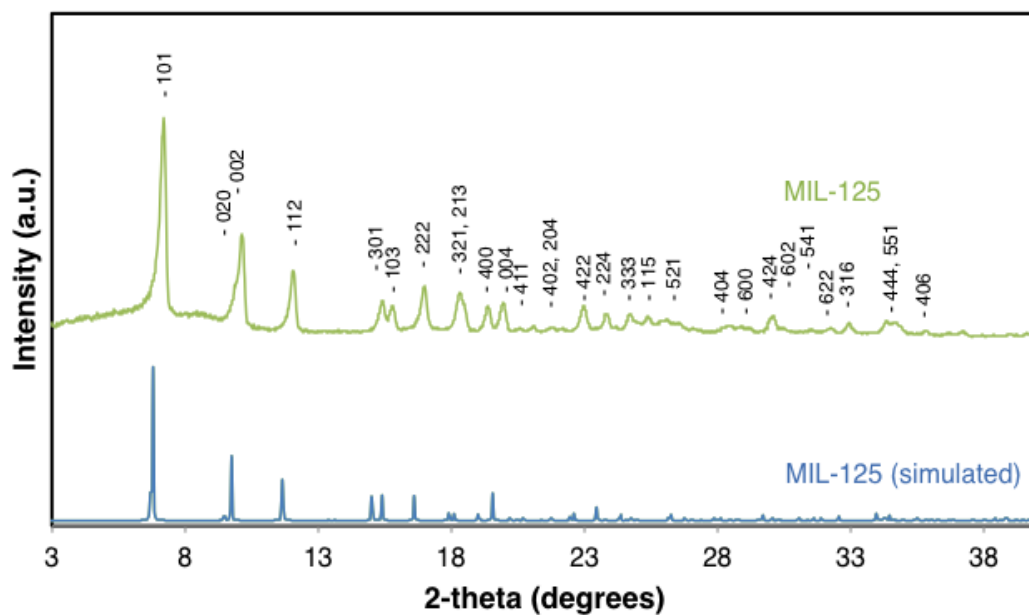
Figure A-3: PXRD of MIL-125 as synthesized, peaks are indexed and compared to simulated pattern from single crystal data.
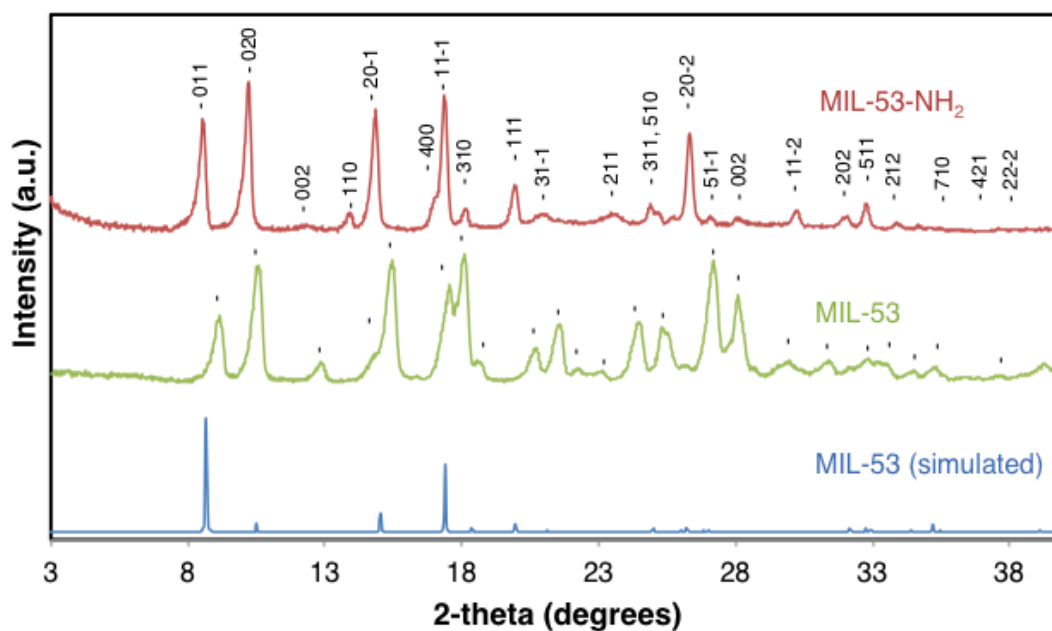
Figure A-4: PXRD of MIL-53 and MIL-53-NH2, peaks are indexed and compared to simulated pattern from single crystal data.

198
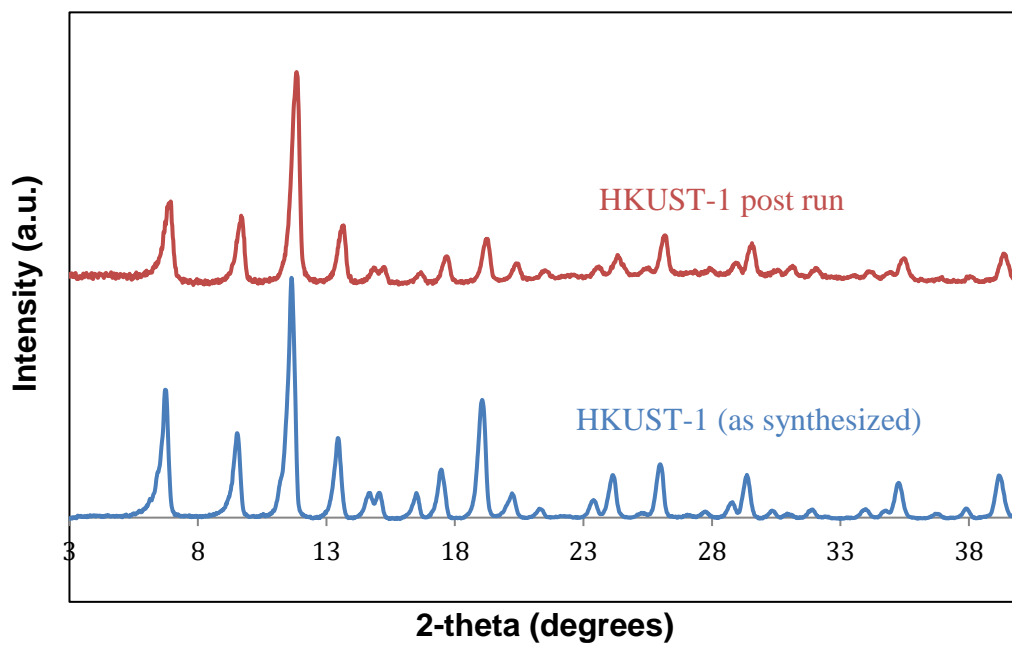
Figure A-5: PXRD of **HKUST-1** as synthesized before and after the photocatalytic oxidation experiments.
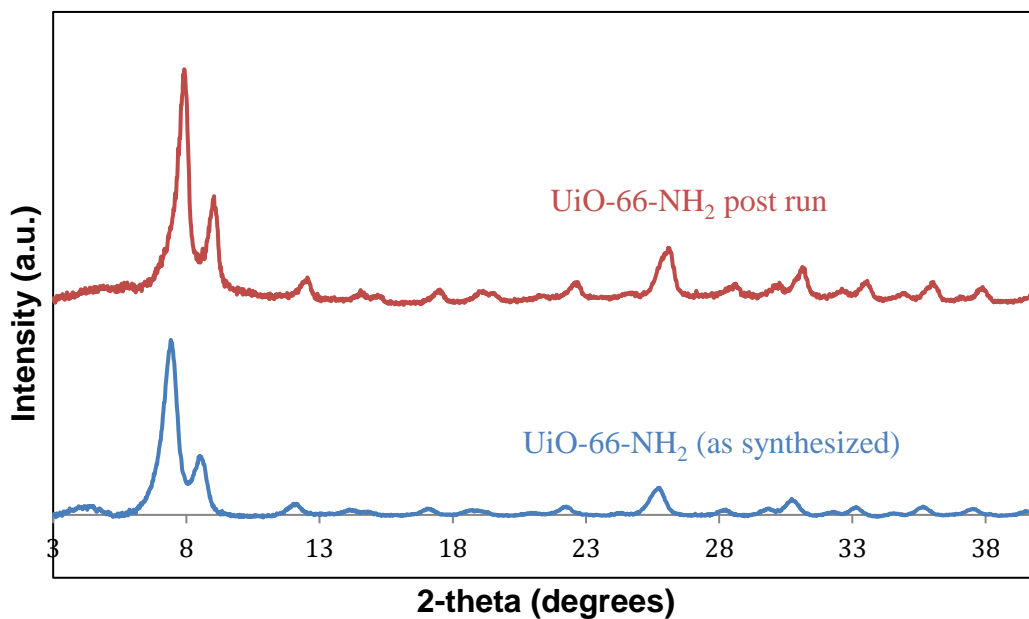
Figure A-6: PXRD of **UiO-66-NH₂** as synthesized before and after the photocatalytic oxidation experiments.
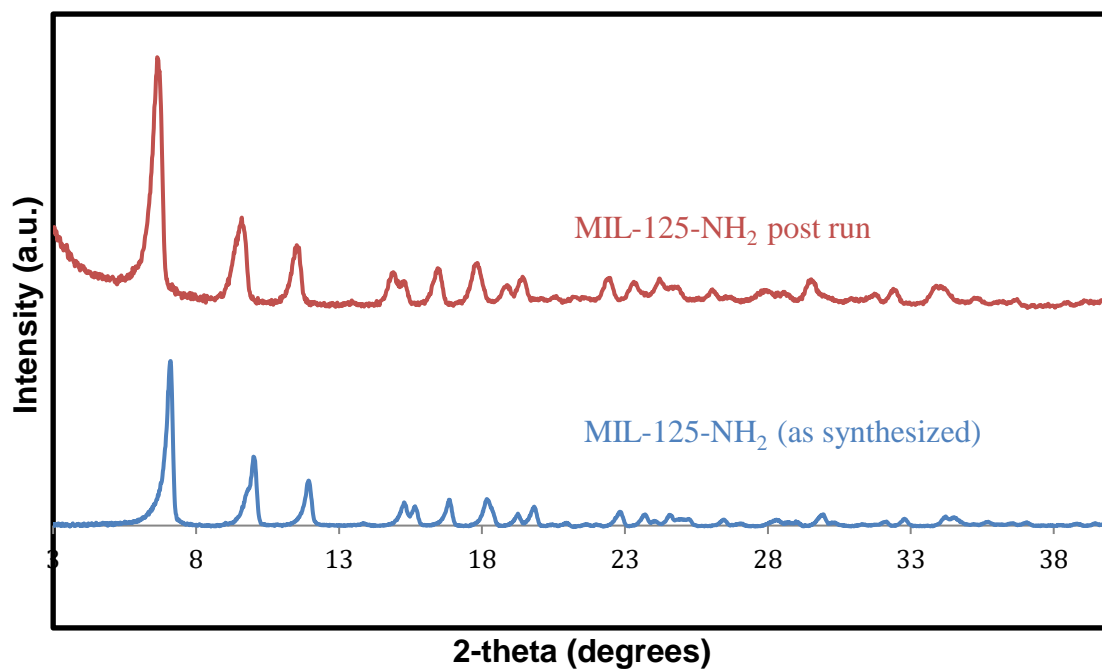
Figure A-7: PXRD of **MIL-125-NH₂** as synthesized before and after the photocatalytic oxidation experiments.

A.2 <u>Scanning Electron Microscopy</u>
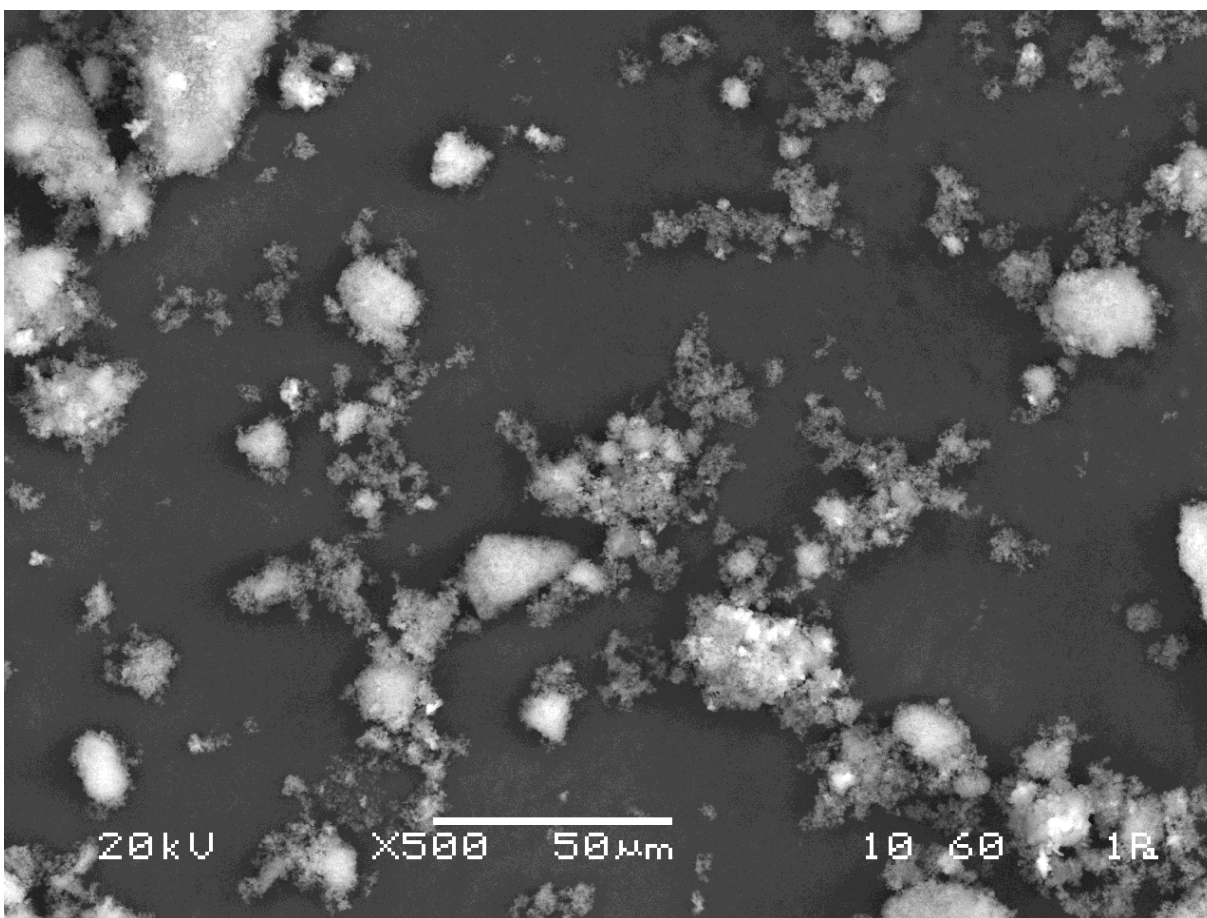
Figure A-8: Scanning electron micrograph images of **MIL-125-NH$_2$** prepared in glass vessel. Scale is indicated.
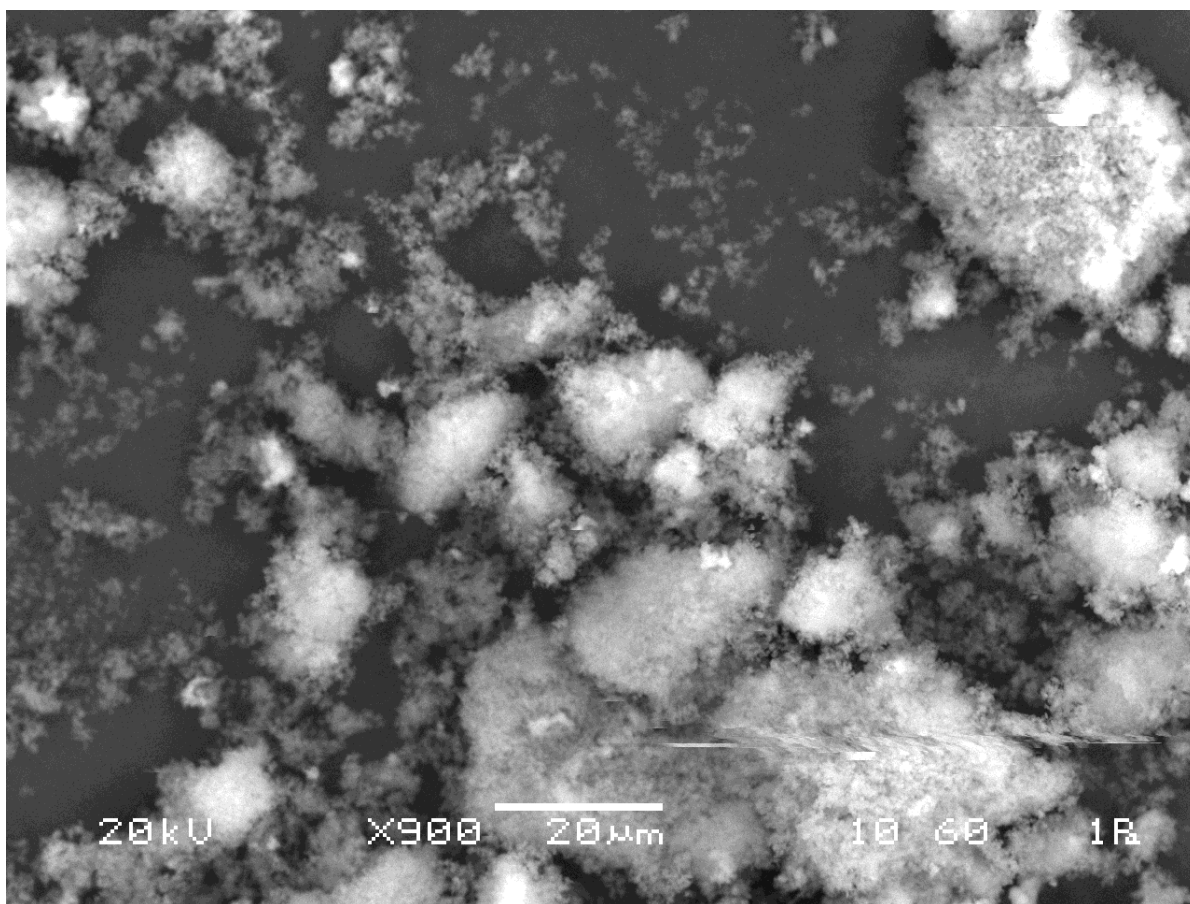
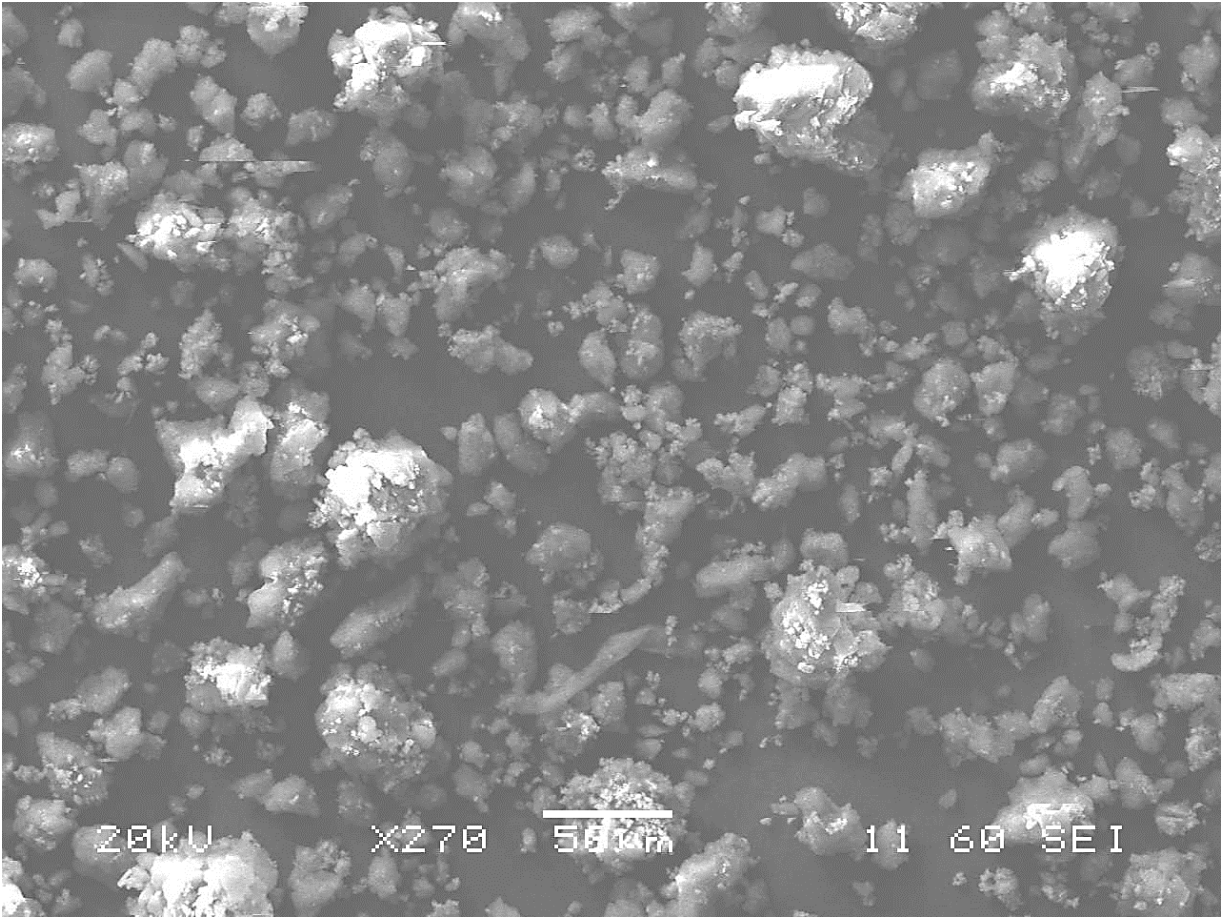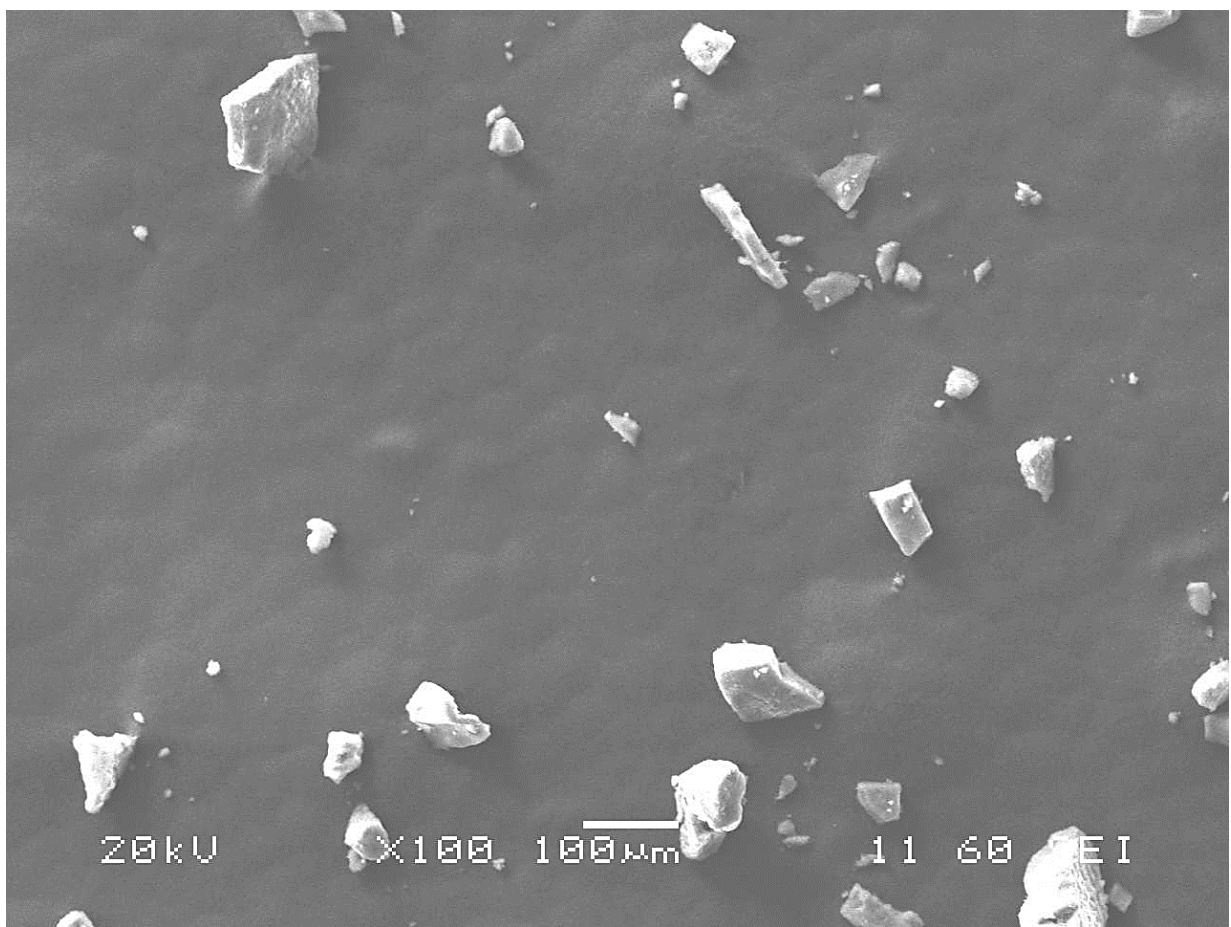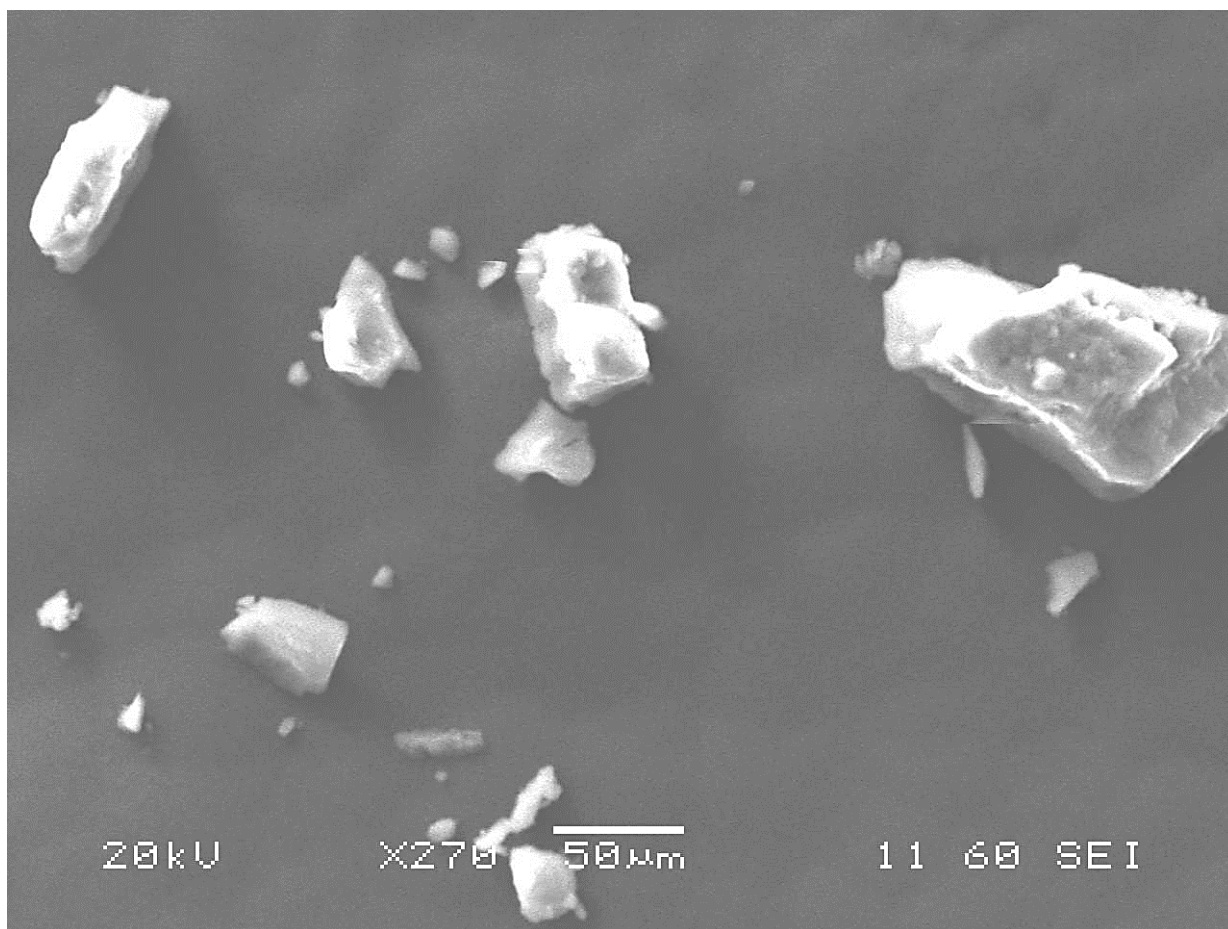Figure A-9: Scanning electron micrograph images of **MIL-125-NH₂** prepared in glass vessel. Scale is indicated.
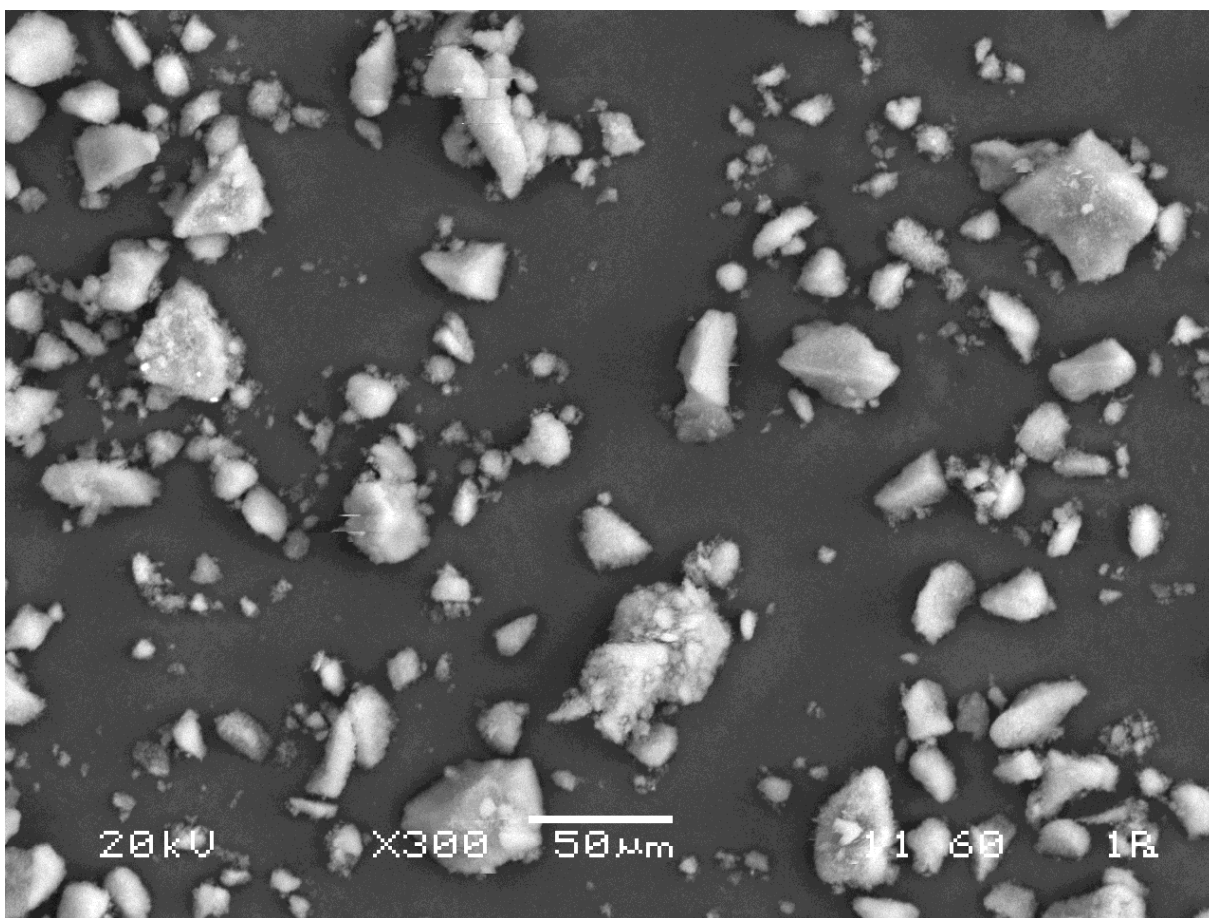
Figure A-10: Scanning electron micrograph images of **MIL-125-NH₂** prepared in PTFE vessel. Scale is indicated.
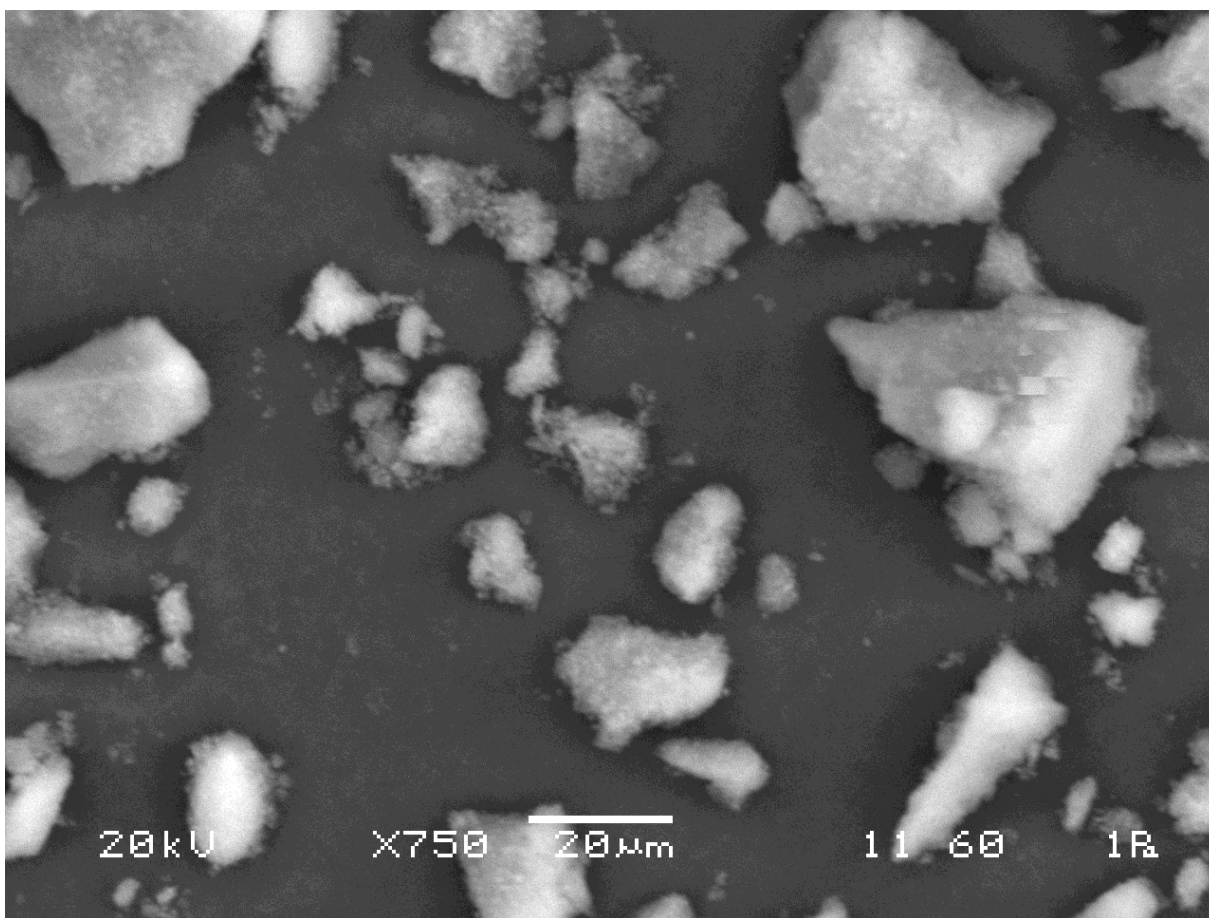
Figure A-11: Scanning electron micrograph images of **MIL-125-NH₂** prepared in PTFE vessel. Scale is indicated.

A.3 Reaction kinetics
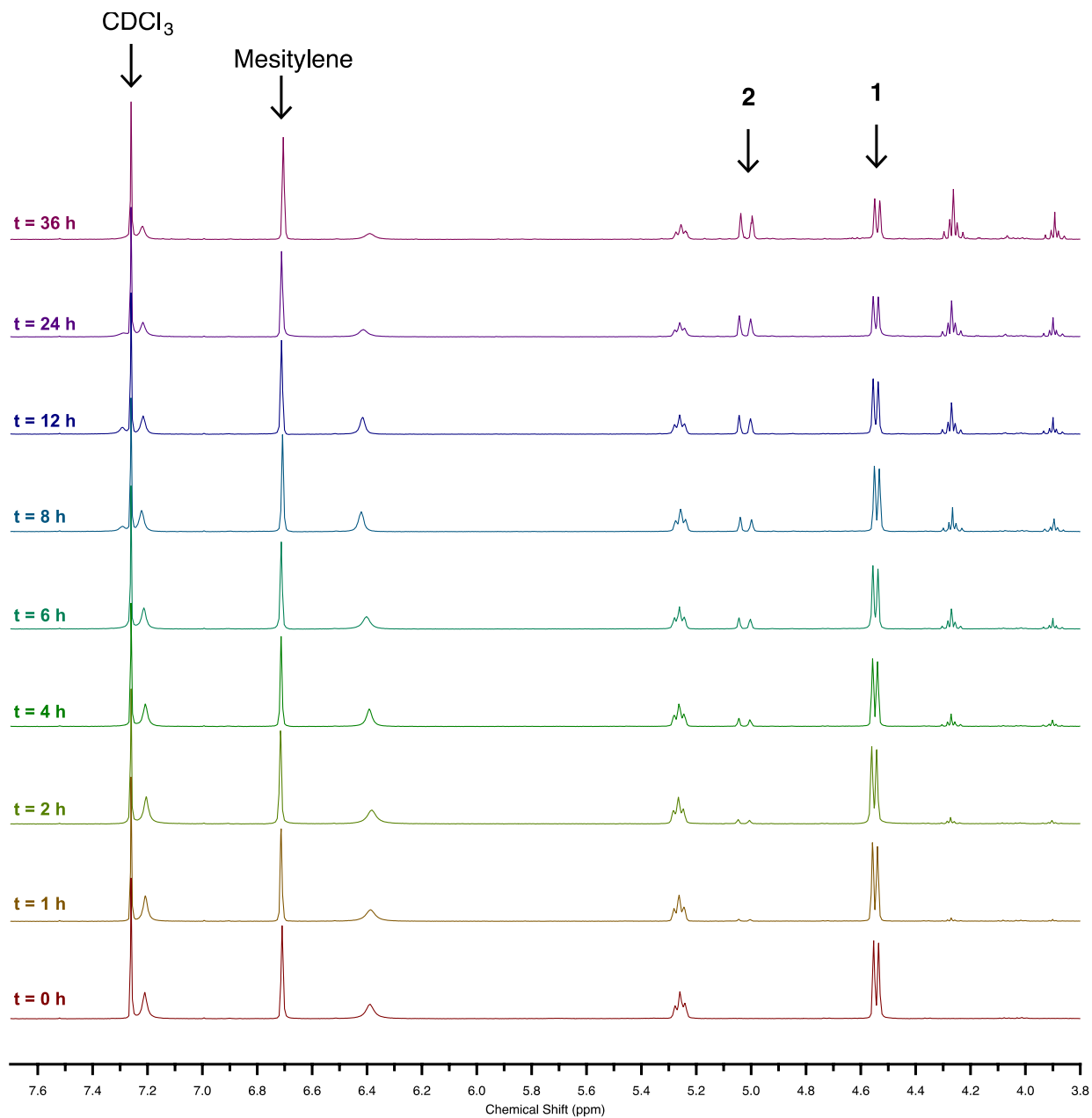

Figure A-12: ^{1}H NMR spectra (400 MHz, CDCl₃, 25 ºC) of the photocatalytic oxidation of **1** vs. time using **MIL-125-NH²** at 25 ºC. The signals of starting material **1** and product **2** used for the quantification are indicated. Mesitylene was used as internal standard (75 mmol L-1).
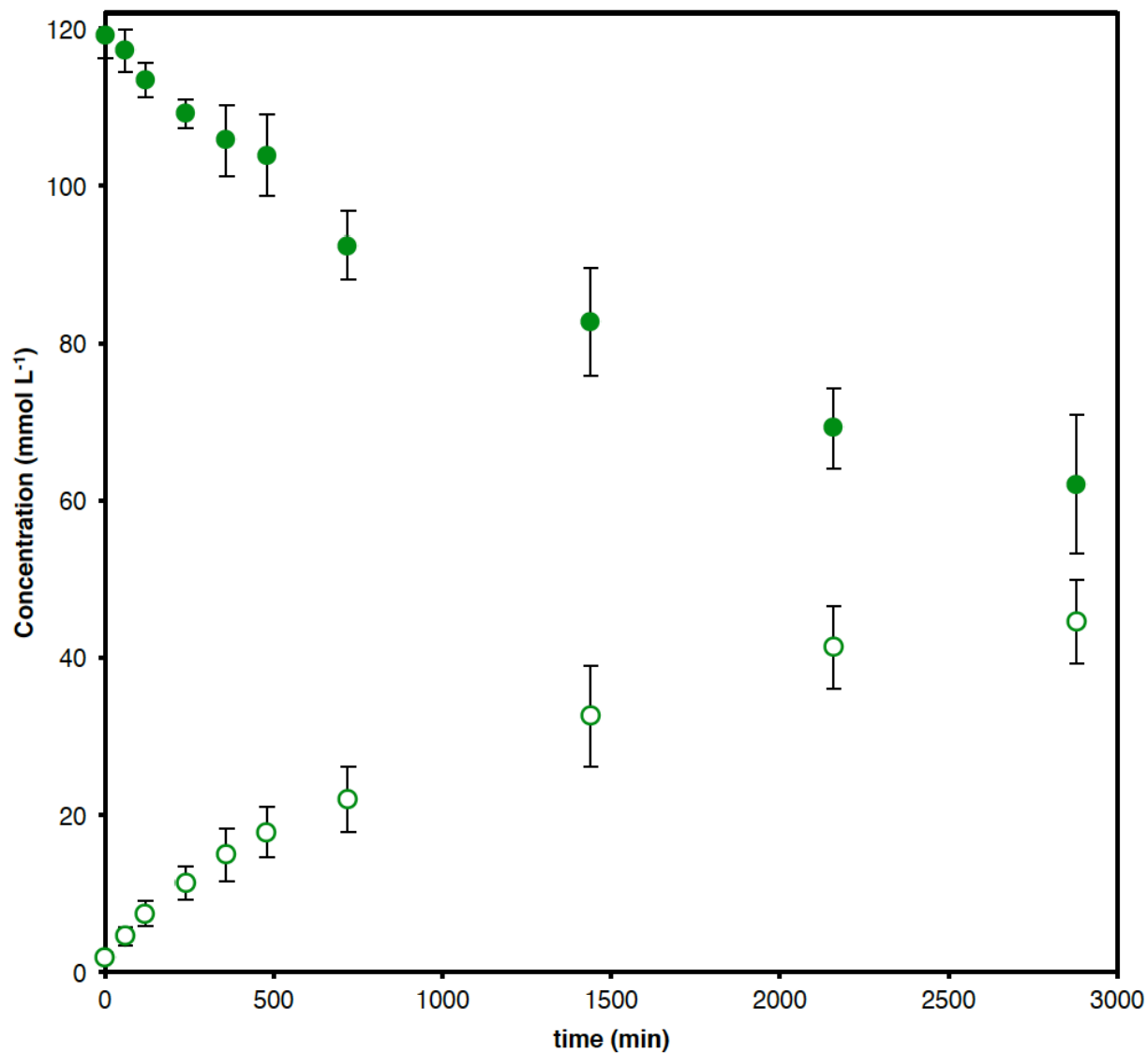
Figure A-13: Concentration vs. time plot of **1** (filled symbols) and **2** (open symbols) using **MIL-125-NH₂** at 25 °C. Concentrations obtained with respect to mesitylene internal standard. Each point is the average of three runs; error bars correspond to one standard deviation.
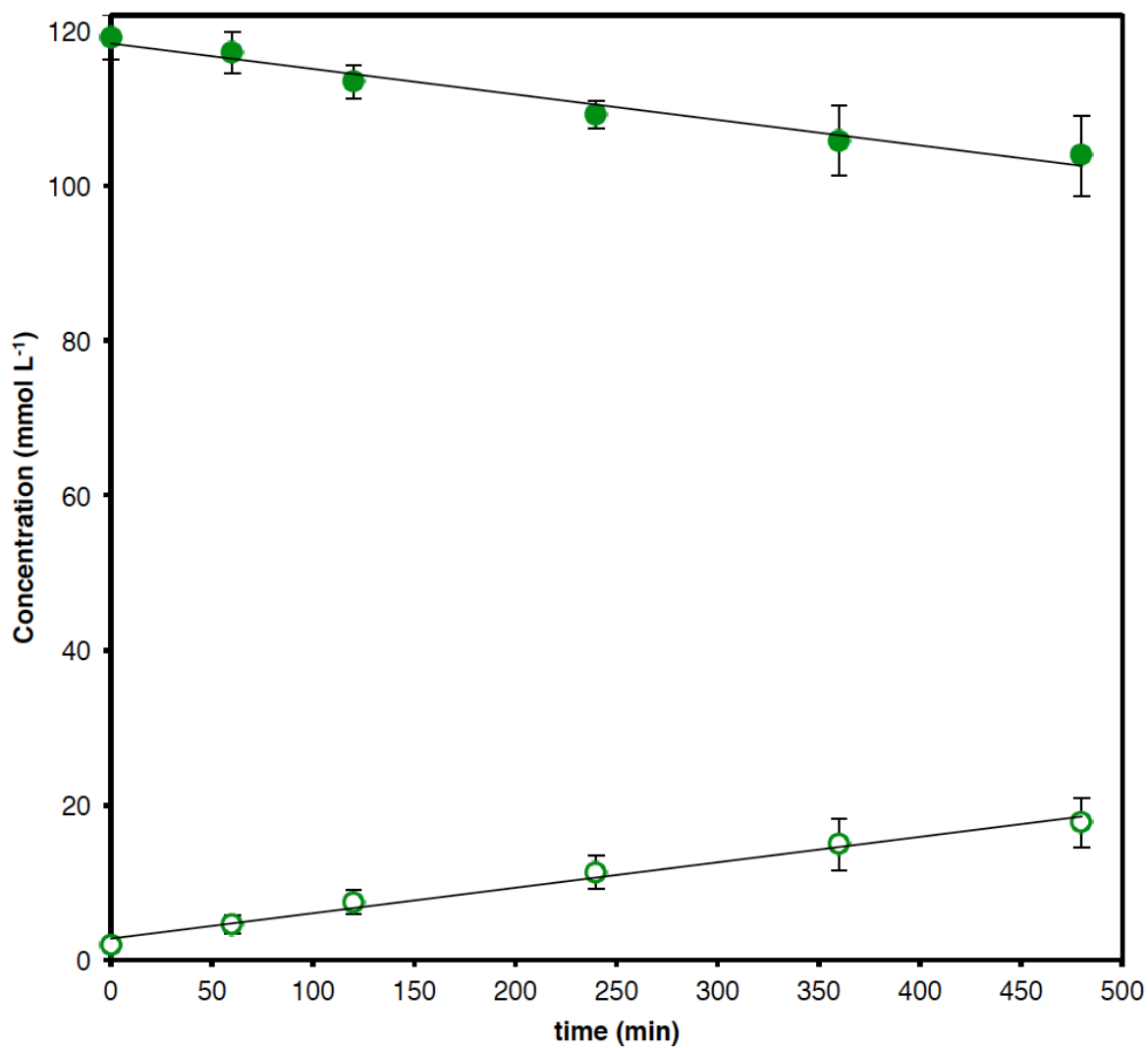
Figure A-14: Linear region of concentration vs. time plot for compounds **1** (filled symbols) and **2** (open symbols) using **MIL-125-NH₂** at 25 ºC. Concentrations were obtained with respect to mesitylene internal standard. Each point corresponds to the average of three runs, and error bars correspond to one standard deviation.

From least-squares linear fitting:

$$\frac{d[1]}{dt} = -k = -32.93 \pm 4.44 \; m\text{mol}\times\text{L}^{-1}\times\text{min}^{-1}$$

and

$$\frac{d[2]}{dt} = 32.87 \pm 2.87 \; m\text{mol}\times\text{L}^{-1}\times\text{min}^{-1}$$

Where k is zero-order rate constant.
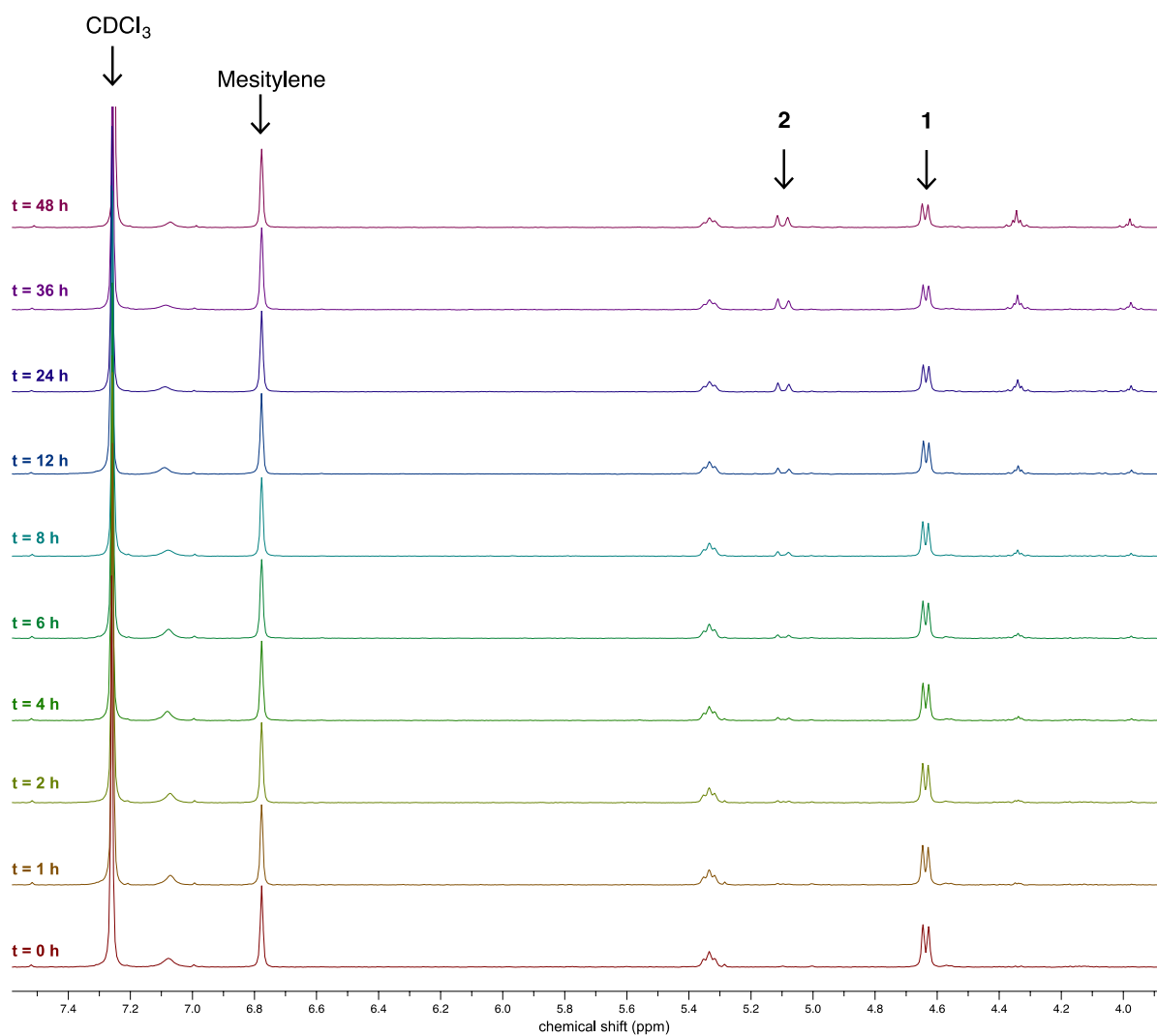
Figure A-15: ¹H NMR spectra (400 MHz, CDCl$_3$, 25 ℃) of the photocatalytic oxidation of **1** vs. time using **UiO-66-NH$_2$** at 25 ℃. The signals of starting material **1** and product **2** used for the quantification are indicated. Mesitylene was used as internal standard (75 mmol L-1).
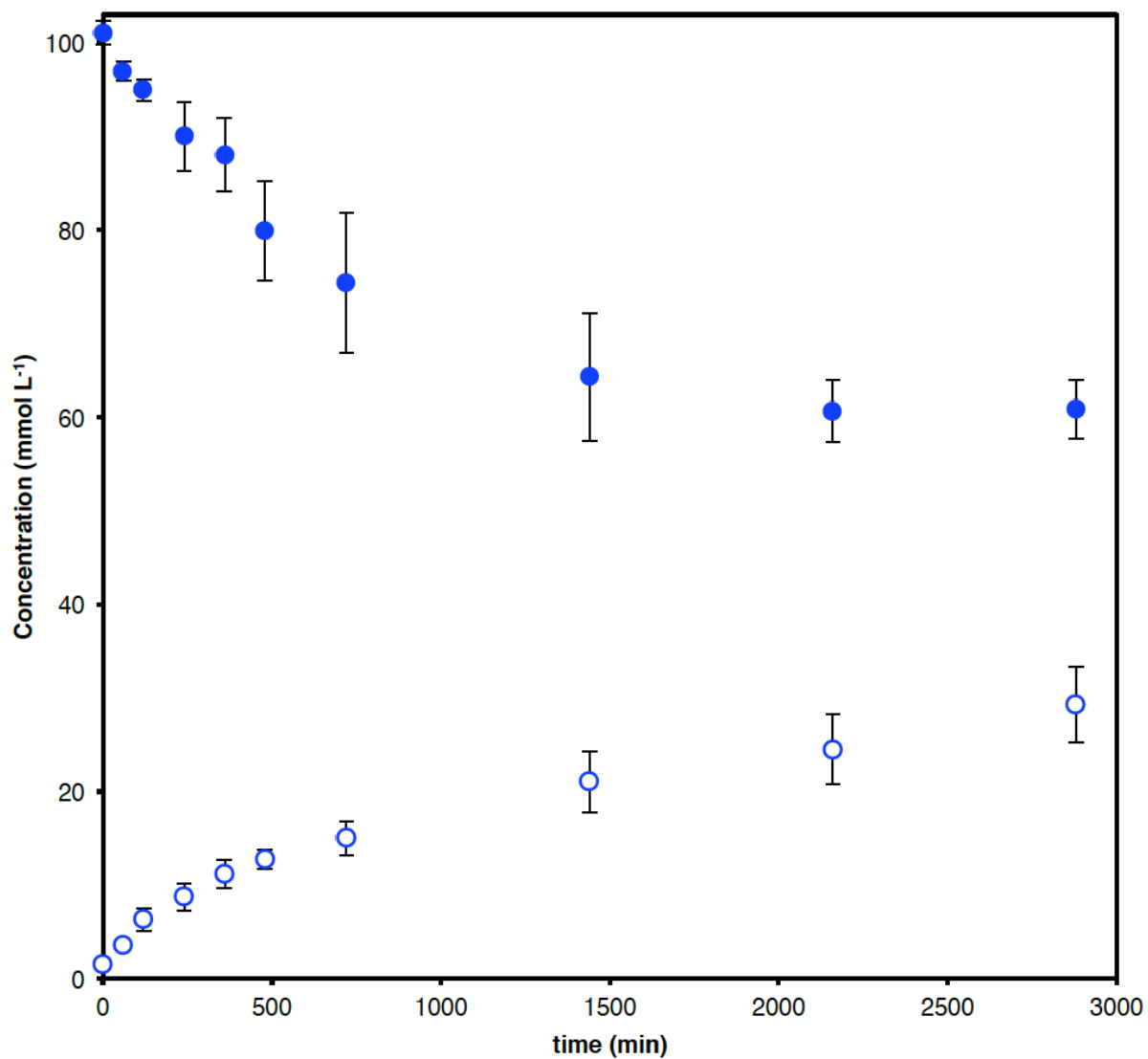
Figure A-16: Concentration vs. time plot of **1** (filled symbols) and **2** (open symbols) using **UiO-66-NH$_2$** at 25 ℃. Concentrations obtained with respect to mesitylene internal standard. Each point is the average of three runs; error bars correspond to one standard deviation.

Figure A-17: Linear part of the concentration vs. time plot of **1** (filled symbols) and **2** (open symbols) using **UiO-66-NH$_2$** at 25 °C. Concentrations obtained with respect to mesitylene internal standard. Each point corresponds to the average of three runs; error bars correspond to one standard deviation.

From least-squares linear fitting:

$$\frac{d[1]}{dt} = -k = -39.98 \pm 4.20 \; m\text{mol×L}^{-1}\text{×min}^{-1}$$

and

$$\frac{d[2]}{dt} = 23.25 \pm 1.75 \; m\text{mol×L}^{-1}\text{×min}^{-1}$$

Where k is zero-order rate constant.
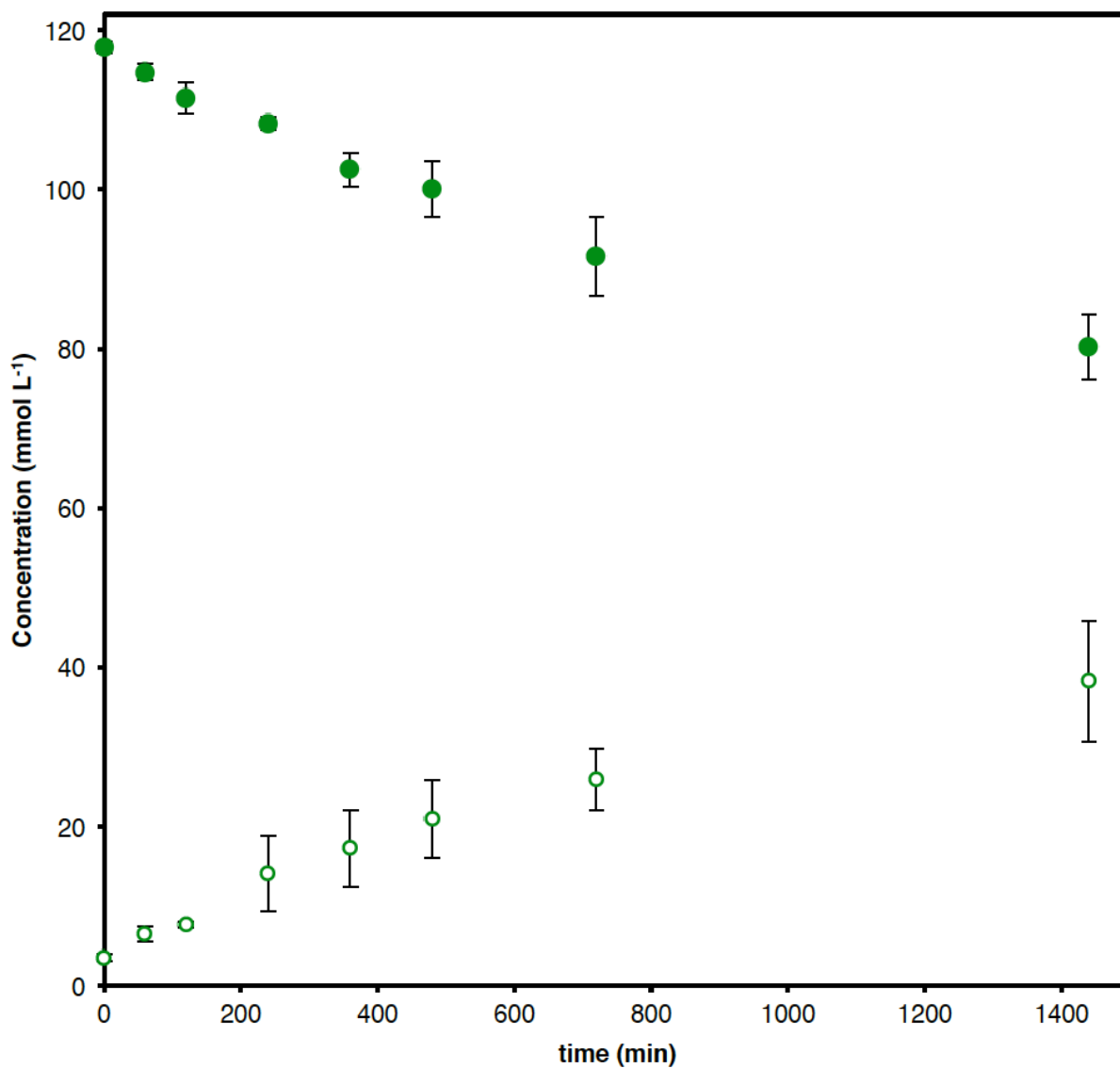
Figure A-18: Concentration vs. time plot of **1** (filled symbols) and **2** (open symbols) using **MIL-125-NH₂** at 50 ºC. Concentrations obtained with respect to mesitylene internal standard. Each point is the average of three runs; error bars correspond to one standard deviation.
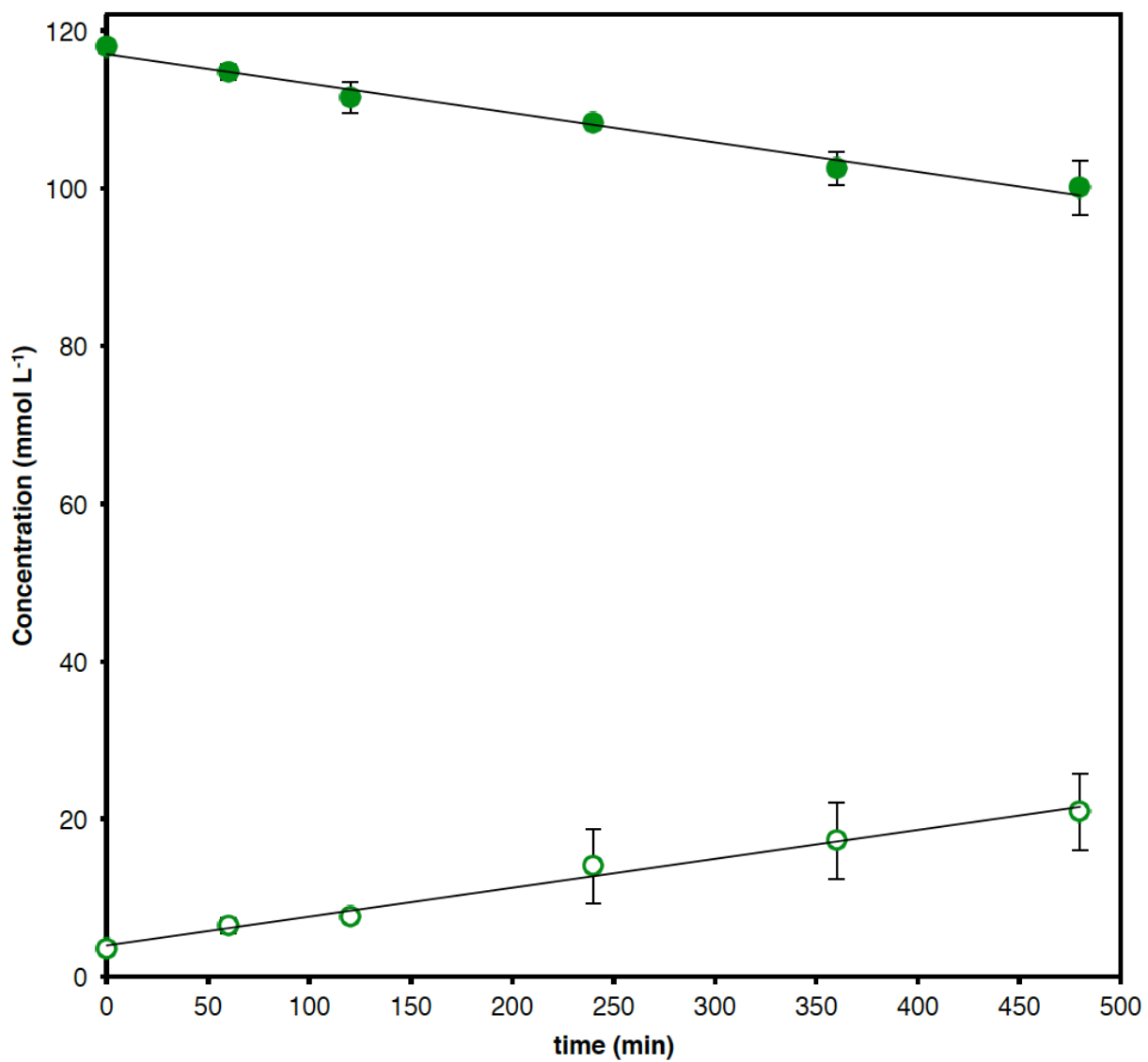
Figure A-19: Linear part of the concentration vs. time plot of **1** (filled symbols) and **2** (open symbols) using **MIL-125-NH$_2$** at 50 ºC. Concentrations obtained with respect to mesitylene internal standard. Each point corresponds to the average of three runs; error bars correspond to one standard deviation.

From least-squares linear fitting:

$$\frac{d[1]}{dt} = -k = -37.29 \pm 2.65 \; m\text{mol} \times \text{L}^{-1} \times \text{min}^{-1}$$

and

$$\frac{d[2]}{dt} = 27.47 \pm 1.80 \; m\text{mol} \times \text{L}^{-1} \times \text{min}^{-1}$$

Where k is zero-order rate constant.
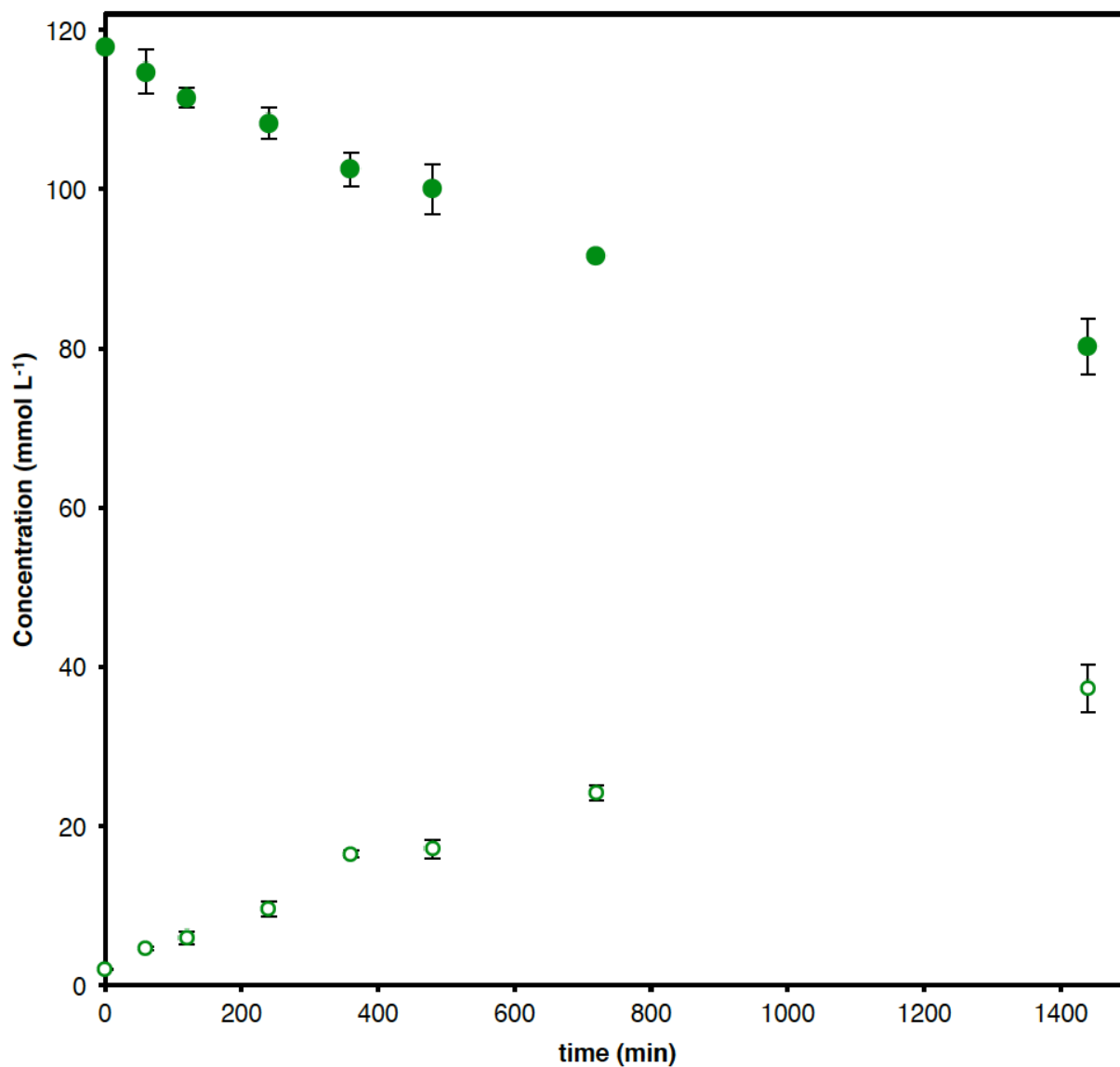
Figure A-20: Concentration vs. time plot of **1** (filled symbols) and **2** (open symbols) using **MIL-125-NH$_2$** at 60 °C. Concentrations obtained with respect to mesitylene internal standard. Each point is the average of three runs; error bars correspond to one standard deviation.
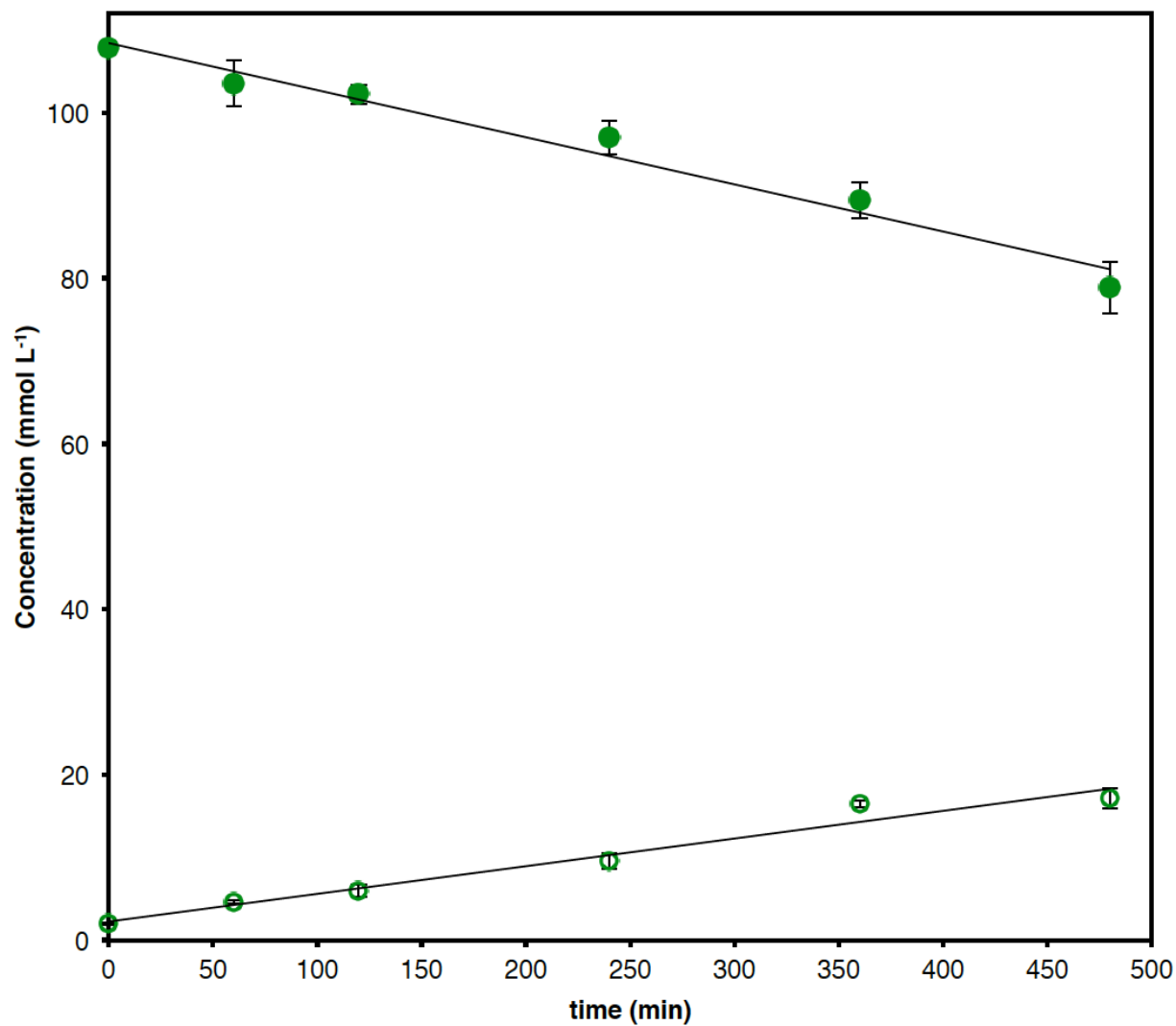
Figure A-21: Linear part of the concentration vs. time plot of **1** (filled symbols) and **2** (open symbols) using **MIL-125-NH₂** at 60 ºC. Concentrations obtained with respect to mesitylene internal standard. Each point corresponds to the average of three runs; error bars correspond to one standard deviation.

From least-squares linear fitting:

$$\frac{d[1]}{dt} = -k = -39.98 \pm 4.20 \; m\text{mol} \times \text{L}^{-1} \times \text{min}^{-1}$$

and

$$\frac{d[2]}{dt} = 23.25 \pm 1.75 \; m\text{mol} \times \text{L}^{-1} \times \text{min}^{-1}$$

Where k is zero-order rate constant.
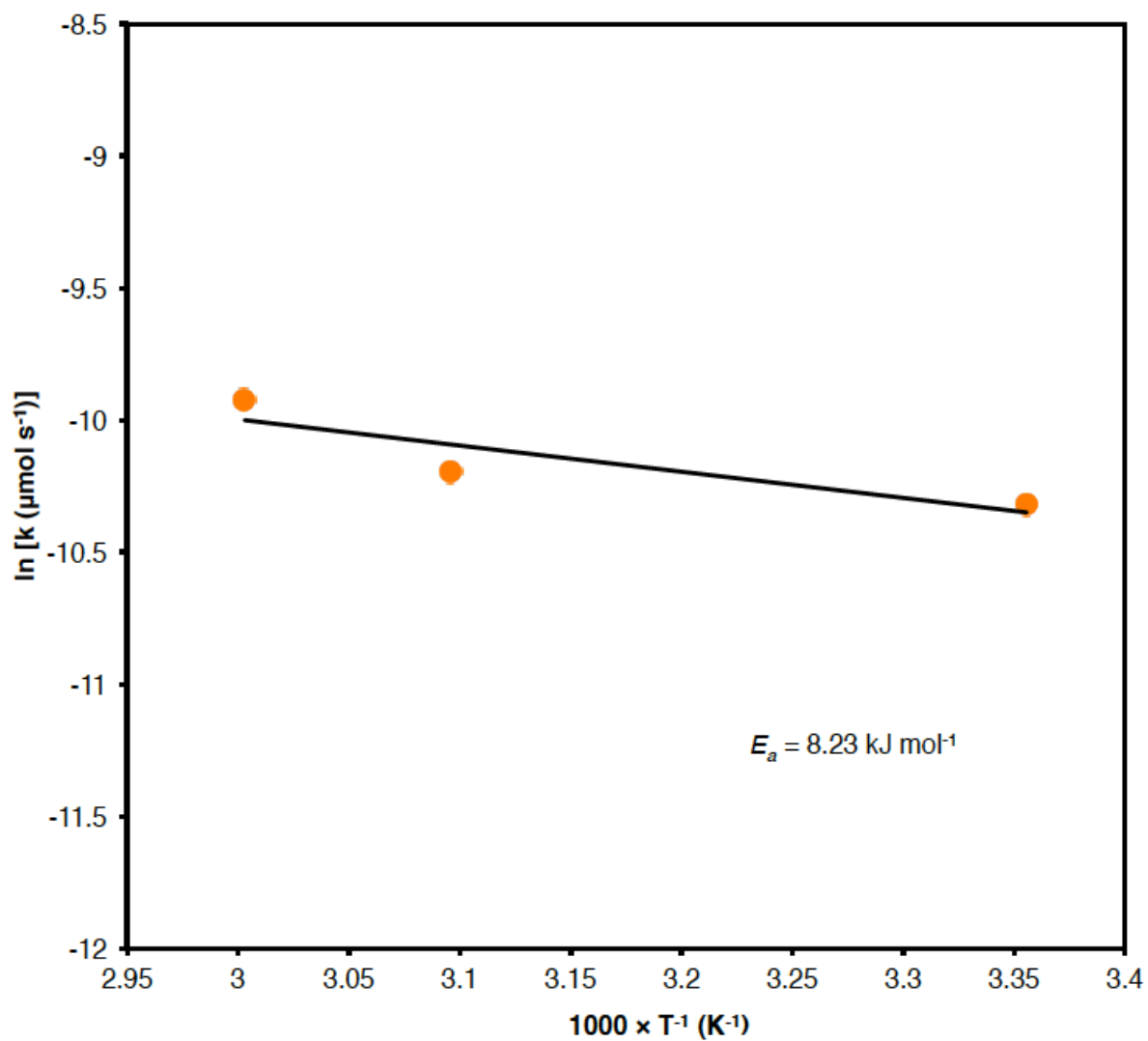
Figure A-22: Arrhenius plot of the photooxidation of **1** using **MIL-125-NH₂**. Activation energy of the reaction is indicated.

A.4 **Photochemical Quantum Yields**
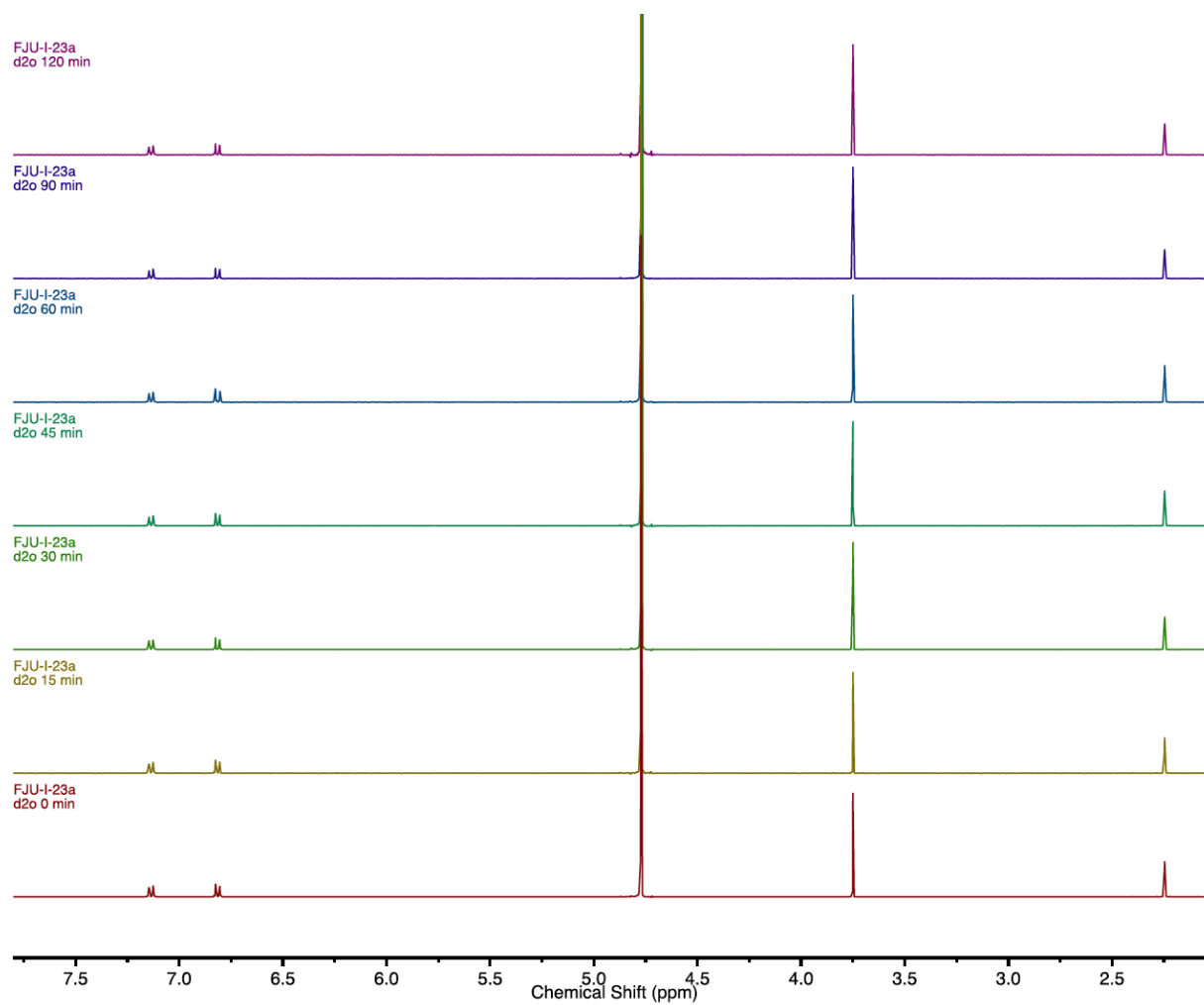
Figure A-23: ^{1}H NMR spectra (400 MHz, D$_2$O, 25 ºC) of the standard photo-decomposition of *p*-cresol by TiO$_2$.

Linear least-square fitting of the data points resulted in:

R^{in}(*p-cresol*) = -239±19 μmol L^{-1} min^{-1}

A.5 NMR Spectra
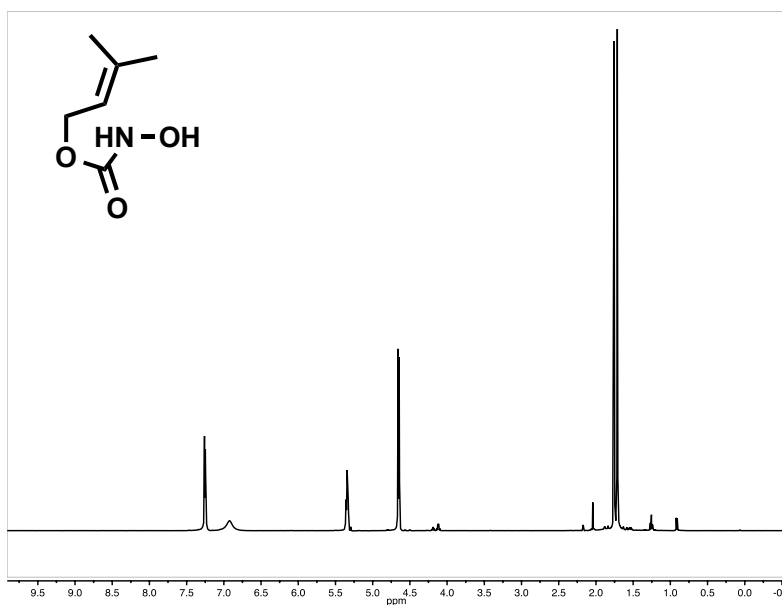
Figure A-24: ^{1}H NMR spectra (400 MHz, CDCl3, 25 °C) of compound **1**.
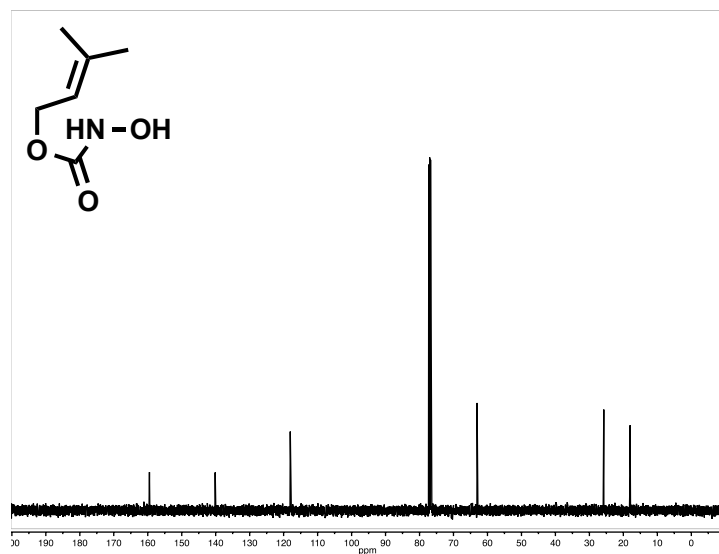
Figure A- 25: ^{13}C NMR spectra (100 MHz, CDCl$_3$, 25 °C) of compound **1**.

221
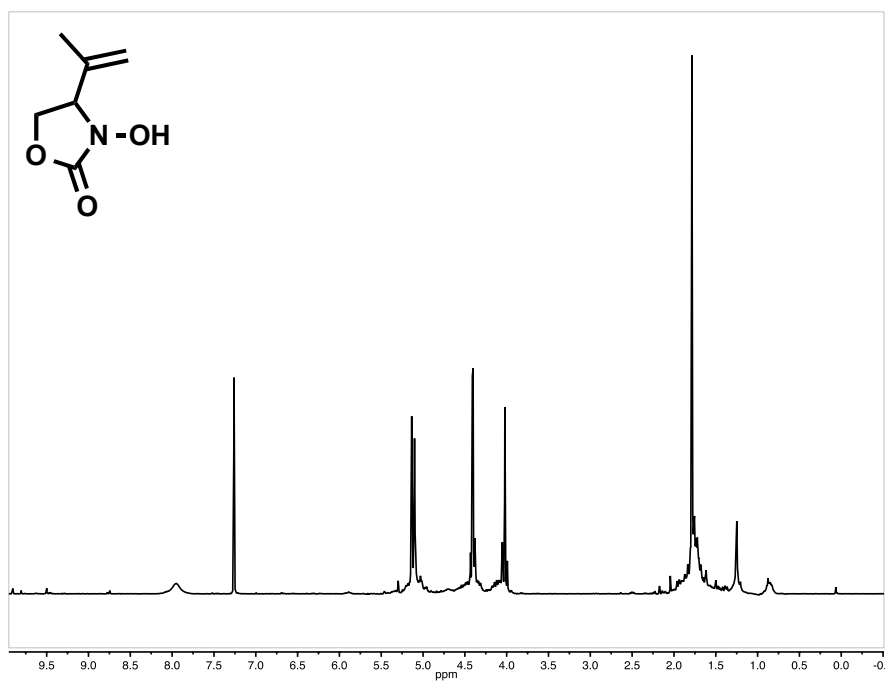
Figure A-26: ₁H NMR spectra (400 MHz, CDCl₃, 25 ℃) of compound **2**.
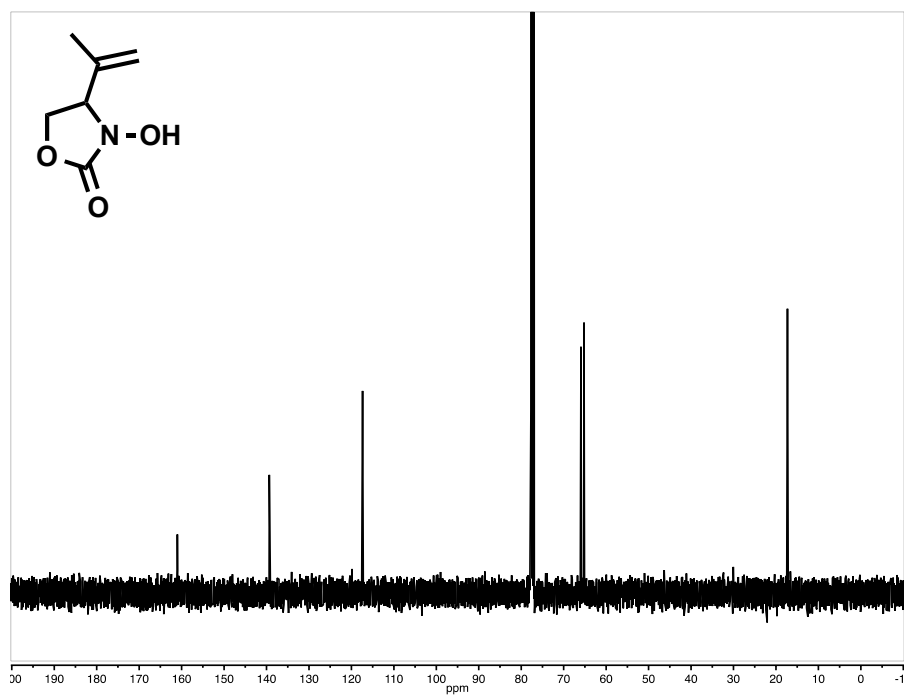
Figure A- 27: ¹³C NMR spectra (100 MHz, CDCl₃, 25 ℃) of compound **2**.
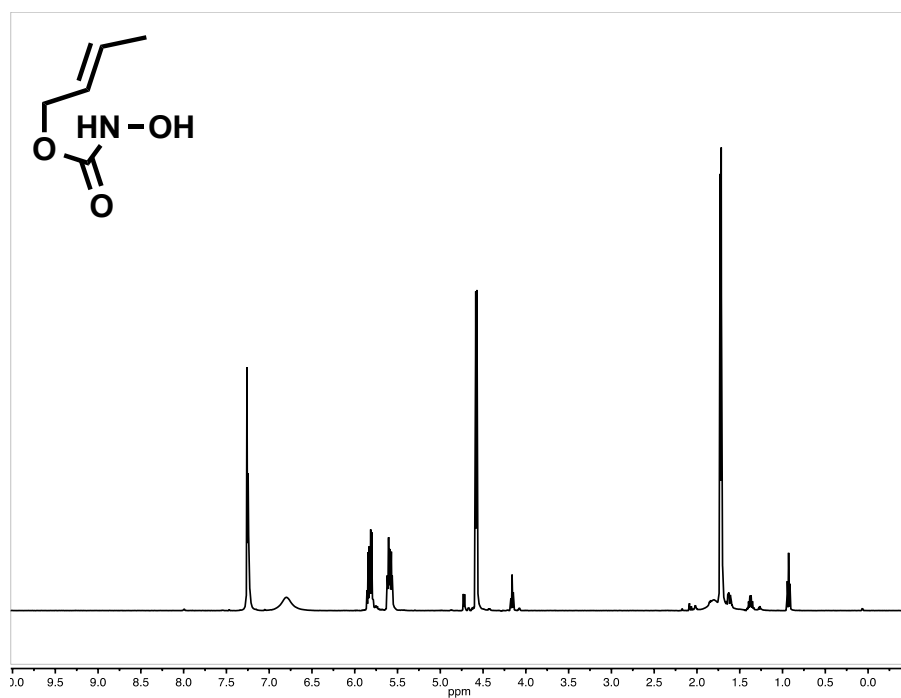
Figure A-28: ^{1}H NMR spectra (400 MHz, CDCl$_3$, 25 ºC) of compound **3**.
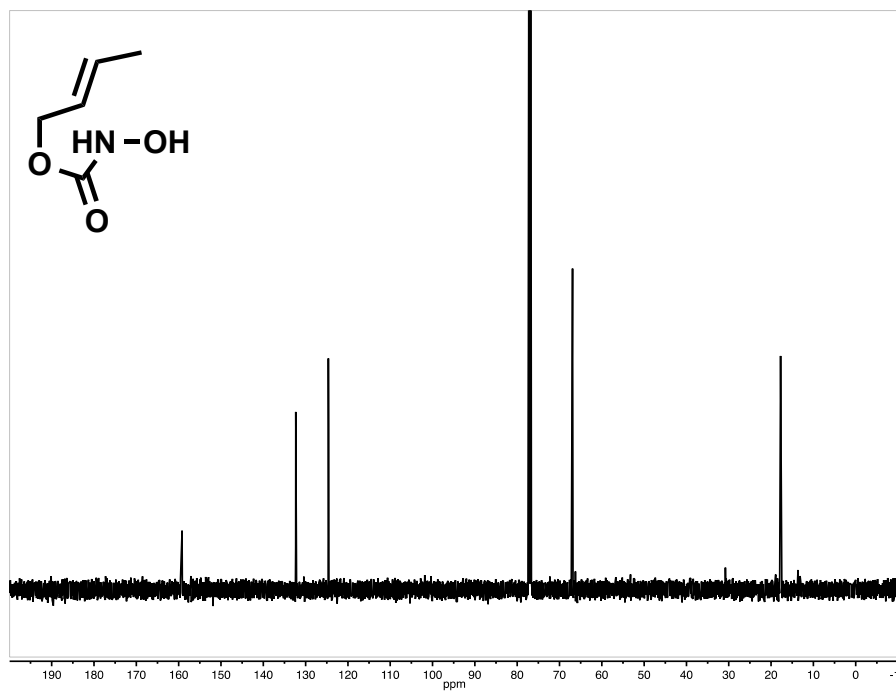
Figure A-29: ^{13}C NMR spectra (100 MHz, CDCl$_3$, 25 ºC) of compound **3**.
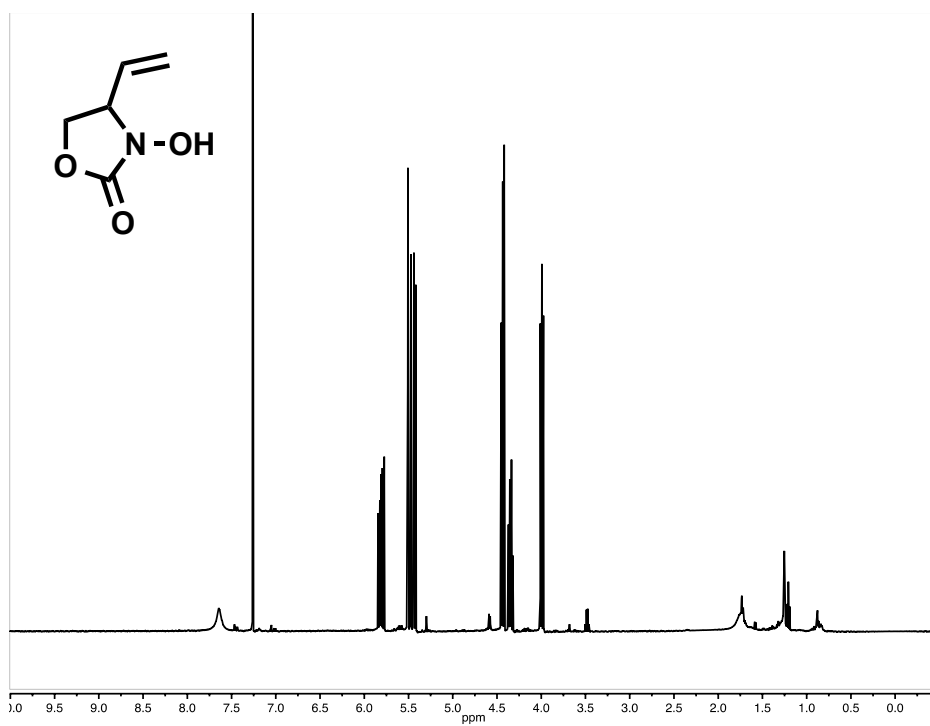
Figure A-30: ^{1}H NMR spectra (400 MHz, CDCl$_3$, 25 °C) of compound **4**.
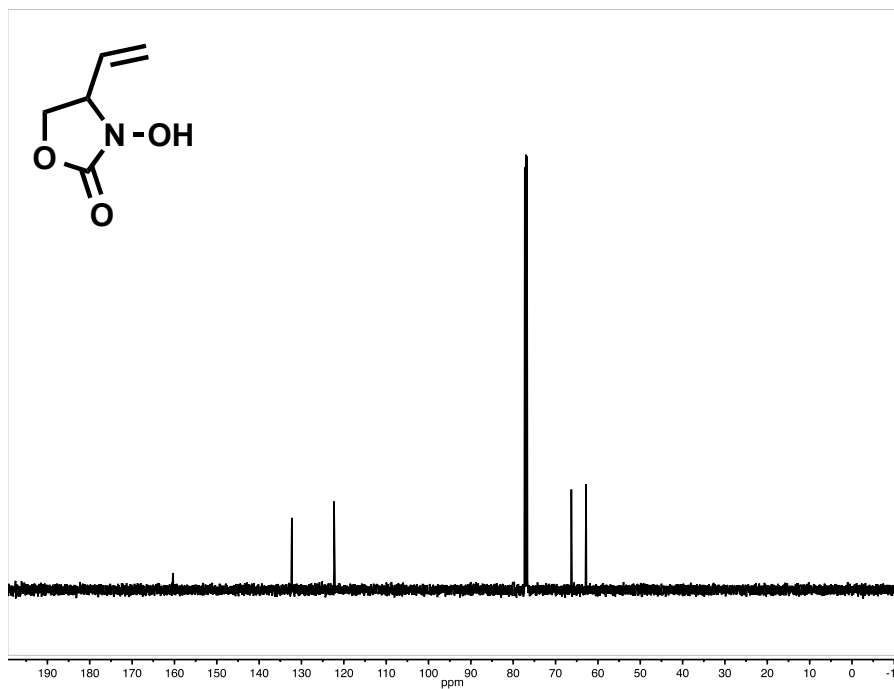
Figure A-31: ^{13}C NMR spectra (100 MHz, CDCl$_3$, 25 °C) of compound **4**.
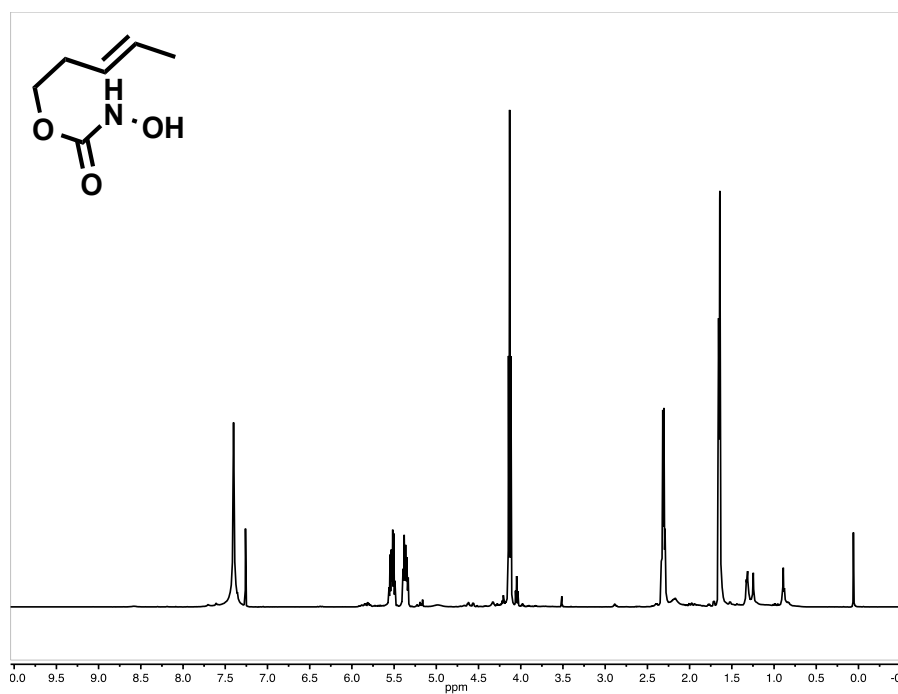
Figure A-32: ^{1}H NMR spectra (400 MHz, CDCl$_3$, 25 ℃) of compound **5**.
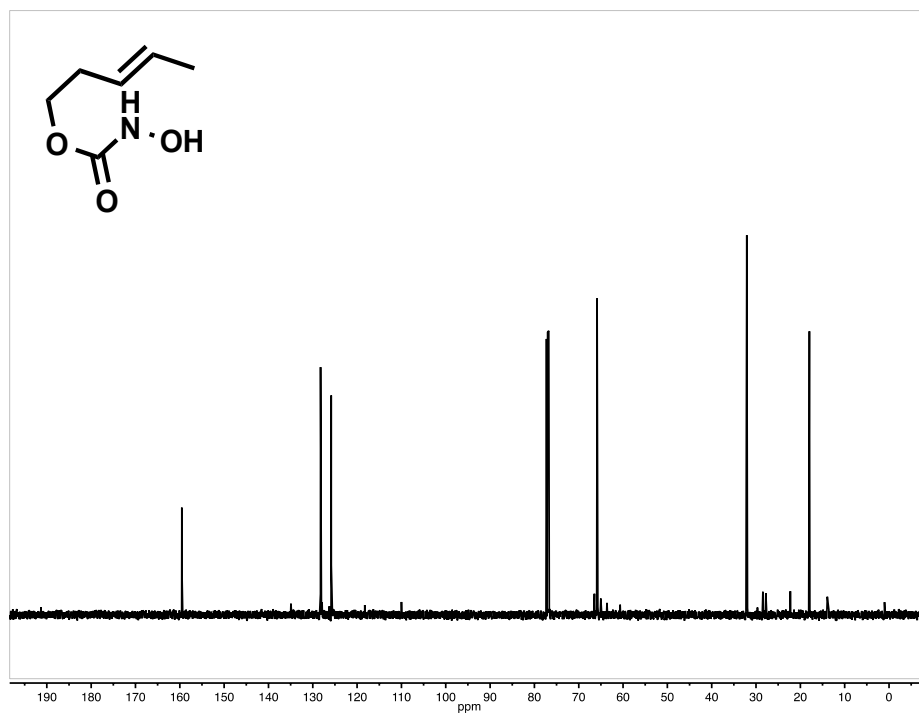
Figure A-33: ^{13}C NMR spectra (100 MHz, CDCl$_3$, 25 ℃) of compound **5**.
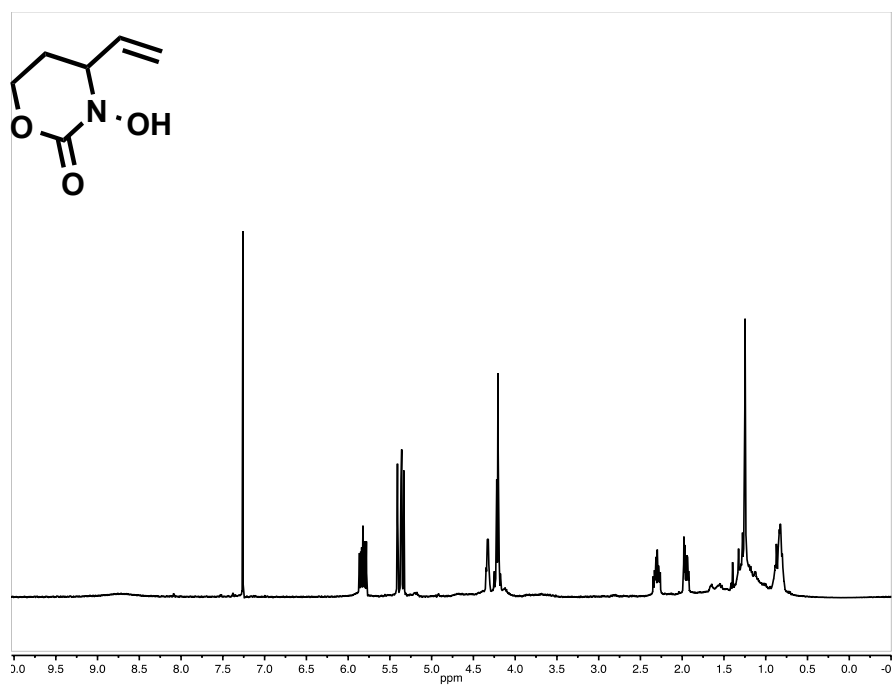
Figure A-34: ^{1}H NMR spectra (400 MHz, CDCl$_3$, 25 ºC) of compound **6**.
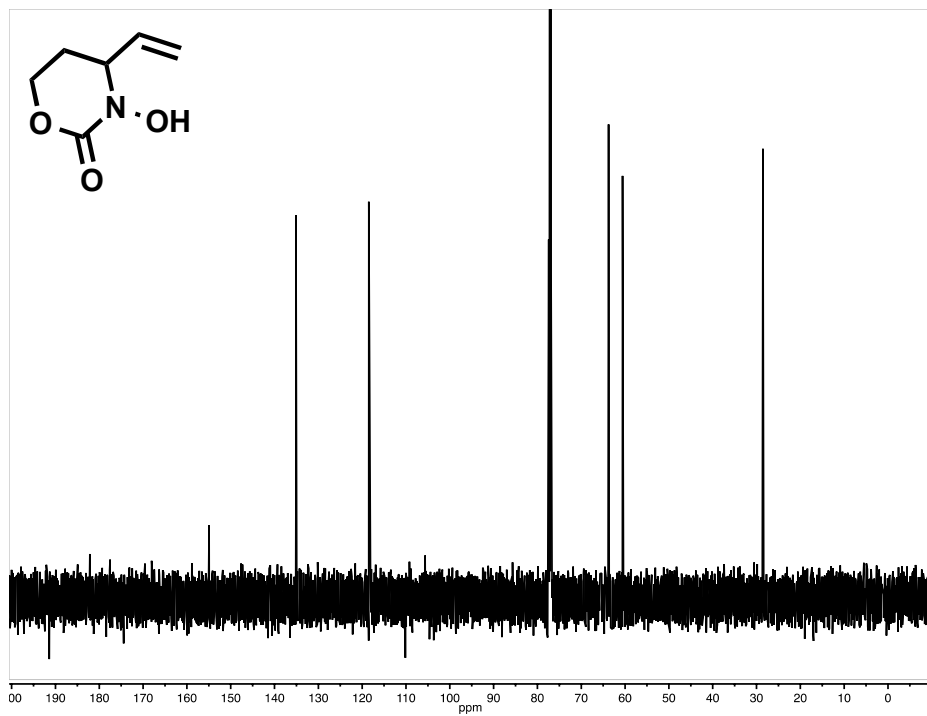
Figure A-35: ^{13}C NMR spectra (100 MHz, CDCl$_3$, 25 ºC) of compound **6.**
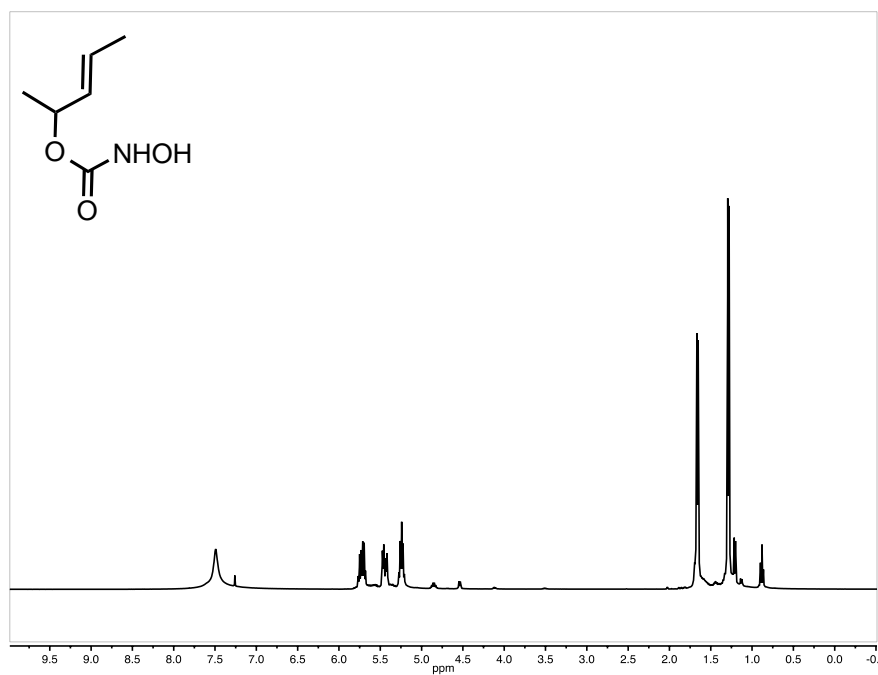
Figure A-36: ^{1}H NMR spectra (400 MHz, CDCl$_3$, 25 °C) of compound **7**.
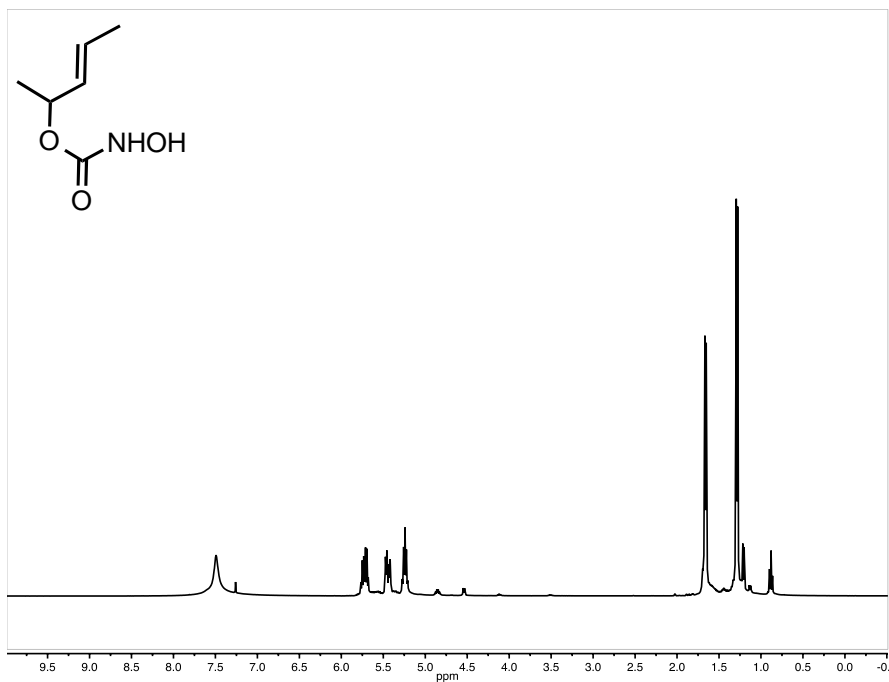
Figure A-37: ^{13}C NMR spectra (100 MHz, CDCl, 25 °C) of compound **7**.
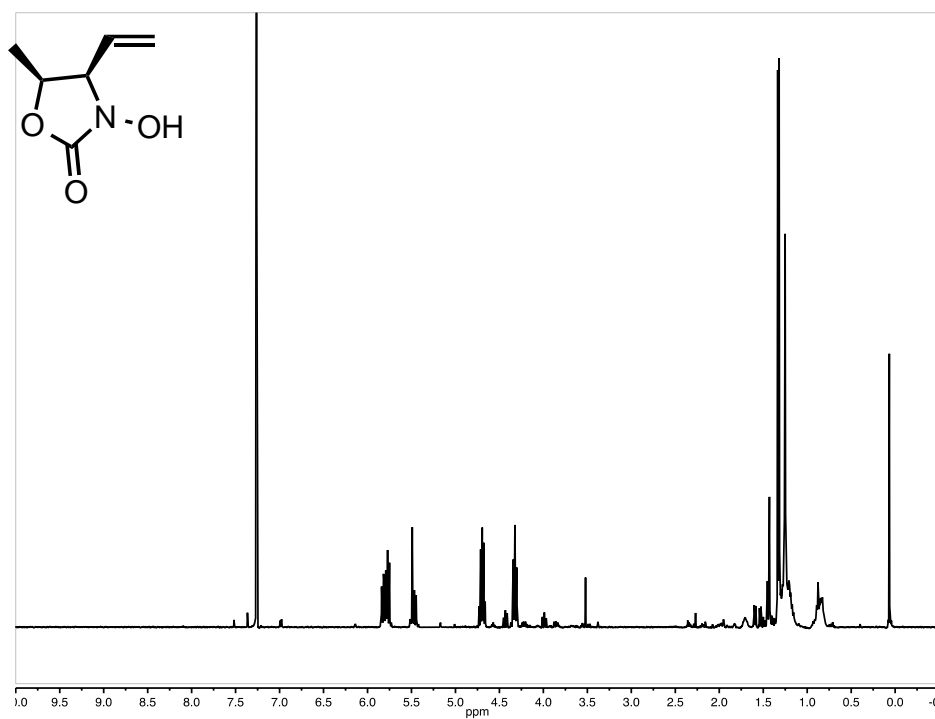
Figure A-38: ¹H NMR spectra (400 MHz, CDCl₃, 25 ℃) of compound **8a**.
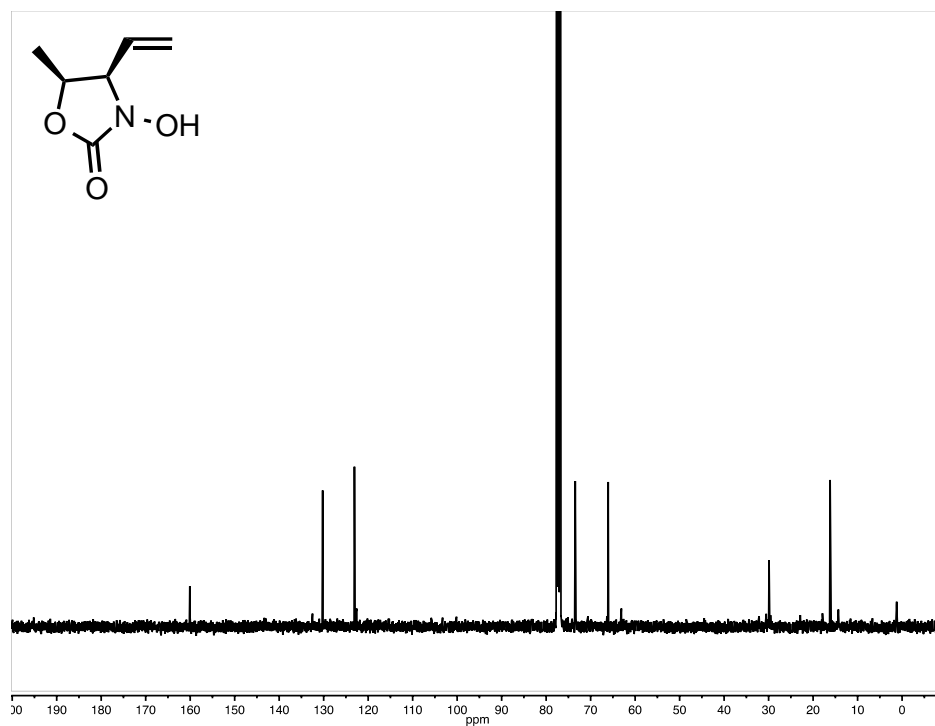
Figure A-39: ¹³C NMR spectra (100 MHz, CDCl₃, 25 ℃) of compound **8a**.
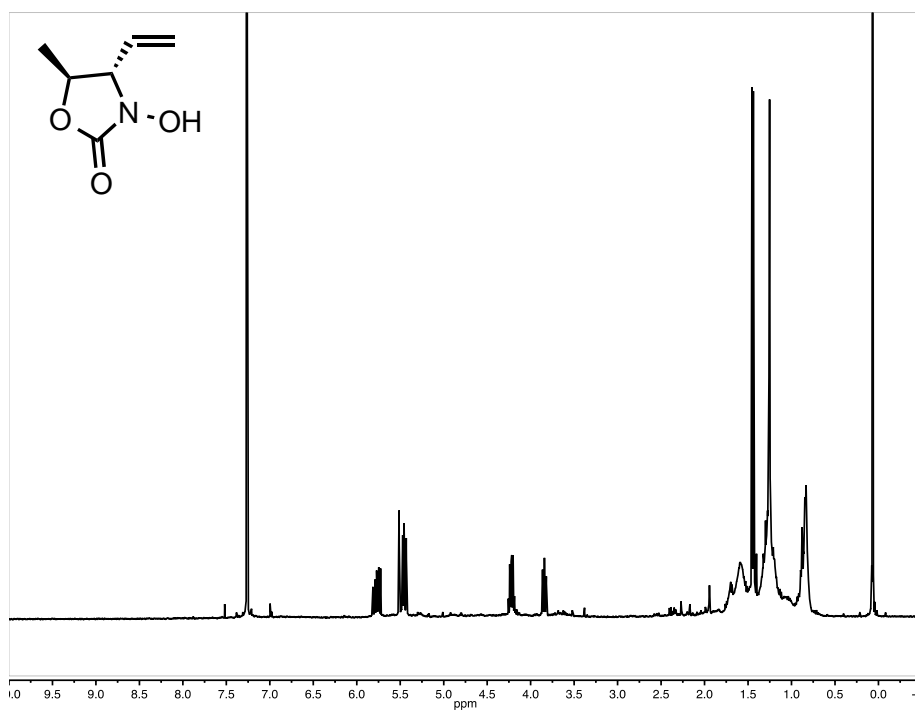
Figure A-40: ^{1}H NMR spectra (400 MHz, CDCl$_3$, 25 ºC) of compound **8b**.
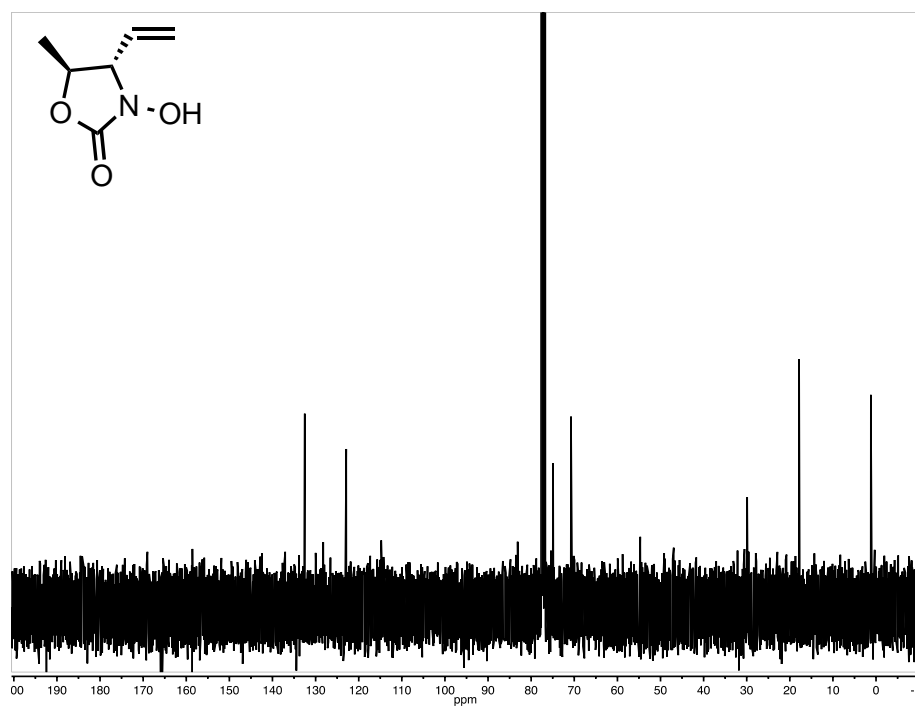
Figure A-41: ^{13}C NMR spectra (100 MHz, CDCl$_3$, 25 ºC) of compound **8b**.
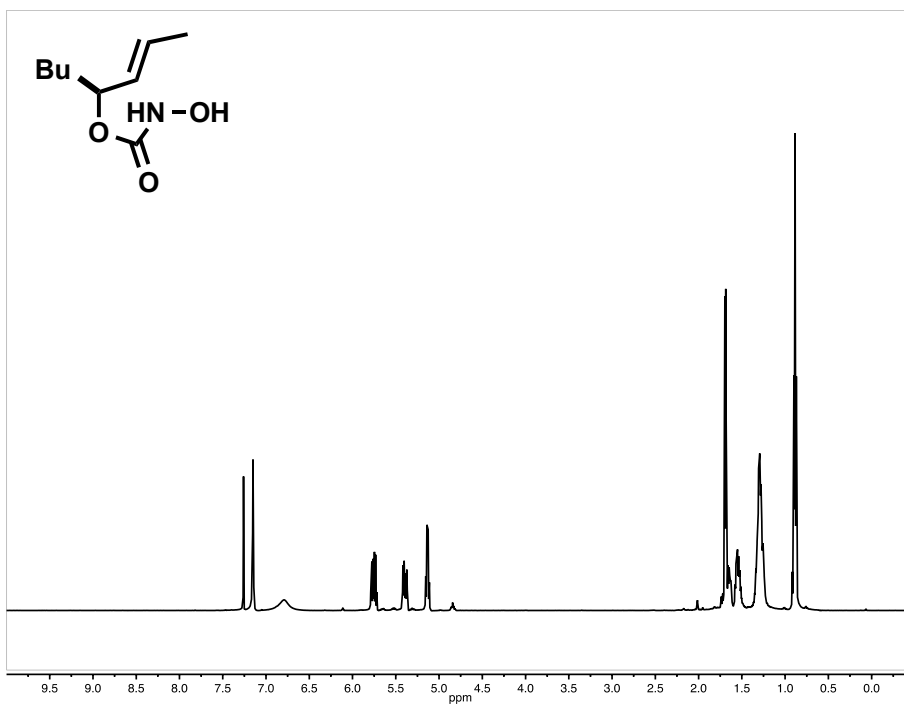
Figure A-42: ^{1}H NMR spectra (400 MHz, CDCl$_3$, 25 °C) of compound **9**.
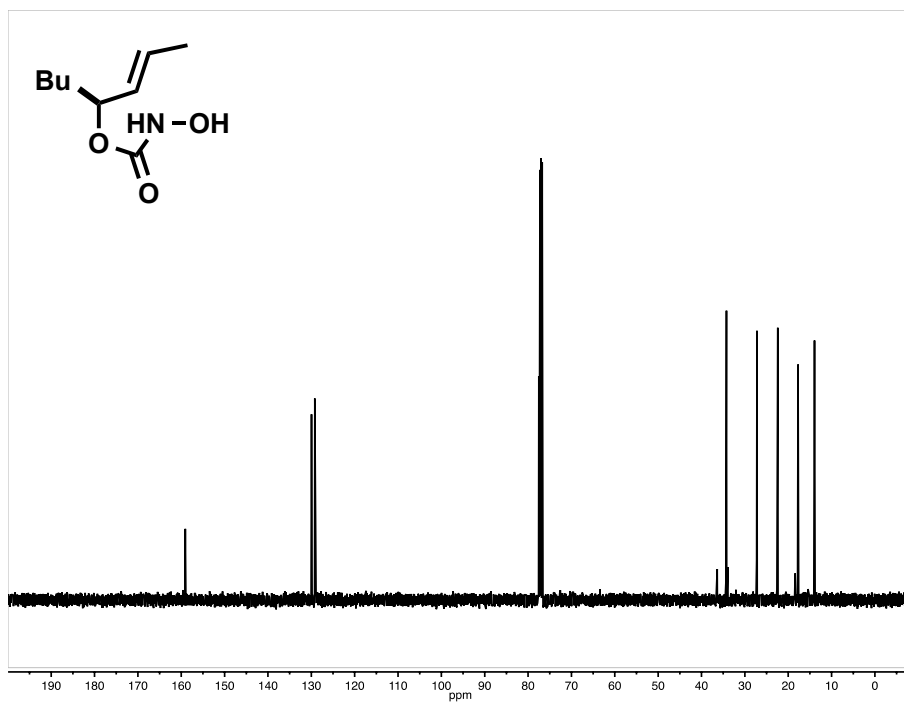
Figure A-43: ^{13}C NMR spectra (100 MHz, CDCl$_3$, 25 °C) of compound **9**.
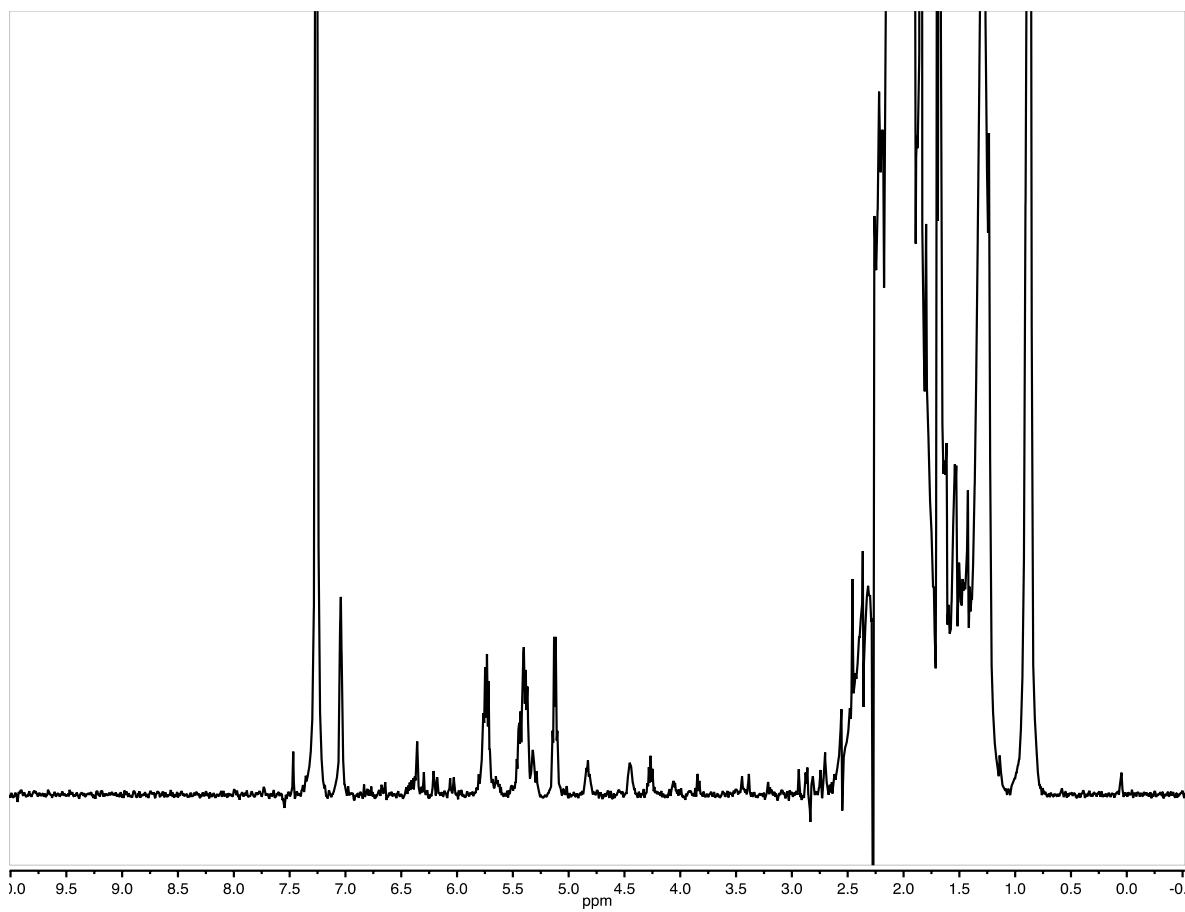
Figure A- 44: ^{1}H NMR spectra (400 MHz, CDCl$_3$, 25 ℃) of compound **10a** and **10b**.

A.6 <u>References</u>

1. Tranchemontagne, D. J.; Hunt, J. R.; Yaghi, O. M., Room temperature synthesis of metal-organic frameworks: MOF-5, MOF-74, MOF-177, MOF-199, and IRMOF-0. *Tetrahedron* **2008,** *64* (36), 8553-8557.

2. Ahnfeldt, T.; Gunzelmann, D.; Loiseau, T.; Hirsemann, D.; Senker, J.; Férey, G.; Stock, N., Synthesis and Modification of a Functionalized 3D Open-Framework Structure with MIL-53 Topology. *Inorganic Chemistry* **2009,** *48* (7), 3057-3064.

3. Gascon, J.; Hernández-Alonso, M. D.; Almeida, A. R.; van Klink, G. P.; Kapteijn, F.; Mul, G., Isoreticular MOFs as efficient photocatalysts with tunable band gap: an operando FTIR study of the photoinduced oxidation of propylene. *ChemSusChem* **2008,** *1* (12), 981-983.

4. Katz, M. J.; Brown, Z. J.; Colon, Y. J.; Siu, P. W.; Scheidt, K. A.; Snurr, R. Q.; Hupp, J. T.; Farha, O. K., A facile synthesis of UiO-66, UiO-67 and their derivatives. *Chemical Communications* **2013,** *49* (82), 9449-9451.

5. McNamara, N. D.; Neumann, G. T.; Masko, E. T.; Urban, J. A.; Hicks, J. C., Catalytic performance and stability of (V) MIL-47 and (Ti) MIL-125 in the oxidative desulfurization of heterocyclic aromatic sulfur compounds. *Journal of Catalysis* **2013,** *305*, 217-226.

APPENDIX B: **SUPPLEMENTARY MATERIAL FOR CHAPTER 3**

B.1 <u>Synthesis.</u>
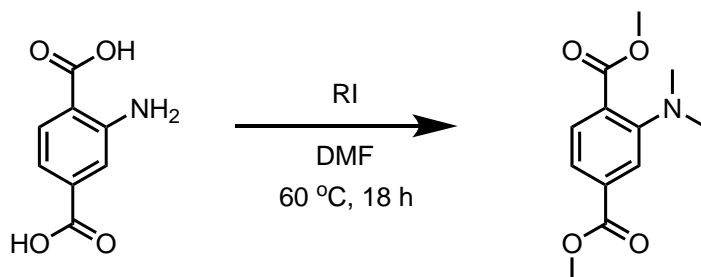
Figure B-1: Synthesis of *N,N*-2-dimethyl amino-terepthlate dimethyl ester

N,N-2-dimethyl amino- terephthalic acid (2.00 g, 9.56 mmol) was suspended in anhydrous DMF (20 mL) and stirred until fully dissolved. K_2CO_3 (5.30 g, 38.2 mmol) was added, followed by dropwise addition of methyl iodide (7.66 g, 54.0 mmol), and the mixture was stirred for 18 h at 60 ºC. The reaction mixture was then cooled to room temperature and quenched with 2 M HCl (*aq*) to a pH = 3. The mixture was extracted with EtOAc (3 × 50 mL), the combined organic extracts were washed with brine (3 × 50 mL), dried over anhydrous $MgSO_4$, filtered through celite and the solvent was removed using a rotary evaporator. The obtained crude was purified using flash chromatography (SiO_2, 15% *v/v* EtOAc:hexanes, dry loading).
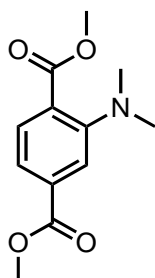
Compound S1: Yellow solid, yield 0.69 g (31%). ^{1}H NMR (400 MHz, CDCl$_3$) δ = 7.65(d, J = 5.9

Hz, 1H), 7.60 (s, 1H), 7.45 (d, J = 7.5 Hz, 1H), 3.91 (d, J = 3.8 Hz, 6H), 2.89 (d, J = 3.1 Hz, 6H).

^{13}C NMR (100 MHz, CDCl$_3$) δ = 168.69, 166.90, 151.95, 133.26, 131.59, 124.43, 119.19, 117.73,

52.44, 43.57.
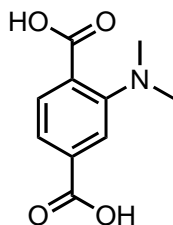
Compound 3: Protocol: The alkylated diester (0.50 g) was dissolved in THF (25 mL), followed by

addition of 1 M NaOH (*aq*, 12.8 mL). The solution was heated to 70 °C and stirred for 8 h. The

mixture was concentrated in a rotary evaporator at 45 °C to remove the excess THF. The mixture

was cooled to room temperature followed by addition of 1 M HCl (*aq*) until a pH = 3. The observed

precipitate was isolated by filtration, rinsed with water, and dried in air at room temperature for 6

h. Yellow solid, yield 0.45 g (90%). ^{1}H NMR (400 MHz, DMSO-d_6) δ = 7.99 (d, J = 1.8 Hz, 1H),

7.95 - 7.89 (m, 1H), 7.76 - 7.71 (m, 1H), 2.86 (s, 6H). ^{13}C NMR (100 MHz, DMSO) δ = 167.11,

166.43, 150.74, 134.69, 130.85, 127.29, 124.41, 120.82, 43.85.

General procedure for solvothermal MOF crystallization in flame-sealed glass tube vessel. A meter-long borosilicate glass tube measuring 10×8 mm (o.d $\times$ i.d), was divided into six equal portions with a marker. Using a glass cutter, the long tube was cut into three shorter tubes by only cutting every other mark. The cut ends of the tube were etched using an oxygen-propane torch. The final glass tubes were made by melting the intermediate glass tubes at the mark with the torch. After the reactants and solvents were loaded into to the glass tubes, a hose adaptor was used to connect the glass tube to a high vacuum (10 mtorr) using a Schlenk line constructed by fitting the open end of the tube inside a short length of standard rubber hose that was further affixed to a ground glass tap which could be closed to insolate this assembly from dynamic vacuum. The mixture was flash frozen at 77 K (liquid N_2), evacuated to an internal pressure of 150 mtorr ($\pm$ 10 mtorr), and sealed under static vacuum. Upon sealing, the length of the tube was reduced to 18-20 cm; the reactant mixture was allowed to thaw and placed in an isothermal oven inside a sand bath. After the reaction was complete, the tube was allowed to cool to room temperature, the tube was opened using a glass cutter, and the solids were isolated by filtration.

B.2 Crystal modeling and Rietveld refinements.
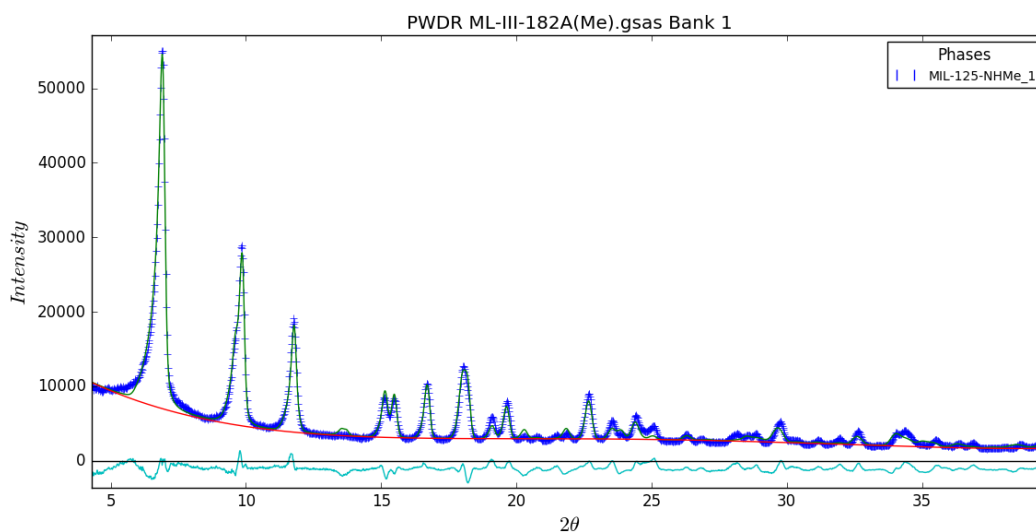
Figure B-2: Rietveld plot of **MIL-125-NHMe**. Blue marks = observed, green trace = refined, teal = difference, red trace = background.
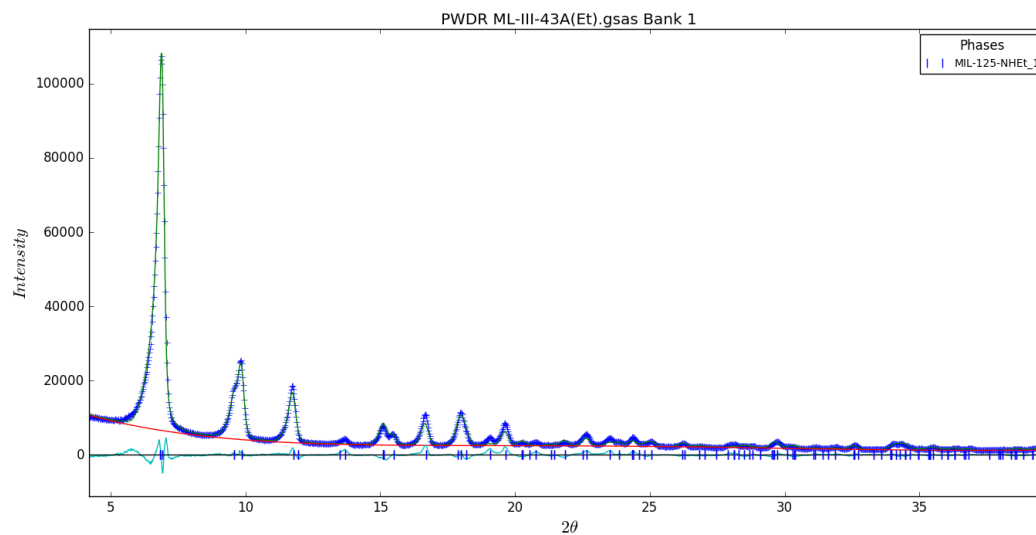
Figure B-3: Rietveld plot of **MIL-125-NHEt**. Blue marks = observed, green trace = refined, teal = difference, red trace = background.
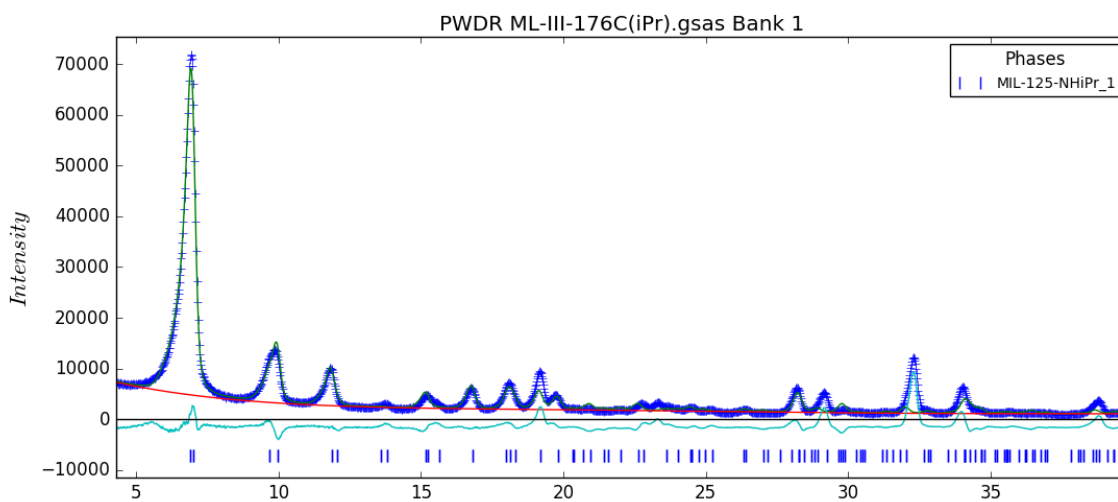
Figure B-4: Rietveld plot of **MIL-125-NHiPr**. Blue marks = observed, green trace = refined, teal = difference, red trace = background.
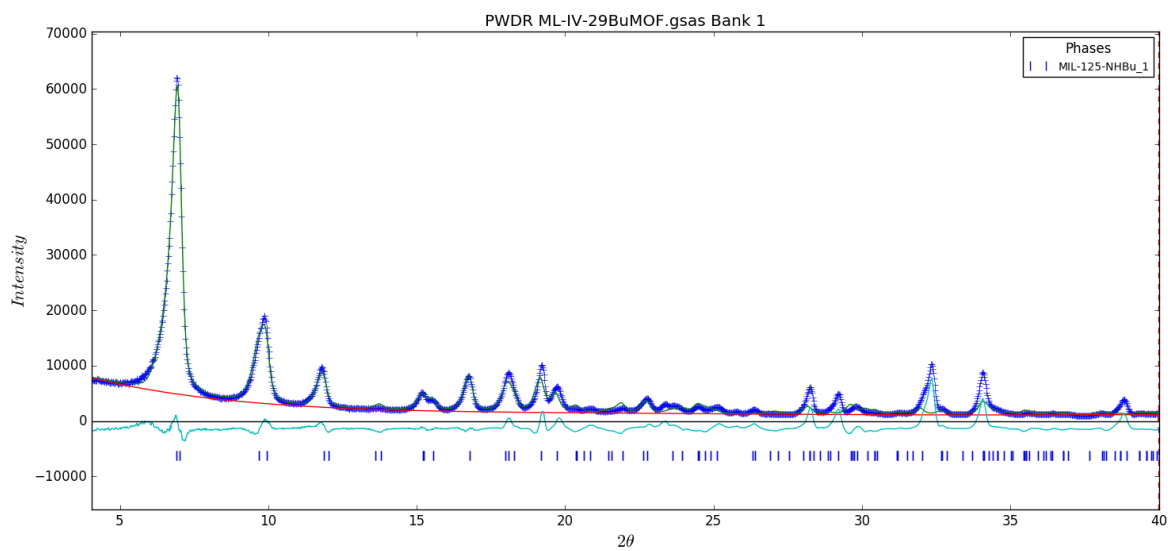
Figure B-5: Rietveld plot of **MIL-125-NHBu**. Blue marks = observed, green trace = refined, teal = difference, red trace = background.
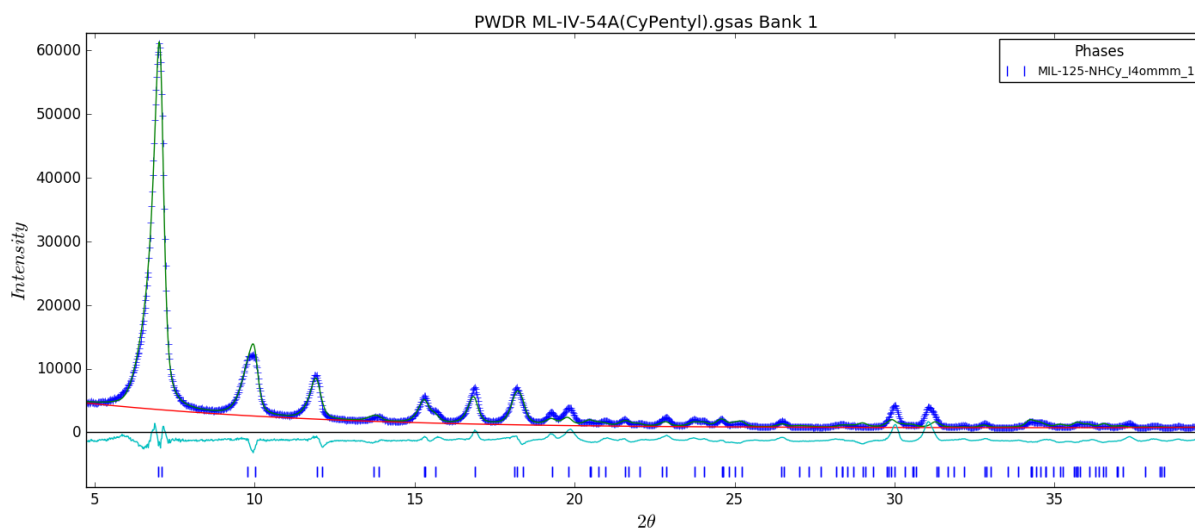
Figure B-6: Rietveld plot of **MIL-125-NHCyp**. Blue marks = observed, green trace = refined, teal = difference, red trace = background.

Figure B-7: Rietveld plot of **MIL-125-NHCy**. Blue marks = observed, green trace = refined, teal = difference, red trace = background.
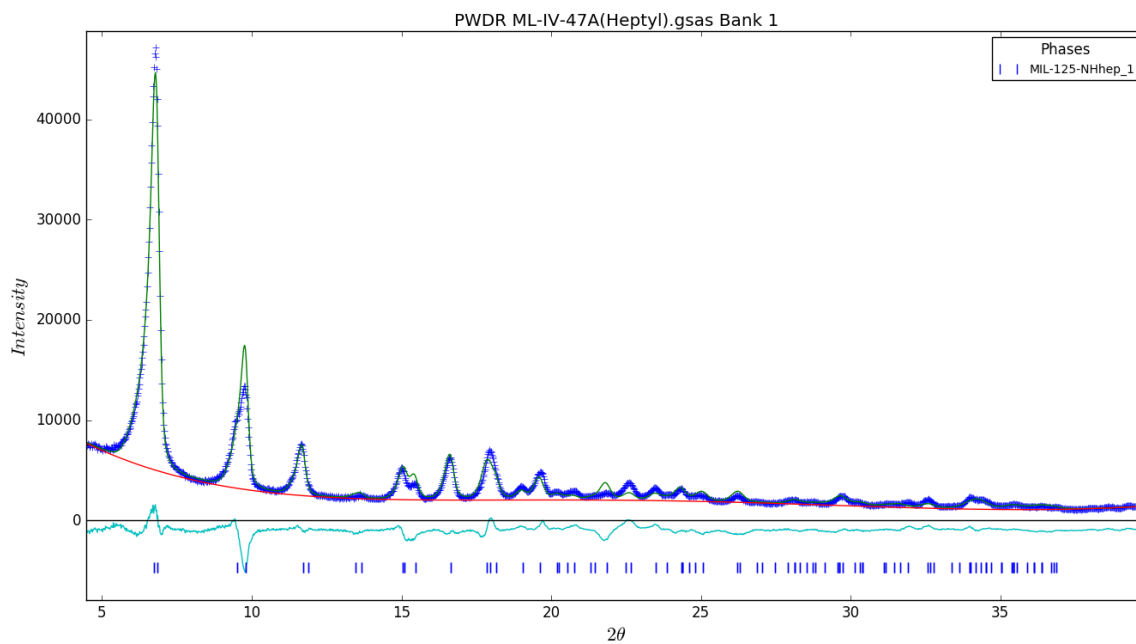
Figure B-8: Rietveld plot of **MIL-125-NHhep**. Blue marks = observed, green trace = refined, teal = difference, red trace = background.

Table B-1: Crystallographic information from Rietveld Refinement.

Name	MIL-125-NHMe	MIL-125-NHMEt	MIL-125-NH^{i}Pr
Assymetric unit composition	$C_{1.395}N_{0.315}O_{2.415}Ti_{0.25}$	$C_{1.785}N_{0.315}O_{2.148}Ti_{0.25}$	$C_{2.175}N_{0.315}O_{3.017}Ti_{0.25}$
Formula weight (g mol^{-1})	71.78	72.19	90.78
Temperature (K)	300	300	300
Z	32	32	32
Crystal system	tetragonal	tetragonal	tetragonal
Space Group	$I4/mmm$ (No. 123)	$I4/mmm$ (No. 123)	$I4/mmm$ (No. 123)
a (Å)	18.635(16)	18.626(20)	18.70(5)
c (Å)	18.131(14)	18.088(18)	18.11(5)
V (Å^3)	6296(15)	6275(20)	6330(50)
Number of independent atoms	23	27	29
Observed reflections	104	103	104
Number of data	1900	1850	1850

points			
Max *d*-spacing resolution (Å)	13.177	13.171	13.226
Min *d*-spacing resolution (Å)	2.256	2.259	2.263
Refined parameters (total)	53	66	97
R_p (%)	6.478	6.175	12.331
wR_p (%)	8.686	8.551	21.211
R_B (%)	5.966	5.884	13.300
GOF (χ^2)	6.26	6.35	14.27

Table B-2: Crystallographic information from Rietveld Refinement.

Name	MIL-125-NHBu	MIL-125-NHCyp	MIL-125-NHCy
Assymetric unit composition	$C_{2.995}N_{0.315}O_{2.833}Ti_{0.25}$	$C_{2.955}N_{0.315}O_{2.149}Ti_{0.25}$	$C_{3.345}N_{0.315}O_{2.019}Ti_{0.25}$
Formula weight (g mol^{-1})	97.68	86.26	88.86
Temperature (K)	300	300	300
Z	32	32	32
Crystal system	tetragonal	tetragonal	tetragonal
Space Group	$I4/mmm$ (No. 123)	$I4/mmm$ (No. 123)	$I4/mmm$ (No. 123)
a (Å)	18.70(4)	18.682(29)	18.675(23)
c (Å)	18.21(4)	18.204(28)	18.147(22)
V (Å^3)	6370(40)	6354(29)	6329(23)
Number of independent atoms	27	34	35
Observed reflections	104	92	100
Number of data	1850	1850	1850

points			
Max d-spacing resolution (Å)	13.225	13.210	13.205
Min d-spacing resolution (Å)	2.264	2.364	2.282
Refined parameters (total)	69	61	70
R_p (%)	12.135	7.869	3.969
wR_p (%)	20.323	13306	5.597
R_B (%)	13.303	7.777	3.445
GOF (χ^2)	13.18	7.60	3.502

Table B-3: Crystallographic information from Rietveld Refinement.

Name	**MIL-125-NHhep**
Assymetric unit composition	$C_{3.735}N_{0.315}O_{2.361}Ti_{0.25}$
Formula weight (g mol^{-1})	99.02
Temperature (K)	300
Z	32
Crystal system	tetragonal
Space Group	$I4/mmm$ (No. 123)
a (Å)	18.854(27)
c (Å)	18.292(23)
V (Å^3)	6502(27)
Number of independent atoms	36
Observed reflections	88
Number of data points	1850

Max d-spacing resolution (Å)	13.332
Min d-spacing resolution (Å)	2.464
Refined parameters (total)	63
R_p (%)	6.291
wR_p (%)	9.196
R_B (%)	7.049
GOF (χ^2)	5.62

B.3 Scanning Electron Microscopy
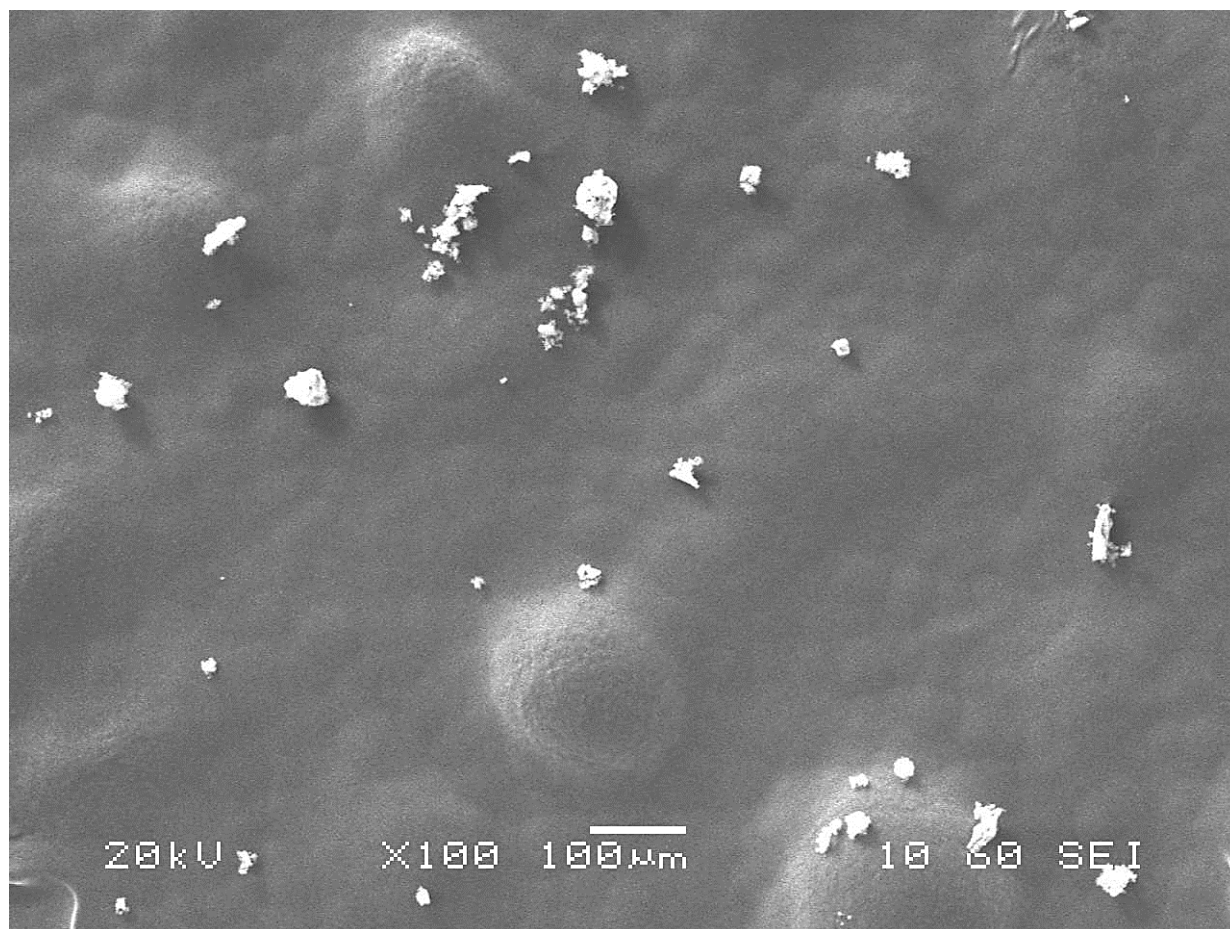
Figure B-9: Scanning electron micrograph images of **MIL-125-NHMe** prepared in glass vessel. Scale is indicated.
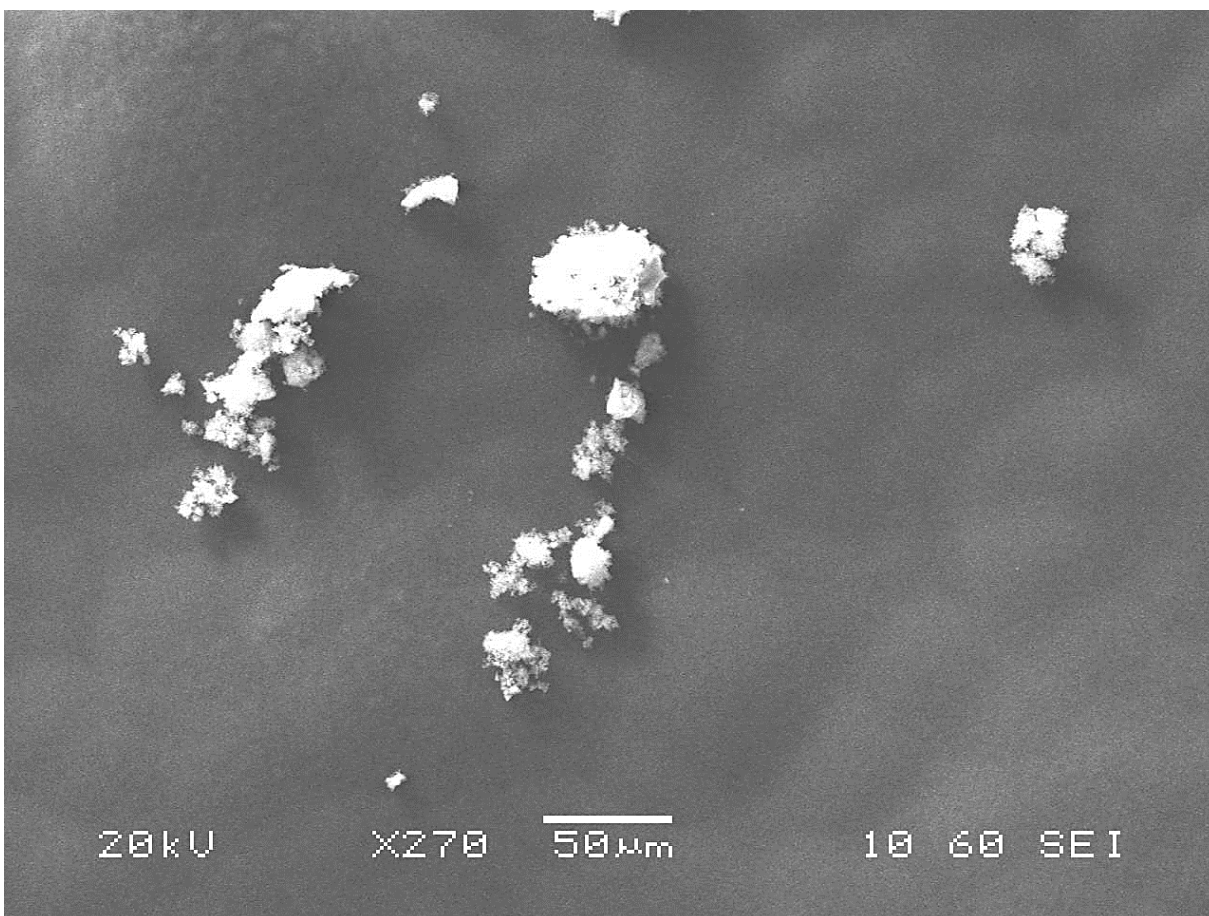
Figure B-10: Scanning electron micrograph images of **MIL-125-NHMe** prepared in glass vessel. Scale is indicated.
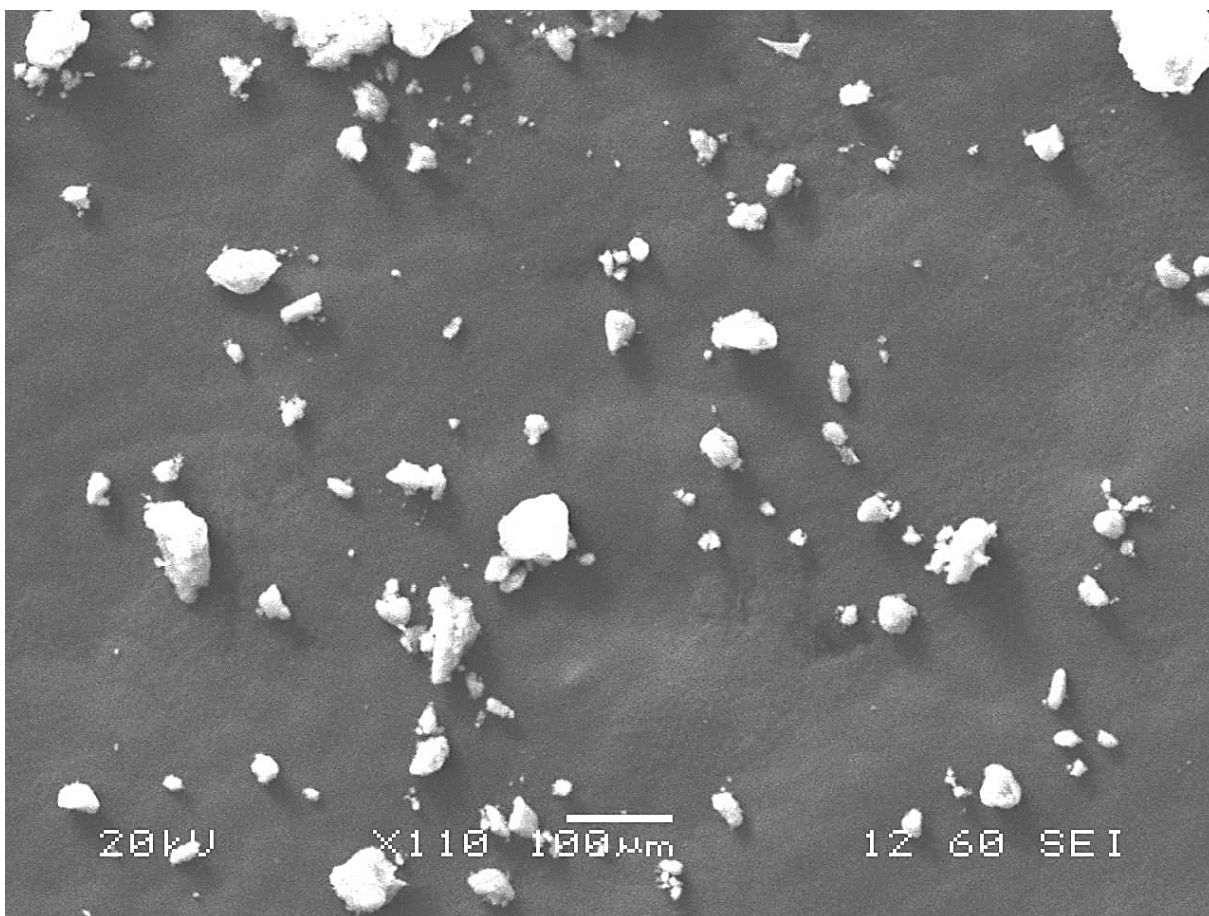
Figure B-11: Scanning electron micrograph images of **MIL-125-NHEt** prepared in glass vessel. Scale is indicated.
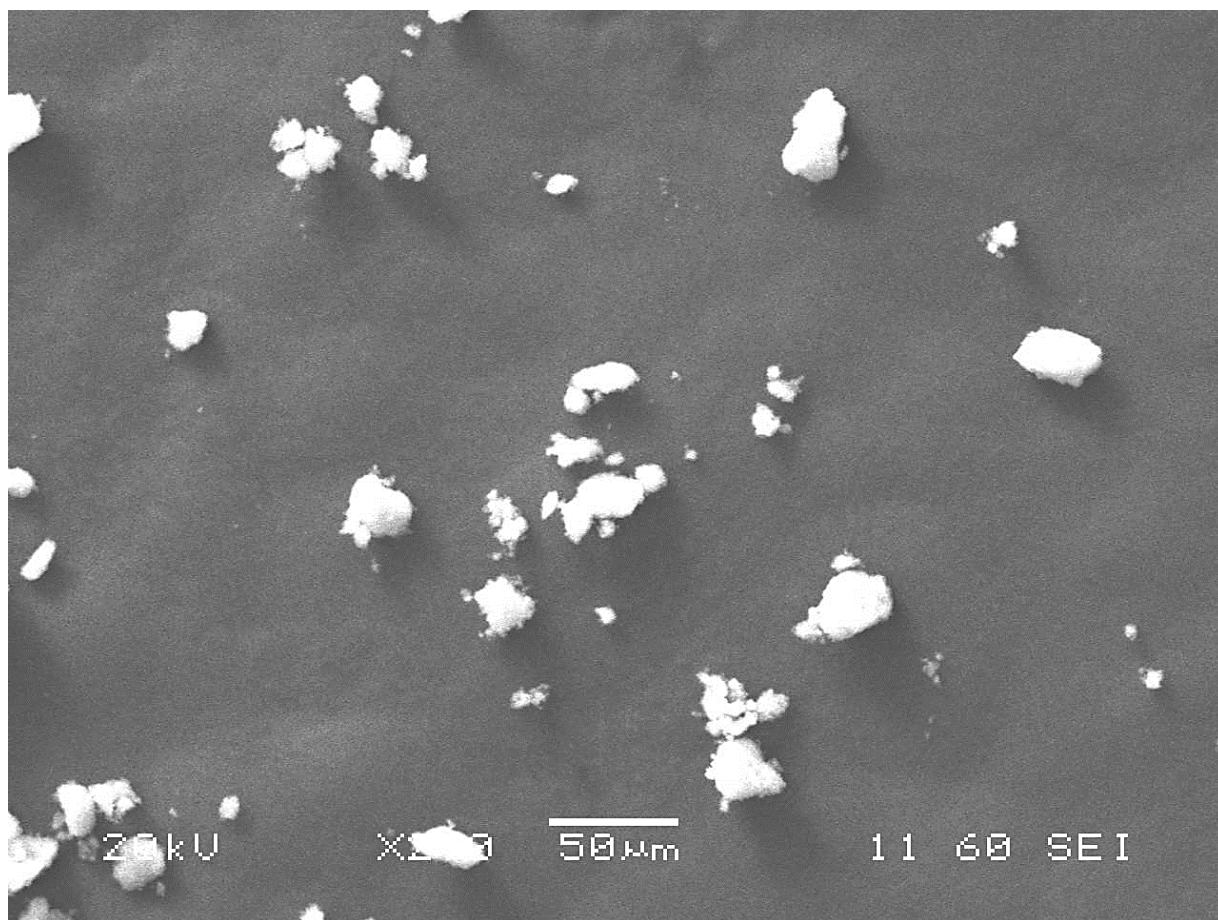
Figure B-12: Scanning electron micrograph images of **MIL-125-NHEt** prepared in glass vessel. Scale is indicated.
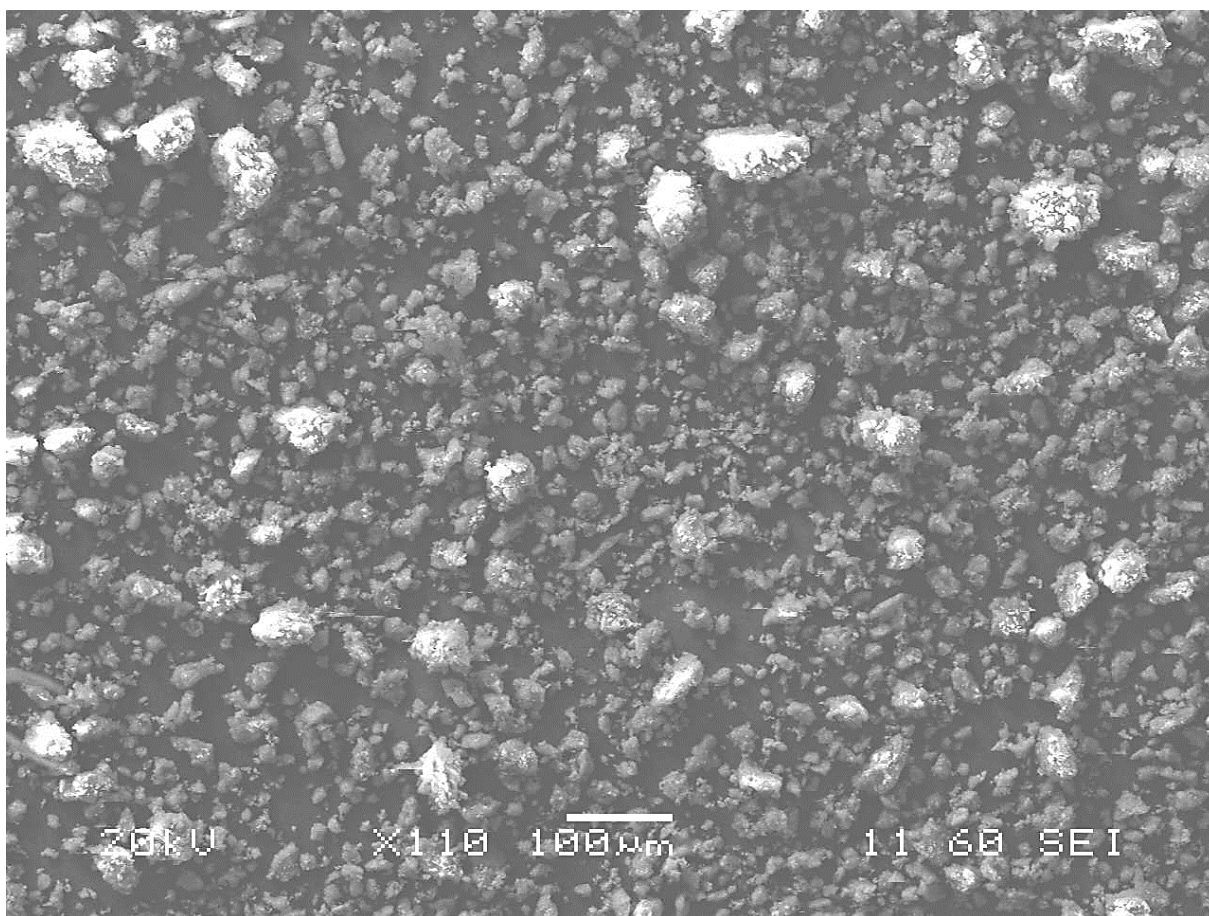
Figure B-13: Scanning electron micrograph images of **MIL-125-NHiPr** prepared in glass vessel. Scale is indicated.

Figure B-14: Scanning electron micrograph images of **MIL-125-NHiPr** prepared in glass vessel. Scale is indicated.

Figure B-15: Scanning electron micrograph images of **MIL-125-NHBu** prepared in glass vessel. Scale is indicated.

Figure B- 16: Scanning electron micrograph images of **MIL-125-NHBu** prepared in glass vessel. Scale is indicated.

B.4 Gas Adsorption
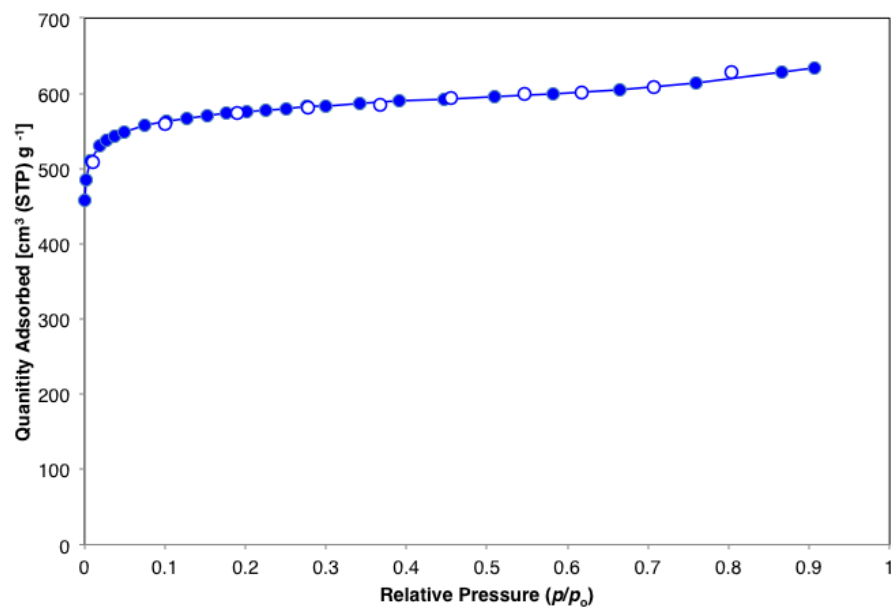
Figure B-17: Nitrogen Gas adsorption isotherm (77 K) of **MIL-125-NH₂**.
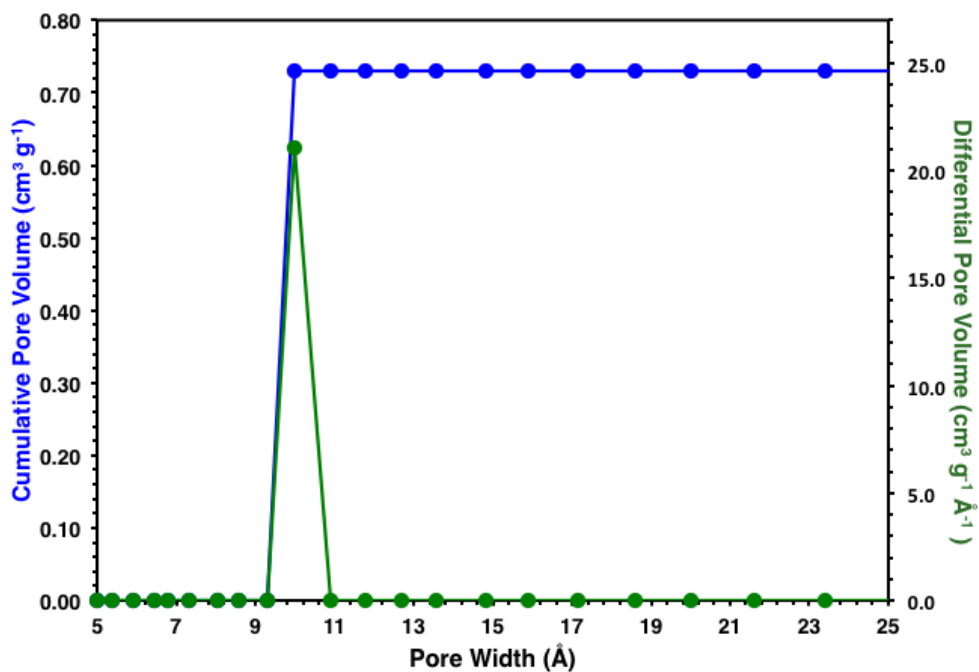
Figure B-18: NLDFT pore size distribution of **MIL-125-NH₂** using data measured from N_2 gas isotherm at 77 K.
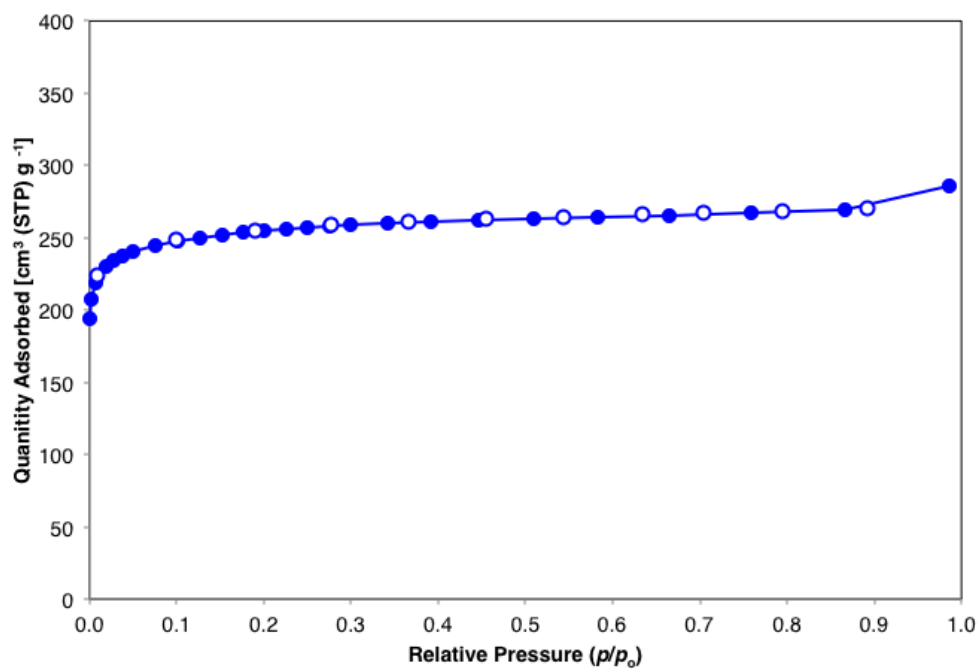
Figure B-19: Nitrogen Gas adsorption isotherm (77 K) of **MIL-125-NHMe**.
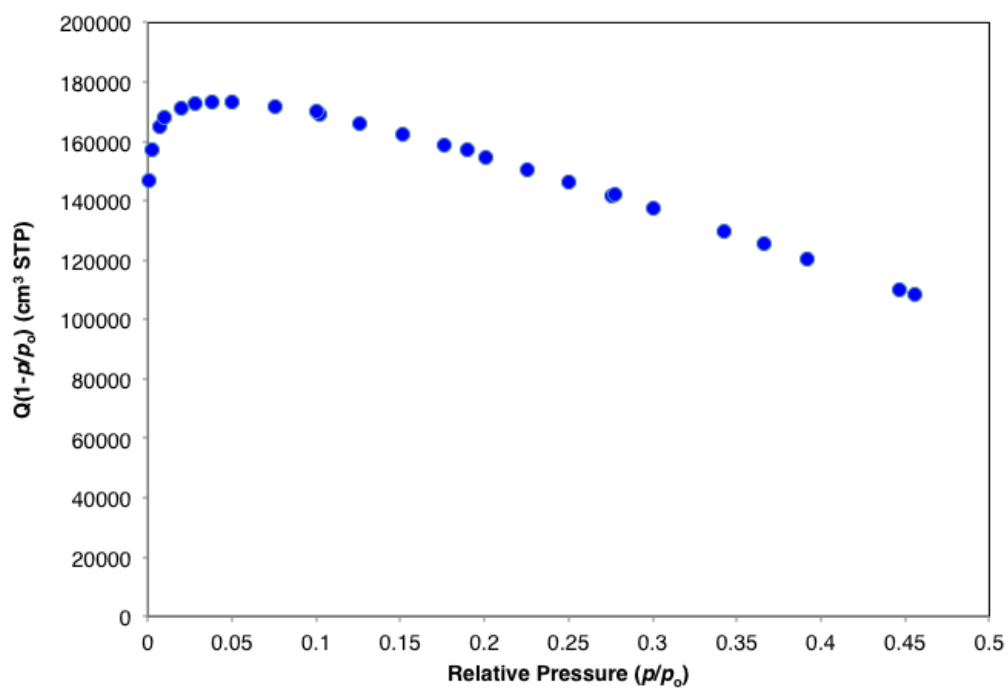
Figure B-20: Rouquerol plot **MIL-125-NHMe**.
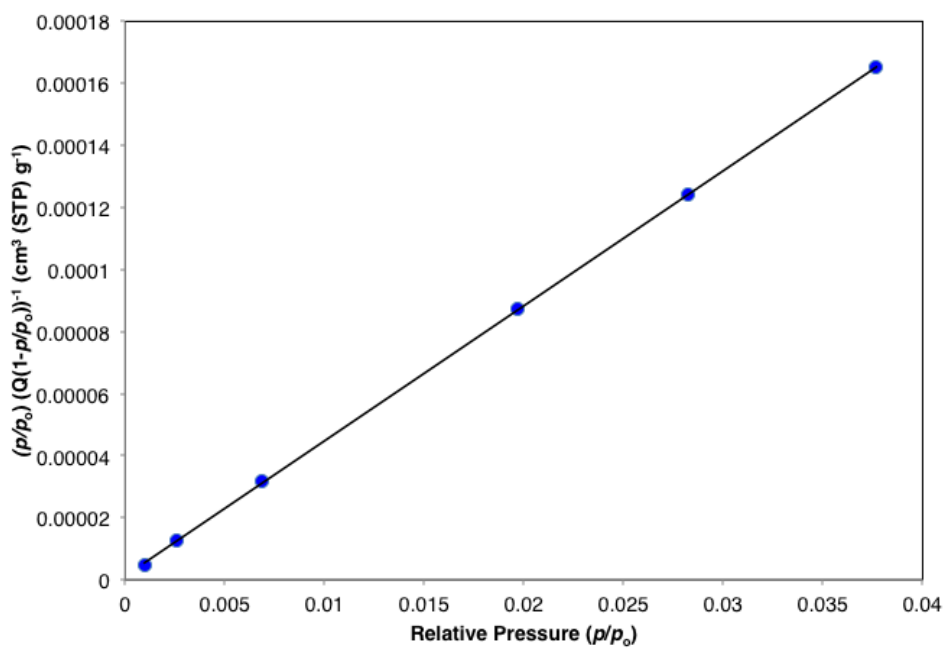
Figure B-21: Linear BET plot **MIL-125-NHMe**.
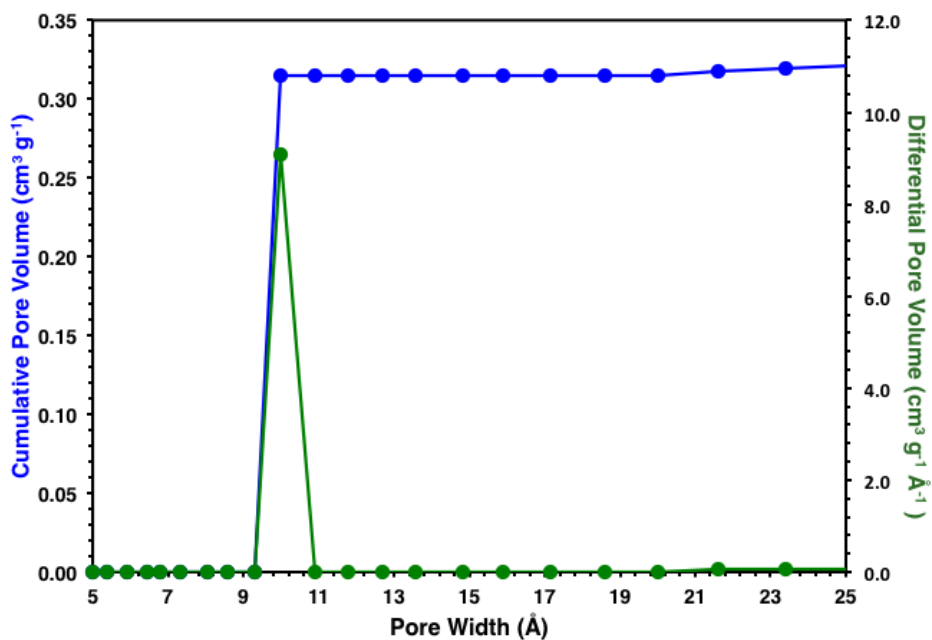
Figure B-22: NLDFT pore size distribution of **MIL-125-NHMe** using data measured from N_2 gas isotherm at 77 K.
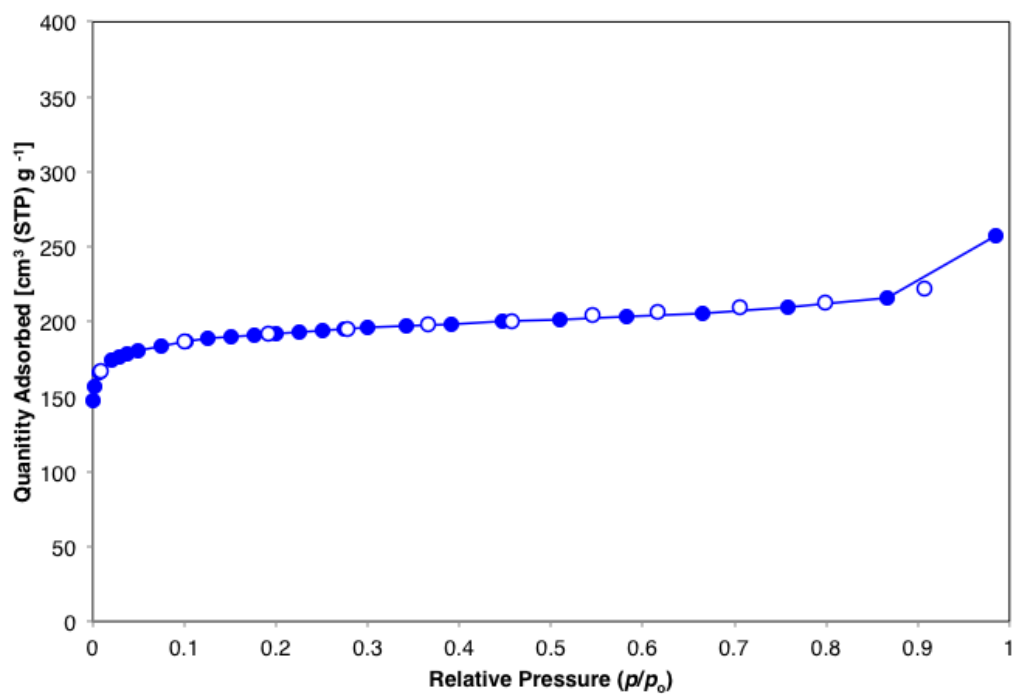
Figure B-23: Gas adsorption isotherm (77 K) of **MIL-125-NHEt**.
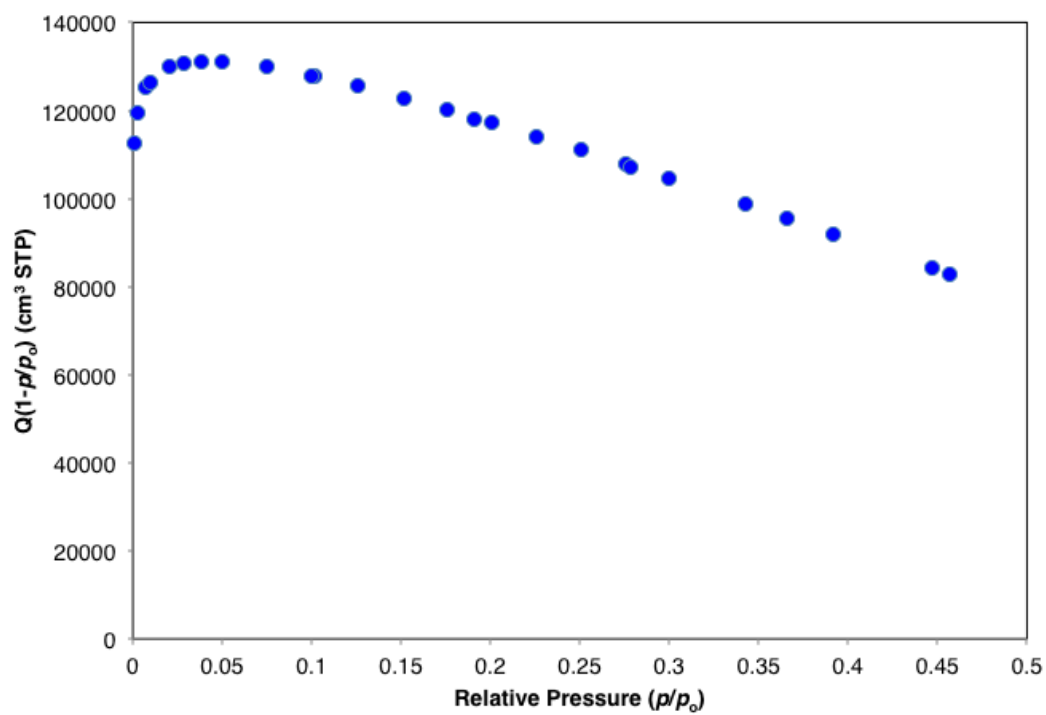
Figure B-24: Rouquerol plot **MIL-125-NHEt**.
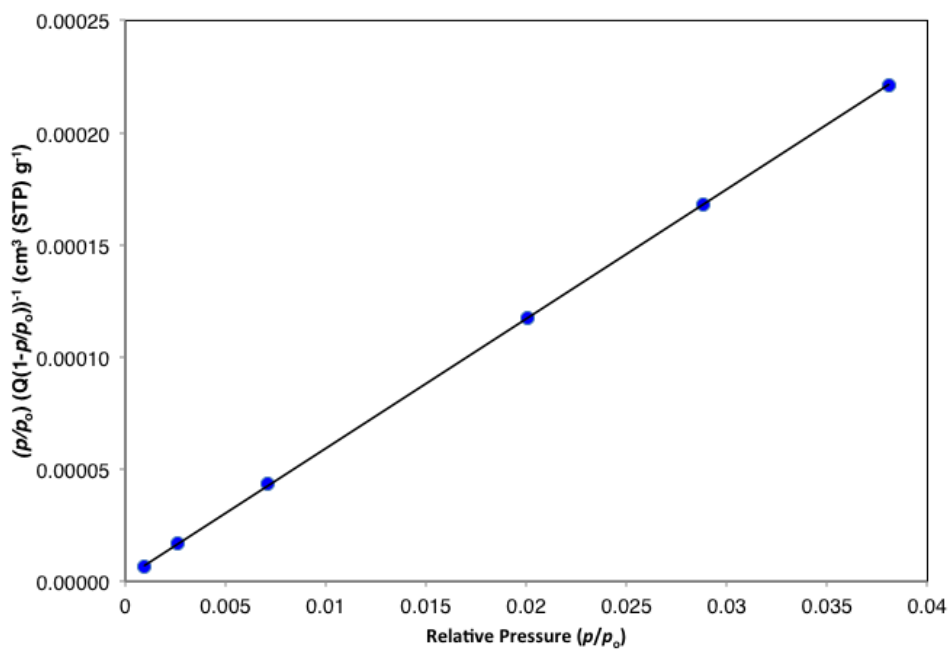
Figure B-25: Linear BET plot **MIL-125-NHEt**.
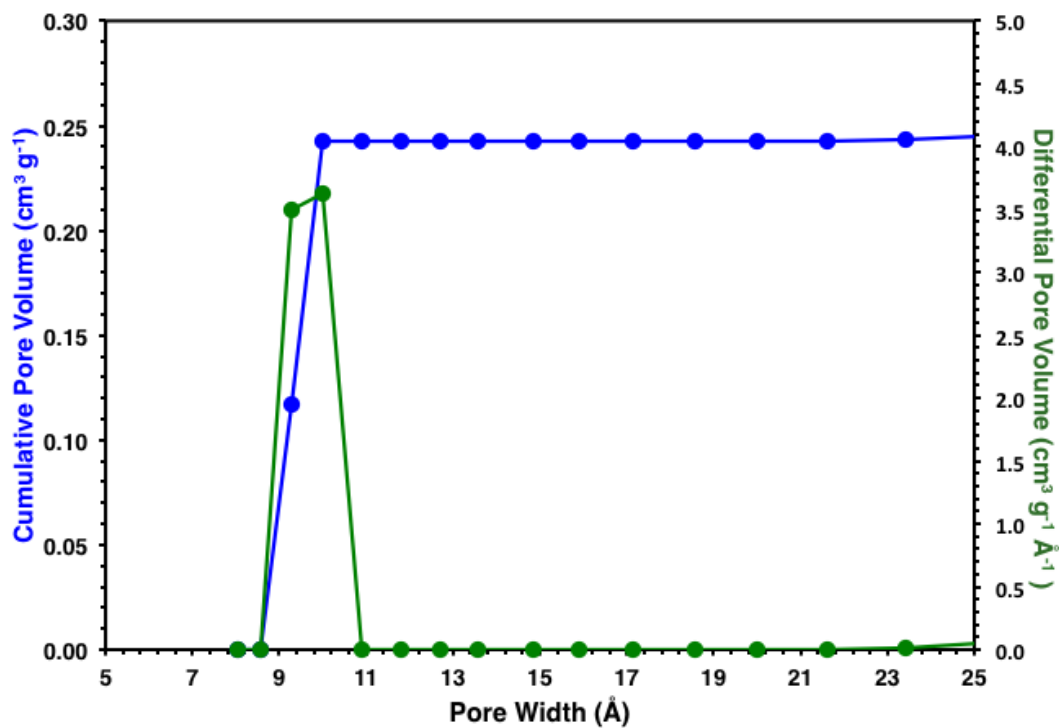
Figure B-26: NLDFT pore size distribution of **MIL-125-NHEt** using data measured from N2 gas isotherm at 77 K.

Figure B-27: Gas adsorption isotherm (77 K) of **MIL-125-NHiPr**.
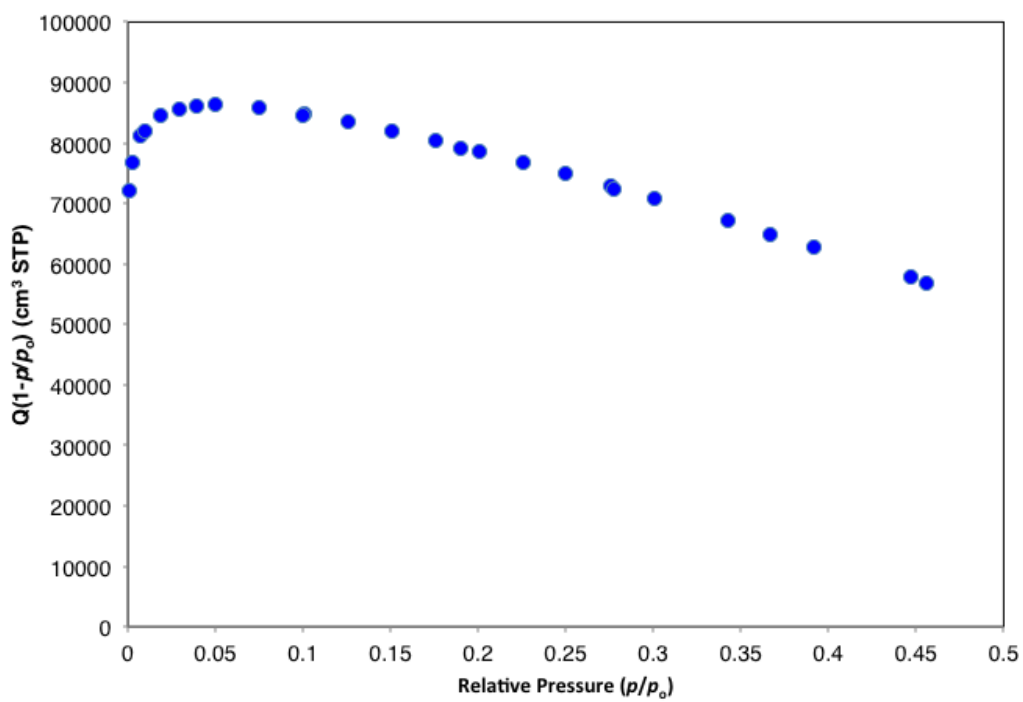
Figure B-28: Rouquerol plot **MIL-125-NHiPr**
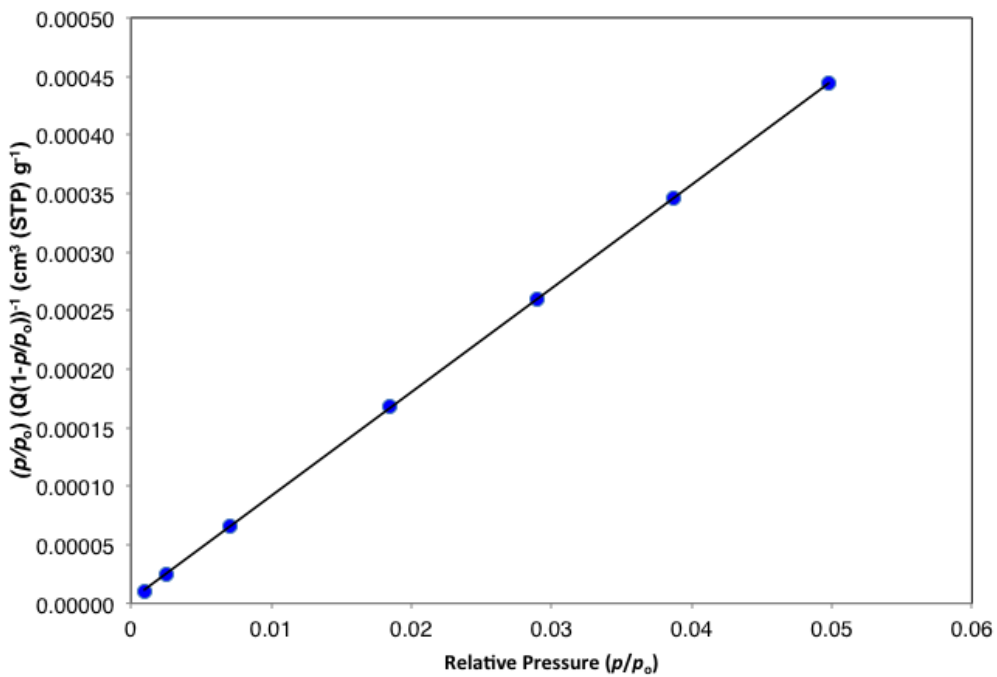
Figure B-29: Linear BET plot **MIL-125-NHiPr**.
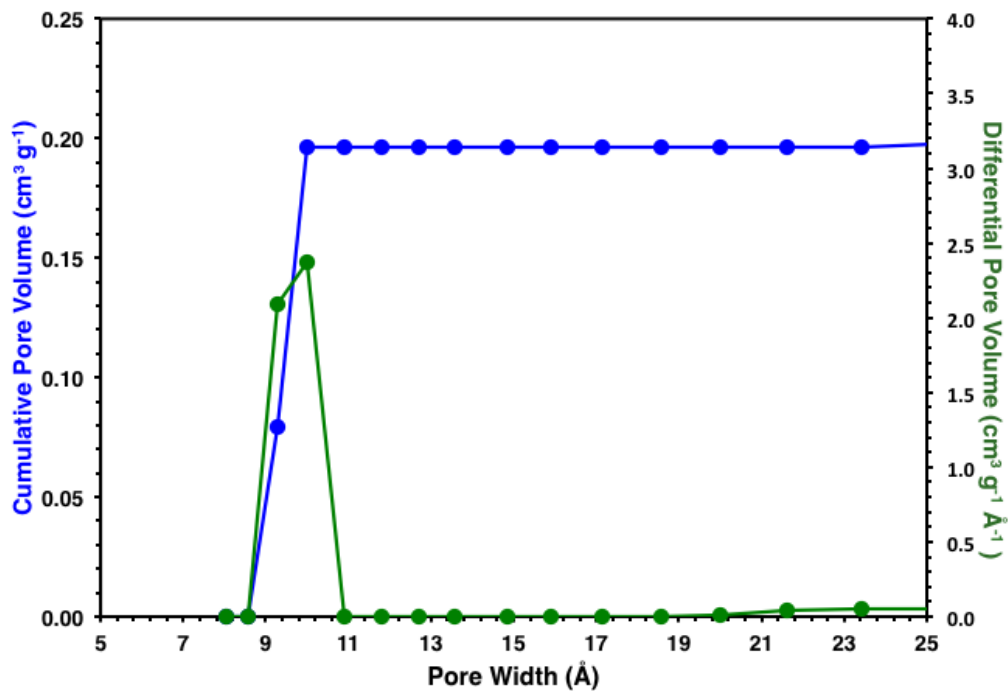
Figure B-30: DFT pore size distribution of **MIL-125-NHiPr** using data measured from N_2 gas isotherm at 77 K.
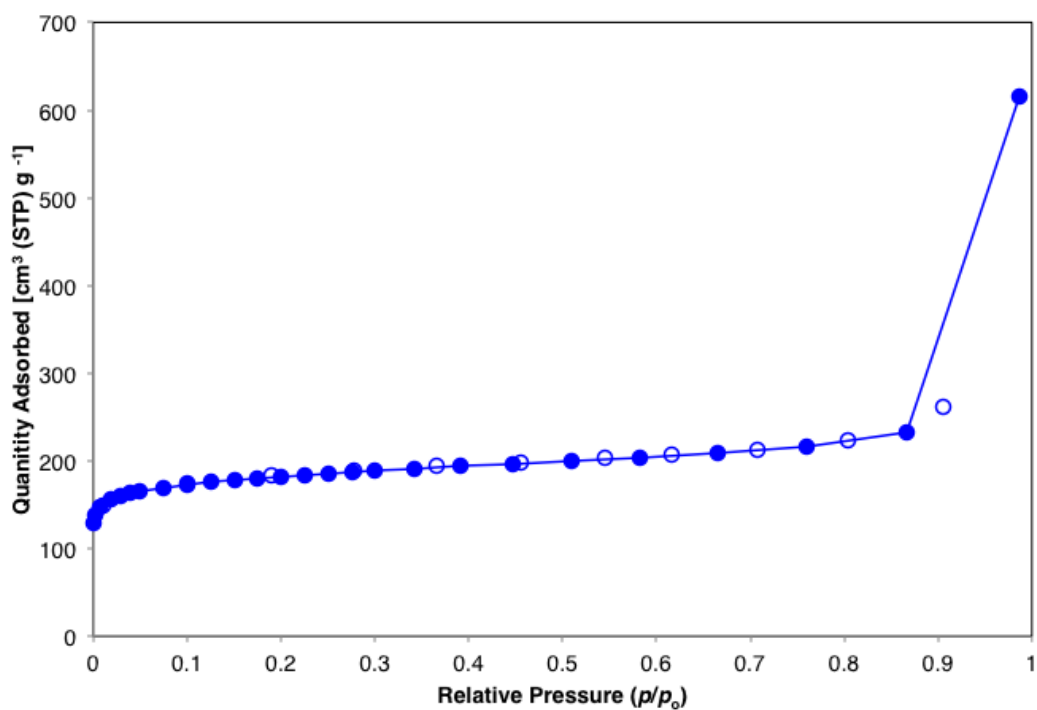
Figure B-31: Gas adsorption isotherm (77 K) of **MIL-125-NHBu**.
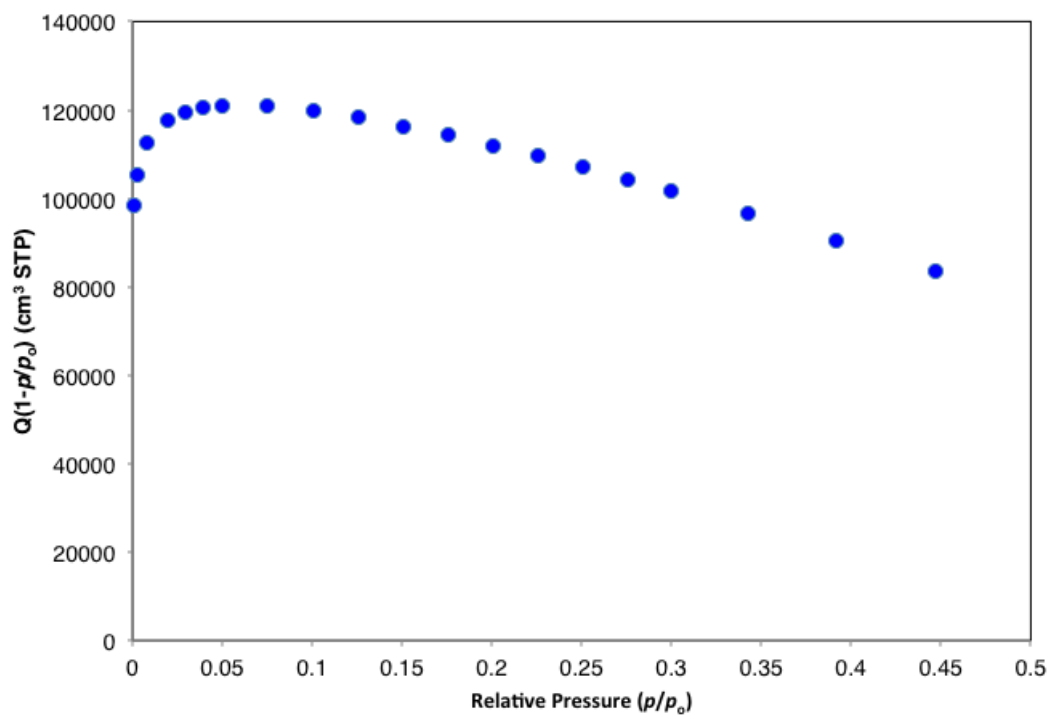
Figure B-32: Rouquerol plot **MIL-125-NHBu**.
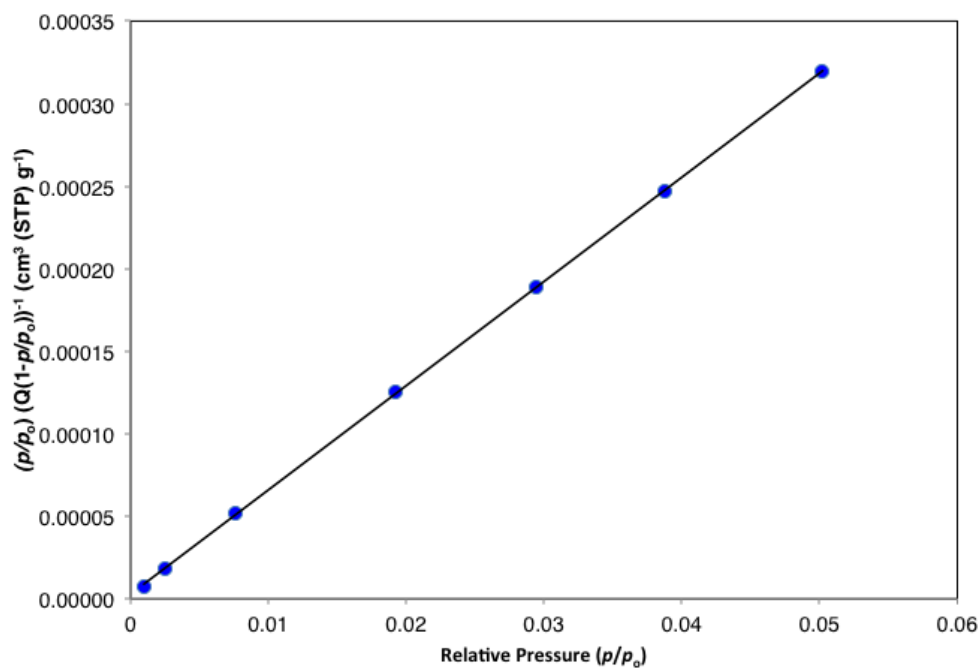
Figure B-33: Linear BET plot **MIL-125-NHBu**.
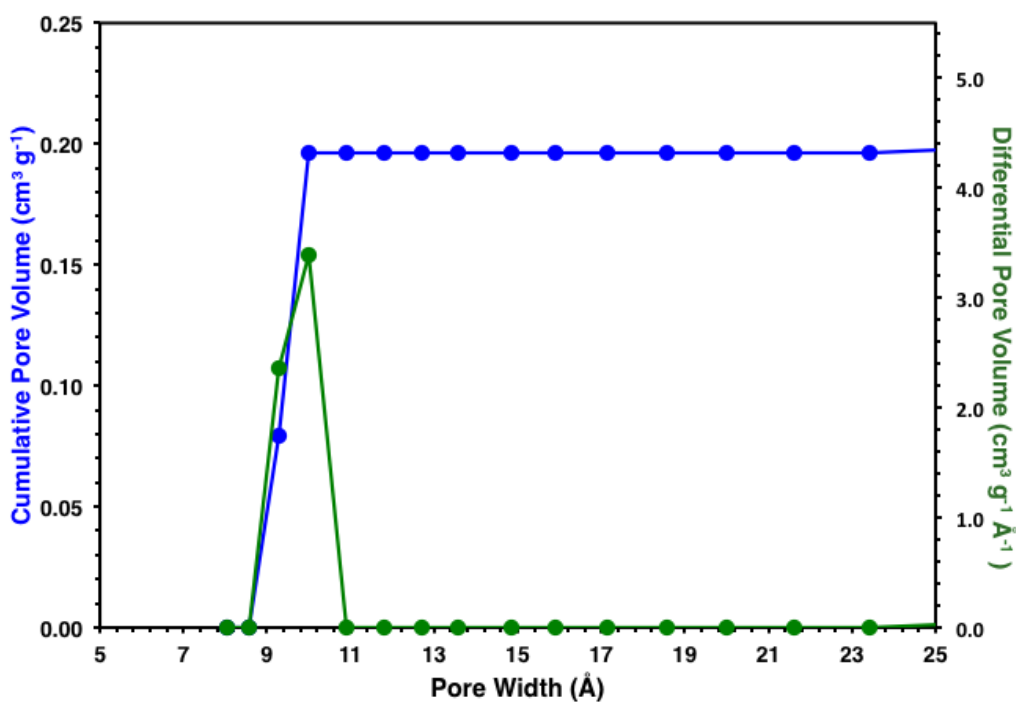
Figure B-34: DFT pore size distribution of **MIL-125-NHBu** using data measured from N_2 gas isotherm at 77 K.
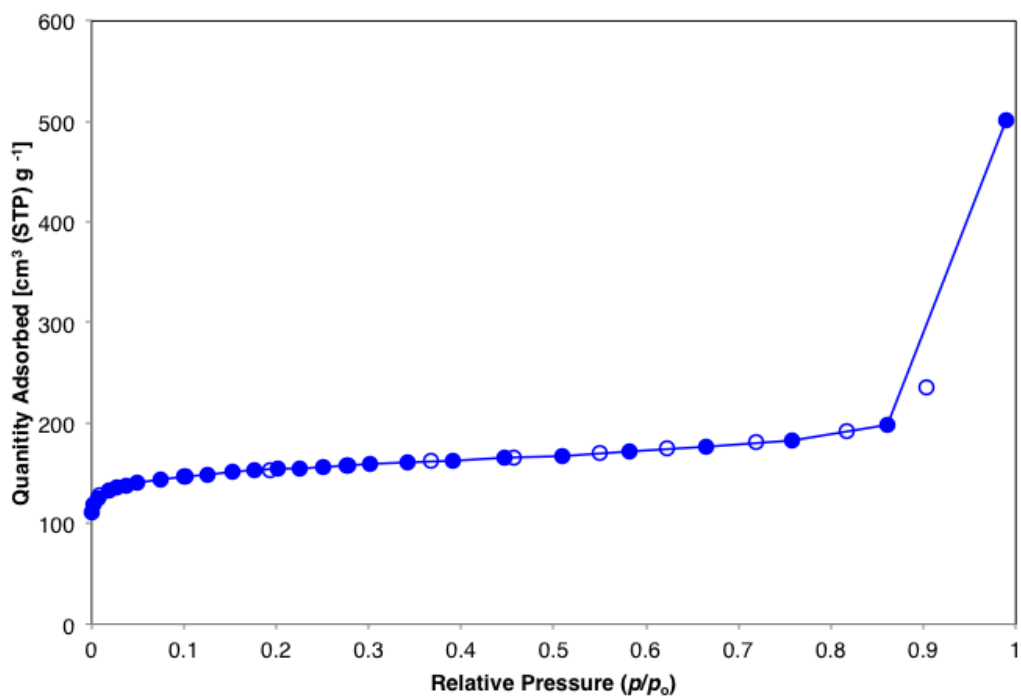
Figure B-35: Gas adsorption isotherm (77 K) of **MIL-125-NHCyp**.
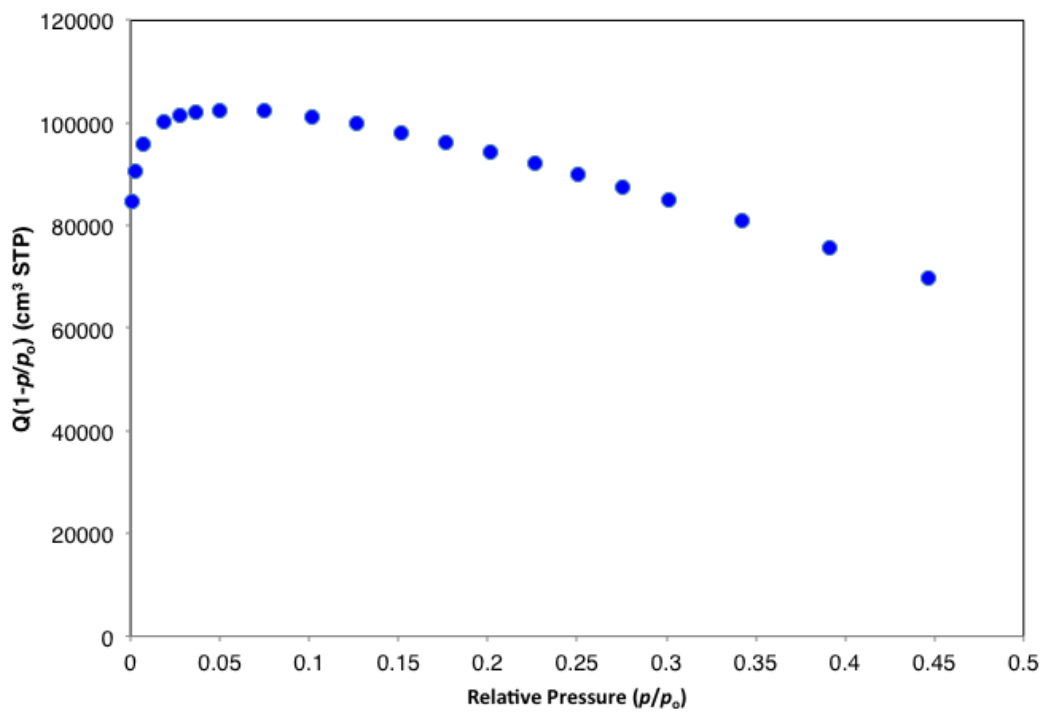
Figure B-36: Rouquerol plot **MIL-125-NHCyp**.
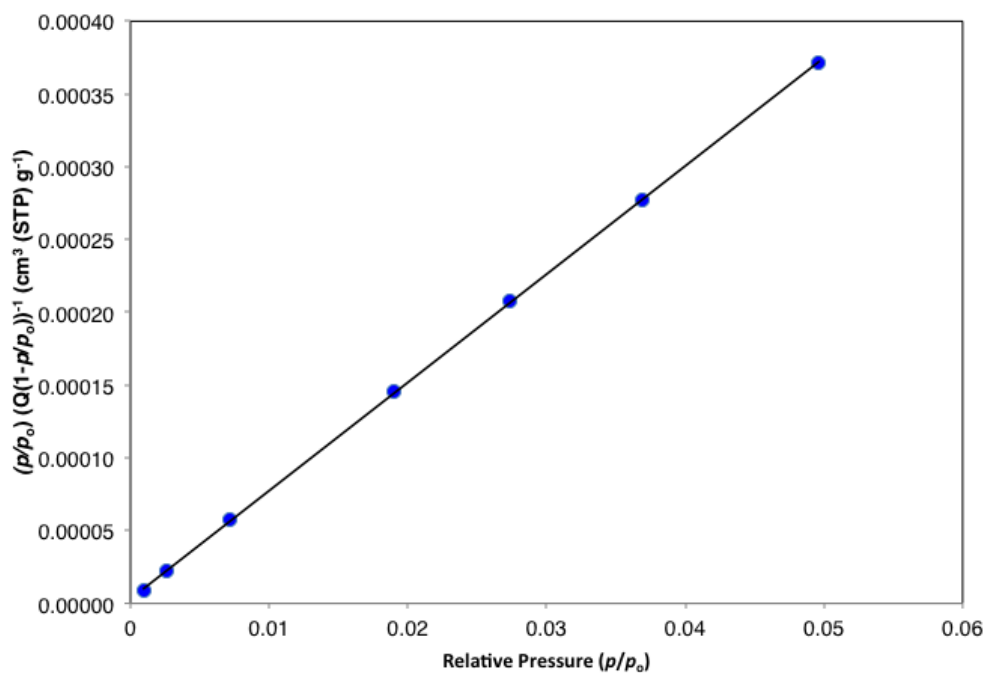
Figure B-37: Linear BET plot **MIL-125-Cyp**.
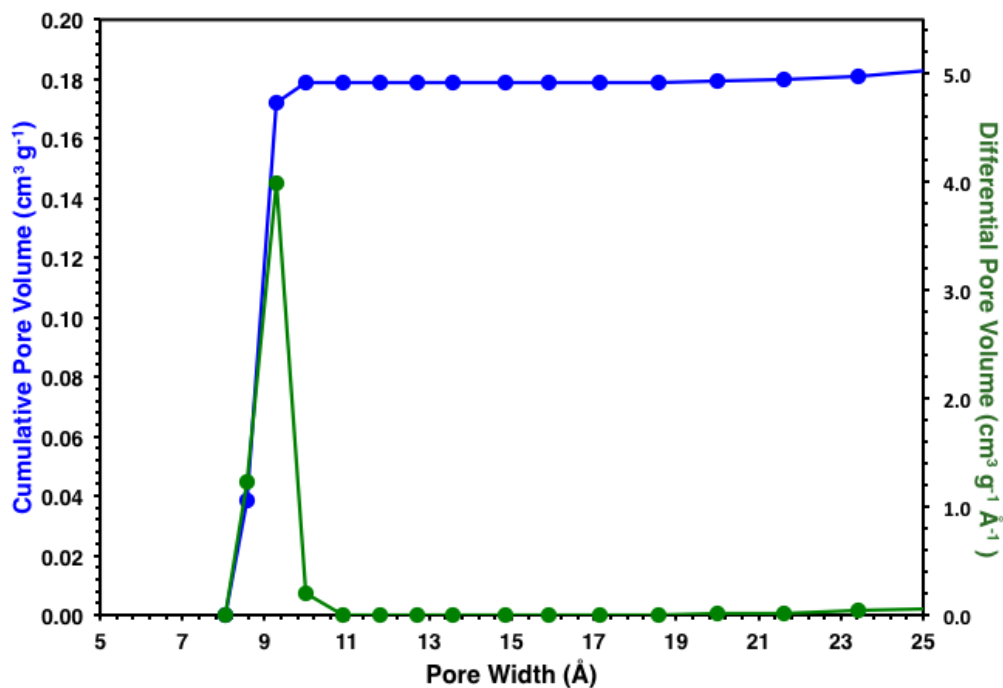
Figure B-38: DFT pore size distribution of **MIL-125-NHCyp** using data measured from N_2 gas isotherm at 77 K.
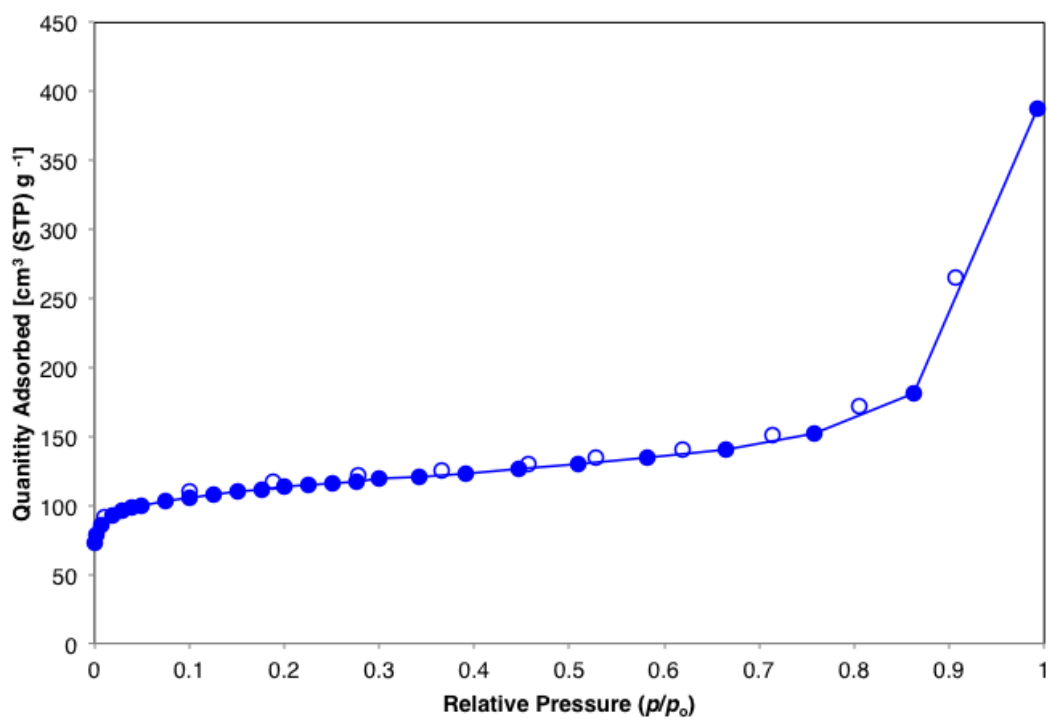
Figure B-39: Gas adsorption isotherm (77 K) of **MIL-125-NHCy**.
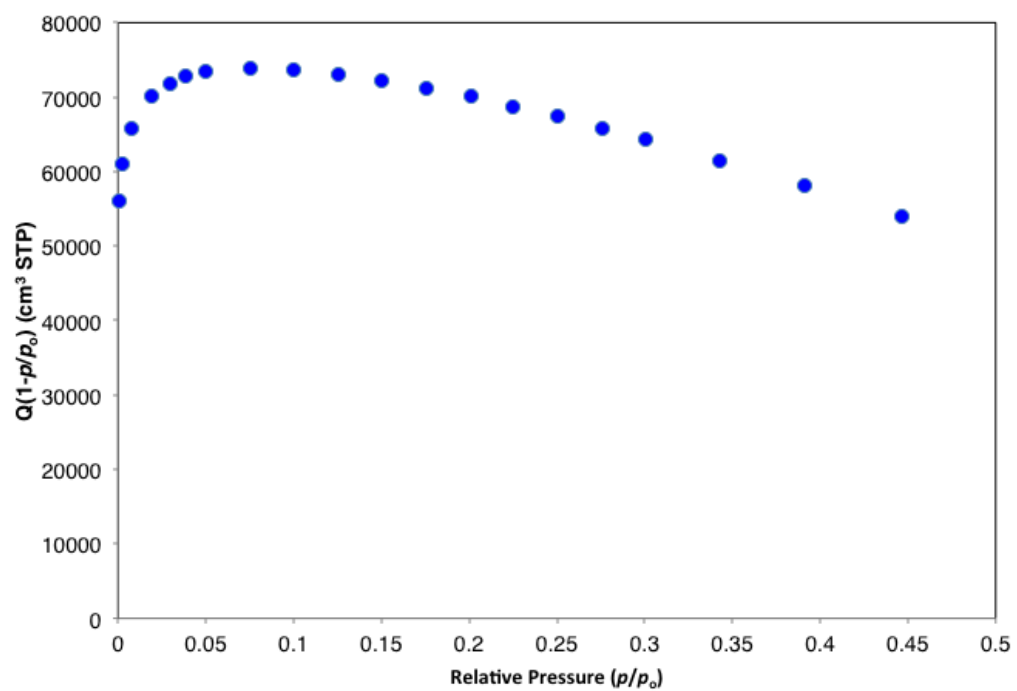
Figure B-40: Rouquerol plot **MIL-125-NHCy.**
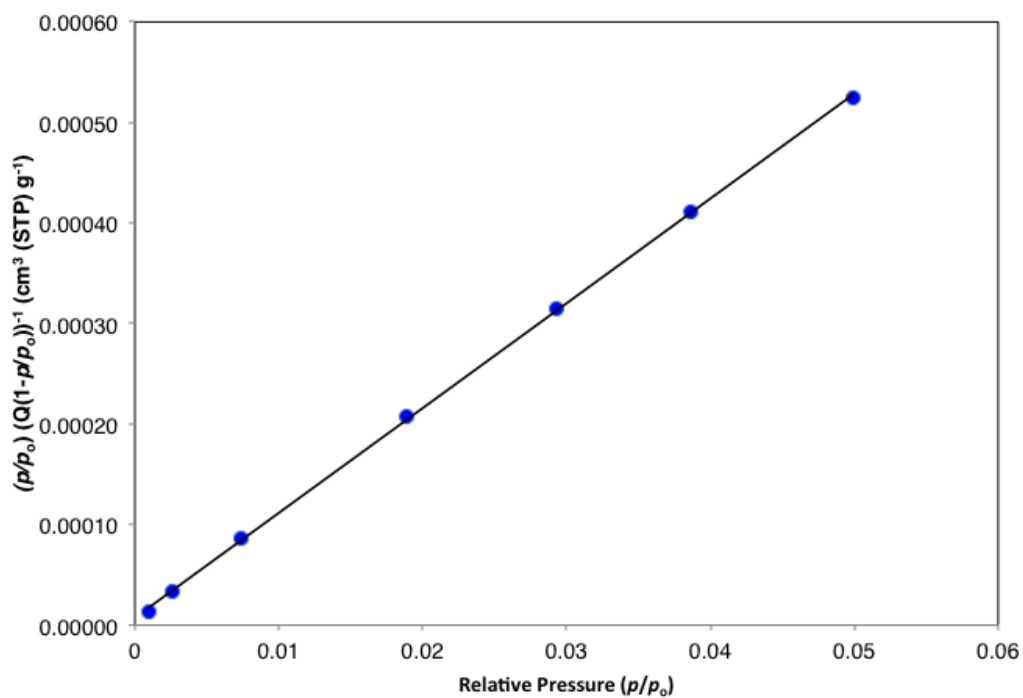
Figure B-41: Linear BET plot **MIL-125-NHCy**.
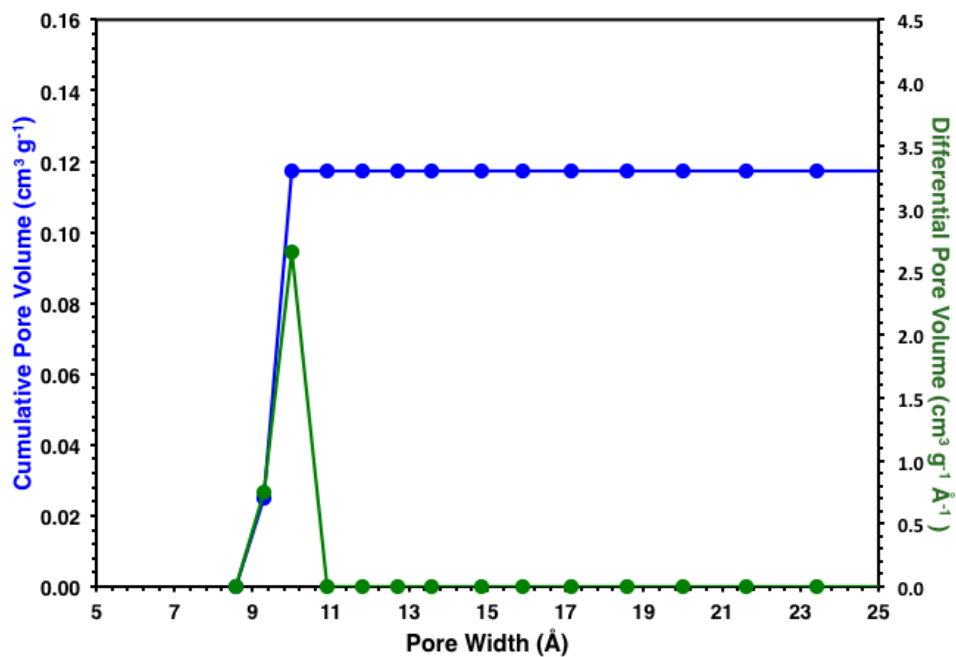
Figure B-42: DFT pore size distribution of **MIL-125-NHCy** using data measured from N_2 gas isotherm at 77 K.
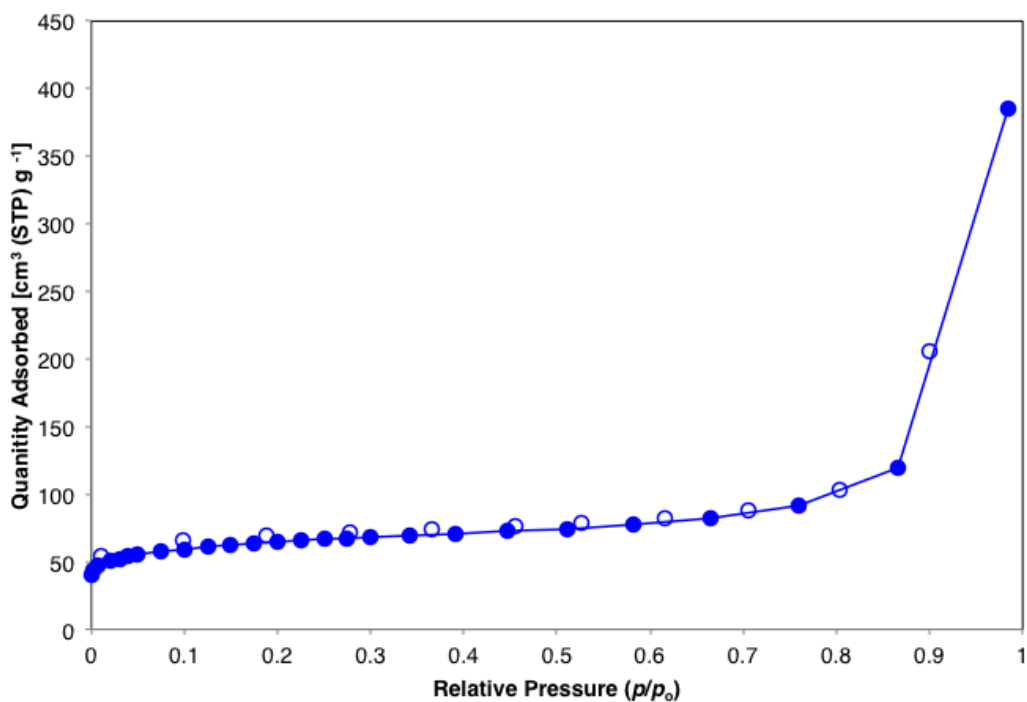
Figure B-43: Gas adsorption isotherm (77 K) of **MIL-125-NHhep**.
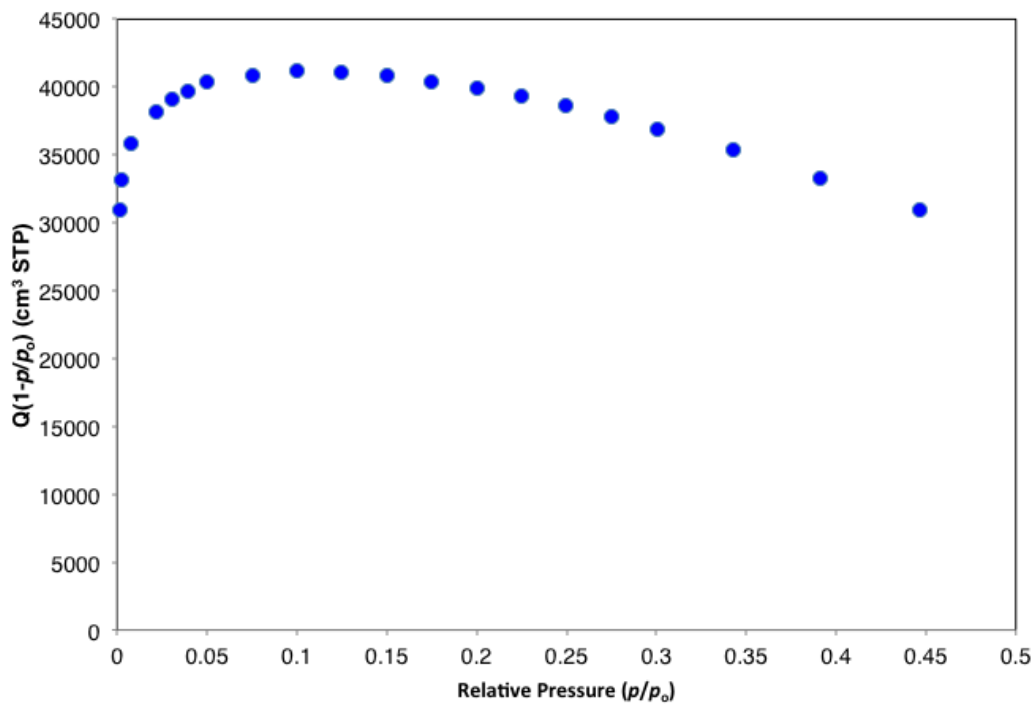
Figure B-44: Rouquerol plot **MIL-125-NHhep.**
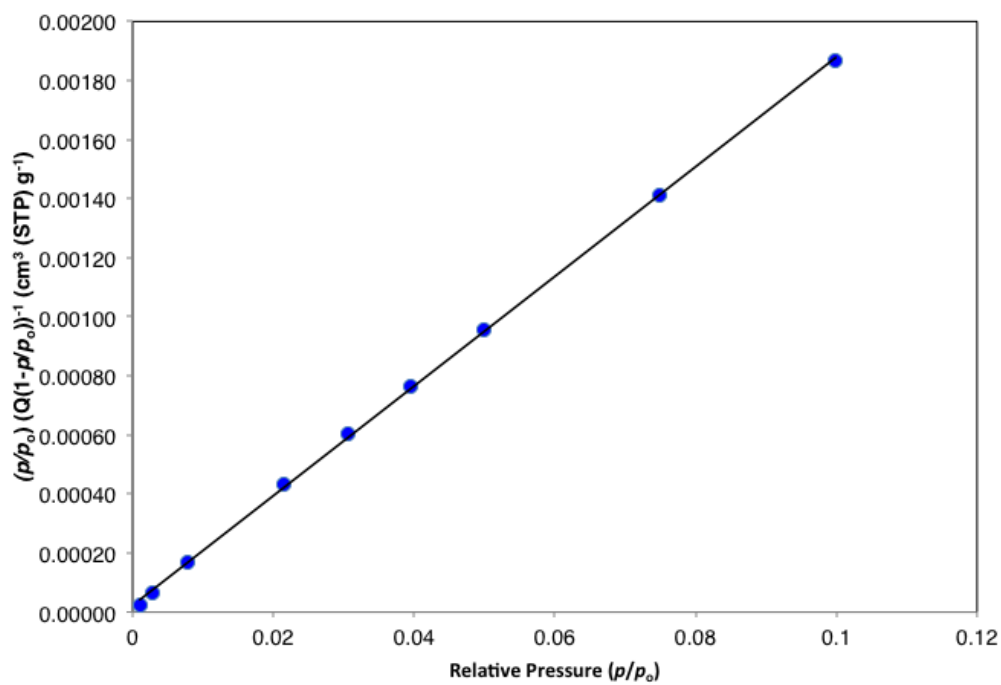
Figure B-45: Linear BET plot **MIL-125-NHhep.**
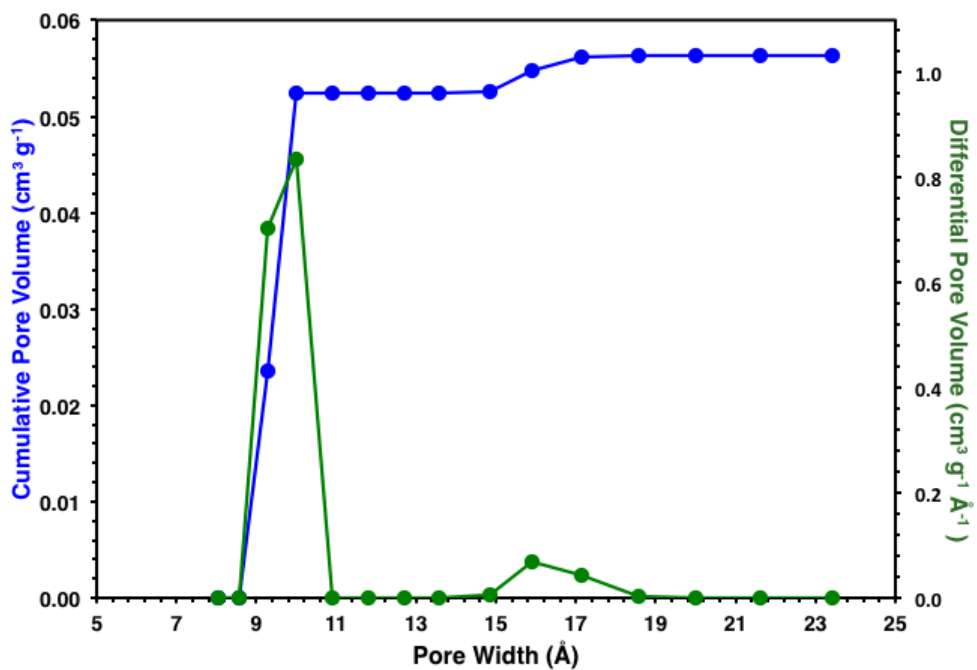
Figure B-46: DFT pore size distribution of **MIL-125-NHhep** using data measured from N_2 gas isotherm at 77 K.

Table B- 4: N_2 BET Surface area parameters.

MIL-125-NHR	**Me**	**Et**	**^{i}Pr**	**Bu**
V_m (cm^3(STP) g^{-1})	229.64	173.09	112.86	158.38
σ_{V_m}	0.62	0.42	0.28	0.61
S_{BET} (m^2 g^{-1})	998.9	752.9	491.0	689.0
σ_{S_BET}	2.7	1.8	1.2	2.6
C_{BET}	3382	3663	2800	2159
σ_{C_BET}	640	676	521	481

Table B- 5: N_2 BET Surface area parameters.

MIL-125-NHR	**Cyp**	**Cy**	**hep**
V_m (cm^3(STP) g^{-1})	134.41	96.37	53.79
σ_{V_m}	0.44	0.46	0.35
S_{BET} (m^2 g^{-1})	584.7	419.2	234.0
σ_{S_BET}	1.9	2.0	1.5
C_{BET}	2424	1262	822
σ_{C_BET}	505	274	205
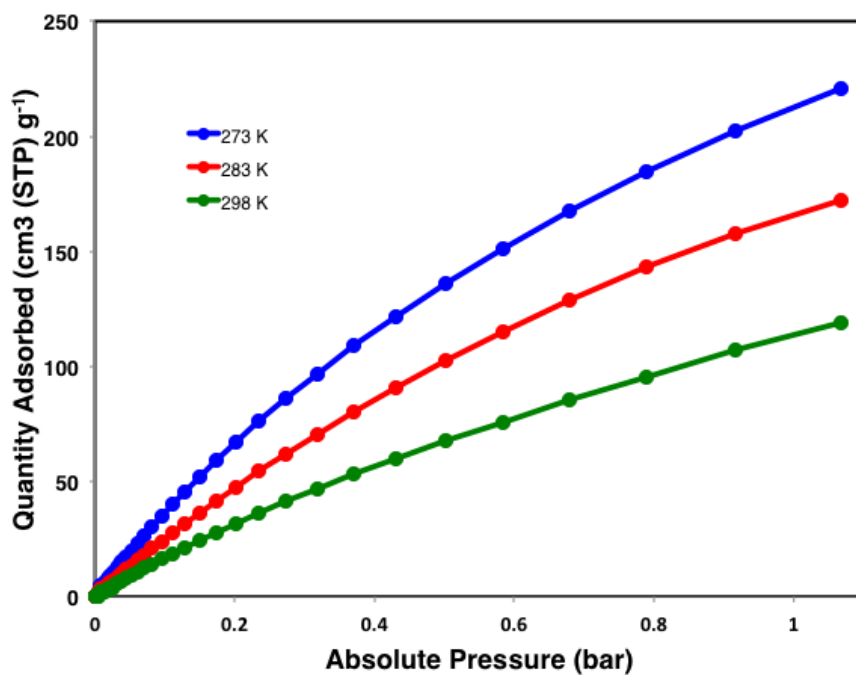
Figure B-47: CO_2 Gas adsorption isotherm of **MIL-125-NH$_2$** at 273 K (blue), 283 K (red), and 298 K (green).
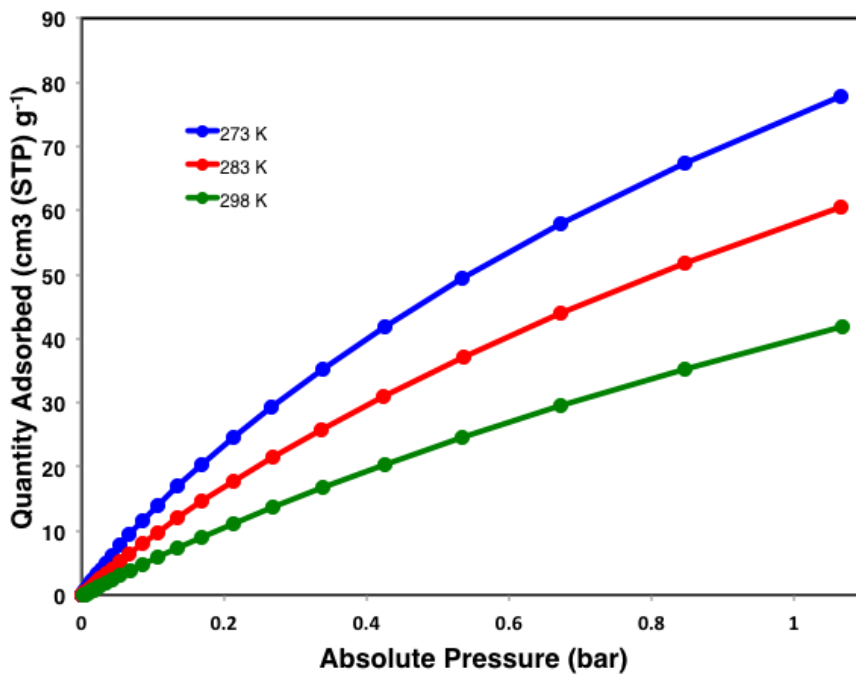
Figure B-48: CO_2 Gas adsorption isotherm of **MIL-125-NHMe** at 273 K (blue), 283 K (red), and 298 K (green).
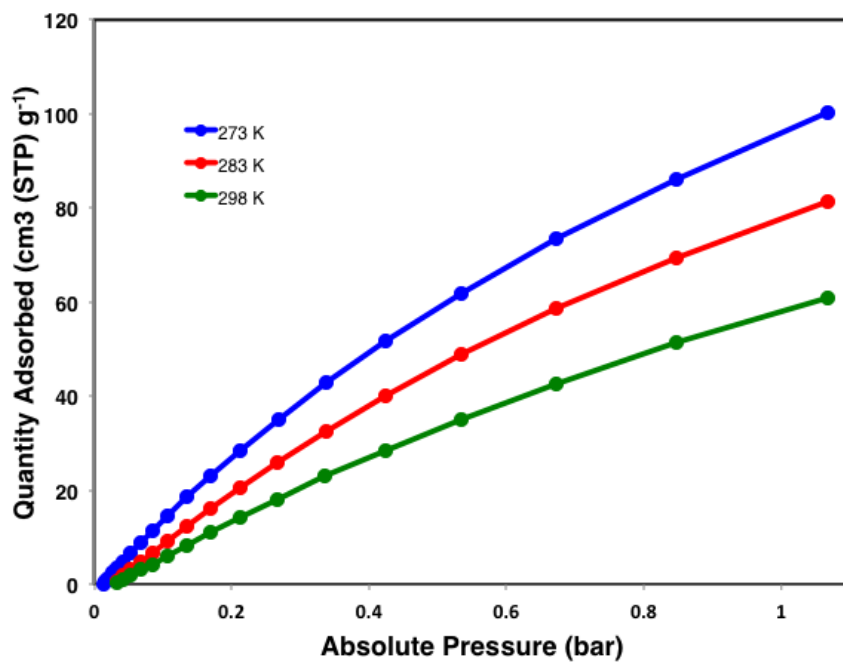
Figure B-49: CO$_2$ Gas adsorption isotherm of **MIL-125-NHEt** at 273 K (blue), 283 K (red), and 298 K (green).
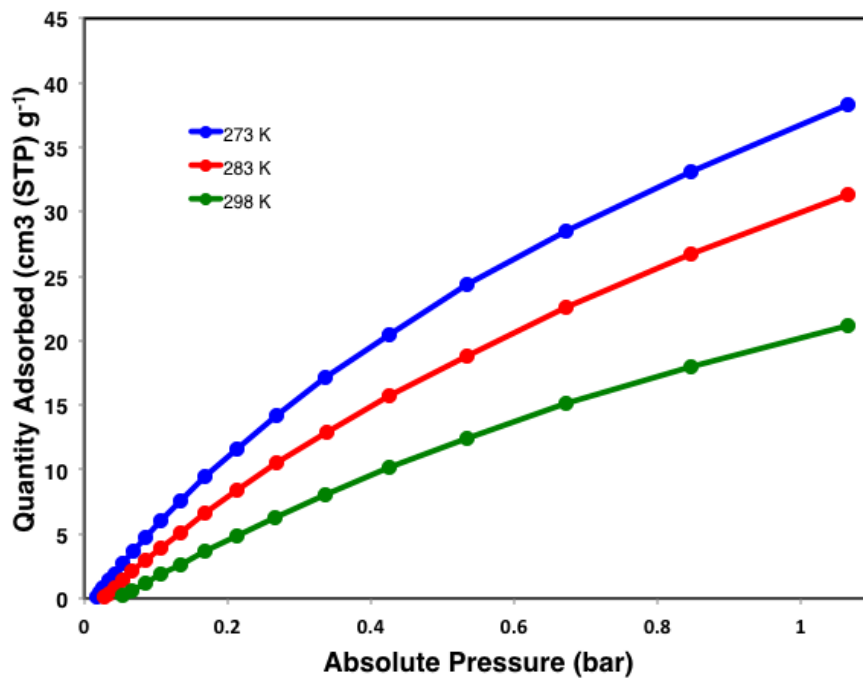
Figure B-50: CO$_2$ Gas adsorption isotherm of **MIL-125-NHiPr** at 273 K (blue), 283 K (red), and 298 K (green).
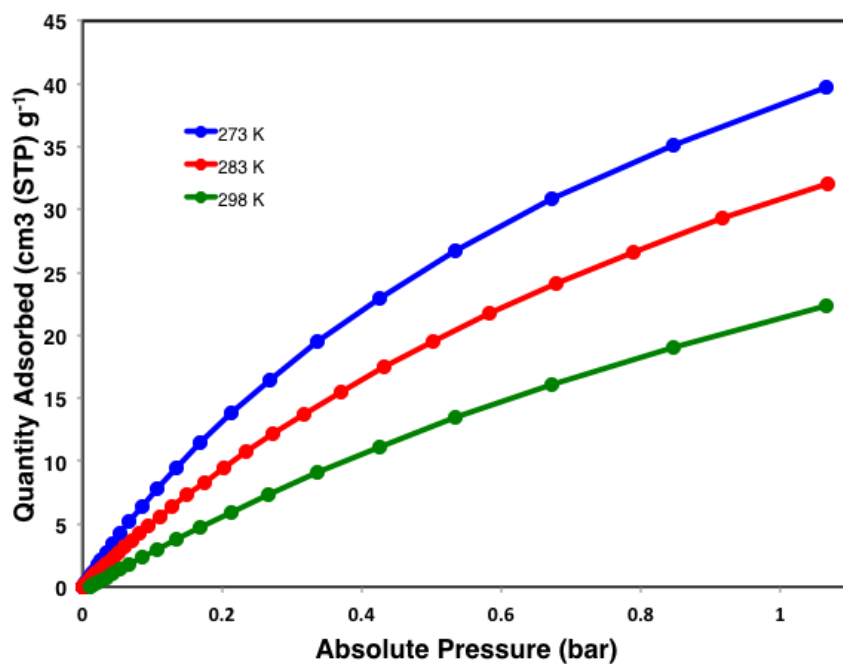
Figure B-51: CO$_2$ Gas adsorption isotherm of **MIL-125-NHBu** at 273 K (blue), 283 K (red), and 298 K (green).
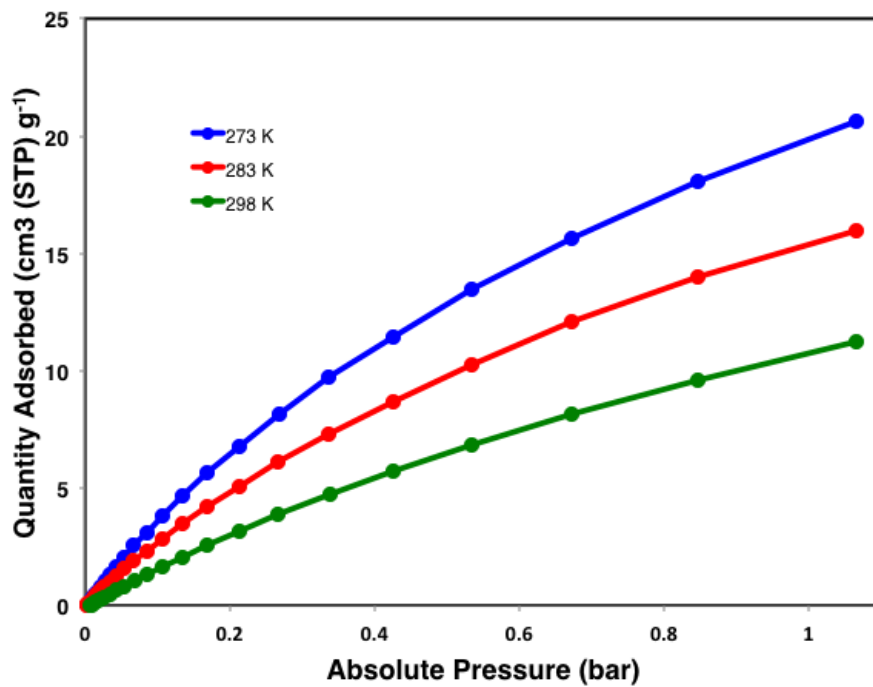
Figure B-52: CO$_2$ Gas adsorption isotherm of **MIL-125-NHCyp** at 273 K (blue), 283 K (red), and 298 K (green).
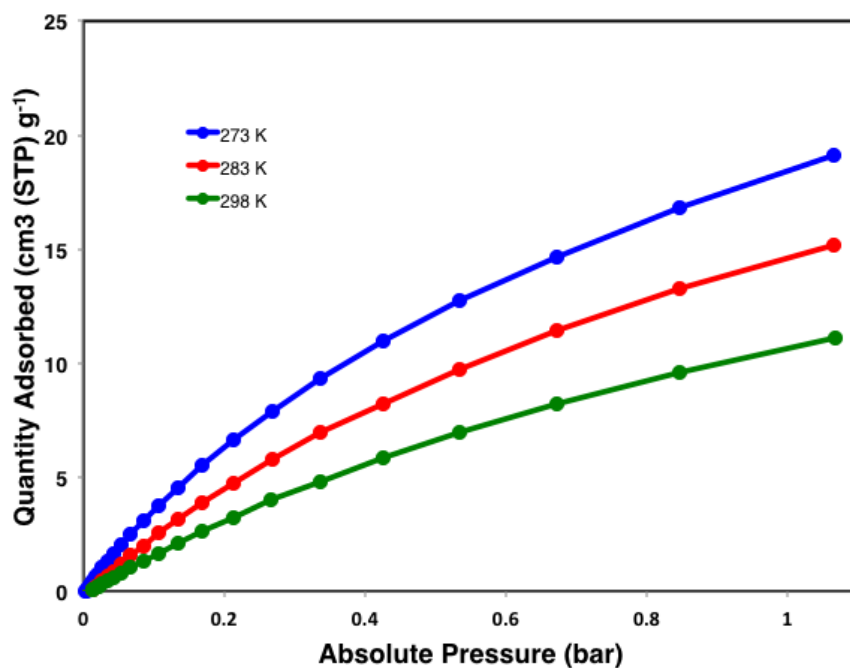
Figure B-53: CO$_2$ Gas adsorption isotherm of **MIL-125-NHCy** at 273 K (blue), 283 K (red), and 298 K (green).
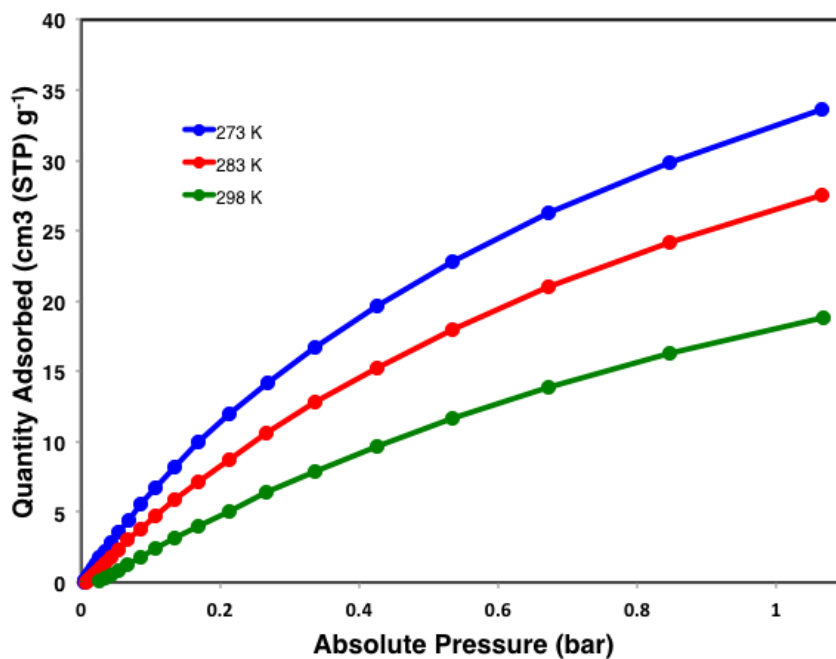
Figure B-54: CO$_2$ Gas adsorption isotherm of **MIL-125-NHhep** at 273 K (blue), 283 K (red), and 298 K (green)

B.5 Optical Band Gap Spectra
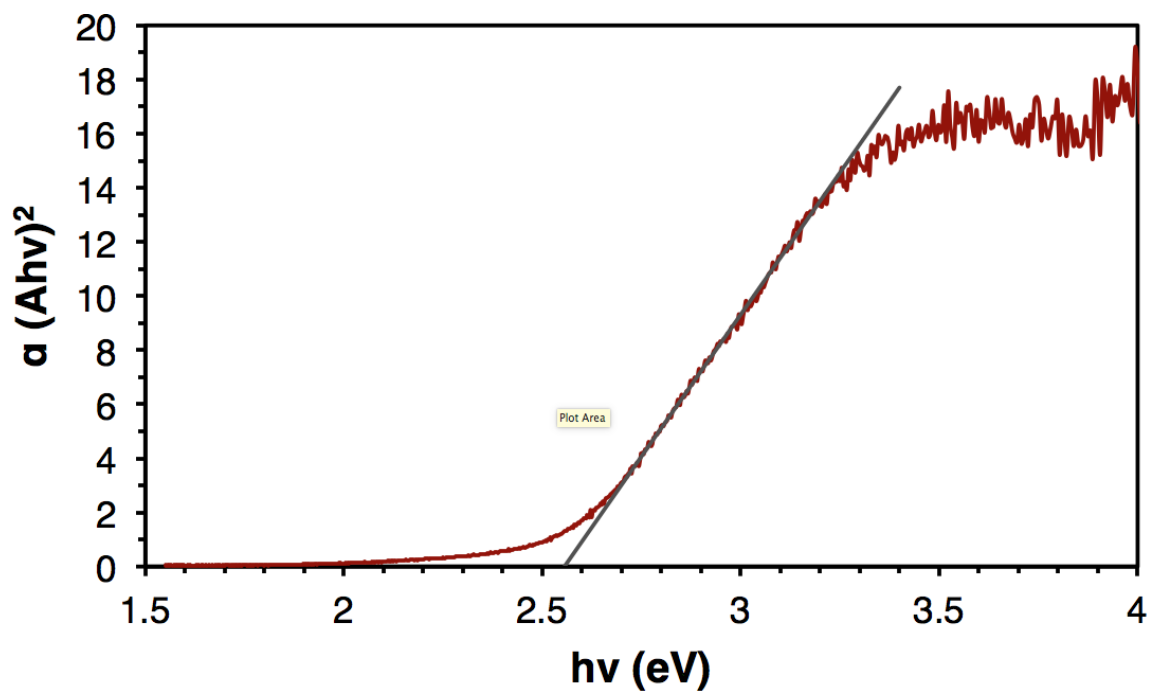
Figure B-55: Tauc plot for **MIL-125-NH₂**. Linear region is indicated.
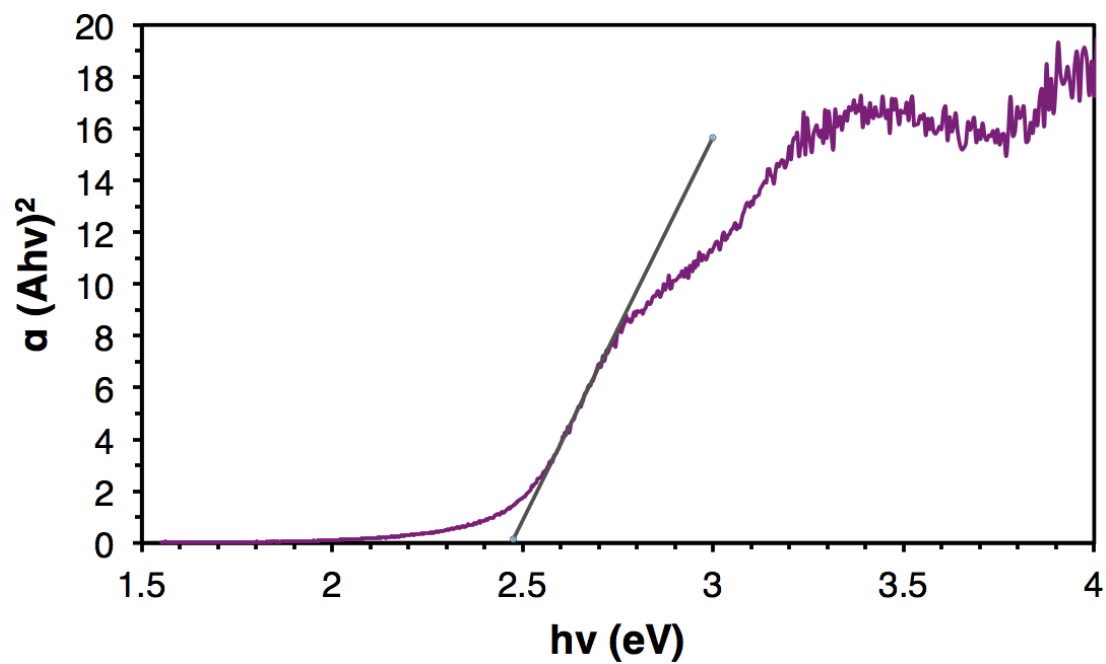
Figure B-56: Tauc plot for **MIL-125-NHMe**. Linear region is indicated.
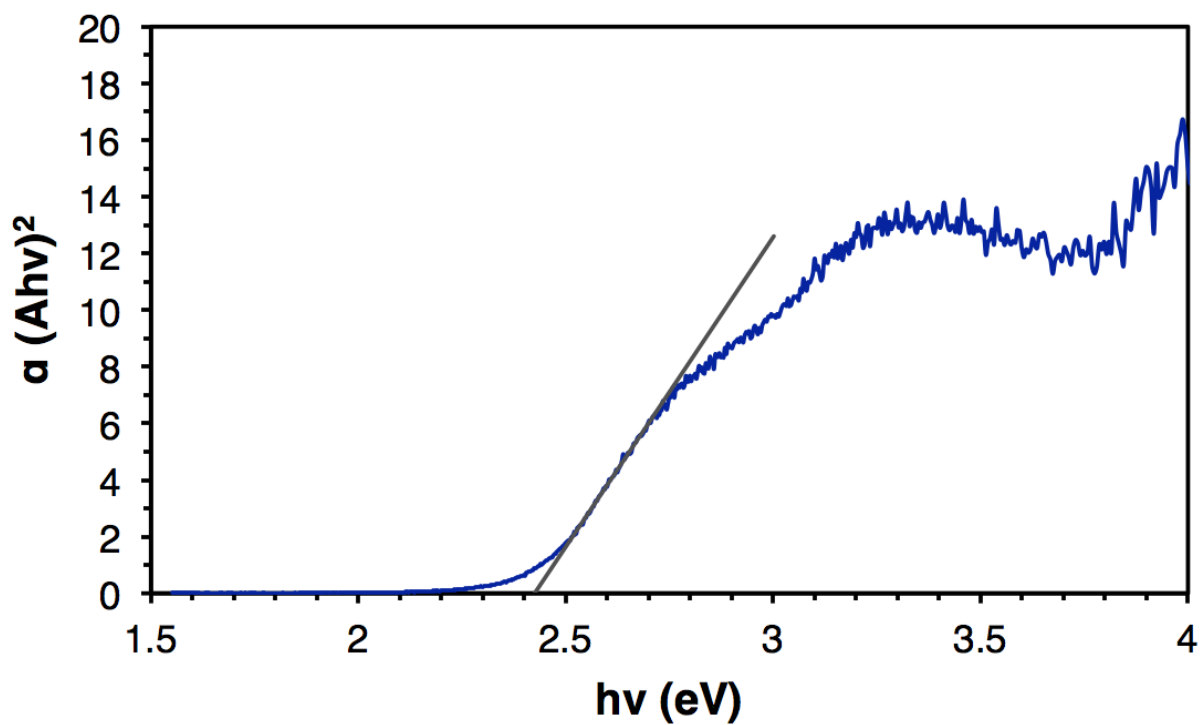
Figure B-57: Tauc plot for **MIL-125-NHEt**. Linear region is indicated.
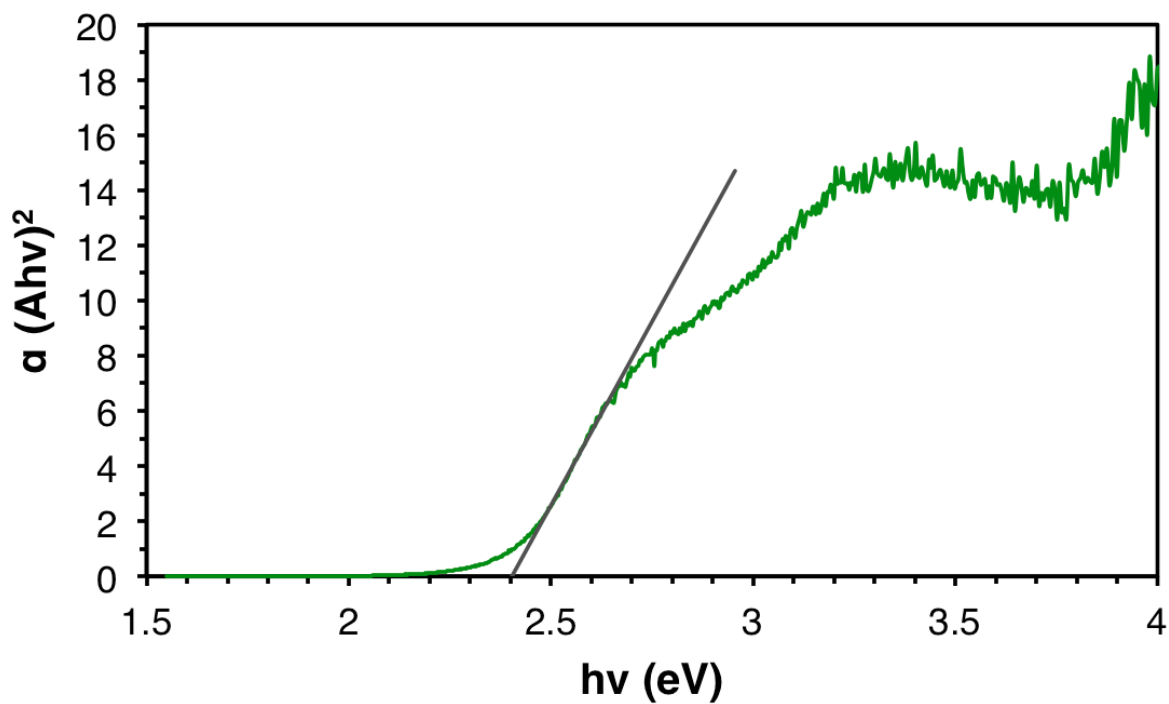
Figure B-58: Tauc plot for **MIL-125-NHiPr**. Linear region is indicated.
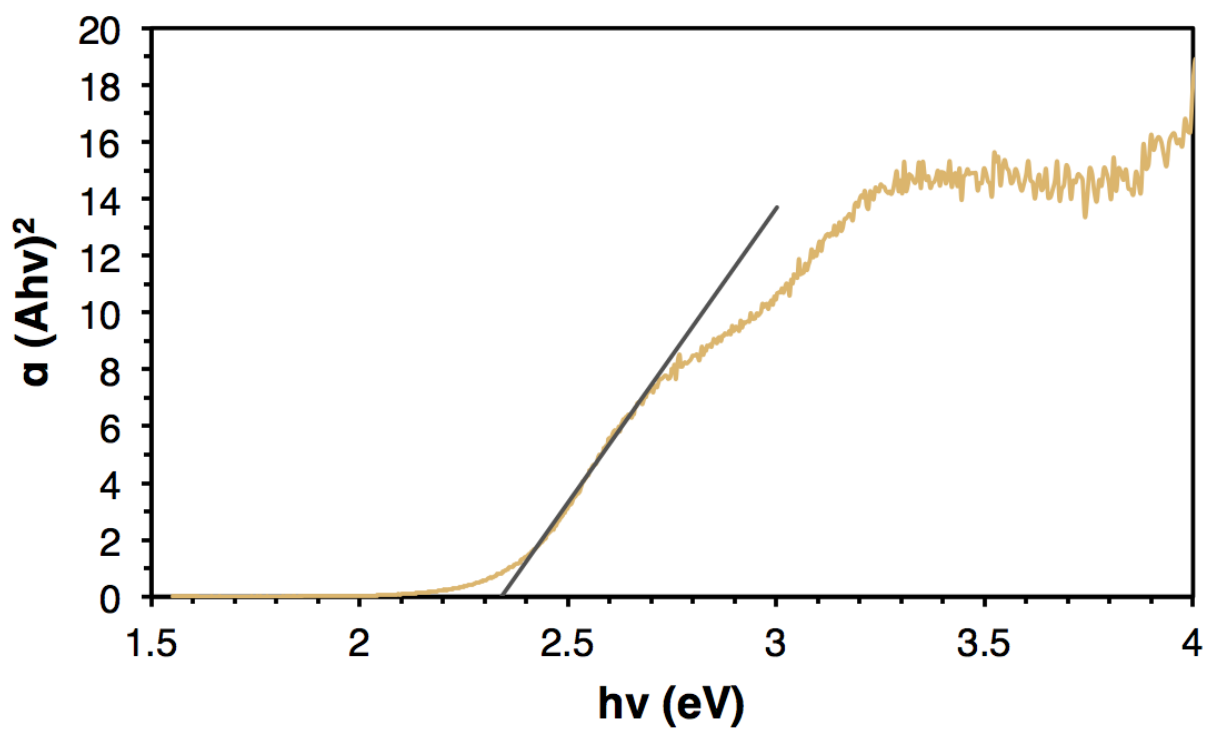
Figure B-59: Tauc plot for **MIL-125-NHBu**. Linear region is indicated.
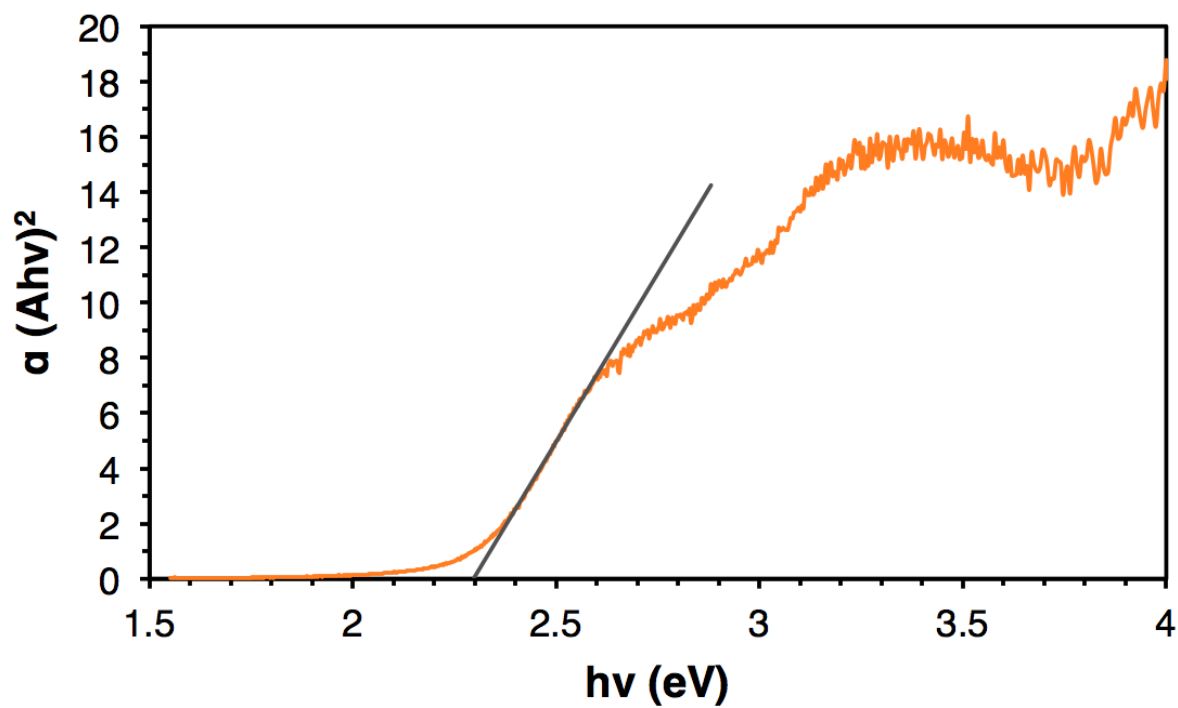
Figure B-60: Tauc plot for **MIL-125-NHCyp**. Linear region is indicated.
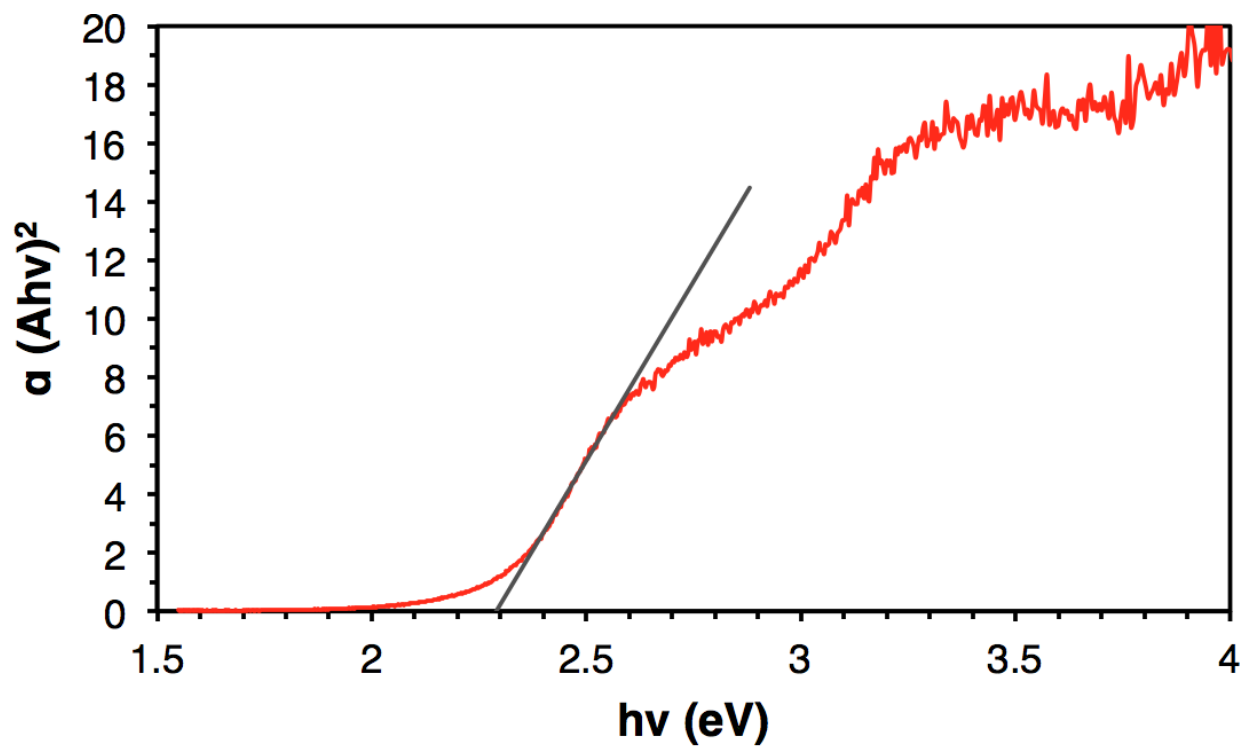
Figure B-61: Tauc plot for **MIL-125-NHCy**. Linear region is indicated.
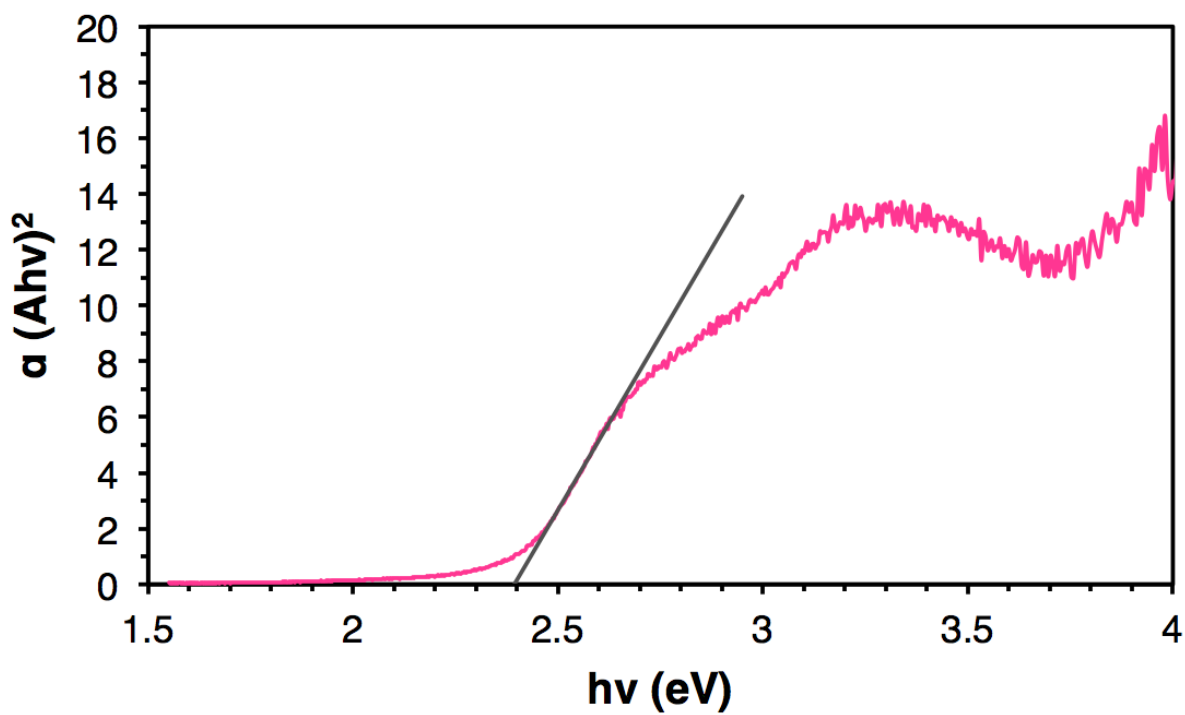
Figure B-62: Tauc plot for **MIL-125-NHhep**. Linear region is indicated.

Table B-6: Optical bandgap of the prepared MOFs.

MIL-125-NHR	E_g (eV)	Std. Dev. (eV)
–NH₂	2.56	0.02
–NHMe	2.46	0.03
–NHEt	2.42	0.02
–NH^{i}Pr	2.40	0.03
–NHBu	2.35	0.04
–NHCyp	2.30	0.02
–NHCy	2.29	0.02
–NHhep	2.39	0.02

B.6 <u>Transient absorption spectra</u>

a)
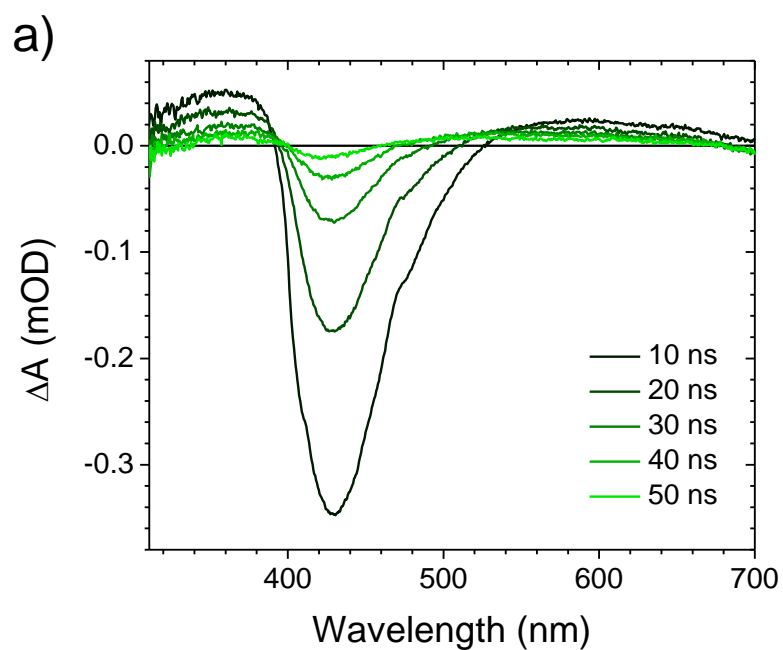
Figure B-63: Transient absorption spectra for a) **MIL-125-NH$_2$**, suspended in MeCN (λex = 405 nm).

b)
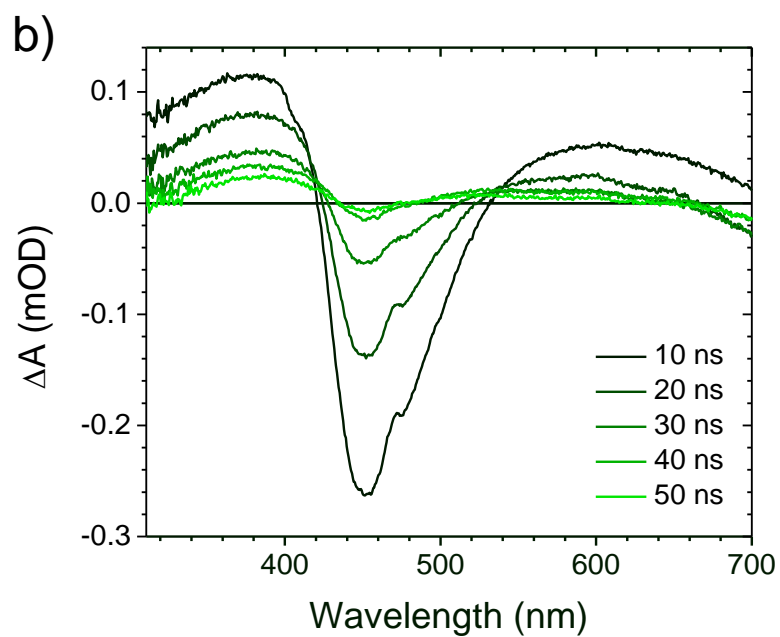
Figure B- 64: Transient absorption spectra for b) **MIL-125-NHMe**, suspended in MeCN (λex = 405 nm).
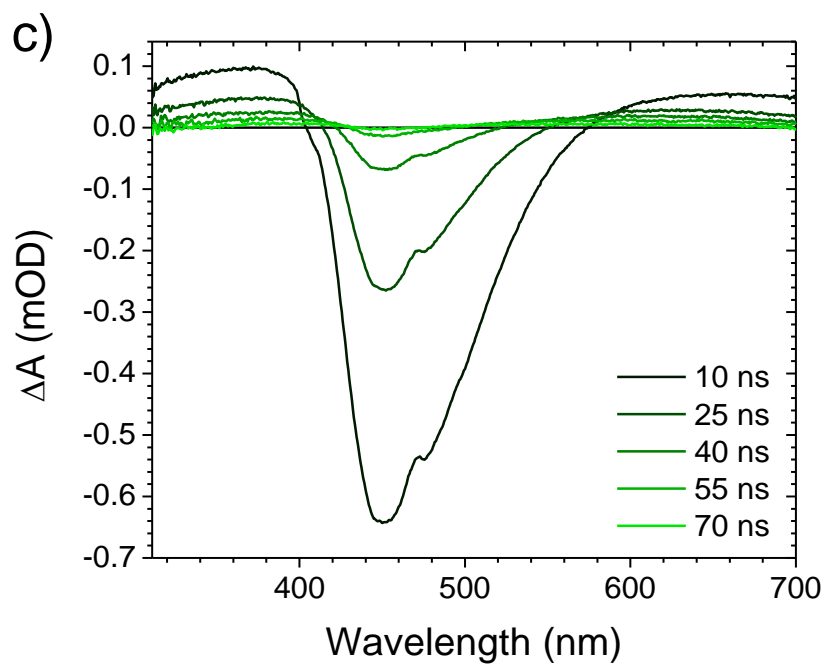
Figure B- 65: Transient absorption spectra for c) **MIL-125-NHEt** suspended in MeCN (λex = 405 nm).
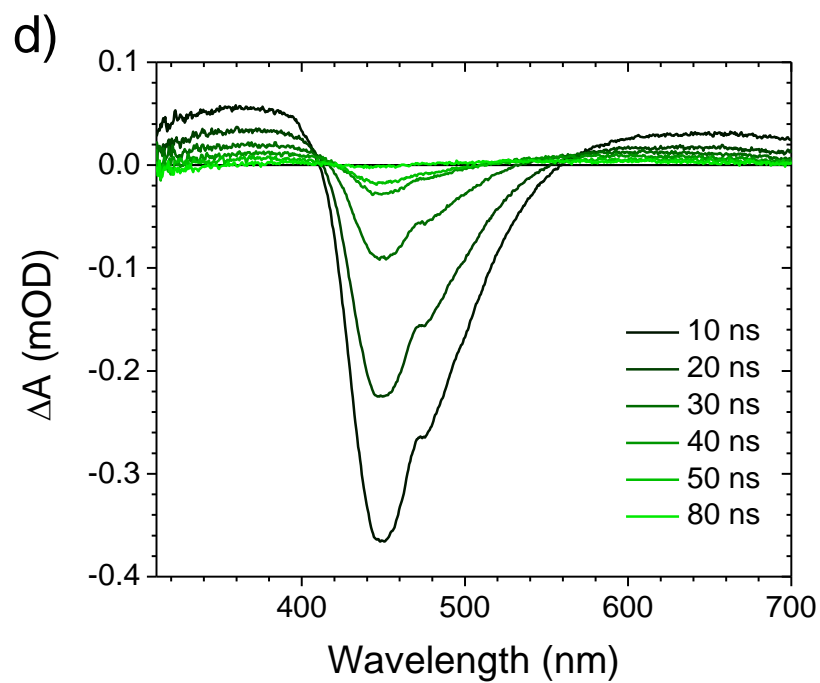
Figure B-66: Transient absorption spectra for d) **MIL-125-NHBu** suspended in MeCN (λ_{ex} = 405 nm).
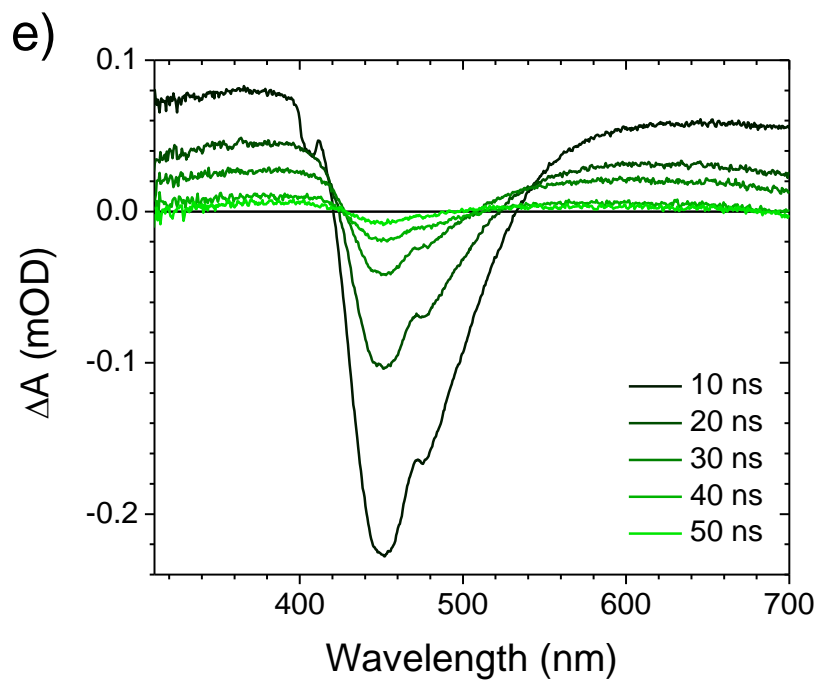
Figure B-67: Transient absorption spectra for e) **MIL-125-NHiPr** suspended in MeCN (λex = 405 nm).

Table B-7: Lifetime constant from time-resolved absorption spectra of the prepared MOFs.

MIL-125-NHR	τ (ns)
–NH₂	12.77
–NHMe	38.19
–NHEt	60.63
–NH^{i}Pr	75.11
–NHBu	52.13
–NHCyp	68.88
–NHCy	91.35
–NHhep	69.17

B.7 <u>Actinometry</u>
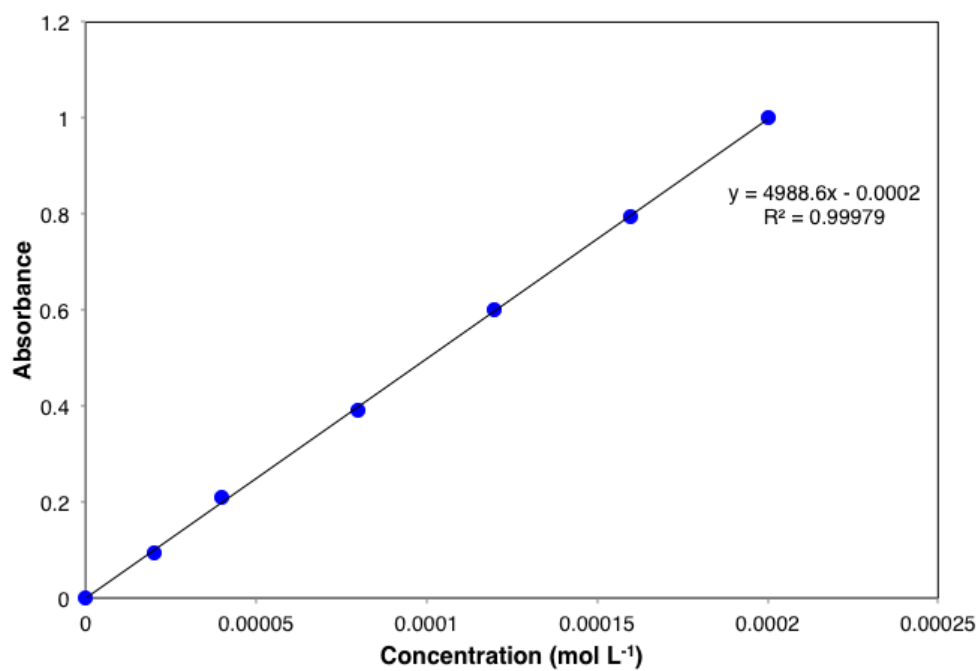
Figure B-68: Calibration curve showing the concentration of Fe(II) vs. absorbance at 510 nm. Plotted with linear regression line and R^2 value.
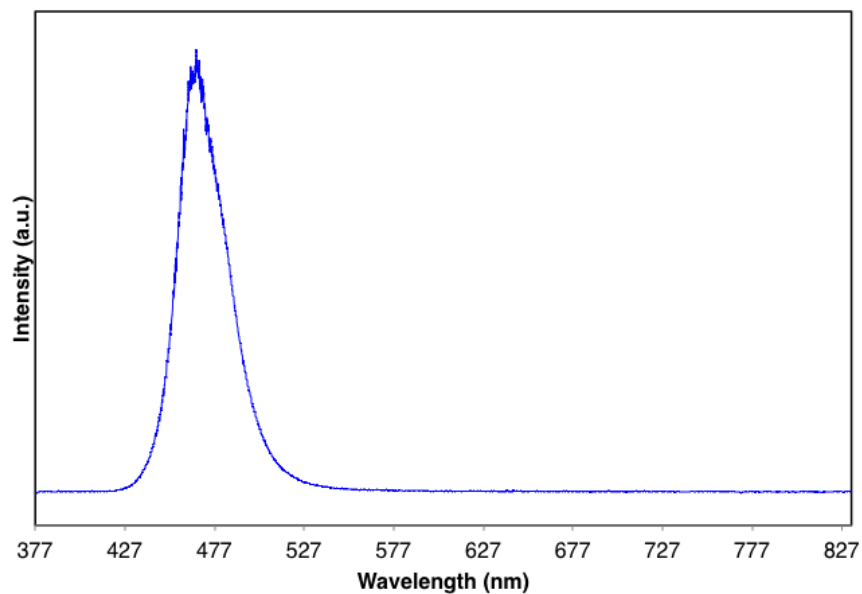
Figure B-69: Emission spectrum of blue LED photoreactor.
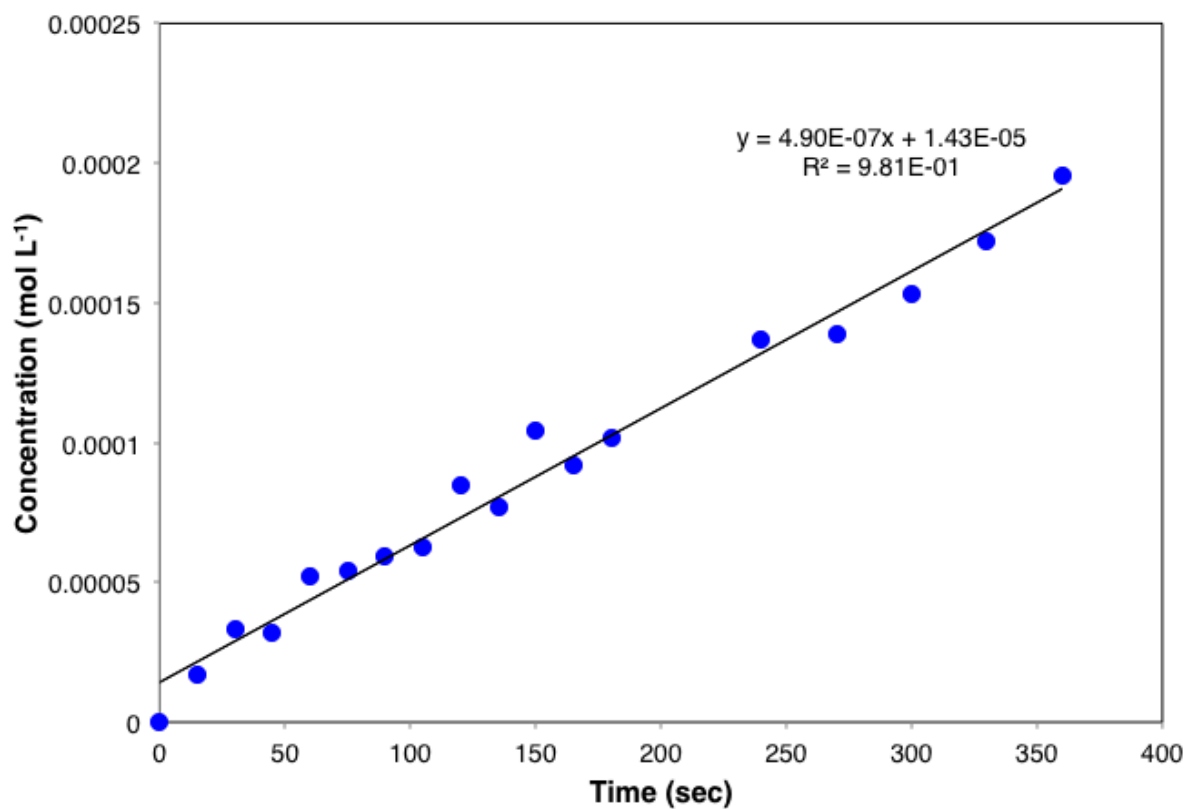
Figure B-70: Photoreduciton of $K_3[Fe(C_2O_4)_3]$ to $Fe((C_2O_4)_2^{-2}$ vs. time in blue LED reactor. Plotted with linear regression line and R^2 value.

B.8 <u>Photocatalysis</u>
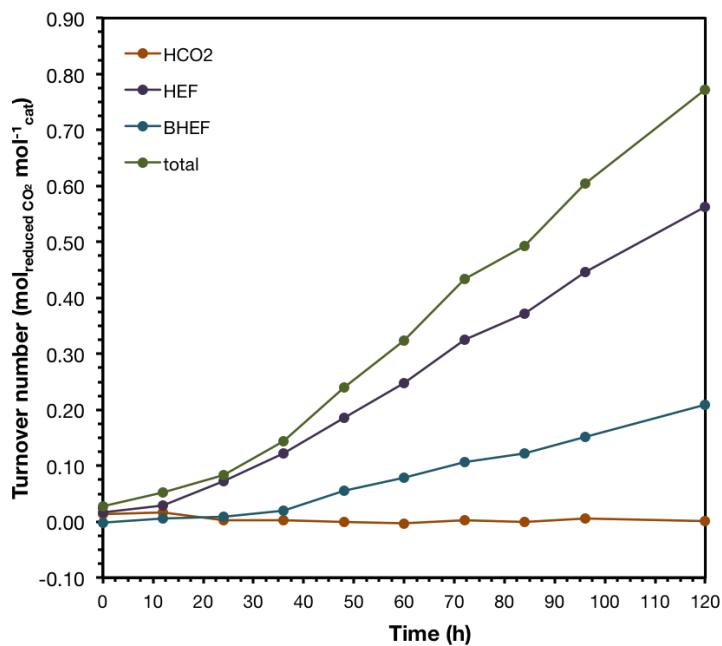
Figure B-71: Kinetic plot of CO_2-photoreduced products using **MIL-125-NH$_2$**.
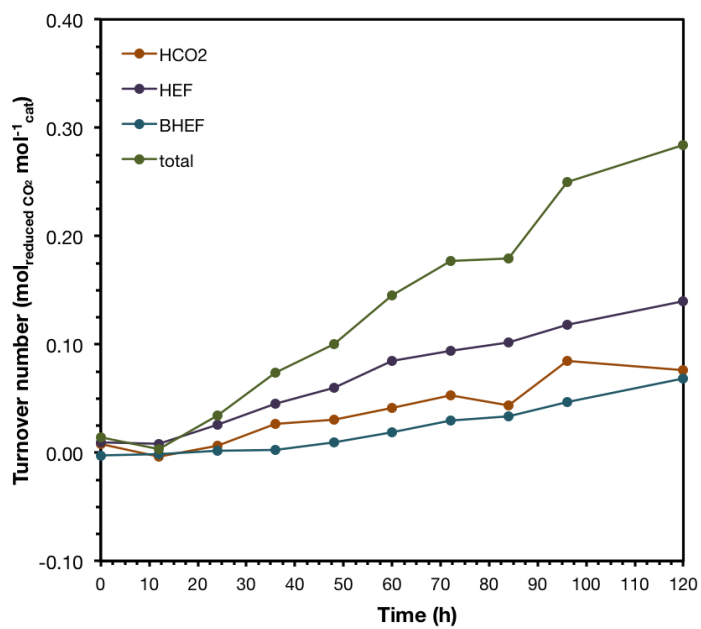
Figure B-72: Kinetic plot of CO_2-photoreduced products using **MIL-125-NHMe**.
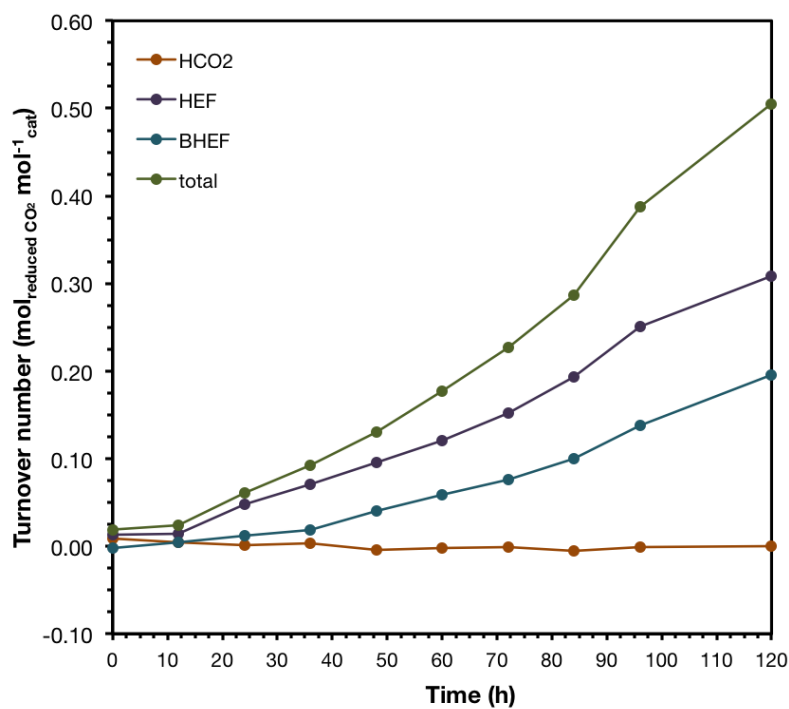
Figure B-73: Kinetic plot of CO_2-photoreduced products using **MIL-125-NHEt**.
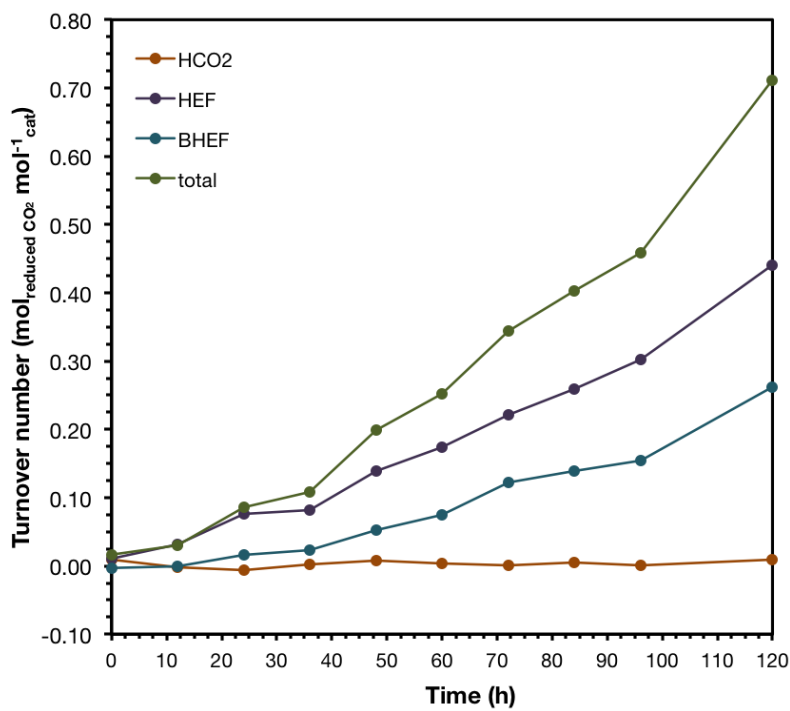
Figure B-74: Kinetic plot of CO_2-photoreduced products using **MIL-125-NH^{i}Pr**.
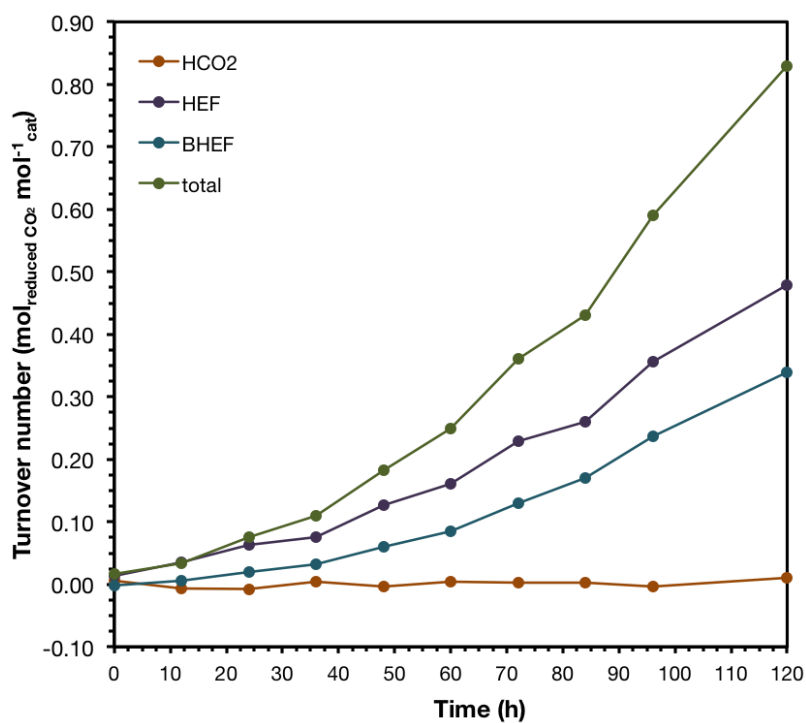
Figure B-75: Kinetic plot of CO_2-photoreduced products using **MIL-125-NHBu**.
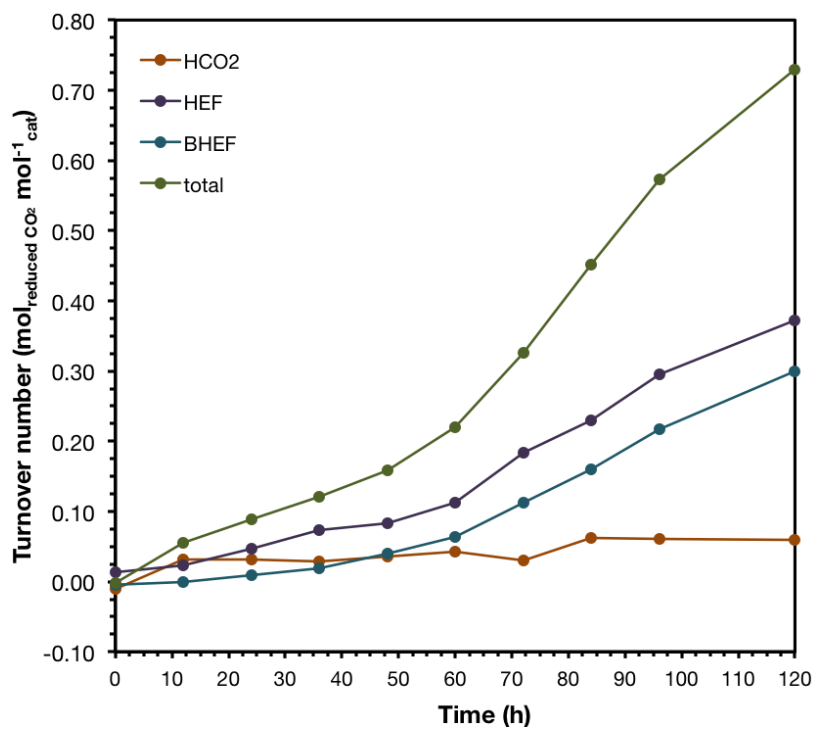
Figure B-76: Kinetic plot of CO_2-photoreduced products using **MIL-125-NHCyp**.
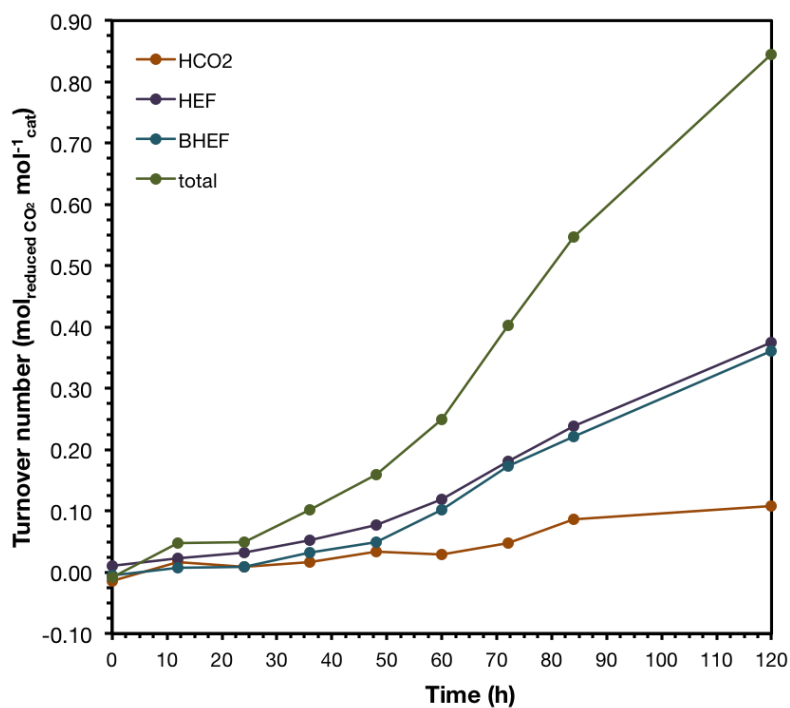
Figure B-77: Kinetic plot of CO$_2$-photoreduced products using **MIL-125-NHCy**.
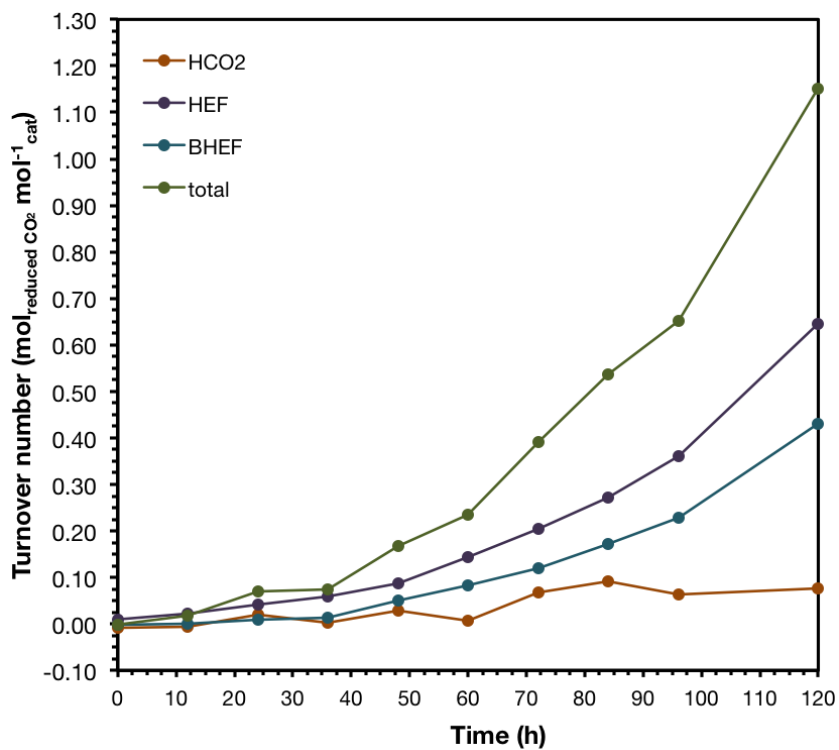
Figure B-78: Kinetic plot of CO$_2$-photoreduced products using **MIL-125-NHhep**.
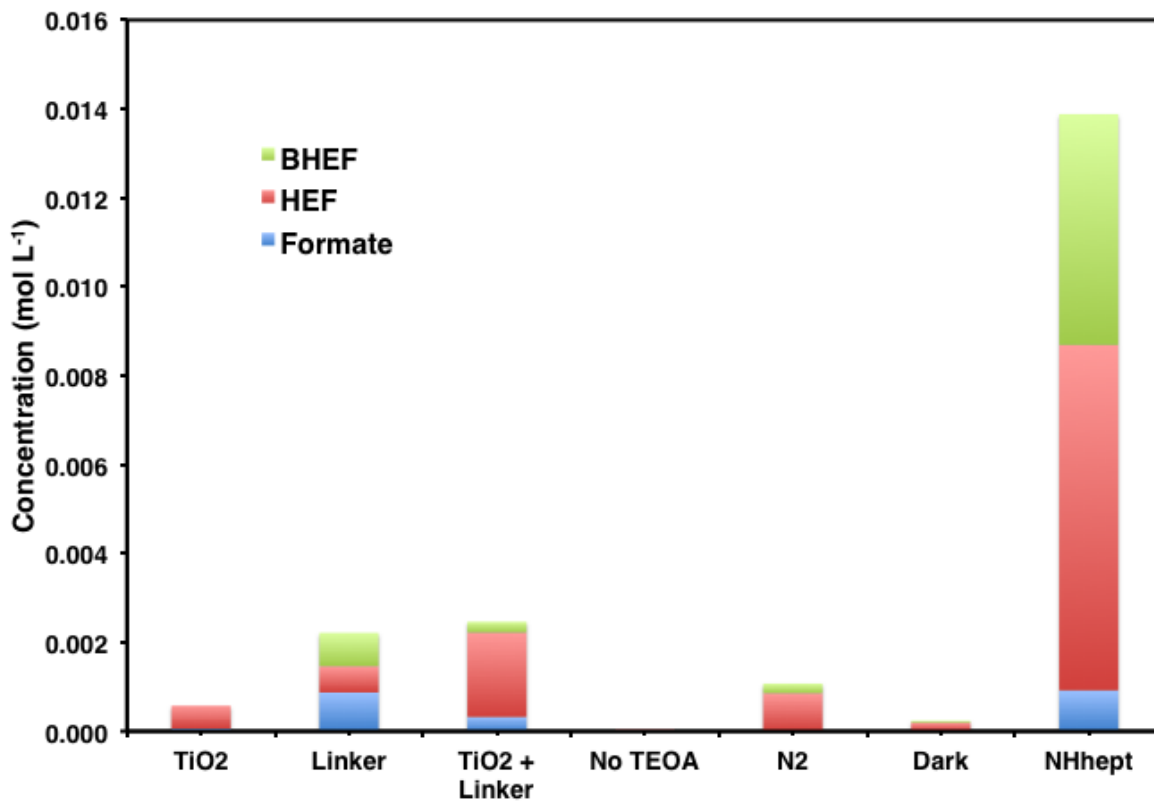
Figure B-79: Control experiments at 120 h blue LED exposure showing the concentration in mol L^{-1}, compared to **MIL-125-NHhept** MOF.

Table B-8: Initial rate of reaction and apparent quantum yield. Initial rate of reaction obtained from evaluation at t = 0 of the first derivative of the 3rd order polynomial fit. Apparent quantum yield obtained according to eq. (2)

MIL-125-NHR	R^{in} (mol L^{-1} h^{-1})	Apparent quantum yield (Φ_{app})
MIL-125-NH$_2$	5.97×10^{-6}	0.31%
MIL-125-NHMe	7.52×10^{-6}	0.39%
MIL-125-NHEt	6.42×10^{-6}	0.33%
MIL-125-NH^{i}Pr	3.00×10^{-5}	1.56%
MIL-125-NHBu	5.71×10^{-6}	0.30%
MIL-125-NHCyp	3.41×10^{-5}	1.78%
MIL-125-NHCy	2.95×10^{-5}	1.54%
MIL-125-NHhep	1.33×10^{-5}	0.69%

B.9 NMR Spectra
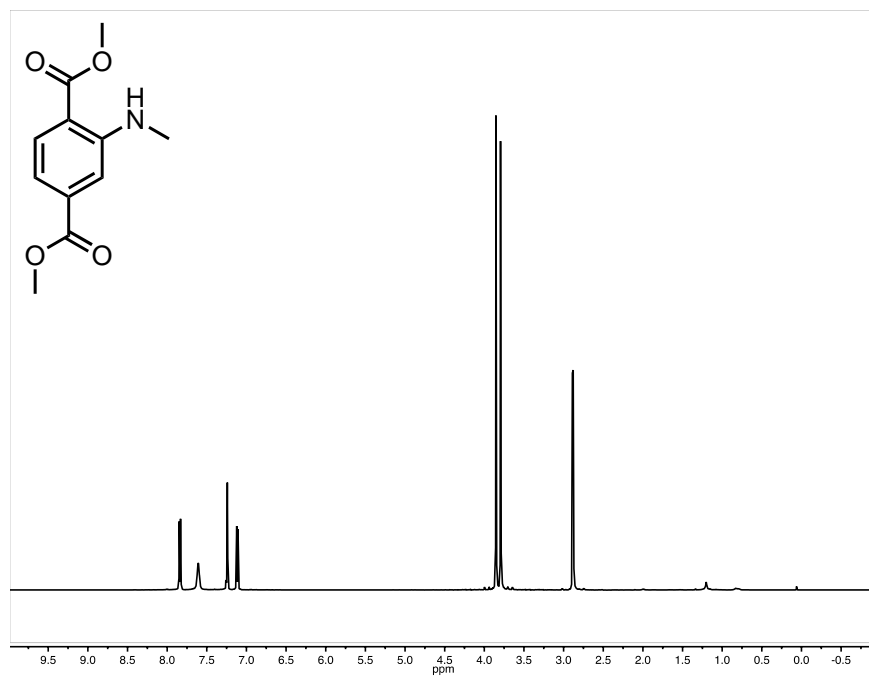
Figure B-80: ^{1}H NMR spectra (400 MHz, CDCl$_3$, 25 °C) of compound 1a.
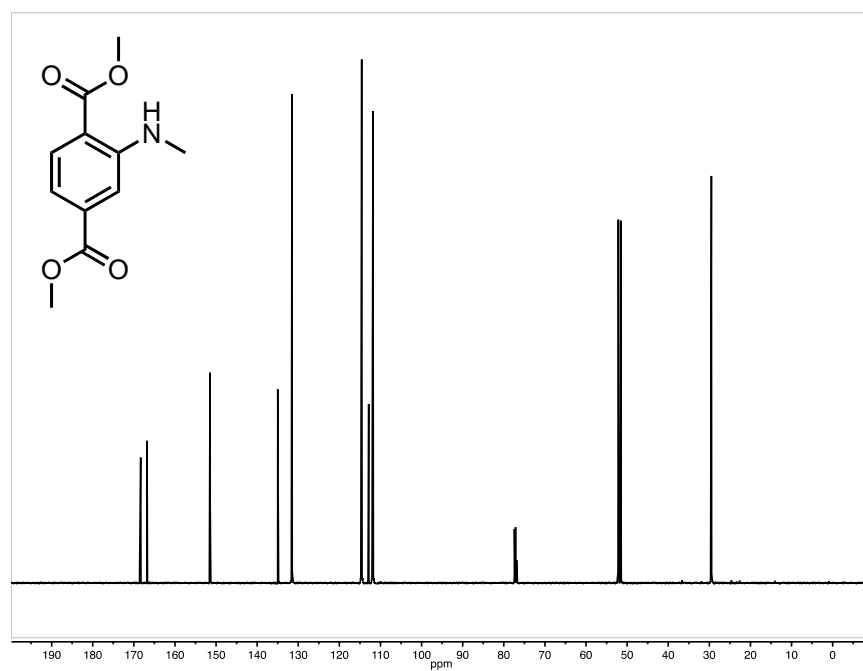
Figure B-81: ^{13}C NMR spectra (100 MHz, CDCl$_3$, 25 °C) of compound 1a.
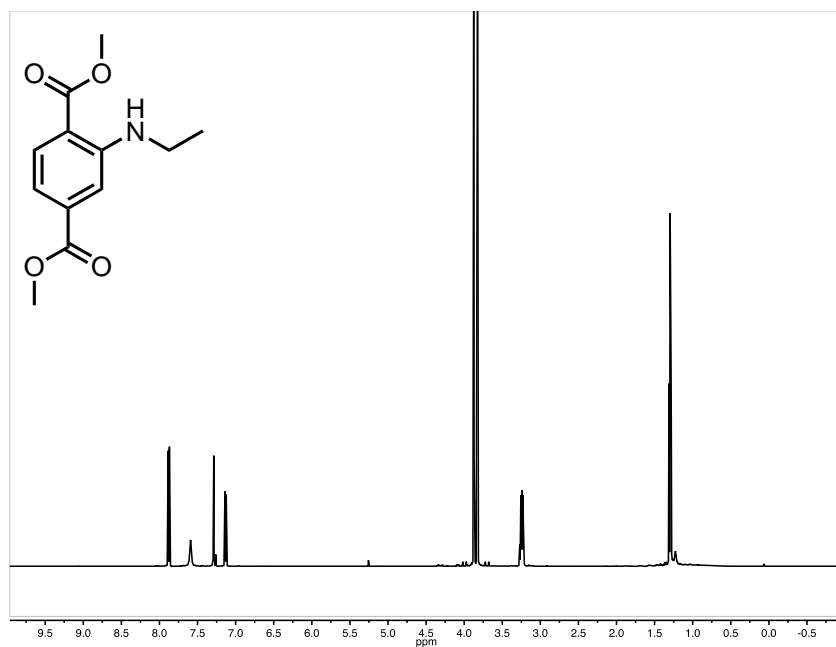
Figure B-82: ^{1}H NMR spectra (400 MHz, CDCl$_3$, 25 ºC) of compound 1b.

Figure B-83: ^{13}C NMR spectra (100 MHz, CDCl$_3$, 25 ºC) of compound 1b.
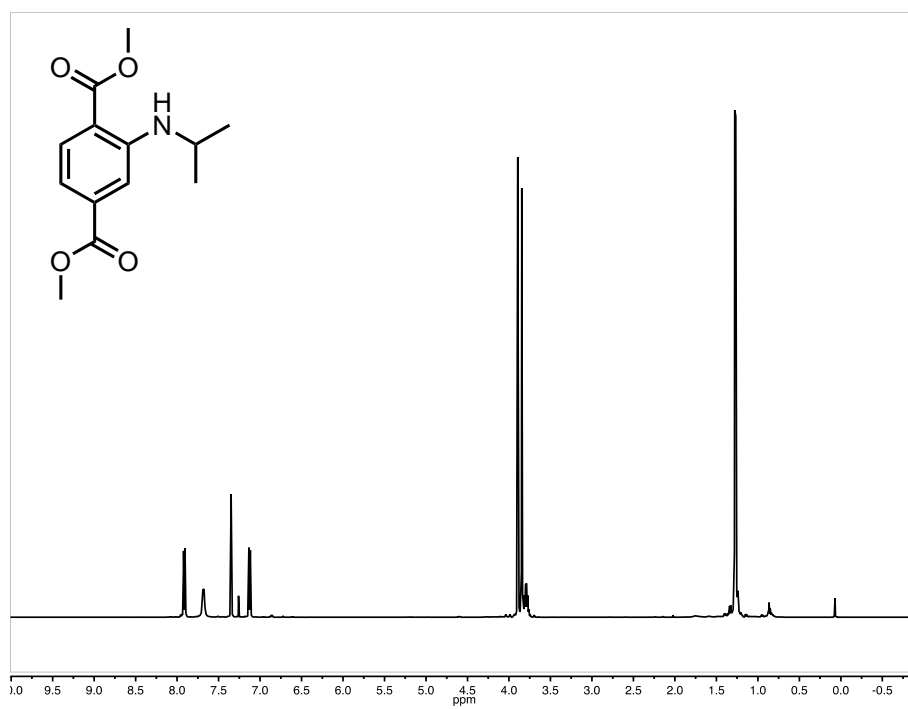
Figure B-84: ^{1}H NMR spectra (400 MHz, CDCl3, 25 ºC) of compound 1c.
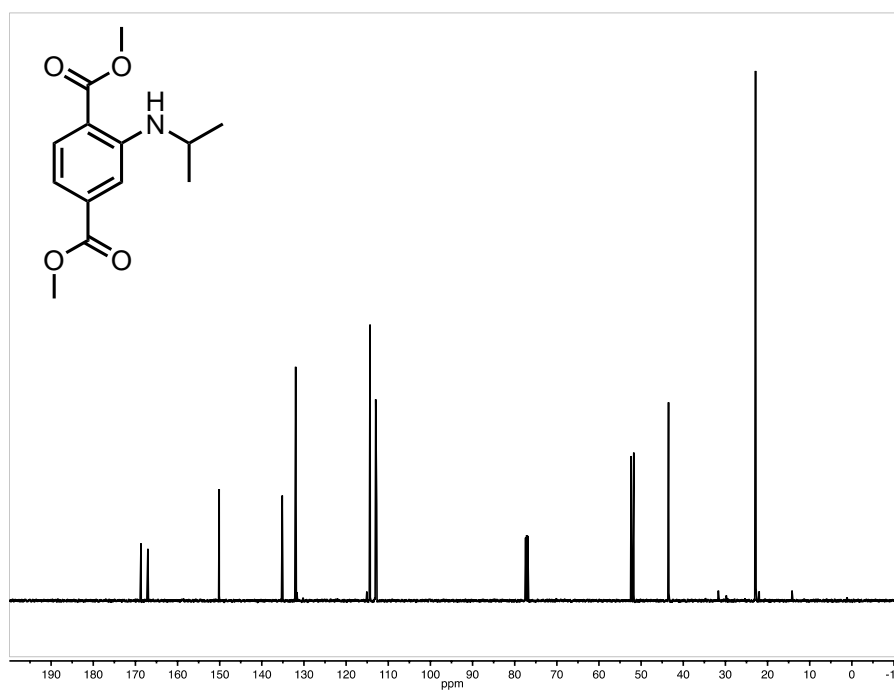
Figure B-85: ^{13}C NMR spectra (100 MHz, CDCl$_3$, 25 ºC) of compound 1c.

Figure B-86: ¹H NMR spectra (400 MHz, CDCl₃, 25 ºC) of compound 1d.
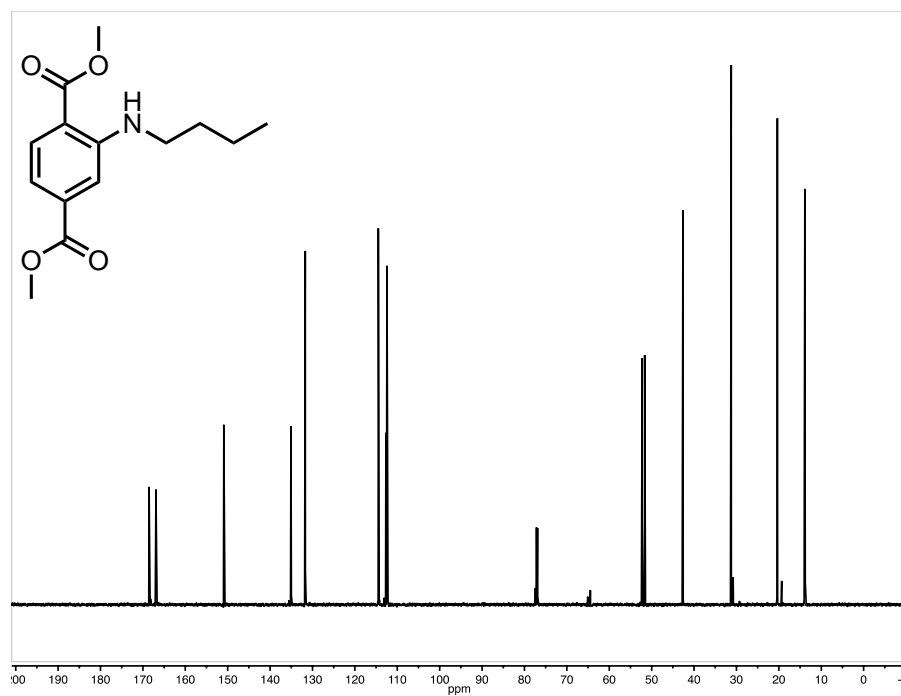
Figure B-87: ¹³C NMR spectra (100 MHz, CDCl₃, 25 ºC) of compound 1d.
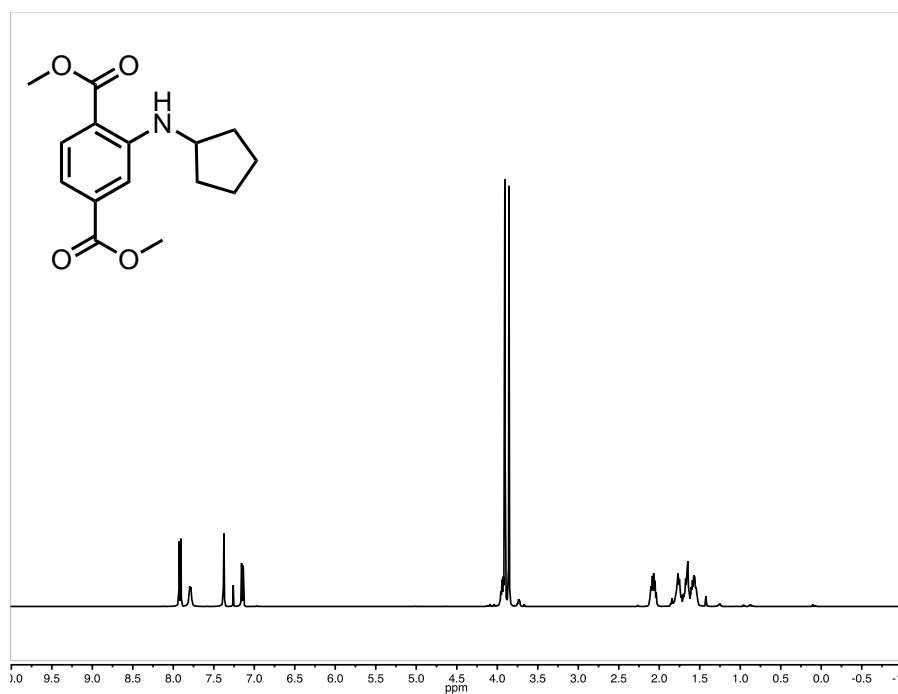
Figure B-88: ^{1}H NMR spectra (400 MHz, CDCl$_3$, 25 ℃) of compound 1e.
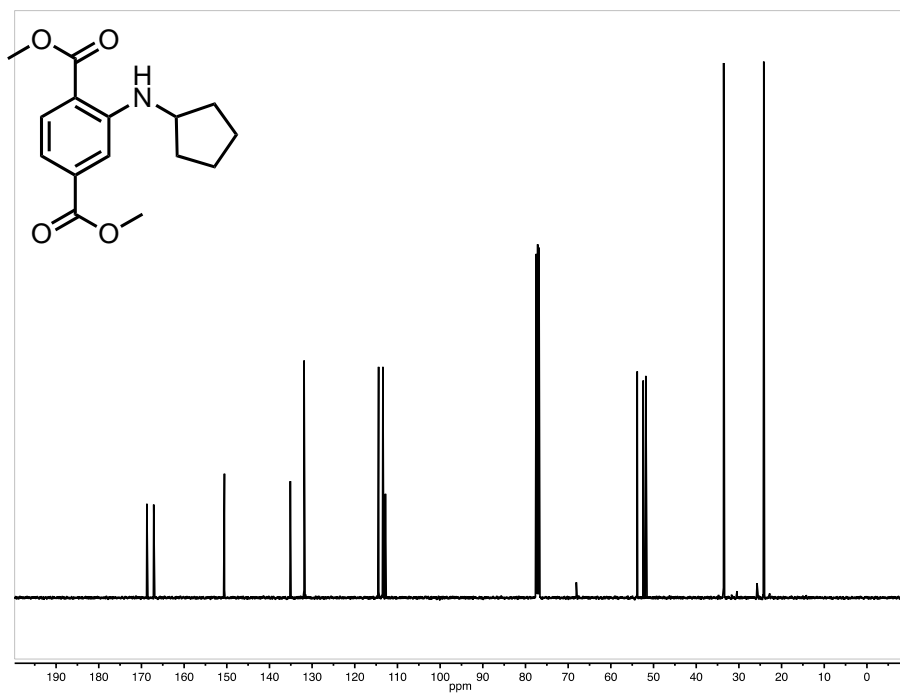
Figure B-89: ^{13}C NMR spectra (100 MHz, CDCl$_3$, 25 ℃) of compound 1e.
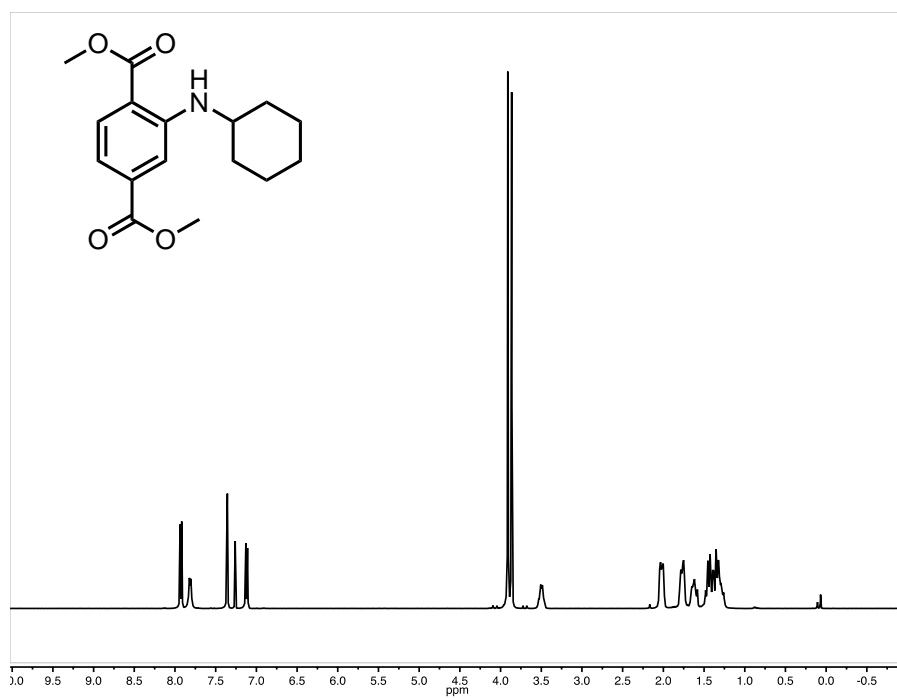
Figure B-90: ^{1}H NMR spectra (400 MHz, CDCl$_3$, 25 ºC) of compound 1f.
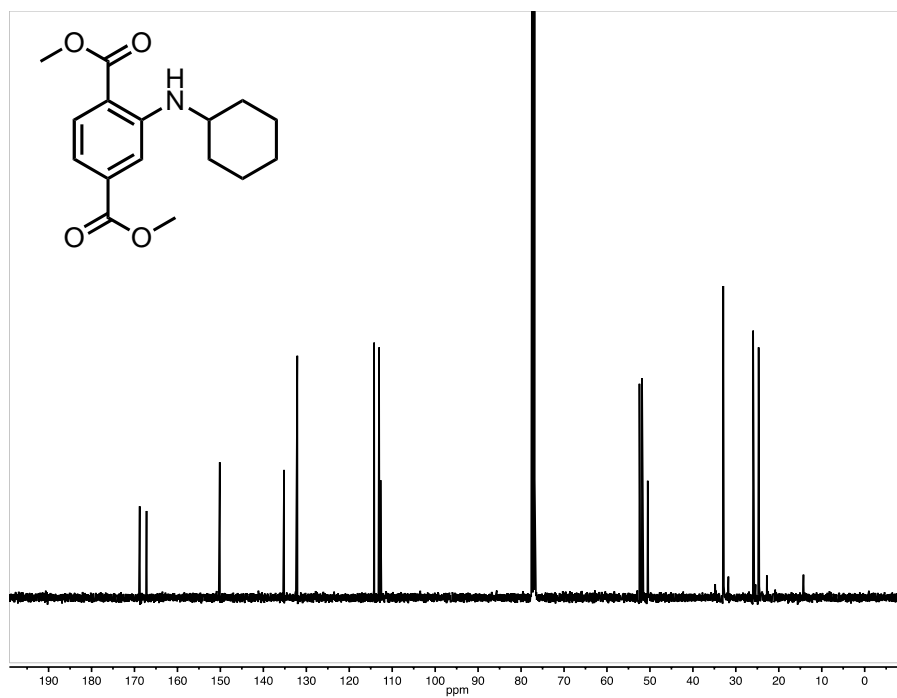
Figure B-91: ^{13}C NMR spectra (100 MHz, CDCl$_3$, 25 ºC) of compound 1f.
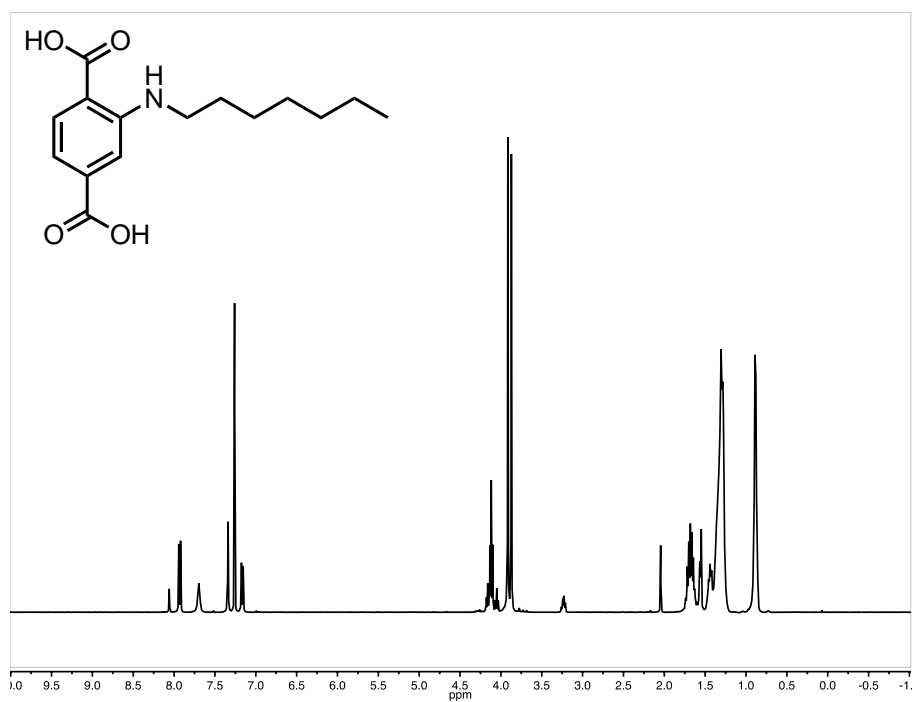
Figure B-92: ^{1}H NMR spectra (400 MHz, CDCl$_3$, 25 ℃) of compound 1g.
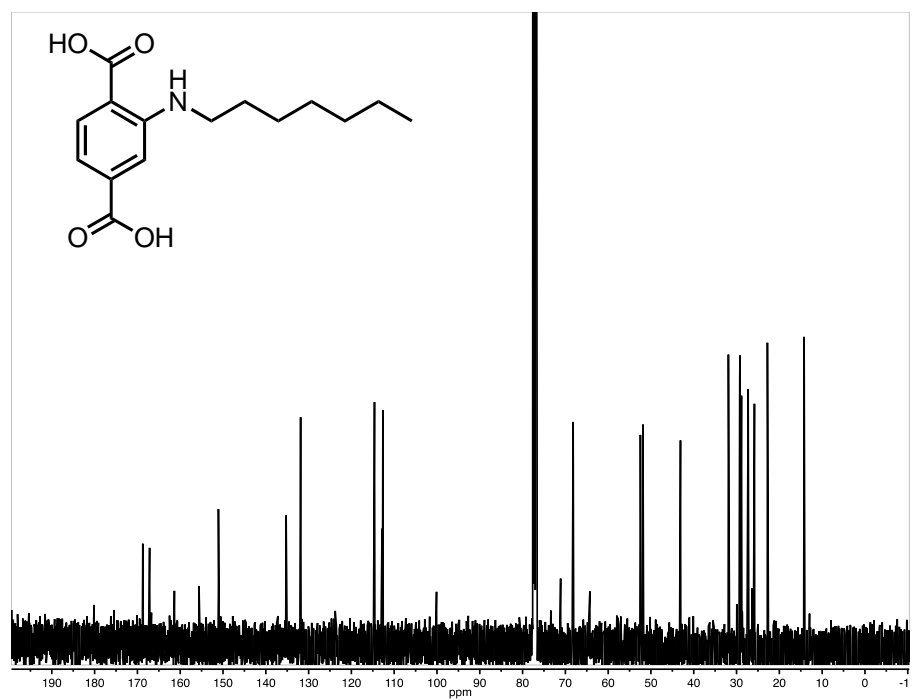
Figure B-93: ^{13}C NMR spectra (100 MHz, CDCl$_3$, 25 ℃) of compound 1g.
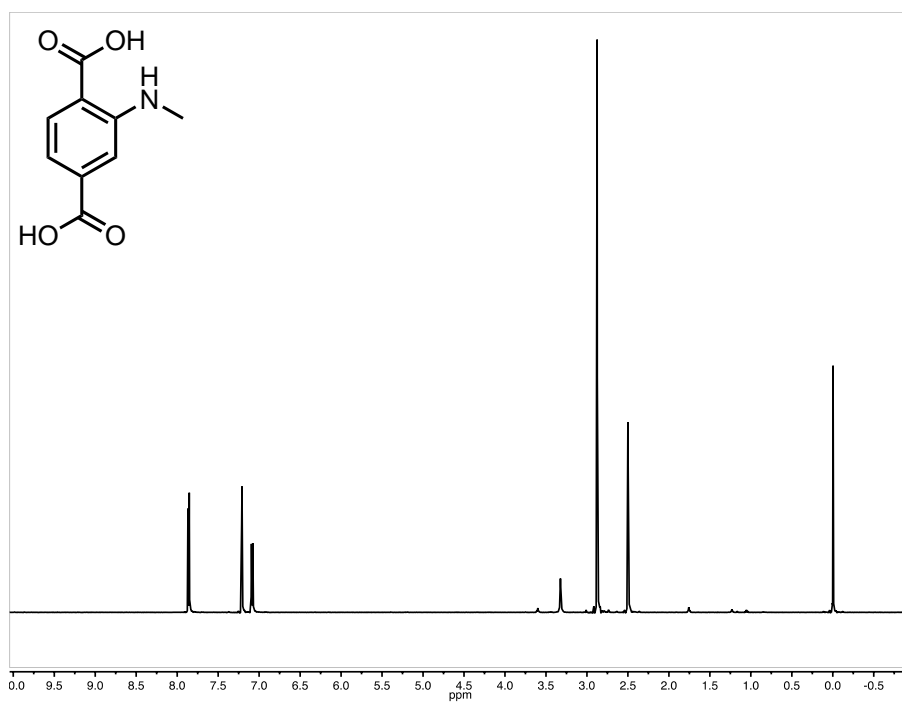
Figure B-94: ^{1}H NMR spectra (400 MHz, DMSO-d$_6$, 25 ºC) of compound 2a.
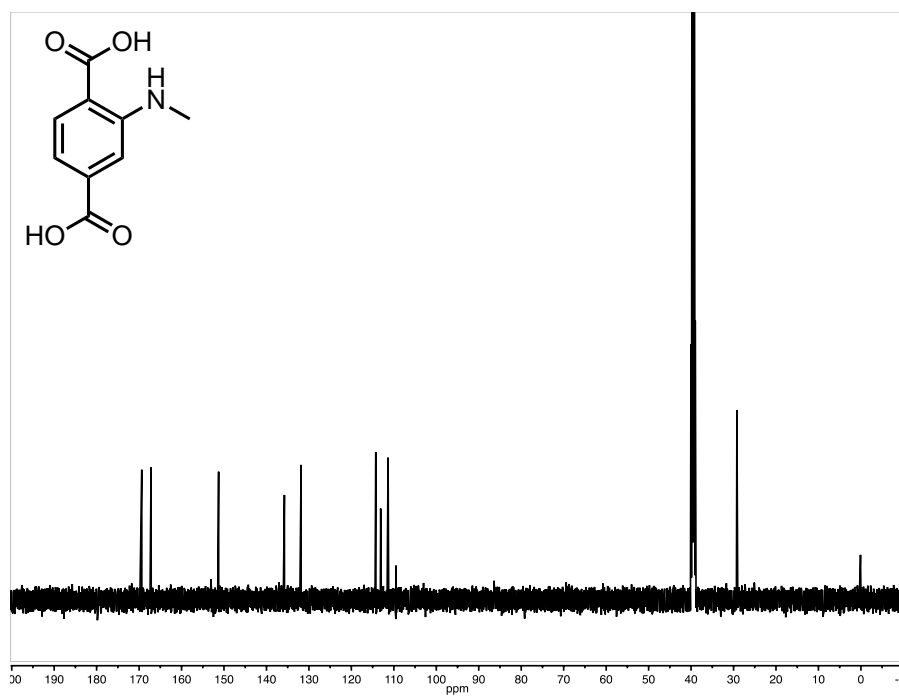
Figure B-95: ^{13}C NMR spectra (100 MHz, DMSO-d$_6$, 25 ºC) of compound 2a.
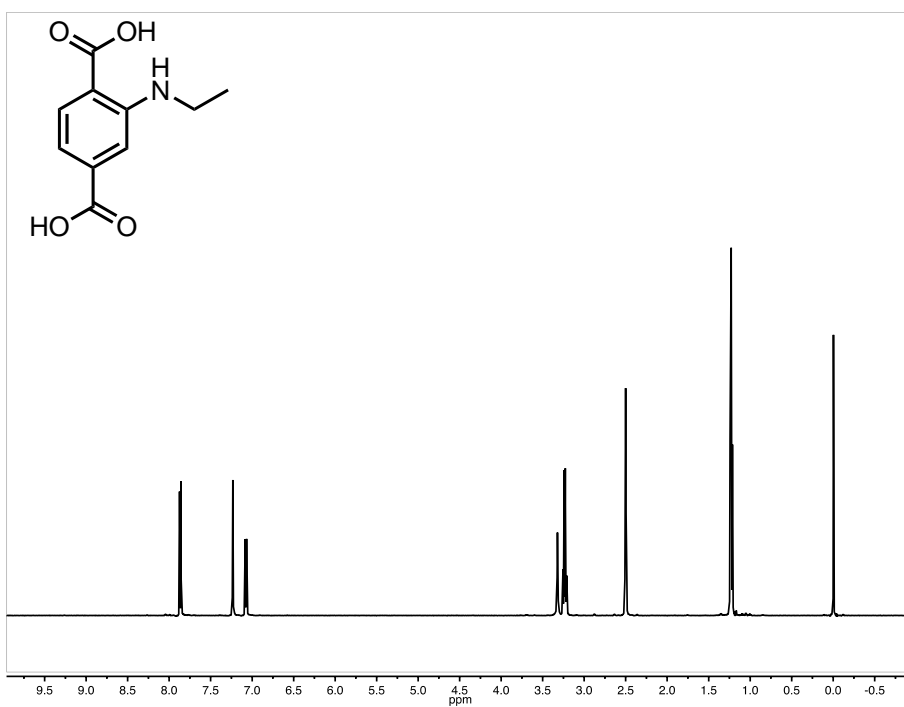
Figure B-96: ^{1}H NMR spectra (400 MHz, DMSO-d$_6$, 25 ºC) of compound 2b.
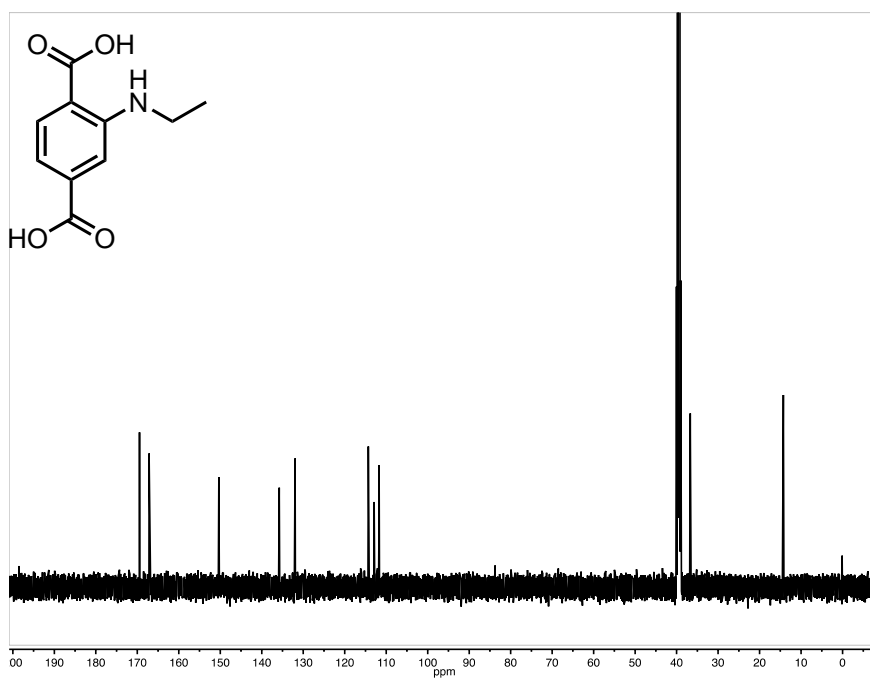
Figure B-97: ^{13}C NMR spectra (100 MHz, DMSO-d$_6$, 25 ºC) of compound 2b.
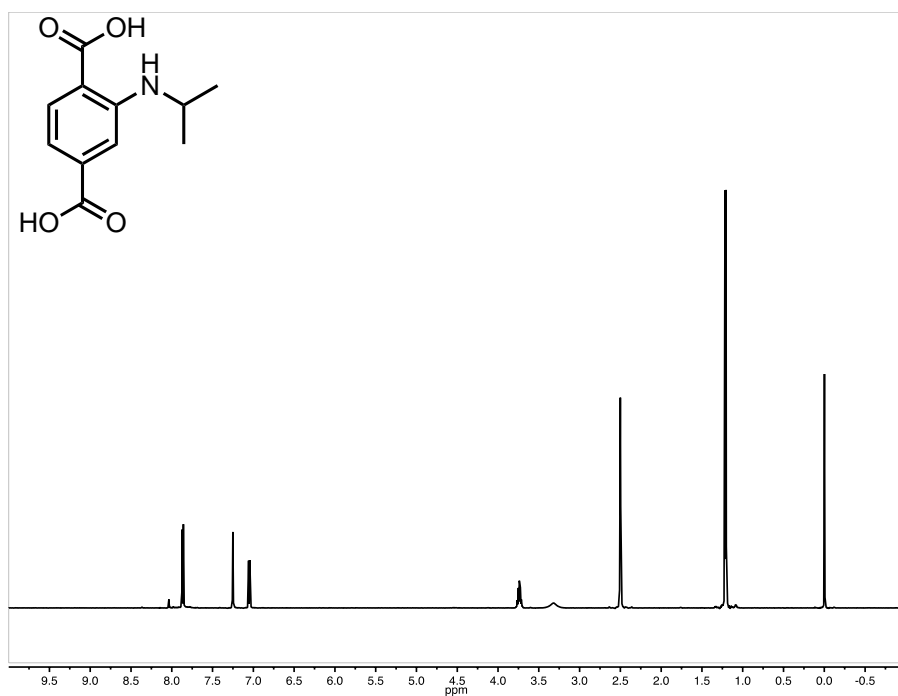
Figure B-98: ^{1}H NMR spectra (400 MHz, DMSO-d$_6$, 25 ºC) of compound 2c.
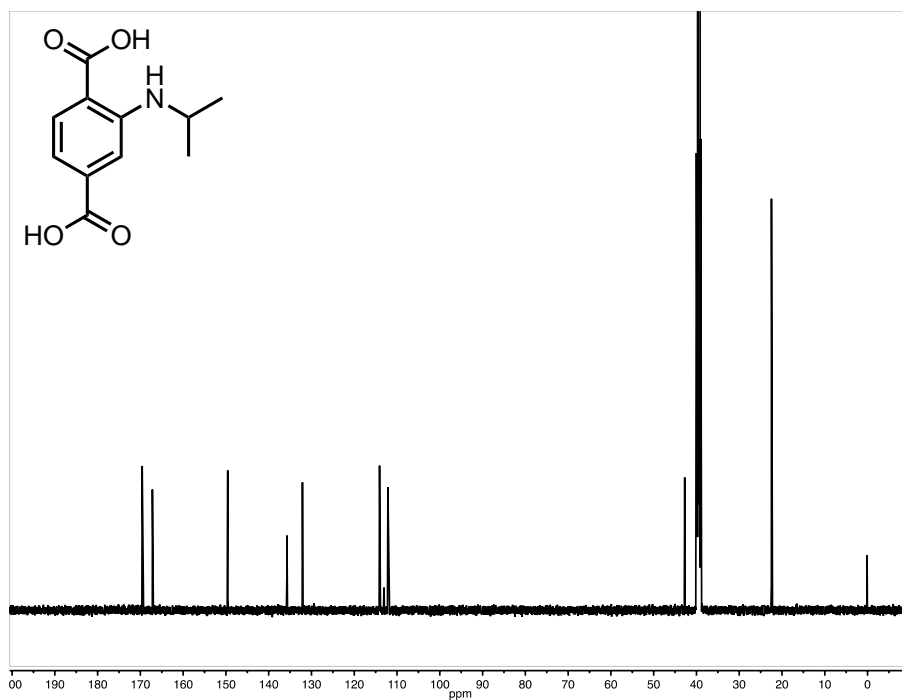
Figure B-99: ^{13}C NMR spectra (100 MHz, DMSO-d$_6$, 25 ºC) of compound 2c.
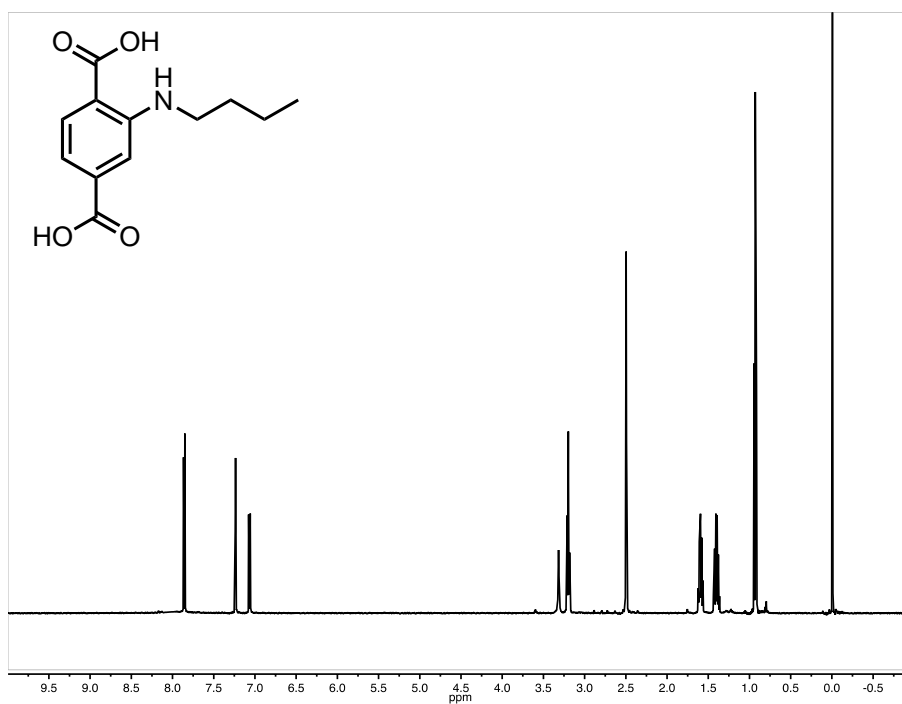
Figure B-100: ^{1}H NMR spectra (400 MHz, DMSO-d$_6$, 25 °C) of compound 2d.
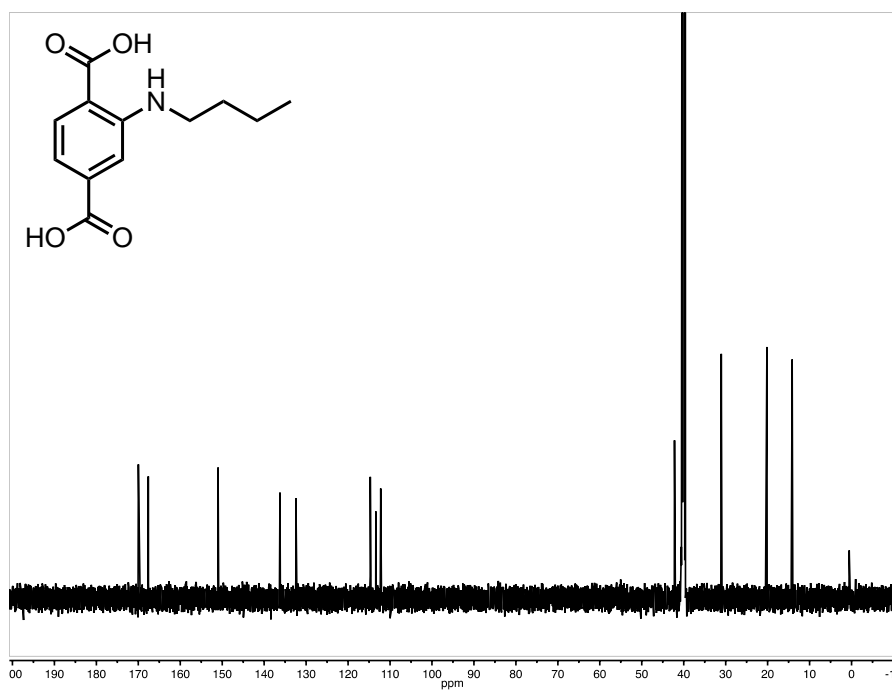
Figure B-101: ^{13}C NMR spectra (100 MHz, DMSO-d$_6$, 25 °C) of compound 2d.
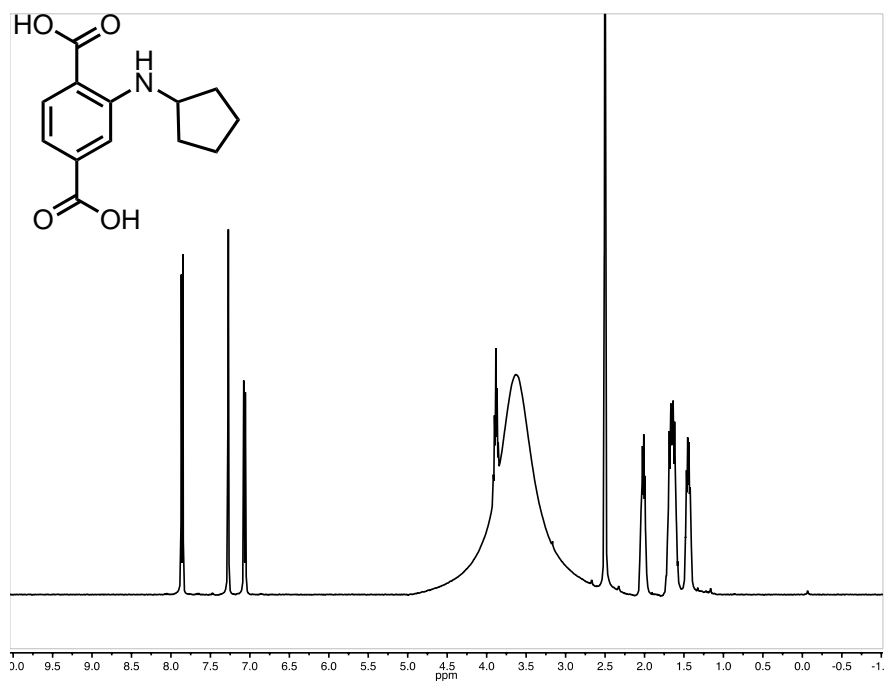
Figure B-102: ^{1}H NMR spectra (400 MHz, DMSO-d$_6$, 25 ºC) of compound 2e. Broad signal at 3.3 ppm corresponds to residual water.
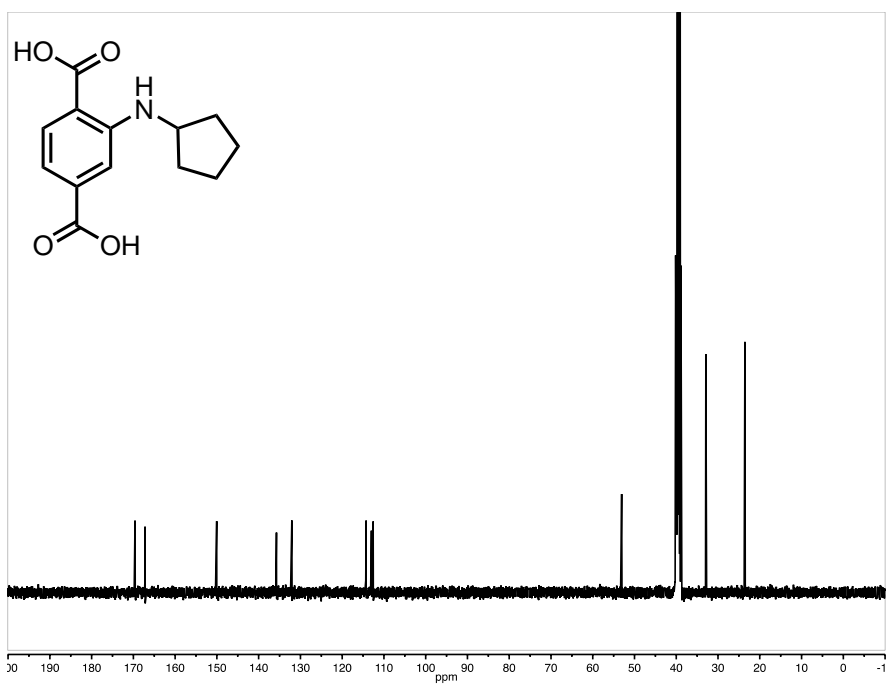
Figure B-103: ^{13}C NMR spectra (100 MHz, DMSO-d$_6$, 25 ºC) of compound 2e.
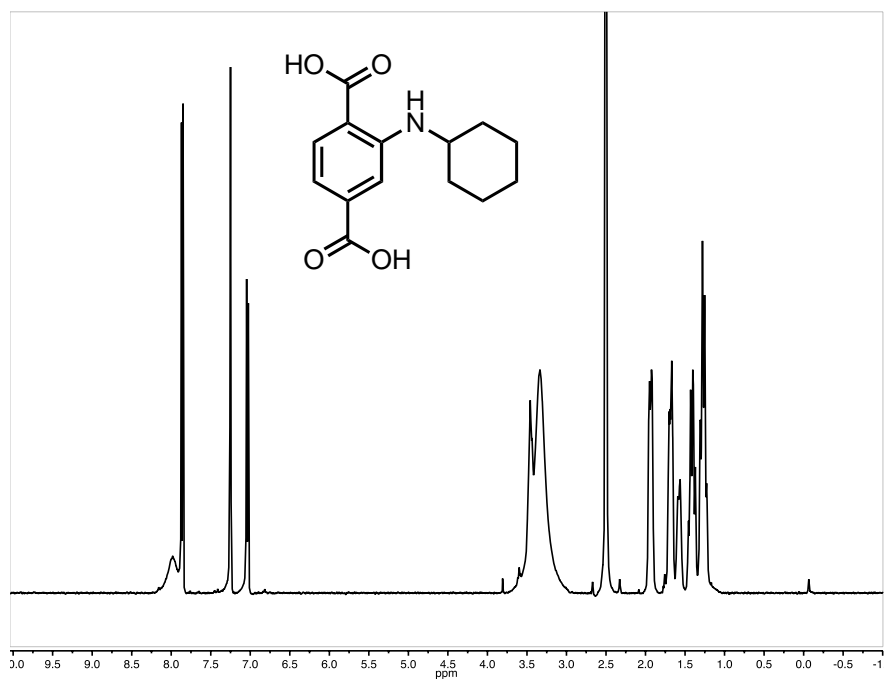
Figure B-104: ^{1}H NMR spectra (400 MHz, DMSO-d$_6$, 25 ºC) of compound 2f. Broad signal at 3.3 ppm corresponds to residual water.
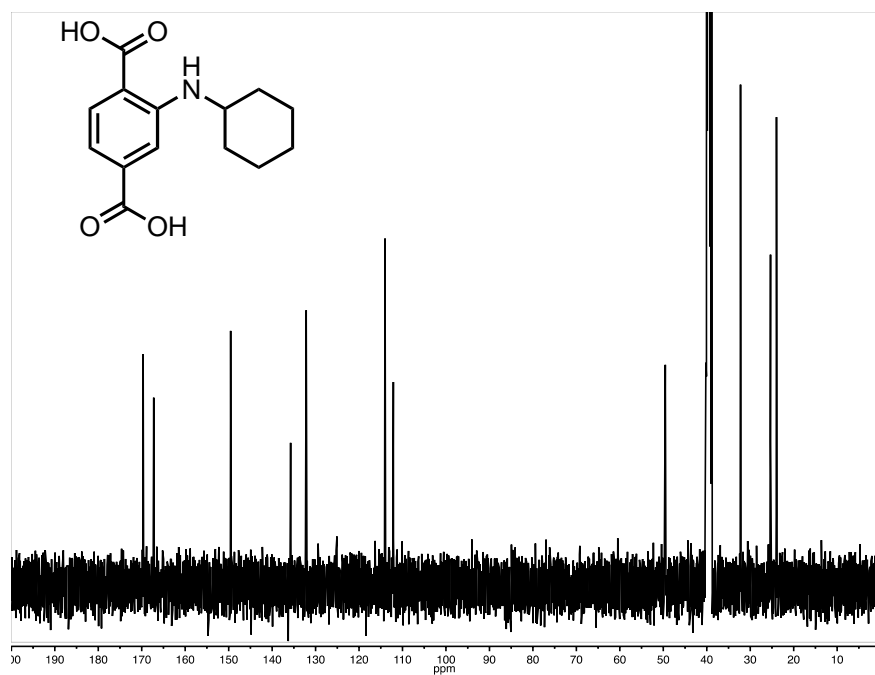
Figure B-105: ^{13}C NMR spectra (100 MHz, DMSO-d$_6$, 25 ºC) of compound 2f.
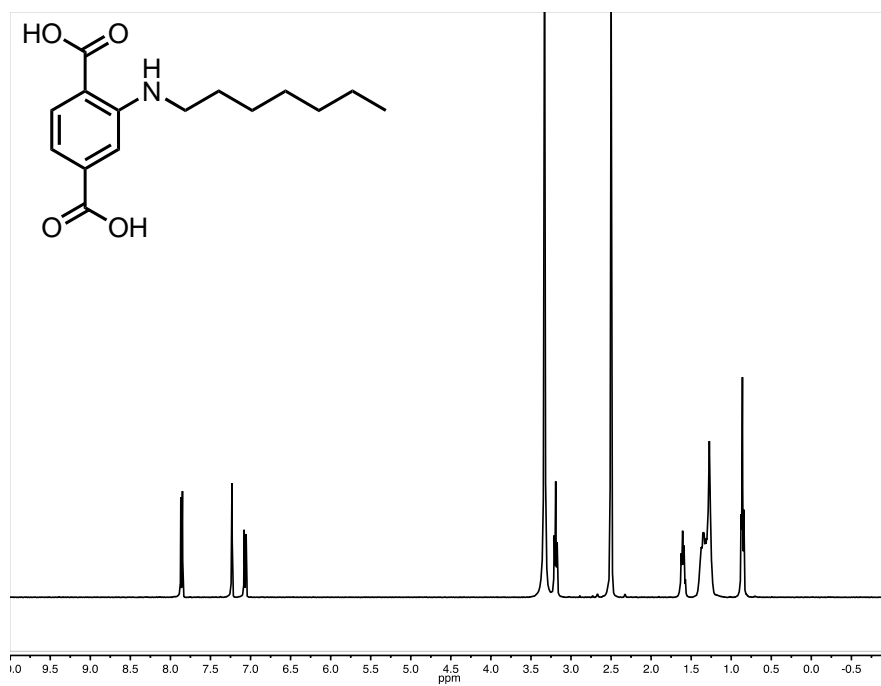
Figure B-106: ^{1}H NMR spectra (400 MHz, DMSO-d$_6$, 25 ºC) of compound 2g.
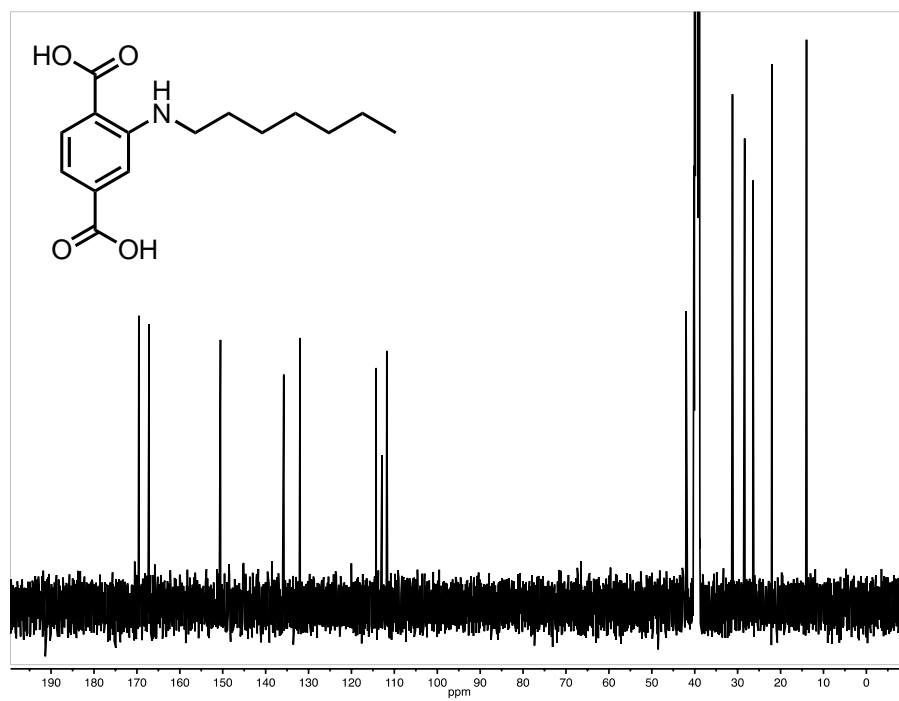
Figure B-107: ^{13}C NMR spectra (100 MHz, DMSO-d$_6$, 25 ºC) of compound 2g.
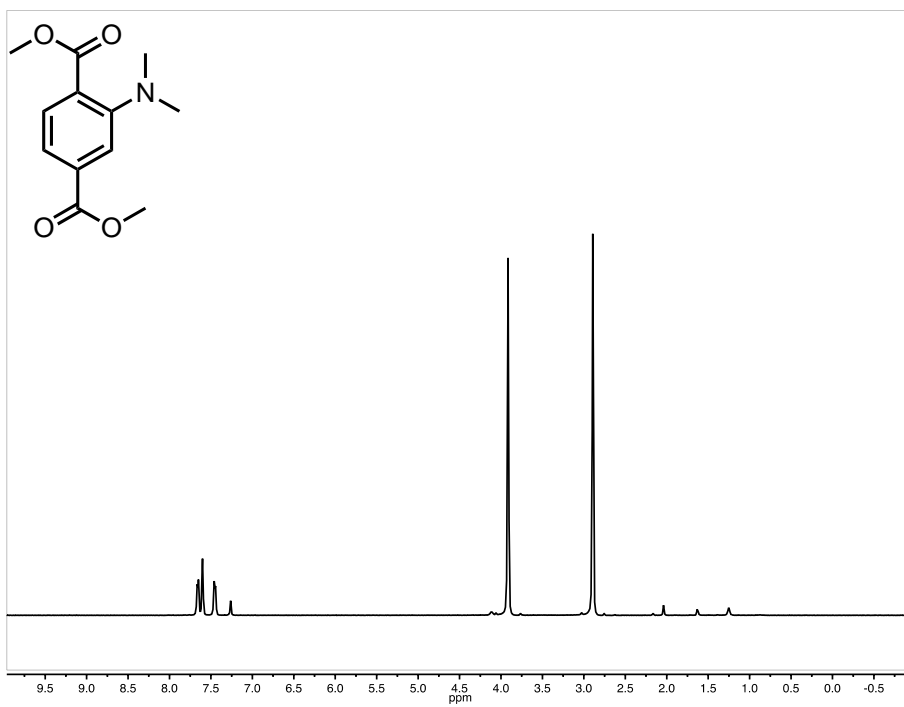
Figure B-108: ^{1}H NMR spectra (400 MHz, CDCl$_3$, 25 ºC) of compound S1.
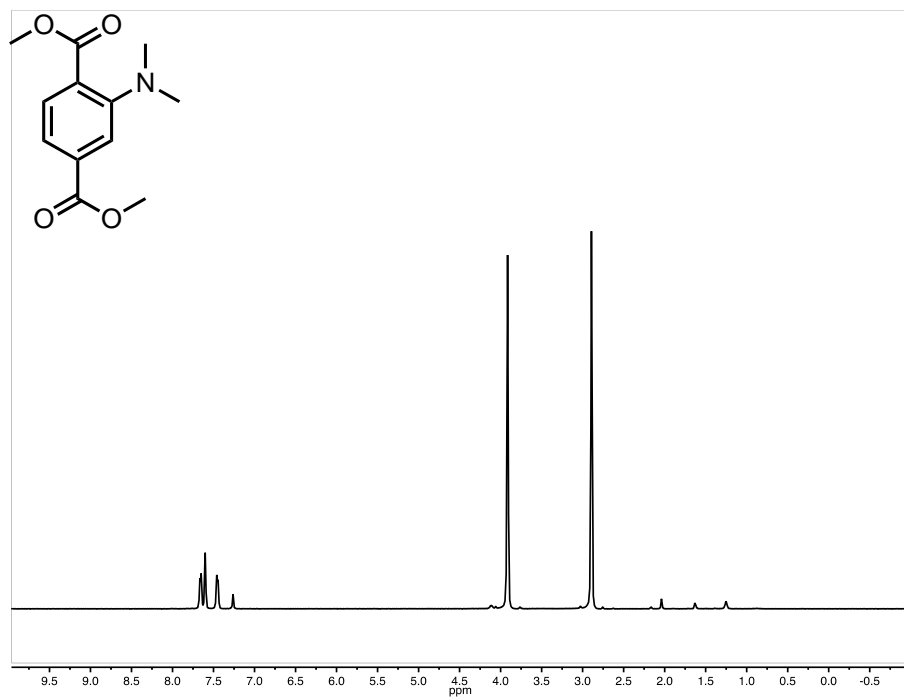
Figure B-109: ^{13}C NMR spectra (100 MHz, CDCl$_3$, 25 ºC) of compound S1.
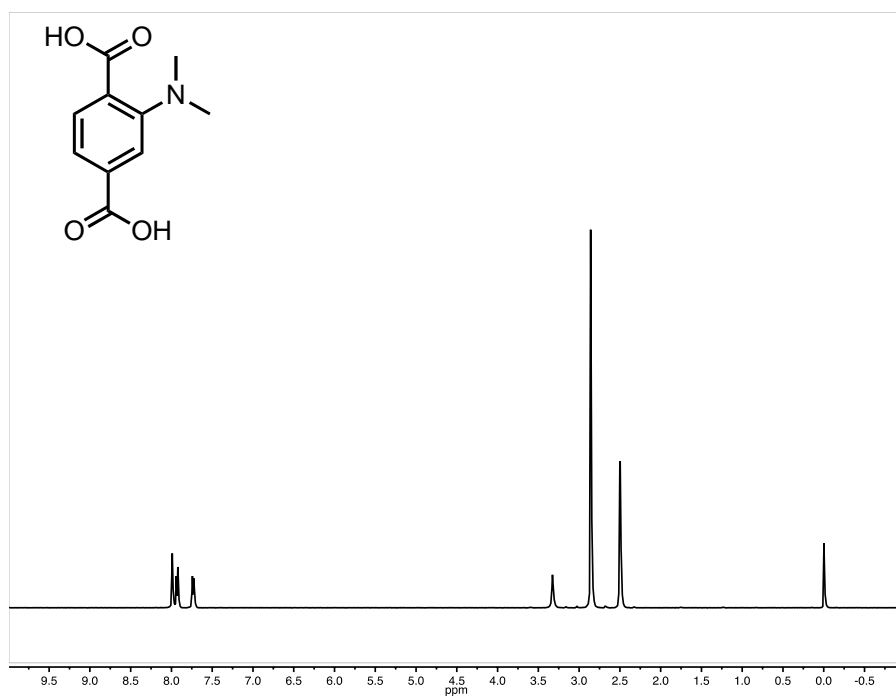
Figure B-110: ^{1}H NMR spectra (400 MHz, DMSO-d$_6$, 25 ºC) of compound 3.
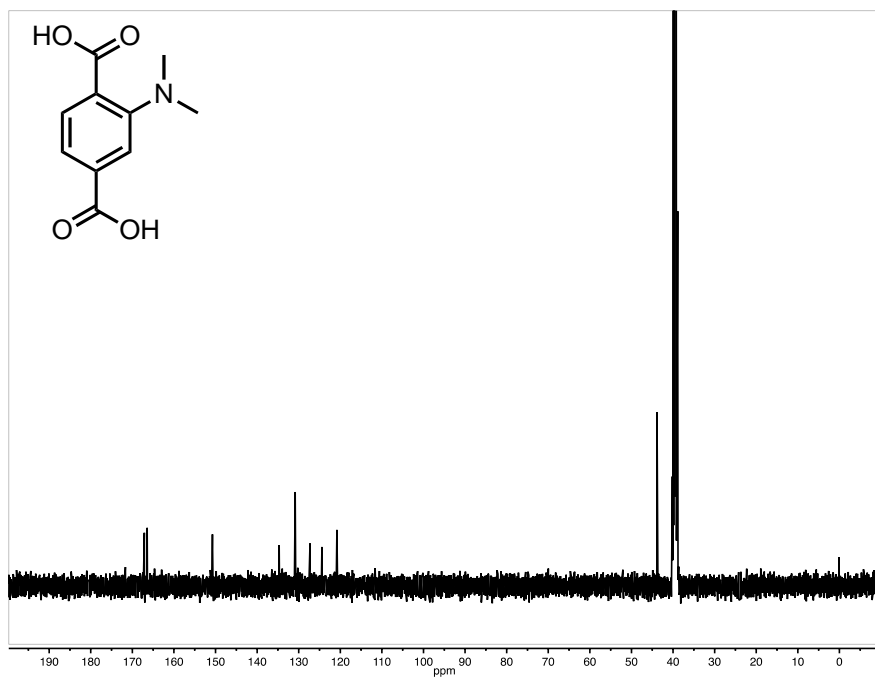
Figure B-111: ^{13}C NMR spectra (100 MHz, DMSO-d$_6$, 25 ºC) of compound 3.

307

APPENDIX C: **SUPPLEMENTARY MATERIAL FOR CHAPTER 4**

C.1 <u>Powder X-ray Diffractograms</u>
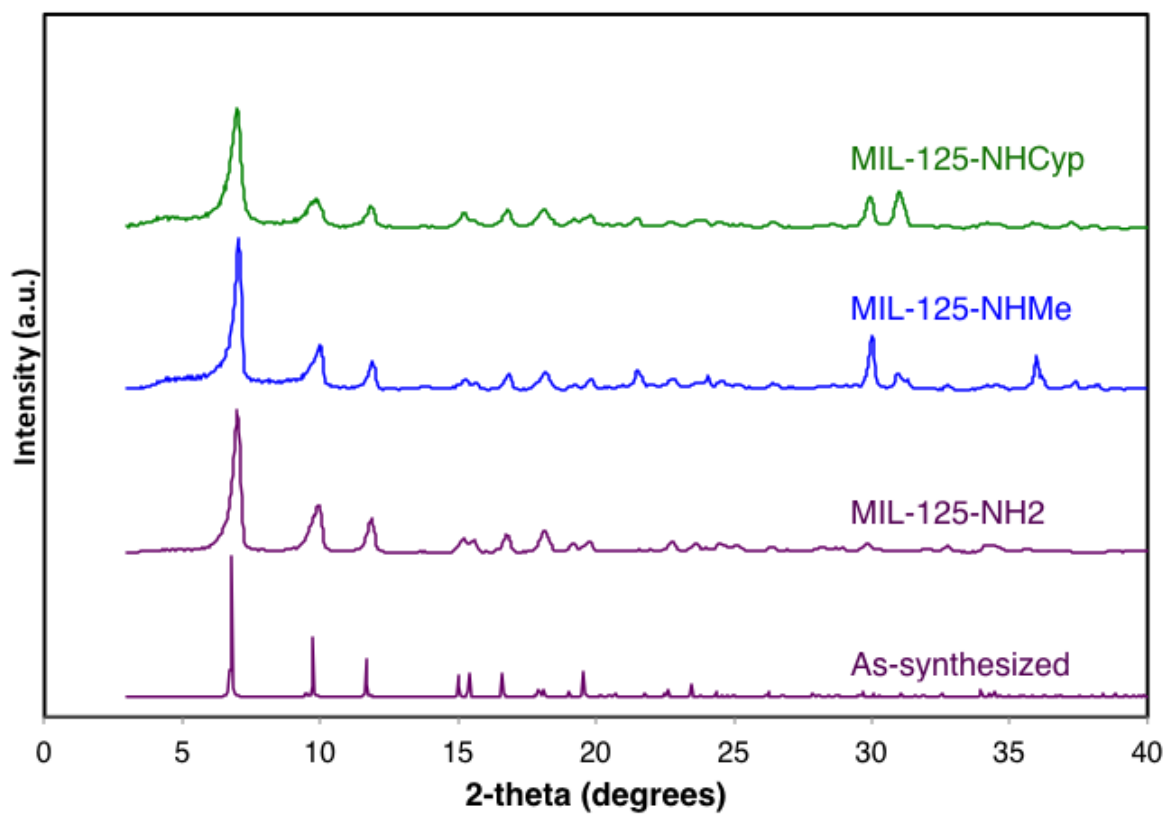
Figure C-1: PXRD of **MIL-125-NH₂**, **MIL-125-NHMe**, and **MIL-125-NHCyp** in purple, green, and blue with corresponding simulated **MIL-125-NH₂**.
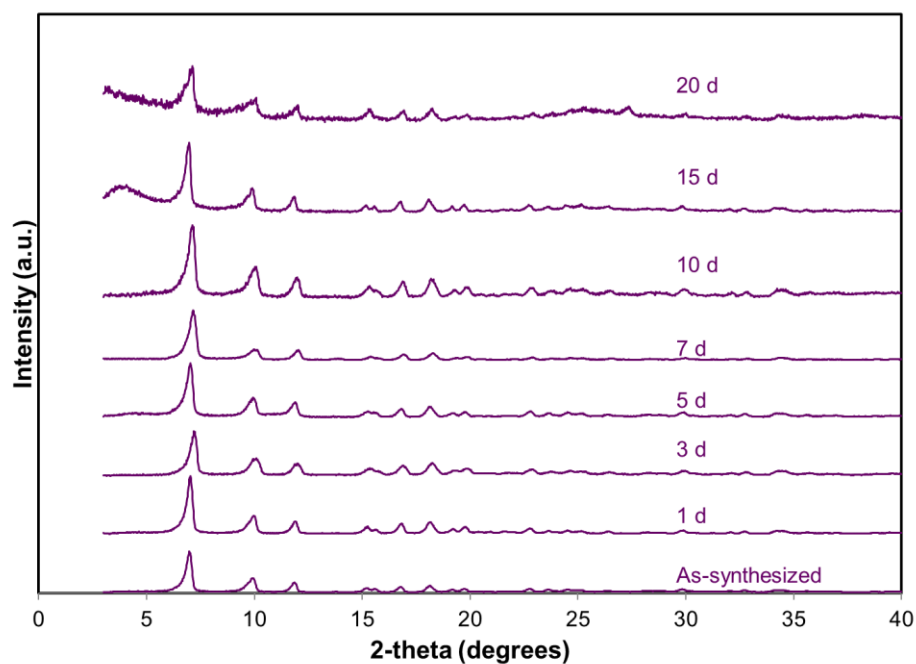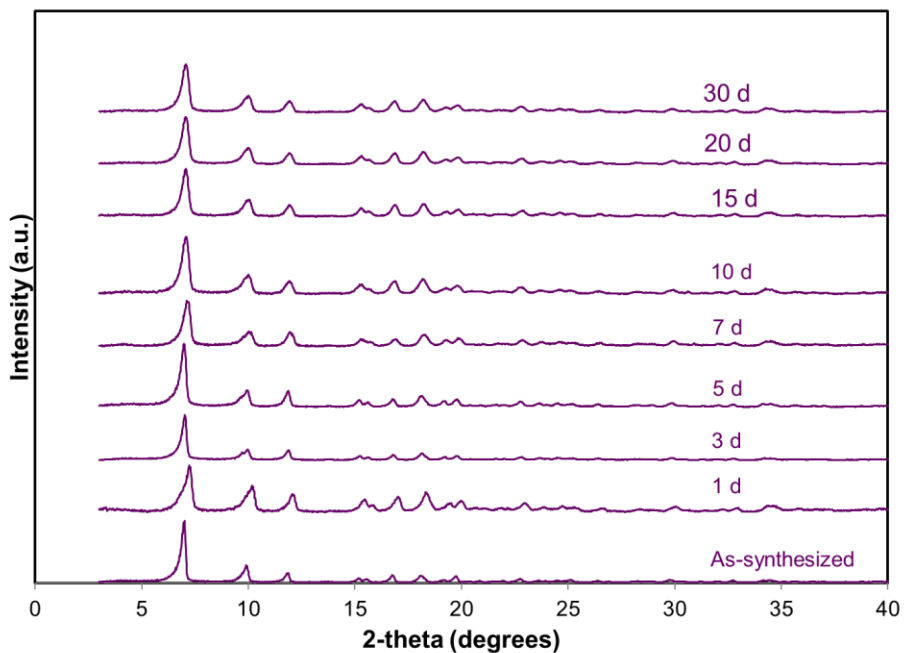
Figure C-2: PXRD of **MIL-125-NH₂** in aqueous environment, pH 7, at rt. Days denoted on right increasing vertically.
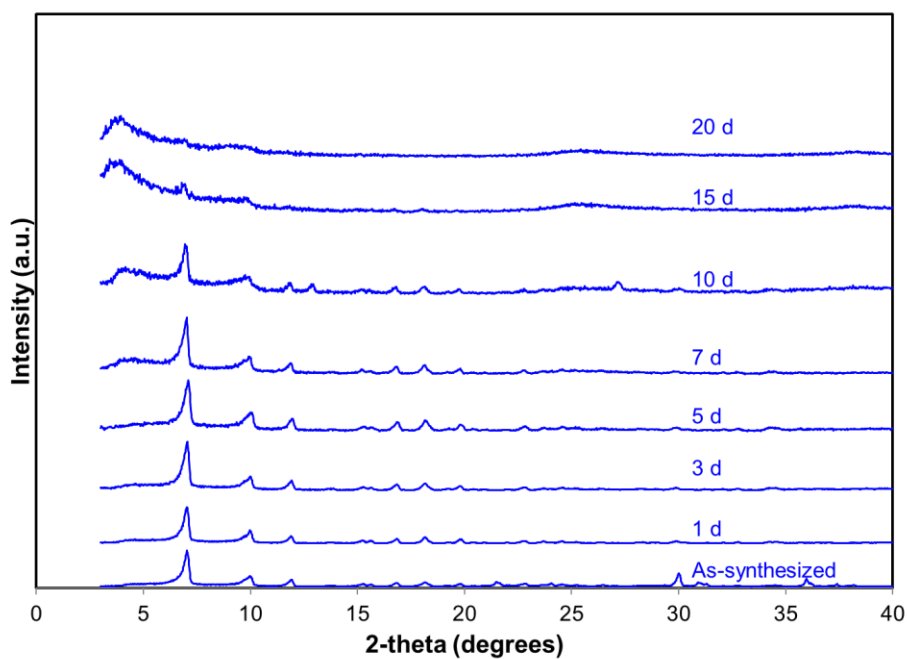

Figure C-3: PXRD **of MIL-125-NHMe** in aqueous environment, pH 7, at rt. Days denoted on right increasing vertically.
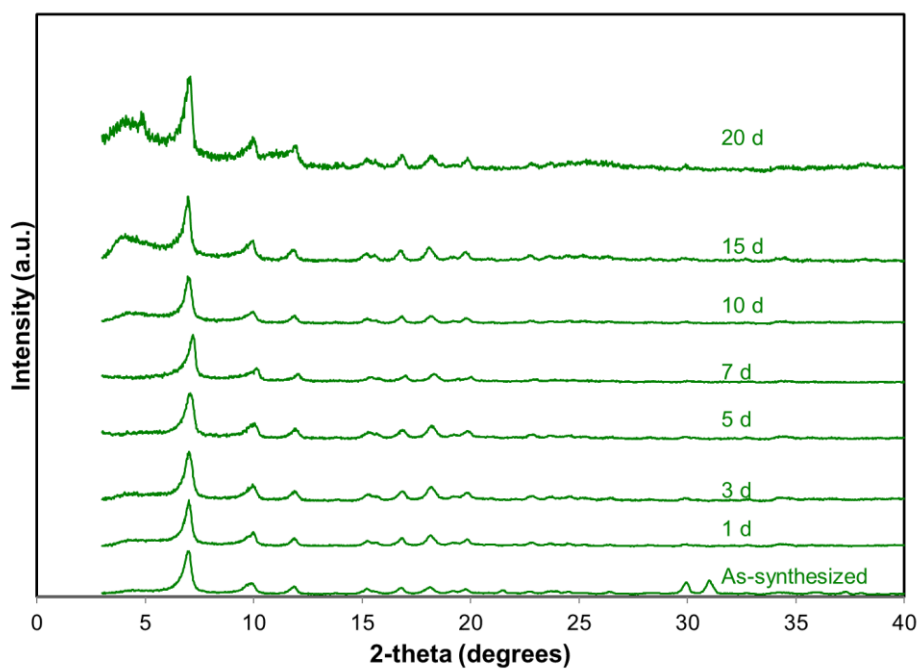
Figure C-4: PXRD of **MIL-125-NHCyp** in aqueous environment, pH 7, at rt. Days denoted on right increasing vertically.
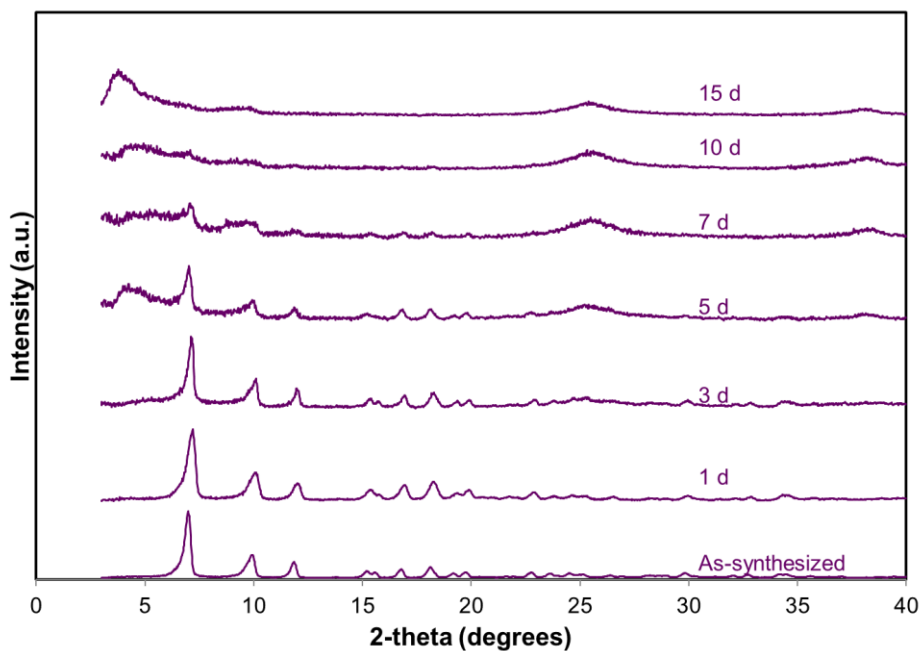

Figure C-5: PXRD of **MIL-125-NH₂** in aqueous environment, pH 7, at 50 °C. Days denoted on right increasing vertically.
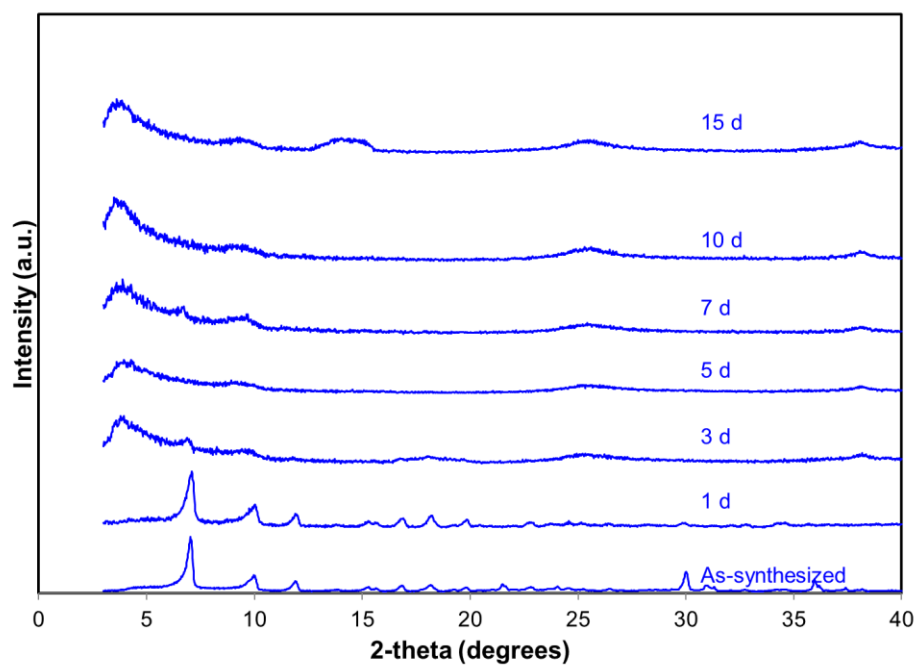
Figure C-6: PXRD of **MIL-125-NHMe** in aqueous environment, pH 7, at 50 ºC. Days denoted on right increasing vertically.
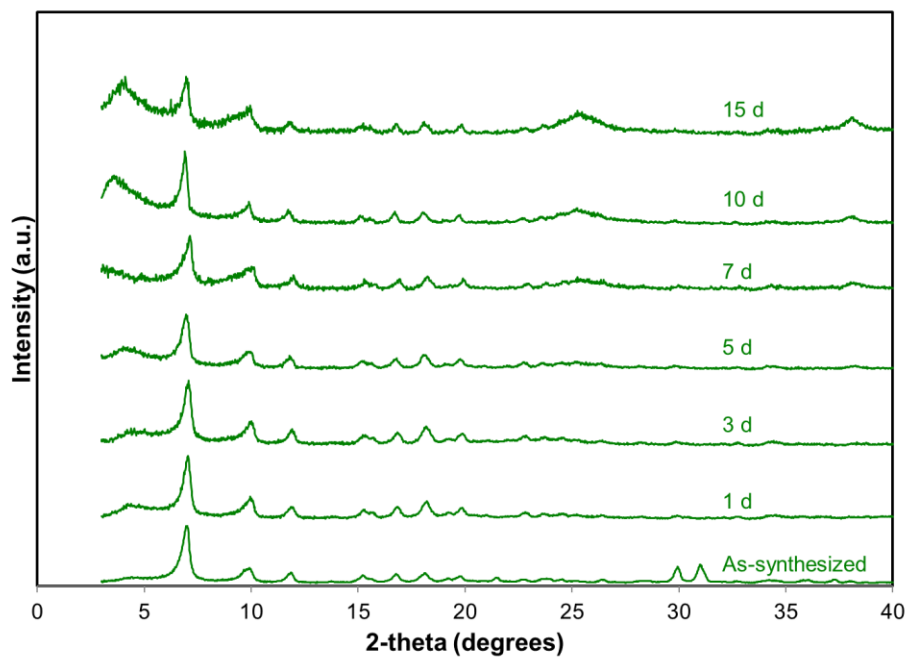
Figure C-7: PXRD of **MIL-125-NHCyp** in aqueous environment, pH 7, at 50 ºC. Days denoted on right increasing vertically.
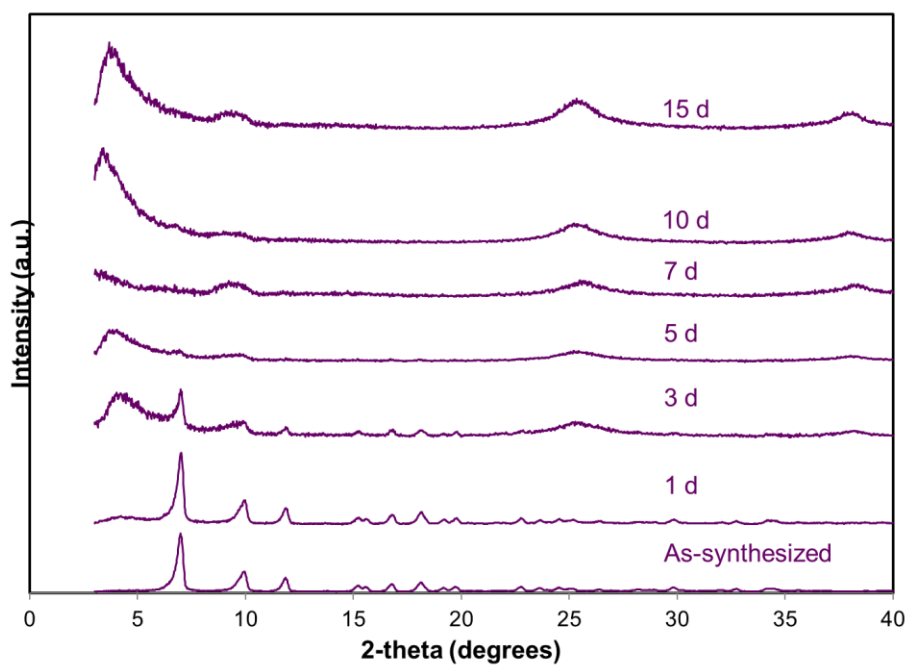
Figure C-8: PXRD of **MIL-125-NH₂** in aqueous environment, pH 7, at 70 °C. Days denoted on right increasing vertically.
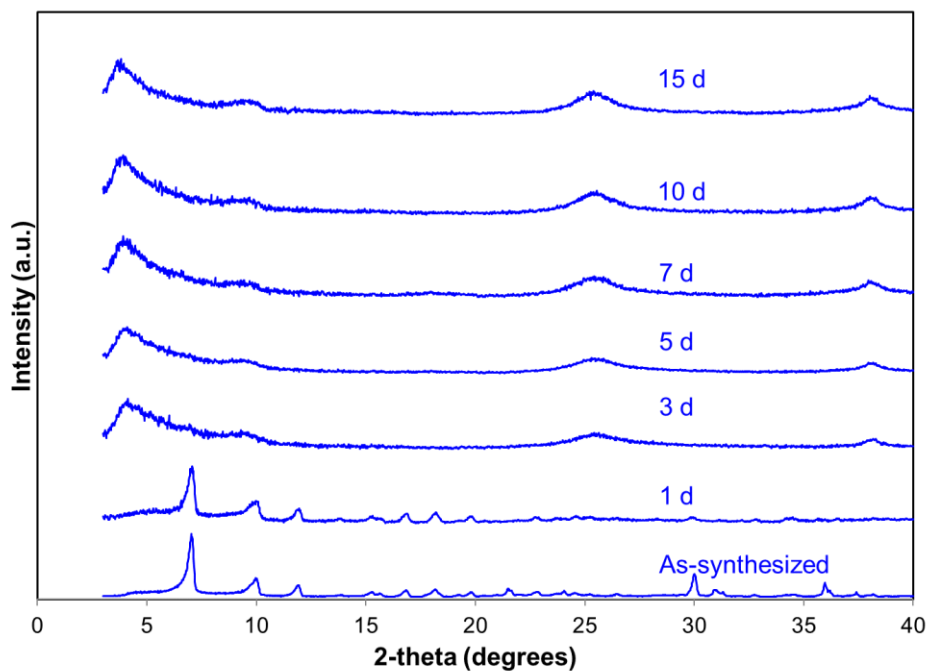
Figure C-9: PXRD of **MIL-125-NHMe** in aqueous environment, pH 7, at 70 °C. Days denoted on right increasing vertically.
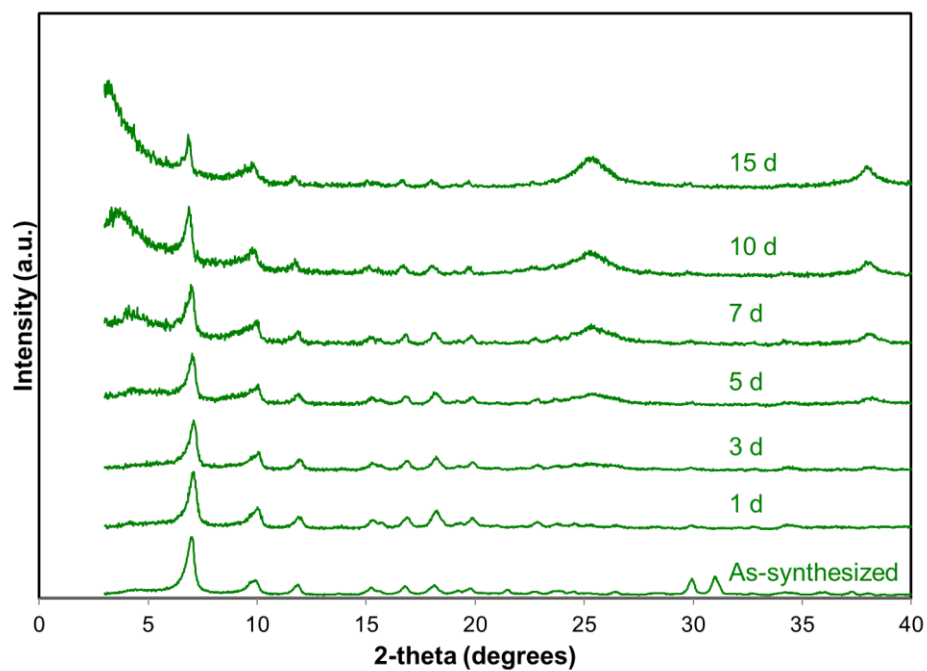
Figure C-10: PXRD of **MIL-125-NHCyp** in aqueous environment, pH 7, at 70 °C. Days denoted on right increasing vertically.
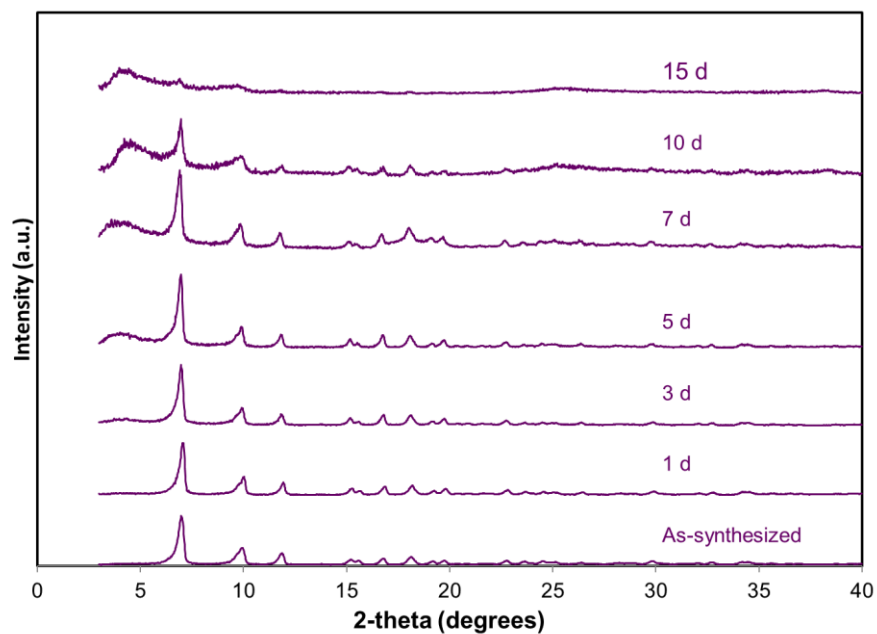
Figure C-11: PXRD of **MIL-125-NH₂** in aqueous environment, pH 9 (NaOH), at rt. Days denoted on right increasing vertically.
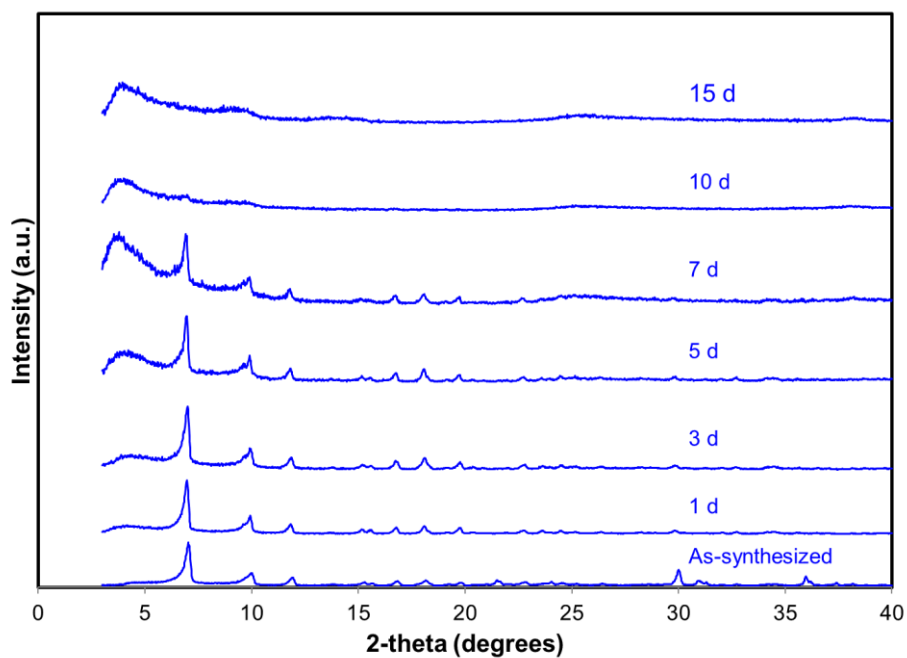
Figure C-12: PXRD of **MIL-125-NHMe** in aqueous environment, pH 9 (NaOH), at rt. Days denoted on right increasing vertically.
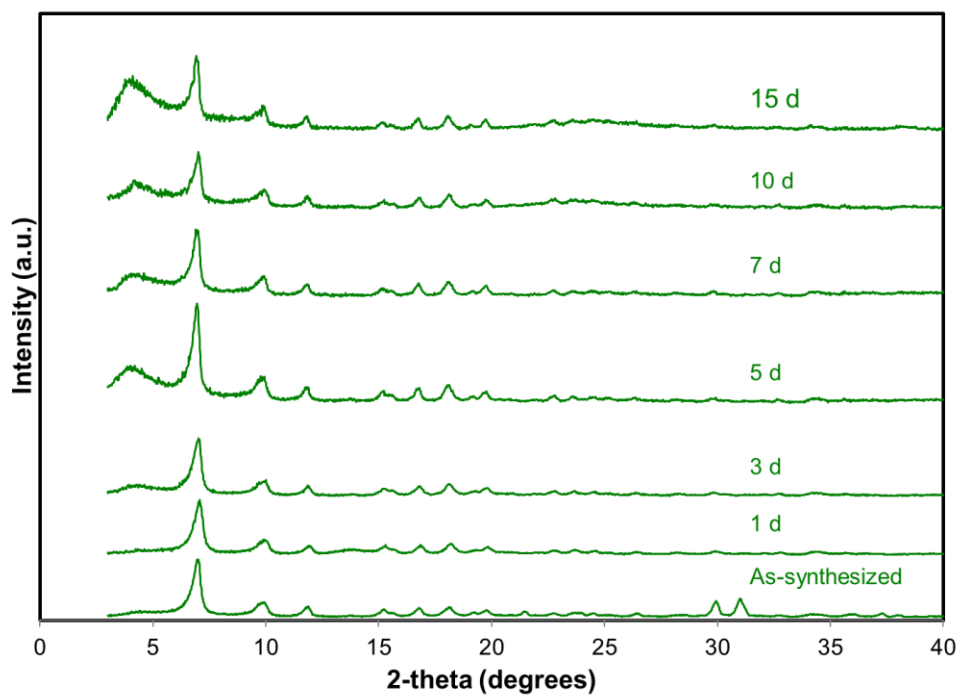
Figure C-13: PXRD of **MIL-125-NHCyp** in aqueous environment, pH 9 (NaOH), at rt. Days denoted on right increasing vertically.
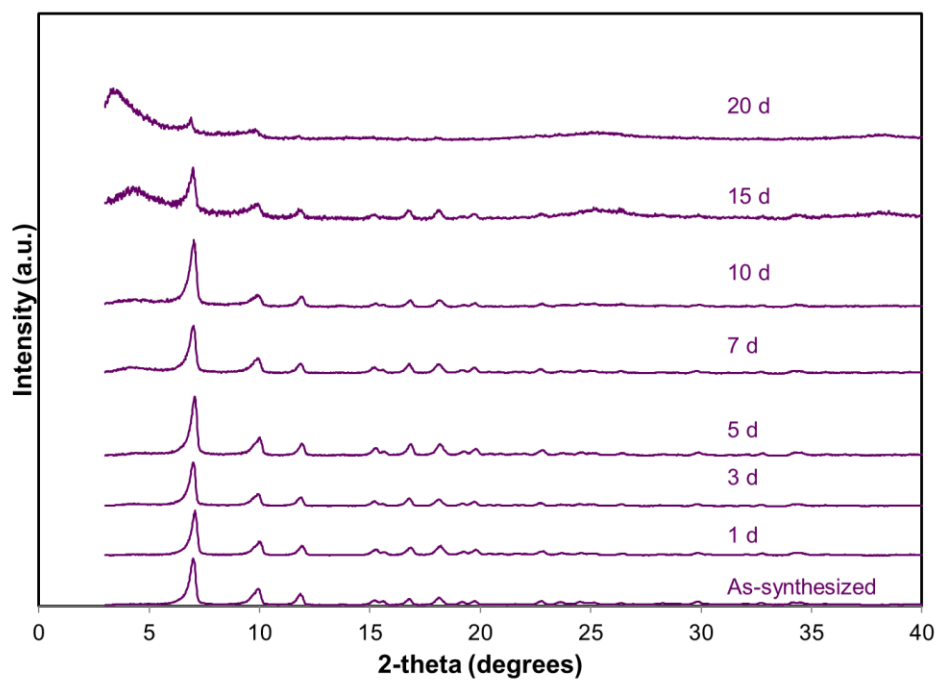
Figure C-14: PXRD of **MIL-125-NH₂** in aqueous environment, pH 4 (HCl), at rt. Days denoted on right increasing vertically.
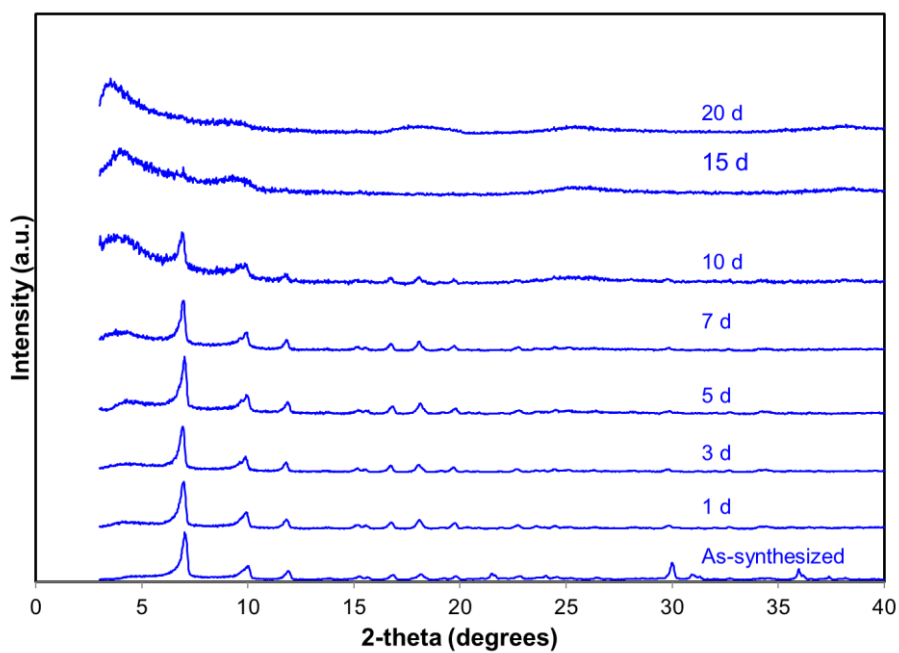
Figure C-15: PXRD of **MIL-125-NHMe** in aqueous environment, pH 4 (HCl), at rt. Days denoted on right increasing vertically.
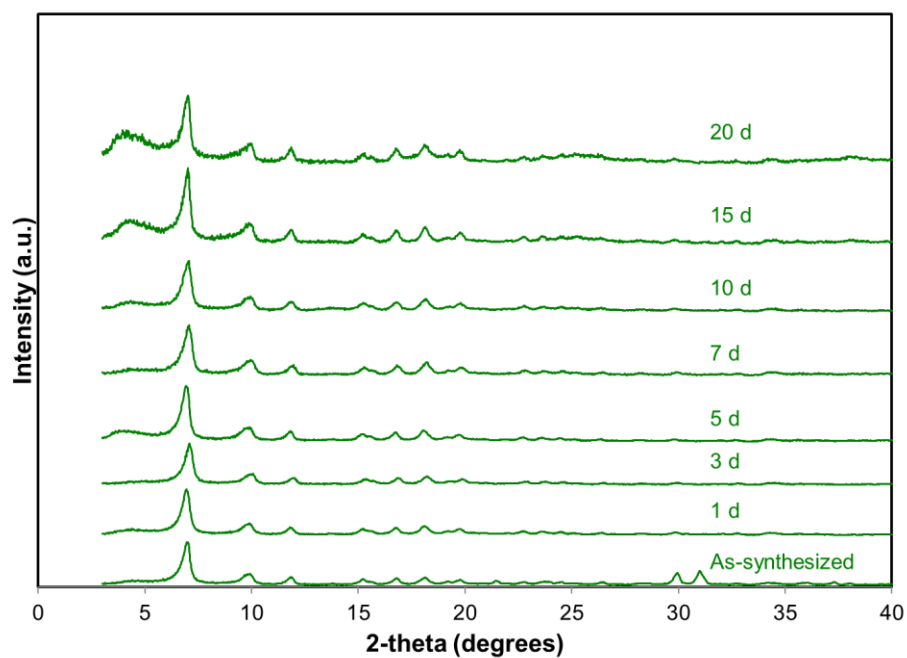
Figure C-16: PXRD of **MIL-125-NHCyp** in aqueous environment, pH 4(HCl), at rt. Days denoted on right increasing vertically.
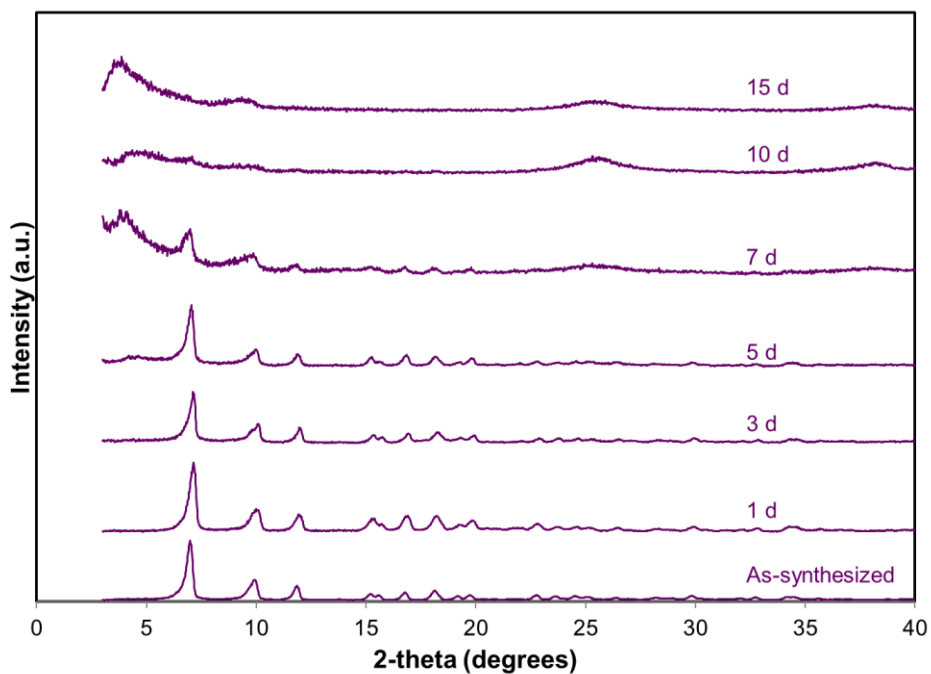
Figure C-17: PXRD of **MIL-125-NH₂** in aqueous environment, pH 1 (HCl), at rt. Days denoted on right increasing vertically.
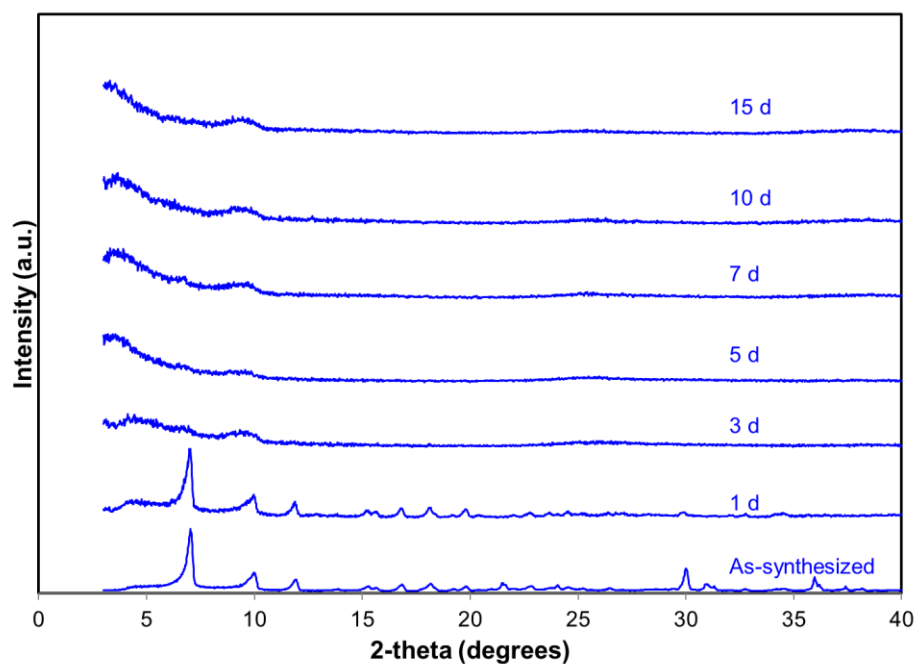
Figure C-18: PXRD of **MIL-125-NHMe** in aqueous environment, pH 1 (HCl), at rt. Days denoted on right increasing vertically.
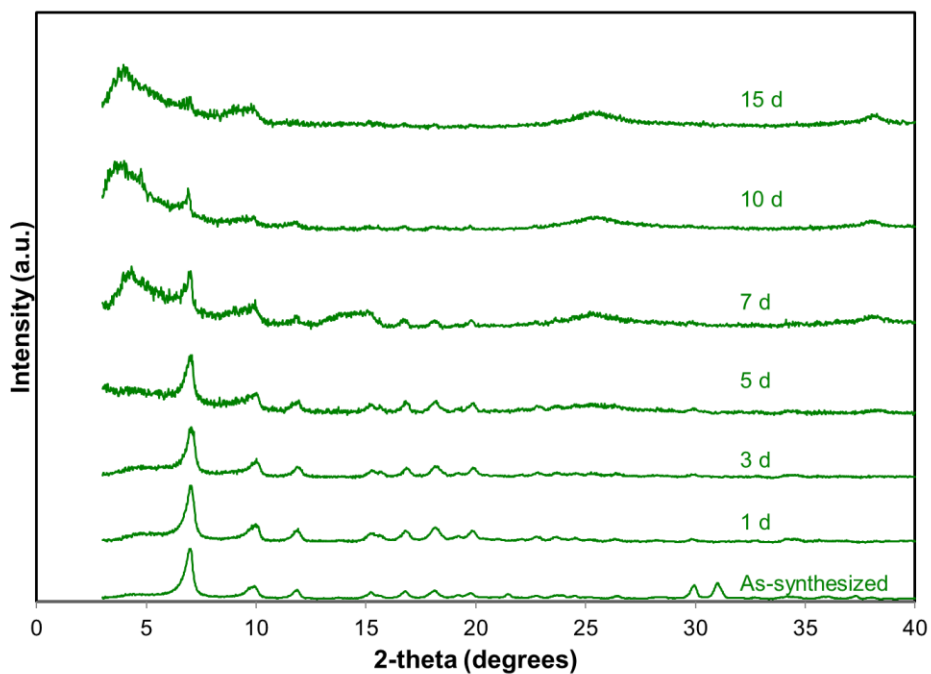
Figure C-19: PXRD of **MIL-125-NHCyp** in aqueous environment, pH 1 (HCl), at rt. Days denoted on right increasing vertically.
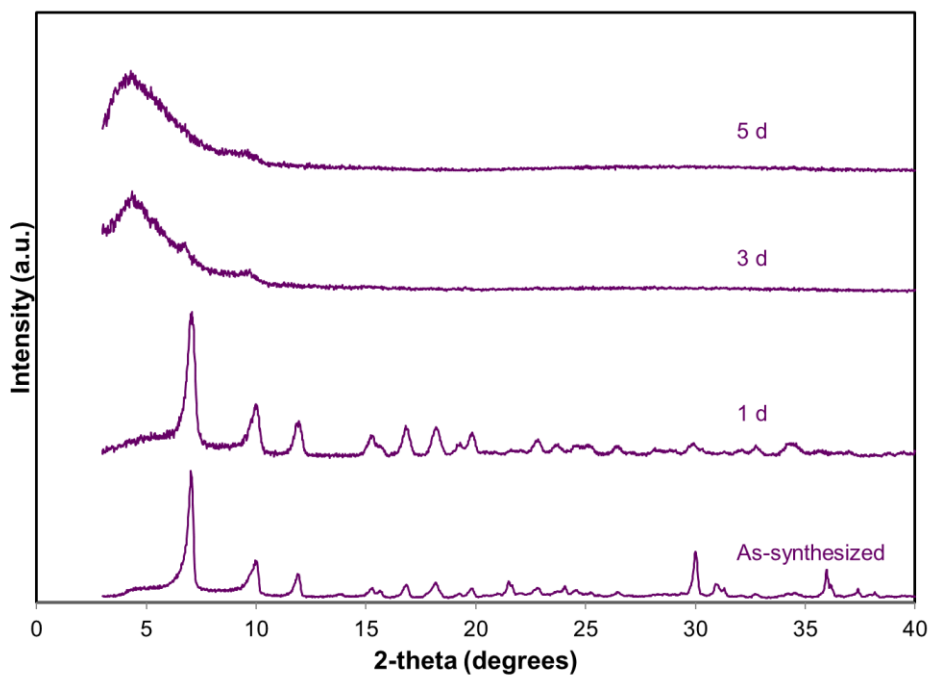
Figure C-20: PXRD of **MIL-125-NH₂** in aqueous environment, 0.15M TEOA, at rt. Days denoted on right increasing vertically.
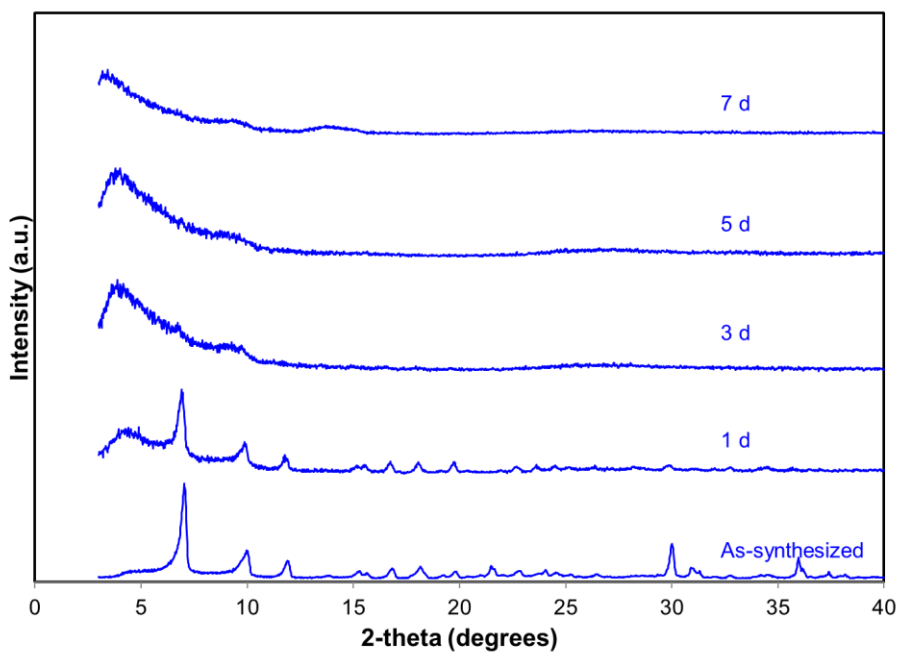
Figure C-21: PXRD of **MIL-125-NHMe** in aqueous environment, 0.15M TEOA, at rt. Days denoted on right increasing vertically.
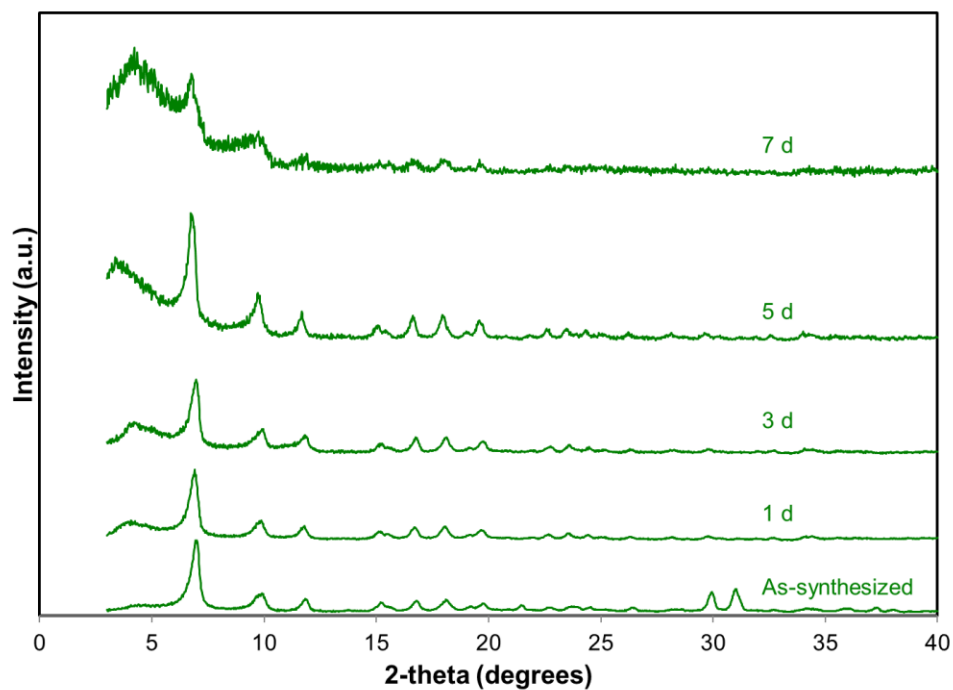
Figure C-22: PXRD of **MIL-125-NHCyp** in aqueous environment, 0.15M TEOA, at rt. Days denoted on right increasing vertically.
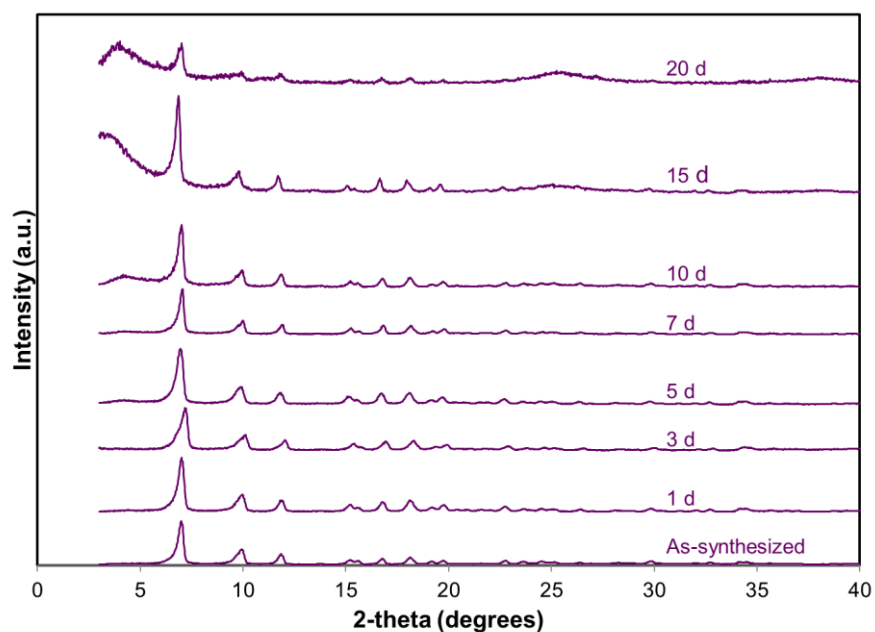
Figure C-23: PXRD of **MIL-125-NH$_2$** in aqueous environment, 0.15M AcOH, at rt. Days denoted on right increasing vertically.
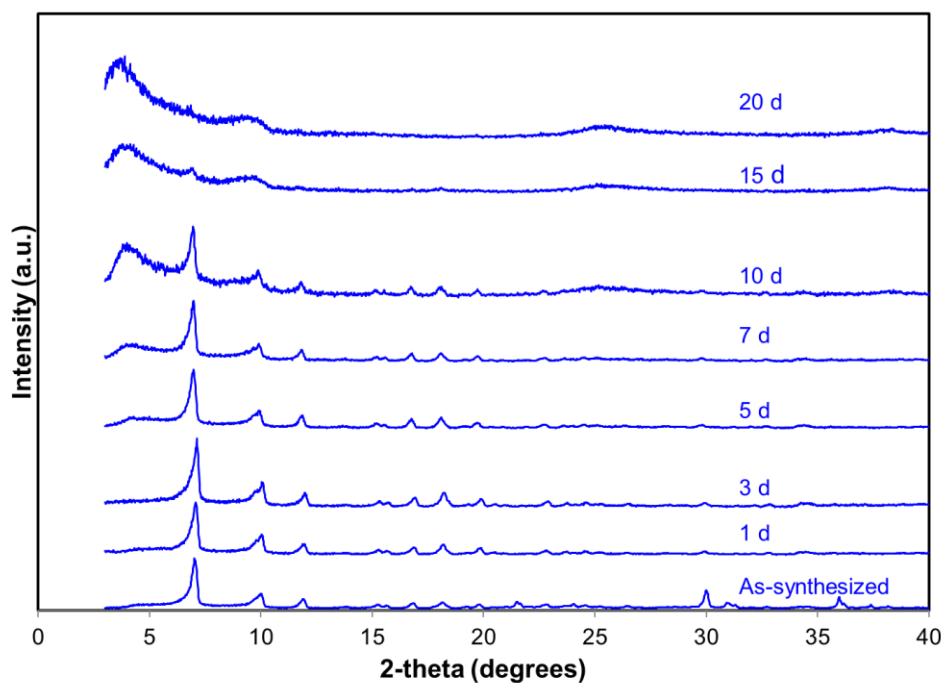
Figure C-24: PXRD of **MIL-125-NHMe** in aqueous environment, 0.15M AcOH, at rt. Days denoted on right increasing vertically.
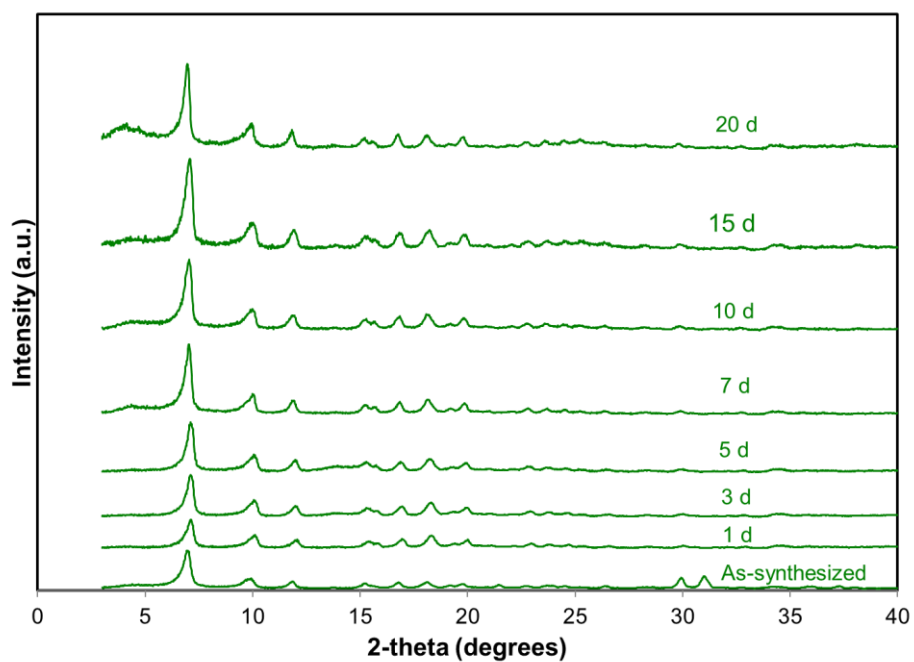
Figure C-25: PXRD of **MIL-125-NHCyp** in aqueous environment, 0.15M AcOH, at rt. Days denoted on right increasing vertically.
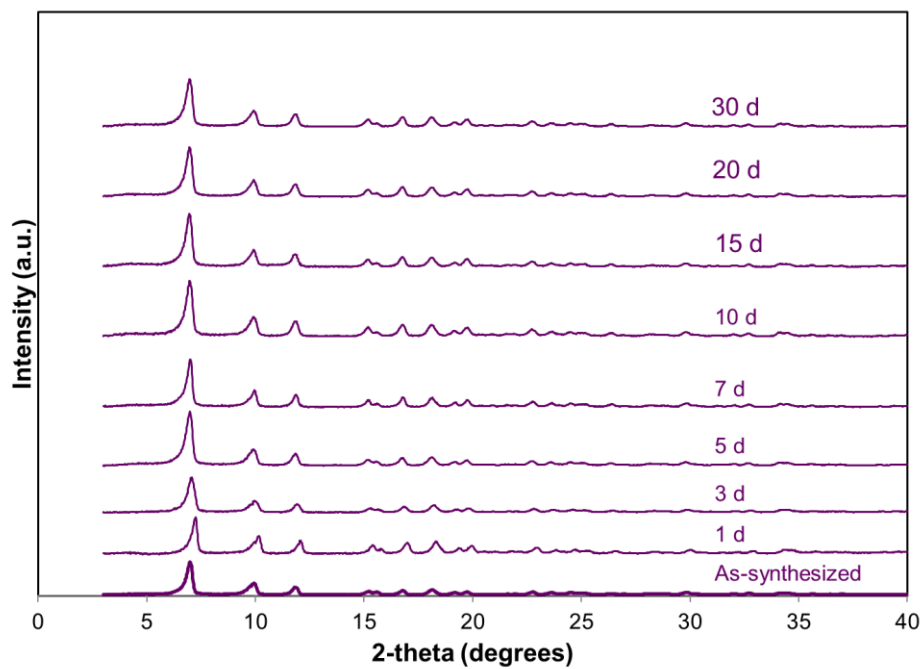
Figure C-26: PXRD of **MIL-125-NH₂** in MeCN, 0.15M TEOA, at rt. Days denoted on right increasing vertically.
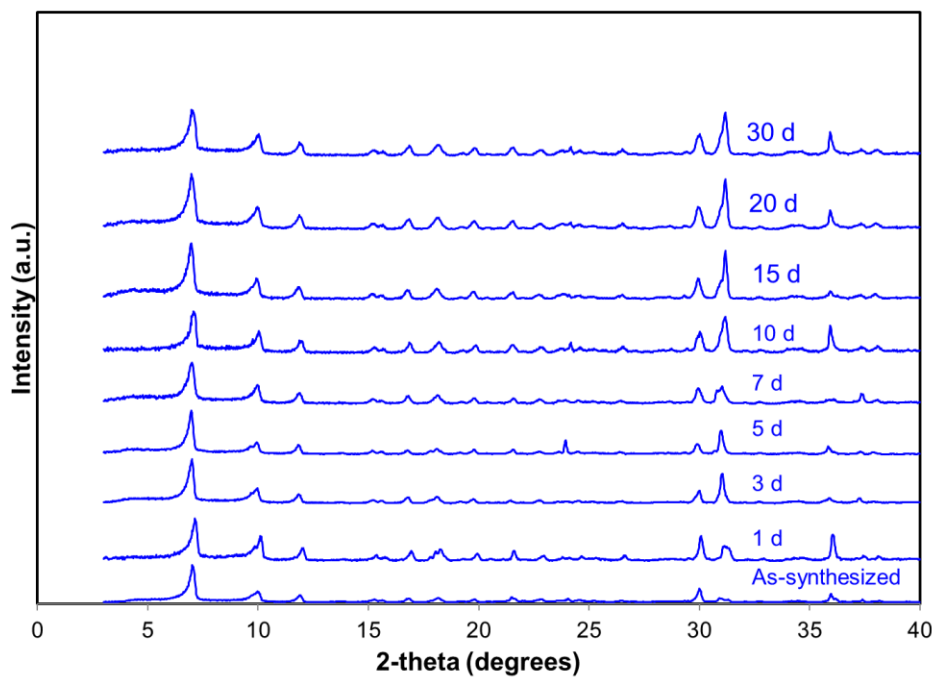
Figure C-27: PXRD of **MIL-125-NHMe** in MeCN, 0.15M TEOA, at rt. Days denoted on right increasing vertically.
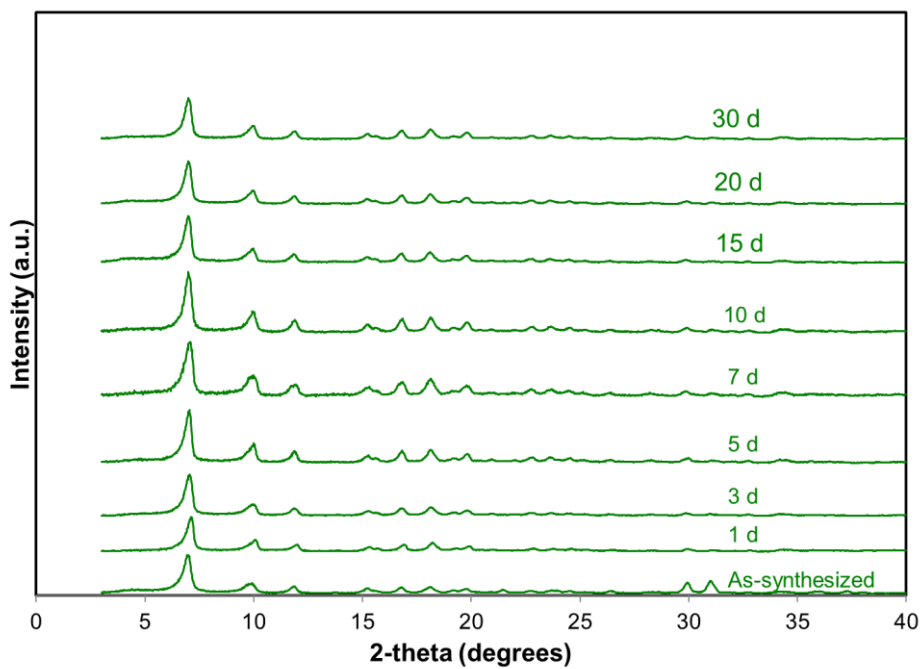
Figure C-28: PXRD of **MIL-125-NHCyp** in MeCN, 0.15M TEOA, at rt. Days denoted on right increasing vertically.

Figure C-29: PXRD of **MIL-125-NH$_2$** in MeCN, 0.15M AcOH, at rt. Days denoted on right increasing vertically.
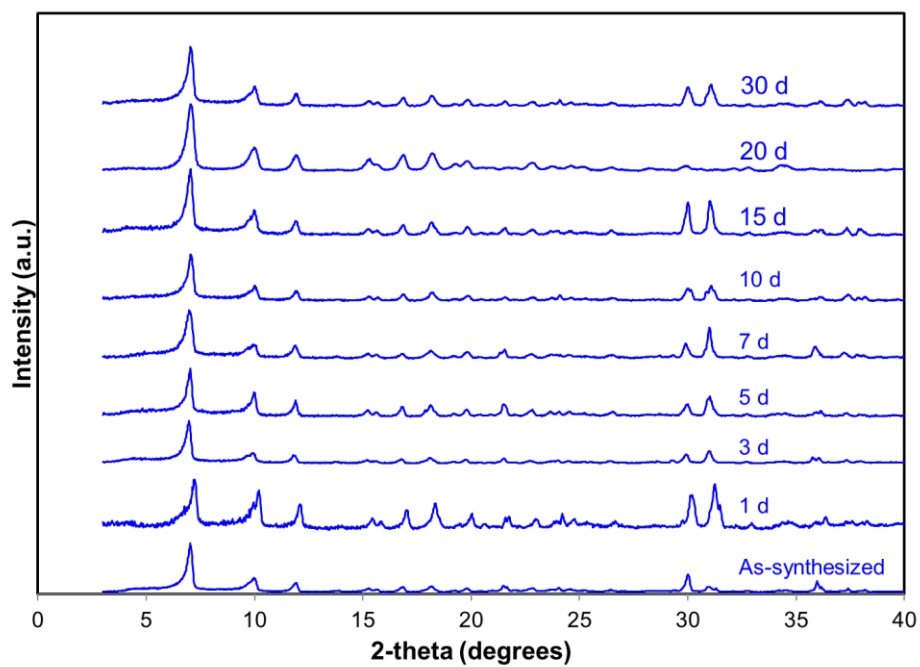
Figure C-30: PXRD of **MIL-125-NHMe** in MeCN, 0.15M AcOH, at rt. Days denoted on right increasing vertically.
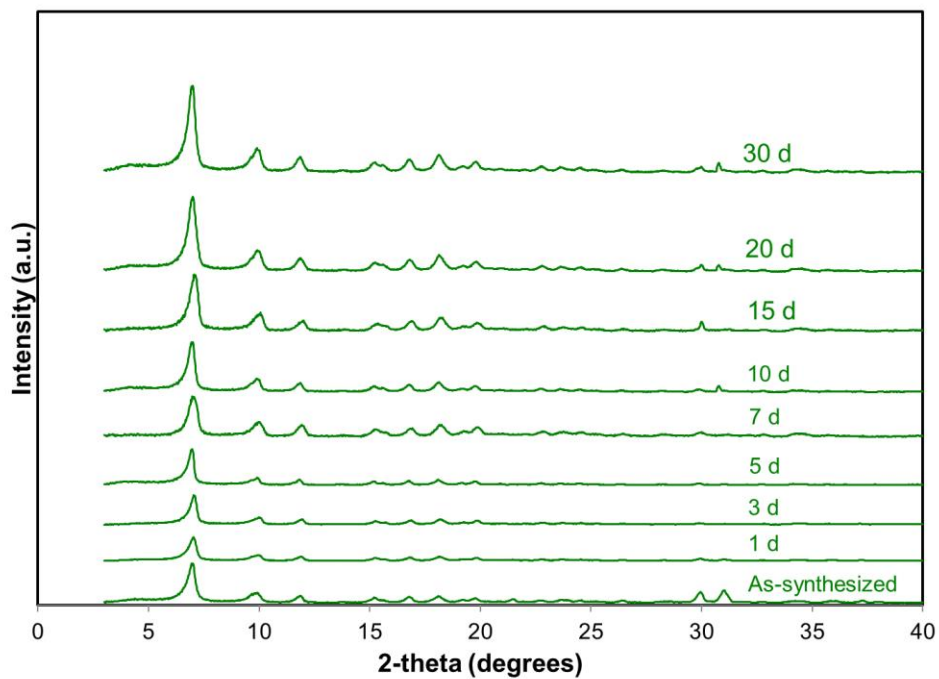
Figure C-31: PXRD of **MIL-125-NHCyp** in MeCN, 0.15M AcOH, at rt. Days denoted on right increasing vertically.
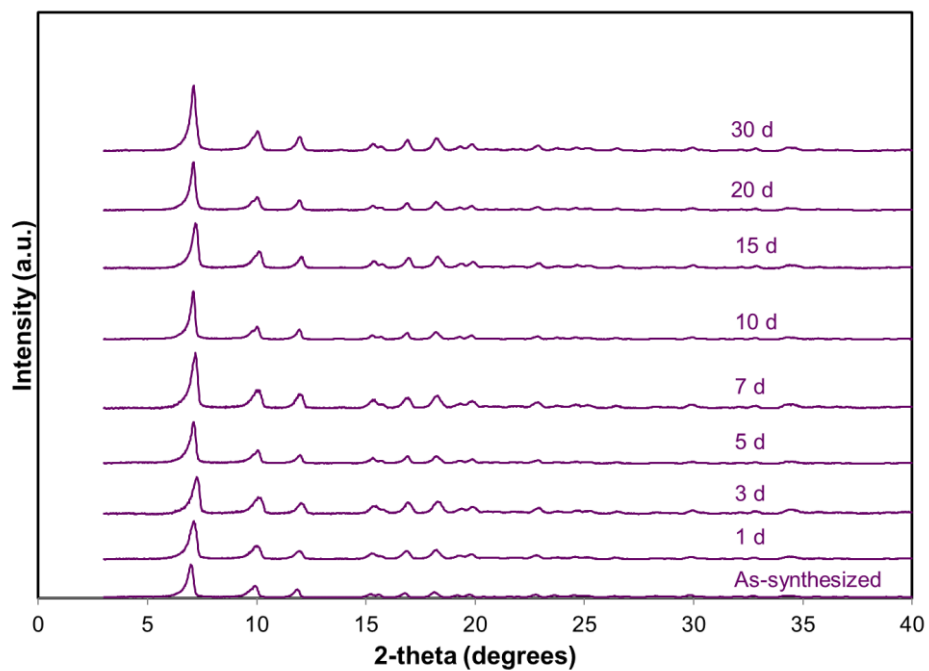
Figure C-32: PXRD of **MIL-125-NH₂** in wet MeCN, 0.15M TEOA, at rt. Days denoted on right increasing vertically.
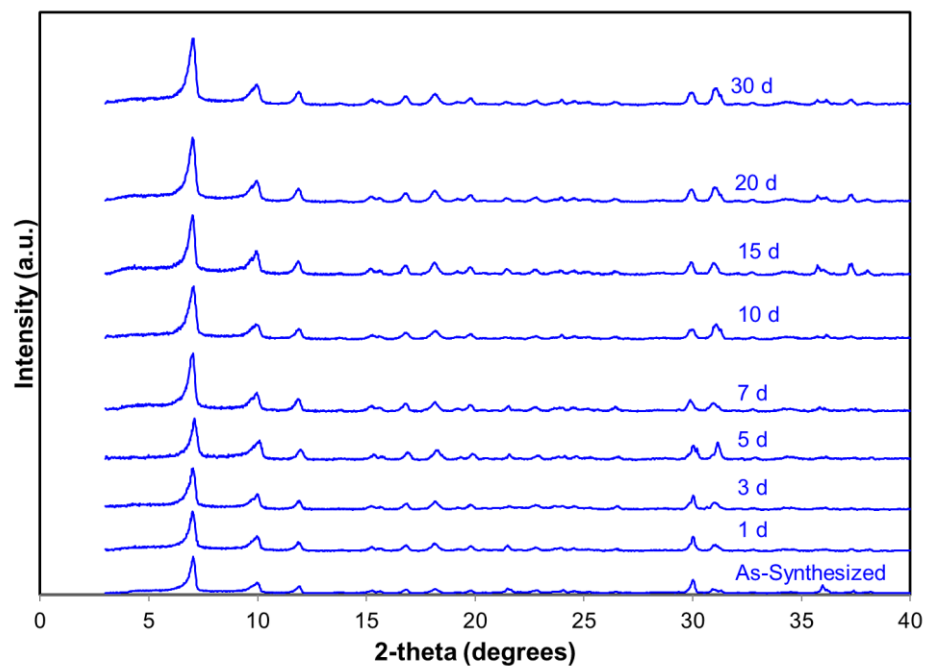
Figure C-33: PXRD of **MIL-125-NHMe** in wet MeCN, 0.15M TEOA, at rt. Days denoted on right increasing vertically.
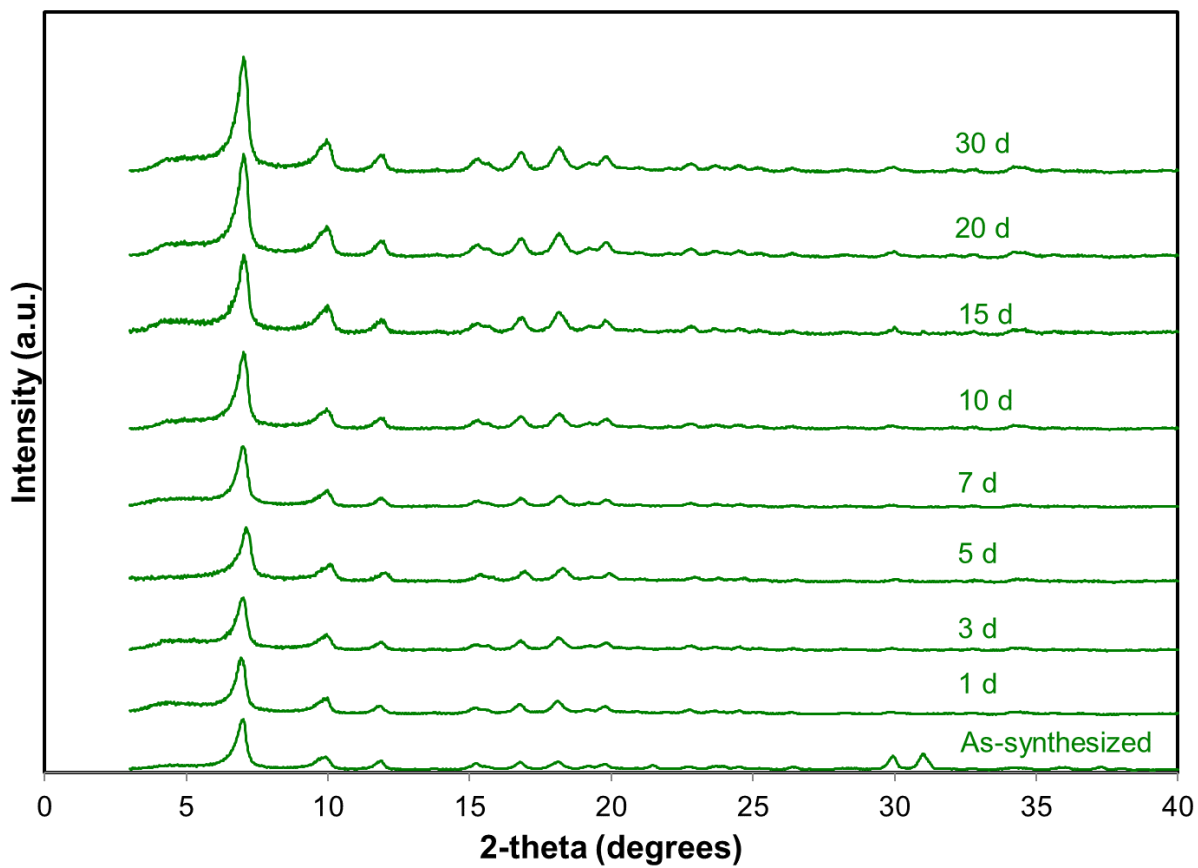
Figure C-34: PXRD of **MIL-125-NHCyp** in wet MeCN, 0.15M TEOA, at rt. Days denoted on right increasing vertically.
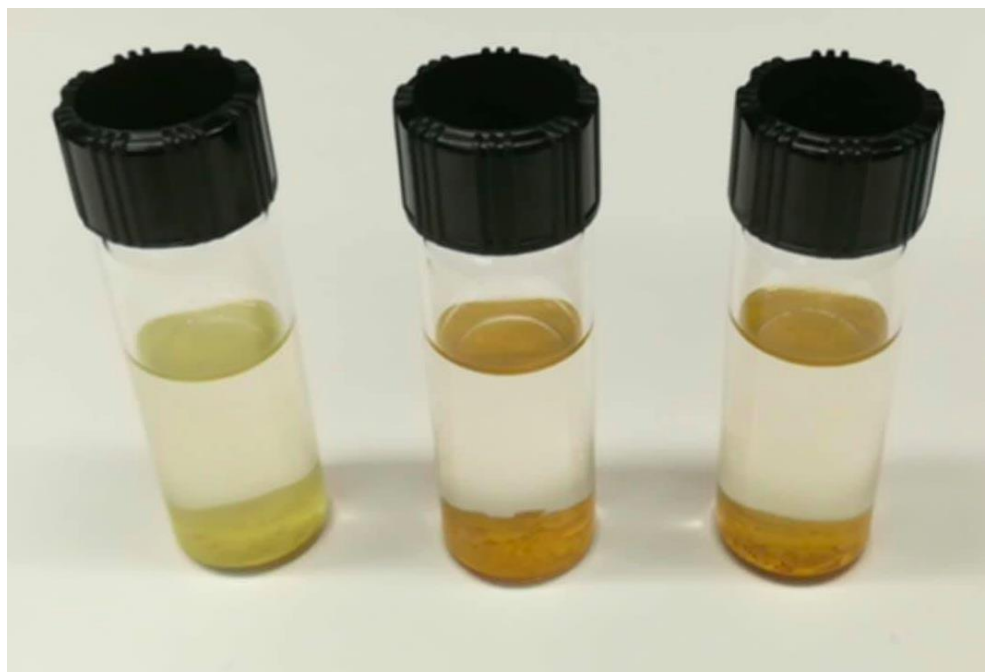
Figure C-35: Day-1 exposure in neutral DI water of **MIL-125-NH$_2$**, **MIL-125-NHMe**, and **MIL-125-NHCyp** (from left to right).
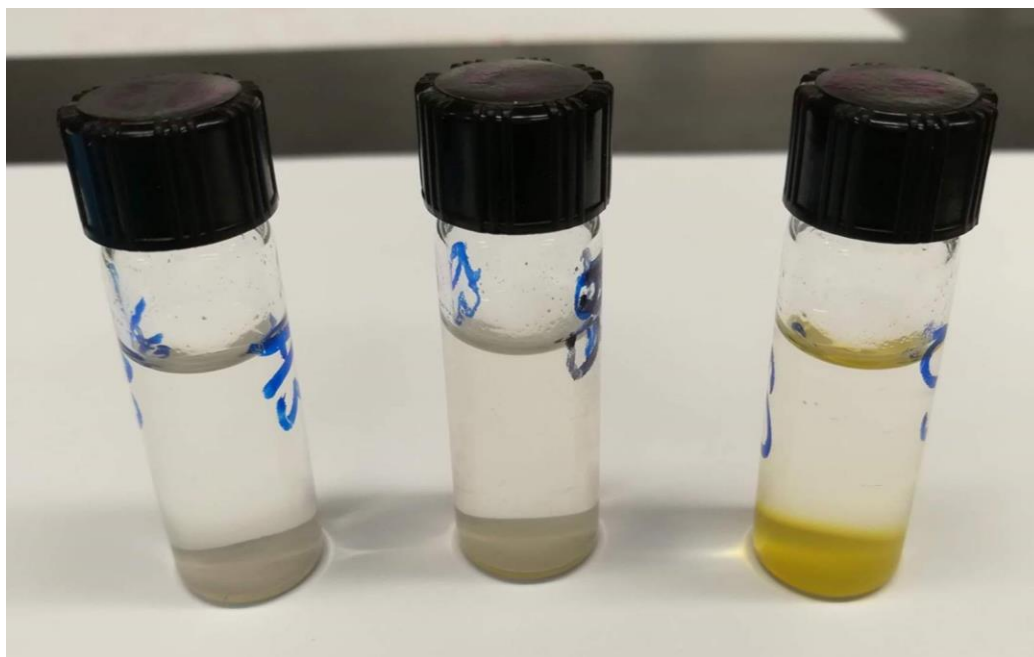
Figure C-36: 10-day exposure in neutral DI water at 70 ºC of **MIL-125-NH$_2$**, **MIL-125-NHMe**, and **MIL-125-NHCyp** (from left to right).

C.2 <u>Gas Adsorption</u>
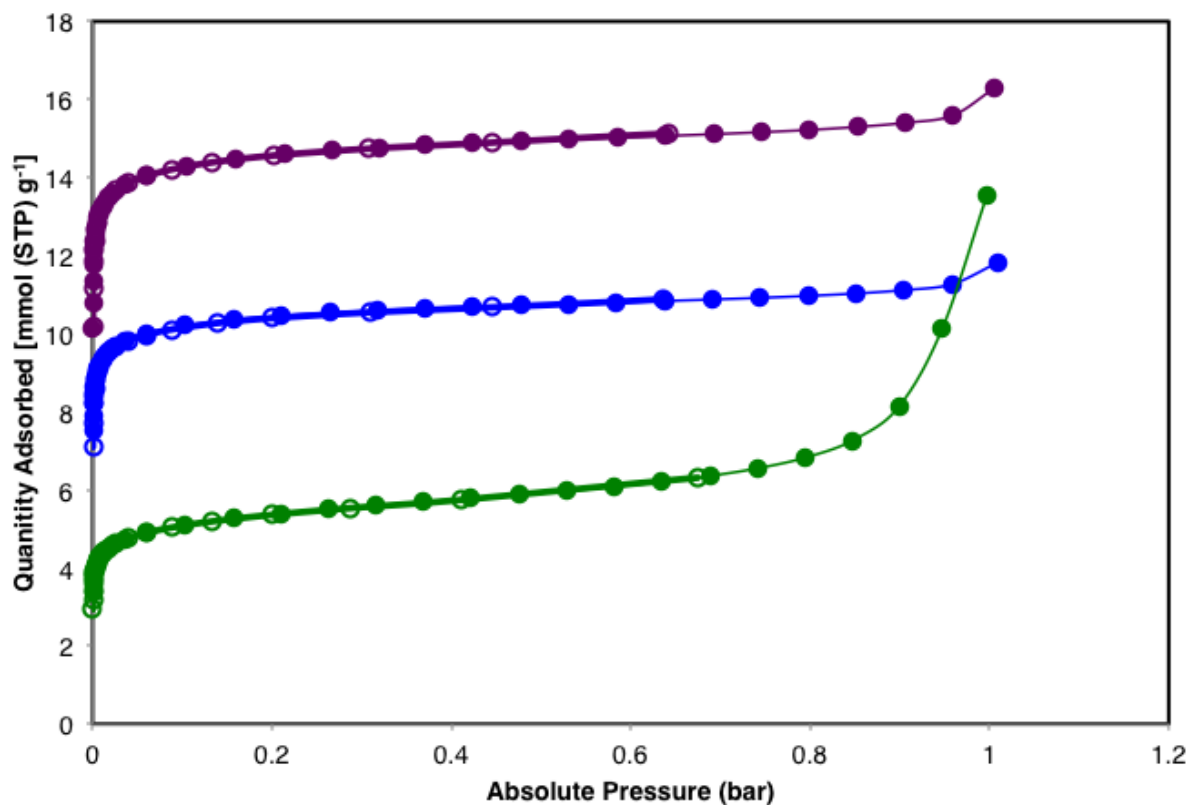
Figure C-37: N$_2$ gas (77 K) adsorption/desorption isotherm for **MIL-125-NH$_2$**, **MIL-125-NHMe**, and **MIL-125-NHCyp** shown in green, blue, and purple, respectively. Closed symbols represent adsorption, open symbols, desorption.
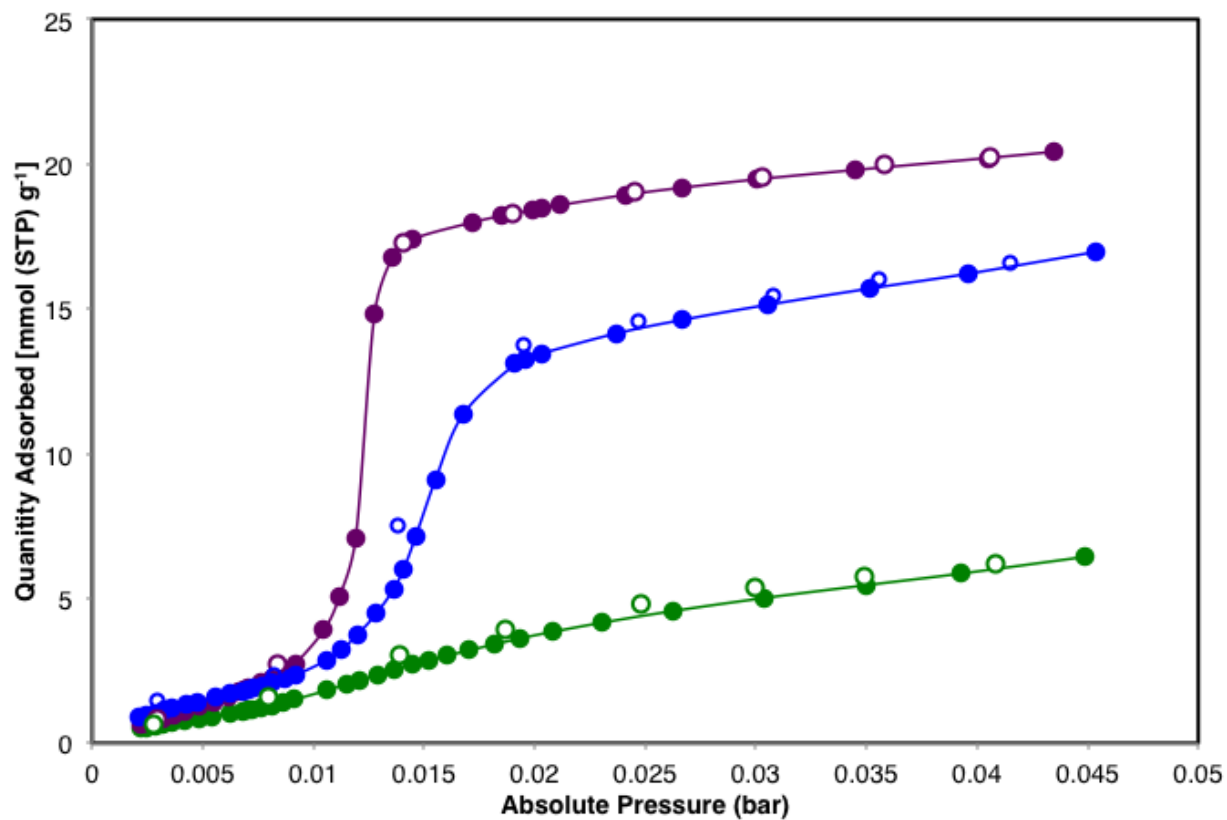
Figure C-38: H$_2$O vapor (308 K) adsorption/desorption isotherm for **MIL-125-NH$_2$**, **MIL-125-NHMe**, and **MIL-125-NHCyp** shown in green, blue, and purple, respectively. Closed symbols represent adsorption, open symbols, desorption.

C.3 <u>Density Functional Theory</u>

Table C-1: Calculated (calc) and experimental value (exp) of pKa of carboxylic acids used in this work.

Molecule	pKa (calc)	pKa (exp[a])
HCOOH	3.60	3.75
CH_3COOH	4.78	4.76
C_6H_5COOH	4.23	4.20
p-$NH_2C_6H_4COOH$	5.03	4.87
Terephthalic acid	3.54, 4.43 [b]	3.54, 4.43[b]
2-amino-terephtalate (–H)	3.87, 4.77 [b]	NA
2-amino-terephtalate (–Me)	3.89, 4.62 [b]	NA
2-amino-terephtalate (–Cyp)	3.88, 4.79 [b]	NA

[a] Experimental values are taken from Ref. 36

[b] The values are for pKa_1 and pKa_2, respectively.

APPENDIX D: **SUPPLEMENTARY MATERIAL FOR CHAPTER 5**

D.1 <u>Pawley Refinement</u>

Table D- 1: Refined crystallographic parameters of synthesized MOFs.

UCFMOF-	2	3-Me$_2$	4-Me$_4$
Formula	C$_{14}$H$_8$O$_7$Ti$_2$	C$_{22}$H$_{14}$O$_7$Ti$_2$	C$_{30}$H$_{32}$O$_7$Ti$_2$
Crystal system	Hexagonal	Hexagonal	Hexagonal
Space group	*P6$_3$/mmc*	*P6$_3$/mmc*	*P6$_3$/mmc*
a (Å)	18.70799 ± 0.09210	22.78755 ± 0.00591	27.17015 ± 0.07251
c (Å)	11.37619 ± 0.00130	11.46098 ± 0.00674	11.53154 ± 0.3056
M$_{20}$	15.39	34.09	75.27
Number of reflections	442	675	908
R$_p$	0.1635	0.0732	0.0565
R$_{wp}$	0.2581	0.1032	0.0964
R$_{wp}$ (w/o background)	0.3983	0.1528	0.1348

D.2 <u>Thermogravimetric Analysis (TGA)</u>
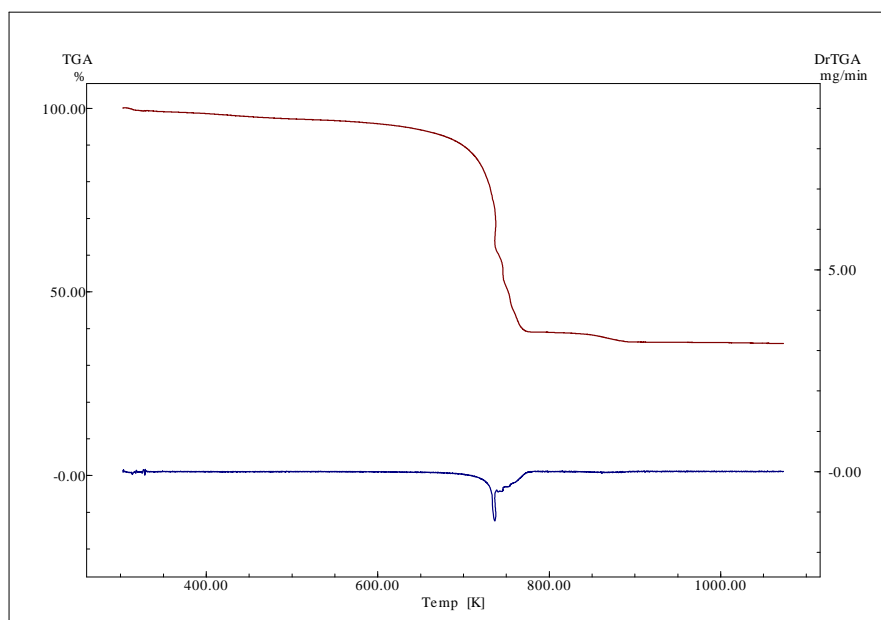
Figure D- 1: TGA and 1ST derivate curve of **UCFMOF-2.**
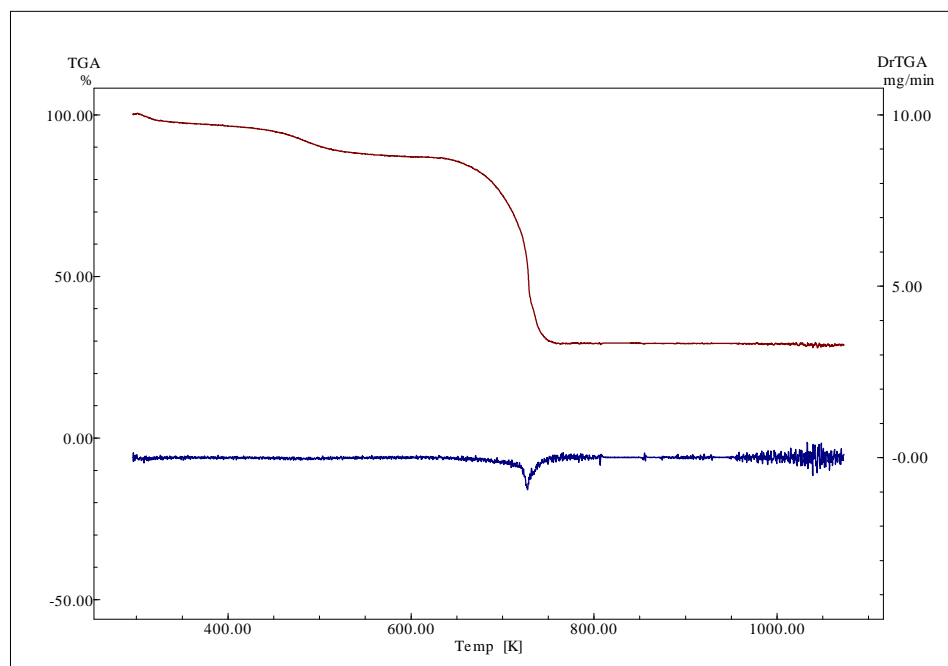
Figure D- 2: TGA and 1st derivate curve of **UCFMOF-3-Me$_2$**.
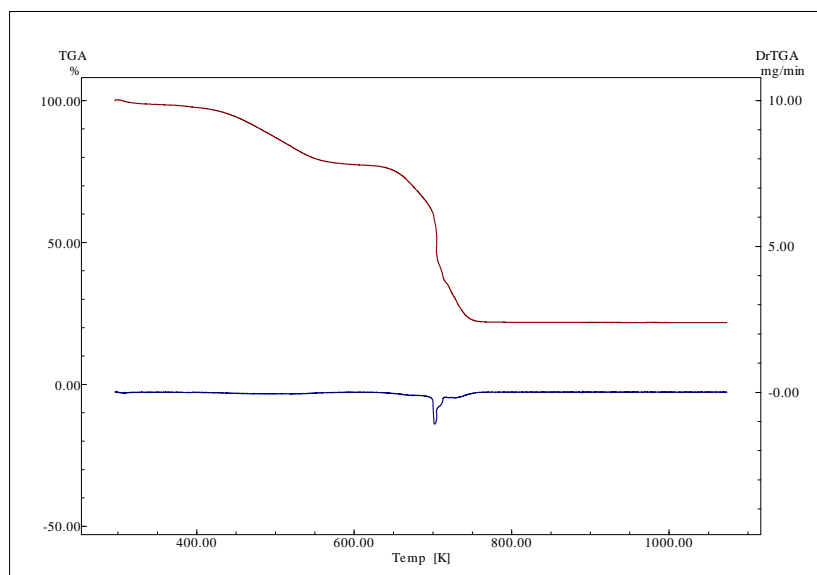
Figure D- 3: TGA and 1st derivate curve of **UCFMOF-4-Me₄.**

D.3 <u>Calculated Surface Areas</u>
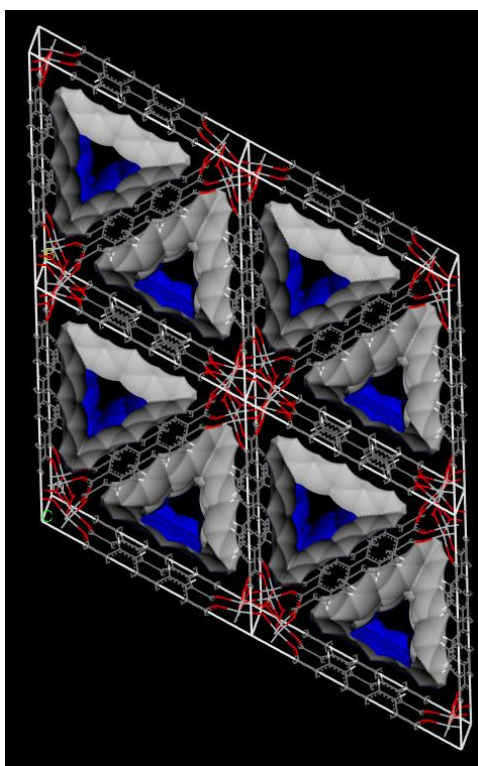
Figure D- 4: Connolly calculated accessible solvent surface area available for **UCFMOF-2.**
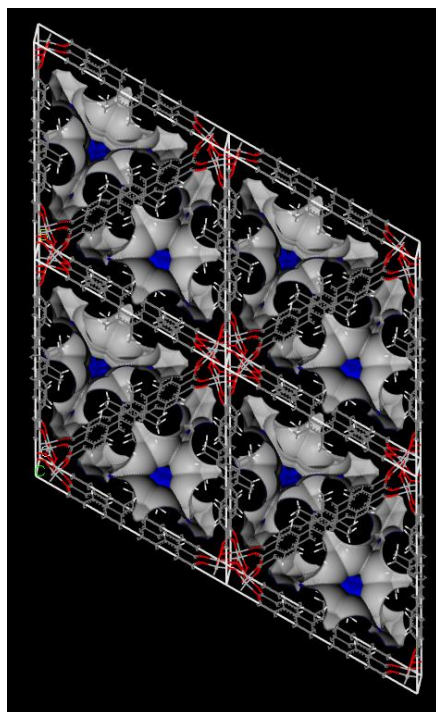
Figure D- 5: Connolly calculated accessible solvent surface area available for **UCFMOF-3-Me₃.**
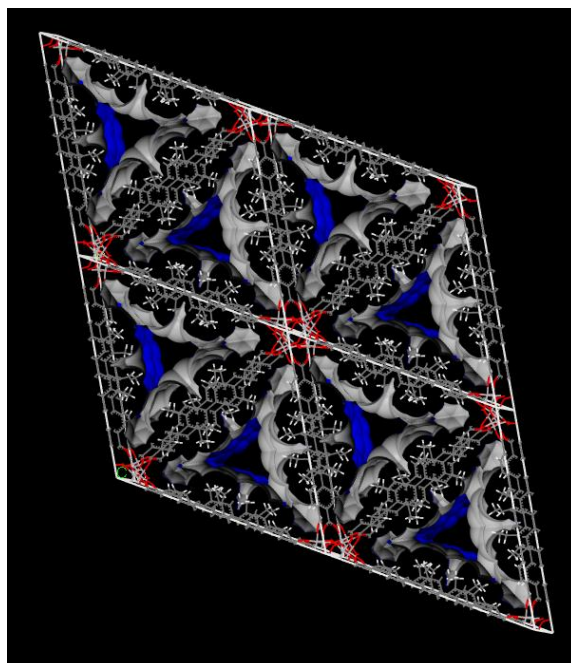
Figure D- 6: Connolly calculated accessible solvent surface area available for **UCFMOF-4-Me₃.**

Table D- 2: Connolly surface area calculations for UCFMOF family.

UCFMOF-	2	3-Me$_2$	4-Me$_4$
Crystal Volume (Å^3)	3448	5154.025	7372.285
Crystal Density (g cm^{-3})	1.1096	0.9397	0.8113
Accessible Solvent Free Volume per Unit Cell (Å^3)	576.97	438.00	1054.98
Accessible Solvent Surface per Unit Cell (Å^2)	603.33	911.41	1254.52
Connolly SA (m^2 g^{-1})	1577	1882	2098

D.4 <u>Gas Adsorption Analysis</u>
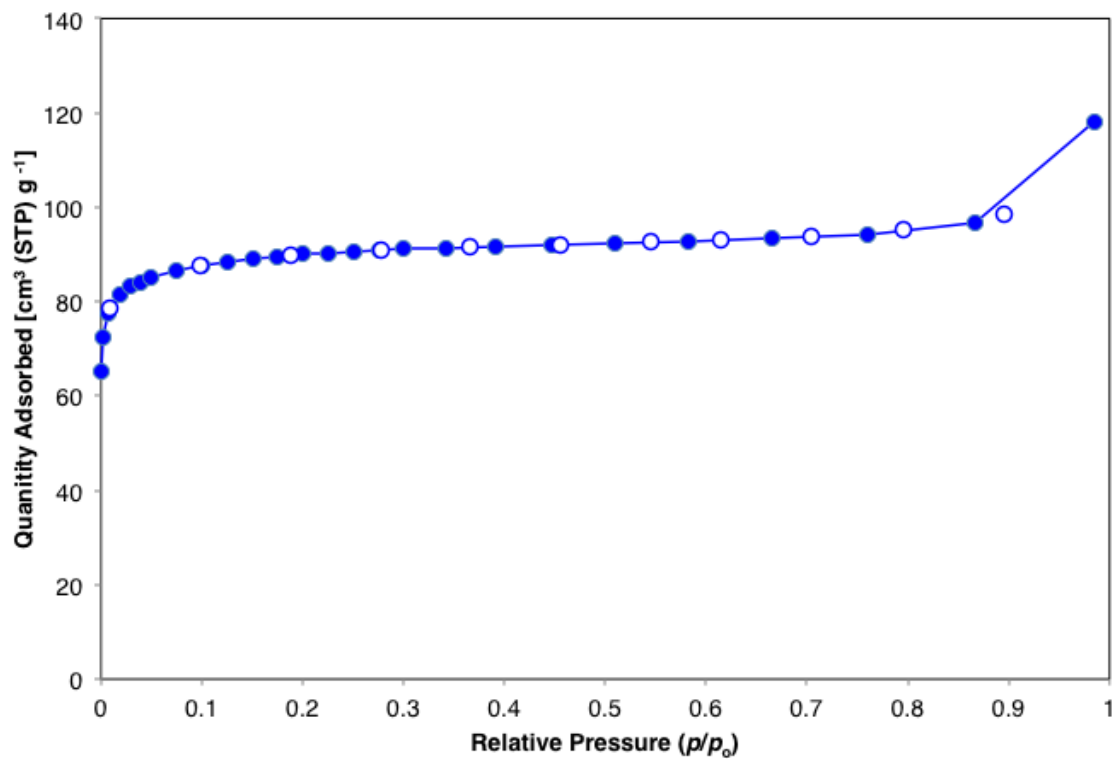
Figure D- 7: Nitrogen Gas adsorption isotherm (77 K) of **UCFMOF-2.**
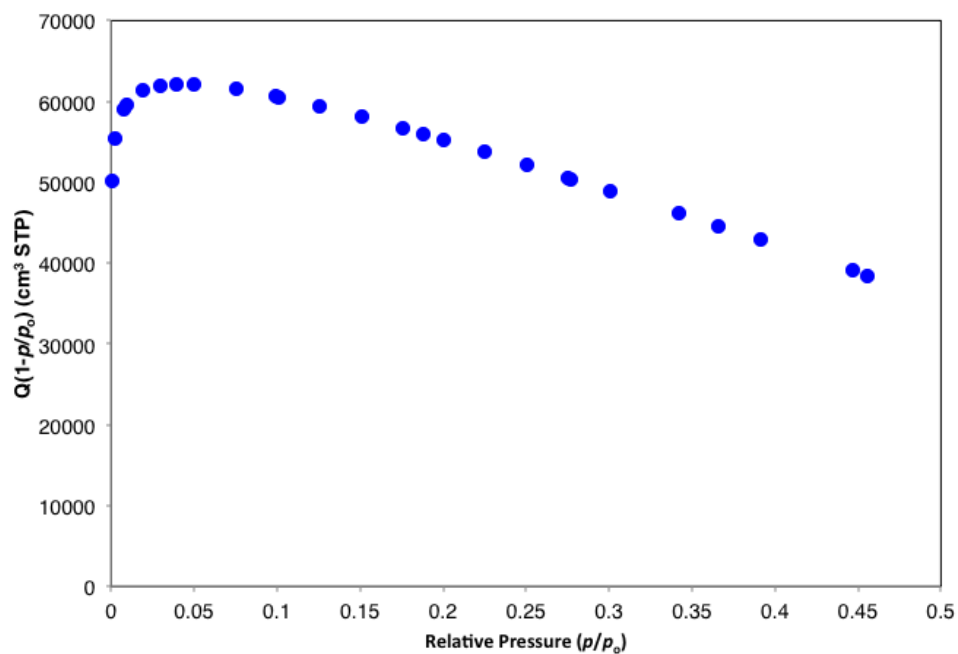
Figure D- 8: Rouquerol plot **UCFMOF-2.**
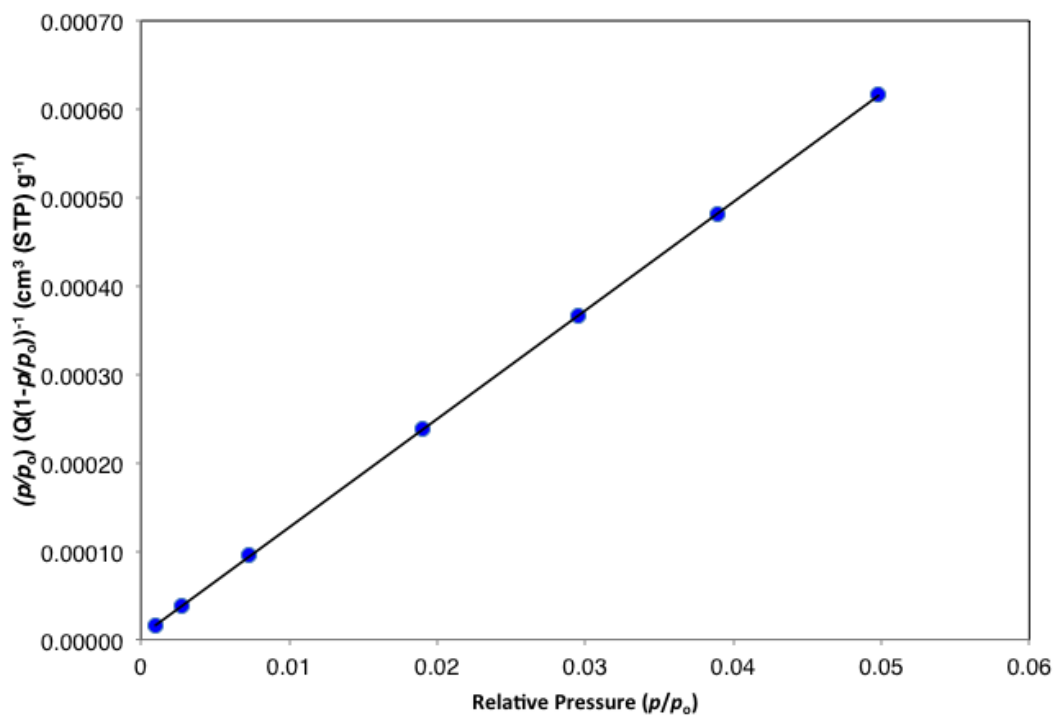
Figure D- 9: Linear BET plot **UCFMOF-2.**
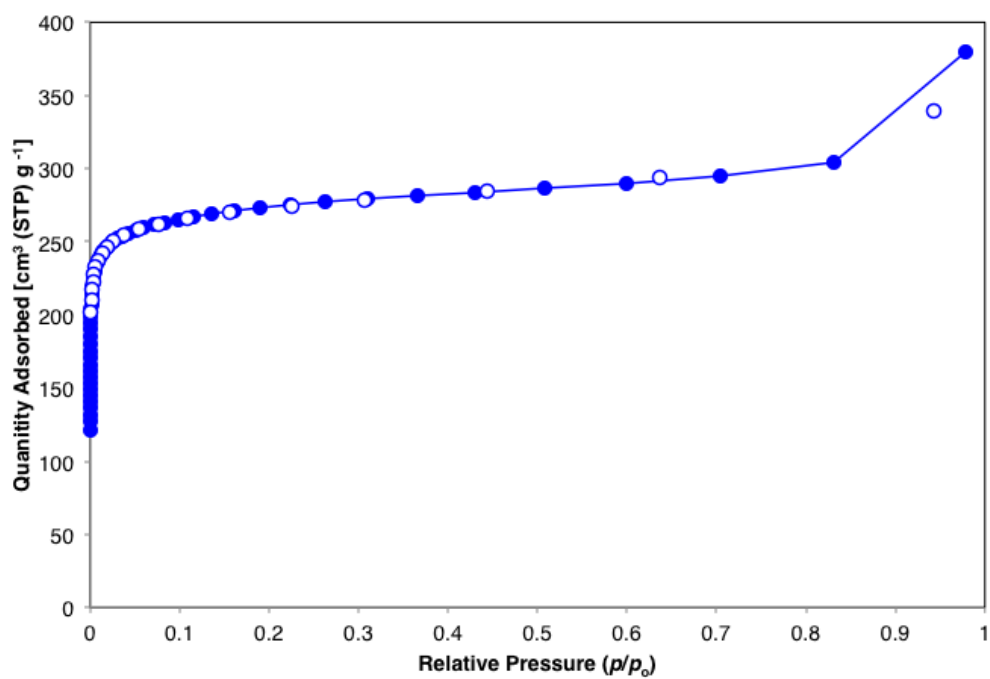
Figure D- 10: PXRD Nitrogen Gas adsorption isotherm (77 K) of **UCFMOF-3-Me₂.**
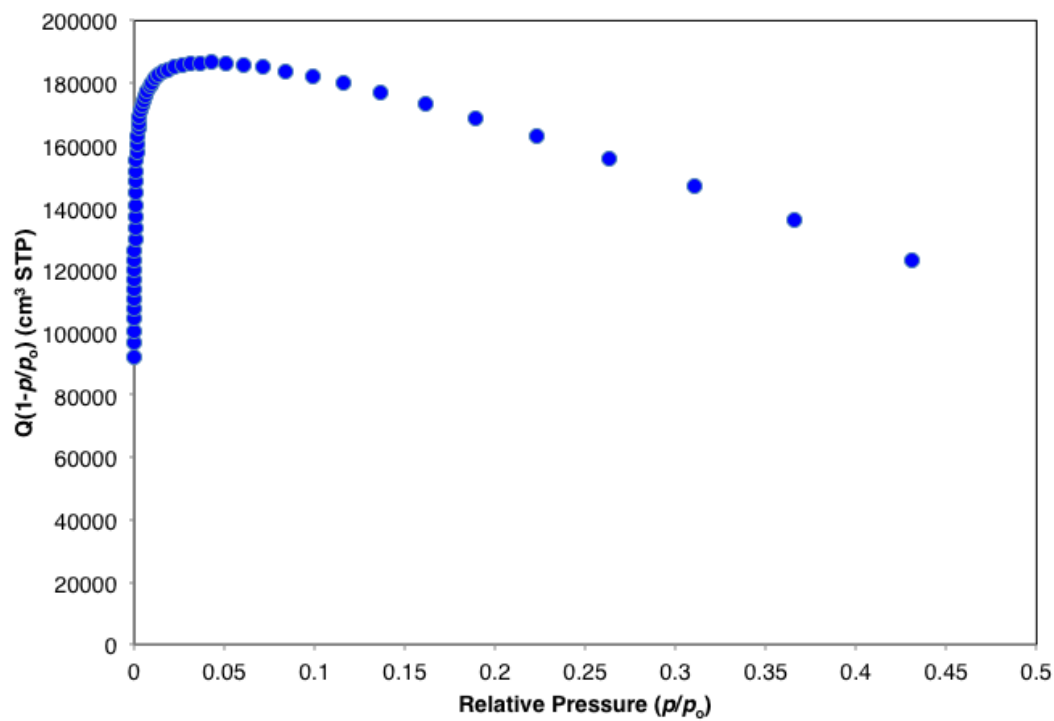
Figure D- 11: Rouquerol plot **UCFMOF-3-Me₂.**

338
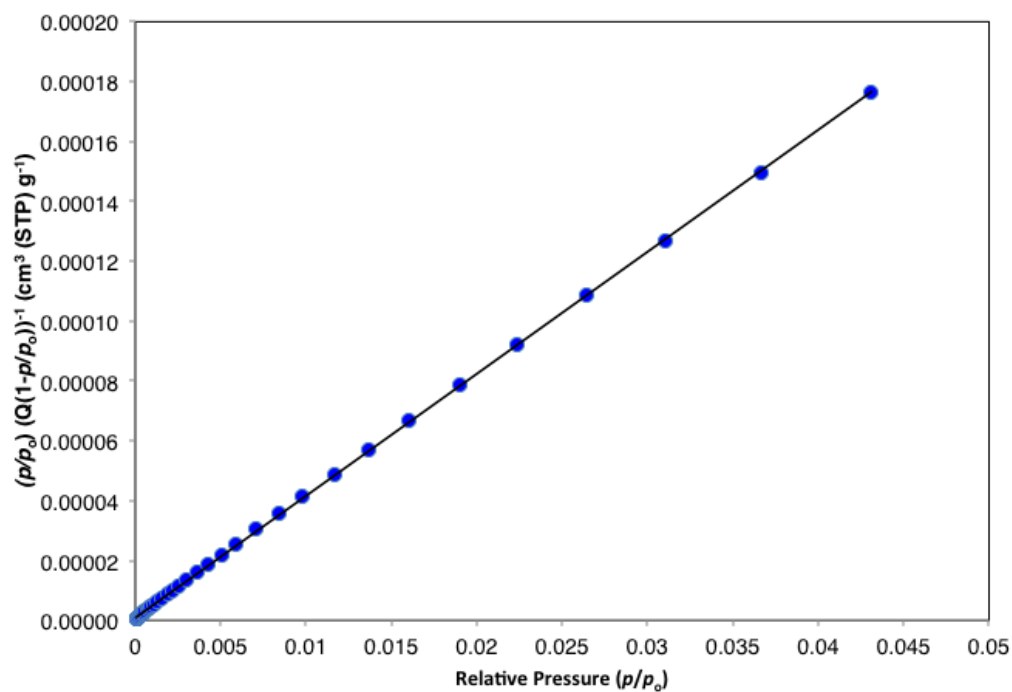
Figure D- 12: Linear BET plot **UCFMOF-3-Me₂.**
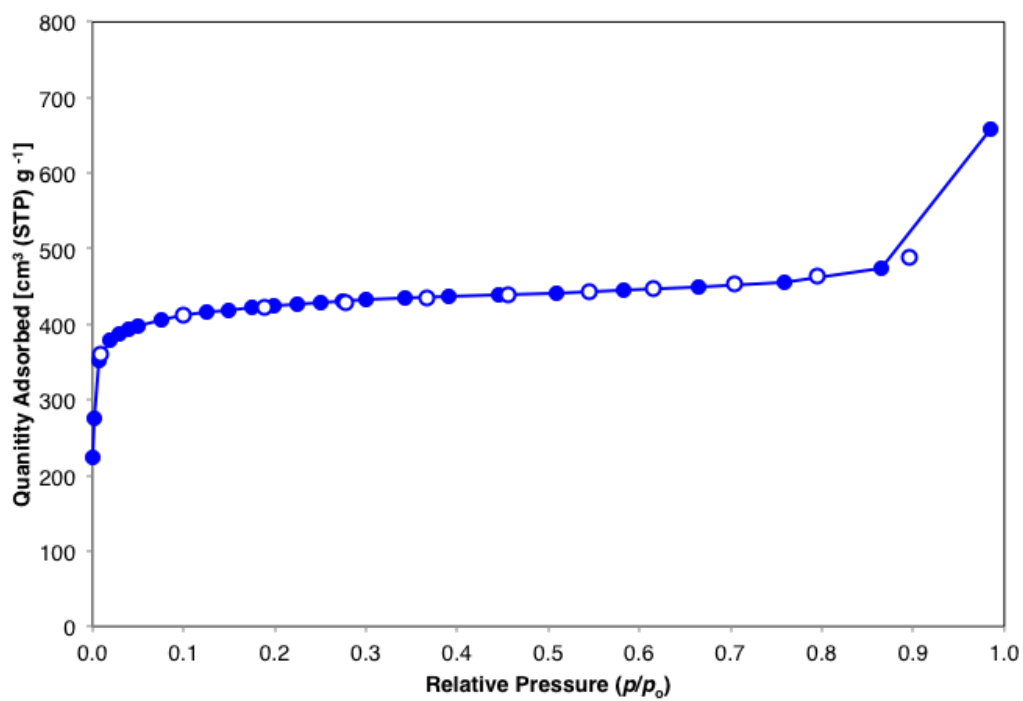
Figure D- 13: PXRD Nitrogen Gas adsorption isotherm (77 K) of **UCFMOF-4-Me₄.**
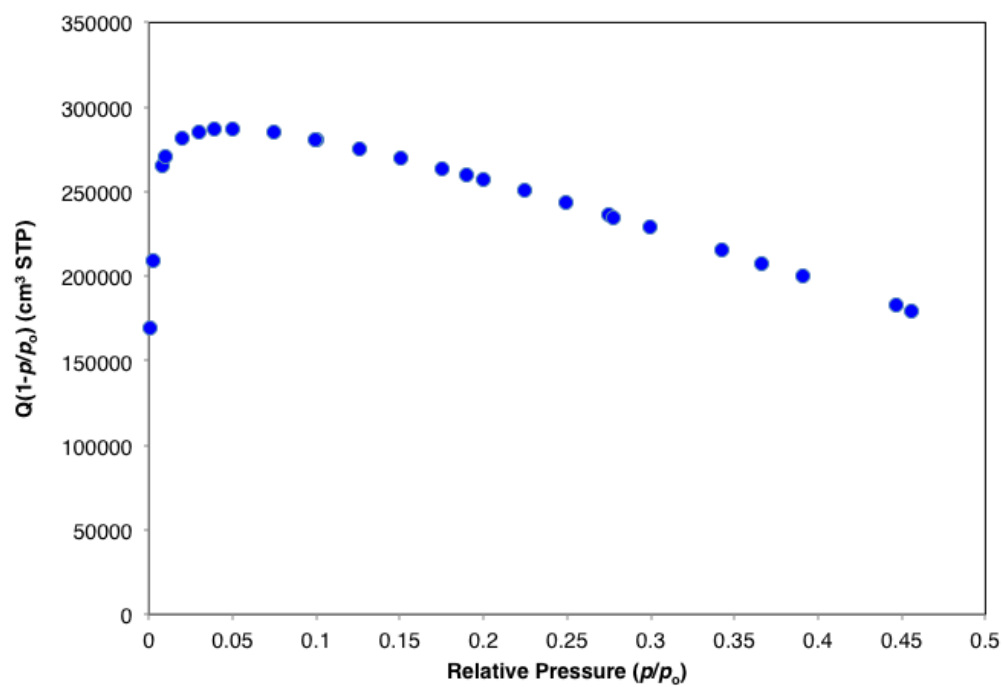
Figure D- 14: Rouquerol plot **UCFMOF-4-Me₄.**
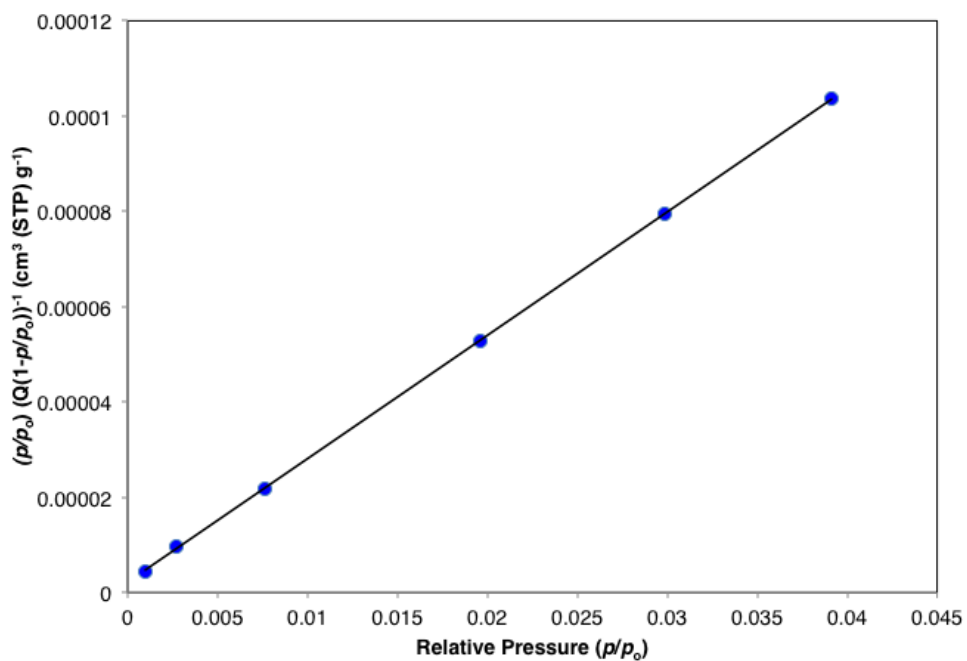
Figure D- 15: Linear BET plot **UCFMOF-4-Me₄.**

Table D- 3: Determination of BET surface area of UCFMOF series.

UCFMOF-	2	3-Me$_2$	4-Me$_4$
BET slope	1.227E-02	4.077E-03	2.589E-03
$\sigma_{BET\ slope}$	1.986E-05	6.311E-06	9.999E-06
BET intercept	4.153E-06	8.697E-07	2.223E-06
$\sigma_{BET\ intercept}$	5.461E-07	8.032E-08	2.188E-07
V_m (cm^3(STP) g^{-1})	81.47	245.24	385.88
σ_{Vm}	0.14	0.38	1.52
S_BET (m^2 g^{-1})	354.4	1066.8	1678.6
σ_{S_BET}	0.6	1.7	6.6
C_BET	2956	4688	1166
σ_{C_BET}	389	433	115

D.5 <u>Fourier-Transform Infrared (FT-IR) Spectroscopy</u>
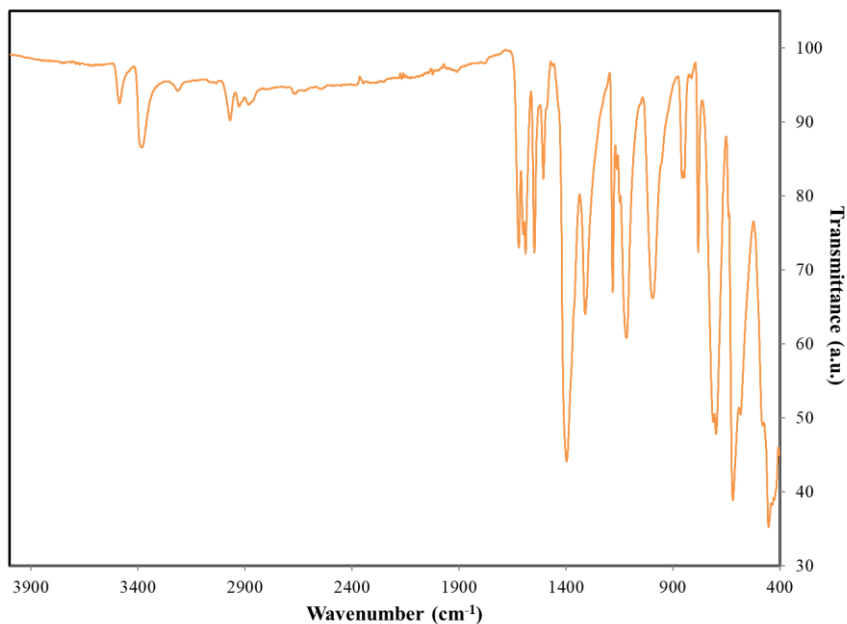
Figure D- 16: FT-IR spectra of compound [Ti$_6$O$_6$(O^{i}Pr)$_6$(abz)$_6$] cluster.
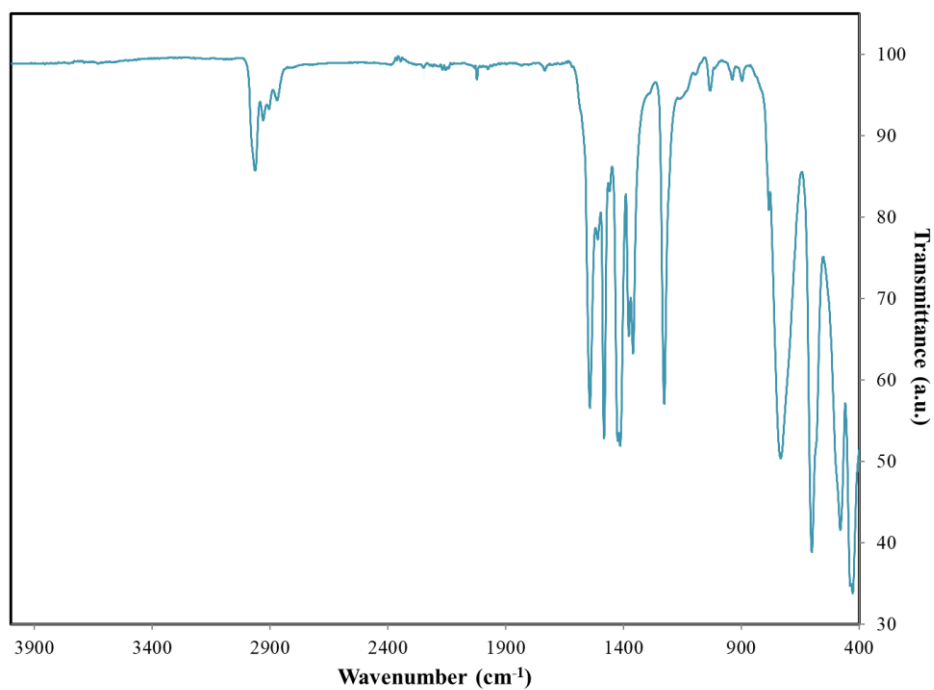
Figure D- 17: FT-IR spectra of compound [Ti$_8$O$_8$(O$_2$C$_2$(CH$_3$)$_3$)$_{16}$] cluster.
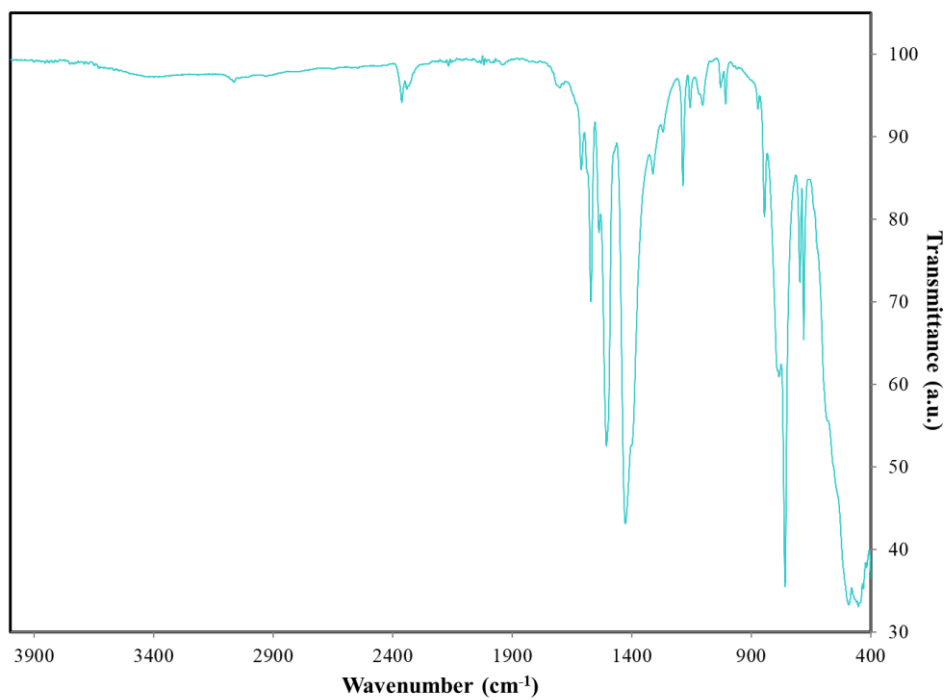
Figure D- 18: FT-IR spectra of compound MIL-125-NH$_2$ cluster.
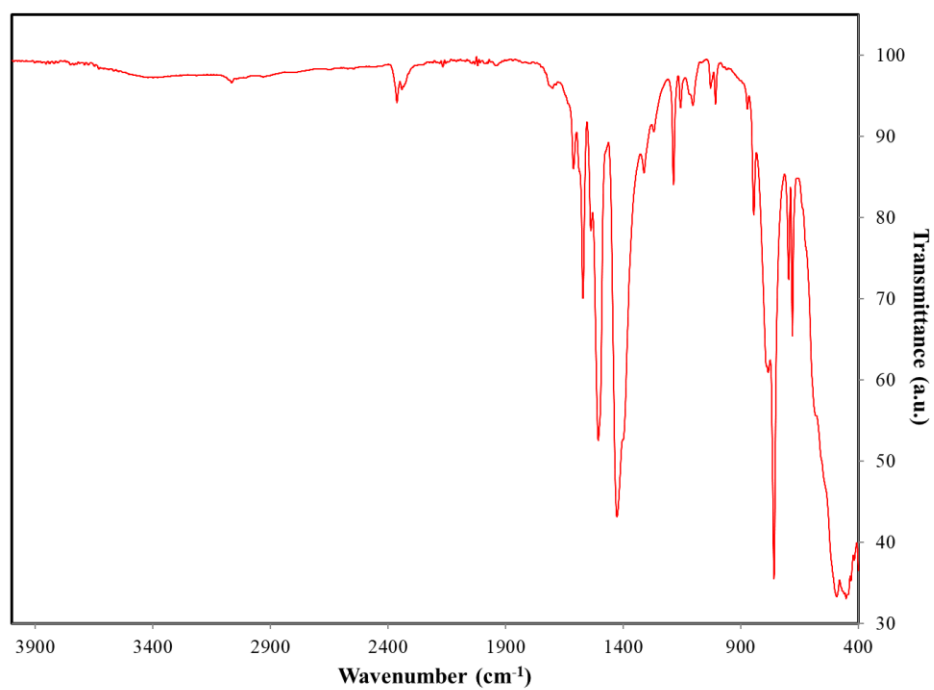
Figure D- 19: FT-IR spectra of compound **UCFMOF-2** cluster.
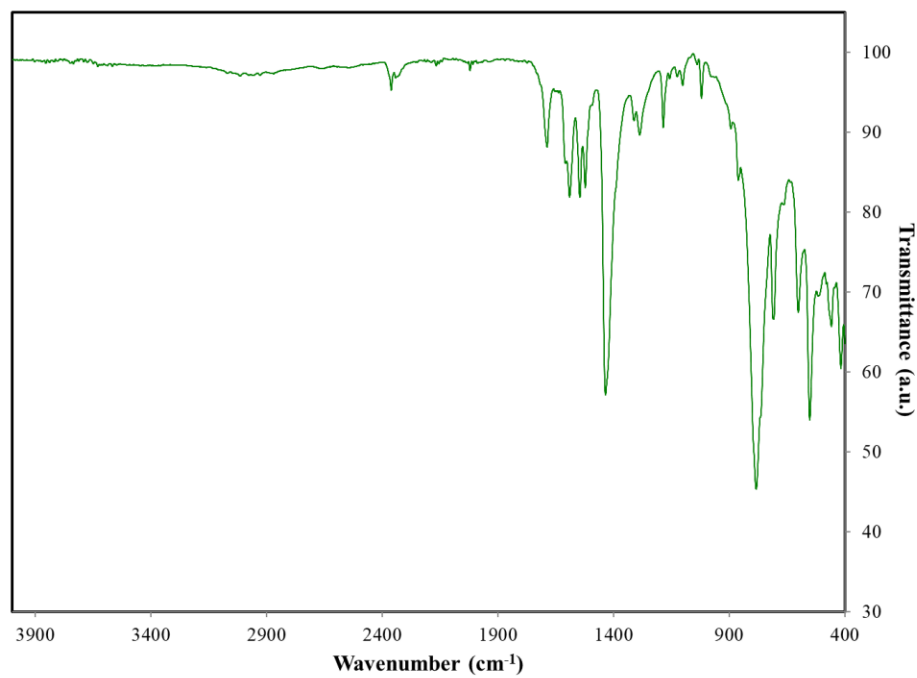
Figure D- 20: FT-IR spectra of compound **UCFMOF-3-Me₂** cluster.
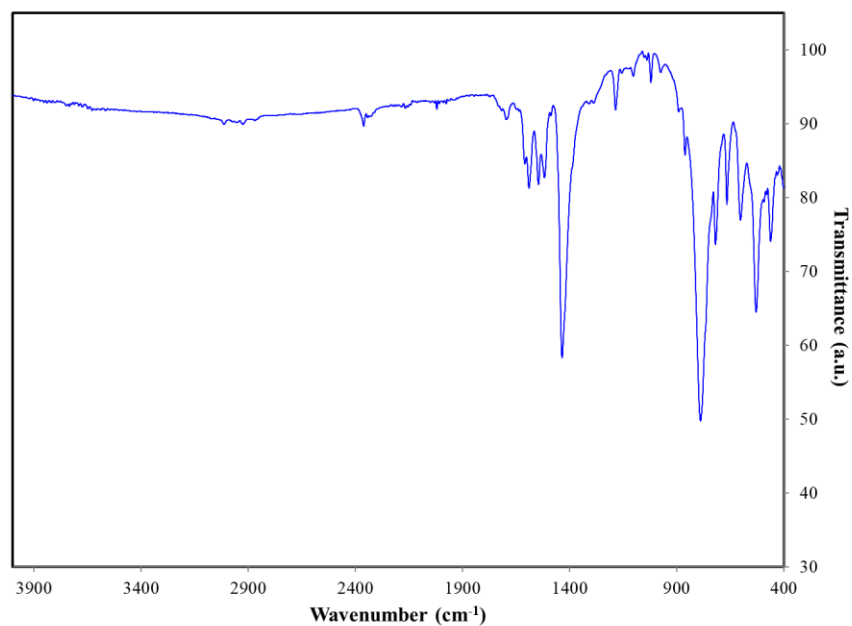
Figure D- 21: FT-IR spectra of compound **UCFMOF-4-Me₄** cluster.

D.6 Nuclear Magnetic Resonance (NMR) Spectroscopy
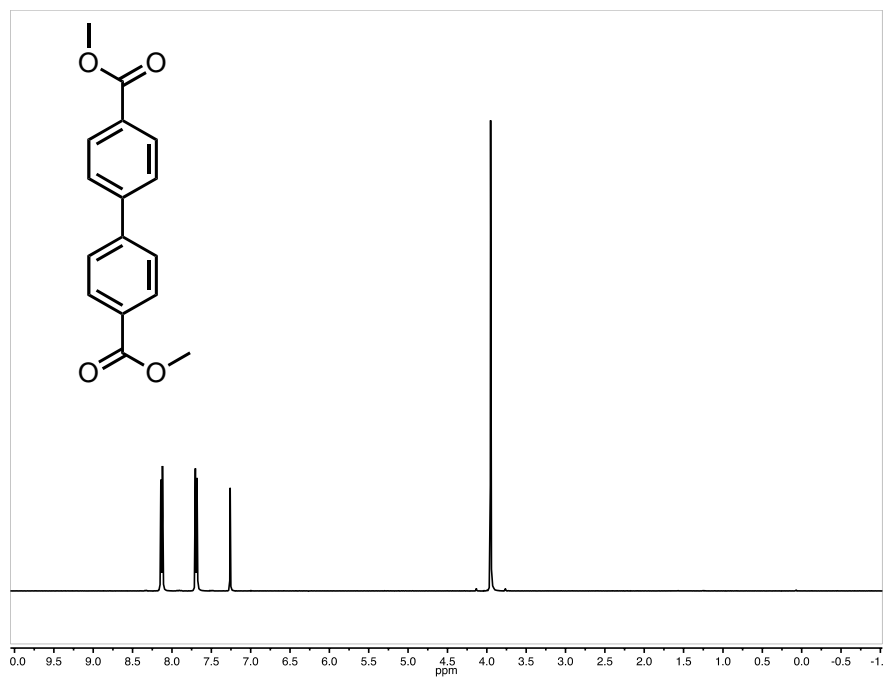
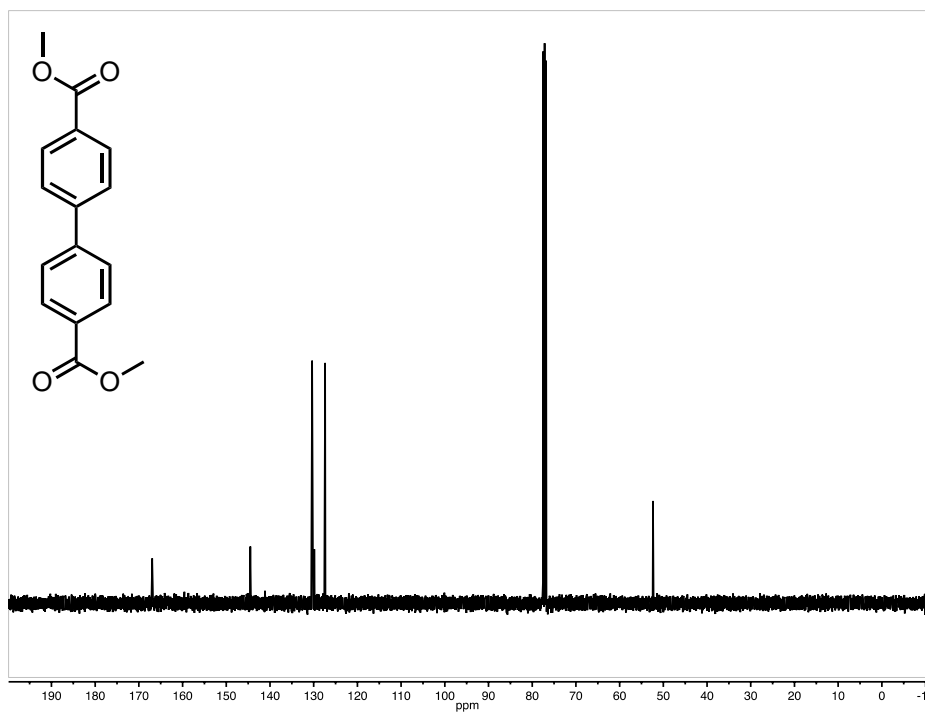Figure D- 22: ₁H NMR spectra (400 MHz, CDCl^3, 25 ºC) of compound **S2**.

Figure D- 23: ^{13}C NMR spectra (100 MHz, CDCl$_3$, 25 ℃) of compound **S2**.
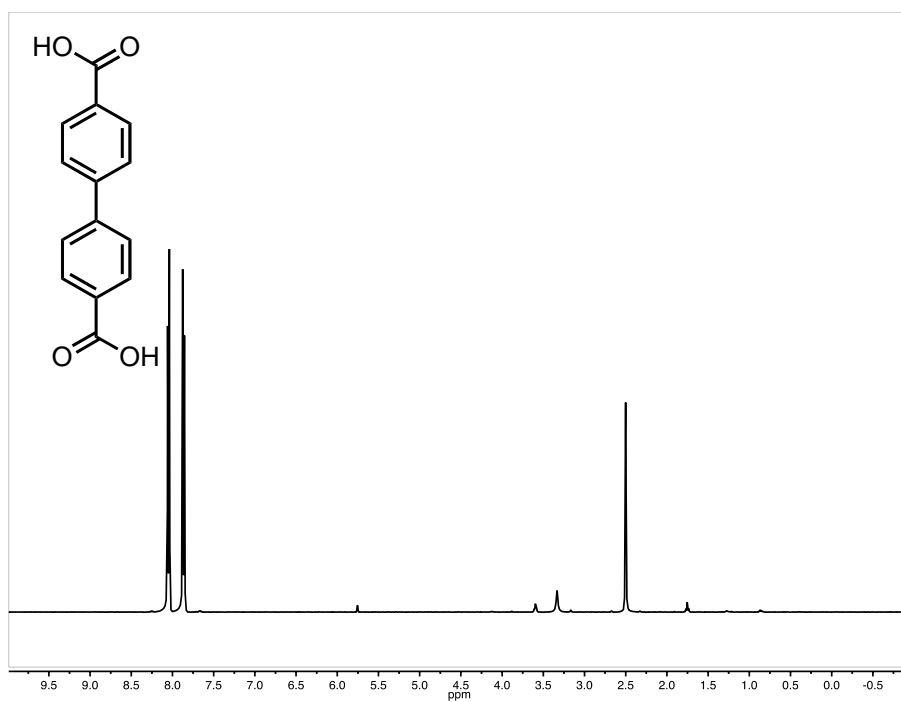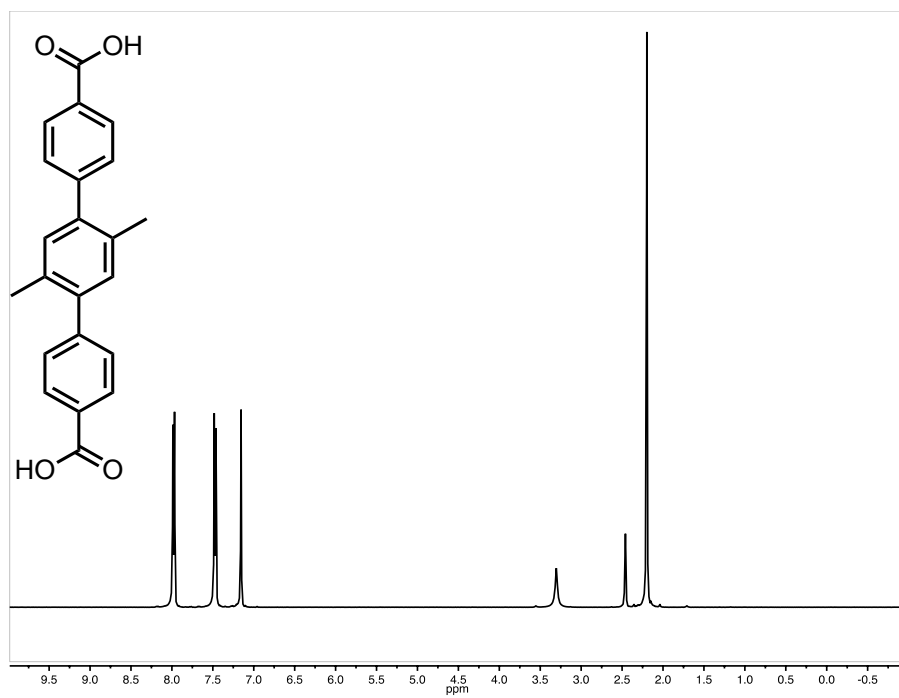

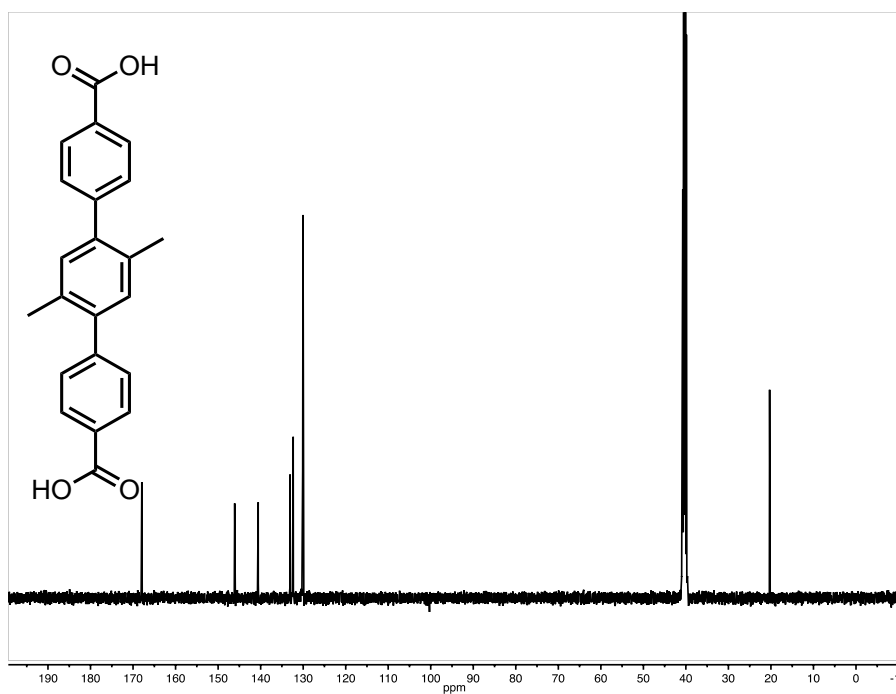Figure D- 24: ^{1}H NMR spectra (400 MHz, DMSO-d6, 25 ℃) of compound **2**.
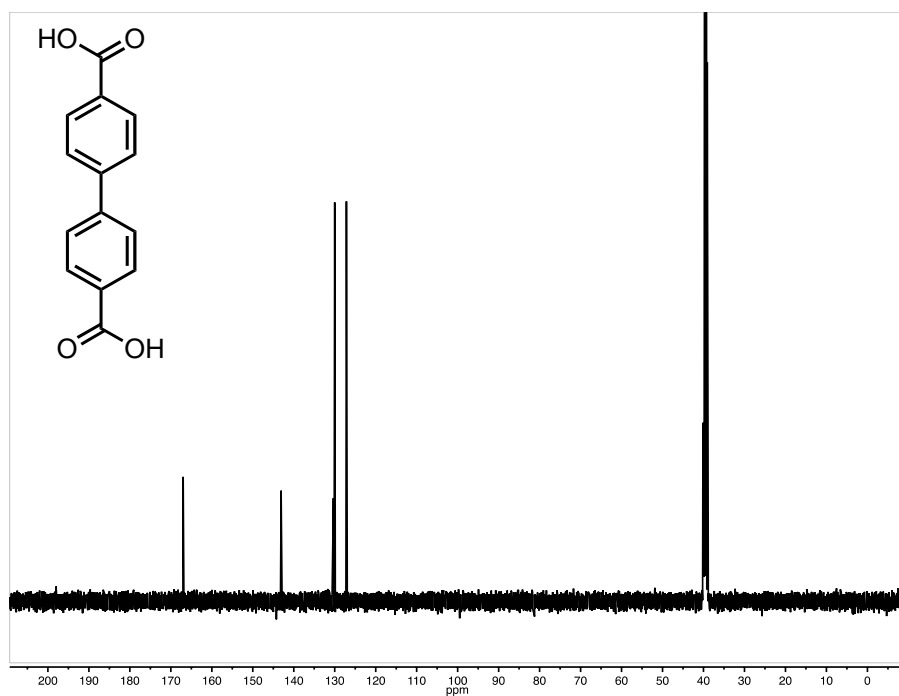
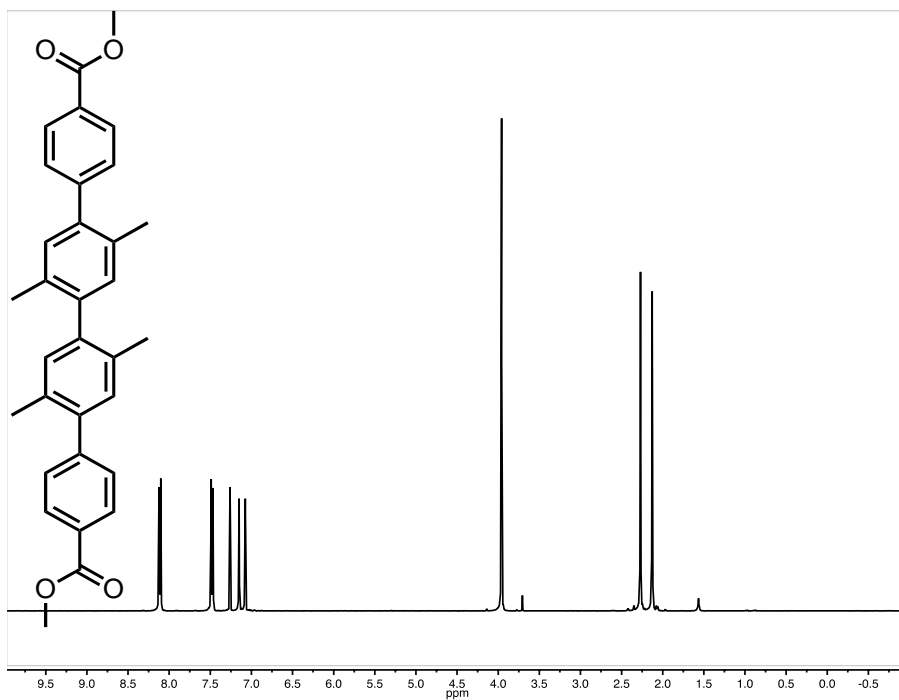Figure D- 25: ^{13}C NMR spectra (100 MHz, DMSO-d6, 25 ºC) of compound **2**.
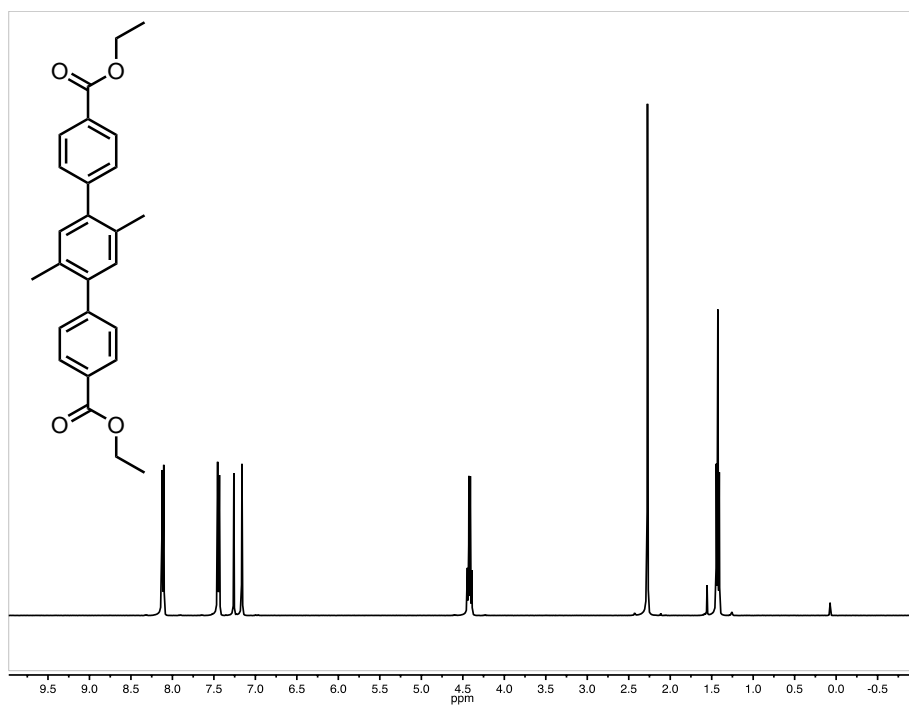
Figure D- 26: ^{1}H NMR spectra (400 MHz, CDCl$_3$, 25 ºC) of compound **S3-Me$_2$**.
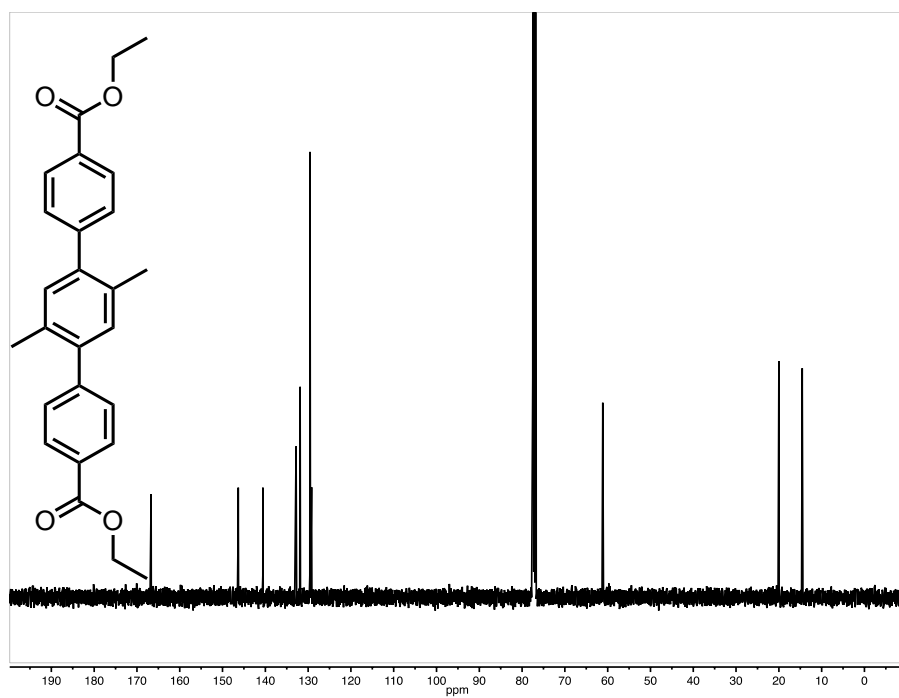
Figure D- 27: ^{13}C NMR spectra (100 MHz, CDCl$_3$, 25 ℃) of compound **S3-Me$_2$**.

Figure D- 28: ^{1}H NMR spectra (400 MHz, DMSO-d$_6$, 25 ℃) of compound **3-Me$_2$**.

347

Figure D- 29: ^{13}C NMR spectra (100 MHz, DMSO-d$_6$, 25 ℃) of compound **3-Me₂**.

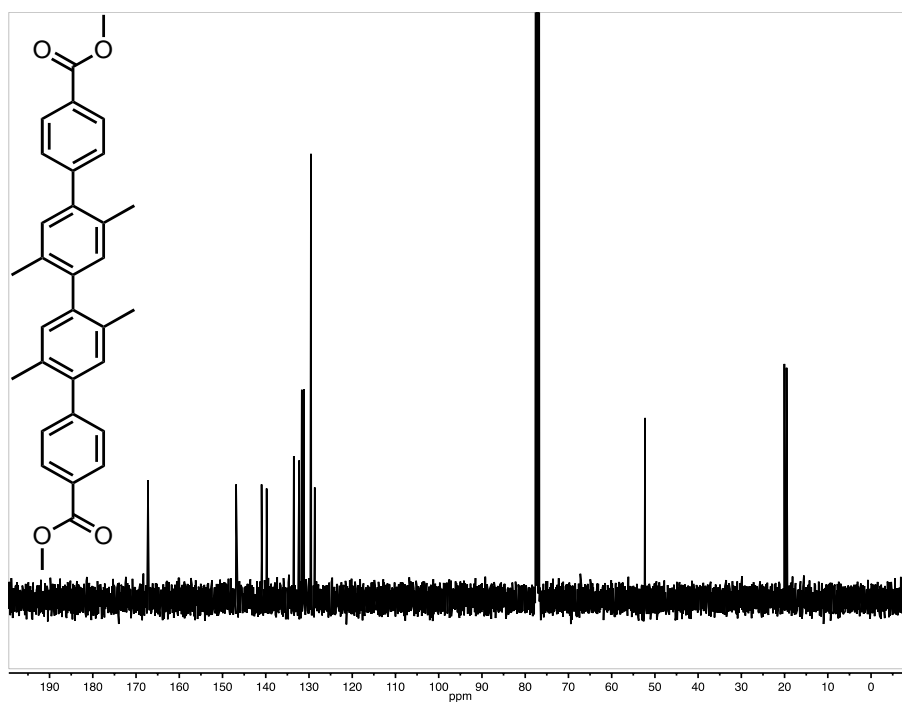Figure D- 30: ^{1}H NMR spectra (400 MHz, CDCl₃, 25 ℃) of compound **S4-Me₄**.

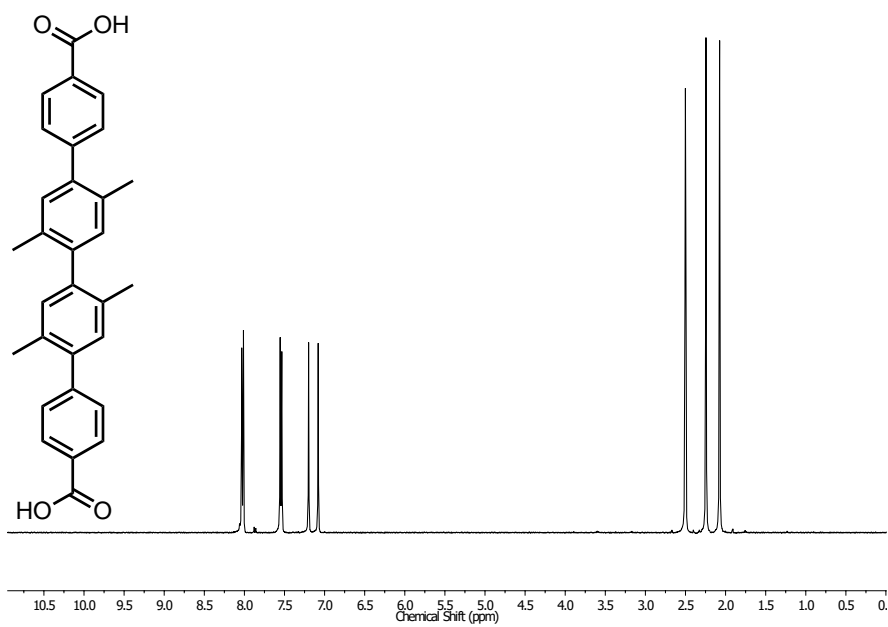Figure D- 31: ^{13}C NMR spectra (100 MHz, CDCl$_3$, 25 ºC) of compound **S4-Me$_4$**.

Figure D- 32: ^{1}H NMR spectra (400 MHz, DMSO-d$_6$, 25 ºC) of compound **4-Me$_4$**.
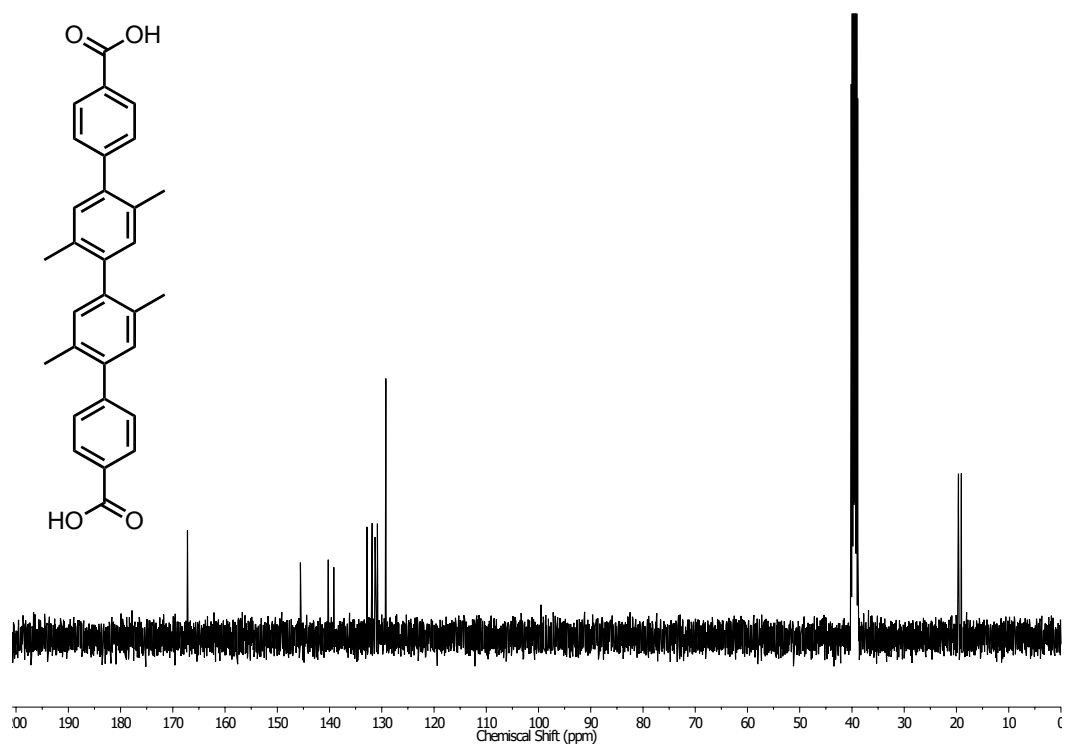
Figure D- 33: ^{13}C NMR spectra (100 MHz, DMSO-d$_6$, 25 ºC) of compound **4-Me$_4$.**